



HAL
open science

Plk1 mitotic phosphorylation in the N-terminal region of the BRCA2 protein: identification, characterization and role in protein interactions

Manon Julien

► **To cite this version:**

Manon Julien. Plk1 mitotic phosphorylation in the N-terminal region of the BRCA2 protein: identification, characterization and role in protein interactions. Structural Biology [q-bio.BM]. Université Paris-Saclay, 2021. English. NNT : 2021UPASQ011 . tel-03341485

HAL Id: tel-03341485

<https://theses.hal.science/tel-03341485v1>

Submitted on 10 Sep 2021

HAL is a multi-disciplinary open access archive for the deposit and dissemination of scientific research documents, whether they are published or not. The documents may come from teaching and research institutions in France or abroad, or from public or private research centers.

L'archive ouverte pluridisciplinaire **HAL**, est destinée au dépôt et à la diffusion de documents scientifiques de niveau recherche, publiés ou non, émanant des établissements d'enseignement et de recherche français ou étrangers, des laboratoires publics ou privés.

Phosphorylation mitotique de la région N-terminale de la protéine BRCA2 par la kinase Plk1 : identification, caractérisation et rôle dans les interactions protéine-protéine
Plk1 mitotic phosphorylation in the N-terminal region of the BRCA2 protein: identification, characterization and role in protein interactions

Thèse de doctorat de l'université Paris-Saclay

École doctorale n°569 : innovation thérapeutique : du fondamental à l'appliqué (ITFA)

Spécialité de doctorat: Biochimie et Biologie Structurale

Unité de recherche : Université Paris-Saclay, CEA, CNRS, Institute for Integrative Biology of the Cell (I2BC), 91198, Gif-sur-Yvette, France

Référent : Faculté de Pharmacie

**Thèse présentée et soutenue à Paris-Saclay,
le 12 mars 2021 par**

Manon JULIEN

Composition du Jury

Herman Van Tilbeurgh Professeur, Université Paris Saclay	Président
Isabelle Landrieu DR, CNRS, Université de Lille	Rapporteuse & Examinatrice
Malene Jensen DR, CNRS/CEA, Grenoble	Rapporteuse & Examinatrice
Mauro Modesti DR, INSERM, Marseille	Examineur

Direction de la thèse

Sophie Zinn-Justin DR, CEA Saclay	Directrice de thèse
François-Xavier Theillet CR, CNRS, CEA Saclay	Co-Directeur de thèse

French summary

Contexte scientifique

Le cancer du sein est le cancer le plus mortel chez les femmes, dans le monde, et la France est le 4^{ème} pays présentant l'incidence la plus élevée (Globocan). Afin de limiter le taux de mortalité lié à ce cancer dans la population générale, le « plan cancer » a été mis en place en France à partir de 2004. Il consiste en un dépistage gratuit proposé tous les 2 ans aux femmes âgées de 50 à 74 ans, les plus à risque. Cette stratégie permet d'identifier le cancer au stade le plus précoce afin d'augmenter l'efficacité du traitement thérapeutique. Ceci a déjà permis de réduire la mortalité du cancer du sein de 21% à 15% (Haute Autorité de Santé).

Cependant, 5 à 10% des cancers du sein sont attribués à un cancer héréditaire, c'est-à-dire qu'une mutation augmentant le risque de développer le cancer du sein est transmise à travers les générations. L'âge d'apparition des cancers du sein héréditaires est plus précoce (40 ans en moyenne). Les stratégies proposées par le « plan cancer » sont donc souvent inadaptées. Dans ce cas, la stratégie proposée consiste à identifier la mutation cancérogène transmise au sein d'une famille. Ceci permet ensuite de proposer un dépistage génétique ciblé à l'ensemble des membres de la famille et de proposer aux personnes à risque un suivi médical adapté.

Dans les années 1990, deux gènes ont été identifiés comme très fréquemment mutés dans les cancers du sein héréditaires : *BRCA1* et *BRCA2* (Hall et al. 1990 ; Wooster et al. 1994). Depuis, plusieurs bases de données répertorient les variations géniques (ou variants) observées sur ces gènes lors du séquençage de patientes atteintes de cancer du sein (Szabo et al. 2000, Caputo et al. 2012, <https://www.ncbi.nlm.nih.gov/clinvar/>). Ainsi, de longues listes de variations géniques de *BRCA1* et *BRCA2* sont disponibles. Cependant, tous les variants observés ne favorisent pas le développement du cancer. Les variants ont donc commencé à être classés soit comme variant causal (qui augmente le risque de cancer du sein), soit comme variant neutre (qui n'influence pas le risque de cancer) grâce à des études épidémiologiques et moléculaires (Plon et al. 2008, Guidugli et al. 2014). Cependant, de nombreux variants faux sens rares sont encore non classés.

Au cours de ma thèse, je me suis intéressée à la protéine BRCA2. Les variants classés de cette protéine, composée de 3 418 résidus, sont principalement localisés dans sa région repliée C-terminale. Cette région ainsi que les 8 motifs répétés BRC dans la région intermédiaire de la protéine sont les plus caractérisées de BRCA2. Ces régions lui permettent

de contribuer à la réparation de l'ADN, la stabilité des télomères et la stabilité de la fourche de réplication en condition de stress.

Cependant, la protéine se compose également d'une région N-terminale de 1000 résidus impliqués en partie dans les fonctions mitotiques de BRCA2. Cette région est prédite comme désordonnée, c'est à dire ne possédant pas de structure tertiaire ou secondaire stable, et est hautement phosphorylée au cours de la mitose par la kinase régulatrice du cycle cellulaire Plk1 (Lin et al., 2003, Takaoka et al., 2014). Les régions désordonnées sujettes aux modifications post-traductionnelles sont connues pour servir de site de recrutement protéique, en particulier suite à des cascades d'évènements de signalisation. Cependant, les sites de phosphorylation par Plk1 n'ont pas pu être tous identifiés par les techniques classiques de spectrométrie de masse ou d'alanine-screening couplé à l'autoradiographie (Lin et al., 2003). En effet ces techniques sont rapidement limitées pour l'identification de modifications multiples dans les régions désordonnées. Ceci a donc largement limité la caractérisation de ces évènements de phosphorylation, seules 2 études ont pu proposer un lien entre ces phosphorylations et les fonctions mitotiques de BRCA2 (Lin et al., 2003, Takaoka et al., 2014).

Objectif de la thèse

Mon projet de thèse a donc eu pour objectif de caractériser à l'échelle du résidu ces évènements de phosphorylation afin d'apporter une meilleure compréhension du rôle de BRCA2 au cours de la mitose. Ces données serviront par la suite à tester l'impact de variants non classés retrouvés dans cette région.

Mes objectifs de thèse se focalisent sur l'étude *in vitro* de la phosphorylation de la région N-terminale de BRCA2 par Plk1, et se scindent en plusieurs sous-objectifs :

- (1) Identification des résidus phosphorylés par Plk1, quantification de la cinétique de phosphorylation et caractérisation du mécanisme de phosphorylation,
- (2) Identification des interactions moléculaires médiées par ces phosphorylations,
- (3) Tests de l'impact de variants rares de signification clinique inconnue.

Résultats

J'ai débuté ma thèse par la production en bactérie du fragment BRCA2₄₈₋₂₈₄ contenant l'ensemble des sites de phosphorylation potentiels de Plk1 (Lin et al., 2003), ainsi que plusieurs fragments plus petits, nécessaires pour faciliter les analyses ultérieures. Puis, j'ai utilisé la

Résonance Magnétique Nucléaire en phase liquide (RMN) pour confirmer expérimentalement le caractère intrinsèquement désordonné de la région. Ces données m'ont permis de publier un premier article sur l'attribution des signaux RMN et l'analyse structurale de BRCA2₄₈₋₂₈₄ (**Julien M et al., 2020, Biomol NMR Assign**). Ensuite, j'ai tiré parti de la résolution à l'échelle du résidu que fournit la RMN pour identifier 4 sites de phosphorylations par Plk1 (produite par la plateforme de l'Institut Curie) sur BRCA2₄₈₋₂₈₄: S193, T207, T219 et T226, les sites S193 et T207 étant très conservés de l'homme jusqu'au poisson.

Pour caractériser le mécanisme de phosphorylation de Plk1 sur BRCA2, je me suis ensuite intéressée à la caractérisation des vitesses de phosphorylation des 4 phosphorésidus en utilisant une stratégie de quantification par RMN en temps réel. L'optimisation des conditions de phosphorylation ainsi que la méthode d'analyse des cinétiques sont présentées dans la revue **Julien M et al., 2020, Methods Mol Biol**. J'ai également participé au développement d'une méthodologie RMN permettant de suivre des cinétiques de phosphorylations à des pH supérieurs ou égaux à 7.5 et des températures excédant 25°C (**Julien* et al., 2020, Angew. Chem. Int. Ed.**), ce qui était inenvisageable précédemment.

Ensuite, j'ai caractérisé l'impact de variants sur les cinétiques de phosphorylation de la région N-terminale de BRCA2. J'ai produit les variants M192T, T200K et T207A, ainsi qu'un mutant contrôle publié comme déficient pour la phosphorylation par Plk1, S193A (Takaoka et al., 2014), mais non observé dans les bases de données. L'analyse par RMN des cinétiques de phosphorylation de ces fragments montre que toutes les mutations testées diminuent globalement la phosphorylation de BRCA2, et que cet effet est particulièrement important dans le cas du variant T207A. La quantification de l'impact des variants à l'échelle du résidu permet de mieux estimer les conséquences moléculaires des mutations associées, afin, par la suite, de proposer quelles fonctions de BRCA2 pourraient être déficientes.

A ce stade, j'ai observé que le motif centré sur T207 phosphorylé (pT207) était similaire au motif consensus reconnu par le domaine régulateur de Plk1 : le domaine PBD qui permet de recruter Plk1 à proximité de ses cibles (Elia et al., 2003). J'ai alors vérifié, par titrage calorimétrique isotherme (ITC), qu'un fragment de BRCA2 centré sur pT207 était capable d'interagir avec le domaine PBD de Plk1, alors que le même fragment non phosphorylé n'en était pas capable. Ces données m'ont permis de mettre en lumière l'importance de la phosphorylation du résidu T207 par Plk1 pour la création d'un site d'interaction pour la kinase. Par ailleurs, la structure cristallographique du complexe BRCA2₂₀₀₋₂₀₉/PBD a été résolue par l'équipe et nous a permis d'identifier que deux résidus sont importants pour l'interaction entre

BRCA2 et Plk1 : S206 et pT207 puisque leur chaîne latérale interagissent directement avec PBD. Ceci nous a permis de conclure que Plk1 est capable de phosphoryler BRCA2(T207) et de s'en servir de site de recrutement pour phosphoryler plus efficacement les autres sites de BRCA2. De plus, les travaux de nos collaborateurs, l'équipe d'Aura Carreira (Institut Curie), ont permis de mettre en évidence que la phosphorylation de T207 est essentielle pour déclencher la formation d'un complexe impliquant BRCA2/Plk1/BubR1/PP2A en mitose. Nos collaborateurs ont pu montrer, en cellules, que ce complexe joue un rôle dans l'alignement des chromosomes, et que des variants de BRCA2 qui présentent un défaut de phosphorylation de T207 (tel que T207A et S206C) causent aussi un défaut mitotique caractérisé par des chromosomes mal alignés, une ségrégation défectueuse et une aneuploïdie. Ces résultats ont été publiés récemment (**Ehlen A, Julien M* et al, 2020 Nat. Commun**).

La description de ce nouveau site d'interaction pour Plk1 sur BRCA2 permet de mieux comprendre son rôle au cours de la mitose. Cependant, un autre site d'interaction Plk1/BRCA2 avait précédemment été identifié : BRCA2_{pT77} (Takaoka et al., 2014, Yata et al., 2014). BRCA2 T77 est phosphorylé en début de mitose par les kinases Cdk et crée un site d'interaction pour le domaine PBD de Plk1. Il a également été montré que pT77 régule en cellule la phosphorylation de S193 (Takaoka et al., 2014). Dans une autre partie de ma thèse, je me suis intéressée à caractériser plus précisément le rôle de pT77 sur la phosphorylation ultérieure de BRCA2 par Plk1.

Pour cela, j'ai d'abord utilisé une stratégie de phosphomimétique (mutation d'un résidu phosphorylé en aspartate ou glutamate pour mimer la présence d'une charge négative). Cependant, le PBD ne reconnaît pas T77D et T77E comme mimes de phosphate. J'ai donc ensuite directement préphosphorylé BRCA2 par des kinases Cdk commerciales. J'ai pu identifier que Cdk1/B1 (présente en mitose) phosphoryle efficacement BRCA2 T77 ainsi que d'autres sites. Cependant, cette kinase était trop peu active et chère pour envisager de mener une étude complète avec ce système. J'ai donc utilisé la kinase commerciale Cdk1/A2 mais j'ai identifié qu'elle ne phosphoryle pas efficacement T77 (site tardif de phosphorylation). Finalement, nous avons opté pour l'utilisation de la MAPK p38, produite au laboratoire et connue pour phosphoryler des sites similaires à Cdk1. p38 phosphoryle efficacement BRCA2 T77 ainsi que d'autres sites également phosphorylés par Cdk1/B1. L'analyse de la cinétique de phosphorylation ultérieure par Plk1 a pu montrer qu'en présence d'une faible préphosphorylation par p38 (3 sites incluant pT77), la vitesse de phosphorylation de BRCA2 par Plk1 est accélérée au niveau des sites S193 et T207. Cependant, en présence d'une forte préphosphorylation par

p38 (7 sites), cet effet est perdu. La complexité d'un système à multiples préphosphorylations nous a empêché de caractériser précisément le rôle de BRCA2 pT77.

Pour revenir à un système plus simple contenant un seul site préphosphorylé (pT77), nous avons initié une collaboration avec le groupe de Vincent Aucagne (CBM, Orléans) afin de produire un fragment de BRCA2 préphosphorylé en utilisant le principe de ligation chimique. La stratégie consiste à produire séparément un peptide N-terminal de BRCA2 préphosphorylé en position T77 par synthèse chimique (groupe de Vincent Aucagne) et un peptide C-terminal ¹⁵N contenant les sites de phosphorylation par Plk1 en bactérie (production au laboratoire). Le protocole de ligation chimique mis au point par nos collaborateurs permet ensuite de lier ces deux peptides. La ligation des peptides, suivi d'une désulfuration de la cystéine laissée pour cicatrice, a déjà montré un bon rendement (70%). Ce projet se poursuivra avec la comparaison des cinétiques de phosphorylation par Plk1 en présence d'un peptide N-ter contenant T77 ou pT77, d'après la méthodologie RMN décrite précédemment.

Enfin, pour continuer à comprendre le rôle de la région conservée et phosphorylée par Plk1, j'ai mis en place des expériences de pull-down analysés par protéomique afin d'identifier de nouveaux partenaires mitotiques dépendant de l'état de phosphorylation de BRCA2 (collaboration avec la plateforme de spectrométrie de masse de l'Institut Curie). L'analyse des résultats de spectrométrie de masse a permis de retrouver Plk1, de manière cohérente avec mes résultats précédents ainsi que d'autres partenaires que j'ai commencé à caractériser.

Finalement, dans une dernière partie de ma thèse, je me suis intéressée à deux projets annexes :

- la production de la kinase Plk1 au laboratoire afin d'en étudier sa dynamique moléculaire,
- la production et la caractérisation *in vitro* de la région 250-500 de BRCA2, identifié comme site de liaison à l'ADN (Von Nicolai et al., 2016).

Ces deux projets sont également brièvement décrits dans mon manuscrit.

Conclusion

Mon projet de thèse a finalement permis de fournir les bases de production recombinante de la région N-terminale de BRCA2 ainsi que la méthodologie RMN nécessaire à l'étude de ses événements de phosphorylation par Plk1. Il nous a également permis d'étudier le rôle de

BRCA2 pT207 dans le contrôle de l'alignement des chromosomes au cours de la mitose. Ceci a servi également de base à l'identification des résidus clés de ce processus et donc à la prédiction de variants néfastes pour l'alignement des chromosomes.

La suite du projet nécessite d'identifier si d'autres partenaires mitotiques de BRCA2 sont reconnus par cette région. La stratégie de pull-down analysé par protéomique reste à vérifier et les partenaires identifiés à caractériser.

Enfin, cette même stratégie pourra être utilisée pour caractériser d'autres régions de BRCA2 afin d'identifier l'ensemble des résidus important pour les fonctions de BRCA2 et donc permettre la prédiction de variants causaux et le test de variants non classés.

Remerciements

Ce travail de thèse a été réalisé au sein du Laboratoire de Biologie Structurale et Radiobiologie (CEA Saclay) et de l'Institut De Biologie Intégrative de la Cellule (CNRS). Je remercie Dr. Jean-Baptiste Charbonnier, Dr. Thierry Meinel et Dr. Frédéric Boccard pour m'avoir accueillie au sein de ces établissements pendant la durée de ma thèse.

Pour ces 4 années, j'ai été financée par le Ministère de l'Enseignement, de la Recherche et de l'Innovation ainsi que par la Fondation ARC. Un grand merci à l'ENS de Cachan pour avoir sélectionné mon projet de thèse ainsi qu'aux donateurs de la Fondation ARC pour leur engagement dans la lutte contre le cancer.

Je remercie l'ensemble des membres de mon jury de thèse pour avoir accepté d'évaluer mon travail : Dr. Isabelle Landrieu, pour avoir suivi ma progression depuis le comité de mi-thèse, pour son soutien et pour son rôle de rapporteur de thèse ; Dr. Malene Ringkjober-Jensen également pour avoir accepté d'être rapporteur ; Pr. Herman Van Tilbeurgh et Dr. Mauro Modesti qui ont accepté de prendre le rôle d'examineurs.

Ce projet a été encadré par Dr. Sophie Zinn-Justin et Dr. François-Xavier Theillet.

Sophie, merci de m'avoir accueillie au sein de l'équipe en stage de M2 et de m'avoir permis de continuer en thèse. Je te remercie particulièrement pour les nombreux congrès auxquels tu m'as permis de participer. Ces occasions ont été très enrichissantes à la fois pour faire évoluer ma vision du projet et pour gagner en culture scientifique. Tous les doctorants n'ont pas cette chance et je t'en suis reconnaissante.

François, je te remercie pour avoir accepté de co-encadrer ma thèse. Tes conseils scientifiques, de présentation et ton soutien m'ont été très précieux. Travailler à tes côtés a été très formateur. Je te souhaite de très belles aventures scientifiques à l'avenir !

Au cours de ces années, j'ai pu croiser de nombreuses personnes au sein du laboratoire. Parmi elles, Dr. Simona Miron, Dr. Virginie Ropars et Ambre Petitalot m'ont aidée à me former aux techniques du laboratoire. Merci d'avoir pris le temps de me les expliquer et merci pour votre enthousiasme à le faire ! Un grand merci à Rania Ghouil pour ses coups de main et sa bonne humeur qui nous ont permis de progresser sur le projet. Je te souhaite bon courage et une belle expérience de thèse à venir ! Un clin d'oeil à Agathe Marcelot et Fouad Ouasti mes compères de thèse. Merci pour votre soutien et pour toutes nos discussions. Je vous souhaite également de belles réussites à l'avenir !

Je voudrais remercier tout le monde, mais cette section serait infinie. Des discussions de bureau ou au spectro, de la laverie aux repas du midi, j'adresse de nombreux merci à tous, pour votre bonne humeur et aussi pour vos râleries !

Mes remerciements s'adressent également aux collaborateurs du projet, Dr. Aura Carreira, Dr. Asa Ehlen, Charlotte Martin, Patricia Duchambon, Dr. Vincent Aucagne et Jean-Baptiste Madinnier. Ce projet de thèse n'aurait pas pu être aussi enrichissant sans vous.

Je souhaite remercier l'ensemble des endadrants de mes stages précédents. Vous m'avez permis de me préparer au mieux à cette expérience de thèse. Dr. Klaartje Houben et Dr. Cecilia Pinto, Dr. Martine Cadène, Dr. Lucie Khemtemourian, Dr. Pierre-Marie Girard et Dr. Joao Santos-Sousa, Dr. Hélène Benedetti, Dr. Daniel Auguin, Dr. Jean-Pierre Gomez et Dr. Patrick Gonzalez, un très grand merci pour le temps que vous avez passé à me former et pour tous vos conseils et encouragements !

Au cours de cette thèse, j'ai pu assurer une mission de 3 années de monitorat. Merci à Dr. Boris Julien et Dr. Caroline Borday pour m'avoir fait confiance pour assurer les enseignements de biochimie, biologie cellulaire et biologie animale à l'Université Paris Sud pendant ces années. Un grand merci à Boris pour m'avoir donné l'occasion de participer à la création des cours en ligne de biochimie. Ce fut très enrichissant pour moi et aussi très formateur. J'ai pris énormément de plaisir à faire partie de l'aventure. Finalement, merci à Dr. Nicolas Graner pour m'avoir recrutée pour cette dernière année dans l'équipe de médiation scientifique du COMPAS de Paris Sud.

« Retourner à l'esprit du débutant. Plus on monte en grade, plus il devrait se manifester », Nobuyoshi Tamura. Un grand merci au karaté club Pascal pour m'avoir donné l'occasion de me vider l'esprit de nombreuses fois au cours de ces dernières années.

Caroline, Fiona, Asma et Norhane, je vous adresse de profonds remerciements pour votre soutien depuis de nombreuses voir de très nombreuses années. Vos encouragements et vos conseils ont été les plus précieux à mes yeux. Je vous embrasse très fort !

La famille, d'immenses merci pour avoir persisté à essayer de comprendre en quoi consistait mon travail et pour toutes les relectures des résumés que j'ai pu vous envoyé. Ces discussions m'ont permis de me rappeler l'objectif de tout ce boulot, je vous en remercie !

Pour finir, un très très grand merci à (B)Agathe et Léa. Cette thèse n'aurait pas été la même sans vous ! Des bisous ♥

Table of contents

Introduction	13
Chapter 1. Breast cancer.....	17
1. The French national program for decreasing the breast cancers mortality rate.....	18
2. Hereditary breast cancers: mutations in <i>BRCA1</i> and <i>BRCA2</i> genes.....	19
3. Identification of breast cancer pathogenic variants of <i>BRCA1</i> and <i>BRCA2</i>	21
Chapter 2. <i>BRCA2</i> structure.....	24
1. <i>BRCA2</i> contains a single folded domain.....	26
2. <i>BRCA2</i> contains 80% of disorder: what is protein disorder?.....	27
3. Roles of IDRs/IDPs.....	28
a. Protein and nucleic acid interaction	29
b. Post-translational modifications regulate IDR-protein interactions.....	31
c. Phase transition	33
4. <i>BRCA2</i> disordered regions contain PTM and interaction sites.....	35
Chapter 3. Functions of <i>BRCA2</i> through the cell cycle	38
1. Homologous recombination	40
a. System description	40
b. Regulation of HR by PTMs.....	43
2. During interphase, <i>BRCA2</i> interacts with other proteins to ensure genome stability and centrosome duplication.....	45
a. Pathways	45
b. Regulation by PTMs.....	45
3. Role of <i>BRCA2</i> during mitosis.....	46
a. Role during chromosome segregation.....	46
b. Phosphorylation by Plk1 regulates <i>BRCA2</i> function in chromosome segregation	47
c. <i>BRCA2</i> phosphorylation by Cdks and Plk1 ensure its localization at the midbody	48
d. Several <i>BRCA2</i> interactions take place in the context of cytokinesis	49
4. Region of interest.....	50
Chapter 4. How does Plk1 work?	52
1. Plk1, a central kinase for mitosis.....	53
2. Plk1 contains a kinase domain and a Polo-Box domain interacting with specific phosphorylated motifs.....	54
3. Dynamics between the two domains of Plk1	58
Chapter 5. Tools for studying phosphorylation.....	61
1. Western Blot necessitates antibody directed against previously identified phosphosites to monitor phosphorylation processes.....	61
2. Mass spectrometry is a powerful technique for studying isolated phosphosites...62	
3. NMR: site-specific identification and monitoring of phosphorylation.....	63

Purpose of the thesis	69
Material & methods	71
1. Commercial products.....	73
2. Plasmids	73
3. Site-directed mutagenesis.....	74
4. Plasmid transformation in <i>E.coli</i> strains.....	76
5. Protein expression	76
6. Protein purification.....	79
7. Production of Plk1 in insect cells.....	90
8. Proteomics.....	92
9. Peptides and DNA.....	93
10. ITC	94
11. Phosphorylation kinetics	94
12. NMR spectroscopy.....	96
13. Phase separation microscopy.....	97
14. Peptide synthesis and Native Chemical Ligation.....	98
15. Figures.....	99
Results	101
Chapter 1. Sample production.....	103
Chapter 2. Identification of BRCA2 residues phosphorylated by Plk1.....	107
1. Delimiting the region of interest: BRCA2 ₄₈₋₂₈₄	107
2. The NMR analysis of BRCA2 ₄₈₋₂₈₄ reveals that it is disordered.....	108
<i>1H, 13C and 15N backbone resonance assignment of the human BRCA2 N-terminal region. Biomol NMR Assign. 2020.</i>	109
3. Plk1 efficiently phosphorylates 4 residues in the BRCA2 ₄₈₋₂₈₄ region.....	110
Chapter 3. Monitoring BRCA2 phosphorylation using NMR.....	112
1. Using ¹ H- ¹⁵ N 2D NMR.....	112
<i>Multiple Site-Specific Phosphorylation of IDPs Monitored by NMR. Methods Mol Biol. 2020.</i>	113
2. Recording 2D ¹³ Ca- ¹³ CO NMR spectra.....	114
<i>Sensitivity-Enhanced 13 C-NMR Spectroscopy for Monitoring Multisite Phosphorylation at Physiological Temperature and pH. Angew Chem Int Ed Engl. 2020.</i>	115
3. Can we obtain complementary data from ³¹ P 1D NMR?.....	116
4. Finding the optimal pH for Plk1 phosphorylation.....	117
5. Impact of the fragment design on phosphorylation kinetics.....	118
Chapter 4. BRCA2 _{pT207} is involved in the spindle assembly checkpoint.....	122
1. BRCA2 _{pT207} interacts with Plk1 _{PBD} and triggers the formation of a quaternary complex.....	122
<i>Proper chromosome alignment depends on BRCA2 phosphorylation by PLK1. Nat Commun. 2020.</i>	123
2. Interaction between BRCA2 ₁₀₉₃₋₁₁₅₈ and PP2A _{B56}	126

Chapter 5. Does phosphoBRCA2 recruit other partners?	133
1. Impact of other VUS on Plk1 phosphorylation of BRCA2.....	133
2. The VUS M192T impairs cytokinesis.....	135
3. Isolating new pBRCA2 ₁₆₇₋₂₆₀ partners using proteomics.....	136
4. Study of the BRCA2/Kif2C interaction	138
5. Study of the BRCA2/Chk2 interaction	144
6. Other interactions tested	145
Chapter 6. Interplay between Cdk and Plk1 phosphorylations	149
1. The phosphomimetics approach.....	149
2. Pre-phosphorylation of BRCA2 by Cdk.....	150
3. Native Chemical Ligation (NCL)	155
Chapter 7. Plk1 production and dynamic study.....	159
1. Plk1 production in insect cells.....	160
2. Design of proteins for bacterial expression.....	162
3. Production of the kinase domain.....	164
4. Production of Aurora A and phosphorylation of Plk1.....	166
5. Production of the PBD.....	168
6. Production of Plk1 _{FL}	170
Chapter 7. Side project: interaction between DNA and N-term BRCA2.....	171
Discussion & perspectives	181
1. BRCA2 ₄₈₋₂₈₄ phosphorylations	183
a. Plk1 phosphorylations.....	184
b. Role of BRCA2 _{pT77} for Plk1 phosphorylation.....	185
c. Strategies for studying IDR monophosphorylation.....	187
2. Interactions and functions mediated by phosphoBRCA2.....	188
a. BRCA2/Plk1 interaction	189
b. Role of BRCA2 _{pT207} in chromosome segregation.....	190
c. Use of proteomics for searching IDRs partners	192
d. Kif2C/phosphoBRCA2 interaction.....	193
e. Chk2/phosphoBRCA2 interaction	195
f. Is the NTD-DBD of BRCA2 functional?	196
3. Plk1, a cancer target with unclear dynamics	197
4. Conclusion.....	201
Bibliography.....	203

List of illustrations

Figures

Figure 1. Estimated numbers of new cancer cases in 2018 in the world and estimated women incidence and mortality per cancer in the world.....	15
Figure 2. Estimated incidence and mortality of breast cancers in the 10 more impacted countries in the world, in 2018.....	17
Figure 3. Origins of breast cancer.....	20
Figure 4. Composition of the BRCA Share™ French database in 2016 according to the variant classification	23
Figure 5. Comparison between BRCA1 and BRCA2 structures reveals no homology.....	25
Figure 6. Ratio between observed and theoretical numbers of variants according to exon length for BRCA1 and BRCA2.....	26
Figure 7. BRCA2 contains only one folded domain.....	26
Figure 8. Common enzymatic post-translational modifications observed in eukaryotes.....	31
Figure 9. LLPS are observed in vitro and in cells and can be regulated by PTMs.....	34
Figure 10. BRCA2 conservation, PTM and interaction sites.....	35
Figure 11. Hypothetical dimer particles of BRCA2 as reported by Shadid et al	37
Figure 12. Expression and localization of BRCA2 through the cell cycle.....	39
Figure 13. Role of BRCA2 during Homologous Recombination	41
Figure 14. PTMs at the S/G2 transition regulate BRCA2 interactions.....	44
Figure 15. BRCA2 is phosphorylated by Plk1 at the entry into mitosis.....	47
Figure 16. BRCA2 is a central component of the spindle assembly checkpoint.....	48
Figure 17. BRCA2 phosphorylated on S193 by Plk1 is localized at the Flemming body.....	49
Figure 18. Exon 6 (aa 172 to aa 210) is conserved.....	50
Figure 19. Polo-like kinase family members and their functions.....	52
Figure 20. Plk1 functions through the cell cycle.....	53
Figure 21. The common architecture shared by Plks.....	54
Figure 22. 3D structure of the kinase domain of human.....	55
Figure 23. Model of human Plk1 from X-Ray structures.....	57
Figure 24. Interaction between Plk1 _(PBD) and a phosphopeptide.....	58
Figure 25. The interaction between the KD and PBD of Plk1 explained its autoinhibition.....	59
Figure 26. Model of multilevel regulation of zebrafish Plk1	60
Figure 27. Comparison between zebrafish and human Plk1 structure.....	60
Figure 28. Protein phosphorylation observed by ¹ H- ¹⁵ N HMQC-SOFAST NMR.....	66
Figure 29. 1X agarose gel of amplification of BRCA2 ₄₈₋₂₁₈ M192T and T207A mutations using site-directed mutagenesis.....	75
Figure 30. 1X agarose gel of BRCA2 _{48-218(C4A)} PCR site-directed mutagenesis for mutations T77D and T77E.....	75
Figure 31. Device for microscopy observation of liquid-liquid phase transition.....	98
Figure 32. BRCA2 constructs used for my PhD project.....	103

Figure 33. Example of overexpression tests in <i>E. coli</i> BL21 (DE3) Star for a IDR expressed in the soluble fraction and an IDR found in the insoluble fraction.	104
Figure 34. BRCA2 ₈₅₋₂₂₀ sample boiled during purification and analyzed by inverse-phase C18 chromatography	105
Figure 35. Prediction of Plk1 phosphosites among the N-terminal BRCA2 sequence.....	107
Figure 36. The N-terminal BRCA2 fragment includes 2 phosphoclusters well-conserved from mammals to fishes.....	108
Figure 37. Plk1 phosphosites in BRCA2 ₄₈₋₂₁₈ and BRCA2 ₁₉₀₋₂₈₄	110
Figure 38. Sequence analysis and conservation of Plk1 phosphosites.....	111
Figure 39. ¹³ Ca- ¹³ CO spectrum assignment of BRCA2 ₁₉₀₋₂₈₄ and BRCA2 ₄₈₋₂₁₈	115
Figure 40. 1D NMR ³¹ P spectra of BRCA2 ₁₆₇₋₂₆₀ phosphorylated by Plk1.....	117
Figure 41. Plk1 presents the same activity profile from pH 7.0 to pH 8.0.	118
Figure 42. Plk1 Vmax and Km determination for BRCA2 _{S193} and BRCA2 _{T207}	119
Figure 43. Comparison of S193, T207, T219 and T226 phosphorylation kinetics in BRCA2 ₄₈₋₂₁₈ , BRCA2 ₁₆₇₋₂₆₀ and BRCA2 ₁₉₀₋₂₈₄	120
Figure 44. Phosphorylation of BRCA2 ₄₈₋₂₁₈ in cell extracts reveals the phosphorylation of S70 that may be executed by PKA.....	124
Figure 45. Interaction between pBRCA2 ₁₆₇₋₂₆₀ and Plk1 _{PBD} , as observed by NMR.....	125
Figure 46. Scheme of the BRCA2/Plk1/BubR1/PP2A quaternary complex, necessary for chromosome segregation.....	126
Figure 47. NMR analysis of BRCA2 ₁₀₉₃₋₁₁₅₈	128
Figure 48. Interaction between BRCA2 ₁₀₉₃₋₁₁₅₈ and PP2A _{B56}	129
Figure 49. Transfer of the BRCA2 ₁₀₉₃₋₁₁₅₈ assignment from 283 K to 298 K.....	129
Figure 50. Phosphorylation of BRCA ₁₀₉₃₋₁₁₅₈ by Plk1.....	131
Figure 51. Comparison of S193, T207, T219 and T226 phosphorylation kinetics between BRCA2 ₁₆₇₋₂₆₀ +/- APB207.....	131
Figure 52. Impact of T200K and M192T VUS on BRCA2 ₁₉₀₋₂₈₄ phosphorylation by Plk1....	133
Figure 53. Comparison of S193, T207, T219 and T226 phosphorylation kinetics between BRCA2 ₁₆₇₋₂₆₀ WT, M192T, S193A and T207A.....	134
Figure 55. 6 mitotic partners were identified by MS for phosphorylated BRCA2 ₁₆₇₋₂₆₀	137
Figure 56. Prediction of Kif2C disorder reveals one large globular domain corresponding to its motor domain	138
Figure 57. Gel filtration elution profile of pBRCA2 ₁₆₇₋₂₆₀ and Kif2C ₂₁₆₋₅₉₈	139
Figure 58. ITC experiments between BRCA2 ₁₆₇₋₂₆₀ and Kif2C ₂₁₆₋₅₉₈	140
Figure 59. Interaction between pBRCA2 ₁₆₇₋₂₆₀ and Kif2C ₂₁₆₋₅₉₈	141
Figure 60. Size exclusion chromatography profiles of Plk1 ₁₋₃₂₈ , Kif2C ₂₁₆₋₅₉₈ and Plk1 ₁₋₃₂₈ +Kif2C ₂₁₆₋₅₉₈	142
Figure 61. Purification of Kif2C FL WT and S715E.....	143
Figure 62. Interaction test between pBRCA2 ₁₆₇₋₂₆₀ and Kif2C _{FL}	143
Figure 63. Sequence and domains of Chk2 and the identified mutation in breast, colon, lung, bladder and ovary cancers.....	144
Figure 64. Interaction between pBRCA2 ₁₆₇₋₂₆₀ and Chk2 ₁₋₂₀₉	145
Figure 65. Interaction test between BRCA2 and DDX5.....	146
Figure 66. Interaction test between BRCA2 and PARP1.....	147

Figure 67. Interaction between BRCA2 and PARP1 ₁₋₃₆₆	148
Figure 68. Calorimetry titration of Plk1 _{PBD} with BRCA2 peptides.....	150
Figure 69. Pre-phosphorylation of BRCA2 ₄₈₋₂₁₈ by Cdk1/B1 qualitatively increases its phosphorylation by Plk1.....	151
Figure 70. Phosphorylation of BRCA2 ₄₈₋₂₁₈ by Cdk1/A2 compared to Cdk1/B1.....	152
Figure 71. Phosphorylation of BRCA2 ₄₈₋₂₁₈ by p38 compared to Cdk1/B1.....	153
Figure 72. Phosphorylation of WT and T77A BRCA2 ₄₈₋₂₁₈ by p38 compared to Cdk1/B1...	154
Figure 73. p38 phosphorylates BRCA2 _{T77} and favors phosphorylation of BRCA2 _{S193} by Plk1 when the p38 phosphorylation of BRCA2 is not complete.....	154
Figure 74. The NCL strategy for studying the effect of pT77 on BRCA2 phosphorylation by Plk1	155
Figure 75. NCL protocol for linking BRCA2 ₄₈₋₈₄ to BRCA2 ₈₅₋₂₂₀	157
Figure 76. NCL reaction and monitoring of BRCA2 ₄₈₋₂₂₀	157
Figure 77. Mass spectrometry identified Plk1 degradation products in the Plk1 sample but couldn't determinate the phosphorylation state of Plk1 _{S137} and Plk1 _{T210}	160
Figure 78. Cloning the Plk1 cDNA sequence into the pKL plasmid for bacmid recombination into DM10EMBacY cells.....	161
Figure 79. Production of Plk1 in sf9 cell.....	162
Figure 80. Construct design for the Plk1 study.....	163
Figure 81. Expression tests of Plk1 _{FL} , Plk1 ₁₋₃₂₈ and Plk1 ₃₆₇₋₆₀₃ constructs in E.coli BL21 (DE3).	164
Figure 82. Coomassie-stained 15% SDS-PAGE analysis of the GF purification step of Plk1 ₁₋₃₂₈	165
Figure 83. Coomassie-stained 15 % SDS-PAGE analysis of Plk1 ₁₋₃₆₆ affinity and GF chromatography purifications	165
Figure 84. Plk1 ₁₋₃₂₈ phosphorylates BRCA2 ₁₆₇₋₂₆₀ at 4 positions: S193, T207, T219 and T226.	166
Figure 85. Coomassie-stained 15% SDS-PAGE analysis of AurA-TPX2 ₁₋₄₃ affinity and GF chromatography purifications.....	167
Figure 86. Phosphorylation of Plk1 ₁₋₃₂₈ by AurA-TPX2 ₁₋₄₃	168
Figure 87. SDS-PAGE of Plk1 ₃₆₆₋₆₀₃ affinity and heparine chromatographies purification...	168
Figure 88. Gel filtration profile of Plk1 ₃₆₆₋₆₀₃	169
Figure 89. Interaction between Plk1 ₁₋₃₂₈ and Plk1 _{PBD}	169
Figure 90. SDS-PAGE 15% analysis of the Plk1 ₁₋₆₀₃ L162C affinity purification.....	170
Figure 91. Interaction between BRCA2 ₂₅₀₋₅₀₀ and ssDNA or dsDNA.....	171
Figure 92. Disordered propensity and conservation analysis of BRCA2 ₂₅₀₋₅₀₀	172
Figure 93. BRCA2 fragments used in the N-terminal DBD study.....	173
Figure 94. ¹ H- ¹⁵ N sofast-HMQC NMR spectra of BRCA2 _{D1}	174
Figure 95. ¹ H- ¹⁵ N sofast-HMQC NMR spectra of BRCA2 _{D1}	174
Figure 96. ¹ H- ¹⁵ N sofast-HMQC NMR spectra of GB1-BRCA2 _{D1}	175
Figure 97. ¹ H- ¹⁵ N sofast-HMQC NMR spectra of BRCA2 _{D1A}	176
Figure 98. ¹ H- ¹⁵ N so-fast HMQC spectra of BRCA2 _{D1} , GB1-BRCA2 _{D1} and BRCA2 _{D1A} in presence of dsDNA or ssDNA.....	177
Figure 99. Light microscopy observation of BRCA2 _{D1} after 36 hrs at 4°C.	178

Figure 100. DIC microscopy of Sox2 ₁₁₅₋₃₁₇ and BRCA2 _{D1}	179
Figure 101. BRCA2/Plk1/BubR1/PP2A quaternary complex upon phosphorylation by Plk1	192
Figure 102. Known interactions between BRCA2, Plk1 and Kif2C.	194
Figure 103. Labeling strategy for studying Plk1 _{KD} /Plk1 _{PBD} interface.....	199

Tables

Table 1. Interaction between disordered regions of BRCA2, proteins, DNA, through BRCA2 cell cycle function.....	40
Table 2. Plasmids for expression of BRCA2 constructs.....	73
Table 3. Plasmids for expression of other constructs including Plk1, Kif2C, PARP1, Chk2 and Aurora A-TPX2.....	74
Table 4. Primers for BRCA2 _{48-218(C4A)} site-directed mutagenesis.	75
Table 5. Composition of LB and M9 media.....	76
Table 6. Optimal protein expression conditions in bacteria for BRCA2, Plk1, AurA-TPX2, PARP1, Chk2 and Kif2C constructs.....	78
Table 7. Molecular weights and molecular extinction coefficients after cleavage (TEV or PreScission) of proteins produced in this study.....	79
Table 8. Primers for hPlk1 and pKL amplification by PCR.	90
Table 9. List of peptides used, their solubilization buffer and their corresponding supplier....	93
Table 10. List of DNA used their sequence and their solubilization.....	93

Annexe

Annexe 1. Link between interaction and PTMs sites and BRCA2 functions.	202
--	-----

Abbreviations

APB207	BRCA2 _{194-210(pT207)} peptide
APC/C	Anaphase Promoting Complex
ARC	Agence de Recherche pour le cancer
BER	Base Excision Repair
BIC	Breast cancer Information Core
BRCA1	Breast cancer susceptibility protein/gene 1
BRCA2	Breast Cancer susceptibility protein/gene 2
CBM	Centre de Biophysique Moléculaire
Cdk	Cycline-dependant kinase
CEA	Commissariat à l'Energie Atomique
Chk	Checkoinp kinase
CTD	C-Terminal Domain
DBD	DNA Binding Domain
DIC	Differential Interference Contrast
DSB	Double strand DNA break
dsDNA	Double-strand DNA
DSS	3-(Trimethylsilyl)Propane-1-sulfonate, sodium salt
DTT	DiThioThreitol
EDTA	Ethylenediaminetetraacetic acid
ELM	Eukaryotic Linear Motif
ESI	Electrospray
FL	Full Length
FRM	Fondation Médicale pour la Recherche
GF	Gel Filtration
HAS	Haute Aurorité de Santé
HEPES	4-(2-hydroxyethyl)-&-piperazineethansulfonic acid
HMBC	Heteronuclear Multiple Bond Correlation
HMQC	Heteronuclear Multiple-Quantum Correlation
HR	Homologous recombination
HSQC	Heteronuclear Single-Quantum Correlation
I2BC	Institut de Biologie Intégrative de la Cellule
ICSN	Institut de Chimie des Substances Naturelles
IDP/IDR	Intrinsically Disordered Protein/Region
IPTG	Isopropyl b-D-A-thiogalactopyranoside
ITC	Isothermal Titration Calorimetry
KD	Kinase Domain
Kif2C	Kinesin-like protein 2C
LB	Luria Browth medium
LLPS	Liquid-Liquid Phase Separation
M9	Minimum medium

MALDI-TOF	Matrix-Assisted Laser Desorption-Ionization – Time Of Flight
MAPK	Mitogen-activated protein kinase
MCAL	Mitotic Centromer Associated Kinesin
MS	Mass Spectrometry
NCI	Native Chemical Ligation
NEB	New England Buffer
NES	Nuclear Export Signal
NLS	Nuclear Localization Signal
NMR	Nuclear Magnetic Resonance
NTD	N-Terminal Domain
OB	oligonucleotide/oligosaccharide-binding
OD	Optical Density
ON	Over night
P/CAF	p300/CBP-associated factor
PBD	PoloBox Domain
PBS	Phosphate Buffer Saline
PDB	Protein DataBank
PI	protease inhibitors
PKA	Protein Kinase A
Plk	Polo-like kinase
PMSF	Phenylmethylsulfonyl fluoride
PTM	Post-Translational Modification
ROS	Reactive Oxygen Species
RT	Room temperature
SDS-PAGE	Sodium Dodecyl Sulfate-PolyAcrylamid Gel Electrophoresis
SEC	Size Exclusion Chromatography
SLIM	Short Linear Motifs
SPOT-dis	Sequence-based Prediction Online Tools for disorder
ssDNA	single-strand DNA
TCEP	tris(2-carboxyethyl)phosphine
TEV	Tobacco Etch Virus endopeptidase
TFA	TriFluoric Acid
UMD	Universal Mutation Database
VUS	Variant of Unknown clinical Significance
WB	Western Blotting

Introduction

Initially, cancers were thought as a single disease with common physical characteristics: veins stretched on all sides as the crab has its feet. The name of cancer is derived from the greek “karkinos” (crab) proposed by Hippocrates around 400 BC. Actually, the term “cancer” is a generic name that refers to a large number of diseases, all characterized by an abnormal proliferation of cells, out of control of the usual regulatory systems. This anarchic multiplication often builds up as a mass, named as the tumor. This can grow and invade nearby tissues or release migrating cells traveling through the vascular system and creating secondary tumors. The term cancer designates all malignant tumors that destroy their physiological environment and jeopardize the organism survival.

In 2018, 18,078,957 of new cancer cases were diagnosed and 9,555,027 deaths were associated to malignant tumors, worldwide (Globocan 2018). Hence, understanding cancers’ development constitutes naturally a central challenge for biology research. The predominant cancers are lung cancers (Figure 1A), which mainly concerns men (65% of incidence in 2018). Breast cancers are those with the highest incidence among women (2,088,849 new cases in 2018), also being the first cause of their death by cancers (Figure 1B). This calls evidently for important research efforts to understand breast cancer(s).

My PhD project is part of the global efforts in breast cancers research. I focused my work on the characterization of a protein often mutated in hereditary breast cancers: the BRCA2 protein. My project aims at describing structurally the molecular function of a conserved yet poorly studied region of BRCA2. The characterization of this region will then make it possible to predict consequences of mutations in BRCA2. This aims at providing information for improving the diagnosis and medical monitoring of hereditary breast cancer patients.

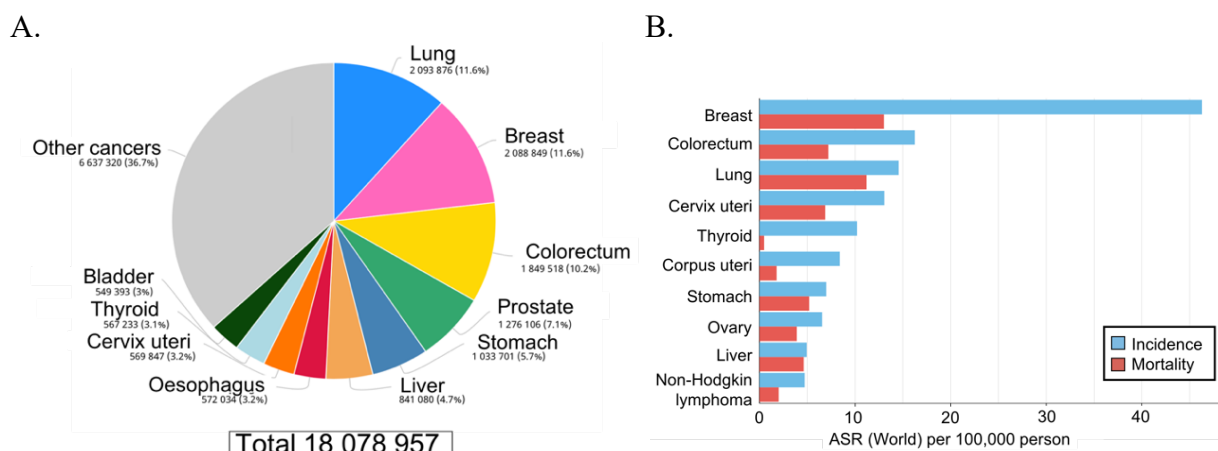


Figure 1. (A) Estimated numbers of new cancer cases in 2018 in the world and (B) estimated women incidence and mortality per cancer in the world (Globocan 2018).

Through my Introduction, I first present the current medical care strategies for limiting breast cancer mortality, emphasizing the particularities of hereditary breast cancer (**Chapter 1**). Then, I focus on the description of the current knowledge on the structure and functions of the BRCA2 protein (**Chapter 2 & 3**), introducing notably the regions where only poor information is available. Finally, I present the kinase Plk1, which phosphorylates BRCA2 in the region that I studied (**Chapter 4**), and the experimental approach to study BRCA2 phosphorylation by Plk1 (**Chapter 5**).

Chapter 1. Breast Cancer

Breast cancers are particularly frequent in industrial regions, i.e. North America, Western Europe and Australia (Globocan 2018). These regions are indeed more exposed to breast cancer risk factors i.e. advanced age, late pregnancy or late menopause, lipid-rich and flesh-eating diets, smocking and exposition to specific chemical compounds or hormones (Anjum F et al., 2017, Kaminska et al., 2015, Chajès et al., 2013, Anothaisintawee et al., 2013). Europe presents the highest breast cancer incidence rate, with France in the top 4 of the most impacted countries (Figure 2).

Current evaluations report that 1 French woman over 9 will develop a breast cancer in her life (INCa 2017). However, the survival rate is not hopeless: 0.87 survival, 5 years after treatment and 0.76, 10 years after treatment (INCa 2017). This can be explained by the efficiency of current breast cancer treatments i.e. surgery, radiotherapy, chemotherapy and hormonotherapy (Les traitements des cancers du sein, 2013). Nevertheless, breast cancer is still the first cause of women cancer mortality in France. New strategies are thus needed for decreasing breast cancer mortality.

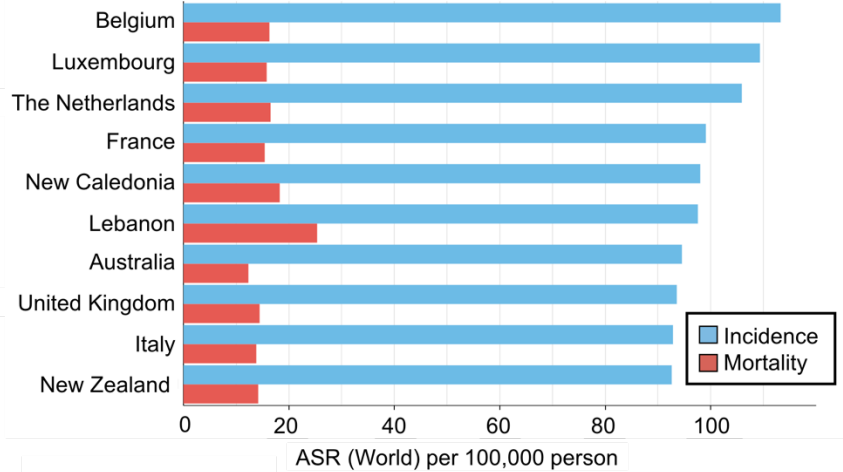


Figure 2. Estimated incidence and mortality of breast cancers in the 10 more impacted countries in the world, in 2018 (Globocan 2018).

1. The French national program for decreasing the breast cancers mortality rate

As breast cancer treatments show currently acceptable efficiencies, the strategy for reducing the mortality rate is focusing on diagnosis improvement. Indeed, detecting the cancer at its first stages of development permits an early treatment of the tumor, which greatly increases the survival probability. With this objective, the French government has set up a national screening program in 2005. Because 85% of breast cancers appear after 50 years old, the program proposes a mammography every 2 years accompanied by a clinical examination of breasts for women from 50 to 74 yo ([1999, Anaes](#)). These exams are free for women and supported by the national health insurance. The participation of the population yielded 40% high at the beginning, and levels off at 50% since 2007 ([Santé publique 2019](#)). Implementing this screening has been highly beneficial: according to the national HAS (Haute Autorité de Santé), the mortality rate linked to breast cancer has decreased from 21% to 15% (for women from 50 to 69 yo).

Beyond its success in the general population, two subpopulations do not take advantage of this tracking program.

The first subpopulation is men. About 500 men are diagnosed with breast cancer every year in France; this represents 0.5% of men cancers ([Fondation pour la Recherche Médicale](#)). The monitoring of male patients has to be highly specific ([Midding et al., 2018](#)) and psychological aspects are important to consider during medical care ([Midding et al. 2019](#); [Skop et al., 2018](#)). However, only scarce data about male breast cancers are available in the literature and published data are restrained to epidemiological studies containing only few cases per country.

The second subpopulation corresponds to patients with a hereditary breast cancer. Certain mutations or group of mutations are transmitted through the generations that increase the risk of developing a breast cancer. Hereditary breast cancers represent about 10 % of breast cancer cases, i.e. 5000 women per year ([Anglian Breast Cancer Study Group 2000](#); [Ghoussaini et al., 2009](#)). Hereditary breast cancer patients are affected by the disease earlier than sporadic cancers, starting from 20's yo ([Ottman et al., 1986](#)). Thus, the general screening program is proposed too late for these patients. To improve their diagnosis, the best strategy would be to propose early genetic screening to families with a breast cancer risk. In turn, this would require an exhaustive identification of all the genetic mutations that increase the breast cancer risk. This

would permit to propose personalized medical care focused on family members carrying risk-enhancing mutations and thus having a real risk of early breast cancer. Several epidemiologic studies are ongoing to localize the frequent breast cancer mutations in patient families.

2. Hereditary breast cancers: mutations in *BRCA1* and *BRCA2* genes

In the 90's, medical centers started to report several examples of families with a high risk of breast cancers. Genetic studies of these families allowed to identify a first gene highly mutated in hereditary breast cancer (Hall et al., 1990). This gene was named *BRCA1* for *BReast CAncer susceptibility gene 1*. Four years later, another study of 15 families suffering early-onset breast cancers revealed that another gene was responsible for high breast cancer risk (Wooster et al., 1994). This second gene was named *BRCA2*. It is now estimated that mutations in *BRCA1* lead to a woman breast cancer risk of 35-40% at 50 yo and 65-70% at 70 yo, whereas mutations in *BRCA2* lead to a risk of 15-35 % at 50 yo and 45-75 % at 70 yo (Stoppa-Lyonnet et al., 2004). Men also carry hereditary breast cancer mutations (Thorlacius et al., 1995, Ottman et al., 1986). However, their identification mainly aims at studying the transmission history of the mutation in the family, due to the weak men hereditary cancer risk (Ravi et al., 2012).

Other genes were also associated with an increased risk of developing breast cancer such as *TP53*, *STK11*, *CDI* and *PTEN* (Wendt et al., 2019). However, their impacts are negligible compared to *BRCA1* and *BRCA2*.

Proteins encoded by the genes *BRCA1* and *BRCA2* have been extensively studied and mechanisms leading to increased cancer risks have been progressively discovered (Figure 3). To explain the role of *BRCA1* and *BRCA2* proteins in cancer risk, we have to briefly present the physiological context.

Breasts are composed of two epithelial tissues (Ellis et al., 2013): the lobules responsible for milk production and the ducts ensuring milk transport to the nipple during lactation (Figure 3.A). These tissues grow during puberty under the action of estrogens and progesterone hormones, produced mainly by ovaries. After menopause, ovaries stop their hormone production and secondary sources increase theirs. Breasts, liver, adrenal gland and adipose tissues are among these secondary hormone production organs. Most of breast cancers take their origins in estrogen level increases after menopause.

The synthesis of estrogen releases reactive oxygen species (ROS) in cells. These highly reactive species are responsible for DNA base oxidation. This kind of DNA damage is normally

fixed by the Base Excision Repair (BER) system, a Single Strand Break DNA repair system that cleaves and replaces damaged bases on the DNA. BRCA1 is known to stimulate BER (Le page et al., 2000). However, when the number of SSBs rises too high, these are converted to double strand breaks (DSBs) (Fridlich et al., 2015). DSB can be repaired by the Homologous Recombination system (HR) (late S, G2 and M phases). BRCA1 and BRCA2 are both involved in the HR pathway. Defect in one of these proteins is thus deleterious for the correct DNA repair upon oxidative stress (Figure 3.B) and can create genome instability, especially after menopause. This scheme gives an explaining frame for connecting breast cancers and defect in BRCA1 or BRCA2. However, the link between BRCA1 and BRCA2 and breast cancer is still under investigation, the ROS rationale being probably insufficient.

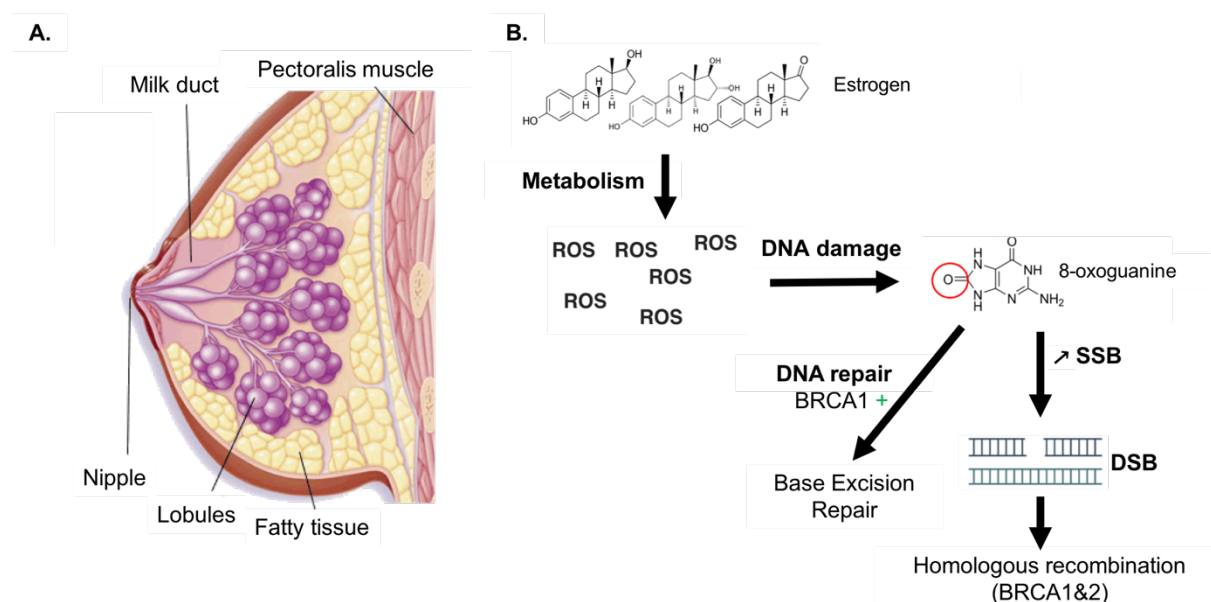


Figure 3. Origins of breast cancer. (A) Sagittal plan of a human breast. (B) Breasts produce estrogen after puberty and increase their production level after menopause. The metabolism of estrogen induces the release of Reactive Oxygen Species (ROS) in cells, causing oxidation of DNA bases such as 8-oxo-guanine. This damage is usually converted into Single Strand Break (SSB) and repaired by the Base Excision Repair (BER) system, which is stimulated by BRCA1. SSBs are converted into Double Strand Breaks (DSBs) if their number is too high for the BER. DSBs are repaired by homologous recombination through the actions of several proteins including BRCA1 and BRCA2 during late S, G2 and M phases of the cell cycle.

BRCA1 and *BRCA2* are also associated with cancer in ovaries, the primary source of estrogen before menopause. Hereditary mutations in *BRCA1* increase the ovary cancer risk of 13-29 % at 50 yo and 39-46 % at 70 yo (Stoppa-Lyonnet et al., 2004, Mersch et al., 2015). *BRCA2* has less influence than *BRCA1* on ovary cancer development (Stoppa-Lyonnet et al., 2004, King et al., 2003). In addition, *BRCA1* mutations increase the risk of prostate cancer

(Castro et al., 2012) and mutations in *BRCA2* favor pancreatic (Martinez-Useros et al., 2016), colorectal (Sopik et al., 2015), prostate (Castro et al., 2012) and melanoma cancer development (Moran et al., 2012, Mersch et al., 2014) or Fanconi Anemia (Meyer et al., 2014). However, the link between *BRCA1/2* and these cancers is not yet understood. This underlines that the hormone metabolism releasing ROS is probably not the only cancer cause.

3. Identification of breast cancer pathogenic variants of *BRCA1* and *BRCA2*

Early after the identification of *BRCA1* and *BRCA2* genes, researchers focused their attention on the identification of key mutations responsible for the increased risk of breast cancer (Li et al., 1999, Nathanson et al., 2001, Wooster et al., 1994, Tavtigian et al., 1996). Several databases regrouping *BRCA* genetic variations observed in breast cancer patients (hereditary or sporadic) emerged in the 2000s. These databases aim at spanning all BRCA's genetic modifications in order to identify causal mutations, i.e. mutations that increase the risk to develop breast cancer. "Genetic variations" or "genetic variants" is a term that corresponds to both the non-pathogenic allelic variations and the causal mutations.

Most of the available databases bring together data of patients from one country: Leiden Open Variation Database for the Netherlands (LOVD-IARC: <http://priors.hci.utah.edu/docs/index.php>), Kathleen Cuningham Foundation Consortium for Research into Familial Breast Cancer for Australia and New Zealand (kConFab: <http://www.kconfab.org/Index.shtml>), The Singapore Human Mutation and Polymorphism Database for Singapore (<http://shmpd.bii.a-star.edu.sg/>)... These national databases are important for the analysis of specific populations, which may present a specific mutation distribution. France also designed a well-documented database named the Universal Mutation Database (UMD) BRCA1/2 (<http://www.umd.be/BRCA2/brca2/> and <http://www.umd.be/BRCA2/brca1>). Since 1995, UMD-BRCA1/2 collects data from 16 licensed laboratories belonging to the French "Groupe Génétique et Cancer" consortium. The 16 licensed laboratories automatically send all the BRCA1/2 variants detected in French families. Presently, the database contains 15,955 records and 3,454 different variations identified for BRCA1 and BRCA2, 95% of variants being observed only once. A description of the UMD-BRCA1/2 content was published in 2012 (Caputo et al., 2012): the database compiled 1,391 distinct BRCA1 variants from 3,743 French families and 1,704 distinct BRCA2

variants from 3,650 families. In 2016, the UMD-BRCA1/2 evolved into a larger project named BRCA2 Share, which aimed at increasing the collection of BRCA variants (Bérout et al., 2016). This new database combines data from the UMD-BRCA1/2 with testing results from two large commercial laboratories, Quest Diagnostics and Laboratory Corporation of America. Now, BRCA Share assembles one of the largest publicly accessible collections of BRCA variants currently available.

International databases have also been built. The most cited one is the Breast Cancer Information Core (BIC: <http://research.nhgri.nih.gov/projects/bic/index.shtml>:BIC). The BIC is a voluntary international collection of variants identified worldwide. BIC data are derived from both the published literature and direct online entries contributed by researchers throughout the world (Szabo et al., 2000). Moreover, BIC aims at facilitating the detection and characterization of these genes by providing technical supports, such as mutation detection protocols, primer sequences, and list of reagents used. However, the database is no longer curated since 2019, but is still the most cited by the community.

Variants are then classified following the 5 classes system proposed by Plon. et al (Plon et al., 2008). Class 1 contains neutral variants, also called non-pathogenic variants, which do not favor the development of breast cancer. Class 5 brings together causal mutants, which significantly increase the risk of developing a breast cancer. Classification in classes 1 or 5 is based on significant evidences, in general coming from epidemiological studies. Intermediate classes 2 and 4 have also been created, named likely neutral and likely causal, respectively. These classes contain variants for which too little information is available to make clinical recommendation. Finally, class 3 is reserved for variants with an unknown clinical significance (VUS).

The classification of these variants aims at associating mutations to phenotypes and providing clear information to clinicians. This represents a decisive help in the decision to screen / follow family members or to establish medical protocols adapted to the mutation (age and degree of cancer development). A better understanding of the variant impact on cancer development also aims at preventing useless prophylactic mastectomy, which were recommended in the past to reduce the cancer risk (90 to 95% risk reduction in BRCA mutation carriers, Ludwig et al., 2016). Furthermore, the characterization of pathological BRCA variants can also improve our knowledge on sporadic breast cancers presenting a “BRCAness” phenotype, i.e. tumors with a deficiency in BRCA functions (Byrum et al., 2019).

The variants resulting in a premature termination codon are directly classified in class 5 (Caputo et al., 2012). However, most of the variants are missense, intronic variants or small insertions/deletions (56.5 % in BRCA1 and 69 % in BRCA2). Their impact on protein function and therefore their clinical significance is most often unknown (Caputo et al., 2012). Epidemiologic studies were initially used for classifying some of these variants. However, the small amount of repetition in variants (95 % are found only once in the UMD-BRCA1/2) forced the community to explore other strategies. Functional assays have notably been developed to investigate the consequences of these variants on the cellular activities of the BRCA1/2 proteins (Guidugli et al., 2014). These assays are homologous recombination assay in human cells, centrosome-amplification assay, mitomycin C survival assay and nuclear localization assay. Biomolecular experiments have also been used to test specific aspects of BRCA properties, such as RNA splicing analysis and protein-protein interaction-based assays. Several studies have already exploited these strategies to screen variants from the databases (Wu et al., 2005, Mesman et al., 2018, Petitalot et al., 2019).

Analysis of the UMD-BRCA1/2 database revealed that most of the identified variants still belong to class 3 (Bérout et al., 2016, Figure 4). To develop molecular assays for the characterization of BRCA variants, in particular BRCA2 variants in the context of my PhD, it would be beneficial to identify all the regions responsible for BRCA functions. My PhD aims at deciphering the function of conserved, yet poorly characterized, regions of BRCA2 corresponding to segments predicted to be disordered. This will further help to design molecular assays for VUS characterization. In addition, the molecular characterization of BRCA2 (partner interactions) may also contribute to identify new therapeutic targets for treating breast cancers (Helleday et al., 2014).

	BRCA1				BRCA2				Combined			
	Records		Unique variants		Records		Unique variants		Records		Unique Variants	
1. Neutral (Benign)	70,388	88.2%	114	4.5%	45,221	78.3%	123	3.3%	115,609	90.2%	237	6.4%
2. Likely Neutral (Likely Benign)	944	1.2%	142	5.6%	2,487	4.3%	218	5.9%	2,487	1.9%	360	9.7%
3. VUS	2,828	3.5%	1,423	56.0%	5,742	9.9%	2,408	64.9%	5,742	4.5%	3,831	103.2%
4. Likely causal (Likely Pathogenic)	39	0.0%	21	0.8%	46	0.1%	34	0.9%	46	0.0%	55	1.5%
5. Causal (Pathogenic)	5,626	7.0%	843	33.1%	4,276	7.4%	928	25.0%	4,276	3.3%	1,771	47.7%
Total	79,825		2,543		57,772		3,711		128,160		6,254	

Figure 4. Composition of the BRCA ShareTM French database in 2016 according to the variant classification (Bérout et al., 2016).

Chapter 2. BRCA2 structure

In the last two decades, BRCA structure and functions were investigated by a number of laboratories.

Initially, BRCA1 and BRCA2 were both characterized as DNA repair proteins ([Bertistle et al., 1998](#)). In the last years, they have been shown to be involved in a larger range of cellular pathways. BRCA1 has also a role in the homologous recombination, mismatch repair pathways, in the regulation of DNA damage checkpoints, centrosome number, chromatin remodeling, gene transcription and apoptosis ([Ohta et al., 2011](#), [Savage et al., 2015](#), [Yi et al., 2014](#), [Densham et al., 2017](#), [Sharma et al., 2018](#), [Takaoka et al., 2018](#)). BRCA2 is involved in genomic stability pathways including DNA repair, stalled replication fork stability, telomere homeostasis and also in mitotic progression, meiosis and centrosome duplication ([Thorlsund et al., 2007](#), [Choi et al., 2012](#), [Mondal et al., 2012](#), [Fradet-Turcotte et al., 2016](#), [Malik et al., 2016](#)). This ability to play roles in so many pathways is probably linked to their large size, their amino acid sequence (more than 1,000 residues) encompassing a number of different functional domains.

While BRCA1 and BRCA2 share a common name and are involved in common pathways, they have no homology in amino acid sequence and structure (**Figure 5**). On one side, BRCA1 is a 1,863 amino acids long protein, which contains three folded domains binding to protein partners. On the other side, the 3,418 amino acids BRCA2 contains only one characterized globular domain that interacts with proteins and ssDNA.

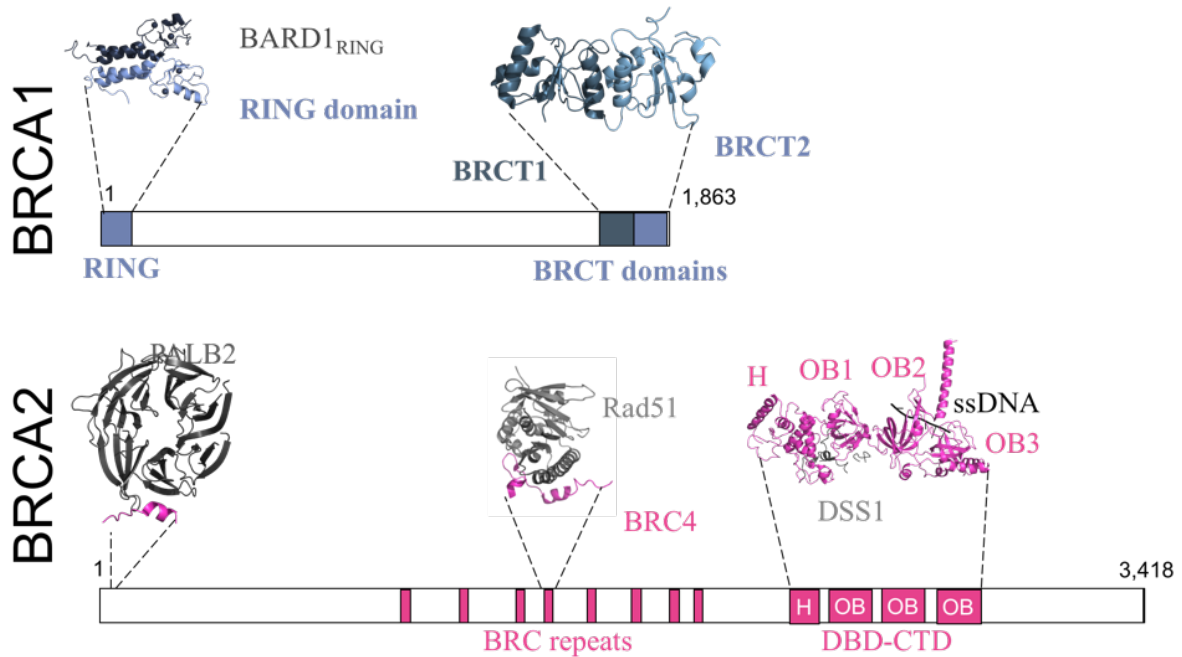


Figure 5. Comparison between BRCA1 and BRCA2 structures reveals no homology.

BRCA1 (top) is a 1,863 amino acids protein containing a cysteine-rich RING domain that forms a zinc-binding domain (aquamarine and zinc atom in grey, PDB: 1JM7). The N-terminus RING domain interacts with the RING domain of BARD1 (grey) to generate a E3 ubiquitin ligase activity. BRCA1 also contains two BRCT domains (BRCT1 in teal and BRCT2 in aquamarine, PDB: 1JNX). The two BRCTs can interact with phosphopeptides, a classical mechanism used to regulate protein-protein interaction through phosphorylation. BRCA2 (bottom) is a 3,418 amino acids protein constituted of a large N-terminal region with a PALB2 interaction site (PDB: 3EU7), PALB2 in grey and BRCA2 in pink) followed by the repetition of 8 BRC motifs. Only one of the BRC repeat structures (pink) was elucidated in interaction with the recombinase Rad51 (grey) (BRC4, PDB: 1N0W). However, due to the similarity in sequence, all the BRCs are expected to share this structure upon Rad51 binding. Interactions with PALB2 and Rad51 are essential for the BRCA2 function in DNA repair. BRCA2 also contains a DBD close to the C-terminal extremity. The mouse BRCA2 DBD structure (pink, PDB: 1MJE) was obtained in interaction with a ssDNA (black) and the protein DSS1 (grey).

The UMD-BRCA1/2 database allows an analysis of variant localization along the protein sequence (**Figure 6**). Interestingly, BRCA1 variants are mostly found in exons 2, 3, 5, 17, 18, 19 and 21, the exons that correspond to the characterized globular domains of BRCA1. However, for BRCA2, the most frequently mutated exons of BRCA2 are not systematically associated with its globular domain (exons 13 to 23). Structural biology and biochemistry studies were initially focused on the characterization of the folded domains. Hence, BRCA2 needs a deeper characterization for improving its variants classification.

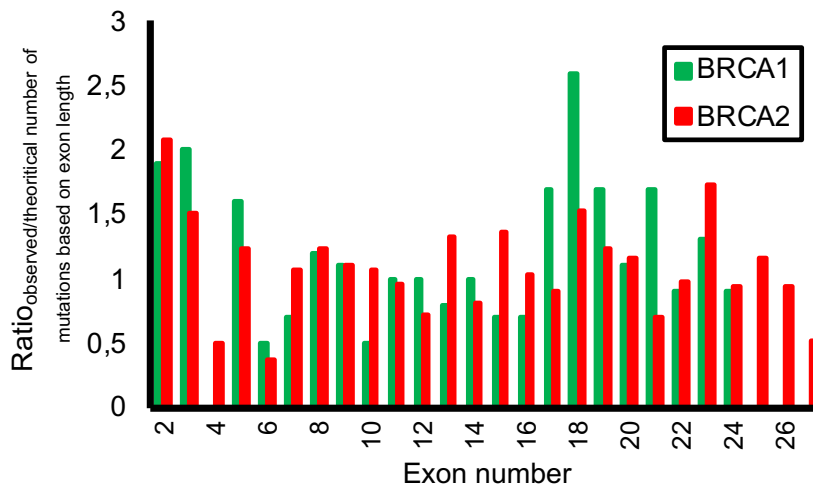


Figure 6. Ratio between observed and theoretical numbers of variants according to exon length for *BRCA1* and *BRCA2* (Caputo et al., 2012)

In this chapter, I report the current knowledge on *BRCA2* structure and I provide information about peculiarities of regions lacking a stable fold. This aims at explaining how the unfolded *BRCA2* regions can contribute to its molecular functions.

1. *BRCA2* contains a single folded domain

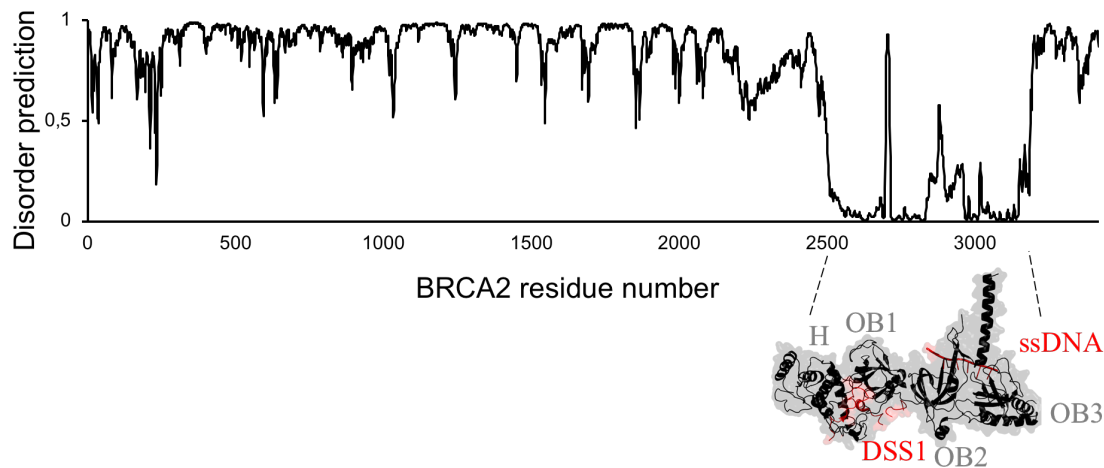


Figure 7. *BRCA2* contains only one folded domain.

BRCA2 contains a single folded domain (PDB: 1MJE, murine *BRCA2*): the DBD-CTD consisting of a helical domain (H), 3 OB-fold domains (OB) and a tower between OB2 and OB3. Other regions of *BRCA2* are predicted to be unfolded/disordered. Prediction was calculated using the server SPOT-disorder (<http://sparks-lab.org/server/SPOT-disorder/index.php>, 1: fully disordered; 0: fully ordered).

The C-terminal globular domain of *BRCA2* is the best-known region of the protein (**Figure 7**). It is the largest conserved region of *BRCA2* from mammals to fishes and its three-

dimensional structure has been resolved by X-ray-crystallography in 2002 (Yang et al., 2002). This region corresponds to a DNA binding domain (DBD) that helps to recruit BRCA2 on single-strand DNA (ssDNA) and to achieve BRCA2 functions in genome stability maintenance. The structure revealed four domains arranged in a linear fashion following this order: a N-terminal helical domain and three oligonucleotide/oligosaccharide-binding (OB) folds. A tower domain, consisting in a helix-turn-helix motif, comes out of the OB2 and supports a three-helix bundle at its top. ssDNA interacts directly with BRCA2 DBD-CTD. More precisely, it binds to the OB2 and OB3 at the base of the tower.

While only rat and mouse BRCA2 DBD-CTD structures have been resolved (Yang et al., 2002), their structure helped to characterize several human breast cancers variants (Caputo et al., 2012, Mesman et al., 2018). In our hands, the human BRCA2 DBD-CTD shows a poor stability. The sequence identity between rat, mouse and human is about 68% (compared with 42% for the entire protein, Yang et al. 2002), which suggests a similar structure. Therefore, our team built a homology model of the human BRCA2 DBD-CTD structure (Philippe Cuniasse, unpublished).

2. BRCA2 contains 80% of disorder: what is protein disorder?

The rest of the BRCA2 sequence is predicted to be disordered (**Figure 7**), i.e. unable to adopt stable secondary and tertiary structures by itself. Such objects are named Intrinsically Disordered Proteins/Regions (IDPs/IDRs) since 1986 (Hernandez et al., 1986). The absence of stable, ordered fold, hence called “disorder” is associated with a lack of deep minimum in their conformational energy landscape, unlike that of a folded globular protein (Fisher et al., 2011, Dunker et al., 2011). In fact, the IDPs/IDRs rather populate broad ensembles of diverse, interconverting conformations in dynamic equilibrium (Forman-Kay et al., 2013), with interconversion times spanning the nanoscale to the millisecond timescale. Full random coils are rare in non-denaturing media: conformation ensembles adopted by IDP/IDRs often show local structural propensities, like transient secondary structures, or long-range organization resulting from electrostatic clusters or repeated amino acids backbone torsion angle propensities, especially for prolines. Hence, IDPs/IDRs have a high diversity of degrees of compactness (Dyson et al., 2002).

IDP/IDRs are often composed of low complexity sequences and show amino acid compositional biases: they are enriched in charged and polar residues, glycine and proline, and

have low content in bulky hydrophobic residues (Val, Leu, Ile, Met, Phe, Trp and Tyr) (Uversky et al., 2000, Williams et al., 2001, Dyson et al., 2005, Theillet et al., 2013, Uversky et al., 2013). The low proportion of hydrophobic residues explains why no hydrophobic core can form in these proteins, leading to high solvent-exposure and peptide conformational behaviors resembling to random coil. In addition, IDP/IDRs can present a high net electrostatic charge, either positive or negative, a mixture of charges or alternating clusters of the same charge.

Disorder can be predicted from the protein sequence. Several servers use the amino acid composition to scan protein sequences and estimated their disorder propensity. Among the early and best-known servers, I can cite PONDR (Romero et al., 1997), DISOPRED (Jones et al., 2003), IUPRED (Dosztanyi et al., 2005), DISpro (Cheng et al., 2005). Progressively, disorder prediction softwares started to use neural networks trained using structural biology data and to incorporate evolutionary profiles and meta-methods servers. In 2019, Nielsen et al. (Nielsen et al., 2019) tested most of the disorder predictors and established that SPOT-disorder (Sequence-based Prediction Online Tools for disorder) (Hanson et al., 2016) was currently the most reliable method. It delivers an efficient prediction of both long and short disordered regions without separated training, although disordered regions of different sizes have different amino acids compositions. We used SPOT-disorder for disorder prediction of BRCA2 in **Figure 7**.

It is estimated that 40% of the eukaryotic proteins content is disordered, 35% of proteins containing disordered regions larger than 20 residues (Ward et al., 2004, Oates et al., 2013, Peng et al., 2015). Looking at the human proteome, more than 30% is estimated to be disordered (Uversky et al., 2000, Dunker et al., 2001, Dunker et al., 2008, Uversky et al., 2010). Since the publication of the first protein 3D structures by Kendrew and Perutz (Kendrew et al., 1960, Perutz et al., 1960), the structure-function dogma focused the attention of structural biologists on folded domains. Protein structures carry indeed dense informative capacities and predictive power. Resolving folded protein structures have had and will have tremendous importance in science. Neglecting the unfolded part of eukaryotic proteomes would however limit our understanding of central biological questions, like cell signaling or cell fate regulation.

3. Roles of IDRs/IDPs

Because of their high solvent accessibility and pliable conformations, IDRs/IDPs are very useful objects for organisms: i) they are exquisite targets for enzymatic post-translational

modifications, and ii) they permit establishing transient protein-protein interactions with high specificity but low affinity. In the last 20 years, an increasing number of examples revealed the importance of disordered proteins and regions of proteins in biological processes. To give an idea about the diversity of the associated functions, we can cite p21, an essential cyclin-dependent kinase inhibitor regulating cell cycle progression at the G1/S transition (Kriwacki et al., 1996), alpha-synuclein, involved in synaptic activity (Weinreb et al., 1996), the helicase subunit Mcm2, which chaperones histones (Richet et al., 2015), and several transcription factors such as p53 and c-myc (Oldfield et al., 2008, Andresen et al., 2012). Hence, IDRs/IDPs are notably carriers of intracellular information.

While folded proteins are usually more strictly positionally conserved than disordered proteins, IDRs can demonstrate high conservation of overall composition (Moesa et al., 2012, Forman-Kay et al., 2013) with an amino acid sequence evolutionarily variable (Tompa et al., 2014, Zarin et al., 2019). The robustness of disordered proteins to sequence variability has been suggested to facilitate rapid evolution of regulatory complexity (Forman-Kay et al., 2013). This could explain the widespread presence of IDP/IDRs in eukaryotes signaling networks (Xue et al., 2012). Disorder is even presented by some authors as an evolutionary tool permitting the emergence of complex eukaryotes (Schlessinger et al., 2011). However, high protein disorder content is also observed in bacteria living in environments requiring fast adaptation such as acid media, low temperature or bacteria exposed to radiations or fast evolution viruses (Tokuriki et al., 2009, Xue et al., 2012).

It is now clear that IDPs are involved in various biological functions through 2 main processes: protein interactions and formation of liquid-liquid phase-separation droplets (LLPS, Dyson et al., 2005, Forman-Kay et al., 2013, Zarin et al., 2019). These aspects of IDP/IDRs are detailed below.

a. Protein and nucleic acid interaction

The first major characteristic of IDP/IDRs is their involvement in low affinity and transient protein-protein interactions with folded domains (Borgia et al., 2018, Tang et al., 2012, Tompa et al., 2015). IDRs act as organizing scaffolds recruiting folded domains of proteins to facilitate signal integration. For example, they can serve as protein platforms that bring closer an enzyme and its substrate (Mittag et al., 2010) or be used in the context of chaperones to mediate the interaction between chaperones and clients (Kovacs et al., 2012, Foit et al., 2013). Albeit specific, IDR interactions are often of low-affinity, usually in the micromolar range (Dyson et al., 2005, Wright et al., 2009, Shammass et al., 2012, Tompa et al., 2014). This enables

ultra-sensitive switch-like (Tang et al., 2012) or rheostat-like (Lee et al., 2010, Mittag et al., 2010) responses depending on the nature of the interaction. Given the significant number of charged residues and the specific charge distribution in IDRs, electrostatic interactions, including cation- π interactions, play prominent roles (Gallivan et al., 1999, Mao et al., 2010, Marsh et al., 2010, Muller-Spath et al., 2010). Many IDRs also contain short amphipathic motifs. These motifs can include large hydrophobic residues, which are often involved in the recognition by the folded binding partner (Fuxreiter et al., 2007, Brown et al., 2010).

Upon binding, IDR can either remain disordered (fuzziness) (Tompa et al., 2008, Mittag et al., 2010), adopt a stabilized structure without secondary structural element (Richet et al., 2015) or adopt a secondary structure such as α -helix or β -strand (Davey et al., 2012, Galea et al., 2008, Wright et al., 2009, Dyson et al., 2002, Schneider et al., 2019). The disorder-to-order transition (sometimes called “folding upon binding”) contributes to the high specificity and low affinity of the interaction (Dunker et al., 1998). Furthermore, the same IDR binding motif can interact with different folded domains by adopting distinct conformations, enabling multi-specificity due to the conformational plasticity of the IDR chain (Oldfield et al., 2008). In other examples, IDRs serve as supplementary docking sites in a protein to enhance an interaction (Wang et al., 2020).

Few cases have shown that IDRs can interact not only with proteins, but also with nucleic acids (Vuzman et al., 2011, Qi et al., 2015). In fact, IDRs are abundant in DNA binding-proteins and they often interact with DNA following a disorder-to-order mechanism. In this situation, IDRs increase the overall protein-DNA interface and increase the affinity and specificity of the neighboring folded domain for DNA. Several examples have also shown that IDRs (including phosphorylated IDRs) can compete with ssDNA to bind to a protein partner (Fuxreiter et al., 2011).

The presence of interaction sites in IDRs is often revealed by the charge and polarity conservation of the interaction motif. Evolution patterns revealed that IDRs involved in protein interactions contain molecular features conserved in amino acid composition (Zarin et al., 2019) and in length (Schlessinger et al., 2011). These experimentally characterized binding motifs, referred as short/eukaryotic linear motifs (ELMs/SLiMs) (Tompa et al., 2014), are listed in the ELM database (<http://elm.eu.org>) in order to facilitate their identification in protein sequences (Davey et al., 2012, Tompa et al., 2014). ELMs are on average 6-7 amino acids long with only 3-4 core positions conferring the interaction specificity (Tompa et al., 2014). On the other side, the number of folded domains involved in ELM recognition has rapidly increased (Stein et al.,

2011). I must here acknowledge the contributions of Norman Davey, Peter Tompa, Toby Gibson and Madan Badu to this field (Tompa et al., 2014, Davey et al., 2017).

b. Post-translational modifications regulate IDR-protein interactions

I have evoked the fact that IDRs often bind to folded domains with affinities lying in the micromolar range. In the cellular environment, these interactions can be dynamically switched on or off by post-translational modifications (PTMs) on the IDR side (Mittag et al., 2010). This mechanism is very common in eukaryotic cell signaling (Iakoucheva et al., 2004, Tompa et al., 2014): it enables fast and reversible regulation of interactions upon the addition or removal of PTMs (Van Roey et al., 2012 & 2013). I present the most common eukaryotic PTMs in **Figure 8**.

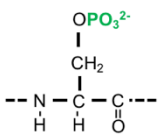
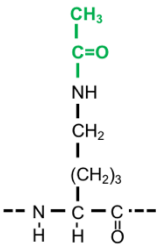
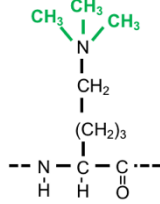
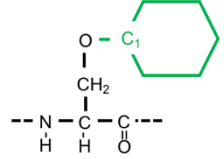
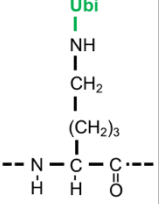
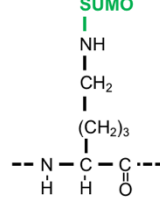
PTM	Phosphorylation	Acetylation	Methylation	Glycosylation	Ubiquitination	Sumoylation
Chemical modification						
Amino acid concerned	Serine, threonine, tyrosine, histidine	Lysine	Arginine and lysine (mono, di, tri)	Asparagine (N-linked) Serine and threonine (O-linked)	Lysine	Lysine
Charge change	0 to -2	+1 to 0	+1 to 0	No change	+1 to 0	No change

Figure 8. Common enzymatic post-translational modifications observed in eukaryotes (in green). Phosphorylation, acetylation, methylation and glycosylation consist in the addition of small chemical compounds, while ubiquitination and sumoylation lead to the addition of a small protein.

While IDRs and folded domains are both subject to PTMs, the high solvent accessibility of IDR favors their modifications by enzymes (Forman-Kay et al., 2013). Thus, IDR sequences are enriched in PTM sites and act as hub proteins in cell signalization networks (Dunker 2005, Higurashi et al., 2008). In 2014, Tompa et al. presented several examples to highlight this phenomenon: p53 (62 PTMs/393 residues in length), the tau protein (123/758), α -synuclein (22/140), Hdm2 (68/491) (Tompa et al., 2014). Their analysis suggested that the human proteome contains up to a million of PTMs, that is to say one modification every ten residues. These modifications are carried out by more than 300 distinct types of enzymes (Jensen et al., 2004).

PTMs can drastically change the net charge and physicochemical properties of a binding motif (Seet et al., 2006, Arif et al., 2010, Deribe et al., 2010, Bicker and Thompson, 2013) and thus, tune its binding/recognition capacities either positively or negatively. For example, the addition of a phosphate group can enhance the helical propensity of an IDR if a phosphoserine and a lysine are found at positions i and $i+4$, respectively (Errington et al., 2005). It has also been proposed that phosphoserines close to the helix N-terminal extremity can stabilize this helix by interfering with the helix dipole, while a phosphoserine at the helix C-terminus would have the opposite destabilization effect (Andrew et al., 2002). If the IDR binding conformation is helical, phosphorylation can thus favor or disturb the corresponding interaction.

Phosphorylation accounts for about half of PTMs detected in humans, whose genomes encodes 518 kinases, the enzymes executing this modification (Manning et al., 2002). A great number of interactions regulated by IDR phosphorylation are described in the literature. They engage in majority folded domains specialized in phosphorylation site recognition, such as WW, BRCT, 14-3-3, FHA or SH2 domains (Reinhardt & Yaffe 2013). One of the most cited examples in the field is however an exception: the phosphorylation of the disordered 4E-binding protein 2 provokes its folding in a conformation incompatible with its recognition by the eukaryotic translation initiation factor 4E, hence preventing the interaction inhibiting RNA translation (Bah et al., 2014). Phosphorylation can also regulate complex binding processes, either initiated by a priming phosphorylation event that triggers phosphorylation of later sites (Kosten et al., 2014, Gebel et al., 2020), or feedback mechanisms depending on the number of phosphorylated sites (Mylona et al., 2016).

Apart from phosphorylation, other modifications regulate IDR functions in various ways: methylation of the FUS protein, involved in neurodegeneration, modulates its nuclear import (Dormann et al., 2012); acetylation of Tau proteins, implicated in Alzheimer disease, has been shown to promote its aggregation (Luo et al., 2014); O-mannosylation can protect IDP from proteolysis (Prates et al., 2018). PTMs of histone tails are also prominent examples of the importance of PTMs on cell fate: at least 12 of the 35 disordered amino acids of Histone H3 have been detected in modified forms for example, PTMs triggering either gene activation or repression (Musselman et al., 2012, Huang et al., 2015).

Ancient PTMs sites are often functional PTMs sites (Studer RA et al. Science 2016), and thus conserved (Nguyen Ba et al., 2012). PTMs sites are also listed in the ELM database (when predicted) and in the Phosphosite database (<http://phosphosite.com>; when

experimentally identified). Most of the PTMs have been detected and identified via high-throughput mass spectrometry proteomic studies, which comes with important limitations as we will see in the next chapters.

c. Phase transition

The last characteristic of IDRs is their ability to form membraneless organelles through phase separation *in vitro* and in cells (Nott et al., 2015, Patel et al., 2015, Riback et al., 2017, Banani et al., 2017, Franzmann et al., 2018, Guseva et al., 2020, **Figure 9**). This role of IDP/IDRs has been fully acknowledged and extensively studied only recently. The membraneless organelles are driven by protein or nucleic acids multi-valent contacts, which IDRs can exquisitely establish via transient interactions of loose specificity (Fujioka et al., 2020). This leads to the formation of micron-sized liquid droplets (Li et al., 2012) that can emulate the co-localization functions of organelles (Malinowska et al., 2013). In the case of IDR intermolecular self-association, the phenomenon is favored by the amino acid composition in polar region, notably by the presence of glutamines or asparagines and of arginines and aromatics (Bergeron-Sandoval et al., 2016, Pak et al., 2016). Protocols for assembling LLPS *in vitro* or in cells have been established (Alberti et al., 2018). Interestingly, these LLPS can also be regulated by PTMs. For example, methylation of arginines or serine/threonine phosphorylation disrupt FUS LLPS (Hofweber et al., 2018, Monahan et al., 2017), and phosphorylation of the translation regulators FMRP and CAPRIN1 control their co-phase separation with RNA (Wong et al., 2020). This new role of IDPs/IDRs opens a field of research that will help to understand the cellular function of LLPS in the next years.

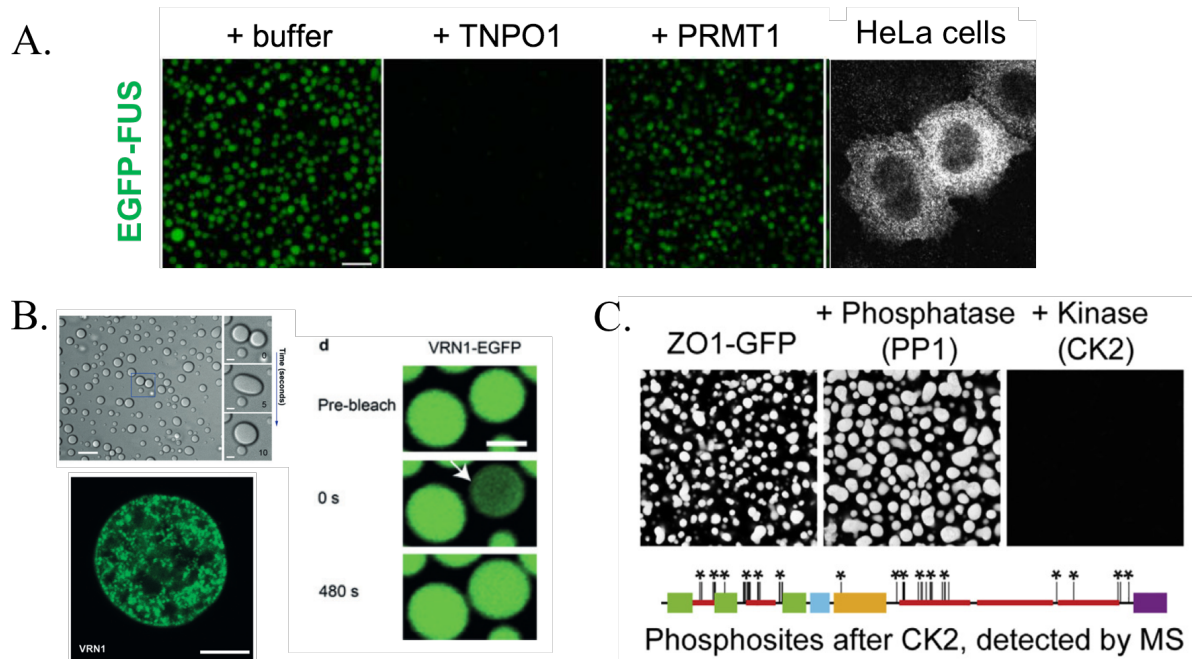


Figure 9. LLPS are observed *in vitro* and in cells and can be regulated by PTMs. **(A)** The FUS protein forms LLPS *in vitro* and in cells as observed by fluorescence microscopy (from Hofweber et al., 2018). This formation is downregulated by the overexpression of the transportin TNPO1 that transfers FUS to the nucleus. However, methylation of FUS via the PRMT1 promotes LLPS formation. **(B)** *Arabidopsis* Vernalization 1 (VRN1) forms LLPS *in vitro* and in cells as seen by contrast and fluorescence microscopies. Bleaching experiments of VRN1-EGFP reveal the fluidity of forming droplets (from Zhou et al., 2019). **(C)** *Zonula occludens* protein 1 LLPS are favored by phosphatase treatment and inhibited by CK2 phosphorylation as seen by confocal imagery (from Beutel et al., 2019).

Over the last years, the essential role of IDPs/IDRs has been revealed for many cellular processes, in particular in eukaryotic signalization pathways. Furthermore, mutations in disordered regions are more and more associated to human diseases (Forman-Kay et al., 2013), via changes in disorder-to-order transitions and binding surfaces (Vacic et al., 2012). The scientific community has been progressively focusing its attention on IDPs/IDRs in order to establish links between their mutations and diseases. This would provide new therapeutic targets (Metallo et al., 2010, Uversky et al., 2010, Rezaei-Ghaleh et al., 2012, Stevers et al., 2017). However, common biochemistry and biophysics protocols, as well as widespread knowledge on proteins, have been established in the past for studying folded domains and high affinity complexes. The relatively recent interest in IDPs/IDRs requires often novel approaches and stimulates new perspectives.

4. BRCA2 disordered regions contain PTM and interaction sites

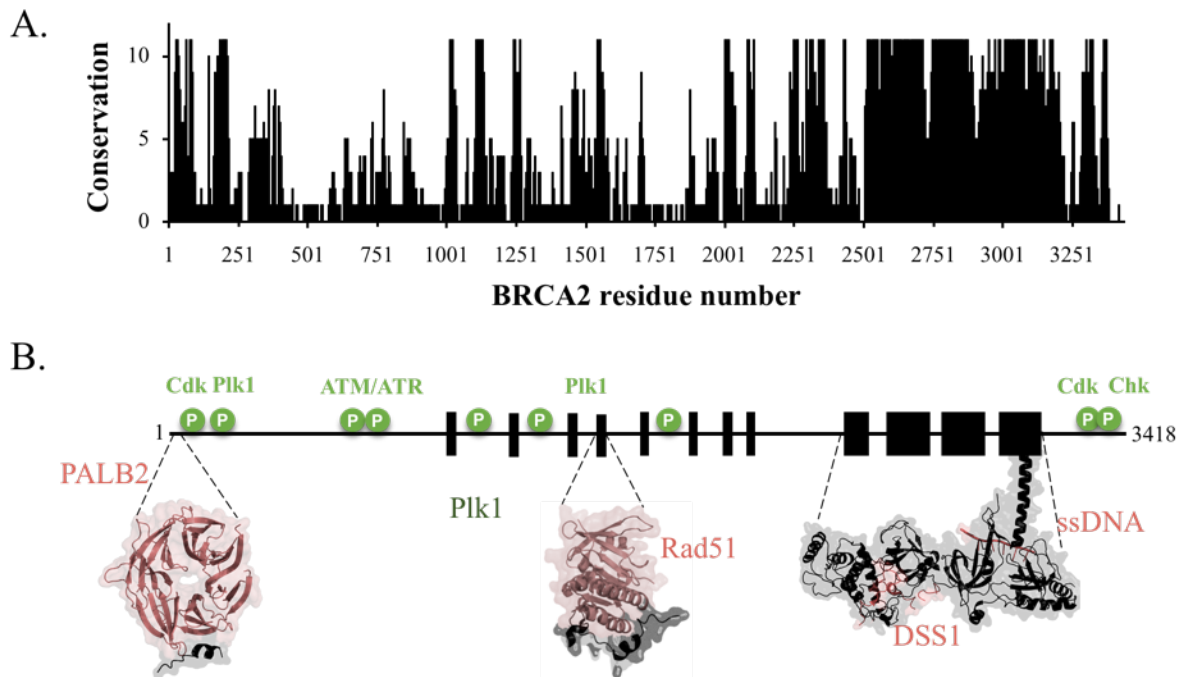


Figure 10. BRCA2 conservation, PTM and interaction sites. **(A)** Conservation of the BRCA2 sequence. Human BRCA2 sequence was aligned with 24 homologous sequences from mammals to fishes: *Mus musculus*, *Rattus norvegicus*, *Felis catus*, *Cavia porcellus*, *Bos taurus*, *Myotis brandtii*, *Heterocephalus glaber*, *Oryctolagus cuniculus*, *Otolemur garnettii*, *Equus caballus*, *Propithecus coquereli*, *Cebus capucinus*, *Rhinopithecus roxellana*, *Nomascus leucogenys*, *Erinaceus europaeus*, *Xenopus laevis*, *Sarcophilus harrisii*, *Ornithorhynchus anatinus*, *Danio rerio*, *Gallus gallus*, *Chelonia mydas*, *Alligator sinensis* and *Oreochromis niloticus*. The conservation score was calculated using Jalview 1.0 (Clamp et al., 2004). A score of 11 corresponds to a position identical in 100% of the sequences, while a score of 1 indicates that only one chemical criteria (size, hydrophobicity, global charge) is common to all variants. **(B)** Phosphorylation and interaction sites. BRCA2 contains several characterized phosphorylation sites by Cdk, (Esashi et al., 2005, Takaoka et al., 2014), Plk1 (Lin et al. 2003, Lee et al., 2004), ATM/ATR (Matsuoka et al., 2007) and Chk1/2 (Bahassi et al., 2008). 3D structures containing BRCA2 regions are displayed below: DBD-CTD with DNA and DSS1 (PDB: 1MJE, murine BRCA2), BRCA2₂₁₋₃₉ in interaction with PALB2 (PDB: 3EU7) and BRCA2_{BRC4} in interaction with Rad51 (PDB: 1N0W).

We estimate from disorder predictions that 80% of the BRCA2 protein is disordered (Figure 7). Interestingly, several of these disordered regions are conserved (Figure 10.A), which may reveal possible roles in BRCA2 functions.

Two interactions between BRCA2 conserved IDRs and protein partners have been described structurally (Figure 10.B). A BRCA2 N-terminal peptide (aa 21 to 39) binds to PALB2 (Oliver et al., 2009), and a central BRCA2 segment (aa 1519 to 1548) binds to Rad51

(Pellegrini et al., 2002). Both structures show BRCA2 peptides binding in helical conformations. The BRCA2 region interacting with Rad51 is called BRC. 8 BRC repeats are found in the BRCA2 sequence. The only published BRC structure has been obtained with the BRC4 fused to the Rad51 ATPase domain (Pellegrini et al., 2002). Interaction sites for BRCA2/PALB2 and BRCA2/Rad51 are conserved through the animal kingdom (**Figure 10.A**). Other conserved patches are observed, in particular in the BRCA2 N-terminal region, but no structural information on their binding properties are described in the literature.

BRCA2 also contains several experimentally detected PTM sites. These sites are represented in **Figure 10.B**. They are mainly phosphorylated by mitotic kinases such as Cdk1, Chk1/2 and Plk1, and by DNA damage response kinases including ATM and ATR. In addition to phosphorylation, another PTM has been identified in BRCA2: asparagine 272 has been shown to be N-glycosylated by the CRB protein (Siddique et al., 2009). However, no functional study has been carried out to understand the role of this glycosylation.

While BRCA2 may be observed as forming foci in cell, especially during DNA repair, no formation of LLPS involving BRCA2 has been described in the literature yet.

In addition, we can mention electron-microscopy studies, which observed BRCA2 multimerization (Shadid et al., 2014, Le et al., 2020). Electron microscopy data of purified BRCA2 from HeLa or HEK cells show a wide range of particle sizes and structural heterogeneity (Le et al., 2020). An early 3-dimensional reconstruction revealed two-fold symmetric particles, interpreted as dimeric BRCA2 particles (Shadid et al., 2014) (**Figure 11**) but the low-resolution model could not help to precisely reconstruct the BRCA2 structure. These results and their significance have been recently questioned by another group, which proposed that DSS1 and DNA binding disrupt BRCA2 multimerization. Shadid et al., 2014 and Le et al., 2020 i) used weak reducing conditions (0.25-1mM DiThioThreitol DTT or tris(2-carboxyethyl)phosphine TCEP at pH7.5, Thorslund et al., 2010) to achieve self-association assays of BRCA2 IDRs showing high cysteine content, and ii) Le et al., 2020 generated EM maps and models from complexes stabilized using cross-linking agents, although these complexes supposedly contain highly flexible regions. These simple remarks may raise concerns and call for cautious consideration. While BRCA2 is predicted to be mostly disordered, the models have globular, donut shapes, which might be an artefact due to sample heterogeneity. In fact, according to our expertise in the field, purification of the entire BRCA2 protein is a challenging task: i) the ~60 IDR solvent-exposed cysteines along BRCA2 sequence are difficult to maintain in their reduced state during the purification process (especially when using only 1 mM DTT at pH7.5 like the evoked studies); ii) the solubility of purified IDRs is

far from being common, their hydrophobic patches requiring chaperones or cognate partner interactions to avoid precipitation. In addition, because BRCA2 is produced in human cells, PTMs and ligands may be present and favor BRCA2 dimerization. Further studies will be necessary to understand whether and how BRCA2 self-organize.

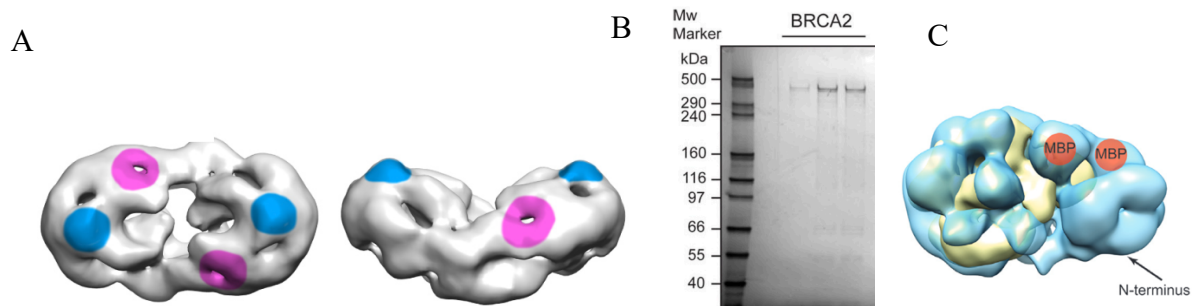


Figure 11. Dimer particles of BRCA2 as reported by Shadid et al., 2014 and Le et al., 2020. **(A)** The 3D model obtained by Shadid et al., 2014 was reconstructed from EM data is seen as a top (left) and a side (right) view. Particles dimensions are 25nmx12nmx13.5nm (in a dimer, folded structure, a 3,418 residues long protein would occupy a 9-10 nm sphere volume) Blue and pink spots respectively revealed the localization of the C-term FLAG tag and BRC repeats. **(B)** SDS-PAGE of purified BRCA2 used for EM images. The protocol did not include any gel filtration step, which generally prevents contamination by aggregates or other proteins before EM analysis. **(C)** 3D reconstruction of the monomeric BRCA2-DSS1-ssDNA complex from Le et al., 2020. Comparison of the crosslinked BRCA2 complex (EMD-21998, blue) versus uncrosslinked complex (EMD-20348, yellow). Mapped MBP tag from D is shown in orange, and N-terminus is labeled.

To conclude, in this **Chapter** we have seen that BRCA2 is a protein mostly constituted of disordered regions, which are associated with interactions and PTM sites. In the **next Chapter**, we will explore the current knowledge about the cellular roles of BRCA2 IDRs.

Chapter 3. Functions of BRCA2

To be able to put my study and its results into their biological context, I felt I needed have a broad view of the known roles of BRCA2 disordered regions. Hence, I initiated a review of the literature focusing on BRCA2 interactions experimentally observed (mainly from pull-downs) and their associated functions. This bibliographic knowledge was necessary to understand the signaling crosstalks occurring on BRCA2 and to draw hypothesis on BRCA2 direct or indirect interactions upon PTMs. This chapter corresponds to the summary of this work and was written in the perspective to publish a review about it.

BRCA2 is expressed in every cell of the human body with tissue-dependent expression levels (<https://www.proteinatlas.org>). Beyond being ubiquitous, BRCA2 is also an essential protein that impairs organism development when depleted at the embryogenic stage (Sharan et al., 1997). After organism development, depletion of BRCA2 by siRNA reveals a wide range of genomic instabilities including defects in DNA repair (Lee et al., 2007), mis-regulation of telomere length (Kwon et al., 2016, Kwon et al., 2019), or meiotic impairment and infertility (Sharan et al., 2004). BRCA2 mutations have been associated with aberrations in both chromosome segregation and cell division (Daniels et al., 2004). Consistently, BRCA2 is involved in several functions related to genome stability such as DNA repair, telomere homeostasis, replication stalled fork stability, and also in mitotic and meiosis progression and centrosome duplication. However, the molecular aspects of its mitotic and meiotic functions are poorly described.

To execute all these functions, BRCA2 is expressed at every stage of the cell cycle, except the G0 phase (Wang et al., 1997, **Figure 12.A**). When overexpressed, it is located in the nucleus and the cytoplasm (**Figure 12.B**). However, endogenous BRCA2 localization revealed that its localization is cell-cycle dependent. In fact, BRCA2 contains 2 Nuclear Leading Sequences (NLS) (Yano et al., 2000), which allow its nuclear localization at every steps of the cell cycle, and one Nuclear Export Sequence (NES), which promotes its transport to the cytoplasm especially during interphase (Jeyasekharan et al., 2013) (**Figure 12.C and 12.D**)

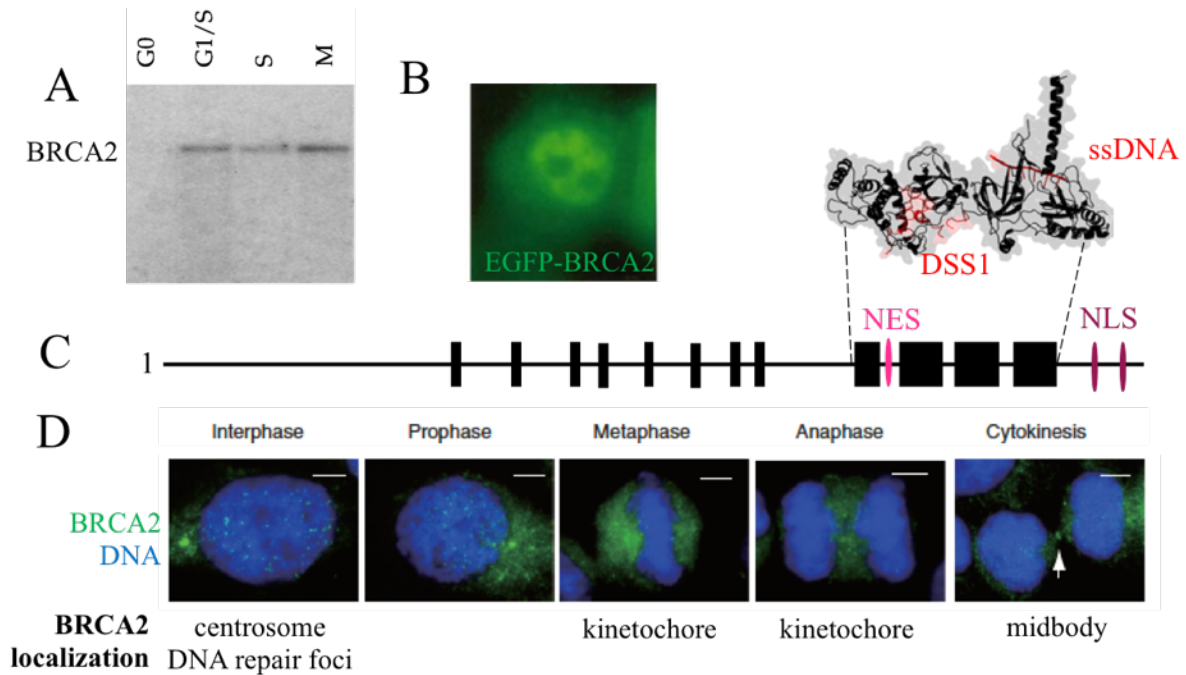


Figure 12. Expression and localization of BRCA2 through the cell cycle. **(A)** Northern blot of BRCA2 mRNA from MCF-10F cell extracts synchronized at different stages of the cell cycle (from Wang et al., 1997). **(B)** EGFP-BRCA2 expressed in HeLa cells under the control of a CMV promoter is localized in the nucleus and the cytoplasm during interphase (from Yano et al., 2000). **(C)** BRCA2 contains one NES between the helical and the OB1 domain of its C-terminal DBD (aa 2681-2700), which is masked by the protein DSS1 (red, Jeyasekharan et al., 2013), and two NLS after the DBD (aa 3266-3269 and aa 3311-3315) (Yano et al., 2000). **(D)** BRCA2 localization during the cell cycle in fixed cells stained for BRCA2 (fluorescent antibody) and DNA (Hoechst 33258 stain), scale bar 5 μ m (from Takaoka et al., 2014).

Throughout this **Chapter**, I present the molecular functions of BRCA2 and especially how IDRs and PTMs contribute to these functions through the cell cycle. Published direct interactions and their associated molecular function are listed in **Table 1** and **Annexe 1**. The mitotic functions of BRCA2 and their associated PTMs are most extensively described in this chapter, because they correspond to the core context of my PhD project.

Table 1. Interaction between disordered regions of BRCA2, proteins, DNA, through BRCA2 cell cycle function.

Partner of BRCA2	Interacting BRCA2 region	Function	Reference
PALB2	21-39	DNA repair	Oliver et al., 2009
EMSY	25-36	DNA repair	Hughes-Davies et al., 2003
DNA	250-500	DNA repair	Von Nicolai et al., 2016
PLK1	885-2115	DNA repair	Lee et al., 2004
Rad51 monomers	BRC1-4	DNA repair	Carreira et al., 2011
FANCD2	2350-2545	DNA repair	Siddiqui et al., 2017
Rad51 filaments	BRC 5-8	DNA repair	Carreira et al., 2011
PLK1	3189-3418	DNA repair	Yata et al., 2014
Rad51 filaments	3270-3305	DNA repair	Esashi et al., 2005
Poln	1338-1781	Replication forks	Buisson et al., 2014
Cytoplasmic dynein 1	2884-2903	Centrome localization	Malik et al., 2016
HSF2BP	2117-2339	Localization to DSB during meiosis	Zhang et al., 2019
DMC1	2382-2411	Meiosis recombination	Thorslund et al., 2007
Plk1	pT77	Chromosome segregation and cytokinesis	Yata et al., 2014
PLK1	pT207 (200-209)	Chromosome segregation	Ehlen et al., 2020
PCAF	290-453	Chromosome segregation	Fuks et al., 1998
BubR1	2861-3176	Chromosome segregation	Futamura et al., 2000
BubR1	3189-3418	Chromosome segregation	Choi et al., 2012
Alix and CEP55	271-836	Cytokinesis	Mondal et al., 2012
HMG20b	BRC5	Cytokinesis	Lee et al., 2014
Filamin A	2973-3001	Cytokinesis	Yuan et al., 2001
CBP	1-188	Unknown	Siddique et al., 2009
BCCIPa	2973-3032	Unknown	Liu et al., 2001

1. Homologous recombination

a. System description

The first identified function of BRCA2 is its role in the Homologous Recombination (HR) DNA repair pathway (Patel et al., 1998). Homologous recombination consists in the repair of double-strand breaks (DSBs) via the search for the lost DNA information on the sister

chromatid (**Figure 13**). HR takes place during S and G2 phases, when two copies of the genome are available in cells. Defects in this process generate unrepaired DNA DSBs, which are highly toxic for the cell, increasing the risk of genome instability, and thus of cancers.

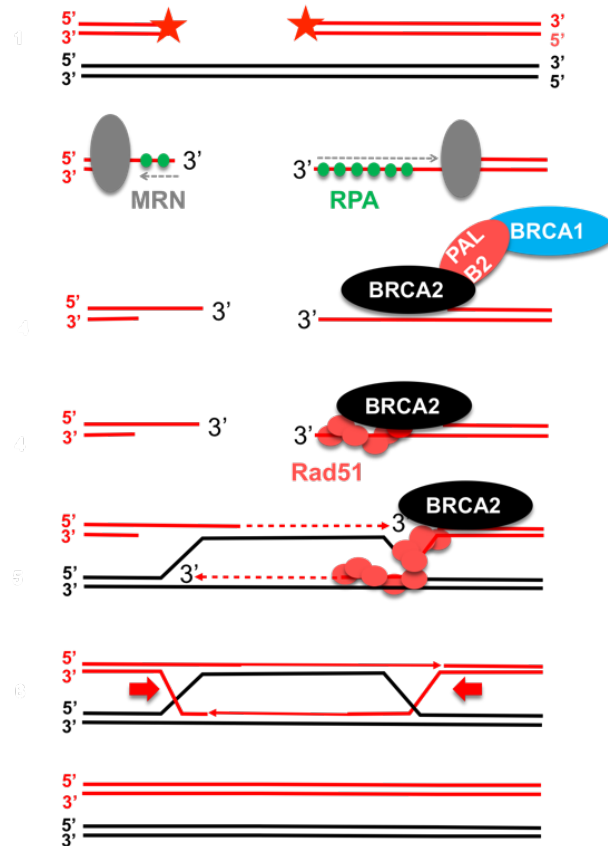


Figure 13. Role of BRCA2 during Homologous Recombination.

Upon DSB breaks (red stars), the MRN complex resects 5' extremities of the broken DNA. It creates 3' single-strand extremities that are protected from nucleases by the small protein RPA. DSB break stimulates the formation of the BRCA1/PALB2/BRCA2 complex, and its localization at the DNA break. Then, BRCA2 loads Rad51 on single-strand DNA and favors its polymerization. Once Rad51 is polymerized, the recombinase invades the sister chromatid and drives homologous recombination. The DNA complex is finally solved by endonucleases and ligases (red arrow) leading to several resolution possibilities, only one is presented here.

The recruitment of BRCA2 to DNA damage sites is mediated by the protein PALB2, that interacts with BRCA2(21-39) (Oliver et al., 2009). PALB2 recognizes DNA breaks via BRCA1, which is bound to resected DNA. A trimeric complex is then formed via the direct interaction between PALB2-BRCA2 and PALB2-BRCA1 (Sy et al., 2009, Oliver et al., 2009), which is responsible for the recruitment of BRCA2 on the lesion. However, until now, only an indirect interaction has been observed between BRCA1 and BRCA2. The localization of BRCA2 via PALB2 is essential for an efficient homologous recombination. In fact, PALB2 mutants with impaired BRCA2 binding decrease the capacity for DNA DSB-induced HR and increase cellular sensitivity to ionizing radiations (Park et al., 2014).

BRCA2 weakly interacts with the broken DNA through its DBD-CTD (Yang et al., 2002), as described in **Chapter 2.1**. The protein DSS1 binds the OB1 domain of BRCA2 DBD-CTD via electrostatic interactions, in presence or absence of DNA (Yang et al., 2002). This interaction hides the BRCA2 NES, which may favor BRCA2 nuclear localization. Furthermore, cell biology and biochemical studies showed that DSS1 stabilizes monomeric BRCA2 and promotes BRCA2-mediated recruitment of Rad51 and thus HR (Gudmundsdottir et al., 2004, Li et al., 2006, Kristensen et al., 2010, Liu et al., 2010).

Another DBD has been identified in the N-terminal region of BRCA2 (250-500) by our collaborators (Carreira and colleagues) (Von Nicolai et al., 2016). While this region is predicted to be disordered, they have established its capacity to interact with a large panel of DNA structures (ssDNA, dsDNA, gapped DNA and 3'/5'-overhang). In addition, DBD-NTD promotes Rad51-mediated HR. In the literature, IDRs interacting with DNA are often located next to a DNA-binding globular domain and tune its DNA affinity (Vuzman et al., 2011). In BRCA2, the contribution of the DBD-NTD region to the BRCA2 DNA binding properties and to the HR process needs further investigations.

After its recruitment to the DNA damage locus, BRCA2 loads the recombinase Rad51 on DNA (Fradet-Turcotte et al., 2016). The recombinase is then polymerized along the broken DNA, further invades the sister chromatid and drives the homologous recombination. BRCA2 interaction with Rad51 is driven by its 8 BRC repeats. Only one of these interactions has been solved by X-Ray-crystallography, namely the BRCA2-BRC4:Rad51 complex (**Figure 10**). BRCs load monomeric Rad51 on ssDNA and favor Rad51 polymerization along the DNA extremity. Nevertheless, all the repeats do not have the same affinity for Rad51. The first 4 repeats have high affinity for monomeric Rad51. They trigger the nucleation of Rad51 polymerization along the ssDNA. They act by reducing the ATPase activity of Rad51 (Carreira et al., 2009) and by enhancing the DNA strand exchange by Rad51 (Carreira et al., 2011). On the other side, BRC5-8 stabilize Rad51 filaments to ensure their growth along DNA (Carreira et al., 2011). This permits the creation of a fiber of Rad51 molecules ready for the chromatid sister invasion and the search of homology.

BRCA2 contains also a Rad51 binding region located in its CTD: the TR2 region. Because its binding interface engages two adjacent Rad51s, this TR2 region shows a high affinity for Rad51 filaments but not for monomers (Esashi et al., 2007). Bahassi et al. (Bahassi et al., 2008) proposed that Rad51 is bound in an inactive form to BRCs in normal cells, and can be transferred to the TR2 to activate Rad51 when needed.

In addition to its role in somatic cells, BRCA2 also contributes to the recombination process during meiosis. Here, BRCA2 interacts with the meiosis-specific recombinase DMC1. This interaction is mediated by several regions of BRCA2. The region comprised between BRC8 and the DBD (between aa 2382 and aa 2411) was initially identified as responsible for binding to DMC1 (Thorslund et al., 2007). The TR2 region is also able to bind DMC1 but with an affinity that is much weaker than for Rad51. The authors suggested that both DMC1 and Rad51 recombinases may act during meiosis. Finally, a more recent study showed that DMC1 interacts with the BRC repeats, especially BRC 6-8, which present a higher affinity for DMC1 than for Rad51, strengthening the idea of a cooperation between both recombinases (Martinez et al., 2016).

The meiotic localizer HSF2BP (also named MEILB2) is proposed to be responsible for the localization of BRCA2, Rad51 and DMC1 during meiotic recombination (Zhang et al., 2019; Brandsma et al., 2019). In fact, disruption of HSF2BP abolishes the localization of Rad51 and DMC1 in spermatocytes and leads to sterility. HSF2BP was shown once to interact directly with BRCA2 and to regulate its association with DSBs during meiosis (Zhang et al., 2019). Interestingly, while HSF2BP is needed during meiosis, its overexpression in somatic cell lines (as observed in some cancer cell lines) triggers BRCA2 degradation and prevents RAD51 loading on DNA inter-strand crosslinks, thus compromising homologous recombination (Sato et al., 2020).

Other proteins such as FANCD2, FANCI and XPG bind BRCA2 and are involved in the regulation of BRCA2 localization to chromatin. Upon DNA damage, BRCA2 forms a complex with the CUE domain of FANCD2 and the ARM repeat in FANCI (Siddiqui et al., 2017). FANCD2 is then monoubiquitylated in its interaction region with BRCA2, favoring the loading of BRCA2 onto chromatin (Wang et al., 2004, Siddiqui et al., 2017). Concerning XPG, the protein interacts directly with BRCA2, Rad51 and PALB2 to favor chromatin binding and Rad51 foci formation (Trego et al., 2016). Further results are needed to understand deeply this mechanism. Finally, the NTD (25-36) region of BRCA2 interacts with EMSY, a transcriptional repressor suggested to interact with chromatin remodelers. However, its role in BRCA2 genome stability functions remains unclear (Hughes-Davies et al., 2003).

b. Regulation of HR by PTMs

Several HR interactions are regulated by PTMs upon DNA damage.

First, in normal cells, the ubiquitin-specific protease 21 (USP21) has been shown to contribute to BRCA2 cellular stability by deubiquitinating it (Liu et al., 2016). The authors showed that BRCA2 deubiquitinylation favored the localization of Rad51 to DSB, ensuring the correct repair of DSB.

Second, upon DNA damage the interaction between TR2 and Rad51 is abolished by phosphorylation. When cells are exposed to DNA damaging agents, kinases Chk1/2 phosphorylate T3387, close to TR2. This leads to the dissociation of Rad51 from TR2 (Bahassi et al., 2008) and triggers the release of active polymerized Rad51 and its re-localization to new DNA damage foci.

Third, at the end of the S-phase, when HR has to be completed before mitosis entry, BRCA2 is phosphorylated by Cdk on residue T77 during late S-phase (Figure 14 Yata et al., 2014). pT77 has been shown to create a docking site that recruit efficiently the kinase Plk1, expressed at early-mitosis. BRCA2 acts as a landing platform bringing Plk1 close to Rad51 during the transition. This favors Rad51 phosphorylation at position S14 by Plk1 and also the phosphorylation of pT13 by CK2 (Yata et al., 2012 & 2014). Phosphorylation of Rad51 by Plk1 and CK2 enhances the interaction between Rad51 and the MNR component Nbs1 involved in the DSB resection (Yata et al., 2012). Hence, these phosphorylation events promote efficient HR repair of DSBs before mitosis.

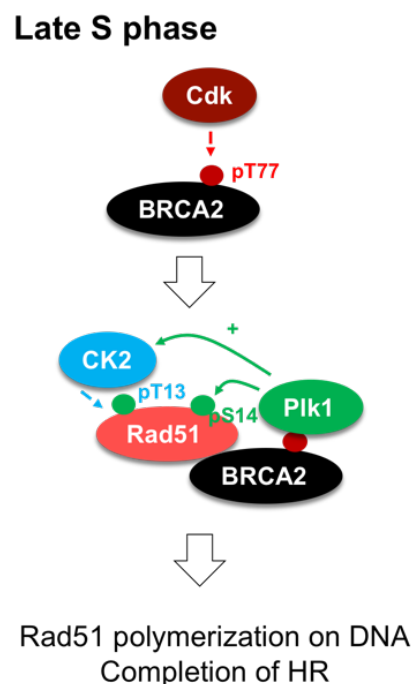


Figure 14. Phosphorylation events by Cdk and Plk1 Cdk enable completion of homologous recombination.

2. During interphase, BRCA2 interacts with other proteins to ensure genome stability and centrosome duplication.

a. Pathways

BRCA2 ability to preserve genome stability through DNA binding and Rad51 polymerization is useful in others pathways.

First, the loading of Rad51 by BRCA2 is essential for preserving telomere stability (Badie et al., 2010). This comes from the observation that BRCA2 depletion leads to shorten telomere extremities and accumulation of fragmented telomeric signals, indicating replication defects at telomeres (Badie et al., 2010). However, the exact mechanism by which BRCA2 helps to protect telomere stability is not yet completely elucidated (Fradet-Turcotte et al., 2016).

BRCA2 is also involved in centrosome duplication. BRCA2 contains a centrosomal localization signal (2884-2903) (Nakanishi et al., 2007), recognized by the cytoplasmic dynein 1, which drives BRCA2 positioning at centrosomes during S-phase (Malik et al., 2016).

Finally, polymerized Rad51 also protects exposed ssDNA upon replication stress (Fradet-Turcotte et al., 2016). Protection of nascent DNA is essential for the replication fork to correctly restart, while preserving at the same time genome integrity. Interaction between the TR2 region of BRCA2 and Rad51 filaments is essential for fork protection: it prevents chromosomal aberrations due to Mre11 upon fork stalling (Schlacher et al. 2011). This was demonstrated using two separation of function mutants, S3291A and S3291E, that abrogate RAD51 binding by the C-terminus; cells bearing the mutations are defective in replication fork protection but their DSB repair by HR remains essentially intact. Furthermore, PALB2 and BRCA2 facilitate the recruitment of Pol η by interacting directly with the polymerase (Buisson et al., 2014). The BRCA2 binding region of PALB2 and BRCA2 region from aa 1338 to aa 1781 (BRC3/4) are responsible for binding to the polymerase. The trimeric complex stimulates the initiation of recombination-associated DNA synthesis by Pol η .

b. Regulation by PTMs

Yata et al., 2014 showed that BRCA2 T77 phosphorylation levels were reduced in BRCA2 bearing a TR2 mutation or C-terminal truncation. TR2 would therefore indirectly alter the Plk1 interaction with the N-terminal region of BRCA2, leading to a reduced level of Rad51 phosphorylation at S14.

BRCA2 is also phosphorylated at the entry into mitosis at S3291 by Cdks (**Figure 14.B** [Esashi et al., 2005](#)) and between BRC repeats by Plk1 ([Lee et al., 2004](#)). Phosphorylation of S3291 of BRCA2 by Cdks increases through G2/M ([Esashi et al., 2005](#)). S3291 is localized close to the TR2 region of BRCA2 and its phosphorylation negatively regulates the interaction between BRCA2 and Rad51 filaments. This event is dispensable for HR, but promotes Rad51 filament disassembly, which, in turn, promotes entry into mitosis ([Ayoub et al., 2009](#)). In addition, Plk1 phosphorylates BRCA2 between repeats BRC1 and BRC2, BRC2 and BRC3, BRC5 and BRC6 of BRCA2 at the entry of mitosis ([Lee et al., 2004](#)). These phosphorylation events are inhibited upon DNA damage; however, their consequences still remain unclear.

All these interactions between BRCA2 and partners, either protein or DNA, suggested that BRCA2 plays the role of a scaffold protein for genome stability during interphase. However, while BRCA2 was initially highly scrutinized for its DNA repair and protection of replication fork functions, it also has functions during mitosis.

3. Role of BRCA2 during mitosis

a. Role during chromosome segregation

BRCA2 interacts with the mitotic checkpoint kinase BubR1 ([Futamura et al., 2000](#), [Choi et al., 2012](#)). BubR1 is a critical component of the mitotic checkpoint that delays the onset of anaphase until all chromosomes have established bipolar attachment to the microtubules. Mutations of the *BUB1B* gene (encoding BubR1) causes premature chromatid separation syndrome, a condition characterized by constitutional aneuploidy and a high risk of childhood cancer ([Hanks et al., 2004](#)). BubR1 is phosphorylated by Plk1 on its two tension-sensitive phosphosites S676 and T680 at the kinetochore ([Elowe et al., 2007](#), [Suijkerbuijk et al., 2012](#)). These phosphorylation events are required for establishing stable kinetochore-microtubule attachments. When the proper tension is achieved at the kinetochore, BubR1 is no longer phosphorylated by Plk1 ([Elowe et al., 2007](#)).

BubR1 is also acetylated by the transcriptional co-activator protein p300/CBP-associated factor (P/CAF). BRCA2 interacts with the lysine acetyl-transferase P/CAF via the BRCA2 region 290-453 ([Fuks et al., 1998](#)). This interaction may bring P/CAF and its substrate BubR1 closer to each other during pro-metaphase, thus favoring BubR1 acetylation ([Choi et al., 2012](#)). However, the contribution of BRCA2 to BubR1 acetylation is still unclear. Furthermore, the interaction sites between BRCA2 and BubR1 are discussed in the literature

(Futamura et al., 2000, Choi et al., 2012). Once the chromosomes are aligned, acetylated BubR1 is recognized by HDAC2/3, polyubiquitinated, becomes a substrate of Anaphase Promoting Complex (APC/C)-Cdc20 and is then degraded (Choi et al., 2009, Yekezare and Pines 2009, Park et al., 2017), leading to the inactivation of the spindle assembly checkpoint (Santaguida et al., 2015), and initiating chromosome segregation.

b. Phosphorylation by Plk1 regulates BRCA2 function in chromosome segregation

Plk1 (Polo-like kinase 1) phosphorylates N-terminal BRCA2 substantially during mitosis (Figure 15.A). Plk1 mitotic phosphorylation sites are located in the region 1-284 of BRCA2 (BRCA2₁₋₂₈₄) (Figure 15.B) (Lin et al., 2003) and deletion of the BRCA2 region 193-207 abolishes BRCA2₁₋₂₈₄ phosphorylation by Plk1 *in vitro* (Figure 15.C). Alanine-mutation of S193, as well as combined alanine-mutation of four residues of this motif (S205A, S206A, T203A, T207A) cause a significant decrease of BRCA2 phosphorylation by Plk1, revealing that Plk1 phosphorylates at least S193 in the 193-207 region of BRCA2 (Lin et al., 2003).

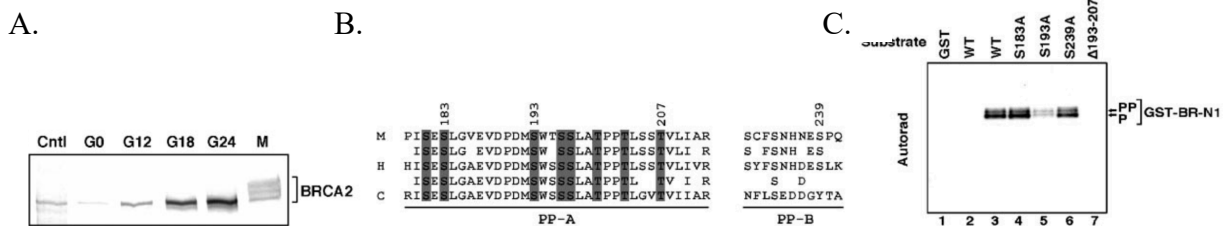


Figure 15. BRCA2 is phosphorylated by Plk1 at the entry into mitosis (from Lin et al., 2003) (A) T24 cells were synchronized, released and analyzed at several time points of the cell cycle (Gxx indicates the number of hours between release and analysis). Cell lysates were immunoblotted with antibodies against BRCA2. In M phase, the smear profile of BRCA2 suggests several phosphorylation states. (B) Two phosphopeptides (PP-A and PP-B) were identified by mass spectrometry. (C) *In vitro* kinase assays were performed to measure phosphorylation of BRCA2₁₋₂₈₄ mutants by Plk1.

These phosphorylation events are not linked to DNA damage (Lin et al., 2003). However, they have been shown to release P/CAF from BRCA2 through an unknown mechanism (Figure 16.A, Lin et al., 2003). In addition, while both BRCA2 and BubR1 have been shown to interact and to be phosphorylated by Plk1 during mitosis (Figure 16.B), it is not clear how all these proteins work together in cell. The two main and non-exclusive hypotheses are summarized in Figure 16.

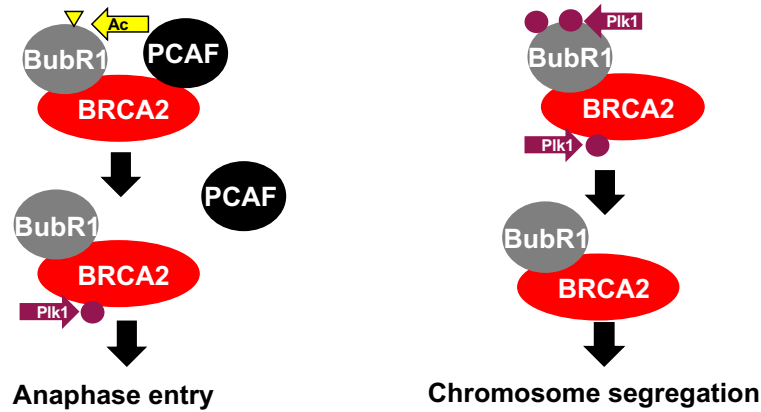


Figure 16. BRCA2 is a central component of the spindle assembly checkpoint. (A) BRCA2 exhibits binding sites for the kinase BubR1 and P/CAF. This favors acetylation of BubR1 by P/CAF (Futamura et al., 2000, Choi et al., 2012). Upon BRCA2 phosphorylation by Plk1, P/CAF is released, which contributes to a decrease in BubR1 acetylation and favors anaphase entry. (B) BubR1 is phosphorylated by Plk1 at two positions: S676 and T680. Dephosphorylation of these sites triggers exit from the spindle assembly checkpoint and chromosome segregation (Elowe et al., 2007).

c. BRCA2 phosphorylation by Cdk1 and Plk1 ensure its localization at the midbody

While all BRCA2 sites phosphorylated by Plk1 are probably not yet fully identified, one phosphoresidue is clearly associated to BRCA2 function during mitosis: phosphorylation of S193 by Plk1 is essential for the localization of BRCA2 at the midbody during cytokinesis, and more precisely at the Flemming body (Figure 17, Takaoka et al., 2014). The mutant S193A fails to localize to the midbody, while the phosphomimic S193E is sufficient to restore BRCA2 localization. This suggests an important role for this phosphoresidue in BRCA2 localization to the midbody.

In addition, an N-terminal region of BRCA2 centered around T77 (aa1-157) competes with full-length BRCA2 for its localization to the midbody (Takaoka et al., 2014). In cells, T77 is phosphorylated from late S-phase to mitosis by Cdk1 (Cyclin-dependant kinase, Yata et al., 2014, Takaoka et al., 2014). This phosphoresidue creates a docking site that efficiently recruits Plk1. Mislocalization of BRCA2 in presence of ectopic expression of BRCA2₁₋₁₅₇ suggests that pT77 is essential for S193 phosphorylation and midbody localization of BRCA2. However, the relationship between pT77 and pS193 and the role of pS193 in BRCA2 localization at the midbody still need to be clarified.

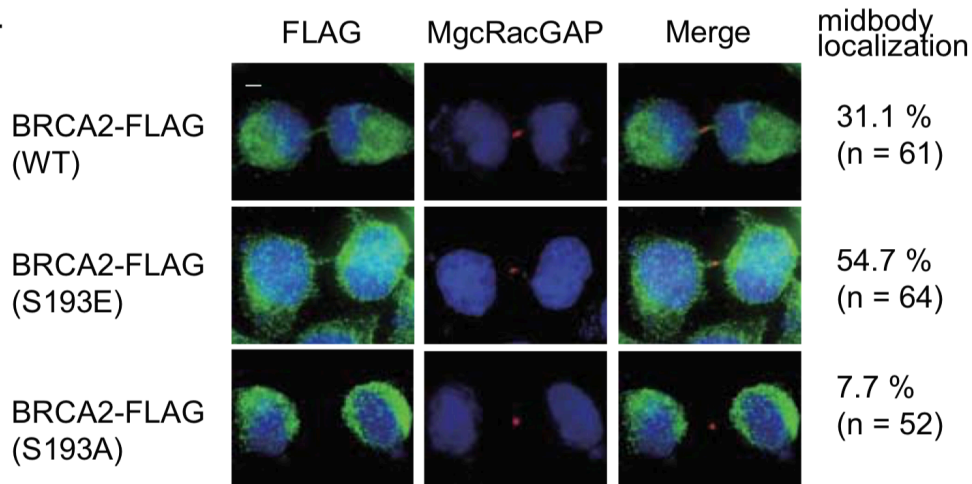


Figure 17. BRCA2 phosphorylated on S193 by Plk1 is localized at the Flemming body (from Takaoka et al., 2014)

Cells transfected with BRCA2-FLAG, BRCA2-FLAG (S193E) or BRCA2-FLAG (S193A) expression plasmid vector were fixed and stained with anti-FLAG (green) and anti-MgcRacGAP (red) antibodies. DNA was stained with DAPI (blue). Midbody localization of BRCA2-FLAG was observed. BRCA2-FLAG (WT) and S193E mutant co-localized with MgcRacGAP, but S193A mutant did not co-localize with MgcRacGAP. Scale bar: 5 μ m

Another region of BRCA2 has been shown to play a role in localizing BRCA2 to the midbody. The actomyosine protein Filamin A interacts directly with BRCA2 aa2973-3001 (Yuan et al., 2001) and mediates BRCA2 localization to the midbody (Mondal et al., 2012). Several BRCA2 breast cancer mutants in the BRCA2 Filamin A binding domain disrupt this interaction and lead to BRCA2 mislocalisation and cytokinesis failure (Mondal et al., 2012). Interestingly, Mondal et al. didn't find that the S193 region was important for directing the BRCA2 localization to the midbody. Thus, further investigations are needed to understand how these two mechanisms contribute to the correct localization of BRCA2 at the end of mitosis.

d. Several BRCA2 interactions take place in the context of cytokinesis

BRCA2 is essential for the localization at the midbody of important cytokinesis regulators such as PRC1, MKLP1 and MKLP2 (Mondal et al., 2012). This suggests that BRCA2 could act as a platform protein essential for the progression of the end of mitosis.

A direct interaction between the N-terminal region of BRCA2 and the protein responsible for the central ring formation, CEP55, was also identified (Mondal et al., 2012). CEP55 is involved in the recruitment of the ESCRT complex that drives the abscission of membranes via an interaction with Alix and Tsg101 (Morita et al., 2007). BRCA2 acts here as a central component by regulating the recruitment of Alix and Tsg101 to the midbody, creating

independent docking sites for CEP55, Alix and Tsg101 and favoring their assembly (Mondal et al., 2012).

BRCA2 interacts with NMH-IIC (Takaoka et al., 2014), the myosin involved in the formation of the cleavage furrow. NMH-IIC forms a 1.5 μm diameter ring needed for the abscission. Interaction with BRCA2 increases the NMH-IIC ATPase activity and thus, favors ring formation by NMH-IIC. It is another essential interaction between BRCA2 and a midbody factor because silencing of BRCA2 prevents the ring formation.

BRCA2 interact with HMG20b (Marmorstein et al., 2001), the kinesin-like coiled-coil protein implicated in G2/M transition, and colocalized at the midbody (Lee et al., 2014). While the function of HMG20b during cytokinesis is not elucidated, it seems to be involved in abscission. Depletion of HMG20b leads to cytokinesis failure (Lee et al., 2011), but the C-terminal region of the protein (173-317) is sufficient to restore the phenotype (Lee et al., 2014).

Lastly, it has been suggested that BRCA2 binds to the Aurora B kinase, an important regulator of midbody function, during cytokinesis (Ryser et al., 2009).

4. Region of interest

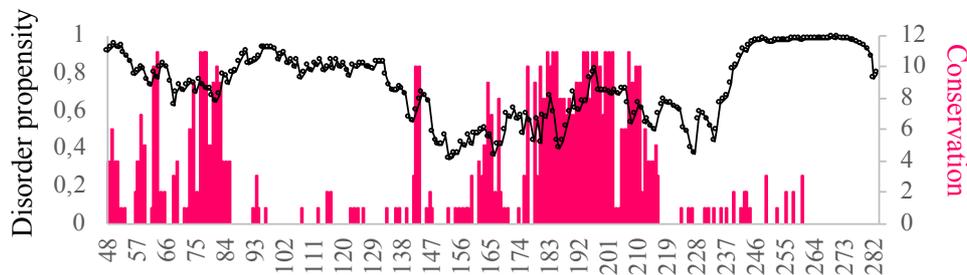


Figure 18. Exon 6 (aa 172 to aa 210) is conserved.

The disorder propensity and conservation of the BRCA2 region from amino acid 48 to amino acid 284. The disorder propensity was calculated using SPOT-Disorder (Hanson et al., 2016). A score of 1 corresponds to a predicted disorder propensity of 100%. The conservation score was calculated using Jalview 1.0 (Clamp et al., 2004). A score of 11 corresponds to a position identical in 100% of the sequences, while a score of 1 indicates that only one chemical criteria (size, hydrophobicity, global charge).

During my PhD, I was interested in the regions encompassing Cdks (T77) and Plk1 (at least S193) phosphosites of BRCA2. As shown in **Figure 18**, these two regions are well conserved among the animal kingdom. Mitotic Plk1 phosphorylations (193-210) are comprised in a large conserved region from aa 180 to aa 217. This suggests that this region may contain BRCA2 Plk1-dependant interactions sites not yet described. In addition, mainly variants of unknown clinical significance are found in exon 6, coding for aa 172 to aa 210, (Caputo et al.

2012). A deeper molecular characterization of this region may thus allow to better understand how PTMs contribute to BRCA2 mitotic functions and characterize a set of VUS to identify new causal variants disrupting BRCA2 functions.

In order to describe thoroughly the role of Plk1 phosphorylation in BRCA2 mitotic functions, I focused on the following questions: which residues of BRCA2 are phosphorylated by Plk1? Which interactions do they regulate? What are the molecular mechanisms triggering and triggered by pT77 and pS193? How does pS193 mediate the BRCA2 localization at the midbody? To answer these questions, I had to understand how Plk1 generally works on its substrates and choose an experimental strategy to monitor the BRCA2 phosphorylation events. **Chapter 4** is thus dedicated to Plk1 and **Chapter 5** describes the technical approaches available for studying phosphorylation.

Chapter 4. How does Plk1 work?

Plk1 is a member of the Polo-like kinases (Plks) family, a serine/threonine kinase family initially identified in *Drosophila melanogaster* (Sunkel & Glover, 1988). Several Plks homologs exist through the animal kingdom including budding and fission yeast (Kitada et al., 1993, Ohkura et al., 1995), *Danio rerio*, *Xenopus laevis* (Duncan et al., 2001), *Caenorhabditis elegans* (Ouyang et al., 1999, Chase et al., 2000), and mammals (Barr et al., 2004).

Plks have been shown to be essential to cell life since their discovery: depletion of Plk in *Drosophila melanogaster* leads to chromosomal aberrations, including abnormal circular chromosomes, multipolar and connected poles during chromosome segregation, defects in chromosome segregation and polyploid cells (Sunkel and Glover, 1988). Through the last 30 years, studies have progressively revealed that Plks are involved in several steps of the cellular division including mitotic entry and exit, spindle formation, cytokinesis and meiosis. All these functions are executed by only one isoform of Plk in yeast, named Cdc5. In contrast, mammals possess 5 isoforms associated with specialized functions (Barr et al., 2004, Figure 19).

Organism	Plk*	Main proposed functions†
Mammals	Plk1	Many roles during mitosis and cytokinesis
	Plk2 (Snk)	DNA-damage response, regulation of synaptic plasticity, G1/S function
	Plk3 (Fnk, Prk)	DNA-damage response, regulation of synaptic plasticity, G2/M function
	Sak (Plk4) [‡]	Mitotic exit
<i>Xenopus laevis</i>	Ptx1	Involved in mitotic entry and mitotic exit
	Ptx2	ND
	Ptx3	ND
<i>Drosophila melanogaster</i>	Polo	Regulation of mitosis and cytokinesis
<i>Caenorhabditis elegans</i>	Plc1, Plc2, Plc3	Required for nuclear-envelope breakdown
<i>Schizosaccharomyces pombe</i>	Plo1p	Regulation of mitosis and cytokinesis
<i>Saccharomyces cerevisiae</i>	Cdc5	Regulation of meiosis, mitosis and mitotic exit

Figure 19. Polo-like kinase family members and their functions (from Barr et al., 2004)

In the context of my PhD, I focused on the Plk1 protein. This Chapter is dedicated to the presentation of the human Plk1 kinase and the emerging questions we had to tackle in the context of its interplay with BRCA2.

1. Plk1, a central kinase for mitosis

Plk1 is an abundant kinase that is activated at the entry of mitosis. It is localized either in the nucleus or the cytoplasm. Plk1 contains 2 Nuclear Localization Signals (NLS) in a conserved region of the N-terminal kinase domain : aa 134 to 146 (Taniguchi et al., 2002). Deletion of these two NLS prevents the correct nuclear localization of Plk1 and stop cells in G2 phase (Taniguchi et al., 2002). Depletion of Plk1 in embryonic mice leads to a lethal phenotype at the 8 steps of development (Lu et al., 2008), and its depletion in cultured human cells leads to a pro-metaphase arrest (Bruskard et al., 2007). These results underline the importance of Plk1 in cell cycle progression. It is now clear that Plk1 functions correspond to an impressive list linked to essential events for the cell-cycle, including DNA replication (S-phase), recovery after DNA damage (G2 phase), centrosome maturation (G2/M transition), mitosis entry through the control of Cdk1 activation (G2/M transition), activation and regulation of the APC/C complex (prophase to metaphase), formation of the kinetochore, attachment and nucleation of microtubules, alignment in the metaphase plate and spindle assembly checkpoint inactivation (prophase to anaphase), Golgi fragmentation (prometaphase) and cytokinesis. All these functions are represented in **Figure 20**. For more details, several reviews on Plk1 functions are available (Liu et al., 2010, Strebhardt et al., 2010, Schmucker et al., 2014, Colicino et al., 2018).

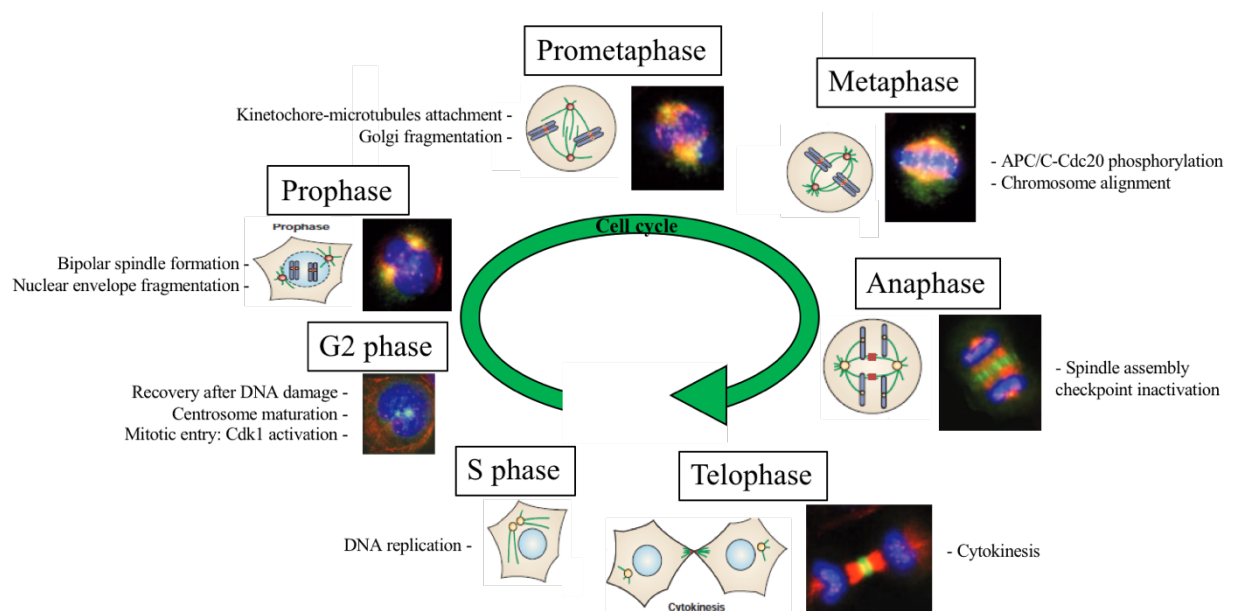


Figure 20. Plk1 functions through the cell cycle (adapted from Barr et al., 2004, Van der Weerd et al., 2006, Archambault et al., 2009, Liu et al., 2010, Strebhardt et al., 2010, Schmucker et al., 2014, Colicino et al., 2018). Microscopy images highlight Plk1 (green), DNA (blue) and tubuline (red) localizations in HeLa cells at different steps of the cell cycle.

2. Plk1 contains a kinase domain and a Polo-Box domain interacting with specific phosphorylated motifs

Plks share a common architecture composed of two globular domains: a N-terminal catalytic S/T kinase domain and a C-terminal regulatory domain containing one or two Polo-Box (PB) motifs (Polo-Box Domain, PBD) (**Figure 21**). In mammals, the PBD of Plk1-3 and Plk4 exhibit two and one PB motifs, respectively ([Barr et al., 2004](#)). Plk5 misses the N-terminal catalytic domain and establishes protein interactions only via the PBD region. The functional selectivity of Plks can be partially explained by the structural variations between isoforms.

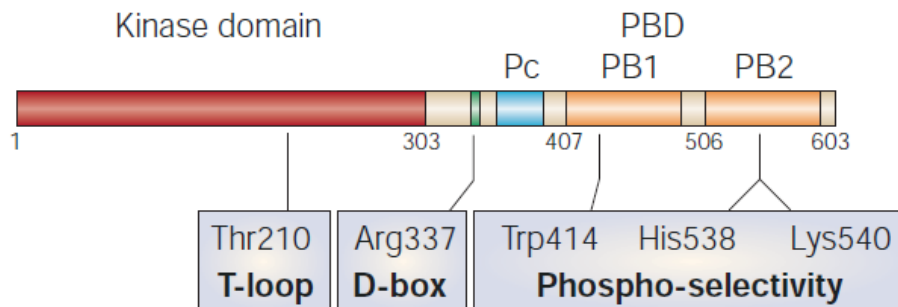


Figure 21. The common architecture shared by Plks. Plks are composed of a N-terminal catalytic domain (kinase domain) that is activated through phosphorylation of its T-loop, a Destruction bod motif (D-box) and a docking region composed of a PBD domain recognizing well-defined phosphorylated motifs (from [Barr et al., 2004](#)).

Plk1 contains one N-terminal kinase domain (KD) and a C-terminal domain composed of 2 PB motifs. The kinase domain of Plk1 executes the catalytic function of the kinase, i.e. the transfer of a phosphate group from ATP to the side chain of the target residue. Plk1 is a S/T kinase, that is to say it only phosphorylates serine and threonine residues on the target protein. The optimal phosphorylation sequence recognized by the kinase domain of Plk1 has been identified from the analysis of variants of Cdc25C, a target of Plk1 phosphorylated at position S198 ([Nakajima et al., 2003](#)). Mutating residues at positions -6 to +5 around the phosphoresidue revealed that residues at positions -2 to +3 were essential for phosphorylation by Plk1. Furthermore, a glycine at position -1 inhibited the phosphorylation reaction. The authors concluded that the optimal target sequence for Plk1 is: D/E-X-pS/pT- Φ , with X for any amino acid and Φ for a hydrophobic amino acid. Other contributions allowed to refine the consensus

sequence to to [S/D/E/N]-X-p[S/T]- ϕ , with ϕ for hydrophobic residue at position $i+1$ or $i+2$ (Alexander et al., 2011 Kettenbach et al. 2012). From this consensus motif, favored phosphosites can be predicted in Plk1 targets (see **Results**).

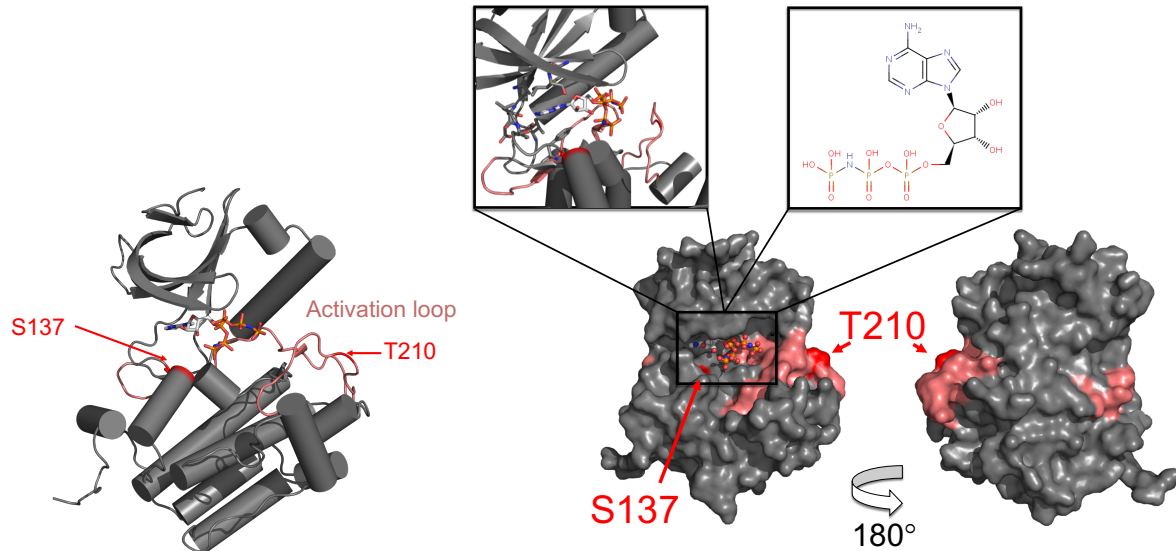


Figure 22. 3D structure of the kinase domain of human Plk1 (PDB: 2OU7, adapted from Kothe et al., 2007)

The kinase domain of Plk1 is represented in dark grey cartoon (left) or surface (right) mode. The activation loop is highlighted in orange (left) or red (right) (zoom in left square), and the two residues involved in Plk1 activation, S137 and T210, are colored in red. The non-hydrolysable ATP (adenylyl-imidodiphosphate, AMP-PNP, zoom in right square) is displayed in grey sticks.

Several 3D structures of human Plk1 KD have been solved by X-ray crystallography. The kinase domain is composed of the top and bottom regions separated by an activation loop (**Figure 22**). The activation loop is responsible for a common regulatory mechanism in kinases (Scheeff et al., 2009). Among others, it partially hides the ATP binding site of the catalytic domain in the inactive kinase.

Activation of the catalytic domain is mediated by the phosphorylation of one threonine in the loop (Jang et al., 2002). Autoinhibited Plk1 is activated by phosphorylation of the conserved T210 (Qian et al., 1999, Jang et al., 2002) by the kinase Slk (Johnson et al., 2008) or a cooperation between Bora and Aurora A kinases (Macurek et al., 2008, Seki et al., 2008) at the entry of mitosis. A study on *Xenopus laevis* Plk1 also proposed that the PKA kinase may activate Plk1, but no equivalent reaction has been demonstrated in mammals, to the best of our knowledge (Barr et al., 2004). Phosphorylation of T210 leads to a change in the conformation of the activation loop that results in global structural changes in the kinase, leading to the adoption of the adequate conformation for ATP binding and substrate

recognition. Upon this activation, the kinase can catalyze with its highest cognate efficiency the transfer of a phosphate group from ATP to its protein target. Activity tests were carried out on the kinase domain of Plk1 in order to confirm the importance of T210: the WT Plk1 kinase domain has a k_{cat} of 4.1 ms^{-1} on Cdc25 (Kothe et al., 2007); a phosphomimetic mutation T210D improved this k_{cat} up to 19 ms^{-1} , while a mutation T210V inhibiting T210 phosphorylation decreased the k_{cat} down to 1.9 ms^{-1} , with little change in the $K_{m(ATP)}$: 3.2, 4.0, and 3.0 μM for Plk1 WT, T210D, and T210V respectively. These results are consistent with an important role of T210 in the activation of Plk1.

Interestingly, another phosphorylated residue was identified as improving the activity of Plk1: S137 (Figure 22). A phosphomimetic mutant S137D led to an increased activity of both Plk1-WT and Plk1-T210D in cells (Jang et al., 2002). These results showed a non-additive effect of the two mutations suggesting a different role for pS137. In fact, while the mutation T210D leads to a spindle assembly checkpoint-dependent delay and delayed M-phase, the mutant S137D results in untimely activation of the anaphase-promoting complex and early S-phase with separated centrosomes (Jang et al., 2002, Van der Weerd et al., 2005). Both phosphosites contribute to proper mitotic progression, with specialized functions for each phosphoresidue. In cell, these two phosphorylations appear during M-phase, T210 phosphorylation preceding S137 phosphorylation and the latter occurring in late mitosis (Van der Weerd et al., 2005). S137 is located at the transition of the hinge region between the top and bottom region of the KD and a helix of the bottom region (Figure 22). The accessibility of this residue for its phosphorylation by a kinase is not obvious and is probably mediated by a first conformational rearrangement (Xu et al., 2013). This phosphorylation may modulate Plk1 substrate specificity (Xu et al., 2013). Plk2, an isoform of the human Plks proteins, has been shown to be able to phosphorylate Plk1 S137 (Matsumoto et al., 2009). However, no further study explored the mechanism by which S137 phosphorylation would regulate Plk1 activity.

The second domain of Plk1 is the C-terminal Polo Box Domain (PBD). Its 3D structure elucidation revealed an arrangement of 2 conserved PB folds (Elia et al., 2003, Figure 23). The two PBs are packed together and form a 12-stranded β -sandwich flanked by helical segments. The domain structure was solved in complex with phosphopeptides: the PBD recognizes selectively peptides containing either a phosphoserine or a phosphothreonine (Figure 24). The target consensus sequence is S-pS/pT-P/X with X for any amino acid (Elia et al., 2003, Elia et al., 2003). Phosphopeptides comprising such a motif have an affinity of about 300 nM for the PBD (Elia et al., 2003, Zhu et al., 2016). The interaction leads to an equimolar complex

engaging one phosphopeptide for one PBD. The phosphopeptide interacts with the two PB folds: the phosphate of the pT interacts with H538 and K540 of PB2 through hydrogen bonds, the side chain of the serine -1 creates H-bonds with W414 and L491 of PB1 (**Figure 24**). This explains the selectivity for the phosphoresidue and the serine at position -1. A proteomic screen identified that 600 proteins have a phospho-dependent interaction with Plk1, through its PBD, showing that this kinase is a central component of the cell ([Lowery et al., 2007](#)).

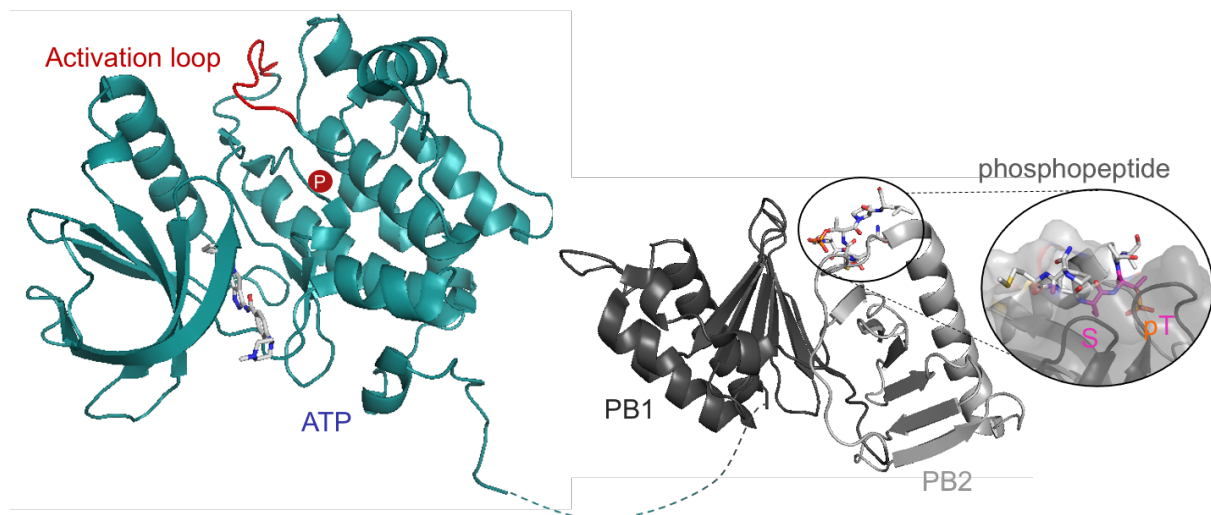


Figure 23. Model of human Plk1 from X-Ray structures.

Plk1 is composed of a kinase domain (blue, PDB: 2OWB), containing an activation loop (red) and an ATP binding site, and a PBD (grey, PDB: 1UMW) made of two PB folds (light and dark grey) binding phosphopeptides. The KD and PBD domains are linked by a 40 amino acids loop.

By interacting with proteins previously phosphorylated by other kinases, the PBD drives the cellular localization of Plk1. The PBD substrates are also genuine targets of Cyclin dependent kinases (Cdk) and MAPKs (Mitogen-activated protein kinases): Cdks and MAPKs phosphorylate S/T-P motifs ([Nash et al., 2001](#)). This creates a priming phosphorylation event on targets, triggering their recognition by Plk1 PBD ([Neef et al., 2007](#), [Zhu et al., 2016](#)). It permits a temporal and spatial regulation of Plk1 recruitment by its targets ([Elia et al., 2003](#), [Barr et al., 2004](#), [Elowe et al., 2007](#), [Wong & Fang, 2007](#), [Yamaguchi et al., 2005](#), [Yamashiro et al., 2008](#), [Zhu et al., 2016](#)). Importantly, the priming phosphoevent can also be created by Plk1 itself ([Neef et al., 2003](#), [Kang et al., 2006](#), [Lee et al., 2008](#)). This mechanism is named “self-priming” and, in cells, it appears that it can also contribute to Plk1 target recognition.

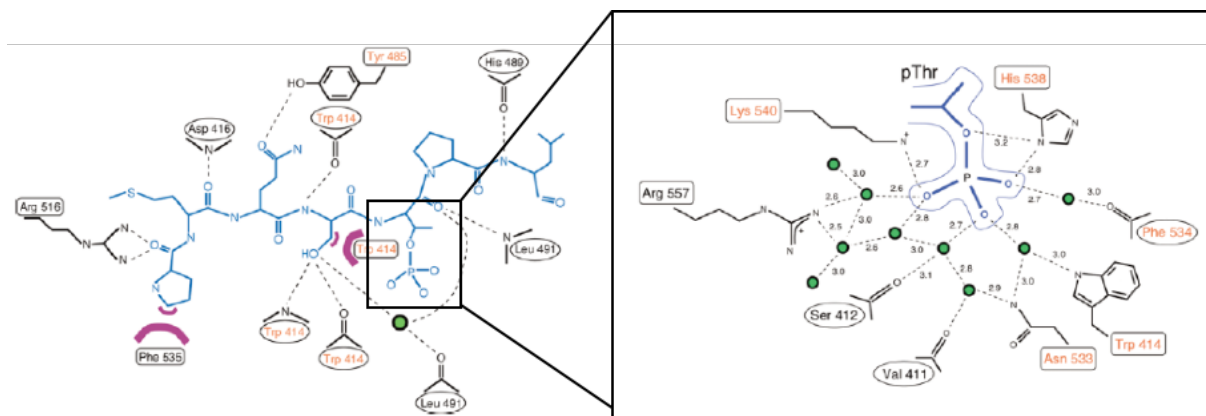


Figure 24. Interaction between Plk1(PBD) and a phosphopeptide (from Elia et al., 2003) The phosphopeptide (blue) interacts with PB1 and PB2: its side- and main-chain atoms established H-bonds with the two PBs, forming a zipper-like structure at the edge of the PB1/PB2 interface. The phosphate group participates in eight hydrogen-bonding interactions, explaining why binding is strictly phosphorylation dependent. The only residues that contact the phosphate group directly are His-538 and Lys-540 from PB2. In contrast, the Ser-1 side-chain is directed toward the PB1 surface, and forms two hydrogen bonding interactions with the Trp-414 main-chain atoms, and one with the Leu-491 carbonyl via a water molecule.

3. Dynamics between the two domains of Plk1

The interplay between the KD and the PBD domains of Plk1 is poorly characterized. This is mainly due to the difficulty to crystallize the full-length kinase. A stable complex KD:PBD has been crystallized though: the complex was generated by co-expression in *E. coli* of the KD and the PBD from *Danio rerio* together with a PBD binding motif of a microtubule associated protein Map205 from *Drosophila* that stabilizes the PBD (Xu et al., 2013). Mutations were introduced in the KD and PBD to eliminate auto-phosphorylation and facilitate crystal packing. In the crystal structure of the complex (Figure 25, PBD: 4J7B), the PBD coordinates the overall architecture by interacting with the KD and the Map205 domain.

The structure revealed how the PBD acts as a negative regulator of the kinase domain. Several intramolecular interactions mediate this autoinhibition. A surface of 2,240 Å² is buried between the two domains, the linkers L1 (between the polo-cap Pc and PB1) and L2 (between PB1 and PB2) of the PBD being mainly responsible for binding to the KD (Figure 25). First, L1 is anchored in the concave surface of the KD (Figure 25.B). This decreases the flexibility of the ATP binding pocket in the KD, as revealed by the B factors (Xu et al., 2013). Second, the disordered L2, between PB1 and PB2, shows a large conformational change upon phosphopeptide binding (Figure 25.C). Because phosphopeptide binding increases the activity of the kinase, L2 appears to play a role in Plk1 activation.

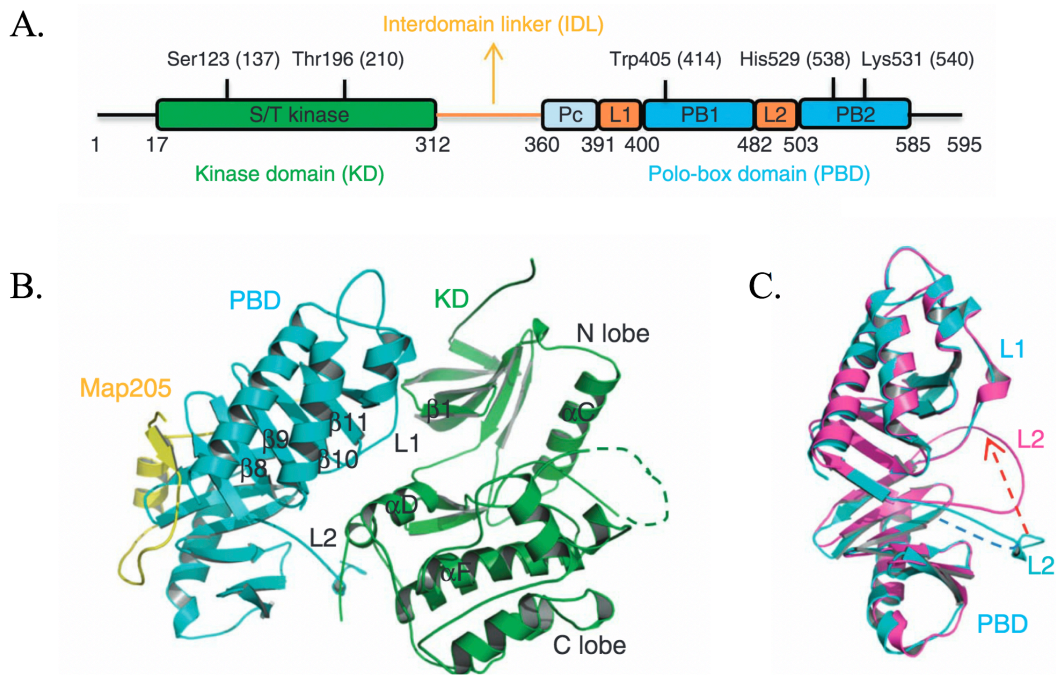


Figure 25. The interaction between the KD and PBD of Plk1 explained its autoinhibition (from Xu et al., 2013).

(A) Architecture of the Plk1 zebrafish kinase. S/T kinase, serine/threonine kinase; Pc, Polo cap; L1, linker region 1; PB1, polo box 1; L2, linker region 2; PB2, polo box 2 (B) Cartoon representation of the interaction between the 2 domains. (C) Conformational change of L2-PBD crystal structures in a KD-bound state and a phosphopeptide-bound state (from blue to pink).

This structure may also explain the activation role of human S137, zebrafish S123. Indeed, S123 is involved in H-bonds, notably with E126, that maintain a local structure and a H-bonds network bridging the KD with L1 (**Figure 26**). S123 phosphorylation may provoke a repulsion of E126, triggering local structural rearrangements and a release of L1. Pulldowns of PBD with KD-WT or KD-S123D confirmed the loss of interaction in presence of a negative charge in position 123. T210 (zebrafish T196) is not involved in the KD/PBD interaction, but its phosphorylation is, nevertheless, indispensable for the ATP pocket activation.

Another interesting point is the role of the 40 amino acids interdomain linker (IDL, **Figure 26**). The KD with the linker but without the PBD display a 10-fold increased activity compared to the full kinase. Furthermore, the KD without the linker shows a five-fold increased activity compared to that of KDs with the linker. This suggests an inhibitory effect of this interdomain linker on the Plk1 activation and activity. However, further studies are needed to understand this effect.

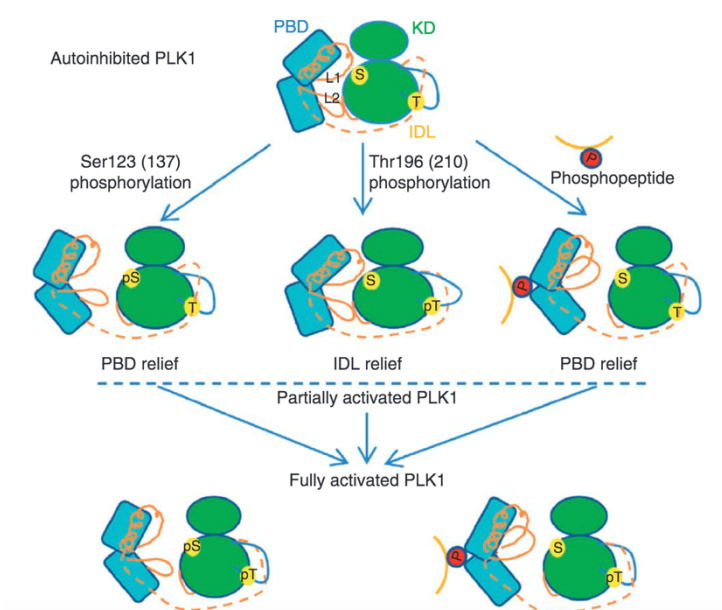


Figure 26. Model of multilevel regulation of zebrafish Plk1 (from Xu et al., 2013). Autoinhibited Plk1 can be activated through phosphorylation of the conserved human T210 in the activation loop, or of S137 at the end of the KD hinge region by upstream kinases. Plk1 can also be activated by phosphopeptide binding with the PBD.

The great structural similarity between zebrafish and human structures of Plk1 suggests similar mechanisms of action (**Figure 27**). Nevertheless, further studies on human Plk1, in particular on the role of the interdomain linker, would permit to better understand this kinase and to provide useful information in the context of new therapeutic strategies.

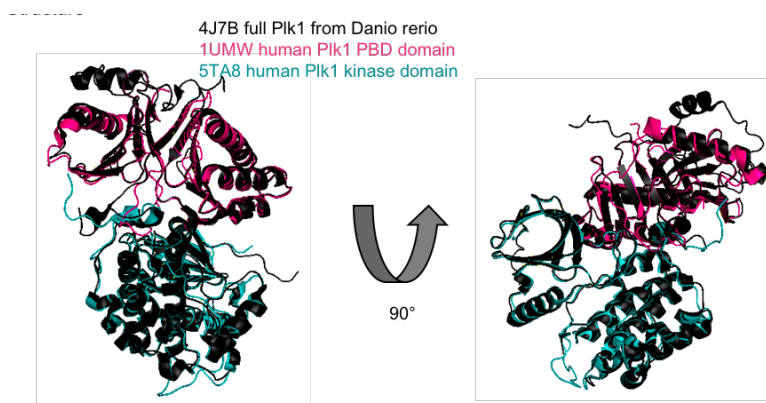


Figure 27. Comparison between zebrafish and human Plk1 structure. Superimposition of *Danio rerio* Plk1 (black) and human KD (blue) and PBD (pink) structures

Chapter 5. Analytical methods for studying phosphorylation

In order to identify Plk1 phosphorylation sites in BRCA2, several techniques are available. Most studies used Western Blotting (WB), and Mass Spectrometry (MS) (Lin et al., 2003, Yata et al., 2014, Takaoka et al., 2014). However, their authors could not identify the phosphorylation sites at the residue level. These methods are the most popular methods to detect protein phosphorylation. Their limitations are explored in this **Chapter**.

1. Western Blot necessitates antibodies directed against previously identified phosphosites to monitor phosphorylation processes

A protein can be detected and quantified in a complex environment, using specific antibodies. Concerning phosphoproteins, antibodies directed against a specific phosphosite are required. A great number of antibodies directed against phosphoserine, phosphothreonine, phosphotyrosine or specific phosphosites of well-known proteins are commercially available (e.g. pT185 and pY187 of Erk1/Erk2, pY419 or pY529 of Src, pS473 of Akt1, pY1022 and pY1023 of JAK1, pT180 and pY182 of p38).

For identifying new phosphosites by WB, alanine screening can be combined with the detection of phosphorylation using antibodies directed against phosphoserine, phosphothreonine or phosphotyrosine, as performed in the studies on BRCA2 phosphorylation by Plk1 (Lin et al., 2003). Alanine screening is actually more convenient to carry out using radio-labeling using ^{32}P ATP, especially for *in vitro* studies. However, the alanine screening method is time-consuming, especially for IDRs that contain many possible phosphosites. Moreover, alanine mutations can modify consensus motifs around the actual phosphosite, or remove priming phosphosites affecting other phosphosites. Hence, they can provide confusing results. WB is thus not the best method to easily identify new phosphosites in a protein.

Moreover, monitoring a phosphorylation process requires a precise quantification of the different phosphoevents. Absolute quantification in WB is notoriously difficult, and necessitates high quality antibodies. Although progressive technical improvements permit better linear correlations between the WB bands intensities and the amount of phosphoresidues (Prabakaran et al., 2011, Mazet et al., 2015, Pillai-Kastoori et al., 2020), a proper quantification requires a number of controls and techniques that are not straightforward to perform (Ghosh et al., 2014, Gorr & Vogel, 2015). Thus, WB is generally used in a semi-quantitative way.

In the case of IDRs, we can highlight two more limitations. First, IDRs often present multiple neighboring phosphorylation sites, which might impair recognition of the phosphosites by specific antibodies, as observed in the case of histones for example (Egelhofer et al., 2011; Fuchs et al., 2011, Bock et al., 2011). Secondly, degenerated (e.g. the S/T-P consensus site of Cdks and MAPKs) or repeated motifs are common in IDRs. The site-specific immunorecognition of a phosphosite in such motifs is logically hindered, ambiguous or even misleading. WB is still very commonly and fruitfully used in cell-biology investigations to assess functional roles of individual phosphorylation sites. However, as far as identification is concerned, most of the community moved to another approach: mass spectrometry.

2. Mass spectrometry is a powerful technique for studying isolated phosphosites

MS is a very powerful technique adapted to the identification and quantification of proteins in simple or complex media. It requires very low amount of sample (about few ng), which favored its use in the two last decades. In the context of phosphoproteins analysis, the protocol often starts with a phospho-affinity chromatography (e.g. using a titanium dioxide TiO₂-coated resin) for enriching the initial sample in phosphoproteins (Riley et al., 2016). Then, two strategies exist for the MS analysis: peptide-based MS and protein-MS (Prabakaran et al., 2011).

Peptide-based MS analysis starts with the digestion of the sample by various proteases (Riley et al., 2015), in order to generate small peptides that can be identified by their weight. In the case of phosphoproteins, MS/MS fragmentation or combining the analysis from different proteases treatments can allow the localization of phosphosites. However, in the context of IDRs, the close proximity between the phosphosites (Schweiger et al., 2010) can make them hardly separable by proteases. MS analysis relies on the possibility to generate peptides having good “flyability” (see below) and that can be identified by their weight. IDRs biased composition make them difficult objects in this regard: i) IDRs can contain long stretches showing high density of Lys/Arg or Glu/Asp, which are the classical targets of common MS-analysis proteases like trypsin or Glu-C, and ii) IDRs show generally low-content of hydrophobic amino acids, targets of other common MS-proteases like pepsin or chymotrypsin. Furthermore, repeated motifs are very complicated to manage with this strategy. After digestion, the sample is analyzed by Matrix Assisted Laser Desorption-Ionization-Time Of Flight (MALDI-TOF) or electrospray (ESI). These two strategies necessitate the ionization of

the sample in order to propel it in the analyzing tube of the MS device. Unfortunately, peptide ionization is amino acid composition-dependent, leading to heterogenous detection of peptides. The final result is thus not always representative of the initial sample, and often contain invisible regions. To fix this problem, new matrices for MALDI-TOF analysis (Fenyo et al., 2007, Patil et al., 2018) and the use of an internal standard have been proposed (Riley et al., 2016, Prus et al., 2019). All these developments largely increased the power of quantitative MS in the last years.

In the case of protein-MS, the full-length protein is analyzed. Recent improvements increased its quantification accuracy (Prabakaran et al., 2011). However, the method by itself does not allow the identification of phosphosites in a protein. The localization of phosphosite(s) requires tandem-MS with the introduction of a collision cell to fragmentate the protein in peptides, which can generate loss or transfer of the phosphate group from one residue to another (Bailey et al., 2019). This strategy is thus not optimal, especially in the context of IDRs that contains several phosphosites.

Even if MS has some limitations, in particular for the analysis of phosphoIDRs, it is the most common method to detect and quantify phosphosites in proteins. The most notorious dataset containing experimentally detected PTMs gathers mostly MS-detected PTMs from phosphoproteomics analysis (<https://www.phosphosite.org/>). This database constitutes a very good starting point in many cases. Nevertheless, sites are identified using different experimental approaches: different MS protocols, cell types, cell culture conditions... Thereby, experimental verification is needed before starting any functional characterization.

To conclude, WB and MS are used for phosphoprotein quantification. Nevertheless, in the context of IDRs, WB and MS present several limitations. Thereby, technical innovation or complementary approaches are welcome for identifying and monitoring IDRs phosphorylation.

3. NMR for site-specific identification and monitoring of phosphorylation

In the last 15 years, an innovative method emerged, based on the use of liquid-state Nuclear Magnetic Resonance (NMR). This technique gives information on the local chemical environment of atom nuclei in a protein (Jensen et al., 2013), which can be very powerful for identifying and quantifying phosphorylation events at an atomic level (Milles et al., 2018).

Every nucleus is characterized by its resonance frequency in the high magnetic field of the NMR spectrometer. This frequency (in Hz) is converted to a chemical shift (in ppm) independent of the spectrometer magnetic field.

The first strategy for monitoring protein phosphorylation is ^{31}P -NMR. This strategy consists in a simple 1D-NMR spectrum. Each peak corresponds to a phosphorus present in a specific chemical environment. ^{31}P NMR was not initially developed for monitoring protein phosphorylation but for the analysis of phosphates in biological contexts. In fact, its first uses were described in the 1970's when a dozen of phosphometabolites were characterized in several mammalian cell types and bacteria (Navon et al., 1977, Hoult et al., 1974, Moon et al., 1973). Notably because ^{31}P occurs at 100% natural abundance, ^{31}P -NMR offers a good sensitivity. Hence, ^{31}P NMR spectroscopy was soon applied to other fields such as enzyme structure (Segall et al., 1993), protein dynamics (Feldmann et al., 1977), reaction analysis (Vogel and Bridger, 1983) and protein phosphorylation (Gassner et al., 1977, Shimidzu et al., 1987, Takahashi et al., 1987). ^{31}P NMR was also developed for clinical applications (Zandt et al., 1999, Gabellieri et al., 2008, van Houtum et al., 2019) and alimentary controls (Belloque et al., 2000).

^{31}P NMR for protein phosphorylation studies was explored in the 1990's. In theory, one single ^{31}P peak can be detected for each phosphoresidue, because every phosphoresidue present a specific local chemical environment. In addition, ^{31}P peak intensities reports quantitatively the advancement of the corresponding phosphorylation reactions. Several studies reported the ^{31}P chemical shifts of phosphorylated amino acids (Mattheis et al., 1984, Hoffmann et al., 1993, Hirai et al., 2000). These chemical shifts are comprised between 1 and 6 ppm and largely depend on temperature and pH. Protocols were then published to identify phosphorylated residues (Hirai et al., 2000).

While this strategy is performed with unlabeled proteins, an NMR probe directly detecting ^{31}P is needed for sensitive detection. Unfortunately, in the era of protein NMR, ^{31}P probes are not that much widespread. Furthermore, it requires the assignment of phosphopeaks, which push us back to the alanine-screening strategy. In principle, HMBC (Heteronuclear Multiple Bond Correlation)-based two- or three-dimensional (2D or 3D) NMR techniques could solve the ^{31}P assignment problem, by establishing correlations between ^{31}P phosphate resonances and backbone ^1H , ^{13}C or ^{15}N resonances. These latter ones should themselves be assigned using the classical protein NMR assignment strategies (HNCO, HNCAO, HNCACB, HN(CA)N, ...). However, multi-dimensional techniques using magnetization transfer from ^{31}P

are extremely time consuming due to sensitivity problems arising from fast transversal ^{31}P relaxation. For all these reasons, other NMR strategies were developed.

Nowadays, the most common approach is the use of ^1H - ^{15}N correlation 2D NMR experiments (Heteronuclear Single Quantum Correlation HSQC or Heteronuclear Multiple Quantum Correlation HMQC). This has been used for the characterization of the phosphorylation of globular proteins (Van Nuland et al., 1993, Smith et al., 2013, Wauer et al., 2015), several IDRs/IDPs (Landrieu et al., 2006, Cordier et al., 2015, Mylona et al., 2016, Noguiera et al., 2017) or even in the case of other PTMs like lysine acetylation or N-terminal acetylation (Theillet et al., 2012). Protocols have also been proposed for monitoring phosphorylation *in vitro* (Theillet et al., 2013, Smith et al., 2015, Danis et al., 2016, Huang et al., 2020), in cell extracts (Selenko et al., 2008, Thongwichian et al., 2015, Theillet et al., 2013) or in cells (Selenko et al., 2008, Milles et al., 2018) using this strategy. In the context of IDRs, this method was optimized using the ^1H - ^{15}N SOFAST-HMQC sequence developed by Schanda et al. for folded proteins (Schanda et al., 2005), but which is also highly beneficial for NMR detection of amino acids showing fast water-amide proton exchange (Theillet et al., 2011).

Before phosphorylation, the ^1H resonances of IDRs are typically found in a specific spectral region, between 7.5 and 8.5 ppm (at 283K-303K, **Figure 28.A**). Upon phosphorylation, the ^1H - ^{15}N HMQC of the protein shows a new fingerprint. First, the new phosphoresidues have new NMR resonances, which are characterized by a ^1H chemical shift comprised between 8.5 and 9.5 ppm (**Figure 28.A**, Bienkiewicz et al., 1999, Hendus-Altenburger et al., 2019). This chemical shift is due to the new chemical environment probed by the backbone amide ^1H - ^{15}N nuclei. The neighbor residues of the phosphosite can also be affected enough to show new peaks upon phosphorylation (**Figure 28.C**). Because NMR peak intensities are proportionnal to the molecular species concentrations, they can report the progressive appearance and disappearance of phospho- and unphospho-residues, respectively. These peak intensities can be measured in series of spectra recorded during the phosphorylation reaction. Hence, one can monitor phosphorylation advancement by tracking intensities of NMR peaks of phosphosites and their neighbors.

Monitoring the peak intensities from non-phosphorylated species in every spectra is the easiest way to get a quantitative estimation of the phosphorylation kinetics: at time 0, the intensity corresponds to 100% of the non-phosphorylated species, hence providing a direct normalization. The normalization of phosphopeak intensities is indeed less evident, because 100% phosphorylation is rarely obtained. It is achievable by anticorrelation with the non-phosphopeak intensities.

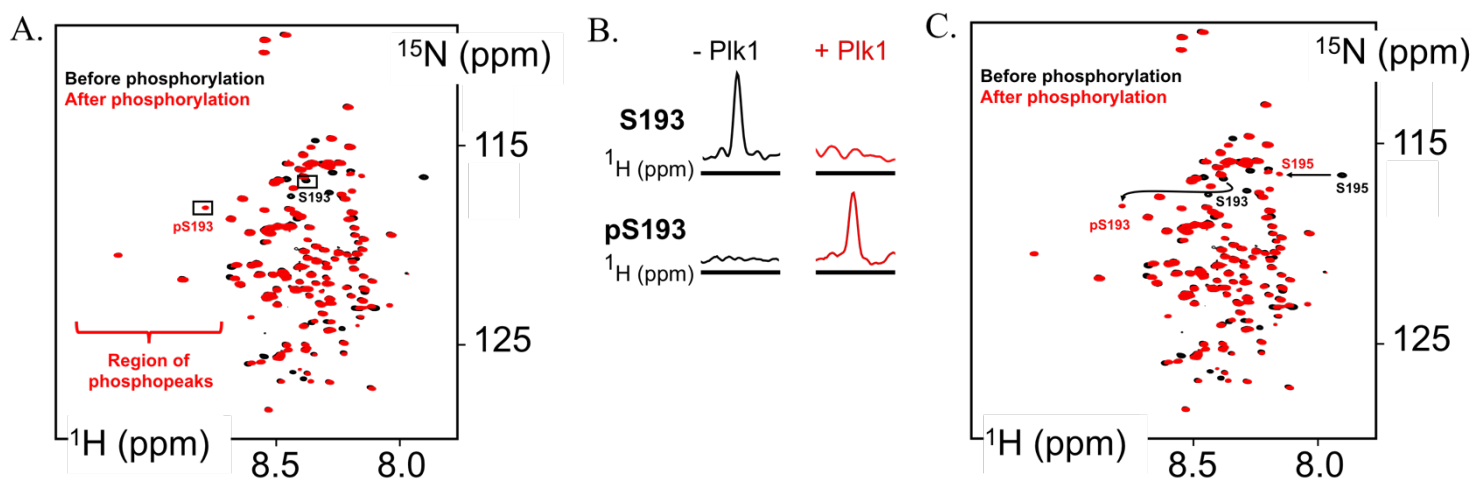


Figure 28. Protein phosphorylation observed by ^1H - ^{15}N HMQC-SOFAST NMR at 700 MHz **(A and C)** Example of superimposition of ^1H - ^{15}N HMQC-SOFAST of BRCA2₄₈₋₂₁₈ at pH 7.0 and 283K before (black) and after phosphorylation by Plk1 (red). Phosphoregion is displayed in **(A)** and **(C)** showed the impact of pS193 on its neighbor S195. **(B)** Intensity of S193 and pS193 peaks before and after complete phosphorylation.

Even if this strategy permits to identify phosphoresidues and monitor their kinetics in one experiment, it presents several drawbacks. First, it necessitates relatively large quantities of protein, at least 2.5 nmol, i.e. 100 μL at 25 μM . Then, it requires protein samples enriched in ^{15}N for being NMR-visible in 2D ^1H - ^{15}N correlation experiments. This is commonly achieved by recombinant production of proteins in a minimum media supplemented with a ^{15}N -nutrient as the unique source of nitrogen, or using culture media supplemented with ^{15}N amino acids. This strategy is more expensive due to the isotope-labeling of proteins. However, the ^1H - ^{15}N spectrum of the protein of interest has first to be assigned in order to associate every peak to its corresponding residue in the protein sequence. This assignment requires the production of a $^{15}\text{N}/^{13}\text{C}$ -labeled NMR sample for recording of a series of 3D NMR spectra necessary for the NMR chemical shift assignment. It is the most time-consuming part of the protocol. Finally, due to their high flexibility, disordered proteins present a narrow ^1H - ^{15}N spectrum, with possible superimposition. In order to prevent superimposition, deleterious for the precise quantification, the size of the construct might be adapted, commonly to 100-200 amino acids. The size is usually a problem for protein solution NMR: large folded proteins tumble slower, which has deleterious consequences on NMR signal. This is less a problem in the case of IDRs, which conserve their fast motion at any size. IDRs larger than 200 amino acids are thus still amenable by solution NMR.

NMR can look time-consuming in comparison to MS. However, it offers several appealing advantages:

- (1) an atomic resolution characterization of the protein of interest, which identifies the phosphoresidues without protease treatment or ionization,
- (2) a very accurate monitoring of the phosphorylation kinetics based on the measurement of the peak intensity decay,
- (3) no need for an internal standard when quantifying the phosphorylation events,
- (4) the NMR analysis gives access to the structural impact of phosphorylations,
- (5) experiments can also be performed in cellular extracts or even in cells, using the ^{15}N -isotope filter that comes for free, because natural abundance of ^{15}N is only 0.4%.

In conclusion, no technique is perfect for studying IDRs phosphorylation. NMR is complementary to other techniques, notably in its capacity to deliver clear and comprehensive data for biochemical characterization *in vitro*. I used this strategy during my PhD to monitor BRCA2 phosphorylation.

Purpose of the thesis

My PhD project aimed at establishing structural and biochemical knowledge on conserved BRCA2 regions that were previously poorly characterized. More precisely, I focused my work on the BRCA2 N-terminal region, which was predicted to be disordered. This region is hyperphosphorylated by Plk1 during mitosis. Several studies have shown that mutations in this BRCA2 N-terminal region can create mitotic defects, including disrupted interaction with chromosome segregation proteins and late cytokinesis, which is highly carcinogenic. However, most of the detected BRCA2 phosphorylation sites targeted by Plk1 during mitosis were not identified previously. This limited the molecular characterization of this region. Among others, characterizing this BRCA2 region may help to identify new BRCA2 mutations causing breast cancers and the mechanisms behind their deleterious effects.

As the “BRCA2 project” started only few years before my arrival at the laboratory, I had two main objectives:

- to set up a methodology to study BRCA2 phosphorylation and to use it to dissect BRCA2 phosphorylation reactions,
- to test hypotheses at the molecular level for understanding the role of these mitotic phosphorylations, either based on the literature or cell biology data from our collaborators.

First, I produced several BRCA2 fragments spanning the N-terminal region (**Chapter 1**) and I used NMR for identifying and monitoring the BRCA2 residues phosphorylated by Plk1 (**Chapter 2**). Then, using a combination of biophysics techniques, I characterized new protein interactions that include this phosphoBRCA2 region (**Chapter 3 and 4**). This strategy also gave me the opportunity to measure the impact of BRCA2 variants of unknown significance on BRCA2 phosphorylation and interaction. My results have been integrated with those of Dr. Aura Carreira team (Institut Curie, Orsay) to describe the role of phosphoBRCA2 during chromosome segregation (**Chapter 4**). I also used a proteomics strategy to identify new phospho-dependent BRCA2 partners. With these results, I initiated the characterization of two newly identified BRCA2 partner: the kinesin Kif2C and the kinase Chk2 (**Chapter 5**).

To better understand the phosphorylation mechanism of BRCA2 by Plk1, I also studied the impact of BRCA2 pre-phosphorylation by Cdks at position T77, which creates a Plk1 docking site (**Chapter 6**). To achieve this goal, I used a new technology based on Native Chemical Ligation, in collaboration with Dr. Vincent Aucagne team (CBM, Orléans).

Because these investigations required to manipulate and use important amounts of Plk1, I first benefited from large amounts of Plk1 produced by the Institut Curie protein production facility, but then I also spent time to optimize its recombinant production. I initiated the production of full-length Plk1 in insect cells and of its separated domains in bacteria. The yields are good enough for future NMR studies (**Chapter 7**).

Finally, I report at the end of the results section my initial main PhD project: I attempted to characterize the molecular bases of the DNA binding properties of the N-terminal region of BRCA2 (**Chapter 8**).

Material & methods

1. Commercial products

PBS 10X was purchased from Sigma Aldrich (D1408-500ML), HEPES 1M from Sigma Aldrich (H0887), EDTA 0.5 M from Sigma Aldrich (E7889-100ML), PMSF 0.1 M from Sigma Aldrich (93482-250ML-F), benzonase from Sigma Aldrich (E1014-25KU), EDTA-free protease inhibitors (PI) from Roche (05056489001), PhoSTOP from Roche (04906837001), affinity and gel filtration column from GE Healthcare (Histrap FF: 17-5255-01, HisTrap excel: 17-3712-05, Heparine: 71-7004-00AU, HiTrap desalting: 17-1408-01; gel filtration columns: HiLoad™ 16/600 Superdex™ 75 PG: 28-9893-33, HiLoad™ 16/600 Superdex™ 200 PG:28-9893-35, Superdex™ 200 Increase 10/300 GL: 28-9909-44), centrifugal units later named concentrators from Amicon (UFC901024).

2. Plasmids

All plasmids used in these studies are summarized in **Table 2** and **Table 3**.

Table 2. Plasmids for expression of BRCA2 constructs

Plasmid name	Protein construct	BRCA2 mutations available	Vector	Antibiotic resistance
BRCA2 ₁₉₀₋₂₈₄	GST-PreScission site-BRCA2 ₁₉₀₋₂₈₄	WT, M192T, T200K, T207A	pGEW-6P-1 (from Dr. Carreira)	Amp
BRCA2 ₅₃₋₂₂₈	GST-TEV site-BRCA2 ₅₃₋₂₂₈	WT	pET-41 b	Kana
BRCA2 ₅₃₋₁₃₁	GST-TEV site-BRCA2 ₅₃₋₁₃₁	WT	pET-41 b	Kana
BRCA2 _{48-218(C4A)} or BRCA2 ₄₈₋₂₁₈	8His-TEV site-BRCA2 ₄₈₋₂₁₈	C132A/C138A/C148A/C161A, C132A/C138A/C148A/C161A/T77A, C132A/C138A/C148A/C161A/M192T, C132A/C138A/C148A/C161A/T207A	pETM-13	Kana
BRCA2 ₄₈₋₂₈₄	8His-TEV site-BRCA2 ₄₈₋₂₈₄	C132A/C138A/C148A/C161A	pETM-13	Kana
BRCA2 ₁₆₇₋₂₆₀	6His-AviTag-BRCA2 ₁₆₇₋₂₆₀	WT, M192T, S193A, T207A	pETM-13	Kana
BRCA2 ₈₅₋₂₂₀	8His-TEV site-BRCA2 ₈₅₋₂₂₀	G85C	pETM-13	Kana
BRCA2 _{T2.2}	8His-TEV site-BRCA2 ₂₅₀₋₅₀₀	WT	pET-M13	Kana
BRCA2 _{T2.3}	8His-TEV site-BRCA2 ₂₅₀₋₃₅₀	WT	pET-M13	Kana
BRCA2 _{D1}	8His-TEV site-BRCA2 ₂₅₀₋₅₀₀	C279A/C393S/C419S/C480S	pET-M13	Kana
BRCA2 _{D1A}	8His-TEV site-BRCA2 ₂₅₀₋₃₅₀	C279A	pET-M13	Kana
BRCA2 _{D2}	8His-TEV site-BRCA2 ₂₅₀₋₅₀₀	C279A/C311S/C315A/C341A/C393S/C419S/C480S	pET-M13	Kana
BRCA2 _{D2A}	8His-TEV site-BRCA2 ₂₅₀₋₃₅₀	C279A/C311S/C315A/C341A	pET-M13	Kana
BRCA2 _{F2}	8His_GB1-TEV site-BRCA2 ₁₀₉₃₋₁₁₅₈	WT	pET-M13	Kana

Table 3. Plasmids for expression of other constructs including Plk1, Kif2C, PARP1, Chk2 and Aurora A-TPX2

Plasmid name	Protein construct	Mutations available	Vector	Antibiotic resistance
GST-Plk1-PBD	GST-TEV-Plk1 ₃₆₅₋₆₀₃	WT	Given by Dr. Anne Houdusse	
His6-SUMO-PBD	His6-SUMO-PBD ₃₂₆₋₆₀₃	WT	pT7-His6-SUMO	Amp
Plk1 _{FL}	6His-TEV site-PLK1 ₁₋₆₀₃	C164L/C212S/C255S/C372S/C405S/C428S/C572S/C573S/L162C C164L/C255S/C372S/C405S/C428S/C572S/C573S C164L/C212S/C255S/C372S/C405S/C428S/C572S/C573	pET-28a	Kana
Plk1 ₃₇₋₆₀₃	6His-TEV site-PLK1 ₃₇₋₆₀₃	C164L/C212S/C255S/C372S/C405S/C428S/C572S/C573S/L162C	pET-28a	Kana
Plk1 ₁₋₃₂₈	6His-TEV site-PLK1 ₁₋₃₂₈	C164L/C212S/C255S/L162C	pET-28a	Kana
Plk1 ₁₋₃₆₆	6His-TEV site-PLK1 ₁₋₃₆₆	C164L/C212S/C255S/L162C	pET-28a	Kana
Plk1 ₃₆₆₋₆₀₃	6His-TEV site-PLK1 ₃₆₆₋₆₀₃	C372S/C405S/C428S/C572S/C573S	pET-28a	Kana
AurA-TPX2	6His-Thrombine site-TEV site-AurA ₁₂₂₋₄₀₃ -PKA _{linker} -TPX2 ₁₋₄₅	C393A	pET-28a	Kana
Kif2C _{motordomain(md)}	6His-Kif2C ₂₁₆₋₅₉₈	R330A/R379A	pET-28a (from Dr. Gigant)	Kana (+Cam for pKg3)
Kif2C _{FL(MCAK)}	Kif2C-6His	WT	pFastBac (from Dr. Friel)	
Kif2C _{FL(46)}	HisTAG-Kif2C	S715E	pSKT46 (from Dr. Welburn)	
Chk2 ₁₋₂₀₉	6His-thioreduxin-TEV-Chk2 ₁₋₂₀₉	WT	pET-32a	Amp
PARP1 ₁₋₃₆₆	HisTAG-PARP1 ₁₋₃₆₆	WT	From Dr. Carreira	Kana+Cam

Most of the genes of interest were synthesized by Genscript with a codon optimization for expression in *E.coli*.

3. Site-directed mutagenesis

BRCA2_{48-218(C4A)} M192T, BRCA2_{48-218(C4A)} T207A, BRCA2_{48-218(C4A)} T77D and BRCA2_{48-218(C4A)} T77E were obtained by site-directed mutagenesis using BRCA2_{48-218(C4A)} as a template.

A first PCR step was realized using either M192T, T207A, T77D or T77E primers (**Table 4**) for the introduction of the corresponding mutation in the BRCA2_{48-218(C4A)} sequence. PCR was conducted with the QuickChange II XL Site-directed mutagenesis kit from Agilent Technologies with the following cycle steps: 2 min at 95°C, (30 s at 95°C, 30 s at 60°C, 14 min

at 68°C)x 18 times, 5 min at 68°C. DNP1 enzyme was then added to the PCR sample and incubated 1 h at 37°C to linearize the amplified plasmid. Samples were then migrated on 1X agarose gel to check the quality of amplification (**Figure 29 and Figure 30**). When amplified, new plasmids were transformed into *E. coli* DH5 α and plate on LB agar. Three colonies of each mutant were grown overnight in 5 mL LB containing kanamycin, spun down 10 min at 3,000 xg and a plasmid miniprep was performed using the Plasmid Miniprep kit from New England Biolabs Inc. Plasmids were then sequenced by Eurofins using BRCA2_{48-218(C4A)} primers.

Table 4. Primers for BRCA2_{48-218(C4A)} site-directed mutagenesis.

	Forward primer (5'-3')	Reverse primer (5'-3')
M192T	AGTTGACCCGGATACGAGCTGGAGCAGC	GCTGCTCCAGCTCGTATCCGGGTCAACT
T207A	ACCCTGAGCAGCGCCGTTCTGATTGTTT	GAACAATCAGAACGGCGCTGCTCAGGGT
T77D	CAACTGGCGAGCGACCCGATCATTTTTAAG	CTTAAAAATGATCGGGTTCGCTCGCCAGTTG
T77E	CAACTGGCGAGCGAGCCGATCATTTTTAAG	CTTAAAAATGATCGGGTTCGCTCGCCAGTTG
BRCA2 _{48-218(C4A)}	AGGCCATGGGTCATCATCATCATCATC	AATGGATCCGCTAGCTTACTCGCTCGCTTCT

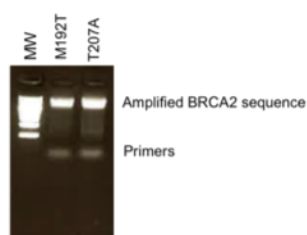


Figure 29. 1X agarose gel of amplification of BRCA2₄₈₋₂₁₈ M192T and T207A mutations using site-directed mutagenesis.

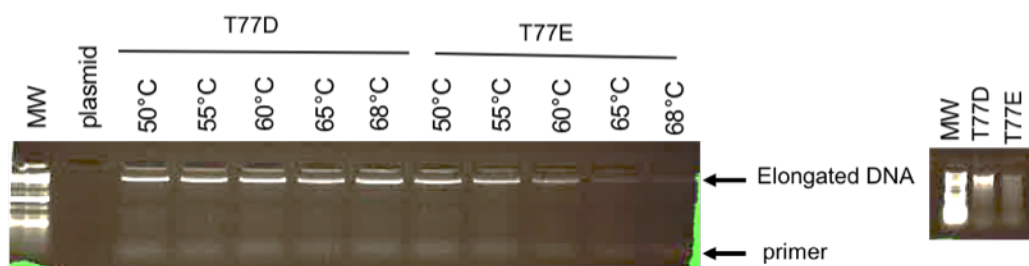


Figure 30. 1X agarose gel of BRCA2_{48-218(C4A)} PCR site-directed mutagenesis for mutations T77D and T77E. Several hybridization temperatures were tested during PCR (left) and hybridizations at 68°C and 50°C were selected for T77D and T77E, respectively (right).

Mutations M192T and T207A were obtained during the first mutagenesis experiment. Despite several trials (**Figure 30**), T77D and T77E mutagenesis were unsuccessful, no colony after transformation into DH5 α were obtained.

4. Plasmid transformation in *E.coli* strains

Plasmids were transformed in *E. coli* (BL21(DE3)Star or Rosetta 2) using a heat-shock protocol. About 100 ng of plasmid were incubated with competent bacteria (see protocol below) and incubated for 20 min on ice. The sample was then heat-shocked for 45 s at 42°C, and then incubated 3 min on ice. 400 uL of LB were added to the bacteria and the sample was incubated for 45 min at 37°C before antibiotic selection. This was achieved by spreading the bacteria on LB-agar plates supplemented with the appropriate concentrations of antibiotics, and incubation overnight at 37°C.

Competent bacteria were obtained by spinning down a bacterial culture in LB at an OD_{600nm} of 0.5. The centrifugation step was realized at 3,000 xg for 10 min at 4°C and bacteria were resuspended in 30 mL cold 100 mM CaCl₂ solution. They were incubated on ice for 10 min and spun-down again. Then, bacteria were resuspended in 8 mL cold 100 mM CaCl₂ 10% glycerol solution, and aliquots of 50-100 uL were flash-frozen in liquid-nitrogen and stored at -80°C.

5. Protein expression

Two culture media were used in this study: Luria Broth (LB) and M9 minimum media (Table 5). As described in Azatian et al., 2019, the use of 2X M9 salts improve the protein yield in minimum media. Thus, since 2019, 2X M9 was used for protein production. Antibiotics were used at concentrations of 100 ug/mL for ampicillin, 30 ug/mL for kanamycin, 30 ug/mL for chloramphenicol.

Table 5. Composition of LB and M9 media

Culture media	LB	1X M9 medium	2X M9 medium
Composition for 750 mL	7.5 g tryptone 3.75 g yeast extract 7.5 g NaCl	6.37 g Na ₂ HPO ₄ , 2H ₂ O 2.5 g KH ₂ PO ₄ 0.35 g NaCl 1X Trace Elements 1.5 g ¹² C or ¹³ C D-glucose 750uL MgSO ₄ 1 M 250 uL CaCl ₂ 1M 750 ug biotine 750 ug thiamine 0.35 g ¹⁴ N or ¹⁵ N NH ₄ Cl	12.74 g Na ₂ HPO ₄ , 2H ₂ O 5 g KH ₂ PO ₄ 0.35 g NaCl 1X Trace Elements 1.5 g ¹² C or ¹³ C D-glucose 750uL MgSO ₄ 1 M 250 uL CaCl ₂ 1M 750 ug biotine 750 ug thiamine 0.35 g ¹⁴ N or ¹⁵ N NH ₄ Cl

100X Trace elements are composed of 13.4 mM EDTA, 3.1 mM FeCl₃, 0.62 mM ZnCl₂, 76 uM CuCl₂, 42 uM CoCl₂, 162 uM H₃BO₃, 8.1 uM MnCl₂.

A single colony taken from LB-Agar plates was resuspended into 35 mL LB and incubated at 30°C overnight to perform a pre-culture. For a final 750 mL culture, a maximum of 20 mL LB preculture was diluted into the larger LB culture erlenmeyer and 5 mL for M9 cultures. When needed (especially for BRCA2₈₅₋₂₂₀ expression in ¹⁵N M9 medium), a 35 mL preculture was spun down and resuspended in fresh minimal media in order to diminish the final ¹²C/¹⁴N content of the culture medium.

Two protocols were used for the optimization of protein expression conditions:

- In the case of disordered proteins (BRCA2 constructs), 3*50 mL culture of bacteria in LB containing antibiotics were incubated at 37°C. Upon OD_{600nm}=0.6-0.8, 1 mM IPTG was added in each culture. Cultures were then separated for incubation either at 20°C, 30°C or 37°C. OD_{600nm} was measured and 100 uL aliquots was collected after i) 2, 3, 4, 5 and 6 hrs of induction at 37°C, ii) 3, 4, 5, 6 hrs and overnight induction at 30°C and iii) 5, 6 hrs and overnight induction at 20°C. The sample were then mixed with Laemmli buffer, boiled 10 min at 95°C and analysed using SDS-PAGE.
- In the case of folded proteins or domains, the protein solubility was checked during the expression optimization step. 2*50 mL cultures of bacteria in LB medium supplemented with antibiotics were incubated at 37°C. After the cultures reached an OD_{600nm} of 0.6-0.8, 1 mM IPTG was supplemented to the media. Cultures were then splitted in 3 flasks, which were incubated either at 20°C, 30°C or 37°C. Cultures at 37°C and 30°C were stopped after 3 hrs of induction, and culture at 20°C was stopped after an overnight (ON) induction. Culture were then spun down 10 min at 3,000 xg, resuspended in 1 mL of a water solution containing Tris-HCl at 50 mM, NaCl at 150 mM, 2 mM DTT, at pH 8.0, supplemented with lysozyme and benzonase. Samples were then sonicated on ice for 2 min and spun down 5 min at 16,000 xg and 4°C. The total, supernatant and pellet fractions were analyzed using SDS-PAGE.

Optimal protein expression conditions are summarized in **Table 6**. In this study, only Kif2C_{md} and PARP1₁₋₃₆₆ expressions were not optimized in the lab.

Table 6. Optimal protein expression conditions in bacteria for BRCA2, Plk1, AurA-TPX2, PARP1, Chk2 and Kif2C constructs.

Construct	Bacterial strain for expression	OD _{600nm} induction	[IPTG]	Other	Induction time	Induction temp.
BRCA2 ₁₉₀₋₂₈₄	BL21(DE3)Star	0.6-0.8	1 mM		4 hrs	37°C
BRCA2 ₅₃₋₂₂₈	BL21(DE3)Star	0.6-0.8	1 mM		4 hrs	37°C
BRCA2 ₅₃₋₁₃₁	BL21(DE3)Star	0.6-0.8	1 mM		4 hrs	30°C
BRCA2 _{48-218(C4A)}	BL21(DE3)Star	0.6-0.8	1 mM		4 hrs	37°C
BRCA2 _{48-284(C4A)}	BL21(DE3)Star	0.6-0.8	1 mM		4 hrs	37°C
BRCA2 ₁₆₇₋₂₆₀	BL21(DE3)Star	0.6-0.8	1 mM		4 hrs	37°C
BRCA2 ₈₅₋₂₂₀	BL21(DE3)Star	0.6-0.8	1 mM		4hrs or ON	37°C or 20°C
BRCA2 _{T2.2}	BL21(DE3)Star	0.6-0.8	1 mM	100 uM ZnCl ₂	6 hrs or ON	20°C
BRCA2 _{T2.3}	BL21(DE3)Star	0.6-0.8	1 mM	100 uM ZnCl ₂	6 hrs or ON	20°C
BRCA2 _{D1}	BL21(DE3)Star	0.6-0.8	1 mM	100 uM ZnCl ₂	ON	20 °C
BRCA2 _{D1A}	BL21(DE3)Star	0.6-0.8	1 mM	100 uM ZnCl ₂	ON	20°C
BRCA2 _{D2}	BL21(DE3)Star	0.6-0.8	1 mM	100 uM ZnCl ₂	ON	20 °C
BRCA2 _{D2A}	BL21(DE3)Star	0.6-0.8	1 mM	100 uM ZnCl ₂	ON	20°C
BRCA2 _{F2}	BL21(DE3)Star	0.6-0.8	1 mM		4 hrs	30°C
GST-Plk1-PBD	BL21(DE3)Star	0.6-0.8	1 mM		4 hrs	30°C
His6-SUMO-PBD	BL21(DE3)Star	0.6-0.8	1 mM		ON	20°C
Plk1 _{FL}	BL21(DE3)Star	0.4-0.6	1 mM		60 hrs	15°C
Plk1 ₃₇₋₆₀₃	BL21(DE3)Star	0.4-0.6	1 mM		60 hrs	15°C
Plk1 ₁₋₃₂₈	BL21(DE3)Star	0.4-0.6	1 mM		60 hrs	14°C
Plk1 ₁₋₃₆₆	BL21(DE3)Star	0.4-0.6	1 mM		60 hrs	15°C
Plk1 ₃₆₆₋₆₀₃	BL21(DE3)Star	0.4-0.6	1 mM		60 hrs	15°C
AurA-TPX2	BL21(DE3)Star	0.6-0.8	1 mM		ON	20°C
Kif2C _{motordomain} Or Kif2C _{md}	Rosetta e-containing pKg3	0.4-0.5	1.5 g D(-)arabinose/L culture, 30 min at RT, add 0.5 mM IPTG, incubation ON at 20°C			
Chk2 ₁₋₂₀₉	BL21(DE3)Star	0.6-0.8	1 mM		ON	20°C
PARP1 ₁₋₃₆₆	Rosetta 2	0.6-0.8	200 uM	100 uM ZnSO ₄	ON	20°C

Because we presumed that a zing finger domain was present in BRCA2₂₅₀₋₃₅₀, ZnCl₂ at a final concentration of 100 uM was added in BRCA2_{T2.2}, BRCA2_{T2.3}, BRCA2_{D1}, BRCA2_{D1A}, BRCA_{D2}, BRCA2_{D2A} culture media. ZnSO₄ at 100 uM was also present for PARP1₁₋₃₆₆ expression because it folds into zinc-finger domain. Kif2C production was performed using Benoît Gigant's conditions and PARP1₁₋₃₆₆ using Aura Carreira's conditions. Addition of D(-)

)-arabinose was used for triggering the expression of protein chaperones (in pKg3) before the Kif2C_{md} expression in order to favor Kif2C_{md} folding.

6. Protein purification

Table 7 summarizes molecular weights and molecular extinction coefficients at 280 nm of the proteins produced in this study. All molecular extinction coefficients at 280 nm were calculated using the ProtParam webserver (<https://web.expasy.org/protparam/>). Purification steps that correspond to column chromatographies were performed at 4°C, with the exception of those performed with urea buffers, which were carried out at room temperature (RT). Samples were stored at -80°C and -20°C for long and short durations, respectively. Protocols correspond to the purification of a 750 mL culture pellet.

Table 7. Molecular weights and molecular extinction coefficients after cleavage (TEV or PreScission) of proteins produced in this study

Proteins	MW (g/mol)	$\epsilon_{280\text{nm}}$ (cm ⁻¹ .M ⁻¹)	pI
BRCA2 ₁₉₀₋₂₈₄	10,363	6,990	5.73
BRCA2 ₅₃₋₂₂₈	20,108	10,220	7.85
BRCA2 ₅₃₋₁₃₁	9,547	4,470	9.65
BRCA2 _{48-218(C4A)}	19,047	9970	8.13
BRCA2 ₁₆₇₋₂₆₀	13,586	12,490	5.74
BRCA2 ₈₅₋₂₂₀	14,961	7,240	7.82
BRCA2 _{T2.2}	27,879	8,855	5.30
BRCA2 _{T2.3}	11,351	1,740	7.00
BRCA2 _{D1}	27,799	8605	5.30
BRCA2 _{D2}	28,194	8480	5,16
BRCA2 _{D1A}	11,319	1,615	7.01
BRCA2 _{D2A}	11,239	1,490	7.04
BRCA2 _{F2}	7,671	1,490	4.78
GST-Plk1-PBD	28,214	36,245	6.35
Plk1 _{FL}	68,195	56,520	9.31
Plk1 ₃₇₋₆₀₃	65,038	56,645	9.20
Plk1 ₁₋₃₂₈	36,742	20,650	9.54
Plk1 ₁₋₃₆₆	41,047	20,650	9.50
Plk1 ₃₆₆₋₆₀₃	27,212	35,870	8.97
Kif2C _{motordomain}	43,789	21,150	8.96
AurA-TPX2	41,711	49,975	6.26
Chk2 ₁₋₂₀₉	23,397	26930	4.95
PARP1 ₁₋₃₆₆	41,263	51,910	9,05

BRCA2₁₉₀₋₂₈₄

Initial protocol (Dr. Simona Miron):

The bacterial pellet is resuspended in 40 mL of 50 mM Tris-HCl pH 7.5, 150 mM NaCl, 2 mM DTT, 1 mM EDTA, 5% glycerol, 1 mM PMSF, 1X protease inhibitors (Roche diagnostics), 1 mM ATP, 5 mM MgSO₄, 2 uL benzonase. Cells are sonicated on ice 2.5 min with 1s ON/1s OFF cycle of sonication (60 % amplitude), and the lysate is clarified by centrifugation during 30 min at 48,000 xg at 4°C. The soluble fraction is incubated with 10 mL Glutathione-coated Sepharose beads (GE Healthcare) during 2 hrs at 4°C on a rotating wheel, washed with 100 mL 50 mM Tris-HCl pH 7.5, 150 mM NaCl, 2 mM DTT, 1 mM EDTA and eluted with 30 mL 50 mM Tris-HCl pH 7.5, 150 mM NaCl, 2 mM DTT, 1 mM EDTA, 20 mM reduced glutathione. 80 uL of PreScission protease (Sigma Aldrich) are added to the sample, which is dialyzed ON against 50 mM HEPES pH 7.0, 1 mM EDTA, 2 mM DTT, 150 mM NaCl using 3.5 kDa cut off dialysis system from Spectrum laboratories. After dialysis, the sample is boiled 10 min at 90°C and spun down 10 min at 16,000 xg. The sample is concentrated using Novagen concentrators with 3 kDa cut off membranes, diluted 10 times with 50 mM HEPES pH7.0, 1 mM EDTA, 2 mM DTT and reconcentrated at 1,500 xg.

Optimized protocol:

The bacterial pellet is resuspended in 35 mL of a solution containing 50 mM Tris-HCl at pH 8.0, 150 mM NaCl, 5 mM DTT, 2 mM EDTA, 1 mM PMSF, 1 mM ATP, 5 mM MgSO₄, 500 ug lysozyme, 0.5 uL benzonase. Cells are sonicated on ice 2.5 min in total with 1s ON/1s OFF cycle of sonication (60 % amplitude), and the lysate is clarified by centrifugation during 15 min at 15,000 xg at 4°C. The soluble fraction is incubated with 10 mL Glutathione-coated Sepharose beads (GE Healthcare) during 1.5 hr at 4°C on a rotating wheel, washed with 100 mL of a solution containing 20 mM Tris-HCl at pH 8.0, 150 mM NaCl, 1 mM DTT, 1 mM EDTA and eluted with 40 mL of a solution containing 20 mM Tris-HCl at pH 8.0, 150 mM NaCl, 1 mM DTT, 1 mM EDTA, 20 mM reduced glutathione. Eluted sample is concentrated to 5 mL using 10 kDa cut off concentrators (Novagen). 30 uL of PreScission protease (Sigma Aldrich) and fresh 1 mM DTT are added to the sample and the sample is incubated 1 h at RT. The sample is boiled 10 min at 95°C and spun down 5 min at 16,000 xg at 4°C. The sample is concentrated at 5,000 xg using Novagen concentrators with 3 kDa cut off membranes and injected on a gel filtration column (Superdex 16/60 HiLoad 75 pg) equilibrated with a solution containing 50 mM HEPES at pH 7.0, 75 mM NaCl, 1 mM EDTA. Fractions are pooled and concentrated using 3 kDa cut off concentrators and a centrifugation at 5,000 xg. 1X protease inhibitors and 2 mM DTT are added and the sample is flash frozen using liquid nitrogen.

BRCA2₅₃₋₂₂₈

The bacterial pellet is resuspended in 35 mL of a solution containing 50 mM Tris-HCl at pH 8.0, 150 mM NaCl, 5 mM DTT, 2 mM EDTA, 1 mM PMSF, 1 mM ATP, 5 mM MgSO₄, 500 ug lysozyme, 0.5 uL benzonase. Cells are sonicated on ice 2.5 min in total with 1s ON/1s OFF cycle of sonication (60 % amplitude), and the lysate is clarified by centrifugation during 15 min at 15,000 xg at 4°C. The soluble fraction is incubated with 10 mL glutathione-coated Sepharose beads (GE Healthcare) during 1.5 hr at 4°C on a rotating wheel, washed with 100 mL of a solution containing 20 mM Tris-HCl at pH 8.0, 150 mM NaCl, 1 mM DTT, 1 mM EDTA and eluted with 40 mL of a solution containing 20 mM Tris-HCl at pH 8.0, 150 mM NaCl, 1 mM DTT, 1 mM EDTA, 20 mM reduced glutathione. The eluted sample is concentrated to 5 mL using 10 kDa cut off concentrators (Novagen) centrifuged at 5,000 xg. 0.4 mg of TEV protease and 2 mM of fresh DTT are added to the sample, which is incubated 1 h at RT. After cleavage, BRCA2₅₃₋₂₂₈ precipitates and therefore is pelleted by centrifugation for 10 min at 16,000 xg, and resuspended in a solution containing 20 mM Tris-HCl, 150 mM NaCl, 1 mM EDTA, 5 mM DTT, 1 mM PMSF, at pH 8 supplemented with 8 M urea. It is finally diluted 10 times in a solution containing 20 mM Tris-HCl, 75 mM NaCl, 1 mM EDTA, 5 mM DTT, 1 mM PMSF, at pH 8 supplemented with 10 mM β-mercaptoethanol. The sample was then injected on a gel filtration column (Highload 16/60 Superdex 75 pg) equilibrated with 50 mM HEPES, 1 mM EDTA, 5 mM tris(2-carboxyethyl)phosphine (TCEP), at pH 7.0. Fractions are pooled and concentrated using 3 kDa cut off concentrators centrifuged at 5,000 xg. 1X protease inhibitors is added and sample is flash frozen using liquid nitrogen.

BRCA2₅₃₋₁₃₁

The bacterial pellet is resuspended in 35 mL of a solution containing 50 mM Tris-HCl at pH 8.0, 150 mM NaCl, 5 mM DTT, 2 mM EDTA, 1 mM PMSF, 1 mM ATP, 5 mM MgSO₄, 500 ug lysozyme, 0.5 uL benzonase. Cells are sonicated on ice 2.5 min in total with 1s ON/1s OFF cycle of sonication (50% amplitude), and the lysate is clarified by centrifugation during 15 min at 15,000 xg at 4°C. The soluble fraction is incubated with 10 mL glutathione-coated Sepharose beads (GE Healthcare) during 1.5 hr at 4°C on a rotating wheel, washed with 100 mL of a solution containing 20 mM Tris-HCl at pH 8.0, 150 mM NaCl, 1 mM DTT, 1 mM EDTA and eluted with 40 mL of a solution containing 20 mM Tris-HCl at pH 8.0, 150 mM NaCl, 1 mM DTT, 1 mM EDTA, 20 mM reduced glutathione. The eluted sample is concentrated to 5 mL using 10 kDa cut off concentrators (Novagen). 0.4 mg of TEV protease and 2 mM of fresh DTT are added to the sample, which is incubated 1 h at RT. The sample is

boiled 10 min at 95°C and spun down 5 min at 16,000 xg at 4°C. The sample is concentrated using Novagen concentrators with 3.5 kDa cut off membranes centrifuged at 5,000 xg, and then injected on a gel filtration column (Superdex 16/60 HiLoad 75 pg) equilibrated with a solution containing 50 mM HEPES at pH 7.0, 75 mM NaCl, 1 mM EDTA, 0.5 mM DTT. Fractions are pooled and concentrated using 3 kDa cut off concentrators centrifuged at 5,000 xg. EDTA-free protease inhibitors (cOmplete EDTA-free) are added at a final 1x concentration and the sample is flash frozen using liquid nitrogen.

BRCA2_{48-284(C4A)} and BRCA2_{48-218(C4A)}

The bacterial pellet is resuspended in 35 mL of a solution containing 50 mM Tris-HCl at pH 8.0, 50 mM NaCl, 5 mM DTT, 2 mM EDTA, 1 mM PMSF, 1 mM ATP, 5 mM MgSO₄, 500 ug lysozyme, 0.5 uL benzonase. Cells are sonicated on ice 2.5 min in total with 1s ON/1s OFF cycle of sonication (50% amplitude), and the lysate is clarified by centrifugation during 15 min at 15,000 xg at 4°C. The soluble fraction is loaded on a Ni-NTA histidine-affinity column (5 mL HisTrap FF, GE Healthcare) using a 2 mL/min flow rate. The column is washed with a solution containing 50 mM Tris HCl, 50 mM NaCl, 1 mM DTT at pH 8.0. Then, the sample is eluted using an imidazole gradient over 45 mL, the final buffer containing 50 mM Tris HCl, 50 mM NaCl, 1 M imidazole, 1 mM DTT at pH 8.0. Fractions of interest are pooled and 0.4 mg of TEV protease and 2 mM of fresh DTT are added to the sample, which is incubated 1 h at RT. The sample is boiled 10 min at 95°C and spun down 5 min at 16,000 xg at 4°C. The sample is concentrated using Novagen concentrators with 3.5 kDa cut off membranes centrifuged at 5,000 xg, and injected on a gel filtration column (Superdex 16/60 HiLoad 75 pg) equilibrated with a solution containing 50 mM HEPES at pH 7.0, 75 mM NaCl, 1 mM EDTA. Fractions are pooled, supplemented with 1 mM fresh DTT and the sample is concentrated using 3 kDa cut off concentrators centrifuged at 5,000 xg. EDTA-free protease inhibitors (cOmplete EDTA-free) are added at a final 1x concentration and the sample is flash frozen using liquid nitrogen.

BRCA2₁₆₇₋₂₆₀

The bacterial pellet is resuspended in 35 mL of a solution containing 50 mM Tris-HCl at pH 8.0, 50 mM NaCl, 5 mM DTT, 2 mM EDTA, 1 mM PMSF, 1 mM ATP, 5 mM MgSO₄, 500 ug lysozyme, 0.5 uL benzonase. Cells are sonicated on ice 2.5 min in total with 1s ON/1s OFF cycle of sonication (50% amplitude), and the lysate is clarified by centrifugation during 15 min at 15,000 xg at 4°C. The soluble fraction is loaded on a Ni-NTA poly-histidine-affinity

column (5 mL HisTrap FF, GE Healthcare) at a 2 mL/min flow rate. The column is washed with a solution containing 50 mM Tris-HCl, 50 mM NaCl, 1 mM DTT at pH 8.0. The sample is then eluted with an imidazole gradient over 45 mL, the buffer containing 50 mM Tris-HCl, 50 mM NaCl, 1 M imidazole, 1 mM DTT at pH 8.0. The sample is boiled 10 min at 95°C and spun down 5 min at 16,000 xg at 4°C. The sample is concentrated using Novagen concentrators with 3.5 kDa cut off membranes centrifuged at 5,000 xg and later injected on a gel filtration column (Superdex 16/60 HiLoad 75 pg) equilibrated a solution containing 50 mM HEPES at pH 7.0, 75 mM NaCl, 1 mM EDTA. Fractions are pooled, 1 mM of fresh DTT is added and the sample is concentrated using 3 kDa cut off concentrators centrifuged at 5,000 xg. EDTA-free protease inhibitors (cOmplete EDTA-free) are added at a final 1x concentration and the sample is flash frozen using liquid nitrogen.

BRCA2_{85-220-G85C}

The bacterial pellet is resuspended in 35 mL of a solution containing 50 mM Tris-HCl at pH 8.0, 50 mM NaCl, 5 mM DTT, 2 mM EDTA, 1 mM PMSF, 1 mM ATP, 5 mM MgSO₄, 500 ug lysozyme, 0.5 uL benzonase. Cells are sonicated on ice 2.5 min in total with 1s ON/1s OFF cycle of sonication (50% amplitude), and the lysate is clarified by centrifugation during 15 min at 15,000 xg at 4°C. The insoluble fraction is resuspended in 30 mL of a solution containing 20 mM Tris-HCl, 50 mM NaCl, 8 M Urea, 5 mM DTT, 1 mM PMSF, at pH 8.0 and incubated 20 min at RT. The solubilized fraction is clarified by centrifugation (10 min, 10,000 xg, RT) and loaded on a Ni-NTA poly-histidine-affinity column (5 mL HisTrap FF) at a 2 mL/min flow rate. The column is washed with a solution containing 50 mM Tris-HCl, 50 mM NaCl, 8 M Urea, 1 mM DTT at pH 8.0. The sample is then eluted with an imidazole gradient over 45 mL, the final buffer containing 50 mM Tris-HCl, 50 mM NaCl, 8 M Urea, 1 M imidazole 1 mM DTT at pH 8.0. Fractions are pooled, concentrated using 10 kDa cut off concentrators (Novagen) centrifuged at 5,000 xg, and diluted to reach 0.5 M Urea with 20 mM Tris-HCl, 50 mM NaCl, 10 mM DTT, 1 mM EDTA, at pH 8.0. 0.8 mg of TEV protease are added to the sample, which is incubated 1 h at RT. The sample is concentrated using Novagen concentrators with 3.5 kDa cut off membranes centrifuged at 5,000 xg, and then injected on a gel filtration column (Superdex 16/60 HiLoad 75 pg) equilibrated with a solution containing 50 mM HEPES at pH 7.0, 75 mM NaCl, 1 mM EDTA. Fractions are pooled and supplemented with 1 mM fresh DTT. The sample is concentrated using 3 kDa cut off concentrators centrifuged at 5,000 xg and diluted 1000 times with 1% acetic acid pH 2.4. Finally, the sample is lyophilized.

BRCA2_{T2.2} and BRCA2_{T2.3}

The bacterial pellet is resuspended in 35 mL of a solution containing 50 mM Tris-HCl at pH 8.0, 50 mM NaCl, 5 mM DTT, 2 mM EDTA, 1 mM PMSF, 1 mM ATP, 5 mM MgSO₄, 500 µg lysozyme, 0.5 µL benzonase. Cells are sonicated on ice 2.5 min in total with 1s ON/1s OFF cycle of sonication (50% amplitude), and the lysate is clarified by centrifugation during 15 min at 15,000 xg at 4°C. The insoluble fraction is resuspended in 30 mL of a solution containing 20 mM Tris-HCl 50 mM NaCl, 8 M Urea, 5 mM DTT, 1 mM PMSF, at pH 8.0 and incubated 20 min at RT. The solubilized fraction is clarified by centrifugation (10 min, 15,000 xg, RT) and loaded on a Ni-NTA poly-histidine- affinity column (5 mL HisTrap FF) at a 2 mL/min flow rate. The column is washed with a solution containing 50 mM Tris-HCl, 50 mM NaCl, 8 M Urea, 1 mM DTT, at pH 8.0 and eluted with an imidazole gradient over 45 mL, the final buffer containing 50 mM Tris-HCl, 50 mM NaCl, 8 M Urea, 1 M imidazole 1 mM DTT at pH 8.0. Fractions are pooled, concentrated using 10 kDa cut off concentrators (Novagen) centrifuged at 5,000 xg, and diluted to reach 0.5 M Urea in 20 mM Tris-HCl, 50 mM NaCl, 10 mM DTT, 1 mM EDTA, at pH 8.0. 0.4 of TEV protease are added to the sample, which is incubated 1 h at RT. After concentration, the sample was very viscous and difficult to manipulate. Thus, I stopped the purification here and focused my attention on BRCA2_{D1} and BRCA2_{D1A}.

BRCA2_{D1}, BRCA2_{D1A}, BRCA2_{D2} and BRCA2_{D2A}

The bacterial pellet is resuspended in 35 mL of a solution containing 50 mM Tris-HCl at pH 8.0, 50 mM NaCl, 5 mM DTT, 2 mM EDTA, 1 mM PMSF, 1 mM ATP, 5 mM MgSO₄, 500 µg lysozyme, 0.5 µL benzonase. Cells are sonicated on ice 2.5 min in total with 1s ON/1s OFF cycle of sonication (50% amplitude), and the lysate is clarified by centrifugation during 15 min at 15,000 xg at 4°C. The insoluble fraction is resuspended in 30 mL of a solution containing 20 mM Tris-HCl 50 mM NaCl, 8 M Urea, 5 mM DTT ,1 mM PMSF, at pH 8.0 and incubated 20 min at RT. The solubilized fraction is clarified by centrifugation (10 min, 15,000 xg, RT) and loaded on a Ni-NTA poly-histidine-affinity column (5 mL HisTrap FF) at a 2 mL/min flow rate. The column is washed with a solution containing 50 mM Tris-HCl, 50 mM NaCl, 8 M Urea,1 mM DTT at pH 8.0 and eluted with an imidazole gradient over 45 mL, the final buffer containing 50 mM Tris-HCl, 50 mM NaCl, 8 M Urea, 1 M imidazole 1 mM DTT at pH 8.0. Fractions are pooled, concentrated using 10 kDa cut off concentrators (Novagen) centrifuged at 5,000 xg.

For BRCA2_{D1}, BRCA2_{D1A}, samples were diluted into buffers containing 0.5 (NMR experiments) or 2 M Urea (phase separation experiments before dilution) with 20 mM Tris-HCl, 50 mM NaCl, 1 mM EDTA, 10 mM DTT, at pH 8.0, incubated at room temperature for 10 min and injected on a gel filtration column (Superdex 10/300 GL 200 pg Increase) equilibrated with a solution containing 50 mM HEPES at pH 7.0, 150 mM NaCl 1 mM EDTA 2 mM DTT and 0 or 2 M Urea buffer.

For BRCA2_{D2}, BRCA2_{D2A}, samples were diluted into a buffer 0.5 M Urea with 20 mM Tris-HCl, 50 mM NaCl, 1 mM EDTA, pH 8.0. and injected on a gel filtration column (Superdex 10/300 GL 200 pg Increase) equilibrated with a solution containing 50 mM HEPES, 150 mM NaCl, 1 mM EDTA at pH 7.0.

After gel filtration, fractions are pooled and supplemented with 2 mM fresh DTT (for BRCA2_{D1} and BRCA2_{D1A}). Sample are concentrated using 3 kDa cut off concentrators centrifuged at 5,000 xg and flash frozen using liquid nitrogen.

BRCA2_{F2}

This protocol was optimized in collaboration with Rania Ghoul.

The bacterial pellet is resuspended in 35 mL of a solution containing 50 mM Tris-HCl at pH 8.0, 50 mM NaCl, 2 mM DTT, 1 mM PMSF, 1 mM ATP, 10 mM MgSO₄, 500 ug lysozyme, 0.5 uL benzonase. Cells are sonicated on ice 2.5 min in total with 1s ON/1s OFF cycle of sonication (50% amplitude), and the lysate is clarified by centrifugation during 15 min at 15,000 xg at 4°C. The insoluble fraction is resuspended in 30 mL of a solution containing 20 mM Tris-HCl, 50 mM NaCl, 8 M Urea, 1 mM PMSF, at pH 8.0 and incubated 20 min at RT. The solubilized fraction is clarified by centrifugation (10 min, 15,000 xg, RT) and loaded on a Ni-NTA poly-histidine-affinity column (5 mL HisTrap FF) at a 2 mL/min flow rate. The column is washed with a solution containing 50 mM Tris-HCl, 50 mM NaCl, 8 M Urea, 1 mM DTT, at pH 8.0 and eluted with an imidazole gradient over 45 mL, the final buffer containing 50 mM Tris-HCl, 50 mM NaCl, 8 M Urea, 1 M imidazole 1 mM DTT, at pH 8.0. Fractions are pooled, concentrated using 10 kDa cut off concentrators (Novagen) centrifuged at 5,000 xg, and diluted into a buffer containing 0.5 M Urea with 20 mM Tris-HCl, 50 mM NaCl, 10 mM DTT, 1 mM EDTA, at pH 8.0. 0.4 mg of TEV protease and 2 mM DTT are added to the sample which is incubated 1 h at RT. The sample is concentrated using Novagen concentrators with 3 kDa cut off membranes centrifuged at 5,000 xg and injected on a gel filtration column (Superdex 16/60 HiLoad 75 pg) equilibrated with a solution containing 50 mM HEPES pH 7.0,

75 mM NaCl, 1 mM EDTA. The fractions of interest are pooled and the sample is concentrated using 3 kDa cut off concentrators centrifuged at 5,000 xg and flash frozen using liquid nitrogen.

GST-Plk1_{PBD}

I optimized this protocol in collaboration with Dr. Simona Miron. The PBD (365-603) was purified by GST-affinity chromatography. After GST cleavage by the TEV protease, the tag and the protease were retained using GST-affinity chromatography, while the PBD was collected in the flow-through and further purified by gel filtration chromatography. The protein was dialyzed against a buffer containing 50 mM Tris-HCl at pH 8, NaCl 150 mM, and 5 mM β -ME (see [Ehlen et al., \(2020\)](#))

His-SUMO-Plk1_{PBD}

The purification protocol of His-SUMO-PBD is described in [Ehlen et al., \(2020\)](#).

Plk1_{FL} and Plk1₃₆₆₋₆₀₃

The bacterial pellet is resuspended in 35 mL of a solution containing 50 mM Tris-HCl at pH 7.5, 50 mM NaCl, 5 mM DTT, 1 mM PMSF, 1 mM ATP, 5 mM MgSO₄, 500 ug lysozyme, 0.5 uL benzonase. Cells are sonicated on ice 2 min in total with 1s ON/5s OFF cycle of sonication (60% amplitude), 15 °C maximum. The lysate is incubated 20 min at RT and then clarified by centrifugation during 10 min at 15,000 xg at 4°C. The soluble fraction is loaded on a Ni-NTA poly-histidine-affinity column (5 mL HisTrap excel) at a 2 mL/min flow rate. The column is washed with a solution containing 50 mM Tris-HCl, 50 mM NaCl, 1 mM DTT at pH 7.5. The sample is eluted with an imidazole gradient over 30 mL, the final buffer containing 50 mM Tris-HCl, 50 mM NaCl, 500 mM imidazole at pH 7.5. The elution fractions are collected and the sample is diluted 100 times with a solution containing 50 mM Tris-HCl at pH 7.5, 50 mM NaCl, 2 mM DTT, 1 mM EDTA. The sample is loaded on a Heparin column (5 mL Heparin Hitrap) at a 2 mL/min flow rate. The column is washed with a solution containing 50 mM Tris-HCl, 50 mM NaCl, 1 mM DTT, at pH 7.5 and the sample is eluted with a NaCl gradient over 30 mL, the final buffer containing 50 mM Tris-HCl, 1 M NaCl, pH 7.5. The elution fractions are collected and 1 mM EDTA and 2 mM DTT are added. The sample is concentrated to 2 mL using 10 kDa cut off concentrators (Novagen) centrifuged at 5,000 xg and injected on a gel filtration column (Superdex 16/60 HiLoad 75 pg for Plk1₃₆₆₋₆₀₃ and 200 pg for Plk1_{FL}) equilibrated with PBS, 1 mM EDTA. Fractions are pooled, 1 mM of fresh DTT is added. The

sample is concentrated using 10 kDa cut off concentrators centrifuged at 5,000 xg and flash frozen using liquid nitrogen.

Plk1₁₋₃₂₈ and Plk1₁₋₃₆₆

The bacterial pellet is resuspended in 35 mL of a solution containing 50 mM Tris-HCl at pH 8.0, 50 mM NaCl, 5 mM DTT, 1 mM PMSF, 1mM EDTA, 1 mM ATP, 5 mM MgSO₄, 500 ug lysozyme, 0.5 uL benzonase. Cells are sonicated on ice 2 min in total with 1s ON/5s OFF cycle of sonication (60% amplitude), 15 °C maximum. The lysate is incubated 20 min at RT and then clarified by centrifugation during 10 min at 15,000 xg at 4°C. The soluble fraction is loaded on a Ni-NTA poly-histidine-affinity column (5 mL HisTrap excel) at a 2 mL/min flow rate. The column is washed with a solution containing 50 mM Tris-HCl, 500 mM NaCl, 1 mM DTT at pH 8.0. The sample was then eluted with an imidazole gradient over 30 mL, the final buffer containing 50 mM Tris-HCl, 50 mM NaCl, 1M imidazole at pH 8.0. The elution fractions are collected and are supplemented with 1 mM EDTA, 2 mM DTT and 1 mM PMSF. The sample is concentrated to 2 mL using 10 kDa cut off concentrators centrifuged at 5,000 xg, and injected on a gel filtration column (Superdex 16/60 HiLoad 75 pg) equilibrated with PBS, 1 mM EDTA. The fractions of interest are pooled, 1 mM of fresh DTT and 1 mM EDTA are added. The sample is concentrated using 10 kDa cut off concentrators centrifuged at 5,000 xg and flash frozen using liquid nitrogen.

AurA-TPX2

The bacterial pellet is resuspended in 35 mL of a solution containing 50 mM Tris-HCl at pH 8.0, 50 mM NaCl, 5 mM DTT, 1 mM PMSF, 1mM EDTA, 1 mM ATP, 5 mM MgSO₄, 500 ug lysozyme, 0.5 uL benzonase. Cells are sonicated on ice 2 min in total with 1s ON/5s OFF cycle of sonication (60 % amplitude), 15 °C maximum. The soluble lysate is then purified by centrifugation during 10 min at 15,000 xg at 4°C. The soluble fraction is loaded on a Ni-NTA poly-histidine-affinity column (5 mL HisTrap excel) at a 2 mL/min flow rate. The column is washed with a solution containing 50 mM Tris-HCl, 50 mM NaCl at pH 8.0. The sample was then eluted with an imidazole gradient over 30 mL, the final buffer containing 50 mM Tris-HCl, 50 mM NaCl, 1 M imidazole at pH 8.0. The elution fractions of interest are collected and concentrated to 2 mL using 30 kDa cut off concentrators centrifuged at 5,000 xg, and injected on a gel filtration column (Superdex 16/60 HiLoad 200 pg) equilibrated with PBS. Fractions are pooled, 1 mM of fresh DTT is added. The sample is concentrated using 30 kDa cut off concentrators centrifuged at 5,000 xg and flash frozen using liquid nitrogen.

Kif2C_{md}

This protocol was kindly communicated to us by Dr. Benoît Gigant's team and reoptimized in the lab by Rania Ghoul.

The bacterial pellet is resuspended in 35 mL of a solution containing 25 mM Tris-HCl at pH 8.0, 1 M NaCl, 5 mM MgCl₂, 5 mM b-mercaptoethanol, 0.1 mM ATP, 500 ug lysozyme, 0.5 uL benzonase. Cells are sonicated 2 min with 1s ON/9s OFF cycle of sonication (60 % amplitude), with a temperature probe set at 10 °C and the soluble lysate is purified by centrifugation during 15 min at 15,000 xg at 4 °C. The soluble fraction is loaded on a Ni-NTA poly-histidine-affinity column (5 mL HisTrap FF) at a 2 mL/min flow rate. The column is washed with a solution containing 25 mM Tris-HCl, 500 mM NaCl, 10 mM imidazole, at pH 7.5. The sample was then eluted with an imidazole gradient over 40 mL, the final buffer containing 25 mM Tris-HCl, 500 mM NaCl, 1 M imidazole, at pH 7.5. The fractions of interest are pooled, concentrated using Novagen concentrators with 10 kDa cut off membranes centrifuged at 5,000 xg, and injected on a gel filtration column (Superdex 16/60 HiLoad 75 pg) equilibrated with a solution containing 50 mM HEPES pH 7.0, 250 mM NaCl, 5 mM b-mercaptoethanol (for ITC study) or 2 mM DTT (for NMR study), 5 mM MgCl₂, at pH 7.0. The fractions are pooled and the sample is concentrated using 10 kDa cut off concentrators centrifuged at 5,000 xg. EDTA-free protease inhibitors (cOmplete EDTA-free) are added at a final 1x concentration and the sample is flash frozen using liquid nitrogen.

Kif2C_{FL(MCAK)} and Kif2C_{FL(46)}

The bacterial pellet is resuspended in 30 mL of a solution containing 20 mM Tris-HCl at pH 8.0, 50 mM NaCl, 5 mM MgCl₂, 5 mM b-mercaptoethanol, 0.1 mM ATP, 500 ug lysozyme, 0.5 uL benzonase. Cells are sonicated for 2 min in total with 1s ON/9s OFF cycle of sonication (60% amplitude) with a temperature probe set up at 10 °C and the soluble lysate is purified by centrifugation during 15 min at 15,000 xg at 4°C. The soluble fraction is loaded on a Ni-NTA poly-histidine-affinity column (5 mL HisTrap excel). The column is washed with a solution containing 20 mM Tris-HCl, 50 mM NaCl, at pH 8.0. The sample was then eluted with an imidazole gradient over 40 mL, the final buffer containing 20 mM Tris-HCl, 50 mM NaCl, 1 M imidazole, at pH 8.0. The fractions of interest are pooled, concentrated using Novagen concentrators with 10 kDa cut off membranes centrifuged at 5,000 xg, and injected on a gel filtration column (Superdex 16/60 HiLoad 200 pg) equilibrated with phosphate at 20 mM and 200 mM NaCl at pH 7.4. The fractions of interest are pooled and the sample is concentrated

using 10 kDa cut off concentrators centrifuged at 5,000 xg. The final sample is supplemented with DTT at a final concentration of 2 mM and flash frozen using liquid nitrogen.

Chk2₁₋₂₀₉

The bacterial pellet is resuspended in 35 mL of a solution containing 50 mM Tris-HCl at pH 8.0, 50 mM NaCl, 5 mM DTT, 1 mM PMSF, 1mM EDTA, 1 mM ATP, 5 mM MgSO₄, 500 ug lysozyme, 0.5 uL benzonase. Cells are sonicated on ice 2 min in total with 1s ON/5s OFF cycle of sonication (60% amplitude), 15 °C maximum. The soluble lysate is purified by centrifugation during 10 min at 15,000 xg at 4°C. The soluble fraction is loaded on a Ni-NTA poly-histidine-affinity column (5 mL HisTrap excel) at a 2 mL/min flow rate. The column is washed with a solution containing 50 mM Tris-HCl, 500 mM NaCl, 1 mM DTT, at pH 8.0. The sample is then eluted with an imidazole gradient over 30 mL, the final buffer containing 50 mM Tris-HCl, 50 mM NaCl, 1 M imidazole, at pH 8.0. The elution fractions of interest are collected, 2 mM DTT and 0.4 mg of TEV protease are added. The sample is incubated 1 h at RT. The sample is then concentrated to 2 mL using 10 kDa cut off concentrators centrifuged at 5,000 xg, and injected on a gel filtration column (Superdex 16/60 HiLoad 200 pg) equilibrated with PBS. Fractions are pooled, 1 mM of fresh DTT and 1 mM EDTA are added. The sample is concentrated using 10 kDa cut off concentrators centrifuged at 5,000 xg, and flash frozen using liquid nitrogen.

PARP1₁₋₃₆₆

The bacterial pellet is resuspended in 35 mL of a solution containing 25 mM HEPES at pH 8.0, 500 mM NaCl, 0.5 mM DTT, 1X protease inhibitors (cOmplete EDTA-free Roche), 1 mM PMSF. Cells are sonicated on ice 2.5 min in total with 1s ON/1s OFF cycle of sonication (50% amplitude, 10°C maximum). The soluble lysate is clarified by centrifugation during 10 min at 15,000 xg at 4°C. The soluble fraction is loaded on a Ni-NTA poly-histidine-affinity column (5 mL HisTrap FF) at a 2 mL/min flow rate. The column is washed with a solution containing 25 mM HEPES at pH 8.0, 1 M NaCl, 20 mM imidazole, 0.5 mM DTT. The sample is then eluted with an imidazole gradient over 35 mL, the final buffer containing 50 mM HEPES at pH 8.0, 500 mM NaCl, 400 mM imidazole, 0.5 mM DTT. The elution fractions of interest are collected and the sample is loaded on HiTrap desalting (5 mL) column, at a 2 mL/min flow rate, equilibrated with a solution containing 50 mM HEPES at pH8.0, 150 mM NaCl, 1 mM EDTA, 0.5 mM DTT. The elutions fractions of interest are pooled and loaded on a Heparin column (5 mL Heparin Hitrap) at a 2 mL/min flow. The column is washed with a solution containing 50

mM HEPES at pH 8.0, 150 mM NaCl, 1 mM EDTA, 0.5 mM DTT. The sample is then eluted with a NaCl gradient over 50 mL, the final buffer containing 50 mM HEPES at pH 8.0, 1 M NaCl, 1 mM EDTA, 0.5 mM DTT. The elution fractions are collected, concentrated to 2 mL using 10 kDa cut off concentrators centrifuged at 5,000 xg, and injected on a gel filtration column (Superdex 16/60 HiLoad 75 pg) priorily equilibrated with a solution containing 50 mM HEPES at pH 8.0, 150 mM NaCl, 1 mM EDTA, 2 mM DTT. The fractions of interest are pooled, concentrated using 10 kDa cut off concentrators centrifuged at 5,000 xg, and flash frozen using liquid nitrogen.

7. Production of Plk1 in insect cells

The plasmid hPlk1 (pTK24 vector) given by Dr Amhed El Marjou (Institut Curie, Paris) (see [Ehlen et al., 2020](#)) was used as a template for human Plk1 cDNA sequence amplification. Primers listed in **Table 8** were used for the PCR amplification of hPlk1 and the pKL vector.

Table 8. Primers for hPlk1 and pKL amplification by PCR.

	Forward primer (5'-3')	Reverse primer (5'-3')
hPlk1	CTGTATTTTCAGGGCATGAGTGCTGCAGTGA CTG	GGCTCTAGACTATTAGGAGGCCTTGAGACGGTTG
pKL	TAATAGTCTAGAGCCTGCAGTCTCG	GCCCTGAAAATACAGGTTTTTCG

The PCR mix was composed of 100 ng DNA template, 2 uM of each primer, 200 uM dNTPs, 1X HF Buffer and 1 uL of ϵ -phusion Q5 polymerase (Phusion High-fidelity DNA polymerase kit from New England BioLabs). PCR was conducted with the following cycle steps: 3 min at 98°C, (20 s at 98°C, 30 s at 64°C, 2.5 min at 72°C)x 35 times, 5 min at 72°C for pKL amplification and 3 min at 98°C, (20 s at 98°C, 30 s at 70°C, 1 min at 72°C)x 35 times, 5 min at 72°C for hPlk1 amplification. PCR products were migrated on 1X agarose gel and purified using the DNA clean and concentrator kit from Zymo Research (D4014). For ligation, 150 ng of purified pKL PCR product was mixed to 115 ng of hPlk1 purified PCR product and to 1X in fusion enzyme premix (TaKaRa) and incubated 1 h at 50°C. Ligation mix was then used to transform Stellar cells (TaKaRa) by heat shock and transformed bacteria were plated on LB-agar containing kanamycin for antibiotic selection. 4 colonies were cultured in 5 mL LB and treated for plasmid extraction using the Plasmid Miniprep kit from New England Biolabs Inc. Plasmids were then sequenced by Eurofins using hPlk1 primers.

After plasmid sequencing, hPlk1-pKL plasmid was used to transform DH10EMBacY cells using heat shock (20 min 4°C, 30 s 42°C, 3 min 4°C, 950 uL of SOC medium, 5 hrs at 37°C) and transformed bacteria were selected on a LB-agar plate containing 30 ug/mL kanamycin, 10 ug/mL tetracyclin, 10 ug/mL gentamycin, 1 mM IPTG, 80 ug/mL X-Gal. This

step permits to achieve the recombination of the hPlk1 sequence from the hPlk1-pKL plasmid into the baculovirus genome sequence contained in the EMBacY bacteria. The hPlk1 sequence is recombined into the β -galactosidase cDNA sequence contained into the EMBaCY bacmid. This recombination results in the disruption of the lacZ gene encoding for the β -galactosidase. Hence, the introduction of Plk1 into the bacmid is screened by growing transformed DH10EMBacY on medium containing IPTG and X-gal. Bacterial clones that contain bacmid carrying the Plk1 cDNA do not express the β -galactosidase, do not digest X-gal and remain uncolored/white, while other clones blue colonies. Two white colonies were incubated in 2 mL LB supplemented with 30 ug/mL kanamycin, 10 ug/mL gentamycin for ON at 37°C. The Plasmid Miniprep kit from New England Biolabs Inc was used until protein precipitation. The supernatant was then supplemented with 44% isopropanol and spun down 10 min at 16,000 xg. EtOH 70% was then used to wash two times the pellet containing the baculovirus genome with hPlk1 and the pellets were dried at RT. Each pellet was then dissolved into 20 uL sterile water, 200 uL of Sf9 medium is added and the transfection mix was completed with 100 uL of sf9 medium and 10 uL of X-TremeGENE (Roche). The mix was then added to a 1.10^6 cell/mL culture of 1 mL. Plates were incubated at 27°C. About 60 hrs later, the supernatant containing the V0 generation of virus was collected and stored at 4°C.

For larger cultures, V0 virus particles were used to infect sf9 cells. Here, I conducted 2 productions of 300 mL. After infection, fluorescence of YFP (contained in the baculovirus genome under the control of the promoter of the polymerase p10, different from the polH promoter used for hPlk1) was monitored to quantify the level of baculovirus-related protein production and cell population. When the fluorescence reached a plateau, cells were collected by centrifugation.

For evaluating the hPlk1 production, I pooled the 2 pellets and resuspended them in 40 mL of a solution containing 20 mM Tris-HCl at pH 8.0, 50 mM NaCl, 1X protease inhibitors (cOmplete EDTA-free Roche), 2 mM DTT, 1 mM EDTA, 1 mM PMSF, 5 mM MgSO₄, benzonase. Suspension was sonicated on ice (1s ON/ 1s OFF cycle for 2 min) with a 10°C maximum temperature allowed. The supernatant was clarified by 15 minutes centrifugation at 10,000 xg and 4°C. Supernatant was loaded on a Ni-NTA poly-histidine-affinity column (HisTrap FF 5 mL), the column was washed with a solution containing 20 mM Tris-HCl at pH 8.0, 50 mM NaCl, 0.5 mM DTT. The sample was eluted through an imidazole gradient of 40 mL, the final buffer containing 50 mM Tris-HCl at pH 8.0, 150 mM NaCl, 500 mM imidazole.

8. Proteomics

This protocol was optimized following the advices of Florent Dingli (MS platform at Institut Curie). All wash steps were performed with beads resuspension unless it is specified.

Recombinant BRCA2 constructs were designed to integrate a 15 amino acid long sequence GLNDIFEAQKIEWHE, so-called Avi-Tag (Fairhead et al., 2015), in the N-terminal end. This permits a specific biotinylation of the lysine contained in the Avi- by the enzyme BirA.

Biotinylation of BRCA2₁₆₇₋₂₆₀ was performed by incubating 100 uM BRCA2₁₆₇₋₂₆₀ in a solution containing 2 mM ATP, 600 uM biotine, 5 mM MgCl₂, 1 mM DTT, 1X protease inhibitors, at pH 7.0 together with 0.7 uM of BirA enzyme (produced by FX Theillet and Chafiaa Bouguechtouli) in a buffer containing 50 mM HEPES, 150 mM NaCl, 1 mM EDTA. The sample was incubated 1h30 at RT and injected on a gel filtration column (Superdex 16/60 HiLoad 75 pg) priorily equilibrated with a solution containing 50 mM HEPES pH 7.0, 75 mM NaCl, 1 mM EDTA. The fractions of interest were pooled, supplemented with 1 mM fresh DTT and the sample ws concentrated using 3 kDa cut off concentrators centrifuged at 5,000 xg. EDTA-free protease inhibitors (cOmplete EDTA-free) are added at a final 1x concentration and the sample was flash frozen using liquid nitrogen.

Either 50 uL or 100 uL of Streptavidine-coated magnetic beads (Streptavidine Mag-Beads, Genscript) were used per sample and loaded with 2 ng or 10 ng of BRCA2 peptide constructs, respectively. All conditions were performed with 5 replicates. Beads were first washed 3 times using 500 uL PBS. 2 ng or 10 ng of recombinant biotinylated Avi-tag-BRCA2₁₆₇₋₂₆₀ in PBS at pH 7.5, 1 mM DTT, 1X protease inhibitors were added to the beads in a 100 uL final volume. The samples and the beads were incubated for 1 h at RT on a rotating wheel, washed 2 times with 500 uL of a solution containing 50 mM HEPES at pH 7.2, 150 mM NaCl, 2 mM EDTA, 10 mM NaF, 0.5 mM PMSF, 1 X protease inhibitors, 1 mM DTT, 1X PhosphoSTOP mixed with 800 ug of lysed cells extracts (HEK cells synchronized or not with nocodazole) in 20 mM HEPES at pH 7.6, 150 mM NaCl, 0.1% NP40, 2 mM EGTA, 1.5 mM MgCl₂, 50 mM NaF, 10% glycerol, 20 mM b-glycerophosphate, 1 mM DTT, 1X protease inhibitors produced by Dr. Aura Carreira's team.

In the experimental conditions using 10 ng of BRCA2 peptides, HEK 293 synchronized (G2/M phase, nocodazole) cell extracts were incubated 30 min at RT on a rotating wheel. In the next steps, the 5 replicates were treated at the same time in order to favor the reproducibility of the experiment. The samples were washed 3 times with 100 uL of a solution containing 50

mM HEPES at pH 7.2 150 mM NaCl, 2 mM EDTA, 10 mM NaF, 0.5 mM PMSF, 1 mM DTT, and washed 3 times with 100 uL of a solution containing 50 mM ammonium bicarbonate at pH 8.25. The beads were resuspended at every step. The beads in 100 uL of 50 mM ammonium bicarbonate pH 8.25 are kept on ice and given to the MS Institut Curie platform (Paris) for MS analysis.

In the experimental conditions using 2 ng of BRCA2 peptides, cell extracts were incubated for 2 hrs at RT on a rotating wheel. In the next steps, the 5 replicates were treated at the same time in order to favor the reproducibility of the experiment. The samples were washed 3 times with 100 uL of a solution containing 50 mM HEPES at pH 7.2, 150 mM NaCl, 2 mM EDTA, 10 mM NaF, 0.5 mM PMSF, 1 mM DTT, and washed twice without resuspension of the beads with 500 uL of a solution containing 50 mM ammonium bicarbonate at pH 8.25. The beads were kept on ice in 500 uL of the buffer containing 50 mM ammonium bicarbonate at pH 8.25 and given to the MS Institut Curie platform (Paris) for MS analysis.

The analysis of the results was later achieved on the website of the platform using MYPROMS.

9. Peptides and DNA

Synthetic peptides used for ITC measurements in this study are listed in **Table 9** and short DNA oligomers used for interaction assays with BRCA2 are listed in **Table 10**. DNA sequences correspond to synthetic nucleotidic sequences from yeast telomeric DNA, previously designed for another project in the lab.

Table 9. List of peptides used, their solubilization buffer and their corresponding supplier.

Name	Peptide	Solubilization buffer	Supplier
T207	Ac-WSSSLATPPTLSSTVLI-CONH ₂	H ₂ O	ProteoGenix
pT207	A-WSSSLATPPTLSSpTVLI-CONH ₂	H ₂ O	ProteoGenix
T207A	Ac-WSSSLATPPTLSSAVLI-CONH ₂	H ₂ O	ProteoGenix
T207D	Ac-WSSSLATPPTLSSDVLI-CONH ₂	H ₂ O	ProteoGenix
T77	Ac-YNQLASTPII-CONH ₂	H ₂ O	ProteoGenix
pT77	Ac-YNQLASpTPII-CONH ₂	H ₂ O	ProteoGenix
T77D	Ac-YNQLASDPII-CONH ₂	H ₂ O	ProteoGenix
T77E	Ac-YNQLASEPII-CONH ₂	H ₂ O	ProteoGenix

Table 10. List of DNA used their sequence and their solubilization

Name	Sequence	Solubilization buffer
R9	5' -TCCTGGTGTGTGGGTGTGCGG	H ₂ O
R9R10	5' -TCCTGGTGTGTGGGTGTGCGG - 3' 3' -CCAGGACCACACACCCACACG- 5'	H ₂ O

10. ITC

All ITC titrations were performed on a VP-ITC instrument (Malvern) and data were analyzed using the Origin 7.0 software (OriginLab).

The ITC titrations for BRCA2/Plk1_{PBD} interactions were performed with 500 uL of BRCA2 peptides at 100 uM in the syringe and 2.4 mL of Plk1_{PBD_Curie} 10 uM in the cell, both in a solution containing 50 mM Tris HCl at pH 8.0, 150 mM NaCl, 5 mM b-mercaptoethanol. Measurements were performed at 20°C with a first injection of 2 uL during 4 s, and then injections of 10 uL in 20 s separated of 240 s intervals.

The ITC titration for BRCA2/Kif2C_{md} interaction was performed with 500 uL of pBRCA2₁₆₇₋₂₆₀ at env. 100 uM in the syringe and 2.4 mL of Kif2C_{md} at env. 10 uM in the cell or 500 uL of Kif2C_{md} at env. 100 uM in the syringe and 2.4 mL of pBRCA2₁₆₇₋₂₆₀ at env. 10 uM in the cell, both in a solution containing 50 mM HEPES at pH7.0, 250 mM NaCl, 5 mM b-mercaptoethanol, 5 mM MgCl₂ buffer. The measurements were performed at 10°C with a first injection of 2 uL during 4 s, and then injections of 10 uL in 20 s separated of 210 s intervals.

11. Phosphorylation kinetics

The following kinases were used in this study:

- Plk1 active but not activated, produced by the protein production platform of the Institut Curie (Dr. Ahmed El Marjou, Paris) in insect cells and purified as described in [Ehlen et al., 2020](#)
- Commercial Cdk1/B1 from Sigma Aldrich
- Commercial Cdk1/A2 from Sigma Aldrich
- Commercial p38 β from Sigma Aldrich
- Home-produced p38 α by Dr. François-Xavier Theillet
- Commercial PKA from NE Biolabs

The general phosphorylation protocol is described in [Julien et al., 2020](#). Briefly, two sorts of protocols can be used: the quenched reaction (pH>7.5) and the continuous readout (pH<7.0).

- Plk1 phosphorylation

BRCA2₁₉₀₋₂₈₄ phosphorylation by Plk1 was initially set up at pH 7.8 using the quenched reaction protocol. BRCA2 peptides at 200 uM were mixed to Plk1 at a final concentration of 1.1 uM in a reaction buffer containing 50 mM HEPES, 1 mM EDTA, 2 mM ATP, 20 mM MgCl₂, 2 mM DTT, 1X protease inhibitors, at pH 7.8. For NMR analysis, 150 uL aliquots of the reaction samples * number of time points were prepared. The samples were incubated at 30°C and boiled for 5 min at 95°C to stop the reaction.

The BRCA2₄₈₋₂₁₈ phosphorylation by Plk1 using the quenched reaction was performed in the same conditions but at a substrate concentration of 50 uM and a Plk1 concentration of 100 nM (different Plk1 stock than for BRCA2₁₉₀₋₂₈₄, with higher activity).

Continuous readout monitoring of BRCA2 phosphorylation by Plk1 was performed with substrate concentrations between 45 and 200 uM and Plk1 concentrations between 150 and 250 nM. Reactions were performed in a buffer containing 50 mM HEPES, 75 mM NaCl, 1 mM EDTA, 5 mM MgCl₂, 2 mM ATP, 2 mM DTT, 1X protease inhibitors, 3-5 % D₂O, 50 uM DSS, at pH 7.0. 300 uL of mix were prepared per reaction. In the case of monitoring using ¹³C-direct detection (¹H-flip)-CaCO NMR spectroscopy, 3 mM V-NOTA were added to the sample.

- Phosphorylation in cell extracts

The continuous NMR readout was performed to monitor this reaction. BRCA2₄₈₋₂₁₈ at 130 uM was mixed to 350 uL of fresh mitotic synchronized cell extracts (DLD1 BRCA2^{-/-} cells) at a final concentration of 2.65 ug/uL in a lysis buffer containing 45 mM HEPES at pH 7.2, 0.5 mM EDTA, 10 mM MgCl₂, 50 mM KCl, 3% NP40, 10% glycerol, 1X PI, 1X antiphosphatase, 3 mM DTT. 2 mM ATP, 2 mM fresh DTT and 10% D₂O were added to a final volume of 500 uL.

- PKA phosphorylation

The continuous NMR readout was carried out to monitor this reaction. BRCA2₄₈₋₂₁₈ was mixed to 1 uL of PKA, 1X NEB buffer supplemented with 1 mM ATP, 1X PI and 5% D₂O in a 150 uL final volume.

- Cdk1/B1 and Cdk1/A2 phosphorylation

The continuous NMR readout was carried out to monitor this reaction. BRCA2₄₈₋₂₁₈ at 50 uM was mixed to 40 uL of Cdk1/B1 or 10 uL of Cdk1/A2 in a reaction buffer containing 50

mM HEPES at pH 7.0, 1 mM EDTA, 10 mM MgCl₂, 2 mM ATP, 4 uM TCEP, 5% D₂O, 1X protease inhibitors in a final volume of 150 uL for 15 hrs.

- p38 β and p38 α phosphorylation

The continuous NMR readout was performed to monitor this reaction. BRCA2₄₈₋₂₁₈ at 50 uM was mixed to a reaction buffer containing 50 mM HEPES at pH 7.0, 1 mM EDTA, 20 mM MgCl₂, 2 mM ATP, 2 mM DTT, 5% D₂O, 1X protease inhibitors in a final volume of 150 uL (or 150 uL * time point for further Plk1 quenched reaction). 15 uL of commercial p38 β or 1-2 uM of home-produced p38 α .

For sequential phosphorylation (Cdk1/B1 and Plk1 or p38 and Plk1), samples were boiled 5 min at 95°C after the first phosphorylation reaction for inactivating the first kinase. Buffer was then exchange either by successive steps of concentrations/dilutions or by gel filtration (Superdex 10/300 GL 75).

- Plk1₁₋₃₂₈ phosphorylation by AurA-TPX2

Plk1₁₋₃₂₈ was mixed to AurA-TPX2 in conditions described in **Figure 77**. The mix was incubated at 25°C. 10 uL aliquots were taken at several time points and mixed to 10 uL 2X Laemmli buffer.

Phos-tag gel preparation were prepared as described in [Kinoshita et al. 2003](#):

Stacking gel: 0.22 mL bis-acrylamide 40%, 1.2 mL H₂O, 0.5 mL 0.5 M Tris-HCl pH 6.8, 25 uL APS 10%, 25 uL SDS 10%, 5 uL TEMED.

Running gel: 1.75 mL bis-acrylamide 40%, 3.1 mL H₂O, 1.75 mL 0.5 M Tris-HCl pH 8.8, 75 uL Phos-tag (alphanabs) 5 mM dissolved in 3% MeOH, 75 uL MnCl₂ 10 mM, 40 uL APS 10%, 70 uL SDS 10%, 4 uL TEMED.

12. NMR spectroscopy

³¹P-NMR spectroscopy experiments were carried out on a 600 MHz Bruker spectrometer equipped with a broadband room-temperature probe at the ICSN spectrometry platform, under the supervision of François Giraud. The acquisition was performed using a 5 mm tube containing ¹⁵N-labeled BRCA2₁₆₇₋₂₆₀ at 300 uM phosphorylated by Plk1 in a buffer containing 50 mM HEPES, 75 mM NaCl, 1 mM EDTA, 5% D₂O, at pH 7.0. The spectra were recorded at 283 K (1024 or 2048 scans) and 300 K (1024 scans).

All the other experiments were recorded either on a 600 MHz Bruker Advance II spectrometer or a 700 MHz Bruker Advance Neo spectrometer, both equipped with a triple resonance cryogenically cooled probe optimized for ^1H -detection (TXI or TCI, Bruker).

The backbone ^1H - ^{15}N assignment of BRCA2₍₄₈₋₂₈₄₎ is described in Julien et al. (2020) NMR Biomol. Assign. The assignment of BRCA2₁₆₇₋₂₆₀ was performed with a sample containing BRCA2₁₆₇₋₂₆₀ at 200 μM in 50 mM HEPES, 75 mM NaCl, 1 mM EDTA, 1 mM DTT, at pH 7.0, 3% D₂O, 50 μM DSS in a 3mm tube. The assignment of pBRCA2₁₆₇₋₂₆₀ was performed using a sample containing BRCA2₁₆₇₋₂₆₀ at 100 μM in the same conditions. ^1H - ^{15}N SOFAST-HMQC, ^1H - ^{15}N HSQC and CBCA(CO)NH spectra were recorded on a 600 MHz Bruker spectrometer.

^1H - ^{15}N SOFAST-HMQC spectra acquisitions for phosphorylation studies are extensively described in Julien et al. (2020) Methods in Mol. Biol. The (^1H -flip) ^{13}C - ^{13}CO -LOWBASHD experiments are detailed in Alik et al. (2020) Angew. Chem. Int. Eng.

The samples from quenched reactions were analyzed in 3 mm NMR tubes (Norell) and the samples used for continuous reading in 5mm Shigemi tubes.

For sample analysis or interaction tests, the samples were analyzed in 3 mm tubes in buffer conditions described in the corresponding figures. ^1H - ^{15}N SOFAST-HMQC spectra were recorded using 1024 or 1536 points in the direct ^1H dimension and 128 or 256 points in the indirect ^{15}N dimension.

For relaxation measurements, R_1 values were derived from peak intensities measured in ^1H - ^{15}N HSQC spectra recorded using 2048 points in the direct dimension, 256 points in the indirect dimension and 12 delays (20, 60, 100, 900, 400, 1300, 60, 2000, 600, 200, 1600 and 600 ms; ns=8). R_2 were obtained from ^1H - ^{15}N HSQC spectra with 2048 points in the direct dimension, 200 points in the indirect dimension and 10 delays (16.96, 33.92, 67.84, 101.76, 135.68, 203.52, 271.36, 339.2, 135.68 and 407.04 ms; ns=8). ^1H - ^{15}N heteronuclear NOEs were measured in 2D spectra recorded with 2048 points in the direct dimension and 512 points in the indirect dimension (ns=24, interscan delay = 5s).

Data were analyzed using Topspin 4.0.6 (Bruker) and CcpNMR Analysis 2.4, R_1 and R_2 fits were performed using CcpNMR Analysis 2.4.

13.Observation of phase separation by microscopy

For the first analysis of phase transition, a $\lambda 50$ Zeiss microscope available at the lab was used with a x50 magnification. For later studies, we used a TCS SP8-X inverted FALCON

(Leica) available on the I2BC microscopy platform. We used a 63x PLAN oil immersion implemented with DIC (NA: 1.4) (Leica). These experiments were performed under the supervision of Romain Le Bars and François-Xavier Theillet. The protein samples were mixed with various concentrations of salts and Ficoll 70 immediately before DIC microscopy observation.

For microscopy experiments, we trapped a sample drop between 2 glass plates with a 2 mm space as shown in **Figure 31**.

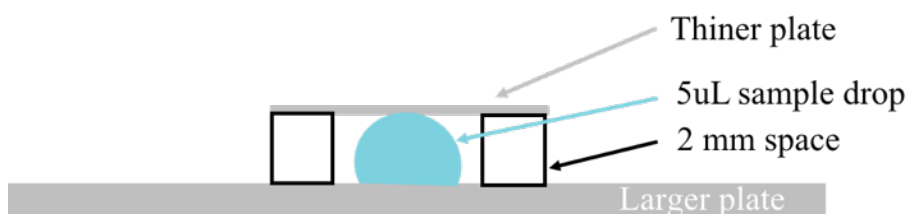


Figure 31. Device for microscopy observation of liquid-liquid phase transition.

14. Peptide synthesis and Native Chemical Ligation

The N-terminal peptide has the same N-terminal extremity as BRCA2₄₈₋₂₁₈. The C-terminal extremity of this synthetic peptide is the residue 84, a glycine, which is usually a favorable C-terminal residue for an efficient NCL. The BRCA2₄₈₋₈₄ peptide was synthesized by Jean-Baptiste Madinier and Dr. Vincent Aucagne using Fmoc-based solid phase synthesis, with and without T77 phosphorylation. A thioester was introduced at the C-terminal extremity for the NCL according to their published protocol (Terrier et al., 2016).

The C-terminal peptide BRCA2_{85-220-G85C} was produced recombinantly in a ¹⁵N-labeled fashion, according to the protocol reported above. The two BRCA2 fragments were purified and analyzed by inverse-phase HPLC and then lyophilized by Jean-Baptiste Madinier. Then, they were weighted, redissolved at 0,5-1 mM concentrations and added to the NCL reaction mix containing 50 mM TCEP (reduction of thiols), 25 mM 4-mercaptophenylacetic acid (MPAA) (serves as a catalyzer by increasing the reactivity of the cryptothioester), 1.5 M NaOH (to adjust the pH to 7.0), 6 M Guanidinium chloride (for removing any potential secondary structure and for increasing the NCL yields) and 20 mM phosphate to buffer the solution. In order to prevent thiol oxidation, the system was submitted to gaseous argon and then incubated at 37°C under agitation for a night. The reaction was monitored overtime by taking 3 uL of the reaction sample mixed to 100 uL of acetonitrile 80:20 H₂O, 0.1 % TFA to quench the reaction. The sample was then loaded on a hydrophobic column linked to a HPLC system and eluted

with a H₂O/acetonitrile gradient (**Figure 76**). The reaction was completed after 24 hrs of incubation.

15. Figures

Figures were prepared using either Microsoft Powerpoint version 16.42 or Affinity Designer 1.7.2.

Results

Chapter 1. Sample production

During my PhD, I produced several BRCA2 fragments spanning the N-terminal region either for the “phosphorylation by Plk1” project (**Figure 32.A**) or for the “NTD-DNA-Binding Domain” (NTD-DBD) project (**Figure 32.B**).

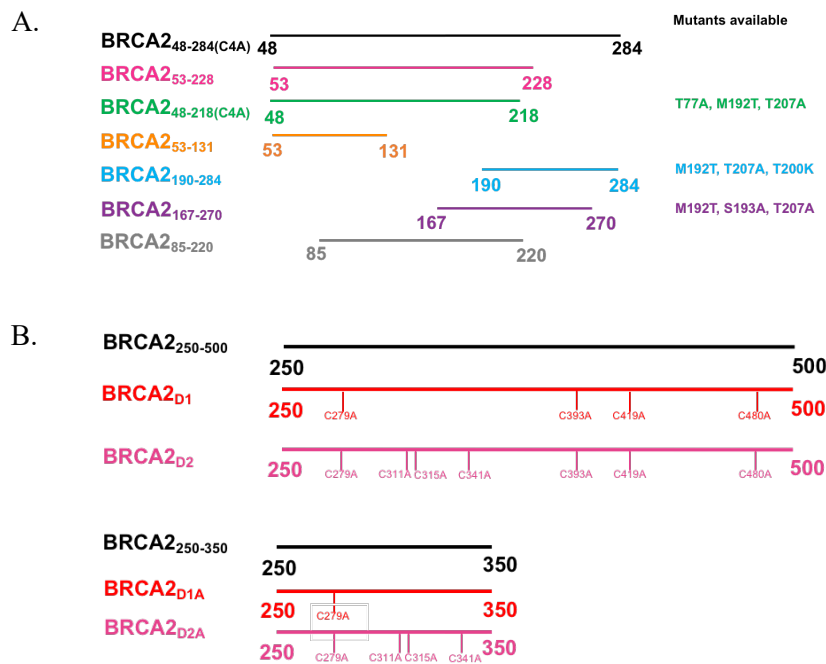


Figure 32. The BRCA2 constructs used for my PhD project (A) The BRCA2 constructs used for the analysis of BRCA2 phosphorylation by Plk1 and (B) the BRCA2 constructs for the DNA-Binding Domain investigations.

Optimizing their production and purification took a large part of my PhD time. However, this work cannot be published *per se*. In this Chapter, I would like to describe experimental principles that I established after purifying several IDRs:

- In most cases, the optimal conditions for their recombinant expression in *E. coli* BL21 (DE3) Star were as follows: induction at 37 °C for 4 hrs for IDRs expressed in the soluble fraction, or at 20 °C overnight for IDRs found in the insoluble fraction (**Figure 33**). At 37 °C, overexpression longer than 4 hrs generates degraded IDR fragments, observable from the first purification step and difficult to remove from the final purified sample.

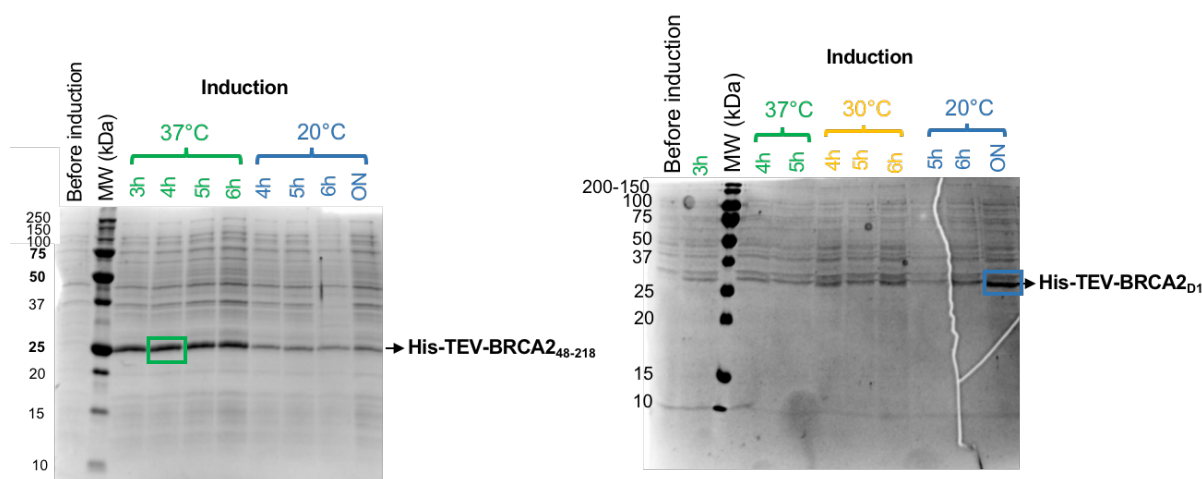


Figure 33. Example of overexpression tests in *E. coli* BL21 (DE3) Star for a IDR expressed in the soluble fraction (left) and an IDR found in the insoluble fraction (right). Total bacteria lysed in 3X Laemmli buffer were loaded on gels, without careful normalization by the OD₆₀₀ of each sample. The best overexpression conditions, without high level of proteolysis, were at 37°C and 4 hrs of induction for the soluble IDR and at 20 °C overnight for the insoluble fragment.

- It is necessary to purify the IDR quickly, in presence of good quantities of protease inhibitors, in order to diminish proteolysis. A protocol containing an affinity chromatography, a cleavage of the tag and a gel filtration chromatography can be performed in one day, which prevents important protein degradation. Also, purification steps should be realized at 4 °C, unless urea is used in the case of His-tag purification of IDRs found in the insoluble fraction upon cell lysis. Furthermore, the addition of adapted protease inhibitors is important. In protocols that I optimized, I use PMSF and EDTA during the sonication step and the first affinity purification, EDTA in all the other steps and finally add to the sample coming out of the last gel filtration a commercial mix of inhibitors (here “EDTA free tablets of protease inhibitors” from Roche), targeting a large set of proteases.
- I also continuously used a freshly prepared disulfide reducer. DTT presents a lifetime of about 20 hrs at 4°C at pH<7. The exposed cysteines present in IDRs are very accessible to oxidation. In most cases, I supplemented the lysis extract with 5 millimolar DTT, and spiked the samples eluted from every column with 2 mM DTT before proceeding with concentration.
- The protocol should include a gel filtration (GF) step in order i) to validate the solubility of the IDR, ii) to remove maximal amounts of as much proteases, nucleic acids and cellular debris, iii) to transfer the IDR in the exact chosen buffer, which is mandatory for conducting reliable NMR spectroscopy (dialysis is too much time consuming for

IDR integrity purposes). GF separates the constituents of samples according to their hydrodynamic radii. Due to the disordered character of IDRs, their elution volume is not comparable to that of classical globular proteins used for column calibration. An IDR elutes commonly at a volume corresponding to a globular protein of about 3-4-fold its molecular weight.

- During my PhD time, several projects about IDRs/IDPs were developed in the lab. I could observe that their biased amino acid composition of these disordered regions/proteins can modify their migration on SDS-PAGE. For example IDRs/IDPs showing high content in acidic amino acids can migrate much slower than standard proteins of the same weight. During the purification analysis, it may be useful to keep it in mind.
- Finally, several IDRs/IDPs purification protocols include a boiling step, at 90-95 °C for 10 min. Most of the contaminants are folded proteins (the *E. coli* proteome is very poor in IDPs) and precipitate at a high temperature, while IDRs/IDPs are commonly still soluble. I initially used this strategy. Nevertheless, thanks to our collaboration with chemists from the Centre de Biophysique Moléculaire (Dr. Vincent Aucagne team), HPLC analysis clearly revealed that this step creates a large chemical heterogeneity in the sample (**Figure 34**). Thus, in the last 2.5 years of my PhD, I removed this step from my protocols.

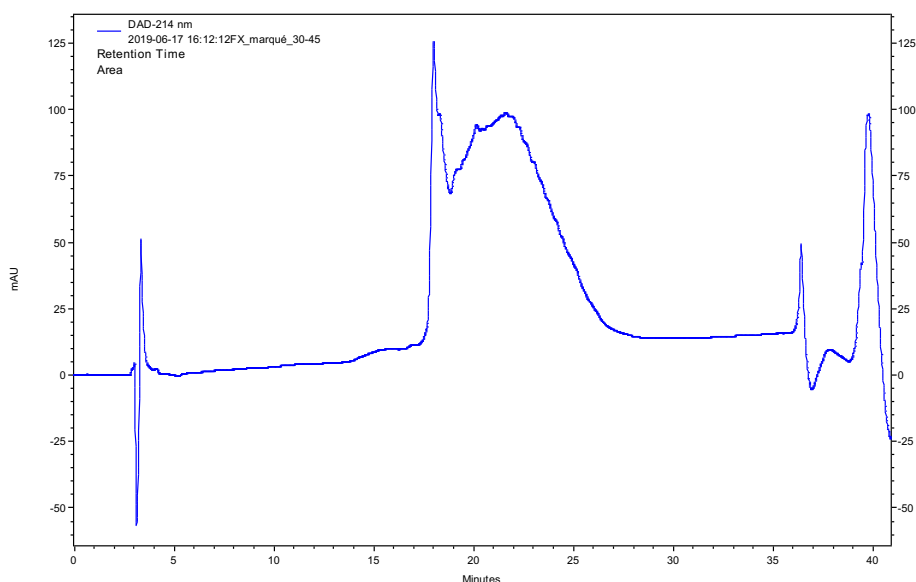


Figure 34. ^{15}N BRCA₂₈₅₋₂₂₀ sample boiled during purification and analyzed by inverse-phase C18 chromatography. The BRCA₂₈₅₋₂₂₀ fragment was correctly eluted after 18.5 min of a H₂O:acetonitrile gradient, however a larger peak is also eluted later (20-25 min). Its analysis by ESI MS revealed that this larger peak also contains BRCA₂₈₅₋₂₂₀ suggesting heterogeneity of the sample.

Using these observations, I conducted the re-optimization of BRCA2₁₉₀₋₂₈₄ purification, initially set up by Dr. Simona Miron:

- induction at 37 °C for 4 hrs instead of 3 hrs,
- substitution of the 30 kDa cut off concentrating step for removing the chaperone contaminant by a gel filtration chromatography,
- purification in 1 day instead of 2.5 days: I shorten the Precision cleavage step to 1h at RT instead of ON at 4°C, I added a gel filtration step for buffer exchange instead of dialysis and I changed the initial concentration at 2,000 xg using 3kDa cut off concentrator devices for centrifugation with 10 kDa cut off (for IDP: minimum 2-folds the MW) at 5,000 xg.

This new protocol decreased proteolysis, thereby increasing sample homogeneity and yields (by ~30%).

These observations also helped me to conduct the production optimization of all the other IDRs used in this study. Further details are provided in the Material and Methods section.

Chapter 2. Identification of BRCA2 residues phosphorylated by Plk1

In order to study the phosphorylation of the N-terminal region of BRCA2 by Plk1, my first objective was to define the construct boundaries and to design protein constructs allowing the production and purification of this region of interest.

1. Delimiting the region of interest: BRCA2₄₈₋₂₈₄

Lin et al., 2003 identified that BRCA2₁₋₂₈₄ is phosphorylated by Plk1 during mitosis at S193 and at least at one other position. I started by predicting the Plk1 phosphosite(s) on BRCA2 based on the Plk1 phosphorylation consensus sequence described in Nakajima et al., 2003, Alexander et al., 2011 and Kettenbach et al., 2012. (Figure 35). Three phosphosites are predicted, at positions S158, S193, and S239. Moreover, analysis of MS data (<https://www.phosphosite.org/>) reveals two conserved phosphorylation clusters in this region (Figure 36). The first cluster contains the residue T77, which is phosphorylated by Cdks and creates a Plk1 docking site (Takaoka et al., 2014). As this cluster may be involved in the regulation of BRCA2 phosphorylation by Plk1, I included it in the region of interest. The second cluster contains the Plk1 phosphoregion including S193 (Lin et al., 2003, Takaoka et al., 2014). Thus, I defined my region of interest from BRCA2 residue 48 to residue 284 (BRCA2₄₈₋₂₈₄).

10	20	30	40	50
MPIGSKERPT	FFEIFKTRCN	KADLGPISLN	WFEELSSEAP	PYNSEPAEES
60	70	80	90	100
EHKNNNYEPN	LFKTPQRKPS	YNQLASTPII	FKEQGLTLPL	YQSPVKELDK
110	120	130	140	150
FKLDLGRNVP	NSRHKSLRTV	KTKMDQADDV	SCPLLNSCLS	ESPVVLQCTH
160	170	180	190	200
VTPQRDKSVV	CGSLFHTPKF	VKGRQTPKHI	SESLGAEVDP	DMSWSSSLAT
210	220	230	240	250
PPTLSSTVLI	VRNEEASETV	FPHDTTANVK	SYFSNHDESL	KKNDRFIASV
260	270	280		
TDSENTNQRE	AASHGFGKTS	GNSFKVNSCK	DHIG	

Prediction of Plk1 phosphosites
Known Plk1 docking site

Figure 35. Prediction of Plk1 phosphosites among the N-terminal BRCA2 sequence using the consensus sequence [S/D/E/N]-X-p[S/T]-φ, with φ for hydrophobic residue at position i+1 or i+2 (Nakajima et al., 2003, Alexander et al., 2011, Kettenbach et al., 2012) and localization of the known Plk1 docking site in this region (Takaoka et al., 2014, Yata et al., 2014).

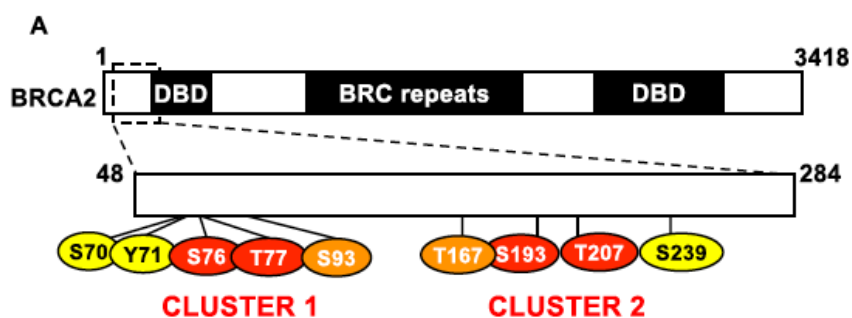


Figure 36. The N-terminal BRCA2 fragment includes 2 phosphoclusters well-conserved from mammals to fishes (<https://www.phosphosite.org/>). Residues identified as phosphorylation sites in more than one mass spectrometry study are displayed. The conservation of these residues was deduced from the analysis of an alignment of 30 BRCA2 sequences from fishes to mammals. The phosphosites are indicated in red if conserved in all 30 sequences, in orange if conserved in more than 80% and yellow if conserved in less than 80% of the sequences. Four phosphosites are 100% conserved: Ser76, Thr77, Ser193 and Thr207.

2. The NMR analysis of BRCA2₄₈₋₂₈₄ reveals that it is disordered

After obtaining good yields and stable samples of BRCA2₄₈₋₂₈₄, my second objective was to assign the NMR signals of BRCA2₄₈₋₂₈₄. To achieve this goal, I analyzed several complementary BRCA2 fragments: BRCA2₄₈₋₂₁₈, BRCA2₅₃₋₁₃₁, BRCA2₁₉₀₋₂₈₄. This diminished the number of peak overlaps in the corresponding NMR spectra, which greatly facilitated the assignment of the NMR signals of BRCA2₄₈₋₂₈₄. Of course, such a strategy relies on the hypothesis that residues did experience the same chemical environment in every truncated construct and in the larger construct. This was demonstrated by the perfect overlap of the NMR resonances generated by every residue in the different constructs, as usually observed for IDRs. The NMR chemical shift assignment and structural characterization of BRCA2₄₈₋₂₈₄ are reported in a publication that I wrote as a first author for the *Biomolecular NMR Assignment Journal*.

In this study, I experimentally confirmed that BRCA2₄₈₋₂₈₄ is a disordered peptide. Furthermore, I assigned the ¹H-¹⁵N backbone signals of the protein, a necessary step for monitoring phosphorylation using ¹H-¹⁵N 2D SOFAST-HMQC NMR.



ARTICLE

^1H , ^{13}C and ^{15}N backbone resonance assignment of the human BRCA2 N-terminal region

Manon Julien^{1,2} · Simona Miron¹ · Aura Carreira^{2,3,4} · François-Xavier Theillet¹ · Sophie Zinn-Justin¹ Received: 21 November 2019 / Accepted: 20 December 2019
© Springer Nature B.V. 2020

Abstract

The Breast Cancer susceptibility protein 2 (BRCA2) is involved in mechanisms that maintain genome stability, including DNA repair, replication and cell division. These functions are ensured by the folded C-terminal DNA binding domain of BRCA2 but also by its large regions predicted to be disordered. Several studies have shown that disordered regions of BRCA2 are subjected to phosphorylation, thus regulating BRCA2 interactions through the cell cycle. The N-terminal region of BRCA2 contains two highly conserved clusters of phosphorylation sites between amino acids 75 and 210. Upon phosphorylation by CDK, the cluster 1 is known to become a docking site for the kinase PLK1. The cluster 2 is phosphorylated by PLK1 at least at two positions. Both of these phosphorylation clusters are important for mitosis progression, in particular for chromosome segregation and cytokinesis. In order to identify the phosphorylated residues and to characterize the phosphorylation sites preferences and their functional consequences within BRCA2 N-terminus, we have produced and analyzed the BRCA2 fragment from amino acid 48 to amino acid 284 (BRCA2_{48–284}). Here, we report the assignment of ^1H , ^{15}N , ^{13}CO , $^{13}\text{C}\alpha$ and $^{13}\text{C}\beta$ NMR chemical shifts of this region. Analysis of these chemical shifts confirmed that BRCA2_{48–284} shows no stable fold: it is intrinsically disordered, with only short, transient α -helices.

Keywords BRCA2 · Mitosis · Breast cancer · Intrinsically disordered protein · Phosphorylation · NMR

Biological context

BReast CAncer susceptibility 2 (BRCA2) is a tumor suppressor gene identified in 1994, commonly mutated in hereditary breast and ovarian cancers (Wooster et al. 1994). BRCA2 was initially characterized as a DNA repair protein involved in the recruitment and loading of the recombinase RAD51, which, in turn, drives the homologous recombination process at DNA double-strand breaks (DSB) (Thorslund and West 2007; Moynahan and Jasin 2010; Jensen et al. 2010). Two decades later, BRCA2 is mainly described as a key platform

protein for genome stability contributing to DNA repair, telomere maintenance, stressed replication fork stabilization (Fradet-Turcotte et al. 2016) and mitosis (Daniels et al. 2004; Mondal et al. 2012; Choi et al. 2012; Venkitaraman 2014). These functions are ensured by the folded C-terminal DNA binding domain of BRCA2 (Yang et al. 2002) and the large regions predicted to be disordered that contain several protein binding motifs. Among them, two short fragments were already structurally characterized in complex with their partner: one of the repeated BRC motifs BRC4 bound to RAD51 (Pellegrini et al. 2002) and BRCA2 fragment between amino acid 21 and amino acid 39 interacting with PALB2 (Oliver et al. 2009). Both of these BRCA2 segments form α -helices upon binding to their partner. Here, we focus on the N-terminal region of BRCA2, which contains 1000 amino acids with a structure that remains elusive. It is predicted to be disordered (Fig. 1b) and contains two clusters of phosphorylation (Fig. 1a) identified by mass spectrometry (<https://www.phosphosite.org/>) between amino acid 75 and amino acid 80 for cluster 1, and amino acid 190 and aa 210 for cluster 2. These two clusters are very well conserved from mammals to fishes and their biological relevance is still

✉ Sophie Zinn-Justin
sophie.zinn@cea.fr

¹ Institute for Integrative Biology of the Cell (I2BC), CEA, CNRS, Univ Paris-Sud, Université Paris-Saclay, Gif-sur-Yvette Cedex, France

² Paris Sud University, Paris-Saclay University CNRS, UMR3348, 91405 Orsay, France

³ Institut Curie, PSL Research University, UMR3348, 91405 Orsay, France

⁴ CNRS, UMR3348, 91405 Orsay, France

unclear. The cluster 1 was reported to be phosphorylated by Cyclin-Dependant Kinases (CDK) at position T77 during late S-phase to mitosis (Yata et al. 2014). This phosphorylation generates a genuine Polo-Like Kinase 1 (PLK1) docking site (Takaoka et al. 2014; Yata et al. 2014) suggested to promote further phosphorylation by PLK1 both on BRCA2 itself (Lin et al. 2003; Takaoka et al. 2014) and on BRCA2 partners such as RAD51 (Yata et al. 2014). However, biochemical data are missing to describe to which extent this BRCA2 phosphorylation by CDKs influences later phosphorylation kinetics by PLK1. The cluster 2 is phosphorylated by PLK1 during mitosis (Lin et al. 2003). This regulates BRCA2 interaction

Fig. 2 Overlapping BRCA2 constructs were used to analyze the two phosphorylation clusters. **a** Five constructs were designed for this study, containing either phosphorylation cluster 1 (BRCA2₅₃₋₁₃₁) or cluster 2 (BRCA2₁₉₀₋₂₈₄) or both (BRCA2₅₃₋₂₂₈, BRCA2_{48-218(C4A)} and BRCA2_{48-284(C4A)}). BRCA2₅₃₋₂₂₈ comprises 4 cysteines (C132, C138, C148, C161). In construct BRCA2_{48-218(C4A)} and BRCA2_{48-284(C4A)}, the four cysteines are mutated into alanines. **b** The ¹H-¹⁵N SOFAST-HMQC spectra of BRCA2₅₃₋₂₂₈ (pink) at 50 μM in buffer A containing TCEP and BRCA2_{48-218(C4A)} (green) at 50 μM in buffer A containing DTT are superimposable, peaks overlap for residues spanning the whole sequence except around the mutated positions (labelled in black) and close to the N-terminal or C-terminal ends (labelled in grey). These spectra were recorded at 283 K and pH 7.0 on a Bruker 700 MHz spectrometer

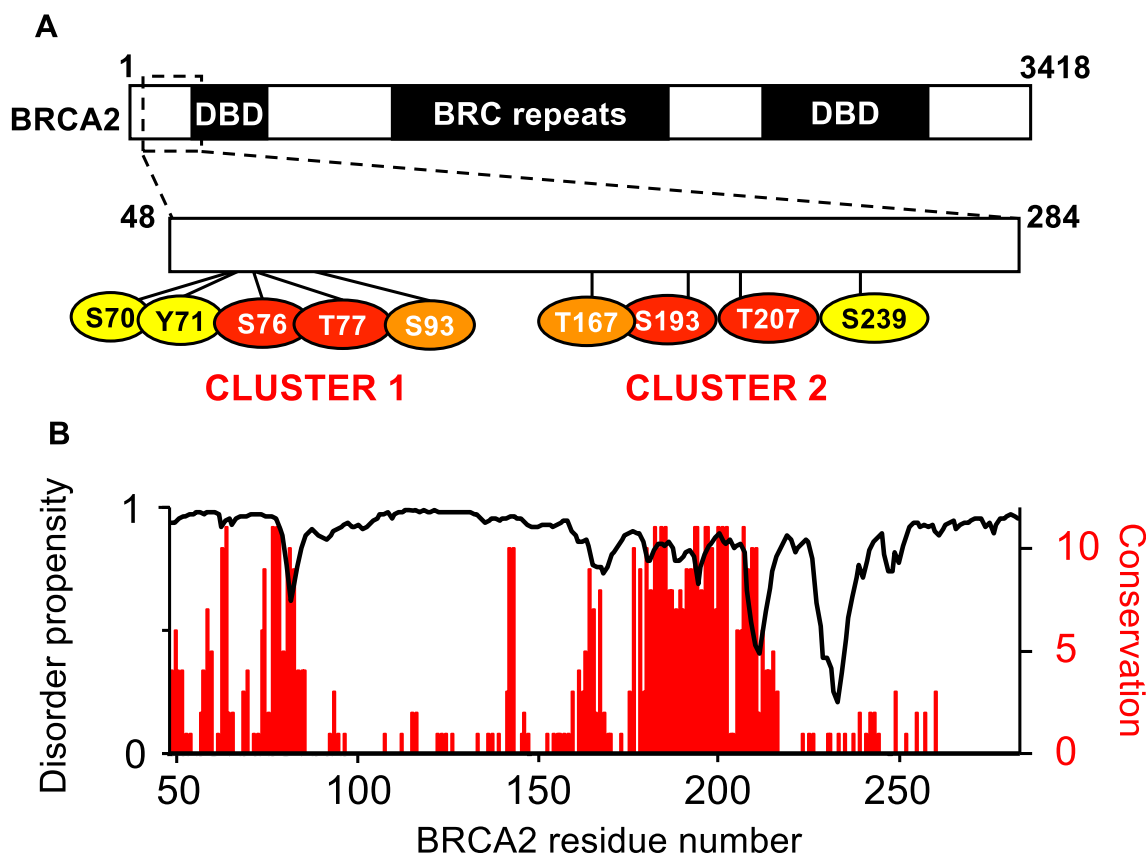
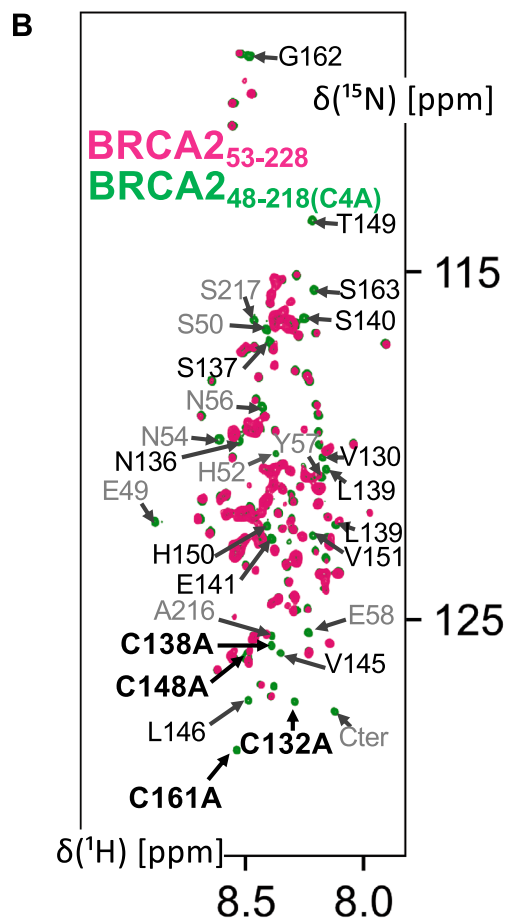
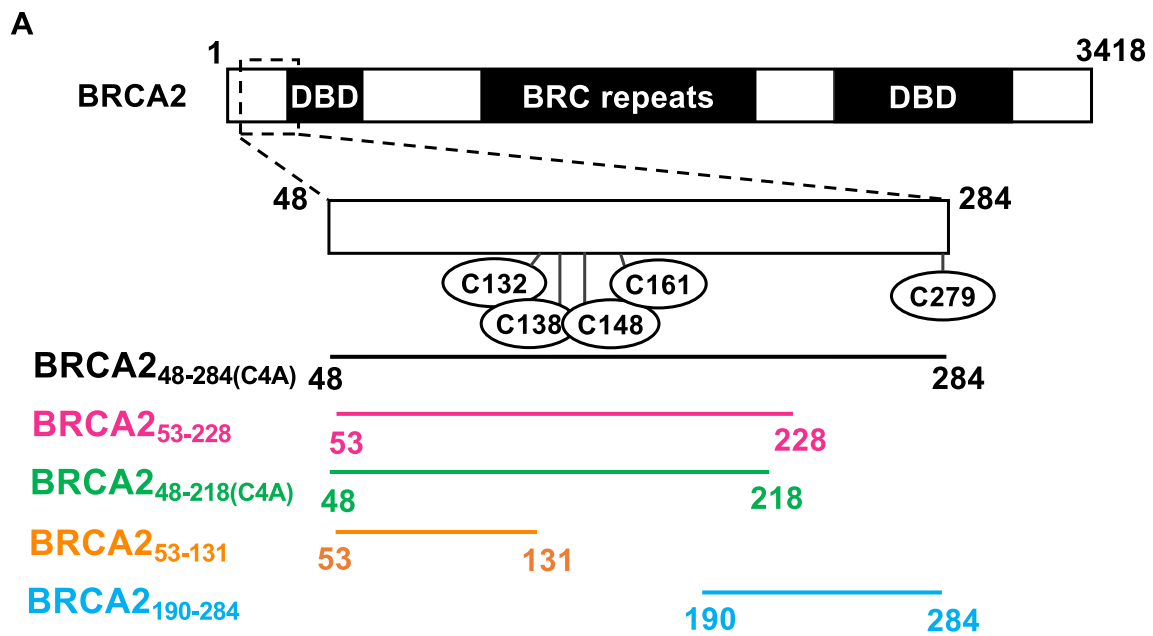


Fig. 1 The N-terminal BRCA2 fragment includes 2 phosphoclusters well-conserved from mammals to fishes. **a** BRCA2 is composed of (i) a 1000 residues long N-terminal region containing the PALB2 binding site (from amino acid 21 to amino acid 39) and a DNA binding domain (DBD) (from amino acid 250 to amino acid 500) (von Nicolai et al. 2016), (ii) an intermediate region made of 8 successive BRC repeats (from amino acid 1002 to amino acid 2085 and (iii) a folded C-terminal DBD (from amino acid 2500 to amino acid 3200). The N-terminal region of the protein contains several phosphorylation sites (<https://www.phosphosite.org/>) organized in two phosphorylation clusters. Alignment of 30 BRCA2 sequences from fishes to mammals revealed that 4 of these positions are 100% conserved: Ser76, Thr77, Ser193 and Thr207. We focused on the BRCA2 region from amino acid 48 to amino acid 284, which includes these 4 phospho-

sites. In this region, residues identified as phosphorylation sites in more than one mass spectrometry study are indicated in red if conserved in all 30 sequences, in orange if conserved in more than 80% and yellow if conserved in less than 80% of the sequences. **b** The disorder propensity and conservation of the BRCA2 region from amino acid 48 to amino acid 284 are displayed as a function of the sequence. The disorder propensity was calculated using SPOT-Disorder (Hanson et al. 2016). A score of 1 corresponds to a predicted disorder propensity of 100%. The conservation score was calculated using Jalview 1.0 (Clamp et al. 2004). A score of 11 corresponds to a position identical in 100% of the sequences, while a score of 1 indicates that only one chemical criteria (size, hydrophobicity, global charge) is common to all the variants



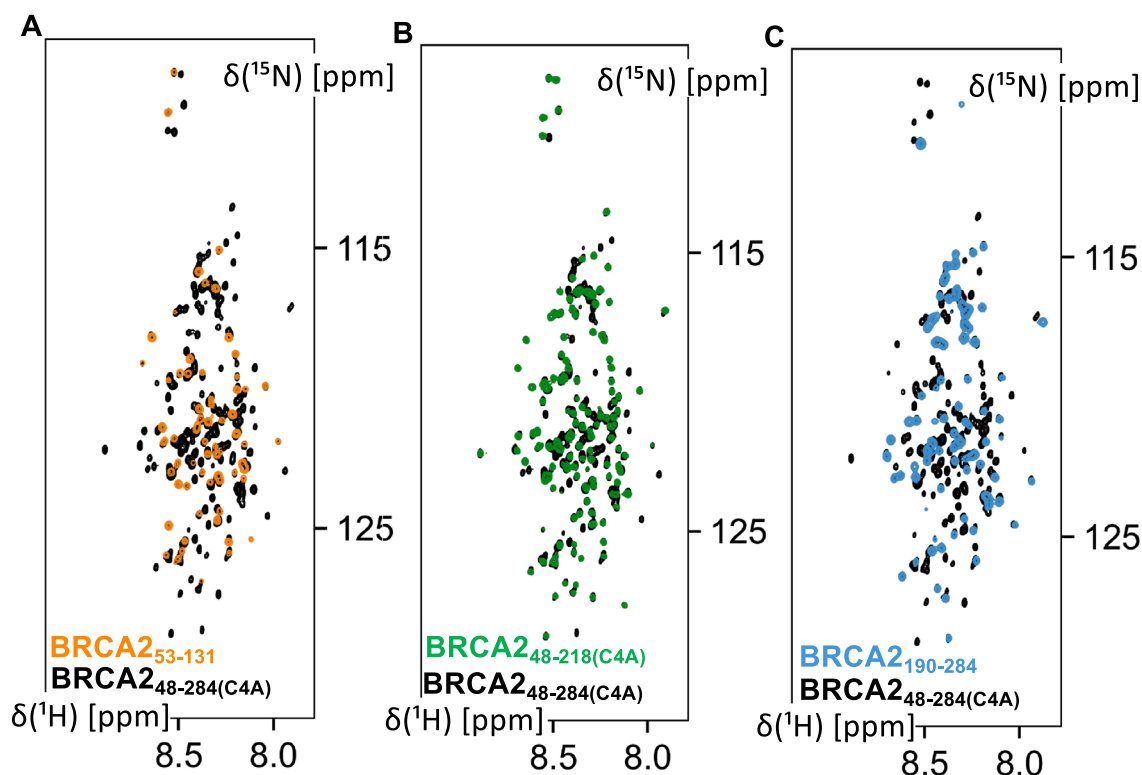


Fig. 3 Superimposition of the constructs spanning the BRCA2 region from amino acid 48 to amino acid 284 confirms the intrinsically disordered behavior of this region. The ^1H - ^{15}N SOFAST-HMQC spectra of **a** BRCA2₅₃₋₁₃₁ (orange), **b** BRCA2_{48-218(C4A)} (green) and **c** BRCA2₁₉₀₋₂₈₄ (blue) are superimposed over BRCA2_{48-284(C4A)} in the different panels. All peptides are at 50 μM in buffer A and spectra

were recorded at 283 K and pH 7.0 on a Bruker 700 MHz spectrometer. Only chemical shifts of residues close to the extremities vary between shorter constructs and BRCA2_{48-284(C4A)}. In order to simplify the figure, peaks corresponding to these residues are not labelled, however, they can easily be highlighted by comparison of chemical shift values available on the BMRB

with the P300/CBP-associated factor (P/CAF) (Lin et al. 2003). It also creates a supplementary PLK1 docking site that ensures chromosome segregation (Ehlen et al. 2019). Furthermore, phosphorylation of S193 by PLK1 leads to the recruitment of BRCA2 at the Flemming body, an important step that warrants a complete cytokinesis (Daniels et al. 2004; Takaoka et al. 2014). While these phosphorylation events have been observed to dynamically regulate these BRCA2 functions throughout the cell cycle, little is known about the structure of the BRCA2 N-terminal region and the phosphorylated residues are only partially identified. Here, we report the assignment of the ^1H , ^{15}N , $^{13}\text{C}\alpha$, $^{13}\text{C}\beta$ and ^{13}CO NMR chemical shifts of the WT BRCA2₄₈₋₂₈₄ fragment.

Methods and experiments

Protein expression and purification

Five fragments spanning the human WT BRCA2 N-terminal phosphorylation clusters were designed: a fragment

from amino acid 53 to amino acid 131 (BRCA2₅₃₋₁₃₁), a fragment from amino acid 53 to amino acid 228 (BRCA2₅₃₋₂₂₈), a fragment from amino acid 48 to amino acid 218 in which all cysteines are mutated into alanines (BRCA2_{48-218(C4A)}), a fragment from amino acid 190 to amino acid 284 (BRCA2₁₉₀₋₂₈₄) and a fragment from amino acid 48 to amino acid 284 with the first four cysteines mutated into alanines (BRCA2_{48-284(C4A)}) (Fig. 2a). All fragments were expressed in *Escherichia coli* BL21 (DE3) Star using a pETM13 vector (BRCA2₅₃₋₂₂₈, BRCA2_{48-218(C4A)} and BRCA2_{48-284(C4A)}), a pGEX-6P-1 vector (GE Healthcare, BRCA2₁₉₀₋₂₈₄) or a pET-41b vector (BRCA2₅₃₋₁₃₁). cDNA of BRCA2₅₃₋₁₃₁, BRCA2₅₃₋₂₂₈, BRCA2_{48-218(C4A)} and BRCA2_{48-284(C4A)} were optimized for expression in *E. coli* (Genscript). Bacteria were grown in M9 medium supplemented with $^{15}\text{NH}_4\text{Cl}$ (0.5 g/L) and ^{13}C -glucose (2 g/L) as sole sources of nitrogen and carbon. Recombinant expression was induced at an optical density of 0.6–0.8 using 1 mM isopropyl β -D-1-thiogalactopyranoside during 4 h at 37 °C. Cells were harvested by centrifugation, resuspended in lysis buffer

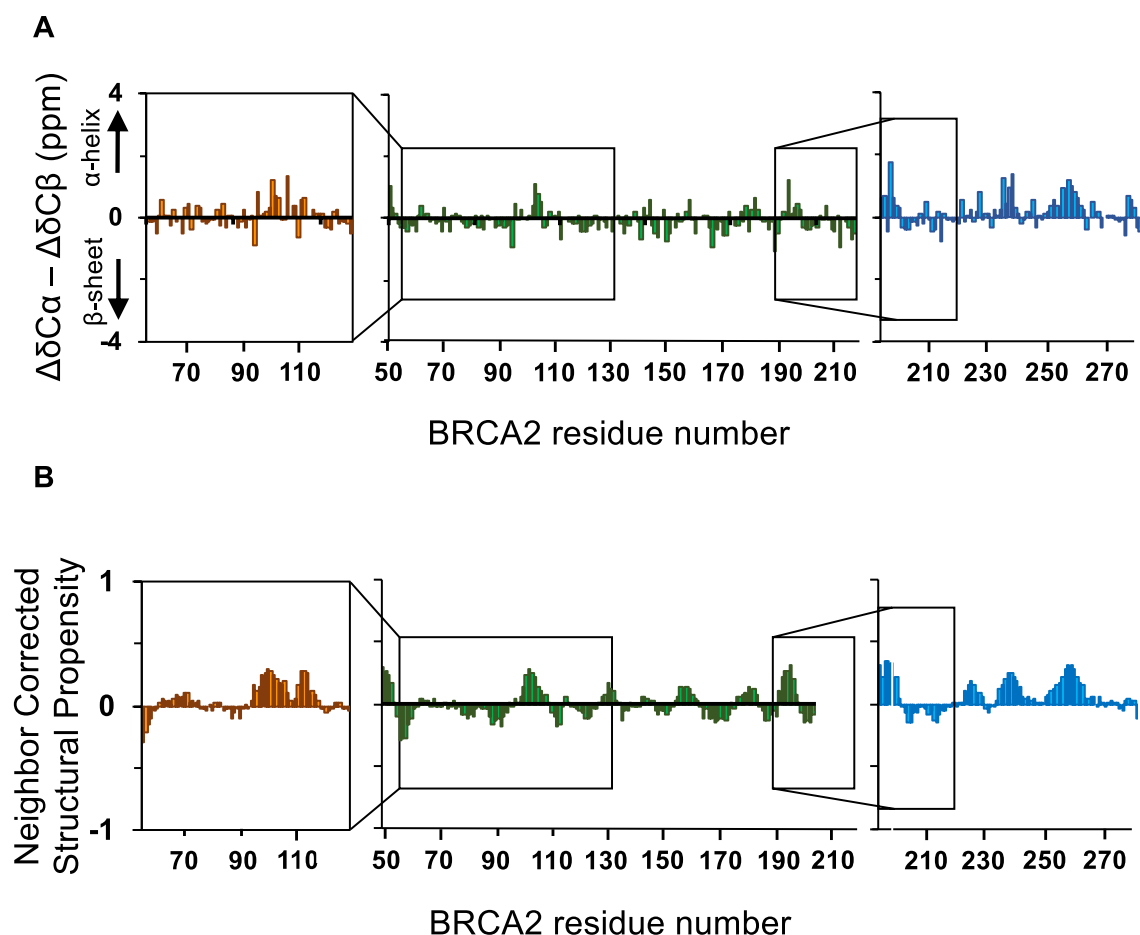


Fig. 4 Analysis of the secondary propensity BRCA2₅₃₋₁₃₁ (orange), BRCA2_{48-218(C4A)} (green) and BRCA2₁₉₀₋₂₈₄ (blue) based on the C α and C β chemical shifts. **a** Analysis of experimental C α and C β chemical shifts compared to predicted values for a disordered region ([https](https://nmr.chem.rug.nl/ncIDP)

[://nmr.chem.rug.nl/ncIDP](https://nmr.chem.rug.nl/ncIDP)) (Tamiola et al. 2010). **b** Analysis based on the calculator available on the website <https://linuxnmr02.chem.rug.nl/ncSPC/> (Tamiola and Mulder 2012) and the library of Tamiola et al. (2010), with an average window of 5 residues

(20 mM Tris, 150 mM NaCl, 1 mM EDTA, 5 mM DTT, 1 mM PMSF, pH 8) and lysed by sonication. The soluble fraction was obtained upon centrifugation of the whole cell lysate at 20,000 \times g during 15 min at 4 °C. BRCA2₅₃₋₁₃₁, BRCA2₅₃₋₂₂₈ and BRCA2₁₉₀₋₂₈₄ were produced with a N-terminal GST tag followed by either a TEV cleavage site (ENLYFQG) or a PreScission cleavage site (LEV-LFQGP) and purified by Glutathione Sepharose affinity chromatography. The tag was cleaved by the TEV protease (BRCA2₅₃₋₁₃₁ and BRCA2₅₃₋₂₂₈) or the PreScission protease (BRCA2₁₉₀₋₂₈₄). The BRCA2₅₃₋₁₃₁ and BRCA2₁₉₀₋₂₈₄ samples were then boiled at 95 °C during 10 min to remove the GST tag, centrifuged 10 min at 16,000 \times g, and the supernatant was later injected on a gel filtration column (Highload 16/60 Superdex 75 pg; GE Healthcare) equilibrated with buffer A (50 mM HEPES, 1 mM EDTA, 2 mM dithiothreitol, pH 7.0). The influence of boiling on structure was verified by ^1H - ^{15}N HSQC NMR (data not shown). BRCA2₅₃₋₂₂₈ precipitates after cleavage,

and therefore was pelleted by centrifugation (10 min, 16,000 \times g), then resuspended into buffer A supplemented with 8 M urea and finally diluted 10 times with buffer A containing 10 mM β -mercaptoethanol before injection on a gel filtration column (Highload 16/60 Superdex 75 pg; GE Healthcare) equilibrated with 50 mM HEPES, 1 mM EDTA, 5 mM tris(2-carboxyethyl)phosphine (TCEP), pH 7.0. BRCA2_{48-218(C4A)} and BRCA2_{48-284(C4A)} were expressed with a N-terminal octa-histidine tag and purified by Ni-NTA affinity chromatography. The tag was cleaved using the TEV protease and the sample was injected on a gel filtration column (Highload 16/60 Superdex 75 pg; GE Healthcare) equilibrated with buffer A at pH 7.0 or buffer A at pH 6.4 for assignment of BRCA2_{48-218(C4A)}. Samples were concentrated to 200–400 μM for assignment experiments (BRCA2₅₃₋₁₃₁, BRCA2_{48-218(C4A)} and BRCA2₁₉₀₋₂₈₄) and to 50 μM for BRCA2₅₃₋₂₂₈ and BRCA2_{48-284(C4A)} characterization.

NMR spectroscopy

NMR experiments were performed on uniformly ^{15}N and ^{13}C labelled fragments in buffer A at pH 7.0 for BRCA2_{53–131}, BRCA2_{48–218(C4A)}, BRCA2_{190–284} and BRCA2_{48–284(C4A)} ($\text{H}_2\text{O}:\text{D}_2\text{O}$ ratio 90:10), in buffer A at pH 6.4 ($\text{H}_2\text{O}:\text{D}_2\text{O}$ ratio 95:5) for BRCA2_{48–218(C4A)} and in 50 mM HEPES, 1 mM EDTA, 5 mM TCEP, pH 7.0 ($\text{H}_2\text{O}:\text{D}_2\text{O}$ ratio 95:5) for BRCA2_{53–228}. All samples were supplemented with 50 μM Sodium trimethylsilylpropanesulfonate (DSS). NMR experiments were recorded at 283 K on a 600 MHz Bruker Advance II spectrometer and a 700 MHz Bruker Advance Neo spectrometer, both equipped with a triple resonance cryogenically cooled probe. Spectra were referenced using DSS ^1H chemical shifts (Wishart et al. 1995) and ^1H , ^{13}C and ^{15}N resonance frequencies were assigned using 2D $^1\text{H}-^{15}\text{N}$ SOFAST-HMQC, 3D BEST-HNCACB, CBCA(CO)NH, BEST-HNCO, BEST-HN(CA)CO and HN(CO)(CA)NH experiments. The data were processed using Topspin 3.6 (Bruker) and analyzed with CCPNMR Analysis (Vranken et al. 2005). The assignments were deposited in the BioMagResBank (<https://www.bmrb.wisc.edu/>) under the following codes: 50077 for BRCA2_{48–218(C4A)}, 50078 for BRCA2_{53–131} and 50079 for BRCA2_{190–284}.

Assignments and data deposition

To facilitate the assignment of the human BRCA2 region from amino acid 48 to amino acid 284, we designed and produced three overlapping fragments: BRCA2_{53–131} centered on the phosphorylation cluster 1, BRCA2_{53–228} containing the two phosphorylation clusters and BRCA2_{190–284} that contains only the cluster 2 (Fig. 2a). BRCA2_{53–131} and BRCA2_{190–284} were purified in sufficient amounts and were stable enough for NMR analysis. However, BRCA2_{53–228} was prone to aggregation due to the oxidation of its four solvent-exposed cysteines. These cysteines are not conserved within BRCA2 from fishes to human. Therefore, we designed the construct BRCA2_{48–218(C4A)}, which corresponds to the fragment from amino acid 48 to amino acid 218 with all cysteines mutated into alanines (C132A, C138A, C148A and C161A; see Fig. 2a). The $^1\text{H}-^{15}\text{N}$ HSQC spectra of BRCA2_{53–228} and BRCA2_{48–218(C4A)} overlap to a large extent: we observed differences only in the vicinity of the mutated residues and N-ter or C-ter ends (Fig. 2b). This shows that the alanine mutations did not modify the average structural ensemble of the peptide. Then, we assigned the ^1H , ^{15}N , $^{13}\text{C}\alpha$, $^{13}\text{C}\beta$ and ^{13}CO chemical shifts of the fragments BRCA2_{53–131}, BRCA2_{48–218(C4A)} and BRCA2_{190–284} using a series of 3D heteronuclear NMR experiments. We obtained

high assignment coverages along the sequences of fragments BRCA2_{53–131}, BRCA2_{48–218(C4A)} and BRCA2_{190–284}: 94%, 97% and 96% of $^1\text{H}-^{15}\text{N}$ pairs, 87%, 98% and 95% of $^{13}\text{C}\alpha$, 99%, 96% and 97% of $^{13}\text{C}\beta$ and 96%, 98%, 95% of ^{13}CO resonances were assigned, respectively. Figure 3 shows a very good crosspeak superimposition between the $^1\text{H}-^{15}\text{N}$ spectra of every fragment and that of BRCA2_{48–284(C4A)}. The narrow range of backbone amide ^1H chemical shifts (between 7.5 and 8.5 ppm) for all BRCA2 fragments reveals their disordered behavior. Furthermore, only the crosspeaks corresponding to the N-terminal or C-terminal residues of each fragment differ from those of the largest construct of BRCA2, i.e. BRCA2_{48–284(C4A)}. The secondary structure analysis, based on $^{13}\text{C}\alpha$ and $^{13}\text{C}\beta$ chemical shifts and the neighbor corrected structural propensity method (Tamiola et al. 2010; Tamiola and Mulder 2012), confirms the absence of a stable fold for BRCA2_{53–131}, BRCA2_{48–218(C4A)} and BRCA2_{190–284} (Fig. 4). We observed α -helical propensities of about 25% around residues 100–110 and 255–260. We concluded that the fragment of BRCA2 from amino acid 48 to amino acid 284 is disordered and that its shorter segments BRCA2_{53–131}, BRCA2_{48–218(C4A)} and BRCA2_{190–284} have the same structural properties when isolated or within BRCA2_{48–284(C4A)}. From this set of data, it is now possible to monitor phosphorylation reactions within the two conserved BRCA2 clusters of phosphorylation using $^1\text{H}-^{15}\text{N}$ and $^1\text{H}-^{13}\text{C}$ NMR spectroscopy.

Acknowledgements This work was supported by CEA, CNRS, University Paris South and ENS Paris Saclay, by the French Infrastructure for Integrated Structural Biology (<https://www.structuralbiology.eu/networks/frisbi>, grant number ANR-10-INSB-05-01, Acronym FRISBI) and by the French National Research Agency (ANR; research grant FUNBRCA2).

References

- Choi E, Park P, Lee H, Lee Y, Kang G, Lee J, Han W, Lee H, Noh D, Lekomtsev S, Lee H (2012) BRCA2 fine-tunes the spindle assembly checkpoint through reinforcement of BubR1 acetylation. *Dev Cell* 22(2):295–308. <https://doi.org/10.1016/j.devcel.2012.01.009>
- Clamp M, Cuff J, Searle S, Barton G (2004) The Jalview Java alignment editor. *Bioinformatics* 20(3):426–427. <https://doi.org/10.1093/bioinformatics/btg430>
- Daniels M, Wang Y, Lee M, Venkitaraman A (2004) Abnormal cytokinesis in cells deficient in the breast cancer susceptibility protein BRCA2. *Science* 306(5697):876–879. <https://doi.org/10.1126/science.1102574>
- Ehlen A, Martin C, Miron S, Julien MT, Ropars FX, Sessa V, Beaurepere G, Boucherit R, Duchambon V, El Marjou P, Zinn-Justin A, Carreira S, A. (2019) Proper chromosome alignment depends

- on BRCA2 phosphorylation by PLK1. *BioRxiv*. <https://doi.org/10.1101/265934>
- Fradet-Turcotte A, Sitz J, Grapton D, Orthwein A (2016) BRCA2 functions: from DNA repair to replication fork stabilization. *Endocr-Relat Cancer* 23(10):T1–T17. <https://doi.org/10.1530/erc-16-0297>
- Hanson J, Yang Y, Paliwal K, Zhou Y (2016) Improving protein disorder prediction by deep bidirectional long short-term memory recurrent neural networks. *Bioinformatics*. <https://doi.org/10.1093/bioinformatics/btw678>
- Jensen R, Carreira A, Kowalczykowski S (2010) Purified human BRCA2 stimulates RAD51-mediated recombination. *Nature* 467(7316):678–683. <https://doi.org/10.1038/nature09399>
- Lin H, Ting N, Qin J, Lee W (2003) M Phase-specific phosphorylation of BRCA2 by polo-like kinase 1 correlates with the dissociation of the BRCA2-P/CAF complex. *J Biol Chem* 278(38):35979–35987. <https://doi.org/10.1074/jbc.m210659200>
- Mondal G, Rowley M, Guidugli L, Wu J, Pankratz V, Couch F (2012) BRCA2 localization to the midbody by filamin A regulates CEP55 signaling and completion of cytokinesis. *Dev Cell* 23(1):137–152. <https://doi.org/10.1016/j.devcel.2012.05.008>
- Moynahan M, Jasin M (2010) Mitotic homologous recombination maintains genomic stability and suppresses tumorigenesis. *Nat Rev Mol Cell Biol* 11(3):196–207. <https://doi.org/10.1038/nrm2851>
- Oliver A, Swift S, Lord C, Ashworth A, Pearl L (2009) Structural basis for recruitment of BRCA2 by PALB2. *EMBO Rep* 10(9):990–996. <https://doi.org/10.1038/embor.2009.126>
- Pellegrini L, Yu D, Lo T, Anand S, Lee M, Blundell T, Venkitaraman A (2002) Insights into DNA recombination from the structure of a RAD51–BRCA2 complex. *Nature* 420(6913):287–293. <https://doi.org/10.1038/nature01230>
- Takaoka M, Saito H, Takenaka K, Miki Y, Nakanishi A (2014) BRCA2 phosphorylated by PLK1 moves to the midbody to regulate cytokinesis mediated by nonmuscle myosin IIC. *Cancer Res* 74(5):1518–1528. <https://doi.org/10.1158/0008-5472.can-13-0504>
- Tamiola K, Mulder F (2012) Using NMR chemical shifts to calculate the propensity for structural order and disorder in proteins. *Biochem Soc Trans* 40(5):1014–1020. <https://doi.org/10.1042/bst20120171>
- Tamiola K, Acar B, Mulder F (2010) Sequence-specific random coil chemical shifts of intrinsically disordered proteins. *J Am Chem Soc* 132(51):18000–18003. <https://doi.org/10.1021/ja105656t>
- Thorslund T, West S (2007) BRCA2: a universal recombinase regulator. *Oncogene* 26(56):1210870. <https://doi.org/10.1038/sj.onc.1210870>
- Venkitaraman A (2014) Cancer suppression by the chromosome custodians, BRCA1 and BRCA2. *Science* 343(6178):1470–1475. <https://doi.org/10.1126/science.1252230>
- von Nicolai C, Ehlén Å, Martin C, Zhang X, Carreira A (2016) A second DNA binding site in human BRCA2 promotes homologous recombination. *Nature Commun*. <https://doi.org/10.1038/ncomms12813>
- Vranken W, Boucher W, Stevens T, Fogh R, Pajon A, Llinas M, Ulrich E, Markley J, Ionides J, Laue E (2005) The CCPN data model for NMR spectroscopy: development of a software pipeline. *Proteins* 59(4):687–696. <https://doi.org/10.1002/prot.20449>
- Wishart D, Bigam C, Yao J, Abildgaard F, Dyson H, Oldfield E, Markley J, Sykes B (1995) ^1H , ^{13}C and ^{15}N chemical shift referencing in biomolecular NMR. *J Biomol NMR* 6(2):135–140. <https://doi.org/10.1007/bf00211777>
- Wooster R, Neuhausen S, Mangion J, Quirk Y, Ford D, Collins N, Nguyen K, Seal S, Tran T, Averill D et al (1994) Localization of a breast cancer susceptibility gene, BRCA2, to chromosome 13q12–13. *Science* 265(5181):2088–2090. <https://doi.org/10.1126/science.8091231>
- Yang H, Jeffrey P, Miller J, Kinnucan E, Sun Y, Thomä N, Zheng N, Chen P, Lee W, Pavletich N (2002) BRCA2 Function in DNA binding and recombination from a BRCA2–DSS1–ssDNA structure. *Science* 297(5588):1837–1848. <https://doi.org/10.1126/science.297.5588.1837>
- Yata K, Bleuyard J, Nakato R, Ralf C, Katou Y, Schwab R, Niedzwiedz W, Shirahige K, Esashi F (2014) BRCA2 coordinates the activities of cell-cycle kinases to promote genome stability. *Cell Rep* 7(5):1547–1559. <https://doi.org/10.1016/j.celrep.2014.04.023>

Publisher's Note Springer Nature remains neutral with regard to jurisdictional claims in published maps and institutional affiliations.

3. Plk1 efficiently phosphorylates 4 residues in the BRCA2₄₈₋₂₈₄ region.

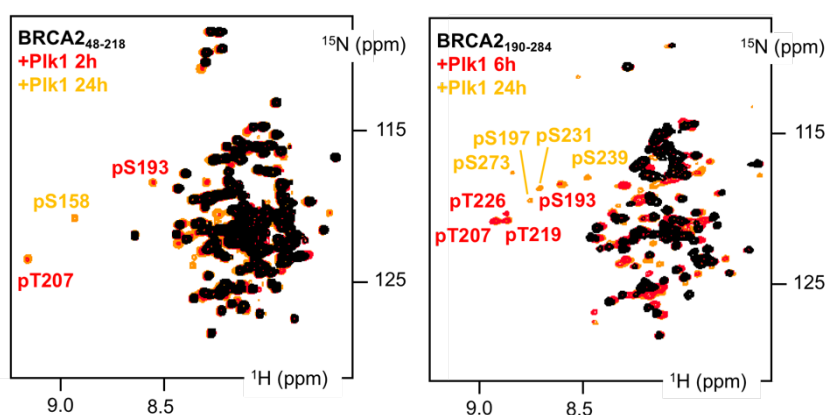


Figure 37. Plk1 phosphosites in BRCA2₄₈₋₂₁₈ and BRCA2₁₉₀₋₂₈₄.

Overlay of ¹H-¹⁵N SOFAST-HMQC spectra of BRCA2₄₈₋₂₁₈ (50 μM) before and after phosphorylation by Plk1 (100 nM) (left). Overlay of ¹H-¹⁵N SOFAST-HMQC spectra of BRCA2₁₉₀₋₂₈₄ (200 μM) before and after phosphorylation by Plk1 (1.1 μM) (right). All spectra were recorded at 283 K, pH 7.0 and 600 MHz.

Finally, I recorded 2D ¹H-¹⁵N SOFAST-HMQC experiments to identify the Plk1 phosphorylation sites in BRCA2₄₈₋₂₈₄, following the phosphorylation protocol designed by Dr. Simona Miron. The two fragments BRCA2₄₈₋₂₁₈ and BRCA2₁₉₀₋₂₈₄ were mixed to Plk1 and NMR spectra were recorded after phosphorylation (**Figure 37.A.B.**). I assigned the phosphoresidues based on the comparison between the NMR spectra before and after phosphorylation, and I confirmed this assignment using 3D heteronuclear NMR experiments.

This led me to identify 4 early phosphoresidues: pS193, pT207, pT219, pT226 (**Figure 37**) and 5 late phosphoresidues: pS158, pS197, pS231, pS239, pS273. The late sites could be either slow phosphosites as it has been observed for other kinase/substrate pairs (Mylona et al., 2016, Gebel et al., 2020) or they could be functionally irrelevant phosphorylation events that are due to our *in vitro* conditions. To discriminate between these two possibilities, one would need at least to quantify their phosphorylation stoichiometries in cells and/or to test the impact of mutating the slow phosphosites on different cellular phenotypes.

Among the 4 identified early phosphosites, 2 are located in a conserved disordered region of BRCA2 (Figure 11A): S193 and T207 are 100% conserved from mammals to fishes, suggesting an essential functional role for these two phosphoevents. At the opposite, T219 and T226 are less conserved (**Figure 38.B**). Within the late phosphosites, only S197 is 100% conserved through evolution.

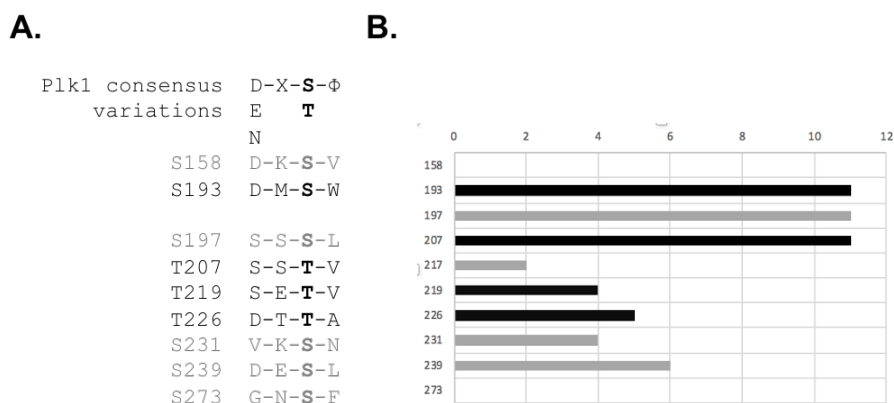


Figure 38. Sequence analysis and conservation of Plk1 phosphosites

(A) Comparison of BRCA2 Plk1 early (black) and late (grey) phosphosites identified in this study with the known consensus phosphosite (Nakajima et al., 2003, Alexander et al., 2011 Kettenbach et al., 2012), φ = hydrophobic residue at position i+1 or i+2 **(B)** Conservation scoring obtained with Jalview 2.10.1 reflecting the conservation of the physico-chemical properties at each phosphosite in an alignment of 40 BRCA2 sequences from fishes to mammals (Livingstone & Barton 1993, 0: no conservation; 11: 100% conserved residue).

Finally, in both BRCA2₄₈₋₂₁₈ and BRCA2₁₉₀₋₂₈₄, the ¹H-¹⁵N resonances remain very similar before and after phosphorylation. Only peaks corresponding to the phosphoresidues and their neighbors show different chemical shifts upon phosphorylation. This indicates that no secondary / tertiary structure is stabilized upon phosphorylation, as usually observed. Only one IDR, to the best of our knowledge, was reported as folding upon phosphorylation (Bah et al., 2015)).

Chapter 3. Monitoring BRCA2 phosphorylation using NMR

1. Using ^1H - ^{15}N 2D NMR

Then, I optimized the conditions for monitoring BRCA2 phosphorylation kinetics by Plk1 using the ^1H - ^{15}N 2D NMR strategy. This led us to propose an updated version of the protocol published by Dr. François-Xavier Theillet in 2013 ([Theillet et al., 2013](#)) in *Methods in Molecular Biology*. In this article, we describe the optimized protocol for monitoring IDRs phosphorylation using liquid-state NMR. This protocol is based on our team expertise, i.e. the NMR analysis of the phosphorylation of several proteins *in vitro* and in cell extracts. For this review, I performed and analysed the experiments, prepared the figures and wrote the manuscript with and under the supervision of Dr. François-Xavier Theillet.



Multiple Site-Specific Phosphorylation of IDPs Monitored by NMR

Manon Julien, Chafiaa Bouguechtouli, Ania Alik, Rania Ghouil, Sophie Zinn-Justin, and François-Xavier Theillet

Abstract

In line with their high accessibility, disordered proteins are exquisite targets of kinases. Eukaryotic organisms use the so-called intrinsically disordered proteins (IDPs) or intrinsically disordered regions of proteins (IDRs) as molecular switches carrying intracellular information tuned by reversible phosphorylation schemes. Solvent-exposed serines and threonines are abundant in IDPs, and, consistently, kinases often modify disordered regions of proteins at multiple sites. In this context, nuclear magnetic resonance (NMR) spectroscopy provides quantitative, residue-specific information that permits mapping of phosphosites and monitoring of their individual kinetics. Hence, NMR monitoring emerges as an *in vitro* approach, complementary to mass-spectrometry or immuno-blotting, to characterize IDP phosphorylation comprehensively. Here, we describe in detail generic protocols for carrying out NMR monitoring of IDP phosphorylation, and we provide a number of practical insights that improve handiness and reproducibility of this method.

Key words NMR spectroscopy, Intrinsically disordered proteins, IDP, Post-translational modifications, Phosphorylation, Cell signaling, Kinases, Multiple phosphosites, Quantitative NMR, Time-resolved NMR

1 Introduction

Living organisms use post-translational modifications (PTMs) as a convenient mechanism to transmit information in a fast and reversible fashion. PTMs can provoke changes in protein conformation or create/abolish binding sites, therefore regulating the activity of proteins. In eukaryotes, serine/threonine phosphorylation represents about 60% of the detected PTMs [1, 2]. Intrinsically disordered regions (IDRs) of proteins carry ~60% of the ~200,000 phosphosites found in the 13,000 human phosphoproteins [3, 4], in line with their importance in cell signaling [5]. Interestingly, phosphosites tend to cluster: about half of them are at a distance of four residues or less [6], while more than 50% of

phosphoproteins have six phosphosites or more [7]. This generates potential crosstalks, collective effects, and improved robustness of signaling [5, 8–10]. A large number of detected phosphorylation sites may also reveal loose specificities that result from the promiscuous access of kinases to IDP residues [11]: a majority of the detected phosphosites in cultured cells shows a fractional occupancy of 25% or less, the functional role of such events being unclear [7, 12].

The most popular methods to detect phosphorylation are mass-spectrometry (MS) and western-blotting because of their ability to detect phosphosites in biological material with high sensitivity. However, multiple neighboring phosphorylation sites hamper immuno-recognition and prevent standard peptide isolation/enrichment/ionization/identification steps in the course of MS analysis, although technical advances have been achieved in this field [13]. Degenerate motifs are also problematic in western-blotting because they hinder site-specific immuno-recognition. Finally, improving phosphoproteome coverage is a perpetual battle: even though novel buffers, enrichment methods, chromatography, and digestion protocols progressively enhance sampling depth [14, 15], accessible data from immunoblots and MS can probably not provide a comprehensive view of the PTM schemes established on your protein of interest.

NMR spectroscopy is a complementary method because of its intrinsic ability to provide quantitative, residue-specific information on IDPs in solution [16]. Using the “NMR isotope-filter,” ^{15}N -labeled proteins are the only observable species in the presence of natural abundance ^{14}N -containing material, which makes it possible to monitor phosphorylation reactions of a ^{15}N -labeled IDP in vitro and in cell extracts [17, 18]. For example, it has been instrumental in solving complex phosphorylation cascades on PTEN [19], or to elucidate the respective kinetics and roles of degenerate Erk phosphosites on Elk1 [20].

NMR spectroscopy provides residue-specific information because nuclei resonance frequencies depend on their chemical environment. Upon phosphorylation, the chemical environment changes in the vicinity of the phosphorylated residues, provoking new chemical shifts for residues neighboring the phosphosites. We illustrate it here with the example of a BRCA2 fragment (aa48–218), phosphorylated at S193 and T207, which generates large chemical shift perturbations for S193 and T207, but also weak but discernable NMR signal displacements of their neighboring residues D189, S195, L198, A199, T203, and V211 (Fig. 1a) [16, 21]. Hence, by recording time series of NMR spectra during the phosphorylation reactions, we can obtain time-resolved quantification or reaction advancement at every phosphosite: new cross-peaks appear while some peaks progressively disappear, corresponding to phosphorylated and non-modified populations,

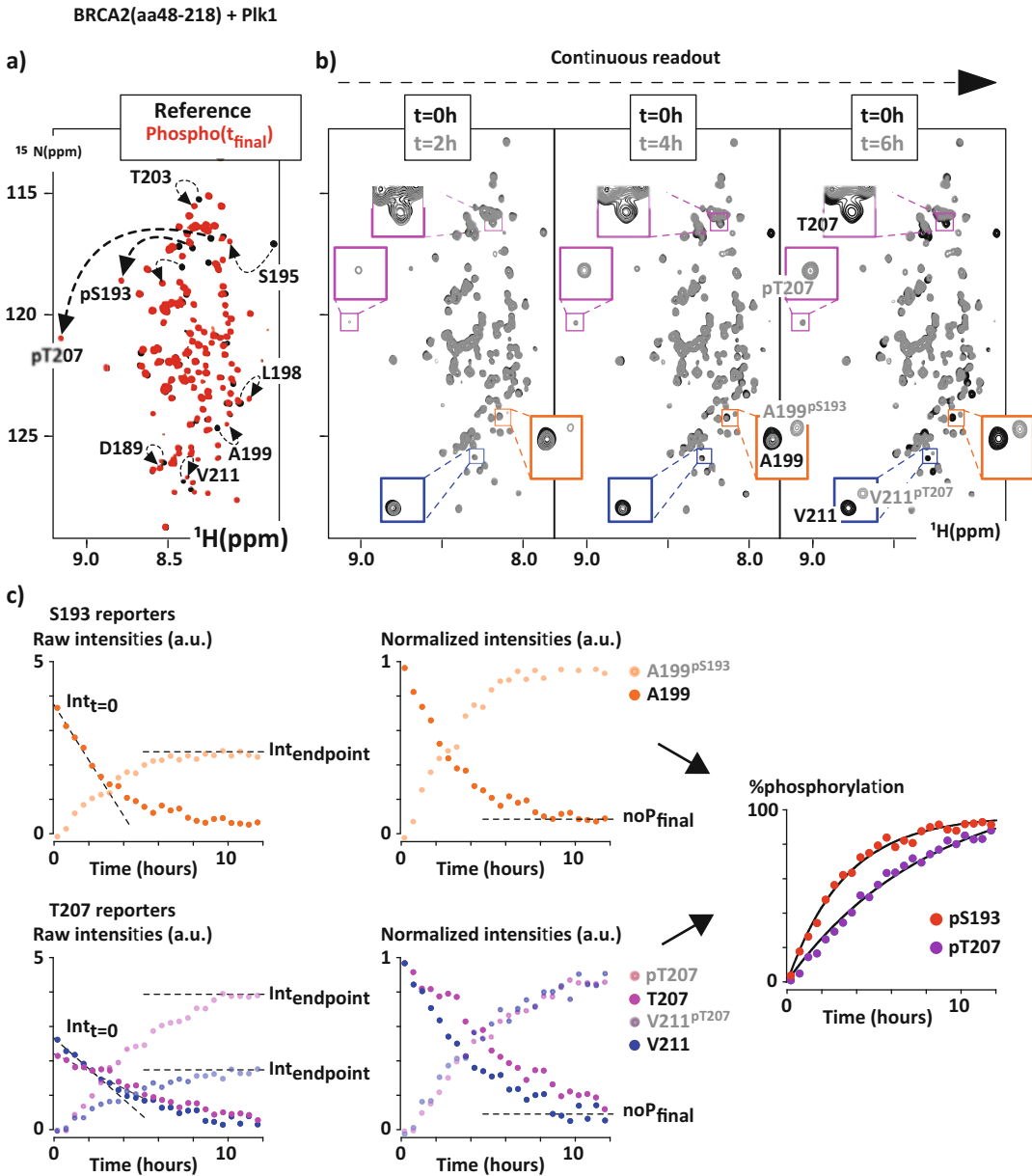


Fig. 1 NMR analysis of BRCA2(aa48-218) phosphorylation by Plk1 ($[BRCA2] = 50 \mu\text{M}$, $[Plk1] = 200 \text{ nM}$, spectra recorded at 700 MHz). **(a)** Overlay of ^1H - ^{15}N 2D HSQC spectra recorded at 283 K before (reference, black) and after the phosphorylation reaction (t_{final} , red). Arrows highlight NMR chemical shift perturbations upon phosphorylation. The two phosphosites S193 and T207 crosspeaks show large perturbation; their neighbor residues D189, S193, S195 and L198, T203 and V211 also shift and can be used as phosphorylation reporters. Measuring the crosspeak intensities of the non-modified species (called later “non-phosphopeaks”) in the two 283 K spectra provides $I_{\text{final}}/I_{\text{ref}}$ ratios, which later permit normalization of the phosphorylation build-up curves. **(b)** Depiction of three time-points in the time series of 2D ^1H - ^{15}N SOFAST-HMQC spectra recorded at 298 K during the reaction (grey spectra). We superimposed them on the reference spectrum at $t=0$ (black spectrum). Close-up views show the evolution of three couples of “non-phosphopeaks” and “phosphopeaks”:

respectively (Fig. 1b). More complex situations can emerge when close residues are concomitantly phosphorylated: two neighboring sites S1 and S2 (separated by ~4–6 amino acids or less) will generate a set of four peaks upon phosphorylation, corresponding to S1–S2, pS1–S2, S1–pS2, and pS1–pS2, where pS1–S2 and S1–pS2 peaks may increase and later decrease (*see* for example [19, 22, 23]).

In the past years, we have successfully monitored phosphorylation reactions using NMR on a large variety of IDPs and kinases. Here, we provide a generic protocol integrating a sum of technical solutions focusing on sample preparation, control of the reaction conditions, and instrument parameters for generating reliable data. We also provide some explanations for the rationale and warnings to avoid misinterpretation (*see* **Note 1**). We illustrate the protocol with results obtained on a BRCA2 fragment (aa48–218) phosphorylated by Plk1.

2 Materials

2.1 Stock Solutions Preparation and Storage

Prepare all solutions using milli-Q water (resistivity of 18.2 M Ω cm at 25 °C). Buffers, reagents stocks, and proteins can be kept at –20 °C for months, but fresh dithiothreitol (DTT) or tris(2-carboxyethyl)phosphine (TCEP) should be added to the samples before performing experiments. DTT half-life in solution is indeed about 1 day at pH ~ 7 and even decreases in presence of metal ions [24], so buffers containing DTT should not be stored. Other reducing agents may be used with profit but also with careful attention (*see* **Note 2**).

We describe standard buffers using Hepes at 50 mM, pH 7.0. Any good buffering molecule in this range of pH would also be acceptable, for example, phosphate, PIPES, and MOPS, whose pKas also have low temperature coefficients (*see* **Note 3**).

Fig. 1 (continued) A199 crosspeaks (orange) report on S193 phosphorylation, while T207 (magenta) and V211 (blue) crosspeaks report on T207 phosphorylation. The non-phosphoT207 peak partially overlaps with other resonances, and is thus a reporter of poor quality. (c) Treatment of peak intensities from raw data, to normalized intensities and interpretation in %phosphorylation. The value $\ln I_{t=0}$ of a non-phosphopeak is obtained from the tangent at $t=0$ of a non-phosphopeak evolution curve, and can then be used for normalizing this evolution. Build-up curves of phosphopeaks are normalized by intensity ratios measured at 283 K $I_{\text{final}}/I_{\text{ref}}$ (*see* Subheading 3.5). To make the graphs clearer, we show only A199 crosspeaks evolution as a reporter of S193 phosphorylation; S193, S195 and L198 crosspeaks can also be used, *see* (a). Similarly, T203 crosspeaks can be used as reporters of T207 phosphorylation. Phosphorylation build-up curves are preferably obtained from non-phosphopeaks decay analysis. They can be normalized easily using the reference intensities at 0% phosphorylation; at the opposite, because a phosphorylation reaction rarely goes to completion, the reference intensities of phosphopeaks at 100% phosphorylation can be difficult to determine

1. Standard IDP Size-Exclusion Chromatography (SEC) buffer (SEC-B): 50 mM Hepes, 100 mM NaCl, pH 7.0.
2. Standard IDP frozen storage buffer (Stor-B): 50 mM Hepes, 100 mM NaCl, pH 7.0, 2 mM DTT, 1× ethylenediaminetetraacetic acid (EDTA)-free protease inhibitors.
3. Standard phosphorylation buffer (Phos-B): 50 mM Hepes, 100 mM NaCl, pH 7.0, 4 mM DTT, 1× EDTA-free protease inhibitors, 4 mM adenosine triphosphate (ATP), 10 mM MgCl₂.
4. Urea buffer (UB): 50 mM Hepes, 100 mM NaCl, pH 6.5, 4 mM DTT, 10 M urea. High urea concentration buffers tend to progressively diverge toward higher pH when stored at room temperature for days.
5. ATP stock solution: 0.1 M ATP, pH 7.0 in water (10 mM Hepes can be added for convenient pH adjustment); store aliquots at -20 °C.
6. DTT stock solution: 1 M DTT in water; store aliquots at -20 °C.
7. MgCl₂ stock solution: 1 M MgCl₂, pH 7.0 (10 mM Hepes can be added for convenient pH adjustment); store aliquots at -20 °C.
8. EDTA-free proteases inhibitors (PI): prepare a 25× stock solution (cOmplete EDTA-free tablets, or any other cocktail of inhibitors that does not contain EDTA). Store aliquots at -20 °C.
9. ¹⁵N-labeled IDP stock solution at a concentration greater than or equal to 200–250 μM is stored at -80 °C. Aliquoting prevents eventual aggregation that often appears upon multiple freeze-thaw cycles.
10. Kinase stock solution: active kinase is obtained either commercially or produced in-house. Prepare low-volume aliquots on ice (2–10 μL, providing a phosphate transfer activity in the range of 50–500 pmol/min) and flash-freeze them before storage at -80 °C. Aliquoting preserves kinase activity which may be lost upon freeze-thaw cycles, and will thus favor experimental reproducibility. Addition of 20% glycerol promotes activity conservation.
11. EDTA or trans-1,2-Diaminocyclohexane-*N,N,N'*,*N'*-tetraacetic acid monohydrate (CyDTA) stock solution: 0.5 M EDTA or CyDTA solution, pH 7.0; store aliquots at -20 °C.
12. D₂O at 99% deuterium enrichment.
13. 4,4-dimethyl-4-silapentane-1-sulfonic acid (DSS) stock solution: 100 mM DSS in water; store at room temperature (RT).

14. Laemmli buffer 4×: 10 mL Tris (1 M, pH 6.8), 4 g sodium dodecyl sulfate (SDS), 20 mL glycerol, 10 mL β -mercaptoethanol, 0.1 g bromophenol blue, 6 mL H₂O.
15. Polyacrylamide gels for SDS-PAGE analysis.

2.2 Sample Preparation

1. SEC column: preparative 16/600 Superdex column containing 75 μ g or 200 μ g resin depending on protein size.
2. Fast protein liquid chromatography (FPLC) system at 4 °C able to carry out SEC, that is, applying constant flow rates of 0.3–1.5 mL/min at a pressure of 0.15–0.5 MPa.
3. 0.22 μ m pore-size membrane filter system.
4. Centrifugal concentrators with a pore size adapted to the IDP molecular weight.
5. Precise pH-meter combined with a pH microelectrode able to measure pH in ~100 μ L samples.

2.3 NMR Spectra Acquisition and Analysis

1. High-field NMR spectrometer (larger or equal to 600 MHz) equipped with a triple-resonance cryoprobe.
2. A ¹H-¹⁵N SOFAST-HMQC pulse sequence program. This can be found in most of the standard pulse sequence libraries. Be careful with the default pulses used in libraries: the central band-selective 180° pulse should be an REBURP and not an r-SNOB to get maximal S/N, as shown by Schanda et al. [25]. Set interscan delays to ~100 ms and use a high number of dummy scans (>64). Set offset frequencies of shaped pulses to 8.5 ppm and use large pulse lengths (>2.4 ms) to avoid saturation of water protons magnetization. Because of fast amide-water proton exchange in IDPs, water protons represent a magnetization reservoir enhancing the apparent amide interscan T₁-recovery [26]. For this reason, great S/N enhancement is obtained for IDPs using long shaped pulses at fields higher than 600–700 MHz, since amide and water proton frequencies become distant enough.
3. A ¹H-¹⁵N HSQC pulse sequence program. Sensitivity-enhanced versions of this pulse sequence provide better S/N for most IDPs. This can be found in most of the standard pulse sequence libraries.
4. NMR tubes. These can be 3 or 5 mm diameter regular tubes, which must be filled with minimal volumes of 150 or 475 μ L, respectively. In standard phosphorylation buffer conditions, 5 mm tubes offer about twice S/N than 3 mm tubes. Using 3 or 5 mm diameter Shigemi tubes optimizes sample efficiency by reducing sample volumes to 90 or 270 μ L, respectively. 4 mm Shigemi tubes (efficient volume: 180 μ L) also exist.

5. NMR data processing and analysis software (e.g., Topspin, NMRPipe, CcpNmr Analysis, Sparky, etc.).
6. Plotting and fitting software (e.g., Prism, Kaleidagraph, Gnuplot, etc.).

3 Methods

The following protocol describes a generic strategy to monitor IDP phosphorylation using NMR spectroscopy. This requires the prior production and purification of the protein of interest uniformly ^{15}N or $^{15}\text{N}/^{13}\text{C}$ labeled. Such labeling is usually obtained by recombinant protein expression in bacteria (*see Note 4*). Bacterial expression is preferred for this protocol because it generates recombinant, non-phosphorylated proteins in most cases (*see Note 5*). We will not detail the corresponding tasks, but we must stress a few points that should be considered with great care for later success in phosphorylation characterization. The IDP of interest can be purified using standard strategies adapted to the presence or absence of affinity tags. First, to avoid any artifactual influence of such tags, their cleavage and removal is generally preferred before executing PTMs' kinetics experiments. Second, because of their high accessibility, IDP's cysteines are prone to establish non-native disulfide bonds in vitro. The complete reduction of cysteine thiols at every step of the purification is mandatory (*see Note 2*). Third, IDPs' susceptibility to proteolysis must be addressed by adding protease inhibitors in lysis buffer and after every purification step.

The protocol starts with the last preparation steps of the IDP sample, then describes a method to optimize the phosphorylation conditions, and later a method to assign the NMR spectra in the phosphorylation conditions. The two final subsections detail the NMR data acquisition and analysis. We have introduced two possible methods to record NMR spectra, either by a continuous readout of a single sample during the phosphorylation reaction (Subheading 3.4.1 NMR continuous readout) or by successive measurements of aliquots quenched at various time points (Subheading 3.4.2 The "Quenched reaction" approach). The first approach is more convenient in many aspects, but it provides too weak S/N for a number of IDPs (*see Note 6*). All other paragraphs are common to all IDPs.

3.1 Preparation of the IDP Stock

We start the protocol with the last preparation step of the IDP, which consists of an SEC. This permits (1) to polish the protein purification, and (2) to transfer the IDP into the exact salt and buffer conditions used for the phosphorylation reaction.

1. Equilibrate the SEC column with two column-volumes of SEC-B, previously filtered on a 0.22 μm pore-size membrane.

Using an FPLC system at 4 °C will lower the risks of IDP proteolysis.

2. Concentrate the purified IDP to a final volume of 2 mL in the presence of 2 mM DTT and PIs (final concentration 1×), using concentrators with centrifugation steps at 10 °C (4000 × *g* for swinging buckets, 5000 × *g* for fixed angle rotors).
3. Add DTT to a final concentration of 10 mM DTT to the concentrated sample and incubate it for 30 min at RT to ensure that all thiols are reduced.
4. Centrifuge the sample for 5 min at 16,000 × *g* and 4 °C to remove aggregates and inject the supernatant on the equilibrated SEC column.
5. Run the SEC with parameters recommended by manufacturers and check the purity of the eluted fractions by SDS-PAGE.
6. Pool the fractions of interest, supplement them with 2 mM DTT (final concentration) and PIs (final concentration 1×), and concentrate the protein to 250 μM by centrifugation at 10 °C (4000 × *g* for swinging buckets, 5000 × *g* for fixed angle rotors).
7. Flash freeze the sample in liquid nitrogen and store it at −80 °C.

3.2 Optimization of Phosphorylation Conditions

For every IDP:kinase pair, phosphorylation kinetics can be first evaluated by SDS-PAGE in order to identify the appropriate concentration of kinase and, eventually, the best buffer conditions. This relies on the fact that phosphorylated amino acids tend to slow down protein migration during SDS-PAGE (Fig. 2). SDS-binding to phosphoproteins is thought to be weaker, which provokes decreased electrophoretic mobility [27]. However, this effect can be negligible for proteins carrying large excess (~15 or more) of negative charges due to a biased composition between Glu/Asp and Arg/Lys; this situation calls for directly moving on to NMR monitoring. Here, we describe the procedure for the SDS-PAGE evaluation of phosphorylation efficiency.

1. Thaw the IDP sample, and prepare three samples of 25 μL containing the IDP at 25 μM in Phos-B.
2. Calculate the amount of kinase to add. As a first estimation, this quantity should correspond to a theoretical capacity to phosphorylate all predicted phosphosites in 1 h, with no consideration for the K_m .

Commercial kinase activity has normally been evaluated, and this information is often presented in nmol/min of phosphate transfer per mg of kinase (together with the kinase concentration). The quantity of kinase to use is thus obtained using the equation:

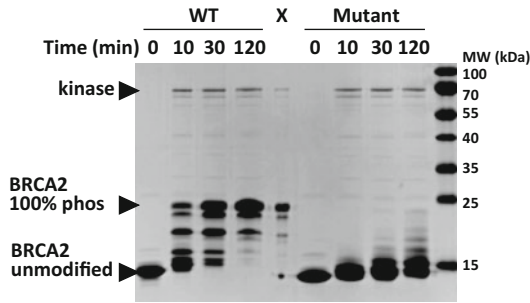


Fig. 2 SDS-PAGE analysis of the phosphorylation kinetics of a BRCA2 fragment presenting five phosphosites. Phosphorylation of the wild-type fragment and a mutant fragment were evaluated at t_0 , $t_{10\text{min}}$, $t_{30\text{min}}$, and $t_{2\text{h}}$. This gel exemplifies the typical phosphorylation shifts provoked by successive phosphorylation events. Although it is not fully characterized, it appears that SDS binds less to phosphoproteins, which slows down electrophoretic migration [27]. Peptides carrying a high net negative charge (~ 15 or more) do not shift as well upon phosphorylation (15% polyacrylamide gel stained with Coomassie blue, lane X shows a default in gel loading)

$$M_{\text{kinase}} = N_{\text{sites-predicted}} \times C_{\text{IDP}} \times V_{\text{reaction}} / (\text{Kin}_{\text{activity}} \times t_{\text{reaction}})$$

With $N_{\text{sites-predicted}}$ the number of phosphorylation sites predicted from the known kinase consensus site (*see Note 7*), C_{IDP} is the IDP concentration in molar, V_{reaction} the reaction volume in liters, $\text{Kin}_{\text{activity}}$ the activity of the kinase in mol/min/mg, and t_{reaction} the incubation time in minutes. M_{kinase} is thus in mg.

Hence, our rough evaluation gives $M_{\text{kinase}} = N_{\text{sites-predicted}} \times 10^{-11} / \text{Kin}_{\text{activity}}$, which often translates into volumes lower than 1 μL of kinase stock solution. Prepare a diluted kinase stock to make it convenient to pipet.

For in-house produced kinase, whose activity has not yet been characterized, (1) if the kinase is activated (phosphorylated or in complex with activators), use $M_{\text{kinase}} \sim 10$ ng (kinase:IDP molar ratio of 1:2500); (2) if the kinase is not activated, use $M_{\text{kinase}} \sim 100$ ng (kinase:IDP molar ratio of 1:250).

For phosphorylation of IDP by cell extract, *see Note 8*.

3. Spike $V_{\text{kinase}} = M_{\text{kinase}} \times [\text{kinase}]$, $3 \times V_{\text{kinase}}$ and $9 \times V_{\text{kinase}}$ in the three pre-phospho mixes prepared in **step 1**. Incubate at 298 K.
4. Take 4 μL of the samples at 0 min, 10 min, 30 min, 1 h, and 2 h, mix them to 4 μL of $2 \times$ Laemmli buffer and heat them immediately for 5 min at 95 $^{\circ}\text{C}$.
5. Load the samples on a polyacrylamide gel.
6. Run the SDS-PAGE, stain with Coomassie Blue or any other better suited staining method. Pick the kinase concentration that will permit to distinguish phosphorylation events using

the NMR time resolution, that is, 15–30 min per time point over 3–5 h (most kinases lose their activity after a few hours at 25 °C).

7. Buffer conditions can also be evaluated. To this purpose, prepare stock solutions of the various conditions to test. One may test a range of pH values (pH 7–7.5–8) and of salt concentrations (50–100–150 mM NaCl). Repeat **steps 1–6**. If the reaction is much faster at high pH, adopting the “quenched reaction approach” may be the method of choice to monitor phosphorylation by NMR. However, if the activity of your kinase is acceptable at pH 7.0, we recommend running the phosphorylation reaction at this pH. For most kinases, pH 7 corresponds to an acceptable compromise between kinase activity and decent quality of IDPs’ NMR spectra.

3.3 Assignment of NMR Spectra in the Conditions Used for Phosphorylation Reactions

To extract residue-specific information, assignment of the IDP’s NMR spectra is a prerequisite. While phosphorylation reactions will typically be executed at 298 K and pH ~7, assignment is usually performed at conditions favorable for NMR analysis of IDPs, that is, low temperature (~283 K) and pH (~6.5), which decrease water/amide proton exchange and consequently maximize S/N. We will not detail this primary assignment strategy relying on the use of 3-dimensional spectra establishing connections between spins of backbone nuclei (the most useful ones in the case of IDPs being HNC(O), HN(CA)CO, HNCACB, and (H)N(CA)NH).

We describe below the next step that aims at inferring the ^1H - ^{15}N crosspeaks assignment in the conditions used for phosphorylation. It relies on a temperature and pH gradient from the assignment conditions to the phosphorylation conditions, using DSS as an internal reference. 2D ^1H - ^{15}N HSQC or SOFAST-HMQC pulse sequences can be used. SOFAST-HMQC will be better suited at higher pH and temperature because of its higher S/N efficiency.

1. Record a 2D ^1H - ^{15}N HSQC spectrum of the IDP at ~100 μM in the pH ($\text{pH}_{\text{assign}}$) and temperature (T_{assign}) conditions used for prior assignment.
2. Record 2D ^1H - ^{15}N HSQC or SOFAST-HMQC spectra at the intermediate temperature ($298\text{ K} - T_{\text{assign}}/2$) and at 298 K.
3. DSS-reference your spectra in both ^1H and ^{15}N dimensions (or apply a 10.5 ppb/K shift if you center the water signal at 4.7 ppm). Then, apply a temperature correction of -7.5 ppb/K in the proton dimension and -6.5 ppb/K in the nitrogen dimension—do not forget that $\gamma(^{15}\text{N})$ is negative. This will account for the average temperature shifts of random coil amino acids [28] and make tracking of peaks easier.

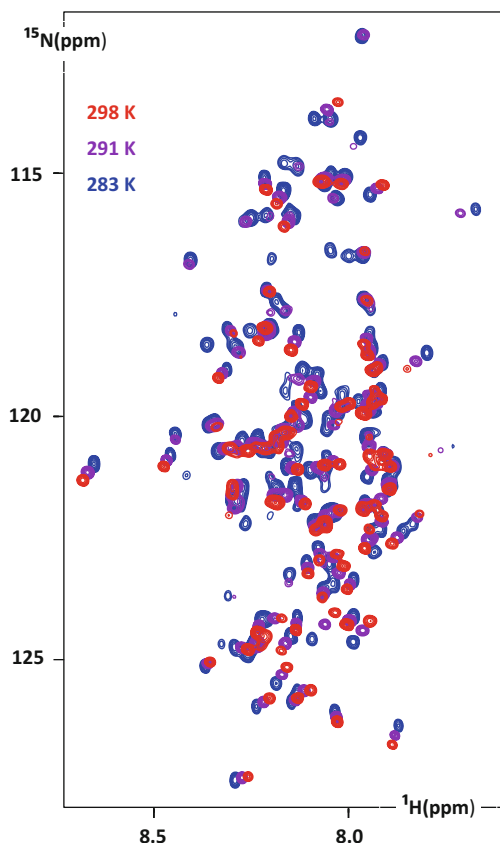


Fig. 3 Temperature gradient from assignment conditions (283 K) to phosphorylation conditions (298 K) allows fast $^1\text{H}_\text{N}$ and ^{15}N assignment at 298 K. 2D ^1H - ^{15}N SOFAST-HMQC spectra of BRCA2(aa48–218) were recorded at 283 K, 290 K and 298 K, and spectral referencing were temperature-corrected according to the rule presented in Subheading 3.3, **step 3**. All spectra are shown at the same contour level. A number of crosspeaks fade away at higher temperature. This is typical of IDPs NMR spectra. The spectra were acquired at pH 7.0 and 700 MHz

4. Assign crosspeaks at 298 K by tracing lines through every set of three resonances across the temperature range (*see* Fig. 3).
5. Apply the same logic for shifting pH progressively from pH_assign to $\text{pH}_\text{phosphorylation}$. Record 2D ^1H - ^{15}N HSQC or SOFAST-HMQC spectra at 3 pH values, DSS-reference your spectra (or apply a 20 ppb/pH unit correction if you center the water peak at 4.7 ppm). In the range of the pH values considered here, that is, pH ~6.5–7.5, crosspeak frequencies should not shift significantly except histidine residues and their close neighbors.

3.4 Phosphorylation Monitoring by NMR

A number of IDPs provide poor S/N at pH 7 or higher due to their high content in hydrophilic amino acids that show fast water:amide proton exchange (Gly, His, Lys, Arg, Ser, Thr). Continuous readout at 298 K can thus be greatly hampered by the absence of reliable reporter crosspeaks. In such situations, it may be more adapted to perform the phosphorylation reaction on the bench, to remove aliquots and quench the reaction at regular intervals, and to record NMR spectra of these aliquots later. This “quenched reactions” strategy has an advantage: low pH and large NMR acquisition times can be used to enhance S/N and resolution. However, the limited number of time points can hinder the robust fitting and interpretation of phosphorylation kinetics.

In the following, we describe protocols for the continuous readout NMR approach (Subheading 3.4.1) and for the discontinuous “quench reaction” approach (Subheading 3.4.2). To choose between these two strategies, you must evaluate the quality of the 2D ^1H - ^{15}N SOFAST-HMQC spectra recorded at $\text{pH}_{\text{phosphorylation}}$ and 298 K (*see* Subheading 3.3). If a number of reporter crosspeaks provide S/N ratios above 10, the continuous readout is probably feasible. S/N will depend of course on the IDP concentration and the tube diameter/volume.

3.4.1 Phosphorylation Monitoring Using Continuous NMR Readout

1. Define the final volume of your sample. This ranges from 90 to 475 μL depending on the NMR tube you want to use (*see* Subheading 2.3, **item 4**). Pipetting losses are difficult to avoid, so start with initial volumes 10–20% higher than the measured ones.
2. Calculate the amount of kinase to add according to Subheading 3.2, that is, the amount leading to measurable levels of phosphorylation within 2–5 h. The reaction should not be too fast because the NMR timeframe is in the order of magnitude of 15–30 min in the described phosphorylation conditions. If you skipped Subheading 3.2 and did not test the kinase activity, you may try an IDP concentration of 50 μM , and a kinase:IDP molar ratio of 1:2500 for an activated kinase, or 1:250 for a non-activated kinase.
3. Prepare the pre-phospho mix containing the IDP at 50 μM in Phos-B, supplemented with 3% D_2O and 50 μM DSS. Check the pH at room temperature using a micro-pH meter and adjust it to 7.0 if necessary.
4. Transfer the pre-phospho mix into the NMR tube, insert the tube in an appropriate spinner and then into the NMR spectrometer equilibrated at 283 K.
5. Tune and match the ^1H circuit of the probehead, lock the HOD signal, and shim the sample tube. Determine the ^1H 90° pulse.

6. Record 283 K reference 1D ^1H spectra and 2D ^1H - ^{15}N 2D SOFAST-HMQC spectra using an FID resolution of ~ 15 Hz in both ^1H and ^{15}N dimensions. This step is recommended to check the quality of your sample (pH control, ATP/ADP concentrations, IDP degradation) and serves to measure IDP reference peak intensities. The acquisition time of the 2D spectrum should be between 30 min and 2 h. Ideally, the S/N of peaks of interest should be 20:1 or more for an accurate quantification of later phosphorylation advancement.
7. Equilibrate the spectrometer sample temperature at 298 K and re-perform wobbling, shimming, and pulse calibration.
8. Record a 298 K reference 1D ^1H -spectrum, record two 2D ^1H - ^{15}N SOFAST-HMQC reference spectra using FID resolutions of 15 Hz in ^1H dimension, and (a) 15 Hz and (b) 30 Hz in ^{15}N dimension. The final acquisition times of the 2D spectra should be about 15 or 30 min. Evaluate the quality of these spectra, try different apodization functions, and pick the parameters that provide the best compromise between resolution and S/N. These will be used for time-resolved NMR monitoring of the phosphorylation reaction.
9. Extract the sample from the tube and add the kinase in quantities defined in Subheading 3.4.1, **step 2**. Mix well by pipetting and load the phosphorylation sample into the same NMR tube.
10. Insert the sample in the magnet, wait for 1 min for temperature equilibration, lock, and shim. Tuning, matching, and pulse calibration should not change after the addition of the kinase, unless the kinase stock is very diluted in a very peculiar buffer.
11. Record a 1D ^1H -spectrum at 298 K and, then, a series of ^1H - ^{15}N 2D SOFAST-HMQC spectra over 4–12 h, using the parameters defined in Subheading 3.4, **step 8**.
12. At the end of the series, shim again and record a 1D ^1H spectrum to evaluate the ADP/ATP ratio (*see Note 9*).
13. Take back the sample from the tube. At this stage, phosphorylation should not progress significantly because of the progressive loss of kinase activity. In the case of a heat-resistant IDP, to definitely stop any enzymatic activity, boil the sample at 90 °C for 5 min, centrifuge 5 min at $16,000 \times g$, and recover the supernatant. Avoid boiling IDPs containing Asn-Gly motifs that may suffer from deamidation. You can alternatively spike EDTA or CyDTA at a final concentration of 15 mM to chelate Mg^{2+} ions, which will not prevent potential interactions between the IDP and the kinase and their consequences on IDPs NMR peak intensities.

14. Measure pH and adjust it to the initial value if necessary. ATP, DTT, and PI hydrolysis usually acidify the solution.
15. Fill the NMR tube with the pH-readjusted sample. Insert it in the magnet, set the sample temperature to 283 K, tune/match, lock, and shim. Record 1D ^1H spectrum and a 2D SOFAST-HMQC spectra at 283 K using the same parameters than in Subheading 3.4, **step 6**. These spectra constitute the endpoint references.

3.4.2 Phosphorylation Monitoring Using Quenched Reactions

1. Quenching can be performed using heat inactivation or urea denaturation. Verify that the studied IDP is resistant to 5 min heating at 90 °C. Test it on an aliquot at the concentration and in the buffer conditions used for the phosphorylation reaction. After 5 min, centrifuge 5 min at $16,000 \times g$, separate the supernatant and the eventual aggregated material and analyze it using SDS-PAGE and NMR. Pay particular attention to the NMR crosspeaks of Asn and Gln, whose decreased intensities may reveal deamidation occurring upon heating.
2. If your protein is not heat resistant, you can quench the phosphorylation reaction by adding phosphorylation reaction buffer supplemented with 10 M urea buffer to the aliquots. The final urea concentration should be over 4 M. This will require a novel NMR assignment at the final urea concentration, which can be performed using a urea gradient with the same logic than for temperature in Subheading 3.3. Recording 2D ^1H - ^{15}N SOFAST-HMQC experiments of IDPs in urea at pH 7 and 283 K provides high quality spectra: IDPs do not adopt any “molten globule” behaviors in these conditions, and urea slows down water-amide proton exchange; hence, favorable relaxation effects generate spectra exploitable for residue-specific analysis.
3. Define the experimental time points (i.e., the number of quenched aliquots) you want to have, and the final volume and concentration of the measured samples. The corresponding aliquots can be diluted after being quenched. Such dilution permits a better control of the later pH adjustment.
4. Calculate the amount of kinase to add according to Subheading 3.2 and the time frame you choose. If you skipped Subheading 3.2 and did not test the kinase activity, you may try an IDP concentration of 50 μM , a total reaction time of 5 h, and a kinase:IDP molar ratio of 1:2500 for an activated kinase, or 1:250 for a non-activated kinase.
5. Prepare the pre-phospho mix containing the IDP at 50 μM in Phos-B supplemented with 3% D_2O and 50 μM DSS. Check

the pH at room temperature using a micro-pH meter and adjust it to $\text{pH}_{\text{phosphorylation}}$ if necessary.

6. Remove an aliquot and heat it 5 min at 90 °C or dilute it in a urea buffer, according to Subheading 3.4.2 step 1. Then, flash-freeze the samples and keep them at -80 °C.
7. Add the kinase in quantities defined in Subheading 3.4.2 step 4. Mix well and place it at 298 K in a dry bath.
8. Remove aliquots at the defined time points, and heat them 5 min at 90 °C or dilute them in a urea buffer. Then, flash-freeze the samples and keep them at -80 °C.
9. After thawing the samples, centrifuge the samples 5 min at $16,000 \times g$ if you heated them. Take the supernatant and complete with the volume of phosphorylation buffer PhosB to reach the final volume that will be measured by NMR.
10. Adjust the pH to 6.5. Flash freeze the aliquots that you will not measure in the next hours; keep the other ones on ice.
11. Transfer the sample into the NMR tube, insert the tube in an appropriate spinner and then into the NMR spectrometer equilibrated at 283 K.
12. Tune and match the ^1H circuit of the probehead, lock the HOD signal, and shim the sample tube. Determine the ^1H 90° pulse.
13. Record 283 K spectra of every aliquot: a 1D ^1H -spectrum and a ^1H - ^{15}N 2D SOFAST-HMQC spectrum using an FID resolution of ~15 Hz in both ^1H and ^{15}N dimensions. 1D ^1H -spectra are useful to compare the eventual differences of IDP concentration in the aliquots. They should thus be recorded with a high S/N. They also permit to check the pH and the ATP/ADP concentrations. The acquisition time of the 2D spectrum should be between 30 min and 2 h. Ideally, the S/N of peaks of interest should be 20:1 or more for an accurate quantification of the phosphorylation advancement.

3.5 Analysis of NMR Data

Although a novel assignment of the phosphorylated IDP spectra is not always necessary (*see Note 10*), it can be very useful in the case where too many phosphosites generate a large number of spectral changes. We will not detail the assignment method relying on the prior phosphorylation of a ^{13}C - ^{15}N labeled IDP and the use of 3-dimensional pulse sequences to establish sequential connections (*see Subheading 3.3*). A single 3D HNCACB spectrum is often sufficient to assign the phosphorylated population. We will not elaborate extensively on curve fitting: because of the progressive kinase loss of activity, the potential IDP degradation, or the competition between phosphosites, fitting models may often become too complicate to provide consistent fitted values. In most cases, it

is safer to only consider the order of phosphorylation events and their initial rates. Crosspeaks whose intensities vary during the phosphorylation reaction reveal phosphorylation advancement, and will be called “reporters.” In the following, we describe how to monitor and quantify the reaction advancement in a residue-specific fashion. We will name “non-phosphopeaks” all crosspeaks found in the reference spectra before phosphorylation, and “phosphopeaks” those appearing in spectra upon phosphorylation.

1. Fourier transform the spectra recorded at 283 K before and after the phosphorylation reaction (*see* Subheading 3.4.1 steps 6 and 15 or Subheading 3.4.2 step 13) using Topspin or any equivalent NMR-data processing software. Process these data with an adapted apodization function, and perform baseline corrections if necessary. The 2D SOFAST-HMQC pulse sequence often generates distorted baselines in the ^{15}N -dimension, which alters absolute peak intensities.
2. Load these 2D 283 K-spectra in an NMR data analysis software (i.e., Ccpnmr or Sparky). Measure intensities of every isolated peak in the reference spectrum (I_{ref}) and after the phosphorylation reaction (I_{final}).
3. Identify the peaks that faded. Because the corresponding residues are either phosphorylated or close to phosphorylated residues, these peaks permit identification of the residues or the segments where phosphorylation reactions occurred. The intensity ratios $I_{\text{final}}/I_{\text{ref}}$ of these peaks reveal the final degrees of advancement of these reactions.
4. If you used the “continuous readout approach,” Fourier transform the spectra recorded at 298 K during the phosphorylation reaction and apply baseline corrections if necessary (*see* Subheading 3.5, step 1). Load these 298 K-spectra in an NMR data analysis software.
5. Measure intensities of every isolated peak in every spectrum, including novel peaks appearing upon phosphorylation. Pay attention to eventual peak displacements due to pH shifts in the time series (*see* Note 11).
6. Plot the evolution curves of every peak using a plot/fit software (Kaleidagraph, Prism, Gnuplot, ...). If you used the “continuous readout approach,” set the time of the first spectrum to $(t_{\text{set-up}} + t_{\text{acq-spectrum}}/2)$, and the later time points to $(t_{\text{set-up}} + t_{\text{acq-spectrum}} \times (n - 1/2))$. $t_{\text{set-up}}$ should be about 5 min. Decay of connected non-phosphopeaks, either of phosphosites or of neighboring residues, should show similar trends.
7. Pay attention to the fact that a given residue can sense more than one phosphorylation reaction, and the decay of its

non-phosphopeak may report on more than one phosphorylation event in its vicinity. Such a situation can be recognized by the appearance of more phosphopeaks than there were non-phosphopeaks.

8. After identifying non-phosphopeaks that report the same phosphorylation reaction, add their individual peak intensities at every timepoint (Fig. 1c). This will increase the S/N of the phosphorylation build-up curves. For every phosphorylation site, evaluate the total intensity $I_{t=0}$ at time = 0 according to the initial slopes of the decay curves. Plot the phosphorylation build-up curve $\%phospho(t) = 1 - I(t)/I_{t=0}$.
9. You may try to assign the phosphopeaks. The peaks corresponding to phosphorylated residues should shift down-field according to the published reference chemical shifts; the neighboring residues should show weaker peak displacements and remain close to the non-phosphopeaks. In both cases, peak intensities of phospho- and non-phospho-populations evolve in a complementary fashion.
10. If no reliable non-phosphopeak reporter can be isolated in the 298 K-spectra, plot the intensities of the assigned phosphopeaks. Evaluate their intensity I_{endpoint} at the end of the time series, according to the last 298 K-spectra (Fig. 1c). Normalize their build-up curve according to the ratio $I_{\text{final}}/I_{\text{ref}}$ of non-phosphopeaks measured at 283 K.
11. You can also add build-up curves from related phosphopeak and non-phosphopeaks to increase S/N. Perform it before intensity normalization and normalize the final build-up curves. Depending on the shape of the build-up curves, there are four possible scenarios:
 12. If the curve looks like a mono-exponential (Fig. 4a), fit it using $\%phospho(t) = \%phospho_{t=\infty}(1 - \exp(-R_{\text{phos}} \times t))$.
 13. If the initial IDP concentration is above the K_m of a phosphosite, the corresponding decay curve may look more linear than exponential (Fig. 4b); in this case, fit it using $\%phospho(t) = \%phospho_{t=\infty}(1 - (\ln(1 + (e^K - 1) \times \exp(-R_{\text{phos}} - t))))/K$, with $K = [\text{IDP}]/K_m$.
 14. If the curve has an S shape, it may reveal a conditional phosphosite P2 that requires a prior phosphorylation of a neighboring site P1 (Fig. 4c), which may be fitted using $\%phospho_{P2}(t) = 1 - [R_{\text{phosP1}} \times \exp(-R_{\text{phosP2}} \times t) - R_{\text{phosP2}} \times \exp(-R_{\text{phosP1}} \times t)]/[R_{\text{phosP1}} - R_{\text{phosP2}}]$. In such situation, a set of two P1 phosphopeaks should appear, corresponding to P1-noP2 and P1-P2. You can fit $\%phospho_{P1\text{-noP2}}(t) = R_{\text{phosP1}}/[R_{\text{phosP1}} - R_{\text{phosP2}}] \times [\exp(-R_{\text{phosP2}} \times t) - \exp(-R_{\text{phosP1}} \times t)]$, and $\%phospho_{P1P2}(t) = \%phospho_{P2}(t)$.

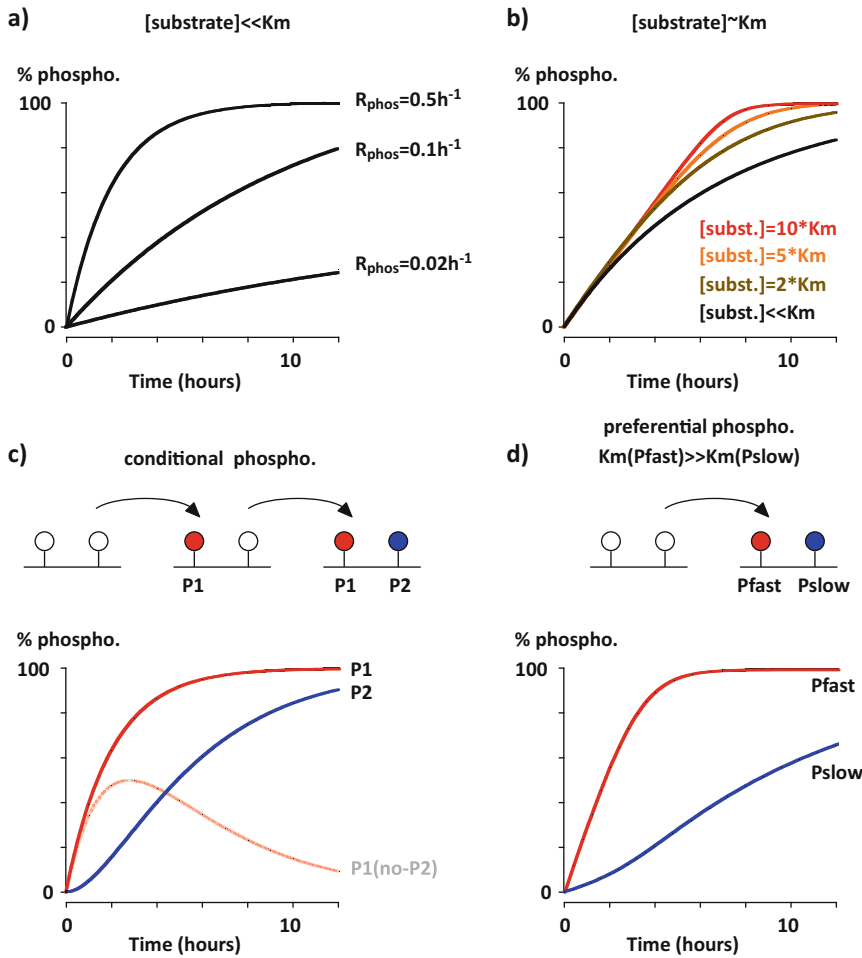


Fig. 4 Theoretical phosphorylation build-up curves. **(a)** Build-up curves in the situation where the phosphorylation target is at a concentration well below its K_m . **(b)** Build-up curves in the situation where the phosphorylation target is at concentrations above its K_m (black: $[substrate] \ll K_m$; brown: $[substrate] = 2 \times K_m$; orange: $[substrate] = 5 \times K_m$; red: $[substrate] = 10 \times K_m$). **(c)** Build-up curves in the situation where the substrate carries 2 phosphorylation sites and the second phosphosites (in blue) is phosphorylated only once the first phosphosite (in red) has been modified. **(d)** Build-up curves in the situation where the substrate carries two phosphorylation sites with $K_m(P1) = 10 \times K_m(P2)$ (P1 is in red, P2 in blue)

15. An S shape can also reveal the late phosphorylation of a poor K_m , slow phosphosite Pslow after the early phosphorylation of a faster site, Pfast (Fig. 4d). This situation does not provoke necessarily the apparition of multiple peaks like in 14. Such a build-up curve is fitted approximately by $\%phospho_{Pslow}(t) = 1 - [1 - \%phospho_{Pfast}]^\delta$, with $\delta = (V_{max-Pslow} \times K_{MPfast}) / (V_{MaxPFast} \times K_{MPslow}) < 1$. Do not pay too much attention to the individual values obtained upon fitting, but consider only the initial rates calculated from fitted parameters (see Note 12).

4 Notes

1. The lowest IDP concentration to obtain sufficient S/N is about 12.5 μM in most cases. Phosphorylation monitoring by NMR is, however, often performed at much higher concentrations in the literature, sometimes at several hundreds of micromolar. Importantly, at high IDP concentrations, kinases are likely to steadily phosphorylate non-specific sites with very high K_m . NMR concentrations may thus generate questionable results if this aspect is neglected. K_m s of kinases for their cognate targets span a wide range of values, from 1 to 100 μM , while k_{cat} values can vary between 0.01 and 100 s^{-1} (we did not find an article providing statistics; these are numbers based on long-term experience; you can try <https://www.brenda-enzymes.org/>). We highly recommend to measure kinetics at a given concentration and at either half or twice this concentration. The measured initial rates (in mol/s) will reveal whether the used concentrations are below or above the K_m of every detected phosphosite, and whether some sites emerge only because of high concentrations. There are three possibilities: (a) if the molar phosphorylation rate is proportional to the substrate concentration, we are well below the phosphosite K_m , which may be odd at concentrations above 100 μM , for example; (b) if it is the same at both concentrations, we are an order of magnitude above the K_m , which may call for running the phosphorylation reaction at lower concentration; (c) intermediate situations mean that we are at a concentration in the order of magnitude of the K_m . Of course, it is ideally preferable to determine k_{cat} and K_m more precisely by measuring initial rates at multiple concentrations following the Michaelis-Menten approach.
2. Cysteine reduction can usually be obtained by supplementing the lysis buffer with 10 mM DTT (final concentration), and by spiking 5 mM DTT (final concentration) in protein samples after every purification step. Avoid β -mercaptoethanol: it is a poor reducing agent and it easily forms mixed disulfides with cysteines. TCEP is advantageous in many regards, but its notorious stability is affected by the presence of phosphate and EGTA [24, 31], it requires pH adjustment after solubilization, and it may cleave progressively the protein backbone near cysteines [32].
3. IDPs are generally very well expressed in *E. coli* strains optimized for protein production. Bacteria are grown in minimum media containing $^{15}\text{NH}_4\text{Cl}$ and ^{13}C -glucose as sole sources of nitrogen and carbon, respectively. Recipes can be found at https://www.embl.de/pepcore/pepcore_services/protein_

[expression/ecoli/n15/](#) or in [29]. IDPs can sometimes be obtained in inclusion bodies: in such situation, they can be first purified in urea using a Histidine tag, before being transferred in a non-denaturant buffer using SEC.

4. High buffering capacity is important because ATP and DTT hydrolysis release protons and can provoke deleterious pH variations. A careful control of the pH is indeed essential to generate NMR data of high quality: crosspeak intensities of IDPs amide functions can vary up to ~10% for a pH shift of 0.1 at pH 7 and 298 K (This is due to the pH-dependency of water/amide proton exchange [37], hence to the residence time of the detected amide protons). Because we calculate phospho and non-phospho populations based on NMR crosspeak intensities, pH variations can thus bias this quantification.
5. Recombinant expression in insect or mammalian cells may produce prephosphorylated protein samples. This may be detected using the Pro-Q Diamond Phosphoprotein Gel Stain kit, Phos-Tag SDS-PAGE [30], Mass Spectrometry, or Western blot with an antibody directed against phosphoSer/Thr. It can also be detected using 2D ^1H - ^{15}N NMR spectroscopy, given the recognizable chemical shifts adopted by phosphoSer/Thr residues [16, 21]. Tyrosine phosphorylation can be nailed using ^1H - ^{13}C NMR spectroscopy because of the Ce chemical shifts perturbation [21]. If prephosphorylation is ascertained, a phosphatase treatment may be carried out during the purification.
6. Adding 10% glycerol to the reaction mix often improves S/N and decreases the pH-dependency of NMR crosspeak intensities. It provokes chemical shift perturbations, which may be large enough to force a supplementary assignment step. This can be carried out similarly to what has been described for temperature-dependent assignment in Subheading 3.3.
7. Kinases achieve substrate specificity in many ways [33]. Several servers exist predicting phosphorylation sites and their associated kinases. They rely mostly on kinase consensus site analysis, reported detection, and existing annotation or interaction networks in databases [34, 35]. An extensive list of methods is available in [36]. A simple consensus site analysis can be obtained using <http://www.cbs.dtu.dk/services/NetPhos/>. Lists of detected phosphorylation sites are available on <https://www.phosphosite.org/>.
8. Monitoring IDP phosphorylation in cell extracts is a challenging task. Which cell line? Which lysis conditions? In exponential growth phase, or after cell-cycle arrest and at which stage? Whole cell extract or separation of specific cell compartment? These parameters will generate very different extracts with

highly variable phosphorylation activities. For this reason, we thought it was difficult to provide a generic protocol, and we prefer to refer to guidelines published previously [17]. Producing active extracts requires fast manipulation of the cellular material. Lysis buffers should of course be non-denaturing and contain large concentrations of protease and phosphatase inhibitors. ATP hydrolysis is usually intense because of the combined activity of several cellular kinases. Extract concentration should be high (1–10 mg/mL). The experimental time-frame is usually about 1 h, although it can be difficult to establish: early phosphorylation can be rapidly compensated by dephosphorylation activity of cellular phosphatases, which often take over anyway after ATP exhaustion. We finally warn the reader that interpretation of phosphorylation kinetics in cell extracts should be cautious: native cellular organization and colocalization is essential in cell signaling, and is lost in cell extracts; the IDP of interest may interact with enzymes that it would not meet in a real cell, and kinase or phosphatase activity regulation may quickly degenerate.

9. Kinases affinity for ATP is in the range of 10–100 μM , and up to the millimolar range in a minority of cases [38]. Affinity for ADP is in the same range and very well correlated to that of ATP [38]. Hence, a large excess of ATP is recommended for monitoring phosphorylation reactions *in vitro* to avoid strong inhibition by growing concentrations of ADP. Moreover, we observed in most cases that kinases hydrolyze more ATP molecules than they transfer phosphate moieties to their substrate. We recommend to measure 1D ^1H spectra before and after the reaction to evaluate the ratio ATP/ADP (Fig. 5), which may help in interpreting the progressive loss of kinase activity.
10. The most prominent chemical shift changes occur for phosphorylated residues. Their crosspeaks show strong downfield-shifts in ^1H - ^{15}N 2D spectra upon phosphorylation: due to a hydrogen bond between the new side-chain phosphate and the backbone amide function, their ^1H resonances move to 8.5–9.5 ppm, which is out of the regular spectral window (7.5–8.5 ppm) for disordered peptides [16, 21]. However, the corresponding peaks move upfield when pH acidifies, and their absolute intensities are also pH dependent. In surprising cases, crosspeaks in this “phospho-region” of 8.5–9.5 ppm can reveal a H-bond between the side-chain phosphate of a phosphorylated residue and the amide proton of a non-phosphorylated residue [39]. $^{13}\text{C}\alpha$ and $^{13}\text{C}\beta$ chemical shifts provide unambiguous information on the nature of these ^1H - ^{15}N crosspeaks (phosphoSer/Thr, or neighboring non-modified residue establishing a H-bond with a phosphate). Recording a 3D HNCACB spectrum is thus often of

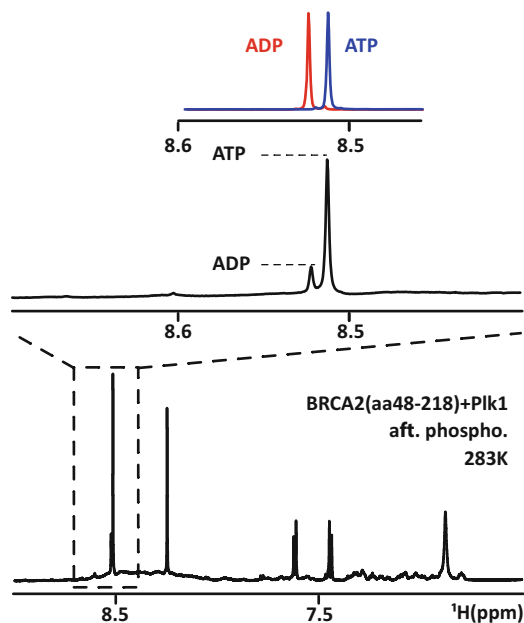


Fig. 5 NMR analysis of the ATP/ADP concentrations. *Upper panel:* Overlay of 1D ^1H spectra of pure ATP (blue) and ADP (red) showing the purine $^1\text{H}_{35}$ resonances. *Lower panel:* 1D ^1H spectrum of BRCA2(aa48–218) at 50 μM at the end of the phosphorylation reaction by Plk1. The close-up view shows the ATP and ADP $^1\text{H}_{35}$ signals allowing their quantification. All spectra were recorded in the phosphorylation buffer (50 mM HEPES, 100 mM NaCl, pH 7.0, 4 mM DTT, 1 \times EDTA-free protease inhibitors, 4 mM ATP, 10 mM MgCl_2) at 283 K and at 700 MHz. ATP and ADP $^1\text{H}_{35}$ chemical shifts depend on pH and on the presence of Mg^{2+} (~ 0.03 ppm)

good help in the analysis of the NMR data, which requires a $^{13}\text{C}/^{15}\text{N}$ -labeled IDP.

11. Because phosphoSer and phosphoThr have pKa values of about 6 and 6.5, respectively [21, 40], their protonation state varies with the potential pH evolution during the phosphorylation reaction, as evoked in **Note 3**. This provokes chemical shift perturbations of the phosphorylated residues and of their neighbors. Hence, it is important to verify that intensities are measured at the peak centers in every spectrum.
12. Complex mechanisms emerging from multiple phosphorylation sites can take place. Assigning all peaks when multiple neighbor phosphosites evolve concomitantly can be tedious. Fitting evolution curves in such situations, or in the case of large K_m differences between phosphosites, is always possible. Equations that can be used to fit complex phosphorylation schemes have been described extensively earlier [17]. However, the fitted parameters should be used cautiously: little differences in the range of the S/N (and thus inside the error bars)

for a couple of early points can provoke large differences in the fitted values; moreover, the progressive loss of kinase activity during the hours-long reaction is very difficult to evaluate. Hence, we argue that one should limit the interpretation of the recorded kinetics to (a) the ranking between phosphorylation sites and (b) the initial rates of phosphorylation.

Acknowledgement

This work was supported by CNRS, CEA, University Paris South and ENS Paris-Saclay, by the French Infrastructure for Integrated Structural Biology (<https://www.structuralbiology.eu/networks/FRISBI>), grant number ANR-10-INSB-05-01, Acronym FRISBI), and by the French National Research Agency (ANR; research grant ANR-14-ACHN-0015). We thank the protein production facility of the Institut Curie for providing the purified kinase Plk1.

References

- Hornbeck PV, Kornhauser JM, Latham V et al (2019) 15 years of PhosphoSitePlus[®]: integrating post-translationally modified sites, disease variants and isoforms. *Nucleic Acids Res* 47: D433–D441. <https://doi.org/10.1093/nar/gky1159>
- Huang K-Y, Lee T-Y, Kao H-J et al (2019) dbPTM in 2019: exploring disease association and cross-talk of post-translational modifications. *Nucleic Acids Res* 47:D298–D308. <https://doi.org/10.1093/nar/gky1074>
- Vlastaridis P, Kyriakidou P, Chaliotis A et al (2017) Estimating the total number of phosphoproteins and phosphorylation sites in eukaryotic proteomes. *GigaScience* 6:1–11. <https://doi.org/10.1093/gigascience/giw015>
- Yu K, Zhang Q, Liu Z et al (2019) qPhos: a database of protein phosphorylation dynamics in humans. *Nucleic Acids Res* 47:D451–D458. <https://doi.org/10.1093/nar/gky1052>
- Wright PE, Dyson HJ (2015) Intrinsically disordered proteins in cellular signalling and regulation. *Nat Rev Mol Cell Biol* 16:18–29. <https://doi.org/10.1038/nrm3920>
- Schweiger R, Linial M (2010) Cooperativity within proximal phosphorylation sites is revealed from large-scale proteomics data. *Biol Direct* 5:6. <https://doi.org/10.1186/1745-6150-5-6>
- Sharma K, D'Souza RCJ, Tyanova S et al (2014) Ultradeep human phosphoproteome reveals a distinct regulatory nature of Tyr and Ser/Thr-based signaling. *Cell Rep* 8:1583–1594. <https://doi.org/10.1016/j.celrep.2014.07.036>
- Theillet F-X, Binolfi A, Frembgen-Kesner T et al (2014) Physicochemical properties of cells and their effects on intrinsically disordered proteins (IDPs). *Chem Rev* 114:6661–6714. <https://doi.org/10.1021/cr400695p>
- Landry CR, Freschi L, Zarin T, Moses AM (2014) Turnover of protein phosphorylation evolving under stabilizing selection. *Front Genet* 5:245. <https://doi.org/10.3389/fgene.2014.00245>
- Nishi H, Shaytan A, Panchenko AR (2014) Physicochemical mechanisms of protein regulation by phosphorylation. *Front Genet* 5:270. <https://doi.org/10.3389/fgene.2014.00270>
- Levy ED, Michnick SW, Landry CR (2012) Protein abundance is key to distinguish promiscuous from functional phosphorylation based on evolutionary information. *Phil Trans R Soc B* 367:2594–2606. <https://doi.org/10.1098/rstb.2012.0078>
- Wu R, Haas W, Dephoure N et al (2011) A large-scale method to measure absolute protein phosphorylation stoichiometries. *Nat Methods* 8:677–683. <https://doi.org/10.1038/nmeth.1636>
- Kanshin E, Pascariu M, Tyers M et al (2018) Combined enrichment/enzymatic approach to study tightly clustered multisite phosphorylation on Ser-rich domains. *J Proteome Res*

- 17:3050–3060. <https://doi.org/10.1021/acs.jproteome.8b00205>
14. Riley NM, Coon JJ (2016) Phosphoproteomics in the age of rapid and deep proteome profiling. *Anal Chem* 88:74–94. <https://doi.org/10.1021/acs.analchem.5b04123>
 15. Humphrey SJ, Karayel O, James DE, Mann M (2018) High-throughput and high-sensitivity phosphoproteomics with the EasyPhos platform. *Nat Protoc* 13:1897–1916. <https://doi.org/10.1038/s41596-018-0014-9>
 16. Theillet F-X, Smet-Nocca C, Liokatis S et al (2012) Cell signaling, post-translational protein modifications and NMR spectroscopy. *J Biomol NMR* 54:217–236. <https://doi.org/10.1007/s10858-012-9674-x>
 17. Theillet F-X, Rose HM, Liokatis S et al (2013) Site-specific NMR mapping and time-resolved monitoring of serine and threonine phosphorylation in reconstituted kinase reactions and mammalian cell extracts. *Nat Protoc* 8:1416–1432. <https://doi.org/10.1038/nprot.2013.083>
 18. Smith MJ, Marshall CB, Theillet F-X et al (2015) Real-time NMR monitoring of biological activities in complex physiological environments. *Curr Opin Struct Biol* 32:39–47. <https://doi.org/10.1016/j.sbi.2015.02.003>
 19. Cordier F, Chaffotte A, Terrien E et al (2012) Ordered phosphorylation events in two independent cascades of the PTEN C-tail revealed by NMR. *J Am Chem Soc* 134:20533–20543. <https://doi.org/10.1021/ja310214g>
 20. Mylona A, Theillet F-X, Foster C et al (2016) Opposing effects of Elk-1 multisite phosphorylation shape its response to ERK activation. *Science* 354:233–237. <https://doi.org/10.1126/science.aad1872>
 21. Bienkiewicz EA, Lumb KJ (1999) Random-coil chemical shifts of phosphorylated amino acids. *J Biomol NMR* 15:203–206
 22. Liokatis S, Stützer A, Elsässer SJ et al (2012) Phosphorylation of histone H3 Ser10 establishes a hierarchy for subsequent intramolecular modification events. *Nat Struct Mol Biol* 19:819–823. <https://doi.org/10.1038/nsmb.2310>
 23. Hendus-Altenburger R, Pedraz-Cuesta E, Olsen CW et al (2016) The human Na(+)/H(+) exchanger 1 is a membrane scaffold protein for extracellular signal-regulated kinase 2. *BMC Biol* 14:31. <https://doi.org/10.1186/s12915-016-0252-7>
 24. Getz EB, Xiao M, Chakrabarty T et al (1999) A comparison between the sulfhydryl reductants tris(2-carboxyethyl)phosphine and dithiothreitol for use in protein biochemistry. *Anal Biochem* 273:73–80. <https://doi.org/10.1006/abio.1999.4203>
 25. Schanda P, Kupče Ě, Brutscher B (2005) SOFAST-HMQC experiments for recording two-dimensional heteronuclear correlation spectra of proteins within a few seconds. *J Biomol NMR* 33:199–211. <https://doi.org/10.1007/s10858-005-4425-x>
 26. Theillet F-X, Binolfi A, Liokatis S et al (2011) Paramagnetic relaxation enhancement to improve sensitivity of fast NMR methods: application to intrinsically disordered proteins. *J Biomol NMR* 51:487–495. <https://doi.org/10.1007/s10858-011-9577-2>
 27. Lee C-R, Park Y-H, Kim Y-R et al (2013) Phosphorylation-dependent mobility shift of proteins on SDS-PAGE is due to decreased binding of SDS. *Bull Kor Chem Soc* 34:2063–2066. <https://doi.org/10.5012/bkcs.2013.34.7.2063>
 28. Kjaergaard M, Brander S, Poulsen FM (2011) Random coil chemical shift for intrinsically disordered proteins: effects of temperature and pH. *J Biomol NMR* 49:139–149. <https://doi.org/10.1007/s10858-011-9472-x>
 29. Azatian SB, Kaur N, Latham MP (2019) Increasing the buffering capacity of minimal media leads to higher protein yield. *J Biomol NMR* 73:11–17. <https://doi.org/10.1007/s10858-018-00222-4>
 30. Kinoshita E, Kinoshita-Kikuta E, Koike T (2009) Separation and detection of large phosphoproteins using Phos-tag SDS-PAGE. *Nat Protoc* 4:1513–1521. <https://doi.org/10.1038/nprot.2009.154>
 31. Hansen RE, Winther JR (2009) An introduction to methods for analyzing thiols and disulfides: reactions, reagents, and practical considerations. *Anal Biochem* 394:147–158. <https://doi.org/10.1016/j.ab.2009.07.051>
 32. Liu P, O'Mara BW, Warrack BM et al (2010) A tris (2-carboxyethyl) phosphine (TCEP) related cleavage on cysteine-containing proteins. *J Am Soc Mass Spectrom* 21:837–844. <https://doi.org/10.1016/j.jasms.2010.01.016>
 33. Miller CJ, Turk BE (2018) Homing in: mechanisms of substrate targeting by protein kinases. *Trends Biochem Sci* 43:380–394. <https://doi.org/10.1016/j.tibs.2018.02.009>
 34. Horn H, Schoof EM, Kim J et al (2014) KinomeXplorer: an integrated platform for kinome biology studies. *Nat Meth* 11:603–604. <https://doi.org/10.1038/nmeth.2968>
 35. Patrick R, Horin C, Kobe B et al (2016) Prediction of kinase-specific phosphorylation sites

- through an integrative model of protein context and sequence. *BBA Proteins Proteomics* 1864:1599–1608. <https://doi.org/10.1016/j.bbapap.2016.08.001>
36. Palmeri A, Ferrè F, Helmer-Citterich M (2014) Exploiting holistic approaches to model specificity in protein phosphorylation. *Front Genet* 5:315. <https://doi.org/10.3389/fgene.2014.00315>
 37. Bai Y, Milne JS, Mayne L, Englander SW (1993) Primary structure effects on peptide group hydrogen exchange. *Proteins* 17:75–86. <https://doi.org/10.1002/prot.340170110>
 38. Becher I, Savitski MM, Savitski MF et al (2013) Affinity profiling of the cellular kinome for the nucleotide cofactors ATP, ADP, and GTP. *ACS Chem Biol* 8:599–607. <https://doi.org/10.1021/cb3005879>
 39. Smet-Nocca C, Launay H, Wieruszkeski J-M et al (2013) Unraveling a phosphorylation event in a folded protein by NMR spectroscopy: phosphorylation of the Pin1 WW domain by PKA. *J Biomol NMR* 55:323–337. <https://doi.org/10.1007/s10858-013-9716-z>
 40. Platzer G, Okon M, McIntosh LP (2014) pH-dependent random coil ¹H, ¹³C, and ¹⁵N chemical shifts of the ionizable amino acids: a guide for protein pK_a measurements. *J Biomol NMR* 60:109–129. <https://doi.org/10.1007/s10858-014-9862-y>

Two strategies are described in this review: i) the continuous readout of the phosphorylation reaction, which can be performed by NMR at pH<7.5, and ii) the delayed NMR analysis of aliquots, whose phosphorylation reaction has been quenched at different time points. The second strategy makes it possible to monitor phosphorylation kinetics at any pH, provided that the quenched samples are readjusted at pH<7.5 for the NMR analysis performed later. It is however more demanding in terms of sample quantities and more labor intensive, because it requires to prepare as many tubes and to set up as many NMR acquisitions as the number of time points (*and to walk 1km about 100 times to the spectrometer :-)*).

For Plk1, an initial optimization of phosphorylation conditions had been set up by Dr. Simona Miron with a first batch of Plk1 produced by Institut Curie. The results of this prior tests suggested to monitor the phosphorylation reaction at pH 7.8 to benefit of the full activity of Plk1. Thus, I initially used quenched reactions for monitoring BRCA2 phosphorylation by Plk1. Although time-consuming and inconvenient because of the number of Plk1 mutants multiplied by the number of time points, it allowed us to report the first phosphorylation kinetics of multiple sites of BRCA2 and its variants by Plk1.

2. Recording 2D $^{13}\text{C}\alpha$ - ^{13}CO NMR spectra

In order to continuously monitor phosphorylation at pH ≥ 7.5 and on large temperature range, we designed a new method based on the acquisition of 2D $^{13}\text{C}\alpha$ - ^{13}CO spectra. All the details of this new method are described in a recent article published in *Angewandte Chemie*. In this article, I produced the BRCA2₄₈₋₂₁₈ and BRCA2₁₉₀₋₂₈₄ samples, I assigned their $^{13}\text{C}\alpha$ - ^{13}CO resonances and those of their phosphorylated versions (**Figure 39**), and I finally acquired and analyzed BRCA2 phosphorylation kinetics using this new strategy, under the supervision of Dr. François-Xavier Theillet.

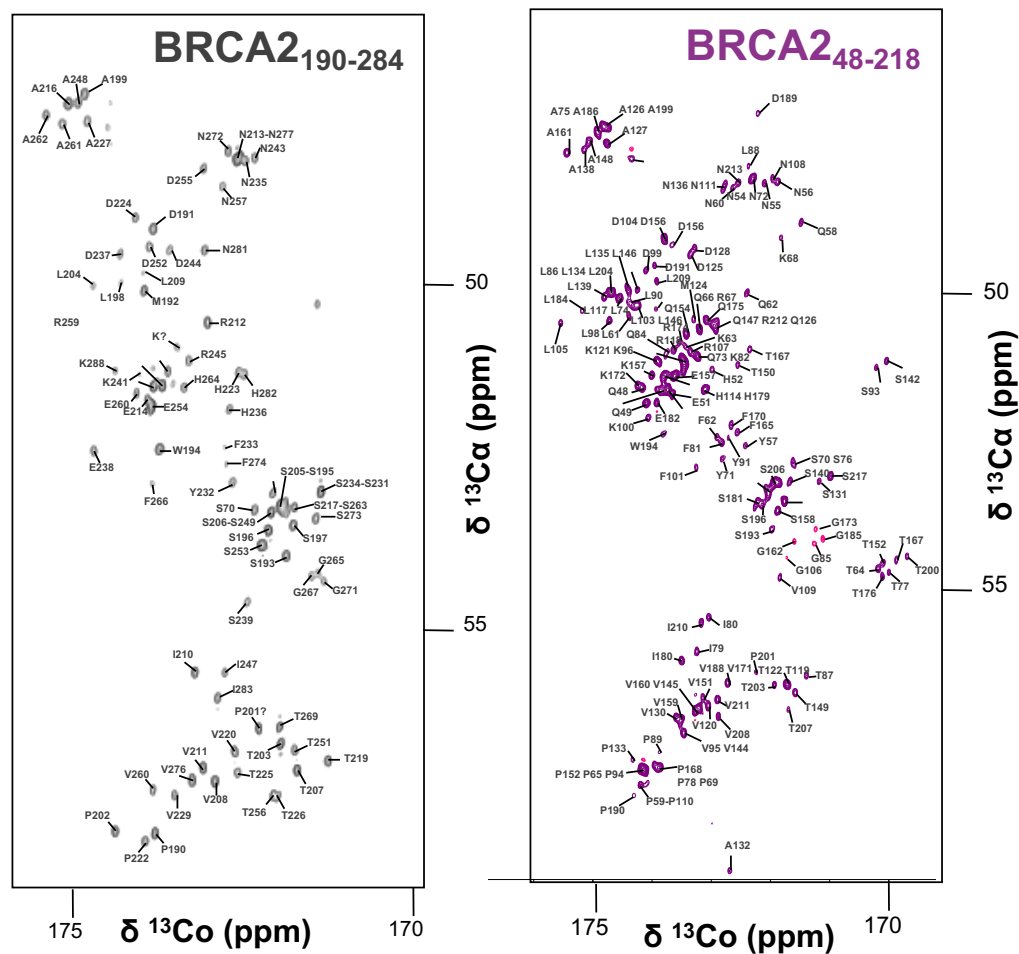


Figure 39. ^{13}Ca - ^{13}CO spectrum assignment of BRCA2₁₉₀₋₂₈₄ and BRCA2₄₈₋₂₁₈ in 50 mM HEPES, 75 mM NaCl, 1mM EDTA, pH 6.8. Spectra were recorded on a 700 MHz spectrometer at 283 K (CEA Saclay).

COMMUNICATION

Sensitivity-Enhanced ^{13}C -NMR for Monitoring Multisite Phosphorylation at Physiological Temperature and pH.

Ania Alik^{[a]#}, Chafiaa Bouguechtouli^{[a]#}, Manon Julien^{[a]#}, Wolfgang Bermel^[b], Rania Ghoulil^[a], Sophie Zinn-Justin^[a], Francois-Xavier Theillet^{*[a]}

[#] These authors contributed equally.

[*] Corresponding author.

[a] A. Alik, C. Bouguechtouli, M. Julien, R. Ghoulil, Dr. S. Zinn-Justin, Dr. F.X. Theillet, Université Paris-Saclay, CEA, CNRS, Institute for Integrative Biology of the Cell (I2BC), 91198, Gif-sur-Yvette, France.
E-mail: francois-xavier.theillet@cns.fr

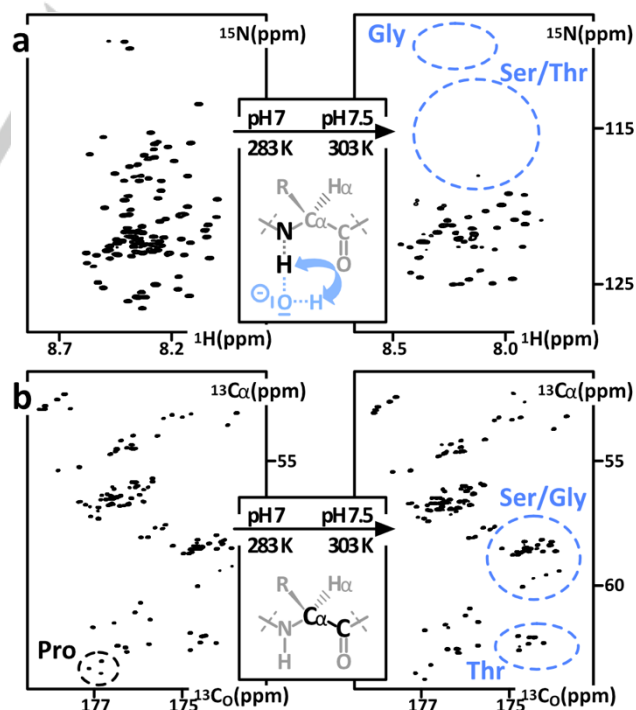
[b] Dr. W. Bermel, Bruker BioSpin GmbH, Silberstreifen, 76287 Rheinstetten, Germany.

Supporting information for this article is given via a link at the end of the document.

Abstract: Abundant phosphorylation events rule the activity of nuclear proteins involved in gene regulation and DNA repair. These occur mostly on disordered regions of proteins, which often contain multiple phosphosites. Comprehensive and quantitative monitoring of phosphorylation reactions is theoretically achievable at a residue-specific level using ^1H - ^{15}N NMR spectroscopy, but is often limited by low signal-to-noise at $\text{pH}>7$ and $T>293\text{K}$. We developed an improved $^{13}\text{C}\alpha$ - ^{13}CO correlation NMR experiment that works equally at any pH or temperature, i.e. also at those where genuine kinase activities occur. This permits to obtain atomic-resolution information in physiological conditions down to $25\ \mu\text{M}$. We exemplified the interest of this approach by monitoring phosphorylation reactions, in presence of purified kinases or in cell extracts, on a range of previously problematic targets, namely Mdm2, BRCA2 and Oct4.

In eukaryotes, intracellular signal transduction largely relies on phosphorylation of intrinsically disordered regions of proteins (IDRs)^[1]. More than 200,000 phosphosites have been detected on the $\sim 13,000$ human phosphoproteins^[2,3]. Many of these phosphosites are clustered in unfolded regions of proteins, which conveniently permits to establish crosstalks or robustness in signaling^[4,5]. Most of them have been detected by mass-spectrometry (MS) or western-blotting (WB). These popular methods are sensitive, but hardly provide a comprehensive characterization in common cases of multiple neighboring or degenerate phosphosites. High-resolution NMR spectroscopy has emerged as a complementary approach to decipher complex phosphorylation schemes: using the classical detection of ^1H - ^{15}N amide resonances, residue-specific information is obtained in 2D ^1H - ^{15}N correlation spectra, even on multiple phosphorylation sites that were not solved by MS/WB^[6-8]. In frequent cases where 2D NMR peaks of IDRs overlap, 3D BT-HNCO combined with non-uniform sampling (NUS) shows superior capacities^[9,10]. However, these approaches rely on amide protons detection, which is efficient for unfolded peptides at $\text{pH}<7$ and $T<293\text{K}$: because water-amide proton exchange rate is proportional to $[\text{OH}^-]$ at $\text{pH}\sim 7$ and gets faster at high temperature^[11], ^1H - ^{15}N signals become weaker in physiological conditions where phosphorylation reactions are carried out, especially for fast-exchanging residues like Ser/Thr (Figure 1a; Figure S1). Moreover, pH changes of ~ 0.1 can generate $\sim 25\%$ variations in the H-N crosspeak intensities, making them delicate to use when a quantitative analysis of phosphorylation reaction advancement is needed.

Indeed, to obtain individual phosphorylation rates, time-series of ^1H - ^{15}N NMR spectra are recorded during the reaction in conditions where kinases are active, i.e. at $\text{pH}=7$ and 298K . Residue-specific peak intensities are then quantified in every spectrum to monitor disappearance or appearance of unphospho- or phospho-species, respectively^[6-8]. The non-phosphopeaks (either from the phosphosites themselves or from neighboring residues) provide the most reliable information: reference intensities at 0% phosphorylation are known and permit a straightforward normalization. However, at physiological pH and temperature, disordered proteins generate overlapping and weak ^1H - ^{15}N signals, as mentioned earlier. The counterpart phosphopeaks display generally more favorable intensities because phosphate groups on the side chain slow down water-



Scheme 1. Figure 1. (a) ^1H - ^{15}N 2D HSQC and (b) $^{13}\text{C}\alpha$ - ^{13}CO 2D (^1H -flip*) $^{13}\text{C}\alpha$ - ^{13}CO -LB spectra of Mdm2(aa284-434) at $\text{pH}7/283\text{K}$ and $\text{pH}7.5/303\text{K}$. Spectral areas of Gly, Ser, Thr resonances are highlighted in blue, those of Pro in black. The same contour levels are applied in all conditions.

COMMUNICATION

amide proton exchange, but exploiting them in a quantitative manner is often problematic: it requires normalization by peak intensities at 100% phosphorylation, a stoichiometry that is often impossible to reach using *in vitro* phosphorylation by purified kinases, especially when these are purchased commercially – commonly at high cost. (Schemes illustrating these normalization issues are shown in Figure S2).

To circumvent these drawbacks, we thought to switch to the observation of proton-less, ^{13}C -detected NMR correlations. This approach became appealing over the last years to characterize unfolded regions of proteins^[12–14]. Still, notably because of the lower ^{13}C gyromagnetic ratio, it suffers from lower S/N than conventional ^1H -NMR. The ^{13}CO - ^{15}N correlation experiments are used to study IDRs because they offer the best crosspeaks dispersion, but necessitate high protein quantities to provide quality spectra ($\sim 500\ \mu\text{M}$ in $\sim 300\ \mu\text{L}$), which is not very adapted to phosphorylation studies: a whole batch of commercial kinase is usually necessary to phosphorylate ~ 100 - $1000\ \text{nmol}$ of high-preference phosphosites. To reach a more favorable NMR sensitivity, we decided to build on the $(^1\text{H}\text{-flip})^{13}\text{C}\alpha$ - ^{13}CO correlation experiment, the most sensitive 2D ^{13}C -detected pulse sequence^[12]. This type of experiment is not spoiled by water-amide proton exchange, at the opposite of the ^{13}CO - ^{15}N experiments (Figure S3). $^{13}\text{C}\alpha$ - ^{13}CO experiments are usually thought to generate unresolved spectra showing abundant crosspeaks overlaps for unfolded peptides. However, using prolonged constant-time $^{13}\text{C}\alpha$ -evolutions, $^{13}\text{C}\alpha$ - ^{13}CO spectra can provide residue-specific information with high coverage along the peptide sequence, as we will see below.

Hence, we thought to improve the $(^1\text{H}\text{-flip})^{13}\text{C}\alpha$ - ^{13}CO sensitivity and adapt the sequence to our application. We first tuned the magnetization transfer delays (we named this first step $^1\text{H}\text{-flip}^*$, see Figure S4), sacrificing glycine resonances but generating a 15% increase for the rest of the amino acids. On average, this pays off in terms of phospho- and unphosphopeak intensities monitoring. Then, we replaced the final IPAP scheme by a homonuclear decoupling scheme LOW-BASHD applied during the acquisition (Figure S4)^[15]. We also implemented a $120\ \mu\text{s}$ triply compensated pulse G5^[16] to invert both carbonyl and alkyl ^{13}C nuclei in the final INEPT block. This yielded on average a 40% increase in S/N without any side-effects on peak line-width (Figure 2a, 2b), as demonstrated by Bax and colleagues^[15]. It left the door open for implementing the preservation of equivalent pathways (PEP) routinely applied to ^1H - ^{15}N HSQC^[17]. Despite multiple trials using various pulses and transfer delays (Figure S3), the best combination provided only a $\sim 40\%$ enhancement in signal, while also increasing the noise by $\sqrt{2}$ because the PEP protocol requires the acquisition of two independent datasets later recombined before processing.

Finally, we thought to use chelated transition metals like Ni-DO₂A for paramagnetic T1 relaxation enhancement, which is a potent way for NMR sensitivity improvement^[18,19]. However, to preserve kinase activity, phosphorylation reactions require i) the presence of Mg^{2+} , which can compete with DO₂A-chelated divalent metal ions, and ii) reducing agents, which react with Ni-DO₂A and most of the transition metals complexes that we tried. Among the commercial DOTA derivatives available, NOTA is attractive because it is tailored to chelate trivalent transition metals, and thus not Mg^{2+} . We found that the vanadium ion complex [$\text{V}^{3+}(\text{NOTA}^{3-})$] (Figure 2c) was the only one to remain stable in presence of Mg^{2+} and DTT, as well as at high pH and temperature.

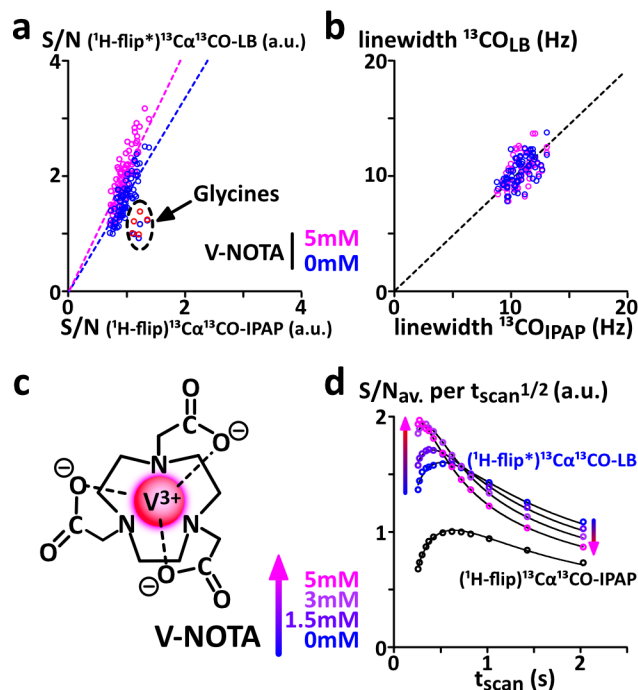


Figure 2. Performances of the $(^1\text{H}\text{-flip}^*)^{13}\text{C}\alpha$ - ^{13}CO -LB sequence, as evaluated on the model protein α -synuclein. (a) S/N of well-separated peaks in 2D $(^1\text{H}\text{-flip}^*)^{13}\text{C}\alpha$ - ^{13}CO -LB with 0mM (blue) or 5mM (red) V-NOTA compared to $(^1\text{H}\text{-flip}^*)^{13}\text{C}\alpha$ - ^{13}CO -IPAP (0mM V-NOTA); (b) Linewidths of isolated peaks in 2D $(^1\text{H}\text{-flip}^*)^{13}\text{C}\alpha$ - ^{13}CO -LB with 0mM (blue) or 5mM (red) V-NOTA compared to $(^1\text{H}\text{-flip}^*)^{13}\text{C}\alpha$ - ^{13}CO -IPAP (0mM V-NOTA). (c) Chemical structure of V^{3+} chelated by NOTA^{3-} ; (d) Sensitivity and time efficiency: average S/N per $\sqrt{t_{\text{scan}}}$ as measured in 1D $(^1\text{H}\text{-flip}^*)^{13}\text{C}\alpha$ - ^{13}CO -IPAP (black) and $(^1\text{H}\text{-flip}^*)^{13}\text{C}\alpha$ - ^{13}CO -LB with 0mM (blue), 1.5mM (violet), 3mM (purple) and 5mM (pink) V-NOTA.

It provided up to a 25% increase in S/N for the $(^1\text{H}\text{-flip}^*)^{13}\text{C}\alpha$ -linewidths (Figure 2). Fast pulsing with low interscan delays ($\sim 0.1\text{s}$) provides the best S/N per experimental time (Figure 2d). Altogether, using a classical cryoprobe optimized for “indirect” ^1H -detection, a $^{13}\text{C}\alpha$ constant-time evolution of 27 ms and 50% NUS^[20,21], we can record in 30 minutes high-resolution 2D $^{13}\text{C}\alpha$ - ^{13}CO correlation spectra providing residue-specific information on IDRs at $50\ \mu\text{M}$ and at any pH or temperature. This can be translated into $25\ \mu\text{M}$ for ^{13}C -direct detection probes. The resulting resolution is often sufficient to get residue-specific information along most of the disordered peptide sequences. To cancel $\text{C}\alpha\text{C}\beta$ coupling in $^{13}\text{C}\alpha$ dimension, a $^{13}\text{C}\alpha$ constant-time evolution of 27, 54 or 81 ms must be used. In case of important peak overlaps, an increased resolution is achievable using a $^{13}\text{C}\alpha$ evolution time of 54 ms, which provides an average 12 Hz linewidth in $^{13}\text{C}\alpha$ -dimension but provokes about 30% losses in S/N (8 Hz linewidth using an evolution time of 81 ms, Figure S5).

With this dedicated analysis tool in hands, we then attempted to characterize challenging phosphorylation reactions that we failed to monitor accurately using only ^1H - ^{15}N experiments. This was the case for human Mdm2, an E3-ubiquitin ligase controlling the abundance of the tumor suppressor p53^[22,23]. Mdm2 activity is regulated by DNA-damage response (DDR) kinases DNA-PK, ATM or ATR^[24,25]. According to the literature, they phosphorylate Mdm2 on 6 sites of its C-terminal region (aa334-434)^[24-26], among which mouse S394 (human S395) phosphorylation has consequences on p53 stabilization and DNA-damage signaling.^[26-28] To investigate the structural mechanism behind

COMMUNICATION

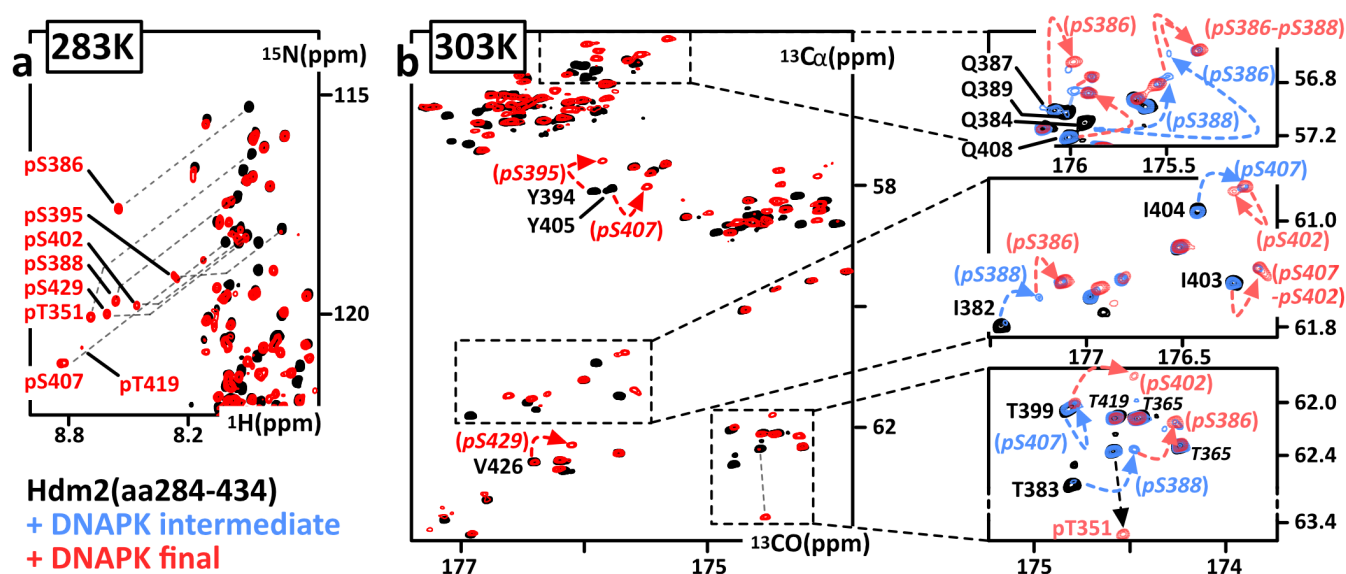


Figure 3. Phosphorylation of human Mdm2(aa284-434) by DNA-PK observed by NMR. (a) Overlay of 2D ^1H - ^{15}N HSQC spectra at 283K before (black) and after (red) the phosphorylation reaction. (b) Overlay of 2D (^1H -flip*) $^{13}\text{C}\alpha$ - ^{13}CO -LB at 303K before (black), in the course (light blue) and at the end (red) of the phosphorylation reaction. At the right: Close-up views of Gln, Ile, and Thr regions. Arrows show peak displacements upon 2 neighbor phosphorylation events: certain sets of peaks report for the 4 phosphostates, e.g. Q384(S386-S388)/Q384(pS386-S388)/Q384(S386-pS388)/Q384(pS386-pS388); in contrast I382(pS388) and T383(pS388) report the appearance of Mdm2(S386-pS388), while I382(pS386) and T383(pS386) both report Mdm2(pS386-S388)+Mdm2(pS386-pS388) (see Experimental Procedures in Supp. Info. for the assignment strategy).

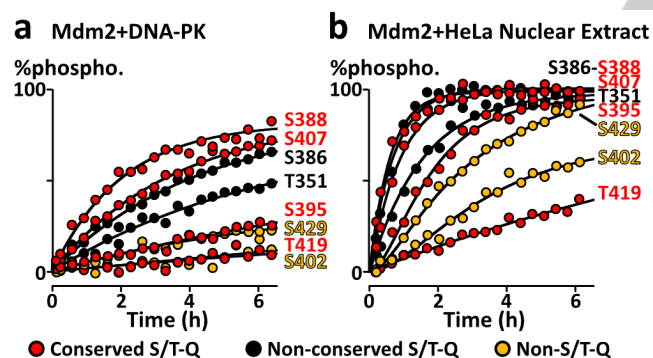


Figure 4. Site-specific phosphorylation kinetics of Mdm2(aa284-434). Build-up curves of phosphorylation reactions as executed (a) by purified DNA-PK or (b) in HeLa cells Nuclear Extract; The phosphosite labels are in line with their corresponding curves. Non-conserved sites are in black, conserved S/T-Q sites in red, non-S/T-Q sites in orange.

this functional switch, we had first to map comprehensively the phosphorylation scheme established by the DDR kinases. We used the segment Mdm2(aa284-434) comprising the region Mdm2(aa334-434) that we characterized as intrinsically disordered (Figure S6). After a prolonged reaction at 298K in the presence of purified DNA-PK, 2D ^1H - ^{15}N spectra of Mdm2(aa284-434) recorded at 283K revealed the phosphorylation endpoint (Figure 3): we identified 8 phosphosites T351, S386, S388, S395, S402, S407, T419 and S429. Initially, we could determine T351, S395 and S429 phosphorylation rates by recording time series of ^1H - ^{15}N SOFAST-HMQC NMR experiments during the reaction at 298K^[29]. In the cases of S386, S388, S402, S407 and T419, we were unable to quantify accurately their kinetics because of ^1H - ^{15}N non-phosphopeaks overlapping or being even non-detectable

for S402 and S407. Together with their uncomplete phosphorylation, these prevented the determination of reference ^1H -detected peak intensities at 0% and 100% phosphorylation. Here, previously published ^1H -detection methods^[6-10] found their limits. Then, we recorded times series of alternated ^1H - ^{15}N SOFAST-HMQC and (^1H -flip*) $^{13}\text{C}\alpha$ - ^{13}CO -LB experiments during the reaction at 298K. These provided complementary information: ^1H - ^{15}N SOFAST-HMQC spectra reported phosphopeaks build-up curves at high S/N, which we normalized using (^1H -flip*) $^{13}\text{C}\alpha$ - ^{13}CO -LB non-phosphopeaks intensities and their decay curves. We found exploitable non-phosphopeak reporters for S386, S388, S402, S407 and T419 in $^{13}\text{C}\alpha$ - ^{13}CO spectra at 298K (Figure 3, see the Material & Methods for a detailed list, a scheme of the rationale is presented in Figure S2). Using these peaks, we quantified and ranked DNA-PK's site preferences on Mdm2 (Figure 4a). Then, we tested our ability to monitor phosphorylation in cell extracts. Our approach mixing ^1H - ^{15}N SOFAST-HMQC and (^1H -flip*) $^{13}\text{C}\alpha$ - ^{13}CO -LB spectra worked in cell extracts containing from 0.2 to 5 mg/mL of cellular proteins: the phosphorylation order observed with purified DNA-PK was very similar in HeLa cells Nuclear Extract that were DNA-damaged by short sonication pulses. Thus, our site-specific absolute quantification revealed i) that S388 is a high-preference novel phosphosite, and T351 and S402 are two new lower preference sites, ii) that S429 and S402, which do not correspond to the DDR kinases S-T/Q consensus motif, were steadily modified, iii) that T383 and T419, two S-T/Q consensus sites, were not or slowly phosphorylated, respectively. Similarly, we monitored site-specific phosphorylation on two other disordered segments of nuclear proteins involved in genome maintenance and expression, namely the Breast Cancer type 2 susceptibility protein (BRCA2 aa190-284, see^[30]) and the pluripotency transcription factor Oct4 (aa1-145) (Figure S7). Our characterization of BRCA2 phosphorylation by Plk1 (pH7.8,

COMMUNICATION

T=303K), an important mitotic event, permitted to quantify properly two novel phosphosites T219 and T226, which were modified with rates comparable to the already known S193 and T207 (Figure 5a,c). We also wanted to examine Oct4 phosphorylation by MAP kinases, which regulates Oct4 transcriptional activity^[31]. In presence of p38 α (pH7.4, T298K), we noticed that the classical MAPK target motifs Ser/Thr-Pro S12, S111 and T118 were modified slower than the non-Ser/Thr-Pro T92 (Figure 5b,d). Here, we bring attention to the fact that $^{13}\text{C}\alpha^{13}\text{CO}$ correlation are very adapted to the study of proline-rich peptides, the residues in N-terminal of Pro showing strong upfield shifts and interesting chemical shift dispersion (see also Figure S8). This is of interest, since the abundant Ser/Thr-Pro motifs are targets of the essential activities of MAP-Kinases and Cyclin-dependent kinases^[32]. Because this method is not limited by temperature conditions, it may also help in studies focusing on temperature-sensitive activities of kinases involved in circadian rhythm or hyperthermia consequences^[33,34]. Hence, our improved ^{13}C -detected NMR approach expands the range of peptides and conditions accessible to NMR phospho-mapping and -monitoring. NMR methods previously published for PTM characterization are based on amide ^1H -detection, which often provides the best sensitivity and possibly higher dimensionality/resolution, using fast acquisition and time-resolved NUS^[6-10]. The proposed ^{13}C -detection scheme makes it possible to obtain residue-specific information with high sequence coverage on disordered proteins by NMR in all conditions of pH and temperature.

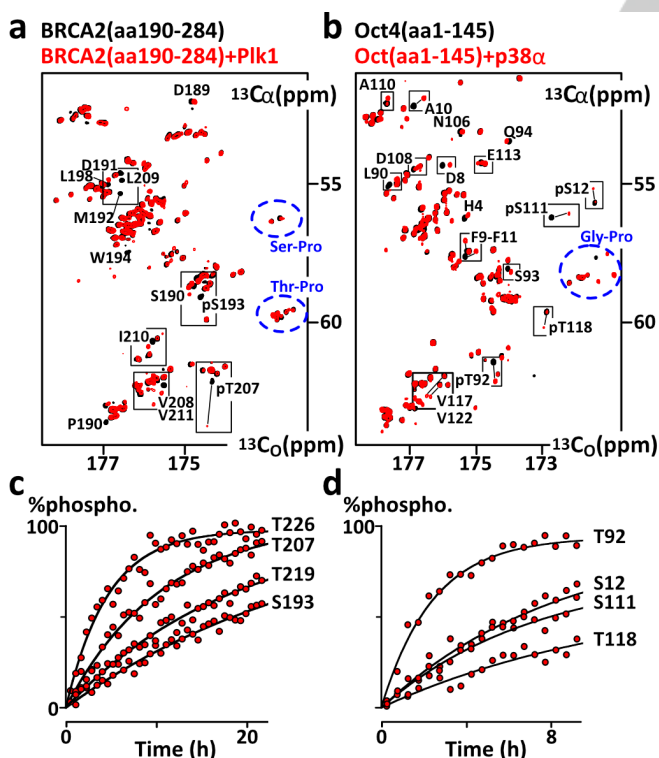


Figure 5. Phosphorylation as observed by 2D (^1H -flip*) $^{13}\text{C}\alpha^{13}\text{CO}$ -LB NMR. Overlays of (^1H -flip*) $^{13}\text{C}\alpha^{13}\text{CO}$ -LB spectra of (a) BRCA2(aa190-284) and (b) Oct4(aa1-145) before (black) and after (red) phosphorylation by Plk1 and p38 α , respectively. Spectral area corresponding to crosspeaks of Ser/Thr/Gly-Pro motifs are in blue. Kinetics were derived from time-series of (^1H -flip*) $^{13}\text{C}\alpha^{13}\text{CO}$ -LB spectra of (c) BRCA2(aa190-284) at 100 μM , pH7.8, T=303K (d) Oct4(aa1-145) at 100 μM , pH7.4, T=298K at 700MHz using a Bruker-TCl probe.

Experimental section

The Supporting Information contains detailed Material and Methods, HN/C α CO/CON NMR spectra of α -Synuclein, Elk1 and BRCA2 fragments at various pH, temperature and resolution, pulse sequence schemes, proteins' primary sequences presentations.

Acknowledgements

This work was supported by CNRS and GEA-Saclay, by the French Infrastructure for Integrated Structural Biology (<https://www.structuralbiology.eu/networks/FRISBI>, grant number ANR-10-INSB-05-01, Acronym FRISBI) and by the French National Research Agency (ANR; research grant ANR-14-ACHN-0015). We thank the protein production facility of the Institut Curie for providing the purified kinase Plk1.

Keywords: Cell signaling • Phosphorylation • NMR spectroscopy • Mdm2 • DNA-damage response

- [1] P. E. Wright, H. J. Dyson, *Nat Rev Mol Cell Biol* **2015**, *16*, 18–29.
- [2] P. Vlastaridis, P. Kyriakidou, A. Chaliotis, Y. Van de Peer, S. G. Oliver, G. D. Amoutzias, *Gigascience* **2017**, *6*, 1–11.
- [3] K. Yu, Q. Zhang, Z. Liu, Q. Zhao, X. Zhang, Y. Wang, Z.-X. Wang, Y. Jin, X. Li, Z.-X. Liu, et al., *Nucleic Acids Res.* **2019**, *47*, D451–D458.
- [4] F.-X. Theillet, A. Binolfi, T. Frembgen-Kesner, K. Ingorani, M. Sarkar, C. Kyne, C. Li, P. B. Crowley, L. Gierasch, G. J. Pielak, et al., *Chem. Rev.* **2014**, *114*, 6661–6714.
- [5] H. Nishi, A. Shaytan, A. R. Panchenko, *Front Genet* **2014**, *5*, 270.
- [6] F.-X. Theillet, H. M. Rose, S. Liokatis, A. Binolfi, R. Thongwichian, M. Stuijver, P. Selenko, *Nat. Protoc.* **2013**, *8*, 1416–1432.
- [7] M. J. Smith, C. B. Marshall, F.-X. Theillet, A. Binolfi, P. Selenko, M. Ikura, *Curr. Opin. Struct. Biol.* **2015**, *32*, 39–47.
- [8] A. Mylona, F.-X. Theillet, C. Foster, T. M. Cheng, F. Miralles, P. A. Bates, P. Selenko, R. Treisman, *Science* **2016**, *354*, 233–237.
- [9] M. Mayzel, J. Rosenl w, L. Isaksson, V. Y. Orekhov, *J. Biomol. NMR* **2014**, *58*, 129–139.
- [10] D. Golowicz, P. Kasprzak, V. Orekhov, K. Kazimierzczuk, *Prog. Nucl. Magn. Reson. Spectrosc.* **2020**, *116*, 40–55.
- [11] Y. Bai, J. S. Milne, L. Mayne, S. W. Englander, *Proteins* **1993**, *17*, 75–86.
- [12] W. Bermel, I. Bertini, I. C. Felli, R. Pierattelli, *J. Am. Chem. Soc.* **2009**, *131*, 15339–15345.
- [13] I. C. Felli, L. Gonnelli, R. Pierattelli, *Nat. Protoc.* **2014**, *9*, 2005–2016.
- [14] J. Lopez, R. Schneider, F.-X. Cantrelle, I. Huvent, G. Lippens, *Angew. Chem. Int. Ed.* **2016**, *128*, 7544–7548.
- [15] J. Ying, F. Li, J. H. Lee, A. Bax, *J. Biomol. NMR* **2014**, *60*, 15–21.
- [16] Y. Xia, P. Rossi, M. V. Subrahmanian, C. Huang, T. Saleh, C. Olivieri, C. G. Kalodimos, G. Veglia, *J. Biomol. NMR* **2017**, *69*, 237–243.
- [17] P. K. Mandal, A. Majumdar, *Concepts Magn. Reson.* **2004**, *20A*, 1–23.
- [18] F.-X. Theillet, A. Binolfi, S. Liokatis, S. Verzini, P. Selenko, *J. Biomol. NMR* **2011**, *51*, 487–495.
- [19] N. A. Oktaviani, M. W. Ris r, Y.-H. Lee, R. P. Megens, D. H. de Jong, R. Otten, R. M. Scheek, J. J. Enghild, N. C. Nielsen, T. Ikegami, et al., *J. Biomol. NMR* **2015**, *62*, 129–142.
- [20] K. Kazimierzczuk, V. Y. Orekhov, *Angew. Chem. Int. Ed.* **2011**, *50*, 5556–5559.
- [21] M. A. Zambrello, A. D. Schuyler, M. W. Maciejewski, F. Delaglio, I. Bezsonova, J. C. Hoch, *Methods* **2018**, *138*–139, 62–68.
- [22] A. C. Joerger, A. R. Fersht, *Annu. Rev. Biochem.* **2016**, *85*, 375–404.
- [23] O. Karni-Schmidt, M. Lokshin, C. Prives, *Annu. Rev. Pathol. Mech. Dis.* **2016**, *11*, 617–644.
- [24] A. Hafner, M. L. Bulyk, A. Jambhekar, G. Lahav, *Nat Rev Mol Cell Biol* **2019**, *20*, 199–210.
- [25] A. N. Blackford, S. P. Jackson, *Mol. Cell.* **2017**, *66*, 801–817.
- [26] D. W. Meek, *Biochem. J.* **2015**, *469*, 325–346.
- [27] T.-A. Nguyen, D. Menendez, M. A. Resnick, C. W. Anderson, *Hum Mutat* **2014**, *35*, 738–755.
- [28] H. S. Gannon, B. A. Woda, S. N. Jones, *Cancer Cell* **2012**, *21*, 668–679.
- [29] P. Schanda,  . Kup e, B. Brutscher, *J. Biomol. NMR* **2005**, *33*, 199–211.

COMMUNICATION

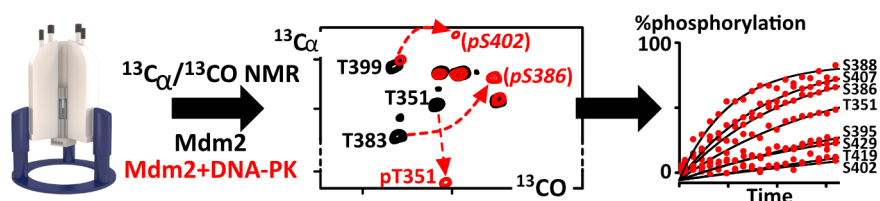
- [30] M. Julien, S. Miron, A. Carreira, F.-X. Theillet, S. Zinn-Justin, *Biomolecular NMR Assignments* **2020**.
- [31] J. Brumbaugh, Z. Hou, J. D. Russell, S. E. Howden, P. Yu, A. R. Ledvina, J. J. Coon, J. A. Thomson, *Proc. Natl. Acad. Sci. U.S.A.* **2012**, *109*, 7162–7168.
- [32] C. J. Miller, B. E. Turk, *Trends Biochem. Sci.* **2018**, *43*, 380–394.
- [33] Y. Shinohara, Y. M. Koyama, M. Ukai-Tadenuma, T. Hirokawa, M. Kikuchi, R. G. Yamada, H. Ukai, H. Fujishima, T. Umehara, K. Tainaka, et al., *Mol. Cell.* **2017**, *67*, 783–798.e20.
- [34] D. Deredge, P. L. Wintrode, M. E. Tulapurkar, A. Nagarsekar, Y. Zhang, D. J. Weber, P. Shapiro, J. D. Hasday, *J. Biol. Chem.* **2019**, *294*, 12624–12637.

WILEY-VCH

Accepted Manuscript

COMMUNICATION

Entry for the Table of Contents



We present an NMR method to monitor site-specific phosphorylation at high pH/T, which are necessary for kinases activity but prevented through characterization of disordered proteins. Our approach uses sensitivity-enhanced $^{13}\text{C}_\alpha$ - $^{13}\text{C}_\text{O}$ experiments. We detail their improvements and efficiency on Mdm2, BRCA2, Oct4. Much more phosphorylation cases are now investigable by NMR.

Supporting Information
©Wiley-VCH 2019
69451 Weinheim, Germany

Sensitivity-Enhanced ^{13}C -NMR for Monitoring Multisite Phosphorylation at Physiological Temperature and pH.

Ania Alik^{[a]#}, Chafiaa Bouguechtouli^{[a]#}, Manon Julien^{[a]#}, Wolfgang Bermel^[b], Rania Ghoul^[a], Sophie Zinn-Justin^[a], Francois-Xavier Theillet^{*[a]}

Abstract: Abundant phosphorylation events rule the activity of nuclear proteins involved in gene regulation and DNA repair. These occur mostly on disordered regions of proteins, which often contain multiple phosphosites. Comprehensive and quantitative monitoring of phosphorylation reactions is theoretically achievable at a residue-specific level using ^1H - ^{15}N NMR spectroscopy, but is often limited by low signal-to-noise at $\text{pH} > 7$ and $T > 293\text{K}$. We developed an improved $^{13}\text{C}\alpha$ - $^{13}\text{C}\text{O}$ correlation NMR experiment that works equally at any pH or temperature, i.e. also at those where genuine kinase activities occur. This permits to obtain atomic-resolution information in physiological conditions down to $25\ \mu\text{M}$. We exemplified the interest of this approach by monitoring phosphorylation reactions, in presence of purified kinases or in cell extracts, on a range of previously problematic targets, namely Mdm2, BRCA2 and Oct4.

DOI: 10.1002/anie.2016XXXXX

SUPPORTING INFORMATION

Table of Contents

Experimental procedures	pages 2-4
Supplementary Figures	pages 5-11
References	page 13
Authors contributions	page 13

Experimental Procedures

Peptide constructs

Codon-optimized genes coding for human Mdm2(aa284-434), Mdm2(aa284-333), Mdm2(aa284-380), Mdm2(aa284-393), Mdm2(aa284-415), and mouse Mdm2(aa282-432) were synthesized by Genscript and cloned into pET41(a+) vector between SacII and BamHI restriction sites. Cys362 and Cys374 (mouse Cys372) were Ala-mutated. Codon-optimized Oct4(aa1-145) was synthesized by Genscript and cloned into pET41(a+) vector between SacII and HindIII restriction sites. Codon optimized gene coding for human alpha-synuclein was synthesized by Genscript and cloned into pET22(a+) vector between NdeI and NotI restriction sites. The plasmid encoding the NatB acetyltransferase was obtained from Addgene. Codon-optimized gene coding for mouse Elk1(aa309-429) was synthesized by Genscript, Ala-mutated by Genscript on positions 325, 337, 418 and 423 and cloned into pET45(b+) vector between KpnI and PacI restriction sites. Codon-optimized gene coding for human BRCA2(aa48-218) Ala-mutated on positions Cys132, Cys138, Cys148 and Cys161 was synthesized by Genscript and cloned in pETM-13 between NcoI and BamHI restriction sites. Codon-optimized human p38 α (aa1-360, full-length) was synthesized by Genscript and cloned into pET41(a+) between NdeI and AvrII restriction sites. Codon-optimized human Erk2(aa8-360) was synthesized by Genscript and cloned into pET45(b+) vector between KpnI and HindIII restriction sites. The plasmid coding for constitutively active MKK6 (GST-MEK4V) was a generous gift from Isabelle Landrieu. It was used to activate both Erk2 and p38 α . All genes contained a coding sequence for the Tobacco Etch Virus Protease (Tev) cleavage site ENLYFQG on the N-terminal side of the peptide of interest. Oct4(aa1-145) was also followed on the C-terminal side by a Tev cleavage site and a GB1 tag to stabilize the construct during recombinant expression. The Tev construct contained a hexahistidine tag (His6), and was produced in-house recombinantly in *Escherichia coli*.

Recombinant protein production

All peptides were produced in BL21(DE3)Star *E. coli* transformed with the plasmids presented above. BRCA2(aa190-284) was produced as previously described [1]. Alpha-synuclein was produced in cells co-transformed with the plasmid encoding NatB following protocols published earlier. [2] Cells were grown in M9 medium containing ¹³C-glucose (2 g/L) and ¹⁵NH₄⁺ (0.5 g/L) as sole sources of carbon and nitrogen, or in LB for kinases. Media were supplemented with 100 μ g/mL ampicillin or 50 μ g/mL kanamycin depending on the plasmids, and in 30 μ g/mL ampicillin and 15 μ g/mL chloramphenicol for alpha-synuclein. Overexpression was induced at an optical density OD₆₀₀=0.8 by supplementing the medium with 1 mM IPTG at 37°C for all peptides except kinases, which were expressed at 30°C. Cells were harvested by centrifugation 4 hours later and cell pellets stored at -80°C. Cell lysis was performed using sonication in Tris 20 mM, NaCl 150 mM, pH 7.5 (TBS), in presence of benzonase (Sigma-Aldrich), lysozyme, protease inhibitors 1x (EDTA-free cOmplete, Roche) and 10 mM DTT. Soluble and insoluble fractions were separated by 15 min centrifugation at 15,000g. All peptides were purified from the soluble fraction except Elk1(aa309-429), which was resolubilized in TBS supplemented with 8 M urea. Alpha-synuclein was purified using protocols published earlier. [2] For the other peptides, the cell extracts were loaded on a His-Trap FF column (5 mL, GE Healthcare) and eluted using a gradient of imidazole. The eluted fractions were later concentrated, submitted to Tev treatment for 1 hour (after transfer in TBS for Elk1) in TBS supplemented with 10 mM DTT, and then re-loaded on His-Trap column. Fractions containing the peptide of interest were finally submitted to a final size-exclusion chromatography using a Superdex 16/60 75 pg (GE healthcare) previously equilibrated with Hepes 40 mM, NaCl 75 mM or 150 mM, pH 7.0 or 7.4 or 7.8.

Vanadium-NOTA production

VCl₃ was purchased from AlfaAesar–Fisher Scientific. NOTA was purchased from Chematech (Dijon, France). NOTA and VCl₃ were solubilized in water at 0.1 M and 1 M, respectively. They were mixed in a 1:1.1 ratio, and pH was progressively shifted from acidic values (about 2-3) to 7. When isolated, NOTA saturation concentration is lower than 0.1 M; it becomes soluble upon V³⁺ complexation, which requires to elevate pH and reach the anion form NOTA³⁻. V(OH)₃ precipitate was sedimented using 14,000 g centrifugation during 10 minutes. 2 mL of the supernatant was applied on a Source 15 RPC column (GE-Healthcare) previously equilibrated with Hepes 1 mM and NaCl 5 mM, pH 7. Salts are eluted first, before the purple-brownish V-NOTA fractions (about 5 mL). These were lyophilized over night before being re-solubilized in water and re-injected on the same Source 15 RPC column and re-lyophilized. The obtained powder was solubilized in ~100-200 μ L water. The most accurate method for weighting the final amount of V-NOTA is the following one: we weight the final microtube filled with the chosen volume of water before and after V-NOTA solubilization. Hepes and NaCl weights from the lyophilized 5 mL must not be forbidden. About 20-30 mg V-NOTA are typically obtained from a starting amount of 30 mg NOTA.

SUPPORTING INFORMATION

HeLa Nuclear Extract production

HeLa S3 cells were grown in DMEM (4.5 g/L glucose, Sigma) supplemented with 10 % FBS. 100 million cells were harvested by trypsinization and lysed using the Qproteome Mitochondria isolation kit (Qiagen). We kept the nuclear fraction and resuspended it in 500 μ L of Hepes 50 mM, NaCl 400 mM, glycerol 10%, protease inhibitors 1x (EDTA-free cOmplete, Roche), 2 mM DTT and phosphatase inhibitors 1x (PhoSTOP, Roche), pH7. We submitted it to three 5s pulses of sonication using a microtip and a 30% output power (VibraCell, Sonics & Material Inc. Danbury, Connecticut, USA). The extract was aliquoted and stored at -80°C. This protocol yields extracts at 5 to 10 mg/mL protein concentration. The final working concentration used for the presented figures is 0.5 mg/mL.

NMR spectroscopy

All NMR spectra were recorded on a 700 MHz Bruker Avance Neo spectrometer, equipped with a cryogenically cooled triple resonance $^1\text{H}[^{13}\text{C}/^{15}\text{N}]$ probe optimized for ^1H detection (TCI Bruker from 2006: ^{13}C ASTM S/N=850, ^1H 0.1% ethylbenzene S/N=7260 when delivered; actual ^{13}C -optimized probes ASTM S/N specifications are about 2500). All spectra were processed in Topspin 4.0.4. 3D spectra analysis was carried out using CccpNmr 2.4.2, and 2D spectra were analyzed using NMRFAM-SPARKY.^[3] DSS at 100 μ M and 3% D_2O were added in all samples.

NMR assignments of backbone amide resonances of uniformly-labeled peptides ($^{13}\text{C}/^{15}\text{N}$) was achieved via BEST-HNCO, -HN(CA)CO, -HNCACB,^[4] (H)N(CA)NH and HNCA 3D experiments, at pH 6.8 and 283K, and at peptide concentrations ranging from 200 to 500 μ M in 5 mm diameter Shigemi tubes. HNCO and HN(CA)CO were carried out with 1536 (^1H) x 92 (^{13}C) x 80 (^{15}N) complex points and sweep widths of 16.23 ppm (^1H), 10 ppm (^{13}C) and 30 ppm (^{15}N), HNCACB 1536 (^1H) x 92 (^{13}C) x 80 (^{15}N) complex points and sweep widths of 16.23 ppm (^1H), 70 ppm (^{13}C) and 30 ppm (^{15}N), (H)N(CA)NH with 1536 (^1H) x 64 (^{13}C) x 64 (^{15}N) complex points and sweep widths of 16.23 ppm (^1H), and 30 ppm (^{15}N), and HNCA 1536 (^1H) x 192 (^{13}C) x 80 (^{15}N) complex points and sweep widths of 16.23 ppm (^1H), 26 ppm (^{13}C) and 30 ppm (^{15}N). Non-uniform sampling was applied (35 to 50%) and processing was achieved using RMDD algorithm implemented in Topspin4.0.4.^{[5][6]} Spectra were processed with linear prediction of 16 complex points in both ^{13}C , and ^{15}N dimensions, cosine apodization in every dimensions, and zero filling to 2048, 512 and 256 complex points in ^1H , ^{13}C , and ^{15}N dimensions, respectively. Assignment 2D ^1H - ^{15}N HSQC spectra were recorded using 1536 (^1H) x 256 (^{15}N) complex points and sweep widths of 16.23 ppm (^1H) and 30 ppm (^{15}N), and processed with zero filling to 4K and 1K in the proton and nitrogen dimensions, respectively.

We used this assignment strategy for backbone amide resonances (BEST-HNCO, -HN(CA)CO, -HNCACB, (H)N(CA)NH and HNCA 3D experiments, at 283K) both for non-modified and phosphorylated species. The assignments at 303K in 2D spectra were transferred from those at 283K by recording spectra at 283K, 293K and 303K: this is sufficient to characterize peak-specific temperature shifts. The spectra and the assignment of "DNA-PK intermediate" phosphorylated Mdm2(aa284-434) were obtained using samples whose phosphorylation was stopped by heating at 323K for 10 minutes (provoking DNA-PK inactivation).

Assignments of unmodified and phosphorylated human Mdm2(aa284-434, C362A-C374A), as well as details of NMR experiments used to derive them have been deposited in the Biological Magnetic Resonance Data Bank (BMRB, accession numbers 28011, 28019, respectively). As reported in the literature by Bycroft et al.^[7], we observed two stable conformations of the Zn-finger that correspond to trans- and cis-prolines (PDB: 2C6A and 2C6B). The relative NMR peak intensities of the two species were the same in the isolated Zn-finger and in Mdm2(aa284-434) (trans:cis~2:1). Secondary structure propensities of unmodified and phosphorylated Mdm2(aa284-434, C362A-C374A) were obtained with the neighbor-corrected structural propensity calculator ncSCP^[8,9] (<http://www.protein-nmr.org/>, <https://st-protein02.chem.au.dk/ncSCP/>) using experimentally determined, DSS referenced $\text{C}\alpha$ and $\text{C}\beta$ chemical shifts as input.

We set up 2D spectra during phosphorylation kinetics as follows: 2D ^1H - ^{15}N SOFAST-HMQC experiments were recorded using 1536 (^1H) x 92 (^{15}N) complex points and sweep widths of 16.23 ppm (^1H) and 30 ppm (^{15}N), 16 scans (128 dummy scans) and interscan delays of 0.12 s, resulting in 7 minutes long spectra; 2D (^1H -flip*) $^{13}\text{C}\alpha$ ^{13}CO -LB experiments were recorded using 1024 (^{13}CO) x 128 ($^{13}\text{C}\alpha$) complex points and sweep widths of 20.28 ppm (^{13}CO) and 14 ppm ($^{13}\text{C}\alpha$), 80 scans (96 dummy scans) and interscan delays of 0.15 s, and 50% non-uniform sampling optimized for a 35 Hz J-coupling (i.e. low sampling around 14 ms $\text{C}\alpha$ evolution time) and 60 ms relaxation, resulting in 31 minutes long spectra. All spectra were processed zero filling to 4K and 1K in the direct and indirect dimensions, respectively. Cosine apodization was applied in ^{13}CO dimension for (^1H -flip*) $^{13}\text{C}\alpha$ ^{13}CO -LB spectra, no apodization was applied for ^1H - ^{15}N SOFAST-HMQC spectra. 2D (^1H -flip*) $^{13}\text{C}\alpha$ ^{13}CO -LB experiments processing was achieved using the CS algorithm implemented in Topspin4.0.4^[10], parameters were set as follows: Mdd_mode=cs, MddCEXP=false, MddCT_SP=true, Mdd_CsALG=IST, Mdd_CsVE=false, Mdd_CsNITER=0. Two 2D ^1H - ^{15}N SOFAST-HMQC spectra were initially acquired, before recording alternately 2D (^1H -flip*) $^{13}\text{C}\alpha$ ^{13}CO -LB and 2D ^1H - ^{15}N SOFAST-HMQC spectra. We used 5 mm diameter Shigemi advanced tubes for phosphorylation kinetics, which increases NMR active volume to 330 μ L, and yields ~13 % higher ^{13}C -direct detection sensitivity, and no ^1H -detection gains or losses.

Phosphorylation reactions

Phosphorylation reactions were carried out using ^{15}N -labeled target peptides concentrations between 12.5 and 100 μ M, in Hepes 40 mM, NaCl 75 mM, DTT 2 mM, ATP 5 mM, MgCl_2 20 mM, protease inhibitors (Roche), 3% D_2O , pH 7.2 to pH 7.8 at 25°C or 30°C in 330 μ L. The spectra and kinetics shown in all figures are from kinetics run with 100 μ M Mdm2, Oct4, Elk1 or BRCA2 fragments. No changes in phosphorylation preferences were observed with concentration changes. Mdm2 phosphorylation by purified DNA-PK was achieved using commercial DNA-PK (ThermoFisher Scientific / Invitrogen): 2.5 μ g of DNA-PK and 35 μ g of DNA-PK activator (ThermoFisher Scientific / Invitrogen), i.e. calf thymus DNA, were spiked in the sample immediately before inserting it in the NMR

SUPPORTING INFORMATION

spectrometer. Regular calf thymus DNA concentrations of 2.5 $\mu\text{g/mL}$ were not reliable enough: initial phosphorylation rates were decreasing with Mdm2 concentration increasing, which goes against kinetics theory and probably reveals an interaction between DNA and Mdm2. We saturated the system with 100 $\mu\text{g/mL}$ of Calf thymus DNA to have constant DNA-PK activation. Moreover, we observed that satisfying reproducibility of DNA-PK phosphokinetics is achievable at 298K, but that this kinase complex appears less stable at 303K, resulting in variable phosphorylation results. BRCA2 kinetics were run at 50 and 100 μM , in hepes 50 mM, NaCl 50mM, pH 7.8 in presence of 250 nM of recombinant Plk1, 2 mM ATP, 1 mM EDTA, 20 mM MgCl_2 , 2 mM DTT, 1x protease inhibitors cocktail cOComplete (Roche), and 3 mM V-NOTA (Plk1 aliquots gently provided by the protein production platform of the Institut Curie, Paris, France). Oct4 kinetics were run at 50 and 100 μM , in hepes 20 mM, NaCl 50mM, pH 7.4 in presence of 500 nM of recombinant p38 α , 2 mM ATP, 5 mM MgCl_2 , 2 mM DTT 1x protease inhibitors cocktail cOComplete (Roche) using recombinant p38 α produced and activated in-house (see the paragraph "Peptide constructs"). Elk1 phosphorylation was performed using recombinant human Erk2 produced and activated in-house (see the paragraph "Peptide constructs").

Phosphorylation kinetics analysis

After processing spectra as detailed in the paragraph "NMR spectroscopy", we measured peak intensities in NMRFAM-SPARKY.^[3] Peaks were centered in every spectra to follow peak shifting because of pH drifts. Progress curves were plotted and fitted in Kaleidagraph 4.5. We used only decay curves to normalize phosphorylation build-up curves. We describe the set of disappearing peaks that we used in the following paragraph.

About Mdm2(aa284-434), we could determine pT351, pS395 and pS429 phosphorylation rates using peaks from 2D ^1H - ^{15}N SOFAST-HMQC NMR spectra. Indeed, we monitored peak intensities of neighboring residues A345+L347 for pT351, Y394+S395 for pS395, L430 for pS429, which all disappear proportionally to the phosphorylation advancement of their closest phosphosite. The other phosphosites (S386, S388, S402, S407, T419) were monitored using 2D (^1H -flip*) $^{13}\text{C}\alpha$ - ^{13}CO -LB spectra as follows. D380, K381, I382 and T383 peaks are good reporters of the concomitant disappearance of non-modified S386 and S388. Even more valuable, a second set of intermediate I382 and T383 peaks appear corresponding to S386/pS388, while a third one report the progressive buildup of pS386/S388+pS386/pS388. In the case of I382 and T383, pS388 does not provoke any further peaks shifting after S386 phosphorylation. At the opposite, (^1H -flip*) $^{13}\text{C}\alpha$ - ^{13}CO -LB peaks of Q384, Q387 and Q387 split in 4 different forms corresponding to the 4 combinations of S386-pS386-S388-pS388, but their interpretation is more tedious because of peak overlaps (Figure 3). Peaks of S402, I403, I404, Y405, S406 and Q408 are good reporters of S407 disappearance, i.e. pS407 appearance, and S398, T399, S402 and I404 of the later appearance of pS402. Finally, E415, R416 and T419 are good reporters of the pT419 reaction advancement. Intensities of peaks that are reporter of a phosphorylation reaction were added to increase the experimental S/N. Decay curves were fitted according to the following equations: $y(t)=I_0\cdot\exp(-k\cdot t)+I_{\text{final}}$ with I_0 and k the fitted values. Normalization was performed using (I_0+I_{final}) , and phosphorylation build-up curves are thus $\% \text{phospho}(t)=1-y(t)/(I_0+I_{\text{final}})$. We also used phosphopeaks of pS386, pS388, pS402, pS407 and pT419 observed in 2D ^1H - ^{15}N SOFAST-HMQC NMR spectra, which are well-separated and identifiable in 2D ^1H - ^{15}N spectra. We normalized them according to the final levels reached at the end of the kinetics, as determined from (^1H -flip*) $^{13}\text{C}\alpha$ - ^{13}CO -LB decay curves. Proton-detected SOFAST-HMQC experiments still provide higher S/N and permit to generate higher quality build-up curves.

BRCA2(aa190-284) phosphokinetics were derived from (^1H -flip*) $^{13}\text{C}\alpha$ - ^{13}CO -LB peak intensities of M192, M192(pS193), S193, W194 and S196 for pS193, T207, pT207, V208, V208(pT207), I210, I210(pT207) and V211 for pT207, A216, T219, pT219 and V220 for pT219, and from H223, A226 and V229 for pT226. Oct4(aa1-145) phosphokinetics were derived from (^1H -flip*) $^{13}\text{C}\alpha$ - ^{13}CO -LB peak intensities of D8, D8(pS12), F9, F9(pS12), A10, A10(pS12), and S12 for pS12, L90, T92 and S93 for pS93, D108, A110, S111 and E113 for pS111, T116, T116(pT118), V117, T118, A121 and V122 for pT118.

Pulse program

We provide two versions of the (^1H -flip*) $^{13}\text{C}\alpha$ - ^{13}CO -LB Bruker pulse program: one for Neo consoles and Topspin4 (c_hcaco_ctre.lowbash.top4), one for earlier systems and Topspin 3 (c_hcaco_ctre.lowbash.top3). They are straightforward to parameterized: only the proton pulse length (p3) has to be determined for each sample, while carbon pulse lengths can be set up only once. The carbon homo-decoupling LOW-BASH pulse is the only pulse that is delicate to parameterize: one should follow carefully the indications provided by Bax and coworkers^[11]. The Shapetool in Topspin4 permits to generate the necessary shape pulse: a center lobe of a sinc function of duration $22,600/\nu_c$ in μs (ν_c is the ^{13}C frequency in MHz) should be amplitude modulated by a cosine function at a frequency of $118 \times \nu_c$. Hence, it applies pulses of equivalent power on both sides of the ^{13}CO carrier frequency, centered at 55 and 191 ppm, which efficiently vanishes Bloch-Siegert shift effects^[11]. This decoupling pulse is automatically applied every 5 ms by the pulse program, as well as the MLEV16 RF phases. We provide the shape pulse Bruker file for a 700 MHz spectrometer as an example in Supplementary data.

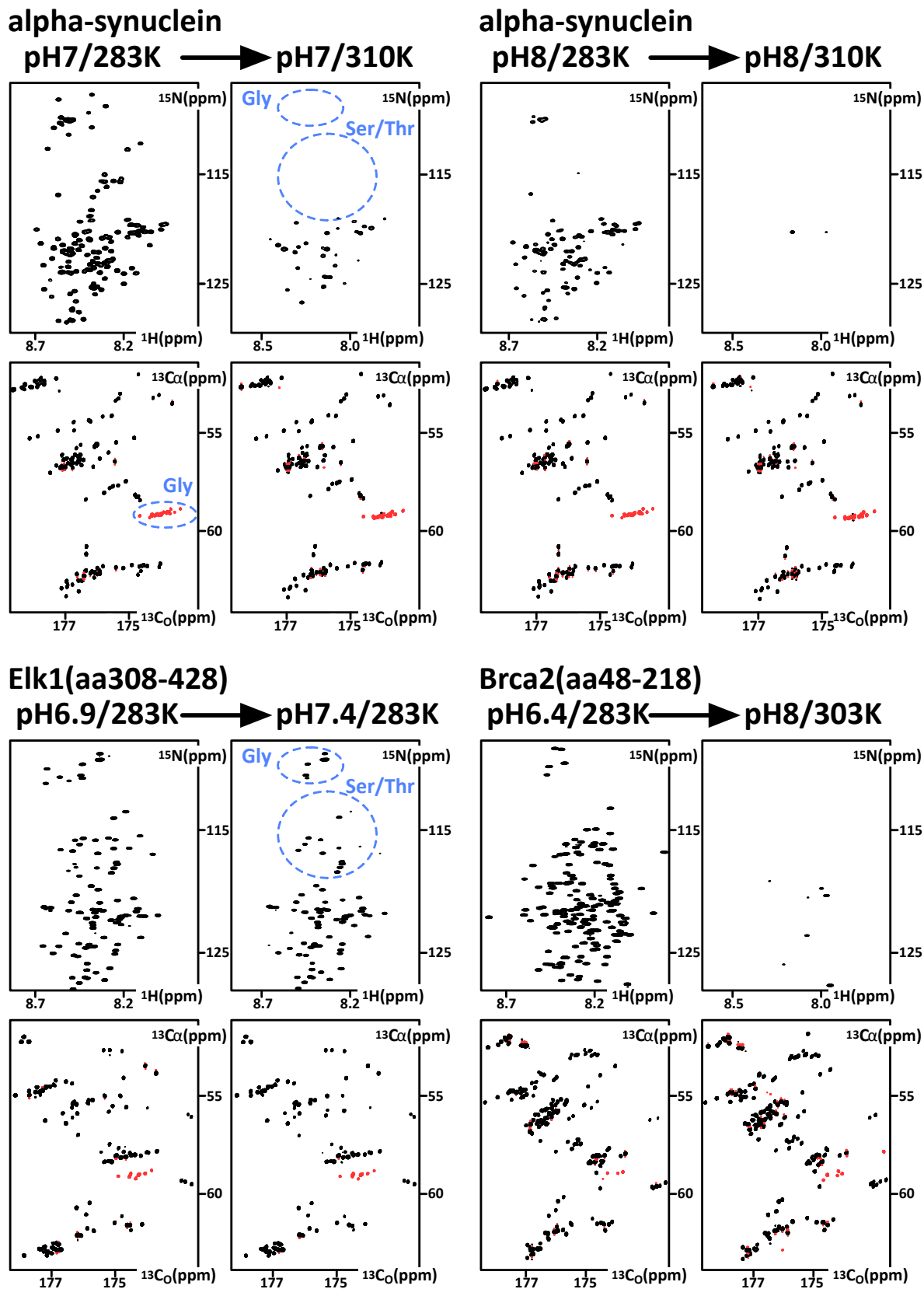
Phosphorylated residues generally provide lower peak intensities than their non-phospho counterparts, due to the difficulties to excite and decouple selectively $\text{C}\alpha$ and $\text{C}\beta$ of pSer and pThr.

It is important to use a low D_2O concentration to avoid high amounts of deuterated amides, which generate significant changes in chemical environment for the neighboring $\text{C}\alpha$ and CO, hence provoking peak splitting or measurable exchange relaxation. We use 3% D_2O .

SUPPORTING INFORMATION

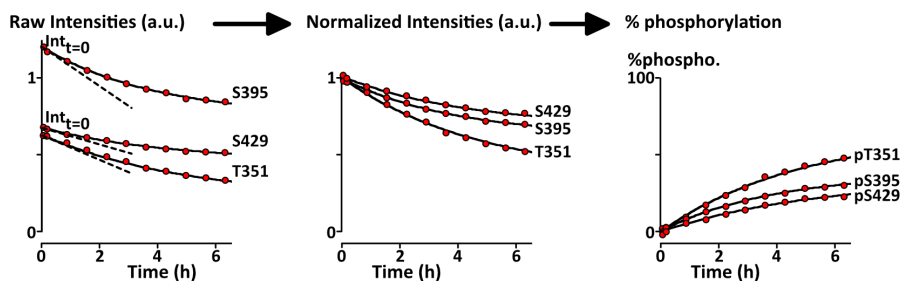
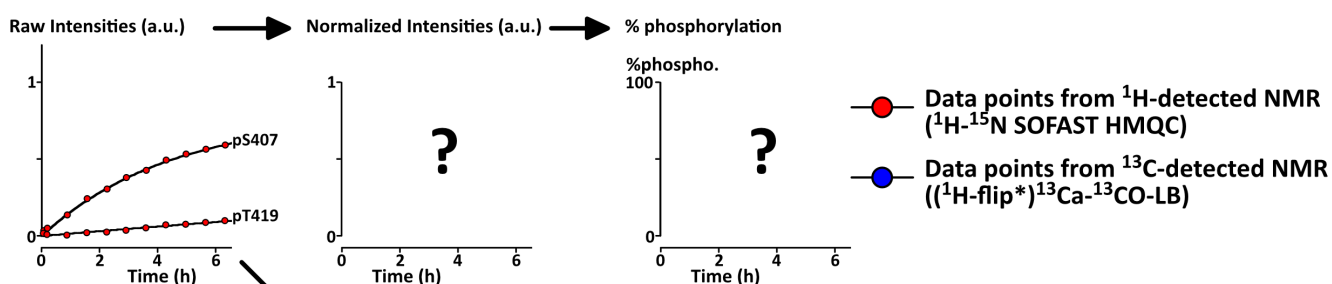
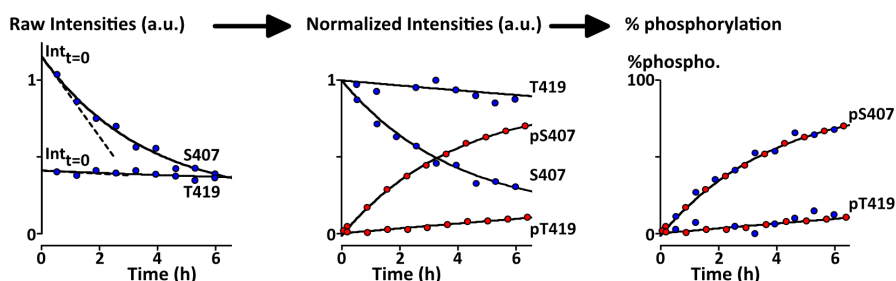
Results and Discussion

Figure S1. ^1H - ^{15}N 2D HSQC and $^{13}\text{C}\alpha$ - ^{13}CO 2D (^1H -flip*) $^{13}\text{C}\alpha$ - ^{13}CO -LB spectra of alpha-synuclein, Elk1(aa308-428) and Brca2(aa48-218) in low pH and low temperature or high pH and high temperature conditions. The same acquisition parameters and contour levels were applied in both conditions. Positive and negative crosspeaks are in black and red, respectively. Negative peaks in red correspond to Gly residues.



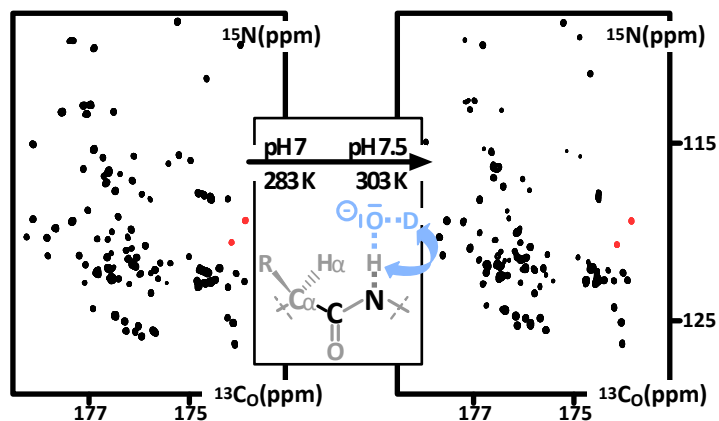
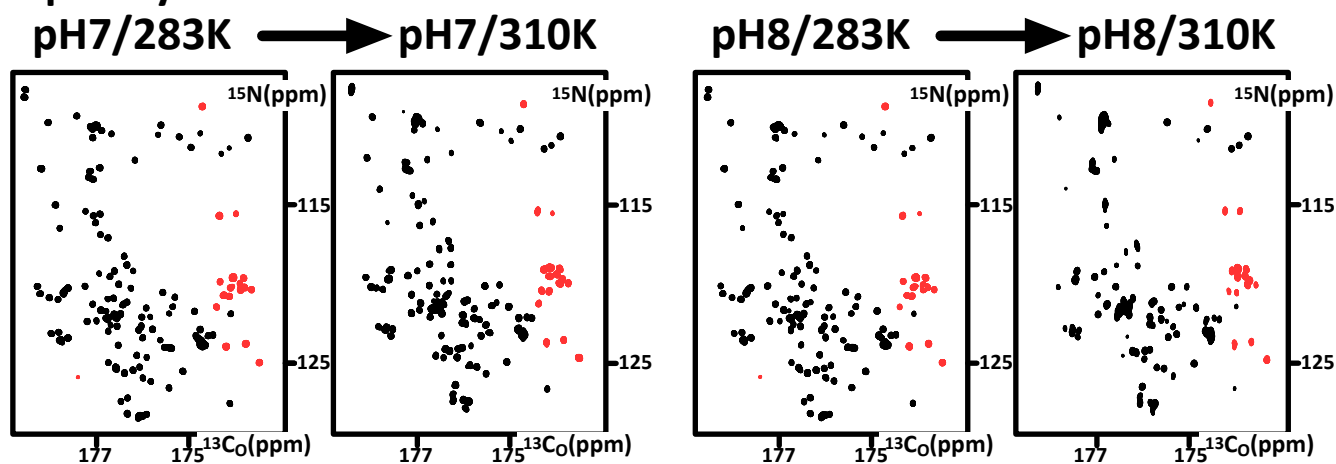
SUPPORTING INFORMATION

Figure S2. Analysis pipeline for data fitting using non-phosphopeaks or phosphopeaks from NMR spectra of Mdm2(aa284-434). **a.** In the case where non-phosphopeaks (from a phosphosite or its neighboring residues) are well-resolved and provide sufficient S/N, intensities measured in every spectrum of the time series can be plotted. They are then fitted using an exponential function $I(t)=I(t=0)*\exp(-t/k)+I(t_{\text{final}})$, the fitted parameters being $I(t=0)$, k and $I(t_{\text{final}})$. Curves are then normalized by $I(t=0)+I(t_{\text{final}})$ and $\% \text{phosphorylation}(t)=1-\text{Normalized}(t)$. **b.** In the case where only phosphopeaks are well-resolved and provide sufficient S/N, intensities from phosphopeaks can be plotted, but not normalized, unless 100% phosphorylation is reached. **c.** Intensities from non-phosphopeaks can be measured in ($^1\text{H-flip}^*$) ^{13}Ca - ^{13}CO -LB spectra and the resulting curves can be fitted and used for normalization of both phosphopeaks and non-phosphopeaks build-up curves.

a Non-phosphopeaks available in 2D ^1H - ^{15}N spectra**b Only phosphopeaks available in 2D ^1H - ^{15}N spectra****c Unphosphopeaks available in 2D ^{13}Ca - ^{13}CO spectra**

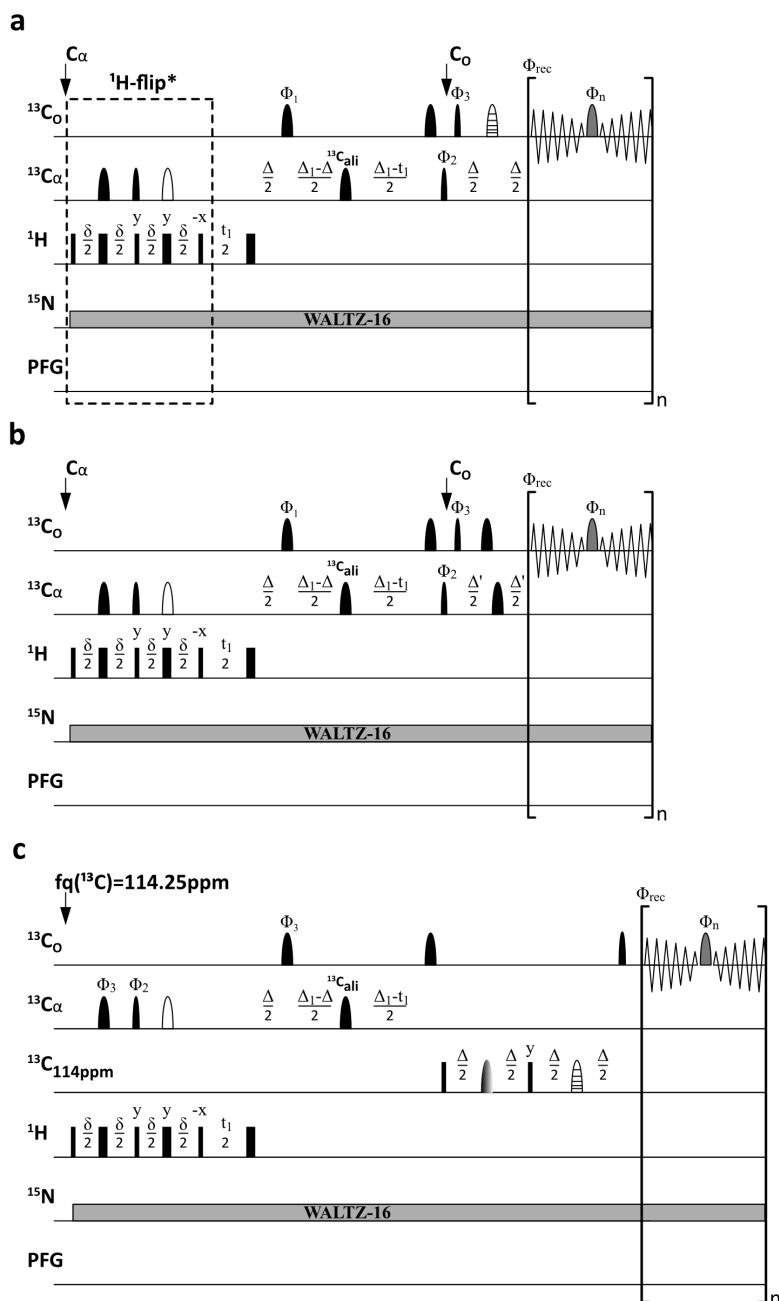
SUPPORTING INFORMATION

Figure S3. ^{15}N - ^{13}CO 2D (^1H -flip*)CON-IPAP $^{12}\text{F}_2$ spectra of Mdm2(aa284-434) and alpha-synuclein at low pH and low temperature or high pH and high temperature conditions. The same acquisition parameters and contour levels were applied in both conditions. Negative peaks in red correspond to Gly residues.

Mdm2(aa284-434)**alpha-synuclein**

SUPPORTING INFORMATION

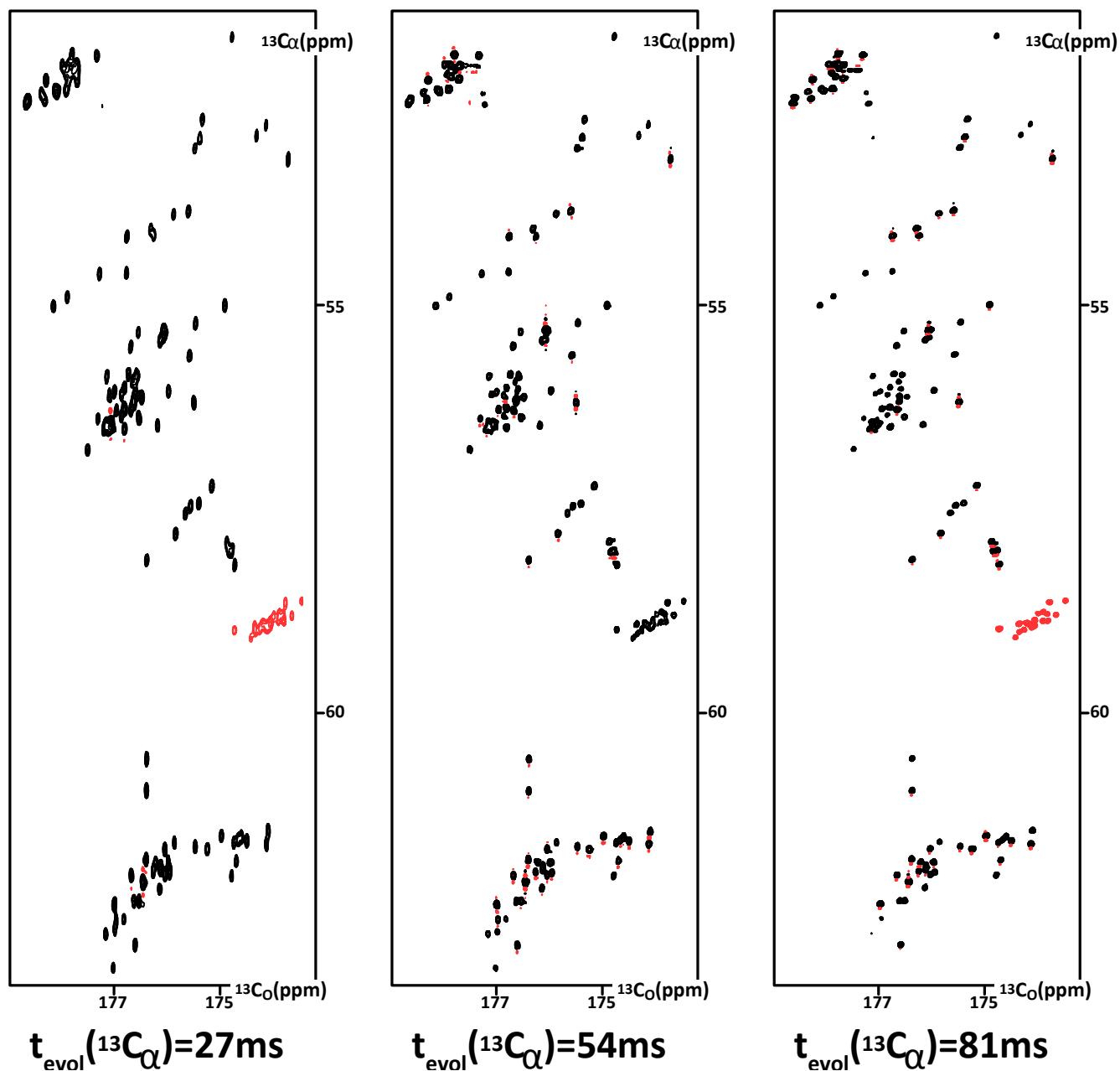
Figure S4. Schemes of the (a) (^1H -flip*) $^{13}\text{C}\alpha^{13}\text{CO}$ -LB_1, (b) (^1H -flip*) $^{13}\text{C}\alpha^{13}\text{CO}$ -LB_2 and (c) (^1H -flip*) $^{13}\text{C}\alpha^{13}\text{CO}$ -LB_3 pulse sequences. Pulse lengths are adapted to a spectrometer field of 700 MHz. Delays are: $\delta=2.9$ ms, $\Delta=9$ ms, $\Delta'=8.4$ ms, $\Delta_1=27^*n$ ms with $n=1, 2$ or 3 . Phase cycle: $\phi_1=x,x,x,x,x,-x,-x,-x,-x$; $\phi_2=x, -x$; $\phi_3=x, x, -x, -x$; $\phi_{\text{rec}}=x,-x,-x,-x,x$; $\phi_n=x,x,-x,-x,x,x,-x,-x,x,x,-x,-x,x$. Filled and open rectangles represent hard 90° and 180° pulses, respectively. Narrow and wide black semi-ellipses are Q5-sebop/Q5tr-sebop 90° (231 μs) and Q3-surbop 180° (300 μs) pulses, respectively. ^{13}CO and $^{13}\text{C}\alpha/\beta$ and $^{13}\text{C}_{\text{ali}}$ carrier frequencies are 173, 55.5 and 41 ppm, respectively. White semi-ellipses are $^{13}\text{C}\alpha$ centered Q3-surbop 180° (634 μs) pulses applied at 41 ppm. The striped semi-ellipse is a 120 μs triply compensated pulse G5^[13,14] applied at 114.25 ppm. The shaded semi-ellipse is a Q3-surbop 180° (900 μs) pulse applied at 114.25 ppm, amplitude modulated by a cosine function at a frequency of 58.75^*v_c (v_c is the ^{13}C frequency in MHz), which inverts selectively both ^{13}CO and $^{13}\text{C}\alpha/\beta$ at the same time. The grey semi-ellipse is a center lobe of a sinc function of duration $22,600/v_c$ in μs (v_c is the ^{13}C frequency in MHz), amplitude modulated by a cosine function at a frequency of 118^*v_c applied n times every 5 ms, with $n=t_{\text{acq}}/5\text{ms}$. Quadrature detection is obtained by incrementing phase ϕ_2 in a States-TPPI manner. The original (^1H -flip*) $^{13}\text{C}\alpha^{13}\text{CO}$ -IPAP sequence uses a pulse field gradient just before the carrier frequency change to ^{13}CO before the final INEPT transfer. We chose not to apply any pulsed field gradients (G_z), because we did not observe any improvement related to it.



SUPPORTING INFORMATION

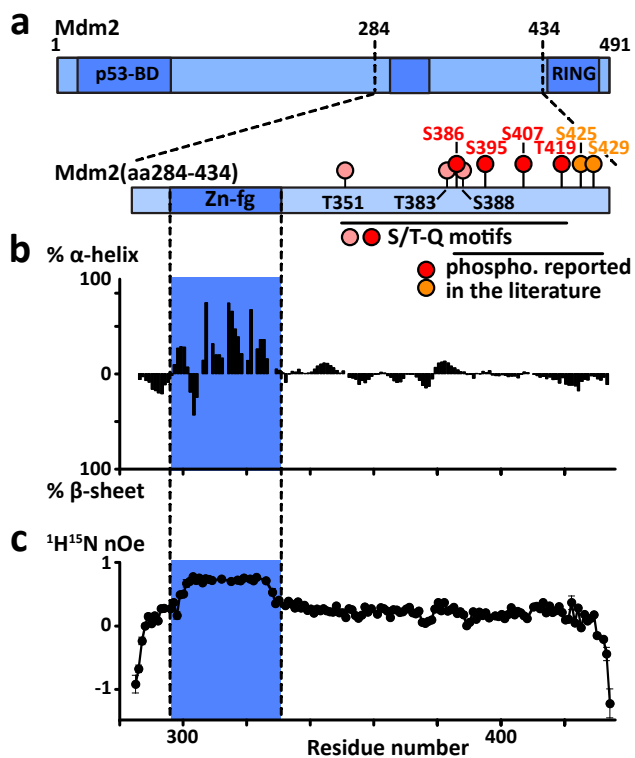
Figure S5. (^1H -flip*) $^{13}\text{C}\alpha$ - $^{13}\text{C}\text{O}$ -LB spectra of alpha-synuclein using growing constant-time (CT) evolution periods of 27, 54 or 81 ms. These correspond to $n/1J(\text{C}\alpha\text{C}\beta)$ with $n=1, 2$ or 3 . This allows the removal of $^1J(\text{C}\alpha\text{C}\beta) \approx 35$ Hz coupling effects during $\text{C}\alpha$ chemical shift evolution. Increasing the constant time by 27 ms provokes on average a 30% loss in S/N for IDPs. It generates at the same time an improved resolution: we measured an average 12 Hz linewidth in $\text{C}\alpha$ -dimension at 54 ms and 8 Hz at 81 ms. In these spectra, the signs of NMR signals oscillate according to J-coupling evolution: they are negative for $\cos(\pi J^* \text{CT}) = -1$, i.e. CT=27 or 81 ms, and positive for $\cos(\pi J^* \text{CT}) = 1$, i.e. CT=54 ms. Gly residues are an exception, because they do not contain any $\text{C}\alpha$ and their signal is always positive. We have changed the phase by 180° so that most of the peaks appear to be positive (black), and those of Gly residues appear negative at CT=27 or 81 ms.

alpha-synuclein pH7/283K



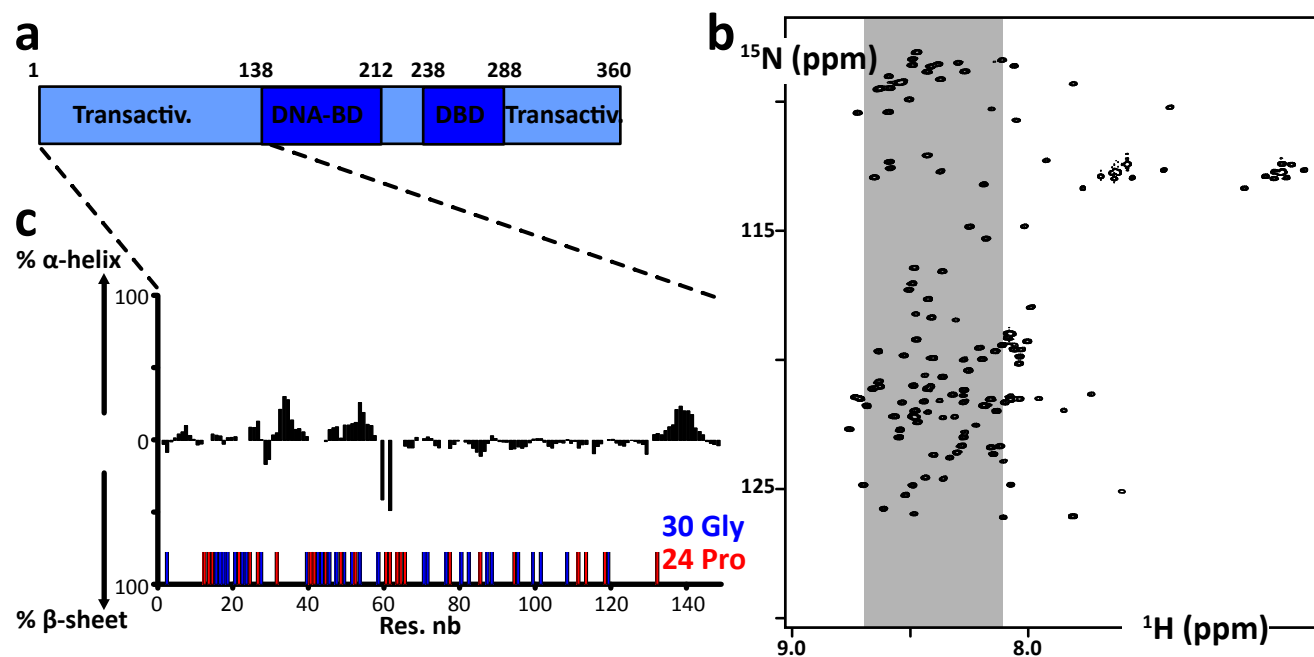
SUPPORTING INFORMATION

Figure S6. (a) Primary structure of human Mdm2 and Mdm2(aa284-434). Folded domains (p53-BindingDomain: p53-BD; Zinc-finger: Zn-fg; RING-ubiquitin ligase domain: RING) are in deep blue and domains predicted to be disordered are in light-blue. DNA-PK/ATM/ATR (DDR kinases) were reported to phosphorylate sites depicted in solid red or orange circles, representing consensus S/T-Q motifs or non-S/T-Q motifs, respectively. S/T-Q motifs not yet detected to be DDR kinases targets are in light red circles.^[15] (b) Secondary structure propensity as calculated from $^{13}\text{C}\alpha/^{13}\text{C}\beta$ chemical shifts using ncSCP.^[8,9] (c) Low ^1H - ^{15}N heteronuclear nOes (700 MHz) reveal ps-ns timescale motion typical of unfolded peptides outside of the Zn-fg domain.



SUPPORTING INFORMATION

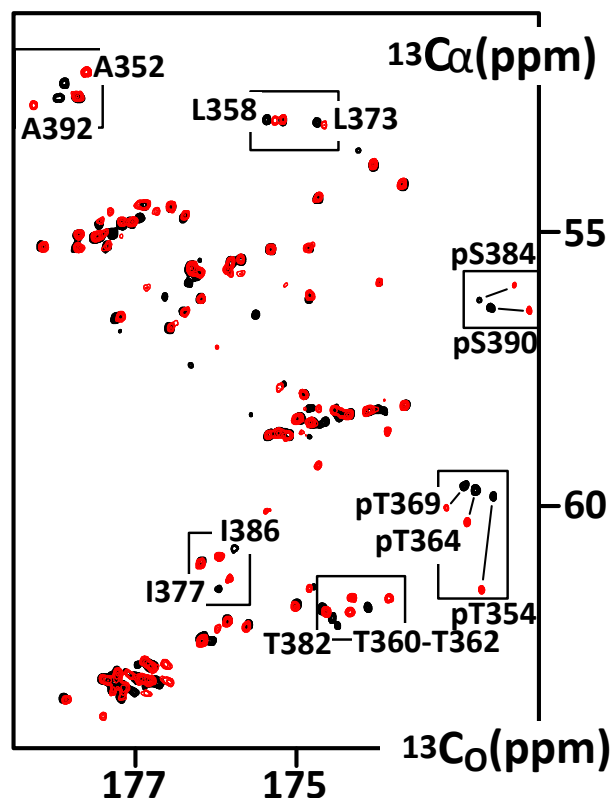
Figure S7. (a) Primary structure of human Oct4 and Oct4(aa1-145). Folded domains (DNA-BindingDomain: DNA-BD or DBD) are in deep blue and domains predicted to be disordered are in light-blue. (b) 2D ^1H - ^{15}N HSQC spectrum of Oct4(aa1-145) showing that most crosspeaks are in the region (in grey) where resonances of unfolded amino acids are found. (c) Secondary structure propensity as calculated from $^{13}\text{C}\alpha/^{13}\text{C}\beta$ chemical shifts using ncSCP.^[8,9] Gly and Pro positions along the primary sequence are indicated by red and blue sticks, respectively.



SUPPORTING INFORMATION

Figure S8. Overlay of (^1H -flip*) $^{13}\text{C}\alpha$ - ^{13}CO -LB spectra of Elk1(aa308-428) before (black) and after (red) phosphorylation by the MAPKinase Erk2.

Elk1(aa308-428) +Erk2



References

- [1] M. Julien, S. Miron, A. Carreira, F.-X. Theillet, S. Zinn-Justin, *Biomolecular NMR Assignments* **2020**, *22*, 295–7.
- [2] F.-X. Theillet, A. Binolfi, B. Bekei, A. Martorana, H. M. Rose, M. Stuiver, S. Verzini, D. Lorenz, M. van Rossum, D. Goldfarb, et al., *Nature* **2016**, *530*, 45–50.
- [3] W. Lee, M. Tonelli, J. L. Markley, *Bioinformatics* **2015**, *31*, 1325–1327.
- [4] E. Lescop, P. Schanda, B. Brutscher, *Journal of Magnetic Resonance* **2007**, *187*, 163–169.
- [5] V. Jaravine, I. Ibraghimov, V. Y. Orekhov, *Nat. Meth.* **2006**, *3*, 605–607.
- [6] V. Y. Orekhov, V. A. Jaravine, *Prog. Nucl. Magn. Reson. Spectrosc.* **2011**, *59*, 271–292.
- [7] G. W. Yu, *Protein Science* **2006**, *15*, 384–389.
- [8] K. Tamiola, F. A. A. Mulder, *Biochem. Soc. Trans.* **2012**, *40*, 1014–1020.
- [9] J. T. Nielsen, F. A. A. Mulder, *J. Biomol. NMR* **2018**, *70*, 141–165.
- [10] K. Kazimierczuk, V. Y. Orekhov, *Angew. Chem. Int. Ed.* **2011**, *50*, 5556–5559.
- [11] J. Ying, F. Li, J. H. Lee, A. Bax, *J. Biomol. NMR* **2014**, *60*, 15–21.
- [12] W. Bermel, I. Bertini, I. C. Felli, R. Pierattelli, *J. Am. Chem. Soc.* **2009**, *131*, 15339–15345.
- [13] V. S. Manu, G. Veglia, *J. Magn. Reson.* **2015**, *260*, 136–143.
- [14] Y. Xia, P. Rossi, M. V. Subrahmanian, C. Huang, T. Saleh, C. Olivieri, C. G. Kalodimos, G. Veglia, *J. Biomol. NMR* **2017**, *69*, 237–243.
- [15] Q. Cheng, B. Cross, B. Li, L. Chen, Z. Li, J. Chen, *Mol. Cell. Biol.* **2011**, *31*, 4951–4963.

Author Contributions

AA, CB, MJ contributed equally. AA, CB, MJ and FXT conducted the research, i.e. sample preparation, data acquisition and analysis. SZJ helped with NMR measurements. FXT achieved resonance assignment, kinetics analysis. WB and FXT optimized the pulse sequences. SZJ and FXT obtained fundings. FXT designed the research and wrote the manuscript. Correspondence and requests for materials should be addressed to FXT.

3. Can we obtain complementary data from ^{31}P 1D NMR?

I also had the opportunity to record some 1D ^{31}P NMR spectra thanks to a collaboration with François Giraud (ICSN, Gif-sur-Yvette). We used an indirect broadband probe detecting ^{31}P on a 600 MHz spectrometer (probe: TBI 600SB ^1H - ^{13}C -BB-D 5mm gradients xyz). This probe offers a moderate sensitivity for ^{31}P acquisition. Recent quadruple cryoprobes optimized for ^{31}P -NMR (QCI probes, Bruker) may provide about 4-5-fold better signal-to-noise performances.

In **Figure 40**, we can observe the ^{31}P spectrum of the phosphorylated BRCA2₁₆₇₋₂₆₀, a new BRCA2 fragment that we will describe later in the Chapter. The sample was phosphorylated at 80-100%, giving rise to the appearance of pS193, pT207, pT219 and pT226, as shown earlier using ^1H - ^{15}N NMR. We observe at least 5 peaks instead of the expected 4. The non-stoichiometric phosphorylation of the neighboring T219 and T226 may generate 4 peaks (T219-T226, pT219-T226, T219-pT226, pT219-pT226). We did not assign ^{31}P resonances.

These experiments required about 10 hours to reach a sufficient S/N ratio from a 300 μM -500 μL sample. A rough calculation indicates that using a ^{31}P -dedicated cryoprobe would probably permit to record similar spectra in 2-4 hours at 25-30°C with a 100 μM -100 μL sample. ^{31}P has unfavorable NMR properties, notably a large CSA of about 80 to 120 ppm for phosphoresidues (Potrzebowski et al. JACS 2003). This provokes fast signal relaxation, hence low signal. We measured peak linewidths of about 20 Hz in our spectra, but, unfortunately, this also corresponds to the used FID resolution (FID res= 18.8 Hz, acquisition time of 53.3 ms). Thus, we estimate a maximal transversal relaxation $R_2 \sim 65$ Hz (minimal $T_2 \sim 15$ ms).

Phosphorylation kinetics should not be performed at too high concentrations: favored phosphosites may have K_m values in the 1 to 100 μM range and may be confounded with poorer, insignificant phosphosites, which can have K_m above 500 μM . Hence, ^{31}P NMR continuous readout is probably not a first-choice method for monitoring protein phosphorylation. To finish our evaluation, we must add that ^{31}P peaks may be delicate to use in the course of phosphorylation reactions that release protons and commonly provoke 0.1-0.2 pH shifts, hence changes in pSer or pThr protonation states (pK_a between 6 and 6.5, respectively) and thus site-specific ^{31}P chemical shift changes in the range of 0.2-0.4 ppm (Bienkiewicz et al. 1999). Supplementary peak overlaps may appear upon pH changes, and assignment would probably require alanine-screening mutations. Altogether, in the case of BRCA2₁₆₇₋₂₆₀, using ^{31}P 1D-NMR has several drawbacks for monitoring protein phosphorylation.

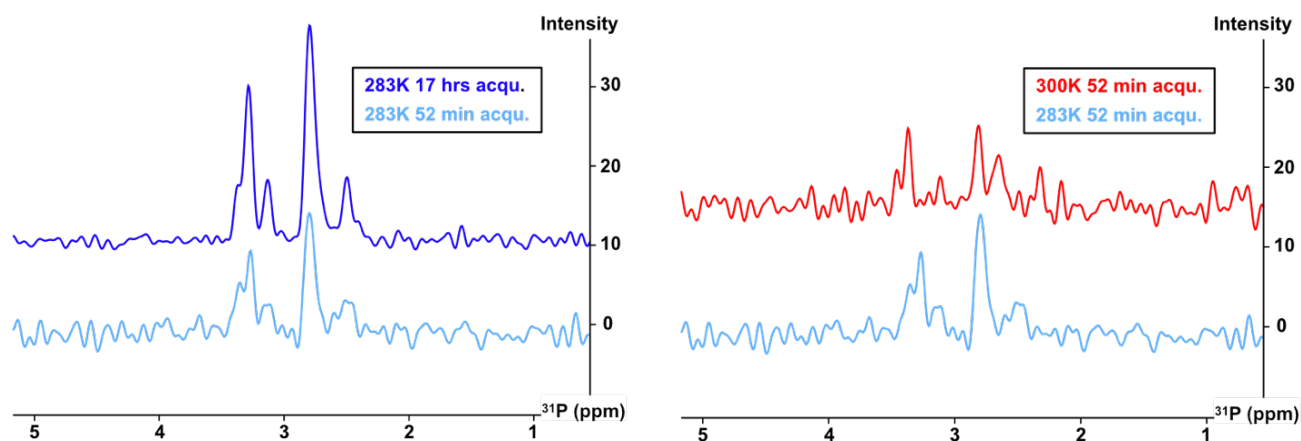


Figure 40. 1D NMR ^{31}P spectra of BRCA2₁₆₇₋₂₆₀ phosphorylated by Plk1 at 283 K (left, 1024 or 20480 scans) and comparison with the same spectrum acquired at 300 K (right, 1024 scans). All these spectra were measured at 300 μM in 50 mM HEPES, 75 mM NaCl 1mM EDTA 5% D₂O pH 7.0 using a 5mm tube and a 600 MHz spectrometer (ICSN, Gif-sur-Yvette). Four residues are phosphorylated by Plk1 in this peptide: S193, T207, T219 and T226.

4. Finding the optimal pH for Plk1 phosphorylation

We were now able to obtain a continuous readout of BRCA2 phosphorylation by Plk1 at any pH. Therefore, I monitored the phosphorylation reaction on BRCA2₄₈₋₂₁₈ at pH 7.0, 7.5 and 8.0 in order to define optimal pH conditions. Here, I used a large new batch of Plk1 from the Institut Curie facility that was more active than previously and sufficient for the rest of my thesis. I first performed an SDS-PAGE analysis, which revealed that Plk1 was active on a broader range of pH than previously found (**Figure 41.A**).

To precisely compare the phosphokinetics at different pHs, I monitored them on BRCA2₄₈₋₂₁₈ between pH 7.0 and 8.0 using the ^{13}C - ^{13}C O method (**Figure 41.B**). The phosphorylation of BRCA2 by Plk1 progressed with the same kinetics at pH 7.0 and pH 8.0.

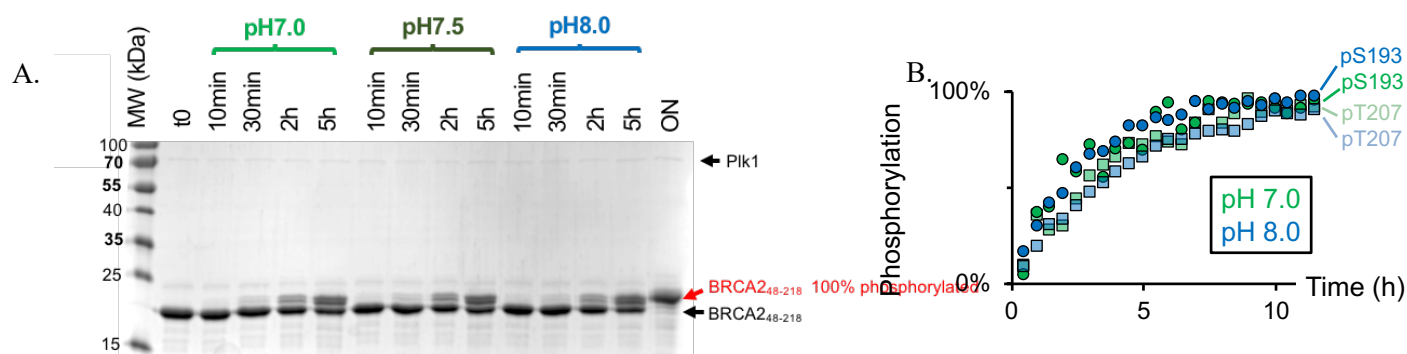


Figure 41. Plk1 presents the same activity profile from pH 7.0 to pH 8.0.

(A) BRCA2 phosphorylation monitored by Coomassie-stained 15% SDS-PAGE gel. Conditions: BRCA2 at 100 μ M in 50 mM HEPES, 75 mM NaCl, 10 mM $MgCl_2$, 2 mM DTT, 2mM ATP, 1.5X PI, pH 7.0 (green), 7.5 (dark green) or 8.0 (blue), incubated at 30°C. **(B)** BRCA2 phospho-kinetics of S193 and T207 monitored by ^{13}C -NMR in the same conditions than in (A).

Thus, during my PhD, I initially monitored BRCA2 phosphorylation by Plk1 using the quenched reaction at pH 7.8 and 30°C, then I used the ^{13}Ca -CO approach at pH 7.8 and 30°C and finally I adopted a more practical approach by using a continuous 1H - ^{15}N SOFAST-HMQC readout at pH 7.0 and 25°C.

As reported in our article in *Methods in Molecular Biology*, I also changed the $MgCl_2$ concentration to 10 mM instead of 20 mM and I added 75 mM of NaCl to the reaction buffer in order to favor kinase stability and specificity. In our initial conditions, we used substrate concentrations of 200 μ M, to ensure high NMR S/N. However, the K_m of pS193 and pT207 have values of about 100-200 μ M (**Figure 42**). According to [Johnson et al., 2008](#), these K_m values look common for sites phosphorylated by Plk1 that is not phosphorylated at T210 (see later **Chapters**). They indicate that we should not work with a substrate concentration exceeding 100 μ M? Indeed, following the Michealis-Menten model, initial rates depends on the substrate concentration. In extreme cases, at millimolar concentrations, phosphorylation kinetics of poor, insignificant sites having high K_m could be faster than those of cognate sites. It is thus important to carefully choose the substrate concentration. We are often focused on the choice of the best conditions according to the technique that we use (high protein concentrations in the context of NMR analysis), and we tend to forget the constraints required for a meaningful interpretation. We performed the following experiments at concentrations between 45-90 μ M.

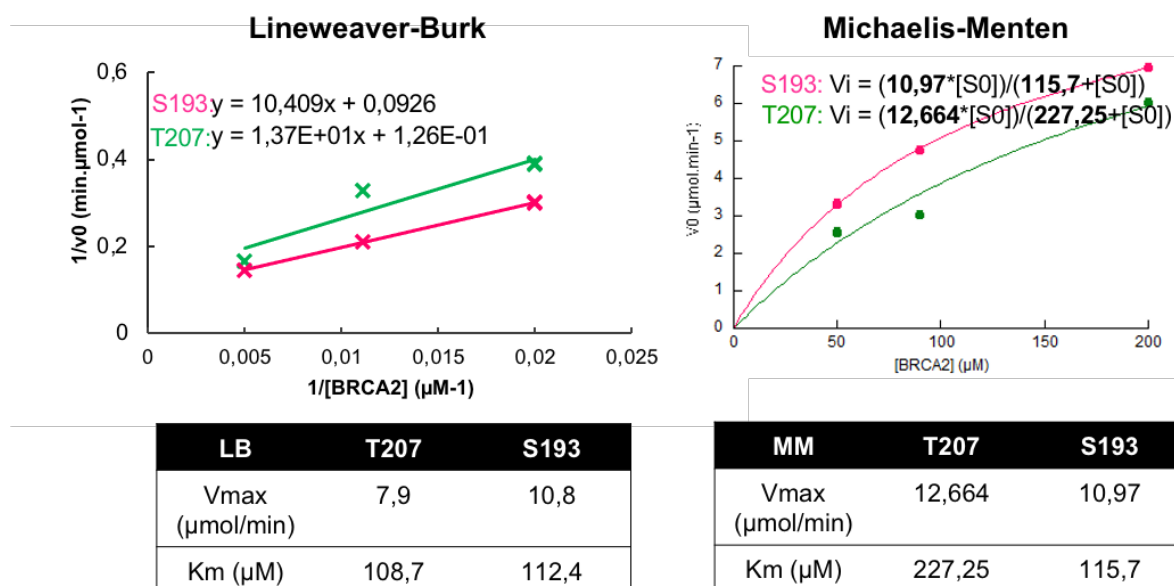


Figure 42. Plk1 Vmax and Km determination for BRCA2_{S193} and BRCA2_{T207}. Several kinetics experiments were carried out with ¹³C-labeled BRCA2₄₈₋₂₁₈ at 50 µM (Plk1 100 nM), 90 µM (Plk1 320 nM), and 200 µM (Plk1 161 nM) in HEPES 50 mM, NaCl 75 mM, 10 mM MgCl₂, EDTA 1 mM, DTT 2 mM, ATP 2 mM at pH7.0 and recorded at 303 K, 700 MHz CEA Saclay, using CaCO spectra. V₀ were determined for each condition and used for Km and Vmax determination using either Lineweaver-Burk (left) or Michaelis-Menten (right) models.

5. Impact of the fragment design on phosphorylation kinetics

Once the phosphoresidues and the optimal phosphorylation conditions were identified, I designed a new BRCA2 fragment (BRCA₁₆₇₋₂₆₀), centered around the 4 fast Plk1 phosphosites and which comprises the conserved region of BRCA2 (**Figure 33**). I used this fragment to characterize the factors influencing the kinetics of phosphorylation of each phosphoresidue.

Interestingly, comparing the kinetics observed with the different BRCA2 fragments highlighted an evident fact: the limits of the protein fragment can influence the kinetics, as illustrated in **Figure 43**. BRCA2₁₆₇₋₂₆₀ and BRCA2₁₉₀₋₂₈₄ both contain the 4 fast phosphosites. In the case of BRCA2₁₆₇₋₂₆₀, pS193 is the fastest phosphorylated residue followed by pT226 and pT207 and finally pT219. Concerning BRCA2₁₉₀₋₂₈₄, all sites are phosphorylated at slower rates, and, remarkably, S193 now exhibits now the slowest build-up kinetics. S193 proximity to the extremity of BRCA2₁₉₀₋₂₈₄ may impair its correct recognition by Plk1. Nevertheless, the phosphorylation scheme is conserved (pT226>pT207>pT219) if we do not consider pS193.

BRCA2₄₈₋₂₁₈ contains only two phosphosites, S193 and T207 instead of 4. This increased the phosphorylation rates of both sites: the kinase has less substrates to phosphorylate. Here too, the preference of phosphorylation is maintained (pS193>pT207).

In conclusion, these results highlight the necessity to design a fragment centered on the phosphosites for monitoring accurate phosphorylation kinetics.

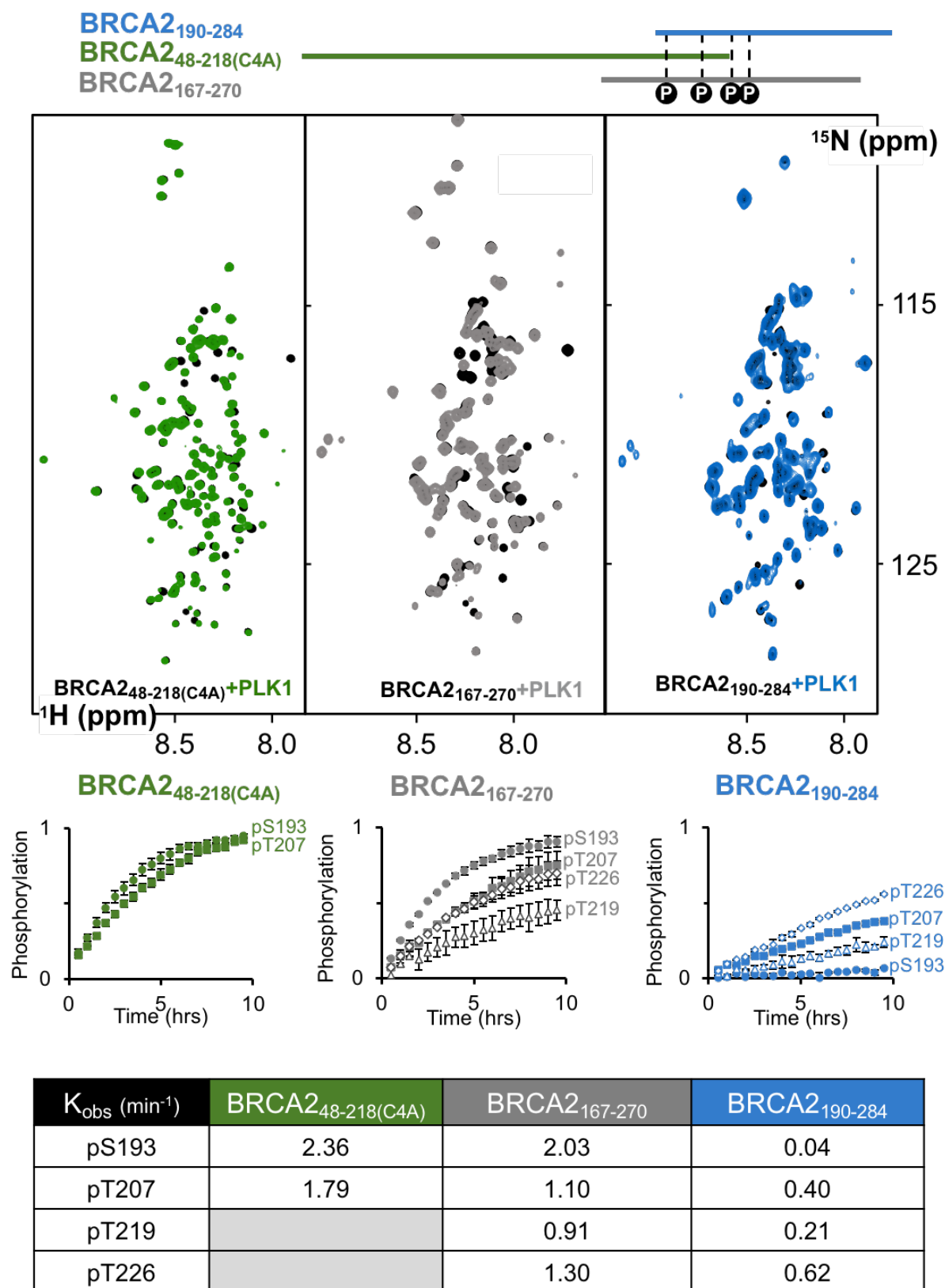


Figure 43. Comparison of S193, T207, T219 and T226 phosphorylation kinetics in BRCA2₄₈₋₂₁₈, BRCA2₁₆₇₋₂₆₀ and BRCA2₁₉₀₋₂₈₄. All these phosphorylation reactions were monitored using

a ^1H - ^{15}N SOFAST-HMQC continuous readout at 298K. BRCA2 fragments at 90 μM were mixed to PLK1 at 200 nM in buffer containing 50 mM HEPES at pH 7.0, 75 mM NaCl, 1 mM EDTA 2 mM DTT, 1X protease inhibitors (Roche), 2 mM ATP, 10 mM MgCl_2 , 50 μM DSS and 5 % D_2O . All experiments were performed in triplicate, corresponding error bars are presented. Fitting the kinetics finally gave access to the apparent rate of phosphorylation k_{obs} (min^{-1}) at each phosphosite, as described in [Julien et al., 2020](#).

In summary, I confirmed experimentally the intrinsically disordered character of BRCA2₄₈₋₂₈₄ and I identified 4 fast BRCA2 residues phosphorylated by Plk1 (S193, T207, T219 and T226). I also designed an optimized fragment for studying BRCA2 phosphorylation kinetics: BRCA2₁₆₇₋₂₆₀, and characterized the phosphorylation rates of Plk1 phosphosites on BRCA2 (pS193>pT226>pT207>pT207). These results constitute a starting point for the elucidation of the functional role of these phosphoresidues in BRCA2. Furthermore, the quantification of phosphorylation kinetics will be useful for characterizing the impact of VUS on BRCA2 phosphorylation by Plk1, as reported in **Chapter 4**.

Chapter 4. BRCA2_{pT207} is involved in the spindle assembly checkpoint

Within the BRCA2 residues phosphorylated by Plk1 (S193, T207, T219 and T226) in BRCA2₄₈₋₂₁₈ and BRCA2₁₉₀₋₂₈₄, the phosphosite S-pT₂₀₇-P corresponds to a potential Plk1 docking site. Indeed, as exposed in the Introduction, the PBD of Plk1 preferentially binds S-pS/pT-P motifs (Elia et al., 2003). The phosphoserine or phosphothreonine of the consensus motif can be either phosphorylated by cyclin-dependent kinases (Cdk, Nash et al., 2001) or by Plk1 itself (Neef et al., 2003, Kang et al., 2006, Lee et al., 2008). Based on our results, we hypothesized that Plk1 may phosphorylate T207 to create its own docking site on BRCA2.

1. BRCA2_{pT207} interacts with Plk1_{PBD} and triggers the formation of a quaternary complex

This hypothesis was confirmed in an article inserted bellow. I contributed to the article as follows: I showed that BRCA2_{pT207} is a Plk1_{PBD} docking site *in vitro*, I quantified the site-specific phosphorylation rates executed by Plk1 on different BRCA2 variants found in breast cancer, and thus identified those that impair BRCA2 phosphorylation at position T207 and BRCA2 binding to Plk1. In the same article, the team of Aura Carreira revealed that the complex BRCA2_{pT207}/Plk1 is at the center of a quaternary complex involving BRCA2_{pT207}, Plk1, BubR1 and PP2A, regulating chromosome segregation during mitosis.

In this study, I was involved in the site-directed mutagenesis of BRCA2_{48-218(T207A)} under the supervision of Ambre Petitalot, the BRCA2₄₈₋₂₁₈ and BRCA2₁₉₀₋₂₈₄ (WT and T207A) production for NMR analysis, I conducted BRCA2 phosphorylation experiments and their analysis by NMR under the supervision of Dr. François-Xavier Theillet and Dr. Sophie Zinn-Justin, I initiated the optimization of Plk1_{PBD} production in the lab and I performed half of the ITC measurements under the supervision of Dr. Simona Miron.

Proper chromosome alignment depends on BRCA2 phosphorylation by PLK1

Åsa Ehlén^{1,2} , Charlotte Martin^{1,2,8} , Simona Miron^{3,8}, Manon Julien^{3,4,8}, François-Xavier Theillet³ , Virginie Ropars³, Gaetana Sessa^{1,2}, Romane Beaupere^{1,2}, Virginie Boucherit^{1,2}, Patricia Duchambon^{5,6}, Ahmed El Marjou^{5,7}, Sophie Zinn-Justin^{3,9}  & Aura Carreira^{1,2,9} 

The BRCA2 tumor suppressor protein is involved in the maintenance of genome integrity through its role in homologous recombination. In mitosis, BRCA2 is phosphorylated by Polo-like kinase 1 (PLK1). Here we describe how this phosphorylation contributes to the control of mitosis. We identify a conserved phosphorylation site at T207 of BRCA2 that constitutes a bona fide docking site for PLK1 and is phosphorylated in mitotic cells. We show that BRCA2 bound to PLK1 forms a complex with the phosphatase PP2A and phosphorylated-BUBR1. Reducing BRCA2 binding to PLK1, as observed in *BRCA2* breast cancer variants S206C and T207A, alters the tetrameric complex resulting in unstable kinetochore-microtubule interactions, misaligned chromosomes, faulty chromosome segregation and aneuploidy. We thus reveal a role of BRCA2 in the alignment of chromosomes, distinct from its DNA repair function, with important consequences on chromosome stability. These findings may explain in part the aneuploidy observed in *BRCA2*-mutated tumors.

¹Institut Curie, PSL Research University, CNRS, UMR3348, F-91405 Orsay, France. ²Paris Sud University, Paris-Saclay University CNRS, UMR3348, F-91405 Orsay, France. ³Institute for Integrative Biology of the Cell (I2BC), CEA, CNRS, Univ Paris-Sud, Université Paris-Saclay, Gif-sur-Yvette, Cedex, France. ⁴Department of Biology, École Normale Supérieure, 94230 Cachan, France. ⁵Protein Expression and Purification Core Facility, Institut Curie, 26 rue d'Ulm, 75248 Paris, Cedex 05, France. ⁶INSERM U1196, 91405 Orsay, Cedex, France. ⁷CNRS UMR144, 12 rue Lhomond, 75005 Paris, France. ⁸These authors contributed equally: Charlotte Martin, Simona Miron, Manon Julien. ⁹These authors jointly supervised: Sophie Zinn-Justin, Aura Carreira. email: sophie.zinn@cea.fr; aura.carreira@curie.fr

The BRCA2 tumor suppressor protein plays an important role in DNA repair by homologous recombination (HR)^{1,2} that takes place preferentially during S/G2 phases of the cell cycle³. BRCA2 has also emerging functions in mitosis, for example, at the kinetochore, it forms a complex with BUBR1^{4,5}, a protein required for kinetochore–microtubule attachment and a component of the spindle assembly checkpoint (SAC)^{6,7}. These two activities of BUBR1 involve different partners and are functionally distinct^{8,9}. BRCA2 has been proposed to contribute to BUBR1 SAC activity^{4,10}, although due to confounding results in the BUBR1 interaction site in BRCA2, it is unclear if this interaction is direct^{4,5}. At the end of mitosis, BRCA2 localizes to the midbody and assists cell division by serving as a scaffold protein for the central spindle components^{11–13}. In mitosis, BRCA2 is a target of phosphorylation by PLK1 both in its N-terminal region^{14,15} and in its central region¹⁵, although the functional role of these phosphorylation events remains unclear.

PLK1 is a master regulator of the cell cycle that is upregulated in mitosis^{16,17}. Among other functions, PLK1 directly binds and phosphorylates BUBR1 at several residues including the two tension-sensitive sites S676¹⁸ and T680¹⁹ in prometaphase allowing the formation of stable kinetochore–microtubule attachments. This activity needs to be tightly regulated to ensure proper alignment of the chromosomes at the metaphase plate^{8,9,18}. The kinase activity of Aurora B is essential to destabilize erroneous kinetochore–microtubule interactions²⁰ whereas the phosphatase PP2A protects initial kinetochore–microtubule interactions from excessive destabilization by Aurora B²¹. This function is achieved through the interaction of PP2A-B56 subunit with BUBR1 phosphorylated at the Kinetochore Attachment and Regulatory Domain (KARD) motif (including residues S670, S676, and T680)¹⁹. Thus, the interplay between PLK1, BUBR1, Aurora B, and PP2A is necessary for the formation of stable kinetochore–microtubule attachments.

PLK1 is recruited to specific targets via its Polo-box domain (PBD)²². PBD interacts with phosphosites characterized by the consensus motif S-[pS/pT]-P/X²³. These phosphosites are provided by a priming phosphorylation event, usually mediated by CDK1 or other proline-directed kinases¹⁷; however, there is also evidence that PLK1 itself might create docking sites (“self-priming”) during cytokinesis^{24,25}.

Several BRCA2 sites have been suggested as phosphorylated by PLK1 in mitosis, some of which belong to a cluster of serines and threonines located in BRCA2 N-terminus around residue S193¹⁴. We set out to investigate which of these sites are phosphorylated by PLK1, and to reveal whether these phosphorylation events play a role in the regulation of mitotic progression. Here, we demonstrate that the two conserved residues S193 and T207 are phosphorylated by PLK1, and that phosphorylated BRCA2-T207 is a bona fide docking site for PLK1. By investigating the phenotype of BRCA2 missense variants that limit the phosphorylation of BRCA2-T207, we reveal an unexpected role for BRCA2 in the alignment of chromosomes at the metaphase plate. We demonstrate that phosphorylation of BRCA2-T207 by PLK1 facilitates the formation of a complex between BRCA2-PLK1-pBUBR1 and the phosphatase PP2A. A defect in this function of BRCA2 is manifested in chromosome misalignment, chromosome segregation errors, mitotic delay and aneuploidy, leading to chromosomal instability.

Results

Breast cancer variants alter PLK1 phosphorylation of BRCA2.

Several missense variants of uncertain significance (VUS) identified in BRCA2 in breast cancer patients are located in the N-terminal region predicted to be phosphorylated by PLK1

(around S193) (Breast information core (BIC)²⁶ and BRCA-Share²⁷), summarized in Supplementary Table 1. To find out if any of these variants affected PLK1 phosphorylation in this region, we purified fragments comprising amino acids 1 to 250 of BRCA2 (hereafter BRCA2_{1–250}) from human embryonic kidney cells (HEK293T) and used an in vitro kinase assay to assess the phosphorylation by PLK1 of the fragments containing either the WT sequence, the different BRCA2 variants M192T, S196N, S206C, and T207A, or the mutant S193A, previously reported to reduce the phosphorylation of BRCA2 by PLK1¹⁴. As expected, S193A reduced the phosphorylation of BRCA2_{1–250} by PLK1 (Fig. 1a, b). Interestingly, variants T207A and S206C also led to a 2-fold decrease in PLK1 phosphorylation of BRCA2_{1–250} (Fig. 1a, b). In contrast, M192T and S196N did not significantly modify the phosphorylation of BRCA2_{1–250} by PLK1 (Fig. 1a, b). The phosphorylation observed in the BRCA2 fragments is specific of the recombinant PLK1 kinase as it is PLK1 concentration dependent (Supplementary Fig. 1a, b) and when replacing the PLK1-WT by a kinase-dead (PLK1-KD) version of the protein (K82R)²⁸, purified using the same protocol, or adding a PLK1 inhibitor (BI2536) to the reaction, the phosphorylation of BRCA2_{1–250} decreased significantly (Fig. 1c, lanes 4 and 5 compared to lane 3; Fig. 1d).

Together, these results show that VUS T207A and S206C identified in breast cancer patients impair phosphorylation of BRCA2_{1–250} by PLK1 in vitro.

BRCA2-T207 is a target of phosphorylation by PLK1. The reduction of BRCA2 phosphorylation in BRCA2_{1–250} containing T207A and S206C variants suggested that these residues could be targets for PLK1 phosphorylation. We investigated this possibility by following the PLK1 phosphorylation kinetics of two overlapping fragments of BRCA2 N-terminus comprising S206 and T207 (hereafter BRCA2_{48–218} and BRCA2_{190–284}) using Nuclear Magnetic Resonance (NMR) spectroscopy (Fig. 2a). Together, these fragments cover a large N-terminal region of BRCA2 including the cluster of conserved residues around S193 (from amino acid 180 to amino acid 210; Supplementary Fig. 1c). NMR analysis allows residue-specific quantification of ¹⁵N-labeled peptide phosphorylation. Figure 2b shows superimposed ¹H-¹⁵N HSQC spectra of BRCA2_{48–218} and BRCA2_{190–284} before (black) and after (red) phosphorylation with recombinant PLK1. Analysis of these experiments revealed phosphorylation of S193 and of three other phosphosites, including T207, by PLK1 in the BRCA2 region from amino acid 48 to amino acid 284. Interestingly, while T219 and T226 conservation is poor, T207 and S193 are conserved from mammals to fishes (Supplementary Fig. 1c) suggesting that both residues are important for BRCA2 function.

BRCA2 variant T207A alters PLK1 phosphorylation kinetics.

Having identified T207 as a target of phosphorylation of PLK1, we next compared the residue-specific phosphorylation kinetics in the polypeptide WT BRCA2_{48–218} containing the variant T207A that displayed reduced overall phosphorylation (Fig. 1a, b). (The production of a ¹⁵N-labeled recombinant fragment comprising S206C yielded an insoluble protein precluding NMR analysis). Time-resolved NMR experiments revealed that PLK1 phosphorylates significantly less BRCA2_{48–218} containing the variant T207A than the WT peptide (Fig. 2c). The initial phosphorylation rate of S193 was decreased by a factor of 2 (Fig. 2d), and T207 was, as expected, not phosphorylated, being mutated into an alanine. Similar results were obtained using BRCA2_{190–284} (Supplementary Fig. 2). This NMR analysis is consistent with the in vitro kinase assay performed using the BRCA2_{1–250} fragment

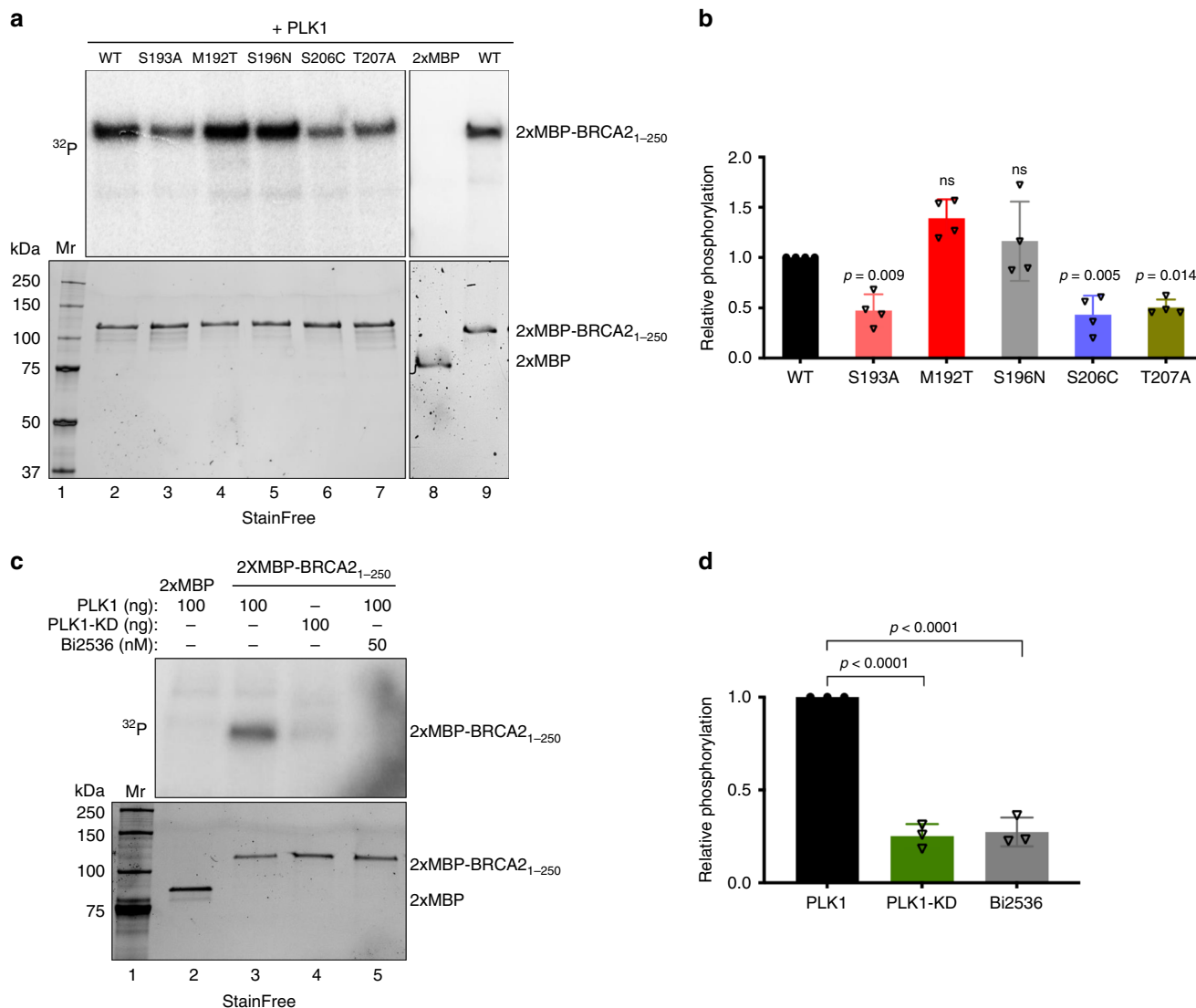


Fig. 1 BRCA2 VUS alter PLK1 phosphorylation of BRCA2₁₋₂₅₀. **a** PLK1 in vitro kinase assay with BRCA2₁₋₂₅₀. Top: The polypeptides encompassing 2x-MBP-BRCA2₁₋₂₅₀ WT or S193A, M192T, S196N, S206C, T207A mutations or the 2XMBP tag were incubated with recombinant PLK1 in the presence of γ -³²P-ATP. The samples were resolved on 7.5% SDS-PAGE and the ³²P-labeled products were detected by autoradiography. Bottom: 7.5% SDS-PAGE showing the input of purified 2xMBP-BRCA2₁₋₂₅₀ WT and mutated proteins (0.5 μ g) used in the reaction as indicated. Mr; molecular weight markers. **b** Quantification of the relative phosphorylation in (a). Data in (b) are represented as mean \pm SD from four independent experiments. **c** PLK1 in vitro kinase assay performed as in (a) with recombinant PLK1 or the PLK1 kinase dead K82R mutant (PLK1-KD) together with BRCA2₁₋₂₅₀ WT as substrate, in the presence or absence of the PLK1 inhibitor Bi2536 (50 nM) in the kinase reaction buffer. Mr; molecular weight markers. **d** Quantification of the relative phosphorylation in (c). Data in (d) are represented as mean \pm SD from three independent experiments. **b, d** One-way ANOVA test with Dunnett’s multiple comparisons test was used to calculate statistical significance of differences (the *p*-values show differences compared to WT (b) or PLK1 (d); ns (non-significant)). Source data are available as a Source Data file.

purified from human cells (Fig. 1), in which T207A reduces the phosphorylation of BRCA2₁₋₂₅₀ fragment by PLK1.

Variants T207A and S206C reduce the interaction of BRCA2 with PLK1. The finding that T207 is efficiently phosphorylated by PLK1 in BRCA2₄₈₋₂₁₈ and BRCA2₁₉₀₋₂₈₄ (Fig. 2b) together with the observation that T207A mutation causes a global decrease in the phosphorylation of these fragments (Fig. 2c; Supplementary Fig. 2) and the prediction that T207 is a docking site for PLK1_{PBD} binding²³ made us hypothesize that T207 might be a “self-priming” phosphorylation event required for the interaction of PLK1 with BRCA2 at this site. If so, the variants that reduce phosphorylation of T207 by PLK1 would be predicted

to alter PLK1_{PBD} binding. To test this hypothesis, we examined the interaction of PLK1 with the VUS-containing polypeptides. We overexpressed 2xMBP-BRCA2₁₋₂₅₀ constructs carrying these variants in U2OS cells to detect the endogenous PLK1 that co-immunoprecipitates with 2xMBP-BRCA2₁₋₂₅₀ using amylose pull-down. As expected, overexpressed BRCA2₁₋₂₅₀ was able to interact with endogenous PLK1 from mitotic cells but not from asynchronous cells (predominantly in G1/S) where the levels of PLK1 are reduced (Fig. 3a, lane 2 compared to lane 1). Furthermore, the variants T207A and S206C showed a weaker interaction with PLK1 than the WT protein (Fig. 3a, pull-down lanes 4, 6 compared to lane 2, Fig. 3b) despite the protein levels of PLK1 remaining unchanged (Fig. 3a, compare PLK1 input lanes 4 and 6 to lane 2). In contrast, the effect of M192T and S196N on the

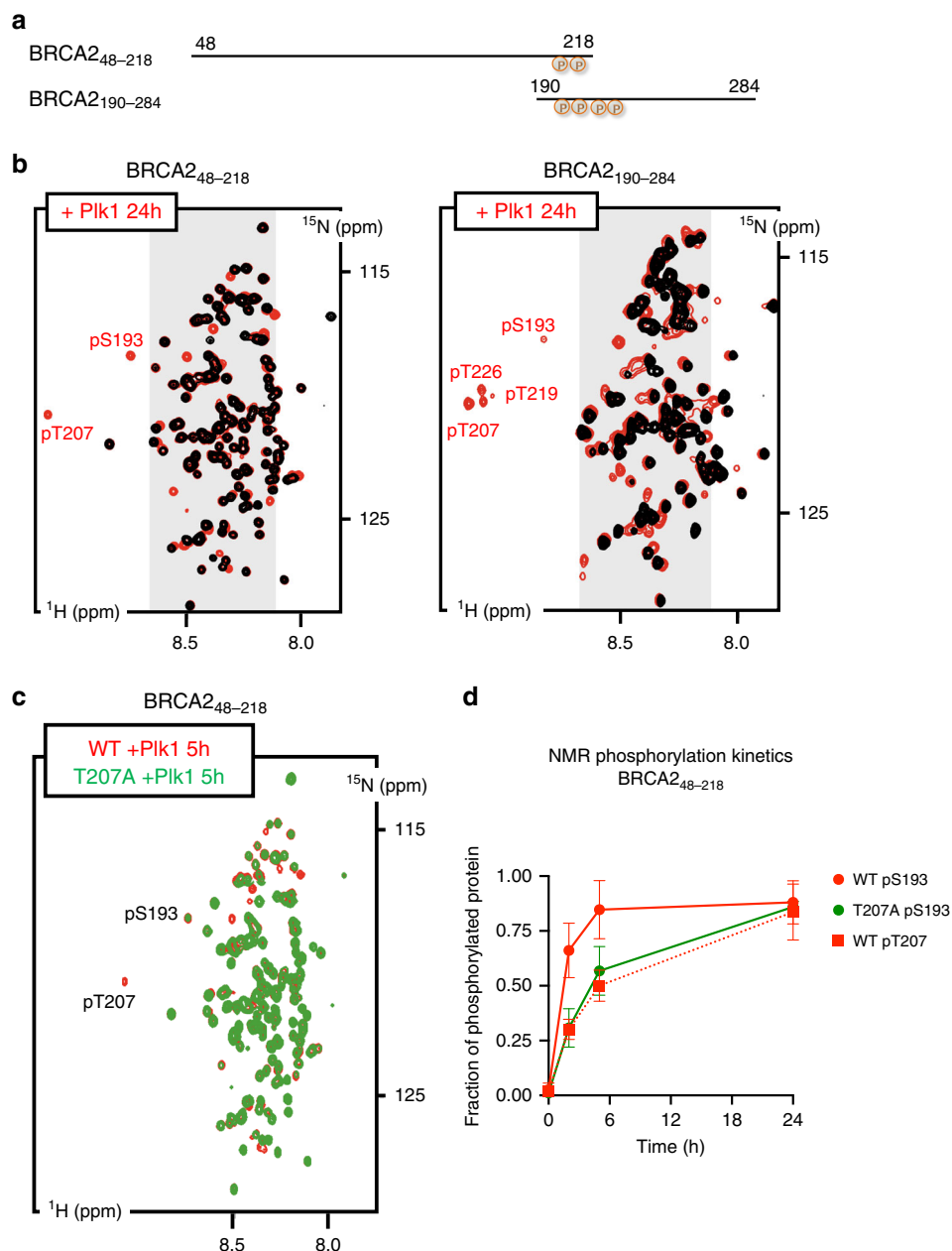
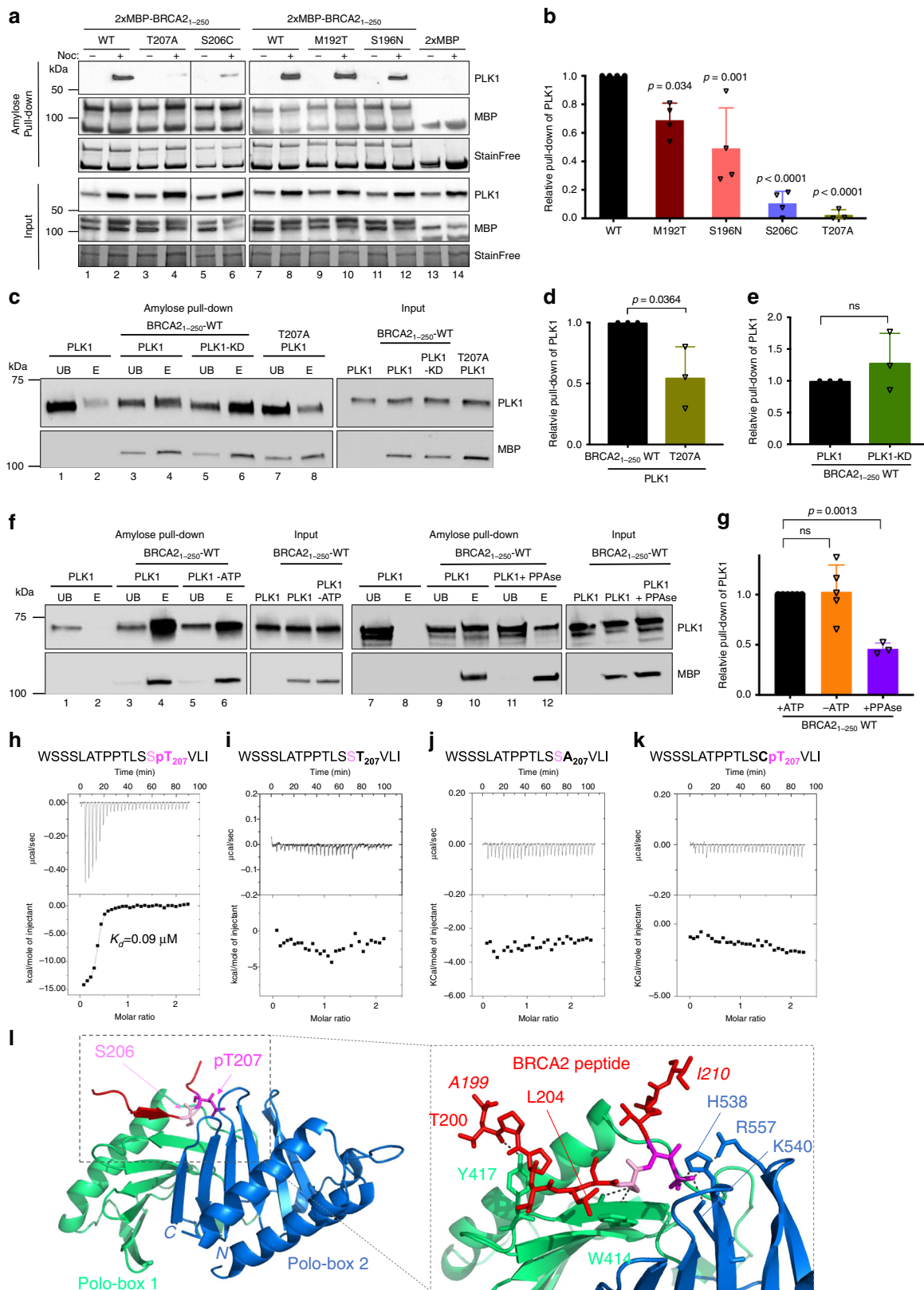


Fig. 2 PLK1 phosphorylates T207 in BRCA2₄₈₋₂₁₈ and BRCA2₁₉₀₋₂₈₄. Phosphorylation of BRCA2₄₈₋₂₁₈ and BRCA2₁₉₀₋₂₈₄ by PLK1 as observed by NMR. **a** Schematic view of the two overlapping BRCA2 fragments analyzed by NMR. Residues identified as phosphorylated in **(b)** are indicated. **b** Superposition of the ¹H-¹⁵N HSQC spectra recorded before (black) and after (24 h; red) incubation with PLK1. Each spectrum contains one peak per backbone NH group. Most peaks are located in the gray region of the spectrum, indicating that they correspond to disordered residues. Assignment of each peak to a BRCA2 residue was performed using a classical heteronuclear NMR strategy. Peaks corresponding to phosphorylated residues are indicated. **c** Comparison of the phosphorylation kinetics recorded for BRCA2₄₈₋₂₁₈ WT and T207A. ¹H-¹⁵N HSQC spectra of BRCA2₄₈₋₂₁₈ WT (red) and T207A (green) recorded 5 h after addition of PLK1 are superimposed to highlight the overall decrease of phosphorylation observed for the mutant compared to the WT. **d** Fraction of phosphorylated protein deduced from the intensities of the peaks corresponding to the non-phosphorylated and phosphorylated residues plotted as a function of time. WT S193 and T207 timepoints are represented by red circles and squares, respectively, while T207A S193 timepoints are represented by green circles. The graph represents data as mean ± SD from three independent experiments. Source data are available as a Source Data file.

interaction was mild (Fig. 3a, compare pull-down lanes 10 and 12 to lane 8, Fig. 3b). These results suggest a self-priming phosphorylation by PLK1 on T207.

To provide further evidence that the PLK1-mediated phosphorylation of BRCA2 favors BRCA2 binding, we performed an in vitro kinase assay with recombinant proteins followed by an amylose pull-down and eluted the bound proteins with maltose. PLK1 was found in the maltose elution with BRCA2₁₋₂₅₀-WT

demonstrating that PLK1-phosphorylated BRCA2₁₋₂₅₀ binds to PLK1 (Fig. 3c lane 4, Fig. 3d). In contrast, the fraction of PLK1 in the eluate of BRCA2₁₋₂₅₀-T207A was substantially reduced (Fig. 3c, lane 8 compared to lane 4, Fig. 3d) indicating that the phosphorylation of T207 is required for efficient binding to PLK1 and confirming our results with cell lysates (Fig. 3a, b). Strikingly, we observed no difference in PLK1 binding between BRCA2₁₋₂₅₀-WT phosphorylated by PLK1 or its kinase dead mutant (PLK1-



KD; Fig. 3c, lane 6 compared to lane 4, Fig. 3e) or in the absence of ATP (Fig. 3f, lane 6 compared to lane 4, Fig. 3g). However, pre-incubating BRCA2₁₋₂₅₀-WT with phosphatase before the addition of PLK1 resulted in a 2-fold decrease in the binding to PLK1 indicating that the phosphorylation of BRCA2 is required for the interaction with PLK1 (Fig. 3f lane 12 compared to 10, Fig. 3g).

T207 is a bona fide docking site for PLK1. To demonstrate the recognition of pT207 by PLK1, we measured the affinity of recombinant PLK1_{PBD} (the target recognition domain of PLK1) for a synthetic 17 aa peptide comprising phosphorylated T207. Using isothermal titration calorimetry (ITC), we found that recombinant PLK1_{PBD} bound to the pT207 peptide with an

Fig. 3 BRCA2 variants showing reduced phosphorylation by PLK1 impair PLK1 binding. **a** Amylose pull-down of U2OS transiently expressing 2xMBP-BRCA2₁₋₂₅₀ (WT), the variants (M192T, S196N, S206C, and T207A) or the 2XMBP-tag treated with nocodazole as indicated. 4–15% SDS-PAGE followed by WB using anti-PLK1 and anti-MBP antibodies. StainFree images are used as loading control (cropped image is shown). **b** Quantification of co-immunoprecipitated PLK1 with WT in **(a)**, relative to the input levels of PLK1. Results are presented as the fold change compared to WT. The data represent the mean \pm SD of three to four independent experiments (WT ($n = 4$), M192T ($n = 4$), S196N ($n = 4$), S206C ($n = 4$), T207A ($n = 3$)). One-way ANOVA test with Dunnett's multiple comparisons test was used to calculate statistical significance of differences (p -values compared to WT). **c** PLK1 (or PLK1-KD) as indicated in vitro kinase assay followed by amylose pull-down of BRCA2₁₋₂₅₀-WT or T207A. 10% SDS-PAGE followed by WB using anti-PLK1 and anti-MBP antibodies. **d, e** Quantification of the PLK1 pull-down in **(c)** relative to the PLK1 levels in the input. Results are presented as the fold change compared to BRCA2₁₋₂₅₀-WT in **(d)** and PLK1-WT in **(e)**. The data represent the mean \pm SD of three independent experiments, two-tailed unpaired t -test was used to calculate significance of differences (ns (non-significant)). **f** PLK1 in vitro kinase assay followed by amylose pull-down assay as in **(c)** Left panel: with or without ATP as indicated. Right panel: The 2x-MBP-BRCA2₁₋₂₅₀-WT polypeptide was pre-treated with phosphatase (FastAP) for 1 h before the amylose pull-down **(c)**. In **(c)** and **(f)**: UB: unbound, E: eluted. **g** Quantification of the PLK1 pull-down in **(f)** relative to the PLK1 levels in the input. Results are presented as the fold change compared to kinase assay performed with non-phosphatase treated BRCA2₁₋₂₅₀-WT in the presence of ATP. The data represent the mean \pm SD of three to five independent experiments (+ATP ($n = 5$), -ATP ($n = 5$), +PPase ($n = 3$)), one-way ANOVA test with Dunnett's multiple comparisons test was used to calculate statistical significance of differences (p -values compared to +ATP; ns (non-significant)). **h–k** Isothermal Titration Calorimetry (ITC) thermograms showing binding of PLK1_{PBD} to a 17 aa BRCA2 peptide containing **(h)** pT207, **(i)** T207, **(j)** A207, **(k)** C206pT207. Residues S206 and pT207 are highlighted in pink (S206) and magenta (pT207) in the peptide sequences. **l** Left panel: 3D cartoon representation of the crystal structure of PLK1_{PBD} (Polo-box 1 in green and Polo-box 2 in blue) bound to the BRCA2 peptide containing pT207 (in red except for S206 (pink, sticks) and pT207 (magenta, sticks)). Right panel: zoom in on the interface between PLK1_{PBD} and the BRCA2 peptide (from A199 to I210). The amino acids of PLK1_{PBD} and BRCA2 involved in the interaction are highlighted in sticks representation with hydrogen bonds depicted as dark gray dots. Source data are available as a Source Data file.

affinity of $K_d = 0.09 \pm 0.01 \mu\text{M}$ (Fig. 3h), similar to the optimal affinity reported for an interaction between PLK1_{PBD} and its phosphorylated target²³. Consistently, PLK1_{PBD} bound to the fragment BRCA2₁₉₀₋₂₈₄ with nanomolar affinity upon phosphorylation by PLK1 ($K_d = 0.14 \pm 0.02 \mu\text{M}$; Supplementary Fig. 3a), whereas it did not bind to the corresponding non-phosphorylated polypeptides (Fig. 3i, Supplementary Fig. 3b). Mutation T207A also abolished the interaction (Fig. 3j), in agreement with the pull-down experiments (Fig. 3a–d). More surprisingly, the phosphomimetic substitution T207D was not sufficient to create a binding site for PLK1_{PBD} (Supplementary Fig. 2c). A peptide comprising pT207 and the mutation S206C could not bind to PLK1_{PBD} (Fig. 3k), as predicted from the consensus sequence requirement for PLK1_{PBD} interaction²³. Last, a peptide containing pS197, a predicted docking site for PLK1, bound with much less affinity to PLK1_{PBD} than pT207 ($K_d = 17 \pm 2 \mu\text{M}$; Supplementary Fig. 2d).

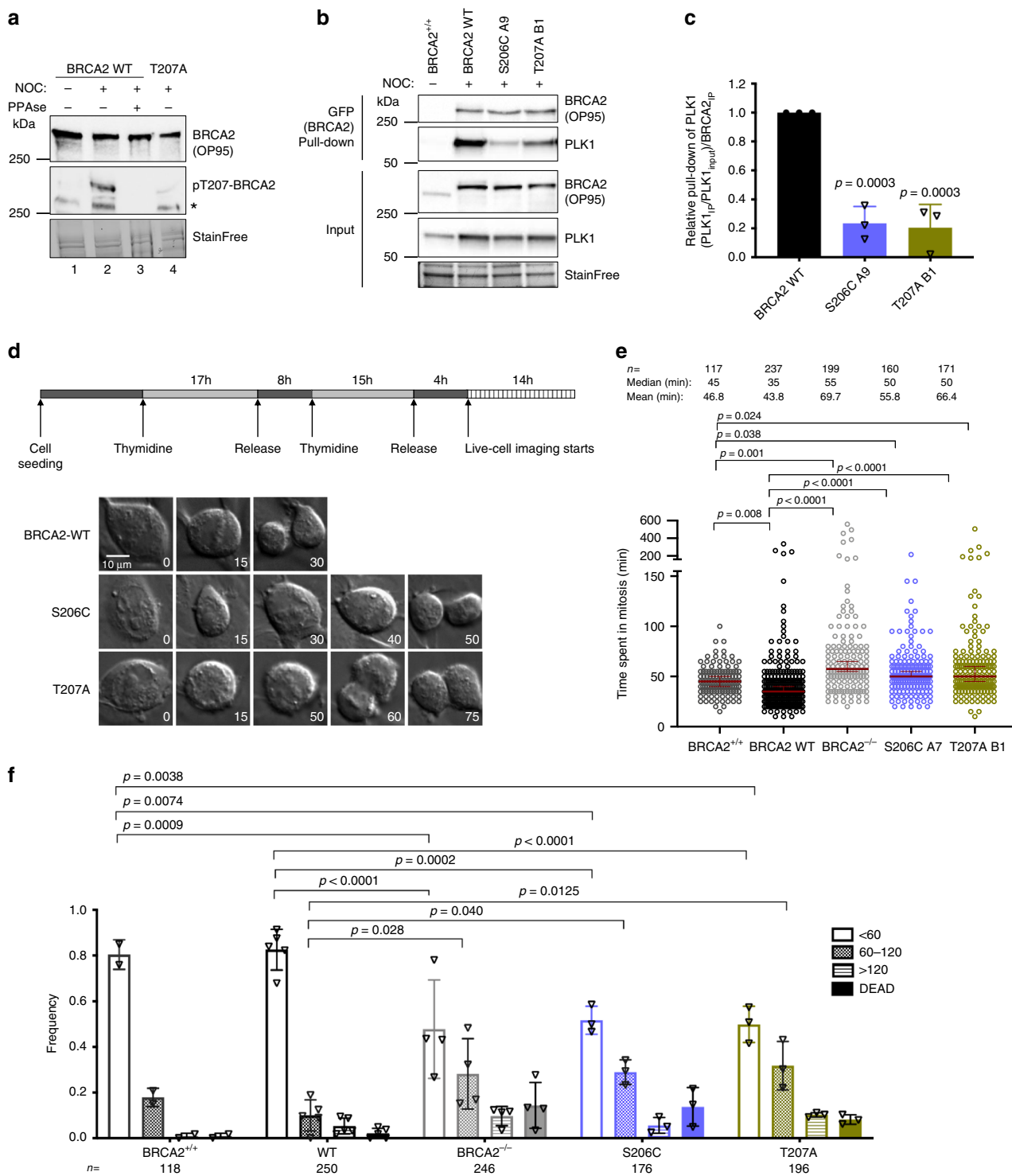
Finally, we determined the crystal structure of PLK1_{PBD} bound to the T207 phosphorylated peptide at 3.1 Å resolution (Supplementary Table 2). Analysis of this 3D structure showed that, as expected, the 17 aa BRCA2 phosphopeptide binds in the cleft formed between the two Polo boxes (Fig. 3l). Twelve residues of the peptide (from A199 to I210) are well structured upon binding, burying about 694 Å² in the interface with PLK1_{PBD}. The interface between BRCA2 and PLK1_{PBD} is stabilized by 12 hydrogen bonds: the backbone of residues T200 to L209 as well as the side chain of S206 are bonded to residues from Polo Box 1, whereas the side chain of phosphorylated T207 is bonded to residues from Polo Box 2 (see the zoom view in Fig. 3l). The side chain of S206 participates in two hydrogen-bonding interactions with the backbone of W414, which explains the strict requirement for this amino acid at this position²³. Moreover, the phosphate group of pT207 participates in three hydrogen-bonding interactions with the side chains of residues H538, K540, and R557 in Polo Box 2 (see the zoom view in Fig. 3l). This explains the critical dependence on phosphorylation for binding observed by ITC (Fig. 3h, i).

Thus, our biochemical and structural analyses demonstrate that the BRCA2-T207 phosphopeptide interacts with PLK1_{PBD} as an optimal and specific PLK1_{PBD} ligand. It supports a mechanism in which phosphorylation of T207 by PLK1 promotes the interaction of PLK1 with BRCA2 through a bona fide docking site for PLK1 and favors a cascade of phosphorylation events. In variant T207A, the absence of T207 phosphorylation impairs

PLK1 docking explaining the reduction of binding to PLK1 and the global loss of phosphorylation by PLK1. S206C eliminates the serine residue at -1 position required for PLK1_{PBD} interaction resulting as well in a strong reduction of BRCA2 binding.

Impairing T207 phosphorylation prolongs mitosis. PLK1 is a master regulator of mitosis¹⁷. To find out whether the interaction between BRCA2 and PLK1 was involved in the control of mitotic progression we examined the functional impact of the variants that reduce PLK1 phosphorylation at T207 (S206C and T207A) in the context of the full-length BRCA2 protein in cells. We generated stable cell lines expressing the BRCA2 cDNA coding for either the GFPMBP-BRCA2 WT or the variants to complement DLD1 BRCA2 deficient human cells (hereafter BRCA2^{-/-}) (Supplementary Fig. 4a). First, to confirm that the phosphorylation of T207 by PLK1 takes place in cells we raised a phospho-specific polyclonal antibody against a peptide encompassing pT207. Using an antibody against BRCA2 we detected a band that corresponds to the size of BRCA2 in cell extracts from BRCA2 WT cells, both in mitotic (nocodazole treated) and asynchronous cells, by Western blotting (Fig. 4a). When the same membrane was re-probed with the pT207-BRCA2 antibody a band corresponding to BRCA2 was detected only in the mitotic cells and not in the asynchronous cells (Fig. 4a, lane 1 and 2). In addition, mitotic cell extracts treated with phosphatase lost the signal indicating that the band corresponds to a phosphorylation event (Fig. 4a, lane 3). Finally, cells bearing BRCA2-T207A were detected with the BRCA2 antibody but showed reduced signal for the pT207 antibody (Fig. 4a, lane 4) providing evidence of the specificity of the antibody. We then tested the interaction of full-length BRCA2 with PLK1 in these stable clones by GFP pull-down assay. As expected, PLK1 readily co-purified with full-length BRCA2 WT from mitotic cells. Importantly, in cells expressing the variants S206C and T207A, the level of co-purified PLK1 was greatly reduced (Fig. 4ba, c), confirming the results obtained with the overexpressed BRCA2₁₋₂₅₀ fragments (Fig. 3a) now in the context of cells stably expressing the full-length BRCA2 protein. Thus, BRCA2 interaction with endogenous PLK1 is impaired in cells bearing variants S206C and T207A.

Also, the binding of BRCA2 to PLK1 in cells stably expressing full-length BRCA2 WT was not reduced by incubating the cells with a PLK inhibitor (BTO) (Supplementary Fig. 4b), consistently with results obtained in vitro (Fig. 3c). Altogether, these data



suggest that another binding site primed by a different kinase (presumably T77 phosphorylated by CDK1²⁹) contributes to BRCA2 binding to PLK1. Consistent with this idea, the binding of overexpressed 2xMBP-BRCA2₁₋₂₅₀ to the endogenous PLK1 in U2OS cells was completely abolished in the presence of the CDK inhibitor (RO3306) (Supplementary Fig. 4c, lane 4 compared to lane 2).

Having confirmed that T207 was a docking site for PLK1 in cells, we next examined the impact of BRCA2 variants on mitosis. Therefore, we monitored the time taken for individual cells from

mitotic entry (defined as nuclear envelope break down) to mitotic exit using live cell imaging. Cells expressing the endogenous BRCA2 (hereafter BRCA2^{+/+}) and the BRCA2 WT cells showed similar kinetics, they completed mitosis, on average, in 47 and 44 min, respectively (Fig. 4d, e) and the majority of the cells (80% for BRCA2^{+/+} and 82% for BRCA2 WT) completed mitosis within 60 min (Fig. 4f). In contrast, cells expressing variants S206C and T207A augmented the time spent in mitosis (average time of 56 and 66 min, respectively, Fig. 4e). This trend was also observed in the frequency of cells dividing within 60 min (~49–51%),

Fig. 4 Cells bearing BRCA2 variants S206C and T207A prolong mitosis. **a** Protein levels of BRCA2 and pT207-BRCA2 in cells bearing BRCA2 WT or the T207A variant from whole cell lysates of nocodazole-arrested (100 ng/μl for 14 h) or asynchronous cells. 4–15% SDS-PAGE followed by WB using anti-BRCA2. The same blot was stripped and re-probed with anti-pT207-BRCA2 antibody. Lane 3 protein extracts were pre-treated with phosphatase (FastAP) for 1 h before loading onto the gel. Asterisk indicates a non-specific band. **(b)** GFP-trap pull-down of EGFPMBP-BRCA2 from cells bearing BRCA2 WT, S206C or T207A. 4–15% SDS-PAGE followed by WB using anti-BRCA2 and -PLK1 antibodies. Asynchronous DLD1 cells with endogenous BRCA2 (BRCA2^{+/+}) were used as control for the pull-down and StainFree images of the gels before transfer as loading control (cropped image is shown). **(c)** Quantification of co-immunoprecipitated PLK1 with EGFP-MBP-BRCA2 in **(b)** relative to the PLK1 protein levels in the input and the amount of pull-down EGFP-MBP-BRCA2 ((PLK1_{IP}/PLK1_{input})/EGFP-MBP-BRCA2_{IP}). Results are presented as the fold change compared to the BRCA2 WT clone. The data represent the mean ± SD of three independent experiments. One-way ANOVA test with Dunnett's multiple comparisons test was used to calculate statistical significance of differences (*p*-values compared to WT). **(d)** Top: Synchronization scheme. Bottom: Representative still images of the time-lapse videos. Numbers represent time (min) after nuclear envelope break down (NEBD). Scale bar represents 10 μm. **(e)** Quantification of the time the cells spent in mitosis in **(d)**. The red line indicates the median (95% CI). Each dot represents a single cell, *n* is the total number of cells from two to four independent experiments (45–60 cells per experiment) (BRCA2^{+/+} (*n* = 2), WT C1 (*n* = 5), BRCA2^{-/-} (*n* = 4), S206C A7 (*n* = 3), T207A B1 (*n* = 3)). Kruskal-Wallis one-way analysis followed by Dunn's multiple comparison test was used to calculate statistical significance of differences. **(f)** Frequency distribution of the time spent in mitosis in **(d)**, including cells that fail to divide (DEAD). The error bars represent mean ± SD of two to four independent experiments (BRCA2^{+/+} (*n* = 2), WT C1 (*n* = 5), BRCA2^{-/-} (*n* = 4), S206C A7 (*n* = 3), T207A B1 (*n* = 3)). Two-way ANOVA test with Tukey's multiple comparisons test was used to calculate statistical significance of differences. Source data are available as a Source Data file.

compared to 82% in BRCA2 WT cells (Fig. 4f). Representative videos of the still images shown in Fig. 4d are included in Supplementary movies 1–3.

Taken together, the phosphorylation of T207 takes place in cells in mitosis. Cells altering this phosphorylation (bearing S206C and T207A variants) display a significant delay in mitotic progression compared to BRCA2 WT cells.

Docking of PLK1 at T207-BRCA2 favors a complex with PP2A and pBUBR1. BRCA2 forms a complex with BUBR1^{4,5}. BUBR1 facilitates kinetochore–microtubule attachments via its interaction with the phosphatase PP2A. Phosphorylation of BUBR1 by PLK1 at the KARD motif comprising the tension-sensitive sites S676 and T680 promotes interaction with PP2A¹⁹. A defect in the phosphorylation of BUBR1 weakens its interaction with PP2A leading to mitotic delay^{20,30}. The mitotic delay phenotype we observed in BRCA2 mutated cell lines led us to ask whether BRCA2 and PLK1 formed a tetrameric complex with pBUBR1 and PP2A. Using a GFP pull-down to capture GFP-MBP-BRCA2 from mitotic BRCA2 WT cells, we observed that PLK1, pT680-BUBR1 and PP2A were pull-down together with GFP-MBP-BRCA2, indicating the formation of a tetrameric complex (Fig. 5a). As described for pBUBR1^{18,19}, PLK1³¹ and PP2A²¹, we found BRCA2 at the kinetochore in mitotic cells (Supplementary Fig. 5a) as previously reported⁴ supporting the idea that this complex takes place at the kinetochore.

Importantly, cells expressing the variants S206C or T207A showed a strong reduction in the interaction of BRCA2 with PLK1, PP2A, BUBR1 and pT680-BUBR1 in the context of the tetrameric complex (Fig. 5a, b). Moreover, the overall levels of BUBR1 and pBUBR1 were also reduced in cells bearing S206C and T207A variants compared to the WT cells, as detected by specific antibodies against BUBR1, pT680-BUBR1 (Fig. 5e–i) and pS676-BUBR1 (Supplementary Fig. 5d), and this was also the case in BRCA2 deficient cells (DLD1 BRCA2^{-/-} cells) or U2OS cells depleted of BRCA2 by siRNA (Fig. 5f, g). Furthermore, we observed an overall reduction in the levels of pBUBR1 at the kinetochore (Fig. 5h, i) in cells expressing T207A compared to WT cells. Consistently, when we immunoprecipitated BUBR1 from mitotic cells and detected the levels of co-immunoprecipitated PP2A (PP2AC antibody), we observed that, although PP2A was readily copurified with BUBR1 in the BRCA2 WT cells, expressing BRCA2 variant T207A reduced the levels of PP2A by ~30% (Fig. 5c, d) suggesting that BRCA2 facilitates the formation of a complex between BUBR1 and PP2A.

Impaired phosphorylation of T207 leads to chromosome misalignment. The association of PLK1-phosphorylated BUBR1 with PP2A is required for the formation of stable kinetochore–microtubule attachments^{18,19}, a defect in this interaction resulting in chromosome misalignment. Therefore, we next examined whether cells expressing the BRCA2 variants S206C and T207A altered chromosome alignment. Following thymidine synchronization, the cells were treated with the Eg5 inhibitor Monastrol (100 μM) for 14 h followed by Monastrol washout and release for 1 h in normal media supplemented with the proteasome inhibitor MG132 to avoid exit from mitosis¹⁸. Chromosome alignment was then analyzed by immunofluorescence. Importantly, the analysis of cells expressing S206C and T207A variants showed high frequency of faulty chromosome congression compared to the BRCA2 WT clone (47% in S206C and 38% in T207 versus 24% in the BRCA2 WT clone), which was exacerbated in BRCA2^{-/-} cells (63%) (Fig. 6a, b), as detected by signals of the centromere marker (CREST) outside the metaphase plate (Fig. 6b). Next, to find out if this defect in alignment was due to impaired stability of kinetochore–microtubule interactions as previously reported^{6,18}, we examined the presence of cold stable microtubules in cells bearing T207A mutation compared to BRCA2 WT cells. Following the same synchronization procedure as before (Fig. 6a), the cells were kept on ice for 15 min before fixation. Under these conditions, BRCA2 WT metaphase cells exhibited relatively intact bipolar spindles with most CREST-stained kinetochores attached to the microtubules (α-tubulin) (Fig. 6c). In stark contrast, almost all the kinetochore–microtubules attachments were lost in T207A mutated cells upon cold treatment (Fig. 6c) as measured by the relative intensity of α-tubulin in these cells with respect to BRCA2 WT cells (~6-fold reduction of the median) (Fig. 6d).

To better understand the mechanism behind the phenotype observed in our clones, we overexpressed a phosphomimic version of BUBR1 RFP-BUBR1-3D (S670D, S676D, T680D) in T207A mutated cells to test whether this form of BUBR1 could restore the misalignment phenotype as previously shown for BUBR1 depleted cells¹⁹. Surprisingly, T207A bearing cells overexpressing RFP-BUBR1-3D exhibited a similar misalignment phenotype (~38% of cells with misalignment) compared to the non-transfected cells (33%) (Fig. 7a, b). Moreover, BUBR1-3D, previously shown to be sufficient to restore PP2A binding in BUBR1 deficient cells¹⁹, could not rescue the interaction of BUBR1 with PP2A in cells bearing BRCA2 S206C variant (Fig. 7c). This effect was not due to an increased localization of PLK1 at the kinetochore in the mutated cells, as the levels of PLK1 at the kinetochores remained unchanged (Supplementary

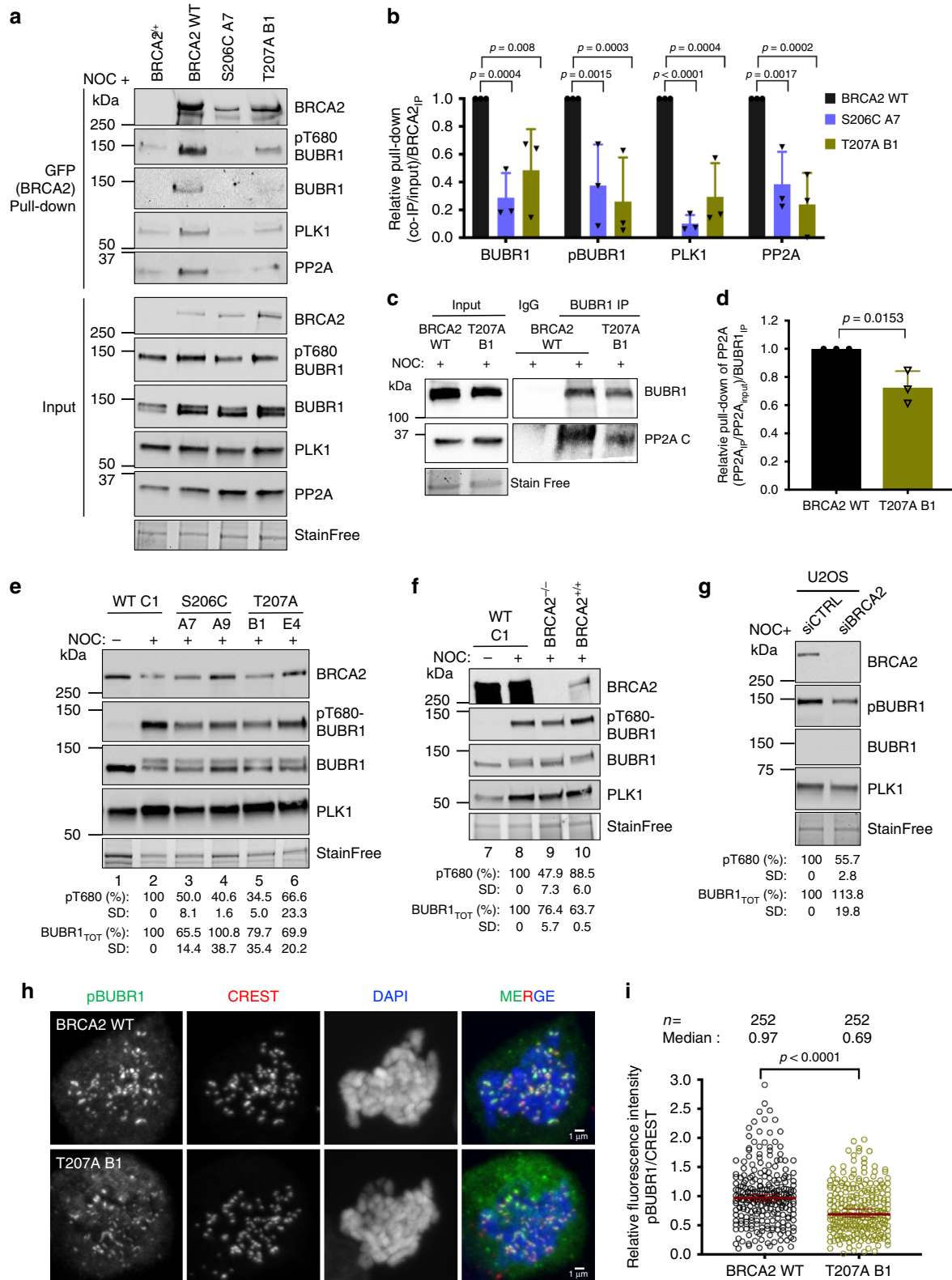


Fig. 6a, b), nor to an increased interaction of PLK1 with BUBR1 in the mutated cells (Supplementary Fig. 6c, d).

Together, these results strongly suggest that docking of PLK1 onto BRCA2 T207 facilitates the formation of a complex between phosphorylated BUBR1 and PP2A at the kinetochore that is essential for the stability of microtubule-kinetochore attachments with direct consequences in chromosome alignment. The fact that BUBR1-3D cannot rescue the phenotype

favors the hypothesis that BRCA2 is required for PP2A-BUBR1 interaction.

Reduced T207 phosphorylation lead to defects in chromosome segregation. Unresolved chromosome misalignment as observed in cells altering BRCA2 phosphorylation by PLK1 is expected to drive chromosome missegregation. To find out if this was the case

Fig. 5 S206C and T207A impair the complex of BRCA2 with PLK1-BUBR1-PP2A and reduce the levels of pBUBR1 at the kinetochore. **a** Pull-down of BRCA2 using GFP-trap beads from mitotic cell extracts of cells bearing BRCA2 WT cells or the variant S206C and T207A. Complexes containing BRCA2-BUBR1/pBUBR1-PP2A-PLK1 were detected by 4–15% SDS-PAGE followed by WB using anti-BRCA2, -BUBR1, -pT680-BUBR1, -PLK1 and -PP2AC (PP2A catalytic subunit) antibodies. Mitotic BRCA2^{+/+} cells were used as control pull-down. **b** Quantification of co-immunoprecipitated BUBR1, pBUBR1, PLK1 and PP2A with EGFPMBP-BRCA2 in **(a)**, relative to the input levels of each protein and the amount of pull-down EGFP-MBP-BRCA2. Results are presented as the fold change compared to the BRCA2 WT clone. The data represent the mean \pm SD of three independent experiments. Two-way ANOVA test with Dunnett's multiple comparisons test was used to calculate statistical significance of differences. **c** IP of endogenous BUBR1 from mitotic cell extracts of BRCA2 WT cells or BRCA2-T207A using mouse anti-BUBR1 antibody. Mouse IgG was used as control. 4–15% SDS-PAGE followed by WB using rabbit anti-BUBR1 and anti-mouse PP2AC antibodies. **d** Quantification of co-IPed PP2A in **(c)**, relative to the input levels and the amount of IPed BUBR1. Results are presented as the fold change compared to the BRCA2 WT clone. The data represent the mean \pm SD of three independent experiments. Unpaired two-tailed *t*-test was used to calculate statistical significance of differences. **e–g** WB showing the protein levels of endogenous BUBR1 and pT680-BUBR1 in nocodazole treated cells bearing BRCA2 WT or the variants, as indicated **(e)** BRCA2^{-/-} or BRCA2^{+/+} **(f, g)** WB showing the protein levels of endogenous BUBR1 and pT680-BUBR1 in U2OS after depletion of endogenous BRCA2 by siRNA. **e–g** The mean BUBR1_{TOT} and pBUBR1 signal relative to the stain free signal is shown for the nocodazole treated samples below the blots, results are presented as percentage compared to BRCA2 WT clone. The data represent the mean \pm SD of three **(e)** and two **(f and g)** independent experiments. The protein levels of PLK1 in **(a, e–g)** are shown as a G2/M marker. **h** Representative images of the localization of pT680-BUBR1 in cells bearing BRCA2 WT or the variant T207A as indicated. CREST is used as centromere marker and DNA is counterstained with DAPI. Scale bar represents 1 μ m. **i** Quantification of the co-localization of pT680-BUBR1 and CREST in **(h)**. The data represent the intensity ratio (pT680-BUBR1:CREST) relative to the mean ratio of pT680-BUBR1:CREST for the GFP-MBP-BRCA2 WT calculated from two independent experiments (252 pairs of chromosomes analyzed). The red line in the plot indicates the median (95% CI) ratio, each dot represents a pair of chromosomes. Mann-Whitney two-tailed analysis was used to calculate statistical significance of differences. Source data are available as a Source Data file.

in cells expressing BRCA2 variants S206C and T207A, we examined chromosome segregation by immunofluorescence in cells synchronized by double-thymidine block and released for 15 h to enrich the cell population at anaphase/telophase stage (Fig. 7d). BRCA2^{-/-} cells displayed, as expected, an increased proportion of chromosome bridges (39% vs 16% in cells expressing BRCA2 WT), whereas the fraction of lagging chromosomes was only mildly increased (7% vs 4% in BRCA2 WT). The percentage of chromosome bridges in cells expressing S206C and T207A was moderately increased (23% and 29%, respectively, compared to 16% in BRCA2 WT). However, the biggest difference was observed in the percentage of lagging chromosomes increasing between 3- and 5-fold in the cells bearing the variants compared to the BRCA2 WT cells (Fig. 7d, e).

Erroneous chromosome segregation generates aneuploid cells during cell division³⁰. Given the strong chromosome segregation defects observed in cells expressing S206C and T207A we next analyzed the number of chromosomes in these cells. Total chromosome counts carried out on metaphase spreads revealed that 37.1% of BRCA2 WT cells exhibited aneuploidy with chromosome losses or gains. In the case of S206C and T207A, this number was elevated to 52.2% and 61.8% of the cells, respectively (Fig. 8a). An example of the images analyzed can be found in Fig. 8b. As the number of chromosomes was difficult to assess for cells with high content of chromosome gains we arbitrarily discarded cells that contained more than 65 chromosomes. Thus, tetraploid cells were not included in this measurement. Therefore, we determined the frequency of tetraploid cells by assessing the incorporation of BrdU and measuring the frequency of S-phase cells with >4N DNA content (Fig. 8c). The frequency of tetraploidy in cells bearing the variants was <1% of the total population as in the BRCA2 WT cells (Fig. 8d), and the number of BrdU positive cells was also equivalent (Supplementary Fig. 7).

Together, these results indicate that, in addition to the severe chromosome misalignment phenotype, cells expressing S206C and T207A display high frequency of chromosome missegregation, including a strong induction of lagging chromosomes and a mild increase in chromosome bridges. As a consequence, the incidence of aneuploidy, but not tetraploidy, is greatly exacerbated in these cells.

The variants reducing PLK1 phosphorylation of BRCA2 do not alter HR. Since BRCA2 has a major role in DNA repair by HR,

the prolonged mitosis observed in the VUS-expressing stable cell lines (Fig. 4) could result from checkpoint activation through unrepaired DNA. Thus, we performed a clonogenic survival assay in the stable clones after treatment with mitomycin C (MMC), an inter-strand crosslinking agent to which BRCA2 deficient cells are highly sensitive^{32–35}. As expected, BRCA2 deficient cells (BRCA2^{-/-}) showed hypersensitivity to MMC treatment whereas BRCA2 WT cells complemented this phenotype almost to the same levels as the cells expressing the endogenous BRCA2 (BRCA2^{+/+}). Cells bearing variants S206C and T207A also complemented the hypersensitive phenotype of BRCA2^{-/-} cells, although there was a mild effect compared to the BRCA2 WT cells (Fig. 9a). These results suggest that the delay in mitosis is not a consequence of checkpoint activation via unrepaired DNA.

Cells expressing VUS S206C and T207A showed a growth defect manifested in a reduced number of colonies (Supplementary Fig. 8a). To exclude a possible bias arising from the different ability to form colonies we used MTT assay. As shown in Fig. 9b, cells expressing S206C and T207A showed similar relative viability upon MMC treatment compared to BRCA2 WT cells or BRCA2^{+/+}, confirming our results. Similarly, the viability upon treatment with the poly (ADP-ribose) polymerase inhibitor (PARPi) Olaparib was not affected in cells bearing the variants (Fig. 9c).

To determine directly the levels of spontaneous DNA damage in these cells and their ability to form DNA repair foci, we measured the number of nuclear foci of the DSB marker γ H2AX and RAD51 protein, in cells unchallenged (–IR) or 2 h after exposure to ionizing radiation (6 Gy, (+IR)). Our results show that in the absence of DNA damage, the number of γ H2AX foci or RAD51 foci is comparable in all cell lines including in cells depleted of BRCA2 (Fig. 9d and Supplementary Fig. 8b); this is probably due to the high genome instability intrinsic to these cancer cells. In contrast, the number of RAD51 foci upon irradiation increased 5-fold in BRCA2^{+/+} and BRCA2 WT cells and 3-fold in T207A bearing cells while it remained low in BRCA2 depleted cells, as expected (Fig. 9e). We conclude that the DNA repair foci are only mildly altered in cells expressing T207A. Representative images of these experiments are shown in Supplementary Fig. 8b.

A typical feature of replication stress is the appearance of micronuclei in daughter cells which generally contain DNA fragments. In contrast, micronuclei with centromeres suggest an event arising from lagging chromosomes involving whole chromosomes or chromatids. BRCA2 deficient cells displayed

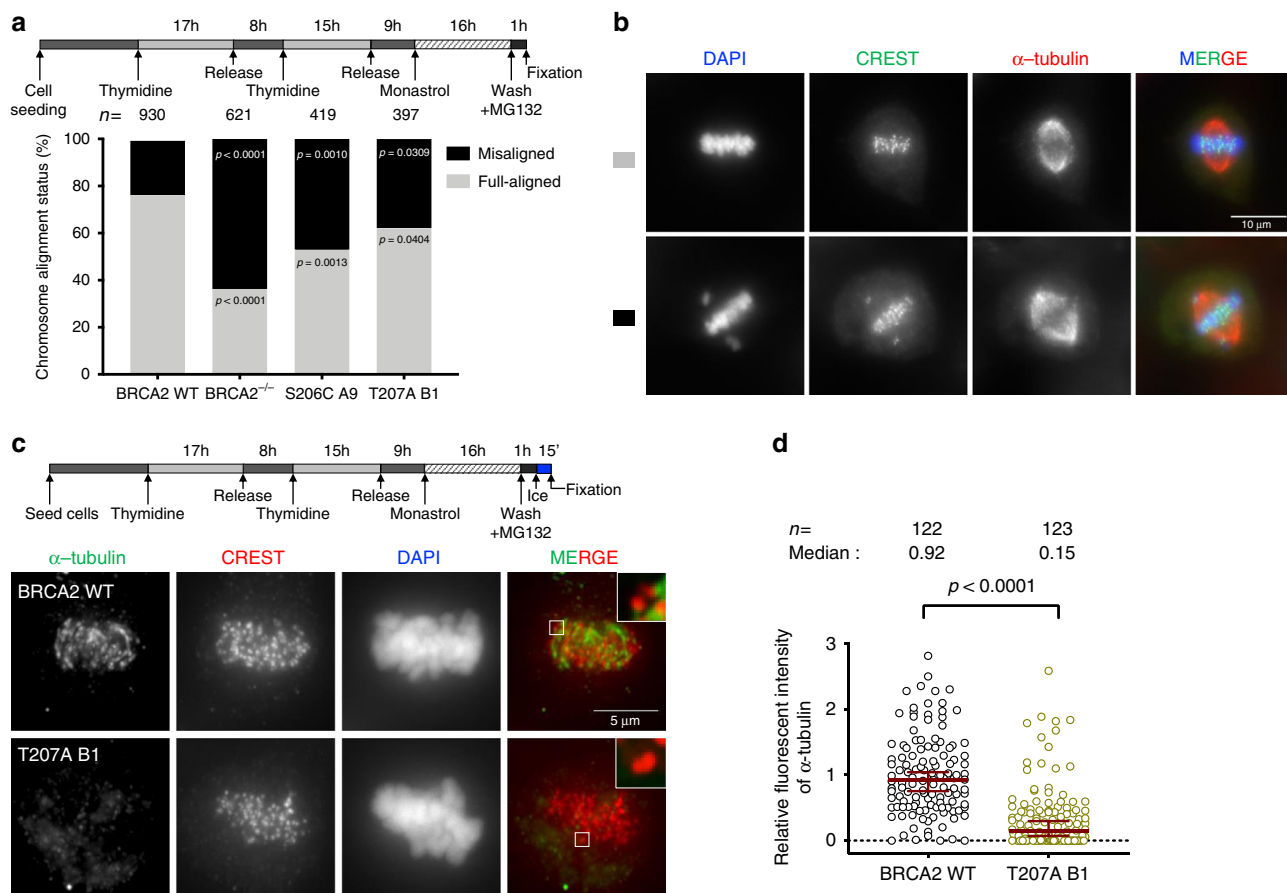


Fig. 6 Cells expressing BRCA2 variants S206C and T207A display reduced stability of kinetochore-microtubule attachments and misaligned chromosomes. **a** Top: Scheme of the double thymidine block procedure used to synchronize the DLD1 cells for the analysis of chromosome alignment. Bottom: Quantification of misaligned chromosomes outside the metaphase plate in DLD1 BRCA2 deficient cells (BRCA2^{-/-}) and BRCA2^{-/-} cells stably expressing BRCA2 WT or the S206C and T207A variants. *n* indicates the total number of cells counted for each clone from two (BRCA2^{-/-}, S206C, and T207A) and four (BRCA2 WT) independent experiments. Statistical significance of the difference was calculated with unpaired two-way ANOVA test with Tukey’s multiple comparisons test, the *p*-values show the significant differences. **b** Representative images of the type of chromosome alignment observed in cells quantified in **(a)**, scale bar represents 10 μm. **c** Top: Scheme of the synchronization procedure for the analysis of cold stable microtubules in the BRCA2-WT and T207A stable clones. Bottom: Representative images of cold stable microtubules in cells expressing BRCA2 WT or the T207A variant. Cells treated according to the scheme were co-stained with α-tubulin and CREST, as centromere marker and DNA was counterstained with DAPI. Scale bar represents 5 μm. A zoom-in inset in the images show representative kinetochore-microtubule attachments in each cell line. **d** Quantification of the relative intensity of α-tubulin normalized to the one in BRCA2 WT cells in **(c)**. The data represent the results from two independent experiments from a total of 122 (WT) and 123 (T207A) cells. The red line in the plot indicates the median intensity (95% CI), each dot representing the intensity for one cell. For statistical comparison of the differences between the samples we applied Mann-Whitney two-tailed analysis, the *p*-values show significant differences. Source data are available as a Source Data file.

an increased number of both types of micronuclei compared to BRCA2 WT cells. In contrast, cells bearing S206C or T207A variant did not change the number of micronuclei (Supplementary Fig. 8d, e) excluding strong replication stress-induced DNA damage in these cells.

Finally, to directly assess the HR proficiency, we performed a cell-based HR assay by DSB-mediated gene targeting using a site-specific transcription-activator like effector nuclease (TALEN) and a promoter-less mCherry donor flanked by homology sequence to the targeted locus³⁶. DSB-mediated gene targeting results in mCherry expression from the endogenous promoter (Fig. 9f) which can be measured by flow cytometry (Supplementary Fig. 9). Using this system, BRCA2^{+/+} and BRCA2 WT cells showed ~5% of mCherry positive TALEN-transfected cells (mean of 5.6% for BRCA2^{+/+} and 4.9% for WT) whereas BRCA2^{-/-} exhibited reduced mCherry expressing cells (1.8%), as expected. Importantly, TALEN-transfected cells expressing BRCA2 variants S206C and T207A showed no significant difference with the BRCA2 WT.

In summary, these results indicate that the role of BRCA2 in conjunction with PLK1 in mitosis is likely independent of the HR function of BRCA2 as the variants S206C and T207A affecting PLK1 phosphorylation of BRCA2 are only mildly sensitive to DNA damage, do not show an increased number of micronuclei, are able to recruit RAD51 to DNA damage sites (as shown for T207A) and are efficient at DSB-mediated gene targeting.

Discussion

Our results demonstrate that residues S193 and T207 of BRCA2 can be efficiently phosphorylated by PLK1 (Fig. 2), thus extending the consensus sequence for phosphorylation by this kinase: position 205 is a serine and not a negatively charged residue, as generally observed at PLK1 phosphorylation sites²³. Moreover, pT207 constitutes a bona fide docking site for PLK1_{PBD} (Fig. 3h–l) that is phosphorylated in mitotic cells (Fig. 4a). Accordingly, BRCA2 missense VUS reducing the phosphorylation

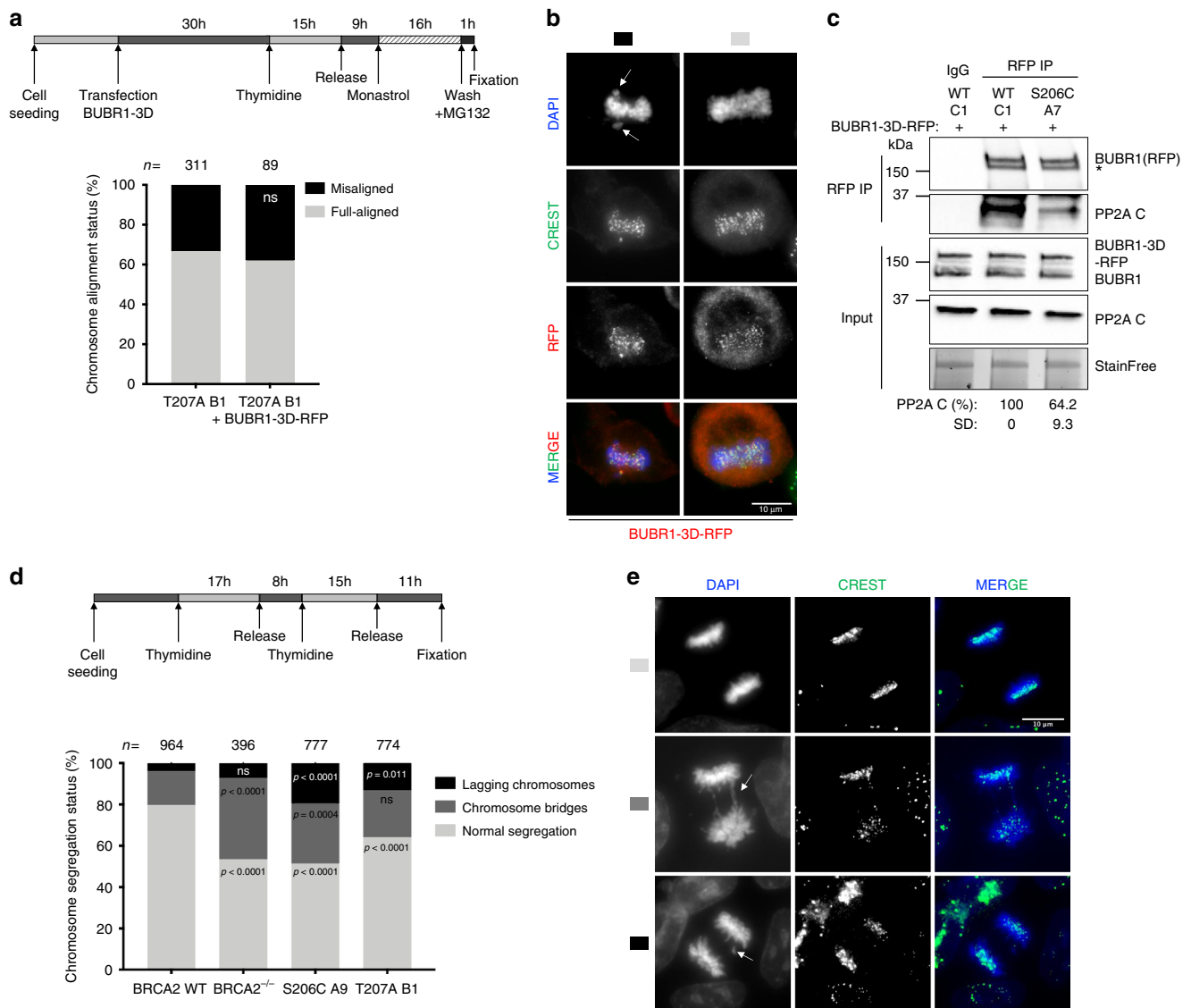
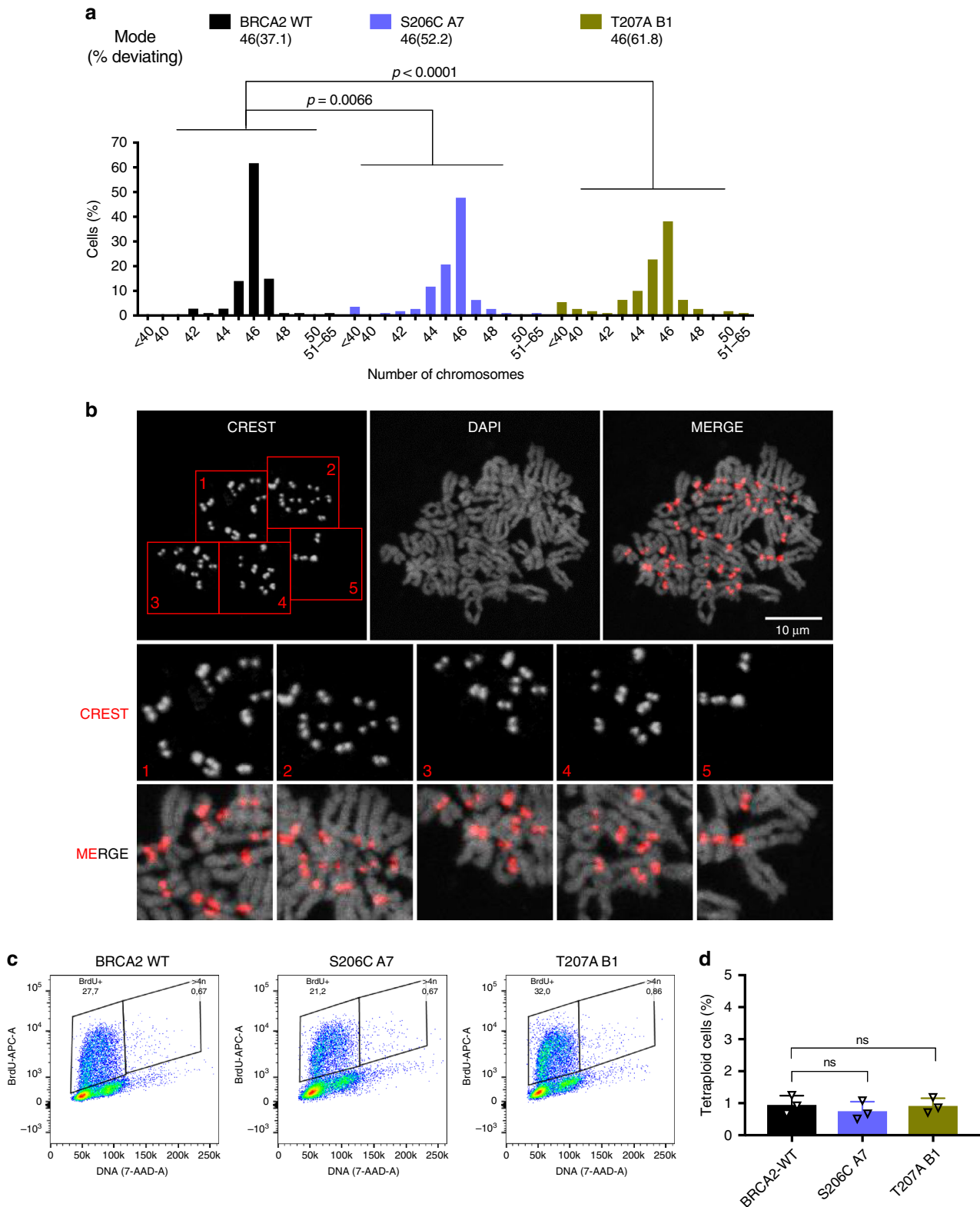


Fig. 7 Cells expressing BRCA2 variants S206C and T207A display aberrant chromosome segregation. **a** Top: Scheme of the synchronization procedure. Bottom: Quantification of misaligned chromosomes in BRCA2-T207A stable clones transiently overexpressing the 3xFLAG-BUBR1-3D-RFP mutant (S670D, S676D and T680D). *n* indicates the total number of cells counted from two independent experiments. Unpaired two-tailed *t*-test was used to calculate statistical significance of differences, ns (non-significant). **b** Representative images of the type of chromosome alignment observed in cells overexpressing 3xFLAG-BUBR1-3D-RFP quantified in (**a**); scale bar represents 10 μm. **c** Co-immunoprecipitation of endogenous PP2A with transiently overexpressed 3xFLAG-BUBR1-3D-RFP mutant from mitotic cell extracts of BRCA2 WT cells or cells bearing the S206C variant using rabbit anti-RFP antibody. Rabbit IgG was used as control for the BUBR1 immunoprecipitation. The immunocomplexes were resolved on 4–15% SDS-PAGE followed by WB using mouse anti-BUBR1 and PP2AC antibodies. The amount of PP2A co-immunoprecipitated with BUBR1-3D-RFP relative to the input levels of PP2A and the amount of immunoprecipitated BUBR1-3D-RFP is presented below the blot as mean ± SD from two independent experiments. The data are presented relative to the non-treated BRCA2 WT. Asterisk denotes a non-specific band (**d**). Top: Scheme of the synchronization procedure. Bottom: Quantification of cells with aberrant chromosome segregation in BRCA2^{-/-} cells and in the clones stably expressing BRCA2 WT, S206C and T207A, as indicated. Two-way ANOVA test with Tukey's multiple comparisons test was used to calculate statistical significance of differences (the *p*-values show the significant differences compared to WT; ns (non-significant)). *n* in (**d**) indicates the total number of cells counted for each clone from two (BRCA2^{-/-}, S206C and T207A) and five (BRCA2 WT) independent experiments. **e** Representative images of the type of aberrant chromosome segregation observed in the cells quantified in (**d**), CREST antibody is used as marker of centromere; nuclei are revealed with DAPI counterstaining. Scale bar represents 10 μm. Source data are available as a Source Data file.

status of T207 (T207A, S206C) result in a decrease in BRCA2-PLK1 interaction (Fig. 3a–k, 4b). Cells expressing these two breast cancer variants in a BRCA2 deficient background display defective chromosome congression (Fig. 6a, b) to the metaphase plate due to a reduced microtubule–kinetochore stability (Fig. 6c, d), causing a substantial delay in mitosis progression (Fig. 4d–f).

Proper kinetochore–microtubule attachments require the interaction of BUBR1 with the phosphatase PP2A-B56 to balance

Aurora B kinase activity^{19,21}. This interaction is mediated through the phosphorylation of the KARD motif of BUBR1 by PLK1. BRCA2 does not alter PLK1 interaction with BUBR1 (Supplementary Fig. 6c, d). However, we found that BRCA2 forms a tetrameric complex with PLK1-pBUBR1-PP2A, and that this complex is strongly reduced in cells bearing BRCA2 variants S206C and T207A (Fig. 5a, b). Furthermore, cells bearing BRCA2 variants S206C and T207A show reduced overall levels of BUBR1



including pBUBR1(pT680) at the kinetochore (Fig. 5i). Importantly, the fact that in the BRCA2 mutated cells the interaction of PP2A with total BUBR1 is reduced (Fig. 5c, d) and that neither this interaction (Fig. 7c) nor the chromosome alignment defect can be rescued by BUBR1-3D overexpression (Fig. 7a, b) strongly suggests that PP2A needs to be in complex with PLK1-bound BRCA2 to bind BUBR1 and facilitate stable kinetochore-microtubules attachment for proper chromosome alignment.

Cells bearing T207A and S206C variants display chromosome segregation errors including lagging chromosomes and chromosome bridges (Fig. 7d, e). Importantly, these accumulated errors ultimately led to a broad spectrum of chromosome gains and losses (aneuploidy) compared to the wild type counterpart (Fig. 8a), but not to tetraploid cells (Fig. 8c, d), suggesting that cytokinesis per se, in which BRCA2 is also involved¹¹⁻¹³, is not affected.

Fig. 8 Cells expressing BRCA2 variants S206C and T207A exhibit aneuploidy. **a** Distribution of the number of chromosomes observed in metaphase spreads of stable clones expressing BRCA2 WT, S206C A7 or T207 B1, total number of cells counted; BRCA2 WT ($n = 105$), S206C A7 ($n = 111$) and T207A B1 ($n = 110$) from two independent experiments. Modal number of chromosomes and percentage deviating from the mode are shown at the top. Kruskal-Wallis one-way analysis followed by Dunn's multiple comparison test was used to calculate statistical significance of differences. The cell passage was between 5 and 9 (BRCA2 WT (p.6 and p.9), S206C A7 (p.5 and p.9) and T207A B1 (p.6 and p.9)). **b** Representative image of two independent experiments of metaphase spreads of the DLD1 BRCA2 deficient stable cells bearing the S206C BRCA2 variant stained with CREST and counterstained with DAPI. In this example, the cell contains 45 chromosomes. **c-d** Analysis of S-phase tetraploid cells in cells bearing BRCA2 WT or the VUS S206C and T207A measured by flow cytometry after 20 min of BrdU incorporation. **c** Representative flow cytometry plots of cells stained with anti-BrdU-APC antibodies and 7-AAD (DNA). **d** Frequency of S-phase tetraploid cells in stable clones expressing BRCA2 WT or the VUS S206C and T207A. The data represents the mean \pm SD of three independent experiments (cell passage: 6–10). One-way ANOVA test with Tukey's multiple comparisons test was used to calculate statistical significance of differences (the p -values show the difference compared to WT, ns: non-significant). Source data are available as a Source Data file.

Finally, the function of BRCA2-PLK1 interaction in mitosis seems to be independent of the HR function of BRCA2 as cells expressing these variants display mild sensitivity to DNA damage (MMC) and PARP inhibitors (Fig. 9a–c), normal recruitment of RAD51 to DNA damage sites (Fig. 9e, Supplementary Fig. 8b), absence of micronuclei (Supplementary Fig. 8d, e), rescue the chromosome bridges phenotype of BRCA2 deficient cells (Fig. 7d) and their HR activity, as measured by a DSB-mediated gene targeting assay (Fig. 9f, Supplementary Fig. 9). Nevertheless, we cannot rule out that the mild phenotype observed in cells bearing S206C and T207A may arise from a disrupted interaction with an unknown DNA repair factor that would bind to the region of BRCA2 where these variants localize.

Putting our results together we reveal an unexpected chromosome stability control mechanism that depends on the phosphorylation of BRCA2 by PLK1 at T207. We show that BRCA2 pT207 is a docking platform for PLK1 that ensures the efficient interaction of BUBR1 with PP2A phosphatase required for chromosome alignment. We propose the following working model (Fig. 9g): in cells expressing BRCA2 WT, PLK1 phosphorylates BRCA2 on T207 leading to the docking of PLK1 at this site. This step promotes the formation of a complex between BRCA2-PLK1-pBUBR1-PP2A in prometaphase at the kinetochore, leading to an enrichment of phosphorylated BUBR1 and the phosphatase PP2A to balance Aurora B activity (Fig. 9g, panel 1). Why is BRCA2 required for PP2A interaction with pBUBR1 and, is this regulated by PLK1? It has been reported that BRCA2 fragment from aa 1001 to aa 1255 (BRCA2₁₀₀₁₋₁₂₅₅) comprising a PP2A-B56 binding motif, binds to the B56 subunit of PP2A; in addition, the phosphorylation of positions 2 and 8 of this motif enhances the binding to B56³⁷. In BRCA2, these positions are occupied by serines that are targets for PLK1. Therefore, it is likely that the recruitment of PLK1 by BRCA2 T207 would favor phosphorylation of BRCA2₁₀₀₁₋₁₂₅₅ and binding of the complex between BRCA2 and PLK1 to PP2A-B56. Non-exclusively, BUBR1 has been reported to bind directly BRCA2 although there are inconsistencies regarding the site of interaction^{4,5}. Thus, either the direct interaction of BRCA2 with PP2A or with BUBR1 or both could be favoring the formation of a complex between PP2A and pBUBR1.

In cells expressing the variants that impair T207 phosphorylation (S206C, T207A), PLK1 cannot be recruited to pT207-BRCA2, impairing the formation of the complex with PLK1, PP2A and BUBR1 (Fig. 9g, panel 1'), which in turn reduces the amount of pBUBR1 and its binding to PP2A for stable kinetochore–microtubule interactions. This leads to chromosome misalignment defects that prolong mitosis (Fig. 9g, panel 2'); as a consequence, these cells exhibit increased chromosome segregation errors (Fig. 9g, panel 3') and aneuploidy.

Although the individual BRCA2 variants analyzed here are rare (Supplementary table 1), the majority of pathogenic mutations recorded to date lead to a truncated protein either not expressed

or mislocalized³⁸ which would be predicted to affect this function. Consistent with this idea, the BRCA2 deficient cells or cells transiently depleted of BRCA2 used in this study exhibit low levels of phosphorylated BUBR1 (Fig. 5f, g). Thus, the chromosome alignment function described here could be responsible, at least in part, for the numerical chromosomal aberrations observed in BRCA2-associated tumors³⁹.

Finally, the lack of sensitivity to the PARP inhibitor Olaparib observed in our cell lines (Fig. 9c) has important clinical implications as breast cancer patients carrying these variants are not predicted to respond to PARP inhibitor treatment (unlike BRCA2-mutated tumors that are HR-deficient).

Methods

Cell lines, cell culture, and synchronizations. The human cell lines HEK293T and U2OS cells (kind gift from Dr. Mounira Amor-Gueret) were cultured in DMEM (Eurobio Abcys, Courtaboeuf, France) media containing 25 mM sodium bicarbonate and 2 mM L-Glutamine supplemented with 10% heat inactive FCS (EuroBio Abcys). The BRCA2 deficient colorectal adenocarcinoma cell line DLD1 BRCA2^{-/-} (Hucl, T. et al 2008) (HD 105-007) and the parental cell line DLD1 BRCA2^{+/+} (HD-PAR-008) was purchased from Horizon Discovery (Cambridge, England). In DLD1 BRCA2^{-/-} cell line, both alleles of BRCA2 contain a deletion in exon 11 causing a premature stop codon after BRC5 and cytoplasmic localization of a truncated form of the protein⁴⁰. The cells were cultured in RPMI media containing 25 mM sodium bicarbonate and 2 mM L-Glutamine (EuroBio Abcys) supplemented with 10% heat inactive FCS (EuroBio Abcys). The DLD1 BRCA2^{-/-} cells were maintained in growth media containing 0.1 mg/ml hygromycin B (Thermo Fisher Scientific). The stable cell lines of DLD1^{-/-} BRCA2 deficient cells expressing BRCA2 WT or variants of interest generated in this study were cultured in growth media containing 0.1 mg/ml hygromycin B and 1 mg/ml G418 (Sigma-Aldrich). All cells were cultured at 37 °C with 5% CO₂ in a humidified incubator and all cell lines used in this study have been regularly tested negatively for mycoplasma contamination.

For synchronization of cells in mitosis, nocodazole (100–300 ng/ml, Sigma-Aldrich) was added to the growth media and the cells were cultured for 14 h before harvesting. For synchronization by double thymidine block, the cells were treated with thymidine (2.5 mM, Sigma-Aldrich) for 17 h, released for 8 h followed by a second thymidine (2.5 mM) treatment for 15 h.

Plasmids. 2XMBP-, human 2XMBP-BRCA2₁₋₂₅₀ and EGFP-MBP-BRCA2 sub-cloning in pHCMV1 expression vector were generated as described^{41–48}. In the case of 2XMBP and 2XMBP-BRCA2₁₋₂₅₀, a tandem of 2 nuclear localization signals from RAD51 sequence was added downstream the MBP-tag.

Point mutations (M192T, S193A, S196N, S206C, and T207A) were introduced in the 2xMBP-BRCA2₁₋₂₅₀, EGFP-MBP-BRCA2 vector using QuikChange II and QuikChange XL site-directed mutagenesis kit (Agilent Technologies), respectively (see Supplementary Tables 3, 4 for primer sequences).

For expression of BRCA2₄₈₋₂₁₈ in bacteria, an optimized gene coding for human His-tagged BRCA2₄₈₋₂₁₈ (WT and T207A) was synthesized by Genscript and cloned in a pETM13 vector (a TEV site being present between the tag and the BRCA2 fragment). For expression of BRCA2₁₉₀₋₂₈₄ in bacteria, the human BRCA2₁₉₀₋₂₈₄ was amplified by PCR using full-length BRCA2 as template (pHCMV1-2xMBP-BRCA2, see Supplementary Table 5 for primer sequences). The PCR product was purified and digested with *Bam*HI and *Sall* and cloned into the pGEX-6P-1 vector (GE Healthcare) to generate GST-BRCA2₁₉₀₋₂₈₄. The point mutation T207A was introduced in the same way in BRCA2₁₉₀₋₂₈₄ as in 2xMBP-BRCA2₁₋₂₅₀ and the EGFP-MBP-BRCA2. The introduction of the point mutation was verified by sequencing (see Supplementary Tables 3, 4 for primer sequences).

The *PLK1* cDNA (Addgene pTK24) was cloned into the pFast-Bac HT vector using Gibson assembly (NEB) (see Supplementary Table 6 for primer sequences).

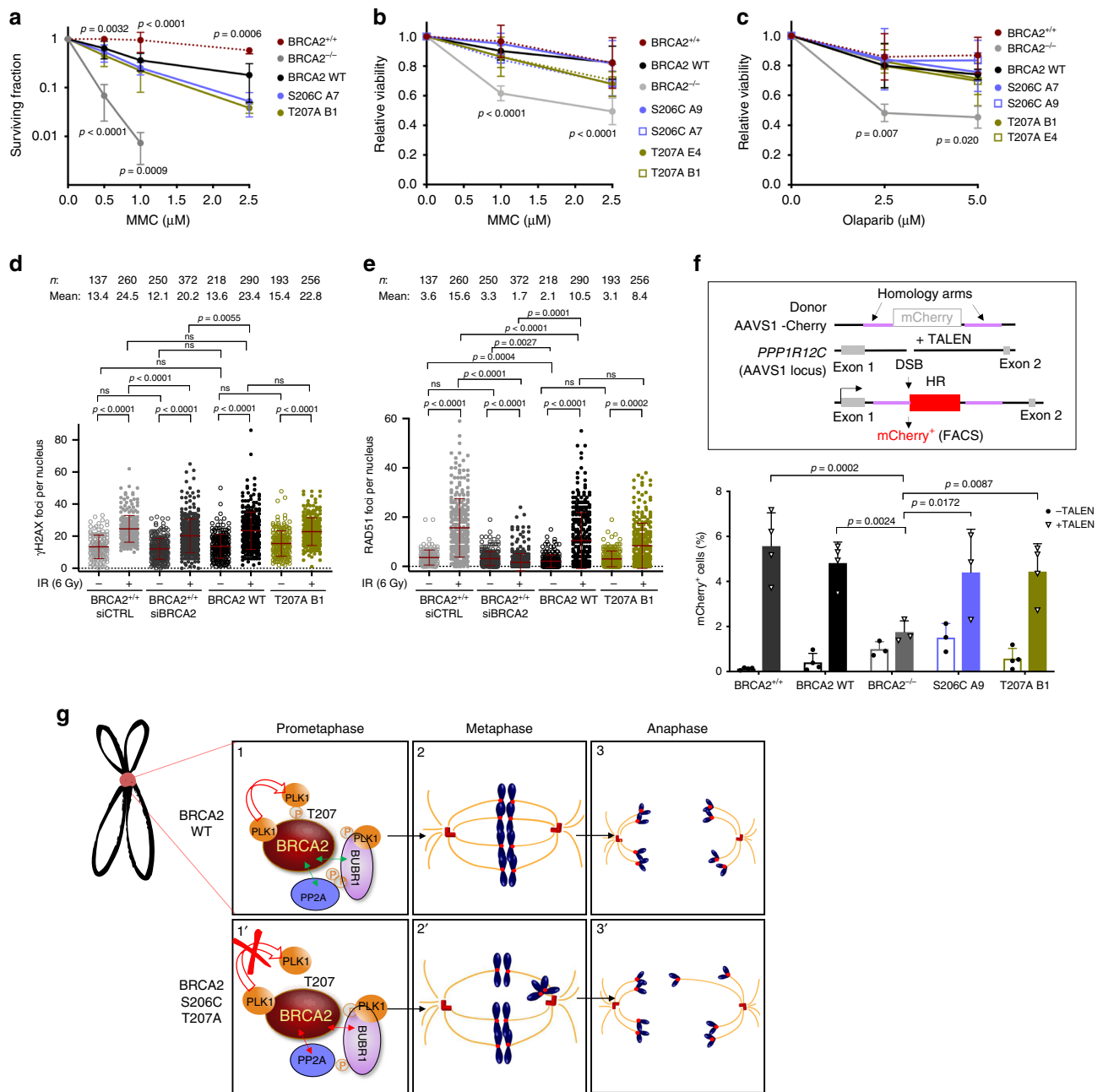


Fig. 9 The DNA repair proficiency is not affected in cells bearing BRCA2 variants S206C and T207A. **a** Quantification of the surviving fraction of BRCA2^{+/+} or stable clones expressing BRCA2 WT or the variants S206C or T207A assessed by clonogenic survival upon exposure to MMC at concentrations: 0, 0.5, 1.0, and 2.5 μM. Data are represented as mean ± SD: BRCA2^{+/+} (red) ($n = 3$), BRCA2^{-/-} (gray) ($n = 6$), WT C1 (black) ($n = 6$), S206C A7 (blue) ($n = 3$), T207A B1 (green) ($n = 4$). **b–c** Quantification of the relative cell viability monitored by MTT assay upon treatment with increasing doses of MMC (**b**) or the PARP inhibitor Olaparib (**c**), as indicated. The data represent the mean ± SD of four (**b**) and three (**c**) independent experiments. **a–c** Two-way ANOVA test with Tukey’s multiple comparisons test was used to calculate statistical significance of differences (the p -values show the significant differences compared to the BRCA2 WT clone). **d–e** Quantification of the number of γ H2AX foci (**d**) or RAD51 foci per nucleus (**e**) 2 h after 6 Gy of γ -irradiation (+IR) versus non-irradiated conditions (-IR), in DLD1 BRCA2^{+/+} cells depleted of BRCA2 (siBRCA2) or control cells (siCTRL) or cells bearing BRCA2 WT or the variant T207A. n indicates the total number of cells counted from two independent experiments. Kruskal-Wallis one-way analysis followed by Dunn’s multiple comparison test was used to calculate statistical significance of differences. The red line in the plot indicates the mean ± SD, each dot represents a single focus. **f** Top: Scheme of the DSB-mediated gene targeting HR assay. Bottom: Frequency of mCherry positive cells in cells transfected with the promoter-less donor plasmid (AAVS1-2A-mCherry) without (-TALEN) or with (+TALEN) nucleases. The error bars represent mean ± SD of three to four independent experiments (BRCA2^{+/+} ($n = 4$), WT ($n = 4$), BRCA2^{-/-} ($n = 3$), S206C A9 ($n = 3$), T207A B1 ($n = 4$)). Two-way ANOVA test with Tukey’s multiple comparisons test. **g** Model for the role of PLK1 phosphorylation of BRCA2 T207A by PLK1 in mitosis (see text for details). In panel 1 and 1’ the two-sided arrows represent a complex between the two proteins as indicated either favored by BRCA2 WT (green) or impaired in the BRCA2 mutated form (red); in panels 2, 2’, 3 and 3’ blue blobs represent chromosomes, red circles represent the kinetochores, red cylinders represent the centrioles and orange lanes represent the spindle microtubules. Source data are available as a Source Data file.

To produce PLK1-KD, the point mutation K82R was introduced in the pFast-Bac HT-PLK1 vector using QuikChange XL site-directed mutagenesis kit (see Supplementary Table 7 for primer sequences).

The Polo-like binding domain (PBD) of PLK1 (amino acid 326 to amino acid 603) was amplified from the pTK24 plasmid (Addgene) and cloned into a pT7-His6-SUMO expression vector using NEB Gibson assembly (Gibson Assembly Master Mix, New England Biolabs, Cat. #E2611S) (see Supplementary Table 7 for primer sequences). A plasmid containing a smaller PLK1 PBD fragment (amino acid 365 to amino acid 603) with a N-terminal GST tag was a kind gift from Dr. Anne Houdusse (Institute Curie, Paris).

To produce the phosphomimic BUBR1 mutant, we introduced the S670D, S676D and T680D point mutations in the pcDNA3-3xFLAG-BUBR1-RFP construct (kind gift from Dr. Geert JPL Kops) using QuikChange XL site-directed mutagenesis kit (see Supplementary Table 8 for primer sequences).

For the DSB-gene targeting assay, we replaced the GFP tag in the promoter-less AAVS1-2A-GFP-pA plasmid (kind gift from Dr. Carine Giovannangeli) with the mCherry tag from the pET28 mCherry plasmid using NEB Gibson Assembly (Gibson Assembly Master Mix, New England Biolabs, Cat. #E2611S). See Supplementary Table 11 for primer sequences.

Expression and purification of 2xMBP-BRCA2₁₋₂₅₀. The 2xMBP-BRCA2₁₋₂₅₀ was purified as previously described⁴⁹. Briefly, ten 150 mm plates of HEK293T were transiently transfected with the 2xMBP-BRCA2₁₋₂₅₀ using TurboFect (Thermo Fisher Scientific). The cells were harvested 30 h post-transfection, lysed in lysis buffer H (50 mM HEPES (pH 7.5), 250 mM NaCl, 1% NP-40, 5 mM EDTA, 1 mM DTT, 1 mM PMSF and EDTA-free Protease Inhibitor Cocktail (Roche)) and incubated with amylose resin (NEB) for 3 h at 4 °C. The 2xMBP-BRCA2₁₋₂₅₀ was eluted with 10 mM maltose. The eluate was further purified with Bio-Rex 70 cation-exchange resin (Bio-Rad) by NaCl step elution. The size and purity of the final fractions were analyzed by SDS-PAGE and western blotting using anti-MBP antibody. The 2xMBP-BRCA2₁₋₂₅₀ fragments containing the BRCA2 variants (M192T, S193A, S196N, S206C, and T207A) were purified following the same protocol as for WT 2xMBP-BRCA2₁₋₂₅₀.

Expression and purification of BRCA2₄₈₋₂₁₈ and BRCA2₁₉₀₋₂₈₄ for NMR. Recombinant ¹⁵N-labeled (WT, T207A) and ¹⁵N/¹³C-labeled (WT) BRCA2₄₈₋₂₁₈ were produced by transforming *Escherichia coli* BL21 (DE3) Star cells with the pETM13 vector containing human BRCA2₄₈₋₂₁₈ (WT and T207A). Recombinant ¹⁵N-labeled (WT, T207A) and ¹⁵N/¹³C-labeled (WT, T207A) BRCA2₁₉₀₋₂₈₄ were produced by transforming *Escherichia coli* BL21 (DE3) Star cells with the pGEX-6P-1 vector containing human BRCA2₁₉₀₋₂₈₄ (WT and T207). Cells were grown in a M9 medium containing 0.5 g/l ¹⁵NH₄Cl and 2 g/l ¹³C-glucose when ¹³C labeling was needed. The bacterial culture was induced with 1 mM IPTG at an OD₆₀₀ of 0.8, and it was further incubated for 3 h at 37 °C. Harvested cells were resuspended in buffer A (50 mM Tris-HCl pH 8.0, 150 mM NaCl, 2 mM DTT, 1 mM EDTA) with 1 mM PMSF and 1X protease inhibitors cocktail (Roche) and disrupted by sonication. For BRCA2₄₈₋₂₁₈, clarified cell lysate was loaded onto Ni-NTA beads (Thermo Scientific) equilibrated with buffer A. After 1 h of incubation at 4 °C, beads were washed with buffer A containing 20 mM imidazole and eluted with buffer A containing 500 mM imidazole. The tag was cleaved by the TEV protease during a 2 hrs dialysis at 4 °C against 50 mM Tris-HCl pH 8.0, 150 mM NaCl, 1 mM EDTA 2 mM DTT. The sample was then boiled 10 min at 95 °C, spun down 5 min at 16,000 xg to remove thermosensitive contaminants and injected on Superdex 75 pg (GE Healthcare) equilibrated with 50 mM HEPES 1 mM EDTA pH 7.0. Sample concentration was calculated using its estimated molecular extinction coefficient of 9970 M⁻¹ cm⁻¹ at 280 nm. The protein sample was characterized for folding using NMR HSQC spectra, before and after the heating at 95 °C.

For BRCA2₁₉₀₋₂₈₄, clarified cell lysate was loaded onto Glutathione (GSH) Sepharose beads (GE Healthcare) equilibrated with buffer A. After 2 h of incubation at 4 °C, beads were washed with buffer A and eluted with buffer A containing 20 mM reduced glutathione. The tag was cleaved by the precision protease during an overnight dialysis at 4 °C against buffer B (50 mM HEPES pH 7.0, 1 mM EDTA) with 2 mM DTT and 150 mM NaCl. The cleaved GST-tag was removed by heating the sample for 15 min at 95 °C and spun it down for 10 min at 16,000g. Sample concentration was calculated using its estimated molecular extinction coefficient of 10,363 M⁻¹ cm⁻¹ at 280 nm. The protein sample was characterized for folding using NMR HSQC spectra, before and after the heating at 95 °C. BRCA2₁₉₀₋₂₈₄ was dialyzed overnight at 4 °C against buffer B with 2 mM DTT.

Expression and purification of PLK1 and PLK1-kinase dead (PLK1-KD). The recombinant 6xHis-PLK1 and 6xHis-PLK1-K82R mutant (PLK1-KD) were produced in sf9 insect cells by infection for 48 h (28 °C, 110 rpm shaking) with the recombinant baculovirus (PLK1-pFast-Bac HT vector). Infected cells were collected by centrifugation (1300 rpm, 10 min, 4 °C), washed with 1xPBS, resuspended in lysis buffer (1xPBS, 350 mM NaCl, 1% Triton X-100, 10% glycerol, EDTA-free Protease Inhibitor Cocktail (Roche), 30 mM imidazole). After 1 h rotation at 4 °C the lysate was centrifuged (25,000 rpm, 1 h, 4 °C) and the supernatant was collected, filtered (0.4 μm) and loaded immediately onto a Ni-NTA column (Macherey

Nagel) equilibrated with Buffer A1 (1xPBS with 350 mM NaCl, 10% glycerol and 30 mM imidazole), the column was washed with buffer A2 (1xPBS with 10% glycerol) and the protein was eluted with Buffer B1 (1x PBS with 10% glycerol and 250 mM imidazole). The eluted protein was diluted to 50 mM NaCl with Buffer A before being loaded onto a cationic exchange Capto S column (GE Healthcare) equilibrated with Buffer A1cex (50 mM HEPES (pH 7.4), 50 mM NaCl and 10% glycerol), the column was washed with Buffer A1cex before elution with Buffer B1cex (50 mM HEPES (pH 7.4), 2 M NaCl and 10% glycerol). The quality of the purified protein was analyzed by SDS-PAGE and the proteins concentration was determined using Bradford protocol with BSA as standard. The purest fractions were pooled and dialyzed against storage buffer (50 mM Tris-HCl (pH7.5), 150 mM NaCl, 0.25 mM DTT, 0.1 mM EDTA, 0.1 mM EGTA, 0.1 mM PMSF and 25% Glycerol) and stored in -80 °C. The purified proteins can be seen in Supplementary Fig. 10.

Expression and purification of PLK1_{PBD}. The pT7-6His-Sumo-PLK1 PBD (326-603) plasmid was expressed in Tuner pLacI pRare cells (Protein Expression and Purification Core Facility, Institut Curie), 2 L of TB medium with Kanamycin and Chloramphenicol antibiotics were inoculated with cells from the pre-culture. The cells were grown at 37 °C until an OD₆₀₀ of ~0.85. The temperature was decreased to 20 °C and the expression was induced by 1 mM IPTG overnight. The cells were harvested by 15 min of centrifugation at 4690g, at 4 °C. The cell pellets were suspended in 80 ml of 1 x PBS, pH 7.4, 150 mM NaCl, 10% glycerol, EDTA-free Protease Inhibitor Cocktail (Roche), 5 mM β-mercapto-ethanol (β-ME). The suspension was treated with benzonase nuclease and MgCl₂ at 1 mM final concentration for 20 min at 4 °C. The suspension was lysed by disintegration at 2 kbar (Cell disruptor T75, Cell D) followed by centrifugation at 43,000g, for 45 min, at 4 °C. The supernatant was loaded at 1 ml/min on a His-Trap FF-crude 5 mL column (GE Healthcare) equilibrated with PBS buffer, pH 7.4, 150 mM NaCl, 10% glycerol, 5 mM β-ME (A) and 20 mM imidazole. The proteins were eluted in a linear gradient from 0 to 100% with the same buffer (A) containing 200 mM imidazole, over 10 column volumes (CV). The purest fractions were pooled and dialyzed (8 kDa cut-off) against 20 mM Tris-HCl buffer, pH 8.0, 100 mM NaCl, 0.5 mM EDTA, 5 mM β-ME, 10% glycerol at 4 °C. 6xHis-SUMO Protease (Protein Expression and Purification Core Facility, Institut Curie) was added at 1/100 (w/w) and incubated overnight at 4 °C to cleave the 6His-SUMO tag. The cleaved PBD-PLK1 was purified using Ni-NTA agarose resin (Macherey Nagel), washed with the following buffer: 20 mM Tris-HCl pH 8.0, 100 mM NaCl, 0.5 mM EDTA, 5 mM β-ME and 10% glycerol. The sample was incubated with the resin for 1 h at 4 °C and the flow-through was collected. The sample was concentrated on an Amicon Ultra Centrifugal Filter Unit (10 kDa cut-off) and injected at 0.5 ml/min on a Hi-Load 16/60 Superdex column (GE healthcare), equilibrated with 20 mM Tris-HCl buffer, pH 8.0, 100 mM NaCl, 0.5 mM EDTA, 5 mM β-ME. The protein concentration was estimated by spectrophotometric measurement of absorbance at 280 nm. The purified protein is shown in Supplementary Fig. 10.

The GST-tagged PLK1_{PBD} (365-603) was expressed in *E. coli* BL21 (DE3) STAR cells, induced with 0.5 mM IPTG at an OD₆₀₀ of 0.6, and grown at 37 °C for 3 h. The PBD (365-603) was purified by glutathione affinity chromatography. After GST cleavage (using a 6His-TEV protease), the tag and the protease were retained using GST- and NiNTA-agarose affinity chromatography, and the PBD collected in the flow-through was further purified by gel filtration chromatography. The protein was dialyzed against a buffer containing 50 mM Tris-HCl pH 8, NaCl 150 mM, and 5 mM β-ME.

In vitro PLK1 kinase assay. 0.5 μg purified 2xMBP-BRCA2₁₋₂₅₀ or 25 ng RAD51 protein, was incubated with recombinant active PLK1 (0, 50 or 100 ng) or PLK1-kinase dead (100 ng) (purchased from Abcam or purified from sf9 insect cells as detailed above, see Figure EV11B for the comparison of the kinase activity of both PLK1 preparations) in kinase buffer (25 mM HEPES, pH 7.6, 25 mM β-glycerophosphate, 10 mM MgCl₂, 2 mM EDTA, 2 mM EGTA, 1 mM DTT, 1 mM Na₃VO₄, 10 μM ATP and 1 μCi [³²P] ATP (Perkin Elmer) in a 25 μl total reaction volume. After 30 min incubation at 30 °C the reaction was stopped by heating at 95 °C for 5 min in SDS-PAGE sample loading buffer. The samples were resolved by 7.5% SDS-PAGE and [³²P] ATP labeled bands were analyzed with PhosphorImager (Amersham Bioscience) using the ImageQuant™ TL software (GE Healthcare Life Science). To control for the amount of substrate in the kinase reaction, before adding [³²P] ATP, half of the reaction was loaded on a 7.5% stain free SDS-PAGE gel (BioRad), the protein bands were visualized with ChemiDoc XRS + System (BioRad) and quantified by the Image Lab™ 5.2.1 Software (BioRad). The relative phosphorylation of 2xMBP-BRCA2₁₋₂₅₀ was quantified as ³²P-labeled 2xMBP-BRCA2₁₋₂₅₀ (ImageQuant™ TL software) divided by the intensity of the 2xMBP-BRCA2₁₋₂₅₀ band in the SDS-PAGE gel (Image Lab™ 5.2.1 Software). In the control experiment where PLK1 inhibitor was used, 50 nM BI2536 (Selleck Chemicals) was added to the kinase buffer.

In vitro protein binding assay. To assess the interaction between recombinant PLK1 and BRCA2₁₋₂₅₀ after phosphorylation by PLK1, a kinase assay was performed with 0.2 μg recombinant PLK1 or PLK1-kinase dead (PLK1-KD) and 0.5 μg purified 2xMBP-BRCA2₁₋₂₅₀ (WT or the VUS T207) in kinase buffer supplemented

with 250 μ M ATP (no [γ^{32} P] ATP) in a total reaction volume of 20 μ l, one control reaction without ATP was performed with PLK1 and 2xMBP-BRCA2₁₋₂₅₀ WT. After 30 min incubation at 30 °C, 15 μ l amylose beads was added to the reaction and incubated for 1 h at 4 °C. The beads were centrifuged at 2000g for 2 min at 4 °C and the unbound fraction was collected before the beads were washed three times in kinase buffer (no ATP) containing 0.5% NP-40 and 0.1% Triton X-100. Bound proteins were eluted from the beads with 10 mM maltose, protein complexes were separated by SDS-PAGE and analyzed by western blotting. To control for the amount of proteins in the reaction, 2 μ l of the kinase reaction (before adding the amylose beads) was loaded as input. The protein bands were visualized with ChemiDoc XRS + System (BioRad) and quantified by the Image Lab™ 5.2.1 Software (BioRad). The relative pull-down of PLK1 was quantified as the intensity of the PLK1 band in the pull-down divided by the intensity of the PLK1 band in the input (ImageQuant™ TL software).

To discard possible remaining phosphorylation of the 2xMBP-BRCA2₁₋₂₅₀ fragment coming from the purification of the protein from HEK293T cells, the 2xMBP-BRCA2₁₋₂₅₀ fragment (WT or the variant T207) was incubated with kinase buffer (no added ATP) supplemented with FastAP Thermosensitive Alkaline Phosphatase (Thermo Fisher Scientific Cat. #EF0654) for 1 h at 37 °C before addition of recombinant PLK1 followed by 30 min incubation at 30 °C and 1 h incubation with amylose beads as described above.

NMR spectroscopy. NMR experiments were carried out at 283 K on 600 and 700 MHz Bruker spectrometers equipped with a triple resonance cryoprobe. For NMR signal assignments, standard 3D triple resonance NMR experiments were recorded on ¹⁵N and ¹³C labeled samples of BRCA2₄₈₋₂₁₈ WT and BRCA2₁₉₀₋₂₈₄ WT and T207A. Analyses of these experiments provided backbone resonance assignment for the non-phosphorylated and phosphorylated forms of these BRCA2 fragments. To follow the PLK1 phosphorylation kinetics, the ¹⁵N labeled fragment BRCA2₄₈₋₂₁₈ (50 μ M) was mixed to a first PLK1 sample at 0.1 μ M and the ¹⁵N labeled fragment BRCA2₁₉₀₋₂₈₄ (200 μ M) was mixed to another PLK1 sample at 1.1 μ M. The mixes were incubated at pH 7.8 and 298 K. For each time point, a 140 μ l sample was heated during 10 min at 368 K to inactivate PLK1, D₂O was added, the pH was adjusted to 7.0 and a ¹H-¹⁵N SOFAST-HSQC experiment⁵¹ was recorded. The HSQC experiments were performed using 2048 \times 256 time-points, 64 scans and an interscan delay of 80 ms. Data processing and analysis were carried out using the Topspin and CcpNmr Analysis 2.4.2 softwares.

Analysis of phosphorylation assays followed by NMR. In the HSQC spectra, the intensity of peaks of the phosphorylated residues pS193 and pT207, as well as the intensity of peaks corresponding to their non-phosphorylated form was retrieved at each time point of the kinetics. In order to estimate the fraction of phosphorylation for each residue at each point, the function $\text{Intensity}_{(\text{phospho})} = f[\text{Intensity}_{(\text{non-phospho})}]$ was drawn for each residue, the trendline was extrapolated to determine the intensity corresponding to the 100% phosphorylated residue and then the percentage of phosphorylation could be calculated at each time point by dividing peak intensities corresponding to the phosphorylated residue by the calculated intensity at 100% phosphorylation. Peaks corresponding to residues closed to a phosphorylated residue (L209 and V211 for pT207; D191, S197, and S195 for pS193) and thus affected by this phosphorylation were also treated using the same protocol and they were used to obtain a final averaged curve of the evolution of the percentage of phosphorylation at positions 193, 207 with time.

Isothermal titration calorimetry. ITC measurements were performed with the PLK1 PBD protein (amino acid 326 to amino acid 603) and BRCA2 peptides in 50 mM Tris-HCl buffer, pH 8.0 containing 150 mM NaCl and 5 mM β -ME, using a VP-ITC instrument (Malvern), at 293 K. We used automatic injections of 8 or 10 μ l. The titration data were analyzed using the program Origin 7.0 (OriginLab) and fitted to a one-site binding model. To evaluate the heat of dilution, control experiments were done with peptide or protein solutions injected into the buffer. The peptides used for the ITC experiments were synthesized by GeneCust (Ellange, LU) or Genscript (Piscataway, NY). The peptides were acetylated and amidated at the N-terminal and C-terminal ends, respectively (see Supplementary Table 9 for peptide sequences). Only peptide BRCA2₁₉₀₋₂₈₄ was expressed in bacteria and purified as detailed above (see “Expression and purification of BRCA2₁₉₀₋₂₈₄ for NMR” section).

Crystallization and structure determination. The purified PBD protein (amino acid 365 to amino acid 603) was concentrated to 6 mg/ml, and mixed to the ¹⁹⁴WSSSLATPPTLSS[pT]VLI²¹⁰ (pT207) BRCA2 peptide at a 3:1 molar ratio. The crystals were obtained by hanging drop vapor diffusion method at room temperature (293 K), by mixing 1 μ l of complex with 1 μ l of solution containing 10% PEG 3350, 100 mM BisTris pH 6.5, and 5 mM DTT. Diffraction data were collected at the Proxima 1 beamline (SOLEIL synchrotron, Gif-sur-Yvette, France). The dataset was indexed and integrated using XDS through the autoPROC package⁵². The software performs an anisotropic cut-off (Tickle et al., STARANISO (2018) Global Phasing Ltd.) of merged intensity data, a Bayesian estimation of the structure amplitudes, and applies an anisotropic correction to the data. The structure was solved by molecular replacement using PHENIX (Phaser) software⁵³.

Two molecules of PBD were consecutively positioned. Electron density for the peptide was clearly visible in the position previously reported in other PBD structures in complex with phosphorylated peptides (PDB 4O56 or 3P35). Refinement was performed using BUSTER⁵⁴ and PHENIX⁵⁵. The model was built with Coot⁵⁶. A summary of crystallographic statistics is shown in Supplementary Table 2. The figures were prepared using Pymol v.1.7.4.0 (Schrödinger, LLC).

Generation of stable DLD1 clones. For generation of DLD1 BRCA2^{-/-} cell lines stably expressing human BRCA2 variants of interest, we transfected one 100 mm plate of DLD1 BRCA2^{-/-} cells at 70% of confluence with 10 μ g of a plasmid containing human EGFP-MBP-tagged BRCA2 cDNA (corresponding to accession number NM_000059) using TurboFect (Thermo Fisher Scientific), 48 h post-transfection the cells were serially diluted and cultured in media containing 1 mg/ml G418 (Sigma-Aldrich) for selection. Single cells were isolated and expanded. To verify and select the clones, cells were resuspended in cold lysis buffer H (50 mM HEPES (pH 7.5), 250 mM NaCl, 1% NP-40, 5 mM EDTA, 1 mM DTT, 1 mM PMSF and EDTA-free Protease Inhibitor Cocktail (Roche)), incubated on ice for 30 min, sonicated and centrifuged at 10,000g for 15 min, 100 μ g total protein lysate was run on a 4–15% SDS-PAGE followed by immunoblotting using BRCA2 and GFP antibodies to detect EGFP-MBP-BRCA2. Clones with similar expression levels were selected for functional studies.

The presence of the point mutations in the genome of the clones was confirmed by extraction of genomic DNA using Quick-DNA™ Universal Kit (ZYMO Research) followed by amplification of the N-terminal of BRCA2 (aa 1-267) by PCR using a forward primers that binds to the end of MBP and a reverse primer that binds to amino acid 267 in BRCA2, the presence of the point mutations was confirmed by sequencing of the PCR product (see Supplementary Table 4 and 10 for primer sequences).

Cell extracts, immunoprecipitation and western blotting. For the interaction between BRCA2₁₋₂₅₀ and endogenous PLK1, U2OS cells were transfected with 2xMBP-BRCA2₁₋₂₅₀ construct (WT, M192T, S193A, S196N, T200K, S206C, and T207A) using TurboFect (Thermo Fisher Scientific), 30 h post-transfection cells were synchronized by nocodazole (300 ng/ml), harvested and lysed in extraction buffer A (20 mM HEPES (pH 7.5), 150 mM NaCl, 0.1% NP40, 2 mM EGTA, 1.5 mM MgCl₂, 50 mM NaF, 10% glycerol, 1 mM Na₃VO₄, 20 mM β -glycerophosphate, 1 mM DTT and EDTA-free Protease Inhibitor Cocktail (Roche)). After centrifugation at 18,000g for 15 min, the supernatant was incubated with amylose resin (NEB) for 1.5 h at 4 °C. The beads were washed five times in extraction buffer before elution with 10 mM maltose. Bound proteins were separated by SDS-PAGE and analyzed by western blotting. Where PLK1 and CDK1 inhibitor was used, the cells were synchronized in mitosis by nocodazole (14 h) followed by 2 h treatment with PLK1 inhibitor (50–100 nM BI2536 (Selleck Chemicals) or 50 μ M BTO-1 (Sigma-Aldrich)) or the CDK1 inhibitor (10 μ M, Ro-3306, (Selleck Chemicals)) before being harvested. The cells were lysed in extraction buffer A, pre-cleared by centrifugation and total protein lysate was separated by SDS-PAGE and analyzed by western blotting. Where proteasome inhibitor was used during the mitotic block, the cells were synchronized by nocodazole for 14 h before the MG-132 (50 μ M, Sigma-Aldrich) was added to the media and the cells were cultured for additional 2 h before harvesting.

For analysis of pBUBR1, BUBR1, pT207-BRCA2 and BRCA2 levels in mitosis, nocodazole (100 ng/ml) treated DLD1 BRCA2^{-/-} clones were lysed in extraction buffer A, pre-cleared by centrifugation and total protein lysate was separated by SDS-PAGE and analyzed by western blotting.

For analysis of the interaction between BRCA2-PLK1, BRCA2-BUBR1 and for the protein complex BRCA2-pBUBR1/BUBR1-PP2A(C)-PLK1 in mitosis, DLD1 BRCA2^{-/-} stable clones expressing EGFP-MBP-BRCA2 (WT or the VUS S206C or T207A) were synchronized with nocodazole, harvested and lysed in extraction buffer A. The lysate were pre-cleared by centrifugation before incubation with GFP-TRAP beads (Chromotek) for 2 h at 4 °C to pull-down EGFP-MBP-BRCA2. Around 3 mg total protein lysate was used per pull-down. The beads were washed 5 times in extraction buffer A and 2 times in extraction buffer A with 500 mM NaCl. Bound proteins were eluted by boiling the samples for 4 min in 3x SDS-PAGE sample loading buffer (SB), eluted proteins were separated by SDS-PAGE and analyzed by western blotting using anti-mouse PLK1, anti-mouse BUBR1, anti-rabbit pT680-BUBR1, anti-mouse PP2A-C and anti-mouse BRCA2 (OP95) antibodies.

For immunoprecipitation of endogenous BUBR1, nocodazole treated DLD1 BRCA2^{-/-} stable clones expressing BRCA2 WT or the variants (S206C or T207A) were lysed in extraction buffer A. After centrifugation, 2000–3000 μ g total protein lysate was pre-cleared by incubation with 20 μ l Protein G PLUS-Agarose (Santa Cruz, sc-2002) for 30 min at 4 °C. The pre-cleared lysate was incubated with 1.25 μ g BUBR1 mouse antibody or control mouse IgG overnight at 4 °C before addition of 40 μ l Protein G PLUS-Agarose, the lysate was incubated for additional 30 min before immunoprecipitates were collected by centrifugation. After four washes in extraction buffer A and two washes in extraction buffer A with 500 mM NaCl, the beads were re-suspended in SB, boiled and the immunocomplexes were analyzed by western blotting using anti-rabbit BUBR1, anti-mouse PLK1 and anti-mouse PP2A-C antibodies.

For the interaction between the phosphomimic BUBR1-3D mutant (S670D, S676D and T680D) and endogenous PP2A, the DLD1 BRCA2^{-/-} stable clones expressing BRCA2 WT or the S206C variant was transiently transfected with the pcDNA3-3xFLAG-BUBR1-3D-RFP construct. The transfection media was replaced 30 h post-transfection with fresh growth media containing 0.1 µg/ml nocodazole and the cells were incubated additional 14 h before harvesting. The cells were lysed and an immunoprecipitation was performed as described above for the BUBR1 immunoprecipitation using rabbit anti-tRFP antibody (Cat.#AB233, Evrogen) to pull-down the 3xFLAG-BUBR1-3D-RFP protein. Immunocomplexes were analyzed by western blotting using anti-mouse BUBR1 and anti-mouse PP2A-C antibodies.

For all Western blots, the protein bands were visualized with ChemiDoc XRS + System (BioRad) and quantified by the Image Lab™ 5.2.1 Software (BioRad). For the relative expression levels (Fig. 5g-i, Supplementary Fig. 5d), the intensity of the band of interest was divided by the intensity of the signal from the stain free gel. The results are presented as percentage compared to BRCA2 WT clone. To calculate the relative co-immunoprecipitation (co-IP)/co-pull-down of a protein of interest, the intensity of the band in the co-IP was divided by the intensity of the band in the input (ImageQuant™ TL software), the ratio co-IP:input of the protein of interest was then divided by the intensity of the band of the immunoprecipitated protein. StainFree images of the gels before transfer were used as loading control for the input and cropped image is shown in the figures.

Antibodies used for western blotting. mouse anti-MBP (1:5000, R29, Cat. #MA5-14122, Thermo Fisher Scientific), mouse anti-BRCA2 (1:1000, OP95, EMD Millipore), rabbit anti-pT207-BRCA2 (raised for this study using the peptide 203^{TLSS}-pT-VLIVRNEEAC as antigen, Genscript) (1:1000), anti-GFP (1:5000, Protein Expression and Purification Core Facility, Institut Curie), mouse anti-PLK1 (1:5000, clone 35-206, Cat. #05-844, EMD Millipore), mouse anti-BUBR1 (1:1000, Cat. #612502, BD Transduction Laboratories), rabbit anti-BUBR1 (1:2000, Cat. #A300-386A, Bethyl Laboratories), mouse anti-PP2A C subunit (1:1000, clone 1D6, Cat. #05-421, EMD Millipore), rabbit anti-pT680-BUBR1 (1:1000, EPR 19958, Cat. #ab200061, Abcam), and rabbit anti-pS676-BUBR1 (1:1000, R193, kind gift from Dr. Erich A. Nigg). Horseradish peroxidase (HRP) conjugated 2nd antibodies used: mouse-IgGκ B-P-HRP (IB: 1:10 000, Cat. #sc-516102, Santa Cruz), goat anti-rabbit IgG-HRP (IB: 1:5000, Cat. #sc-2054, Santa Cruz), goat anti-mouse IgG-HRP (1:10 000, Cat.#115-035-003, Interchim), goat anti-rabbit IgG-HRP (1:10 000, Interchim, Cat.#111-035-003).

siRNA transfection. For analysis of the pT680-BUBR1 levels in U2OS cells after transient depletion of endogenous BRCA2 with RNAi, U2OS cells were transfected with 200 nM siRNA targeting the 3'UTR of BRCA2 (siBRCA2 #1: SI00000966, Qiagen) using jetPRIME (Polyplus Transfection, Cat.#114-07). As control, the cells were transfected with the 200 nM of the si-control RNA (siRNA control ON-TARGETplus Non-targeting Pool. D-001810-10-05, Thermo Scientific) The transfection media was replaced 30 h post-transfection with fresh growth media containing 0.1 µg/ml nocodazole and the cells were incubated additional 14 h before harvesting. Total protein lysate was extracted as described above and 30–50 µg total protein lysate was resolved on a 4–15% SDS-PAGE and analyzed by western blotting using anti-mouse BRCA2 (OP95), anti-mouse BUBR1, anti-rabbit pT680-BUBR1 and anti-mouse PLK1 antibodies (see above for reference number).

For depletion of endogenous BRCA2 in DLD1 BRCA2^{+/+} cells for analysis of γH2AX and RAD51 foci, the cells were transfected with a combination of the BRCA2 5'UTR siRNA (SI00000966, Qiagen) and IAC204 (Dharmacon D-003462-04) (100 nM each) or the ON-TARGET plus Non-targeting oligonucleotide D-001810-04-20, Thermo Scientific 100 nM) and fixed and expose to IR 30 h post-transfection (see Supplementary Fig. 8c for the Western blot showing BRCA2 depletion) for analysis of DNA repair foci (see Supplementary Fig. 8c for the Western blot showing BRCA2 depletion).

Phosphatase treatment. DLD1 BRCA2^{-/-} cells stably expressing EGFP-MBP-BRCA2 WT were synchronized in mitosis by nocodazole (14 h), harvested, lysed in extraction buffer A without phosphatase inhibitors (NaF, Na₃VO₄ and β-glycerophosphate), and pre-cleared by centrifugation. For detection of pT207-BRCA2 and BRCA2, 20 U FastAP Thermosensitive Alkaline Phosphatase (Thermo Fisher Scientific Cat. #EF0654) was added to 200 µg of total protein lysate in FastAP Buffer in a total reaction volume of 60 µl. After 1 h incubation at 37 °C the reaction was stopped by heating at 95 °C for 5 min in SDS-PAGE sample loading buffer, 30 µl of the reaction was loaded on a 4–15% SDS-PAGE gel, the gel was transferred onto nitrocellulose membrane and the levels of pT207-BRCA2 were analyzed by western blotting using anti-pT207-BRCA2 antibody. For detection of pBUBR1 and BUBR1, increased amount (0–20U) of FastAP Thermosensitive Alkaline Phosphatase was added to 15 µg of total protein lysate in FastAP Buffer in a total reaction volume of 60 µl followed by same protocol as described for pT207-BRCA2, the levels of pS676/pT680-BUBR1 were analyzed by western blotting using anti-pS676/pT680-BUBR1 antibodies.

Cell survival and viability assays. For clonogenic survival assay, DLD1 BRCA2^{-/-} cells stably expressing full-length EGFP-MBP-BRCA2 and the variants (S206C

and T207A) were treated at 70% of confluence with Mitomycin C (Sigma-Aldrich) at concentrations: 0, 0.5, 1.0, and 2.5 µM. After 1 h drug treatment the cells were serially diluted in normal growth media containing penicillin/streptomycin (Eurobio) and seeded in triplicates into 6-well plates. The media was changed every third day, after 10–12 days in culture the plates were stained with crystal violet, colonies were counted and the surviving fraction was determined for each drug concentration.

Cell viability was assessed with 3-[4,5-Dimethylthiazol-2-yl]-2,5-diphenyltetrazolium bromide (MTT, #M5655, Sigma Aldrich) after treatment with MMC and the PARP inhibitor Olaparib (AZD2281, Ku-0059436, #S1060, Selleck Chemicals). For MMC, the cells were plated in triplicates in 96-well microplates (3000–5000 cells/well) the day before treatment. The cells were washed once in PBS before addition of serum-free media containing MMC at the concentrations: 0, 1.0 and 2.5 µM. After 1 h treatment the cells were washed once in PBS and incubated for 72 h in normal growth media before the viability was measured by MTT assay. For PARP inhibition, the cells were seeded 4 h before 4 days treatment in normal growth media with Olaparib at concentrations: 0, 2.5 and 5.0 µM.

HR assays. We applied a DSB-mediated gene targeting strategy using site-specific TALEN nucleases to quantify HR in cells. DLD1 BRCA2^{-/-} cells stably expressing full-length GFPMBP-BRCA2 and the variants (S206C and T207A) were transfected using AMAXA technology (Lonza) nucleofector kit V (Cat. #VCA-1003) with 3 µg of the promoter-less donor plasmid (AAVS1-2A-mCherry) with or without 1 µg of each AAVS1-TALEN encoding plasmids (TALEN-AAVS1-5' and TALEN-AAVS1-3', see Supplementary Table 12 for sequences, kind gift from Dr. Carine Giovannangeli). For each transfection, 1 × 10⁶ cells were transfected using program L-024, the cells were seeded in 6-well plate in culture media without selection antibiotics. The day after transfection the media was changed to media with selection and 48 h post-transfection the cells were trypsinized and reseeded on a 10-cm culture dish and cultured for additional 5 days. The percentage of mCherry positive cells was analyzed on a BD FACSAria III (BD Bioscience) using the FACSDiva software and data were analyzed with the FlowJo 10.4.2 software (Tree Star Inc.).

Analysis of tetraploid cells. For the analysis of S-phase tetraploid cells in the DLD1 BRCA2^{-/-} stable clones, the cells were incubated with 10 µM BrdU for 20 min before they were harvest, fixed and stained for cell cycle analysis using a APC-BrdU flow kit (BD Bioscience, Cat. #552598) following the manufacturer's instructions.

Labeled cells were analyzed on a BD FACSCanto II (BD Bioscience) using the FACSDiva software and data were analyzed with the FlowJo 10.4.2 software (Tree Star Inc.).

Immunofluorescence. Kinetochores localization: For staining of pT680-BUBR1 and PLK1 at the kinetochore, DLD1 BRCA2^{-/-} stable clones expressing EGFP-MBP-BRCA2-WT or the variant T207A were seeded on coverslips and treated with nocodazole (0.25 µg/ml) for 4 h, fixed with 4% PFA in PBS containing 0.5% Triton X-100 for 20 min at room temperature. The coverslips were rinsed three times in PBS-T and blocked for 30 min with 4% BSA in PBS before incubation with primary antibodies (human anti-CREST (1:100, Cat. #15-234-0001, Antibodies Online) together with either rabbit anti-pT680-BUBR1 (1:500, clone EPR 19958, Abcam, Cat. #ab200061) or mouse anti-PLK1 (1:500, clone F-8, Santa Cruz Biotechnology, Cat. #sc-17783), diluted in PBS-T with 5% BSA overnight at 4 °C. After three washes of 5 min in PBS-T the coverslips were incubated for 2 h incubation at room temperature with respective Alexa Fluor conjugated secondary antibody (for pBUBR1; goat anti-human Alexa-488 (1:1000, Cat. #A11013, Life Technologies) and donkey anti-rabbit Alexa-488 (1:1000, Cat. #A-21206, Thermo Fisher Scientific), for PLK1; goat anti-human Alexa-633 (1:500, Cat. #A21091, Life Technologies) together with either donkey anti-rabbit Alexa-488 (1:1000, Cat. #A-21206, Thermo Fisher Scientific) or donkey anti-mouse Alexa-488 (1:1000, Cat. #A-21202, Thermo Fisher Scientific) diluted in PBS-T with 5% BSA. After two washes of 5 min in PBS-T and one rinse in PBS the coverslips were mounted on microscope slides.

For staining of BRCA2 at the kinetochore, U2OS was transiently transfected with GFPMBP-BRCA2 construct using TurboFect (Thermo Fisher Scientific). The cells were seeded on coverslips 24 h post-transfection and incubated for another 24 h before nocodazole (0.25 µg/ml) was added. The cells were treated for 4 h followed by fixation as described above for kinetochore localization of pBUBR1, pAuroraB and PLK1. BRCA2 was detected by rabbit anti-BRCA2 (1:500, CA1033, EMD Millipore) and Alexa-488 secondary antibody (donkey anti-rabbit Alexa-488 (1:1000, Cat. #A-21206, Thermo Fisher Scientific), CREST was detected by human anti-CREST (1:100, Cat. #15-234-0001, Antibodies Online) and Alexa-633 secondary antibody (1:500, Cat. #A21091, Life Technologies), diluted in PBS-T with 5% BSA.

Phosphatase inhibitors (50 mM NaF, 1 mM Na₃VO₄, and 20 mM β-glycerophosphate) were added to all buffers.

Cold stable kinetochore-microtubules, chromosome alignment and segregation: DLD1 BRCA2^{-/-} cells and the stable clones expressing EGFP-MBP-BRCA2 WT or the variants (S206C and T207A) were seeded on coverslips in 6-well tissue

culture plates and synchronized in mitosis. For analysis of chromosome alignment, the cells were synchronized by double thymidine (2.5 mM, Sigma-Aldrich) block, released for 9 h followed by treatment with Monastrol (100 μ M, Sigma-Aldrich) for 16 h. After incubation with Monastrol the cells were washed twice in PBS before 1 h incubation in media containing the proteasome inhibitor MG-132 (10 μ M, Sigma-Aldrich). To detect cold-stable microtubules cells were synchronized using the same protocol as for the chromosome alignment followed by 15 min of cold treatment on ice before fixation. For chromosome segregation analysis, the cells were synchronized by double thymidine block and released in normal growth media for 11 h.

After synchronization, the cells were fixed with 100% methanol for 15 min at -20°C , rinsed once in PBS before permeabilization with PBS containing 0.1% Triton-X for 15 min at room temperature. Nonspecific epitope binding was blocked with 4% BSA (Sigma-Aldrich) in PBS. The coverslips were rinsed in PBS, incubated with primary antibody (mouse anti- α -tubulin (1:5000, GT114, Cat. #GTX628802, Euromedex) and human anti-CREST (1:100, Cat. #15-234-0001, Antibodies Online) diluted in PBS containing 0.1% Tween-20 (PBS-T) and 5% BSA for 1 h at room temperature. After incubation, the coverslips were washed three times of 5 min in PBS-T before being incubated for 1 h at room temperature with Alexa Fluor conjugated secondary antibody (donkey anti-mouse Alexa-594 (1:1000, Cat. #A-21203, Thermo Fisher Scientific) and goat anti-human Alexa-488 (1:1000, Cat. #A111013, Life Technologies)) diluted in PBS-T with 5% BSA. The coverslips were washed two times of 5 min each in PBS-T followed by one rinse in PBS before being mounted on microscope slides.

For the analysis of chromosome alignment in cells expressing the phosphomimic BUBR1-3D mutant (S670D, S676D and T680D), the DLD1 BRCA2^{-/-} stable clones expressing the T207A variant was transiently transfected with the pcDNA3-3xFLAG-BUBR1-3D-RFP construct using TurboFect. The day after transfection the cells were seeded on coverslips in 6-well tissue culture plates, synchronized in mitosis and prepared for immunofluorescence.

Aneuploidy: For aneuploidy analysis the cells were treated with nocodazole for 14 h (0.1 μ g/ml) to enable chromosome spread; the cells were rinsed in PBS, incubated for 10 min with KCl (50 mM) at room temperature before they were spread on coverslips at 900 rpm for 5 min in a Cytospin 4 (Thermo Scientific). The cells were fixed with 3% paraformaldehyde (PFA) in PBS for 20 min followed by 15 min permeabilization in PBS containing 0.1% Triton X-100. The coverslips were rinsed three times in PBS, blocked with 5% BSA in PBS before incubation with human anti-CREST primary antibody (1:100, Cat. #15-234-0001, Antibodies Online) diluted in PBS overnight at 4°C . After incubation the coverslips were washed three times of 5 min in PBS before 1 h incubation at room temperature with Alexa Fluor conjugated secondary antibody (goat anti-human Alexa-555 (1:1000, Cat. #A-21433, Thermo Fisher Scientific)) diluted in PBS. After three washes of 5 min in PBS the coverslips were mounted on microscope slides.

γ H2AX and RAD51 foci: For the detection of γ H2AX and RAD51 foci, the cells were seeded on coverslips the day before 6 Gy γ -irradiation (GSR D1, Cs-137 irradiator). Two hours after irradiation, the coverslips were washed twice in PBS followed by one wash in CSK Buffer (10 mM PIPES, pH 6.8, 0.1 M NaCl, 0.3 M sucrose, 3 mM MgCl₂, EDTA-free Protease Inhibitor Cocktail (Roche)). The cells were permeabilized for 5 min at room temperature in CSK buffer containing 0.5% Triton X-100 (CSK-T) followed by one rinse in CSK buffer and one rinse in PBS before fixation for 20 min at room temperature with 2% PFA in PBS. After one rinse in PBS and one in PBS-T, the cells were blocked for 5 min at room temperature with 5% BSA in PBS-T before incubation for 2 h at room temperature with primary antibodies diluted in PBS-T with 5% BSA. After primary antibody incubation, the coverslips were rinsed in PBS-T followed by two washes of 10 min in PBS-T and blocked for 5 min at room temperature with 5% BSA in PBS-T before incubation for 1 h at room temperature with respective Alexa Fluor conjugated secondary antibody diluted in PBS-T with 5% BSA. After one rinse in PBS-T and two washes of 10 min in PBS-T the coverslips were rinsed in PBS before being mounted on microscope slides. γ H2AX foci were detected by mouse anti-pSer139- γ H2AX (1:1000, clone JBW301, EMD-Millipore, Cat. #05-636) and secondary antibody donkey anti-mouse Alexa-594 (1:1000, Cat. #A-21203, Thermo Fisher Scientific). RAD51 foci were detected by rabbit anti-RAD51 (1:100, clone H-92, Santa Cruz Biotechnology, Cat. #sc-8349), followed by secondary antibody donkey anti-rabbit Alexa-488 (1:1000, Cat. #A-21206, Thermo Fisher Scientific).

For the analysis of γ H2AX and RAD51 foci in DLD1 BRCA2^{+/+} cells depleted of BRCA2 by siRNA, the DLD1 BRCA2^{+/+} cells were transiently transfected with siRNA targeting BRCA2 (see section siRNA transfection above). The day after transfection the cells were seeded on coverslips in 6-well tissue culture plates and radiated as described above.

Micronuclei: For analysis of micronuclei, DLD1 BRCA2^{-/-} cells and the stable clones expressing EGFP-MBP-BRCA2 WT or the variants (S206C and T207A) were seeded on coverslips in 6-well tissue culture plates the day before fixation. Centromeres were detected by human anti-CREST primary antibody (1:100, Cat. #15-234-0001, Antibodies Online) and Alexa Fluor conjugated secondary antibody (goat anti-human Alexa-555 (1:1000, Cat. #A-21433, Thermo Fisher Scientific)).

All coverslips were mounted on microscope slides with ProLong Diamond Antifade Mountant with DAPI (Cat. #P36966, Thermo Fisher Scientific).

Image acquisition and analysis: For analysis of DNA repair foci, chromosome alignment and segregation, images were acquired in an upright Leica DM6000B wide-field microscope equipped with a Leica Plan Apo 63x NA 1.4 oil immersion

objective. The camera used is a Hamamatsu Flash 4.0 sCMOS controlled with the MetaMorph2.1 software (Molecular Devices). For Fig. 6a and 7a, 7 to 20 Z-stacks were taken at 0.2 μ m intervals to generate a maximal intensity projection image using ImageJ. For the analysis of γ H2AX and RAD51 foci, 26 Z-stacks were taken at 0.2 μ m intervals to generate a maximal intensity projection using the Image J software (1.51 s, NIH). For the BUBR1-3D-RFP chromosome alignment experiment, RFP negative cells on the same coverslips were used as control.

The number of γ H2AX foci per nucleus were counted by a customized macro using a semi-automated procedure; the nucleus was defined by an auto-threshold (Otsu, Image J) on DAPI, a mask was generated and applied onto the Z-projection to count foci within the nucleus. For the definition of foci we applied the threshold plugin IsoData (ImageJ software (1.51 s, NIH)) and for the quantification of foci we used the tool Analyze Particles (ImageJ software (1.51 s, NIH)) setting a range of 5-100 pixels² to select only particles that correspond to the size of a focus. RAD51 foci were quantified using the plugin Find Maxima onto the Z-projection with a prominence of 1000.

For analysis of cold stable microtubules images were acquired in an upright Leica DM6000B wide-field microscope equipped with a Leica Plan Apo 100x NA 1.4 oil immersion objective. The camera used is a Hamamatsu Flash 4.0 sCMOS controlled with the MetaMorph2.1 software (Molecular Devices), 20 Z-stacks were taken on metaphase cells at 0.5 μ m intervals to generate a maximal intensity projection image using the ImageJ software (1.51 s, NIH). The quantification of the intensity of α -tubulin in metaphase cells was performed in the area of the spindle subtracting the background of α -tubulin signal from a different area in the same cell. The data were then normalized to the mean intensity of the BRCA2 WT cells.

For analysis of aneuploidy, kinetochore localization and micronuclei images were acquired in an inverted confocal Leica SP5 microscope with a plan Apo 63x NA 1.4 oil immersion objective with the lasers 405, 488, 561 and 633 nm. For Fig. 8b (aneuploidy), Z-stacks were taken at 0.13 μ m intervals to generate a maximal intensity projection image using the ImageJ software (1.51 s, NIH). For the counting of chromosomes in the aneuploidy experiment, the quantification was performed in zoomed areas counting the CREST signal in separated stacks to ensure the counting of all chromosomes. We were able to count up to 65 chromosomes with certainty, thus >65 CREST signals were discarded and not included in the analysis.

For the analysis of kinetochore localization, Z-stacks were taken at 0.21 μ m intervals to generate a sum slice projection image using ImageJ, six pairs of chromosomes per cell were analyzed in 15-21 cells per experiment from two individual experiments. The results from the quantifications (Fig. 5i, Supplementary Fig. 6b) is represented as the ratio between the intensities for pBUBR1/PLK1 and the CREST signal relative to the mean ratio observed for the BRCA2 WT complemented cells. For the images in Fig. 5h (pBUBR1:CREST), Supplementary Fig. 6a (PLK1:CREST) and Supplementary Fig. 8e (micronuclei), Z-stacks were taken to generate a maximal intensity projection image using the ImageJ software (1.51 s, NIH), except for DAPI where the image is from one Z-stack.

Time-lapse video microscopy of mitotic cells. For phase-contrast video-microscopy DLD1 BRCA2^{-/-} cells stably expressing full-length EGFP-MBP-BRCA2 and the variants (S206C and T207A) were seeded in 35 mm Ibidi μ -Dishes (Ibidi, Cat. #81156), synchronized by double thymidine block, released and cultured for 4 h in normal growth media before the filming was started. The cells were imaged for 16 h every 5 min, at oil-40X using an inverted video-microscope (Leica DMi6000) equipped with electron multiplying charge coupled device (EMCCD) camera controlled by the MetaMorph2.1 software (Molecular Devices). Images were mounted using the Image J software (1.51 s, NIH).

Statistical analysis. In all graphs error bars represent the standard deviation (SD) from at least three independent experiments unless otherwise stated, scatter dot plots show median with 95% CI. Statistical significance of differences was calculated with unpaired two-tailed *t*-test, one/two-way ANOVA with Dunnett's or Tukey's multiple comparisons test, Mann-Whitney two-tailed or Kruskal-Wallis one-way analysis followed by Dunn's multiple comparisons test as indicated in the figure legends. All analyses were conducted using GraphPad Prism version Mac OS X 8.3.0 (328).

Reporting summary. Further information on research design is available in the Nature Research Reporting Summary linked to this article.

Data availability

The data that support the findings of this study are available from the corresponding authors upon reasonable request. The source data for Fig. 1a-d; Fig. 2; Fig. 3a-k; Fig. 4a-f; Fig. 5a-i; Figs. 6a, 6d; Fig. 7a, c, d; Fig. 8a, d; Fig. 9a-f; Supplementary Fig. 1a, b; Supplementary Fig. 2b, c; Supplementary Fig. 3a-d; Supplementary Fig. 4a, c; Supplementary Fig. 5b-d; Supplementary Fig. 6b-d; Supplementary Fig. 7d; Supplementary Fig. 8c-d; Supplementary Fig. 10a, b; are available as a Source Data file.

The PDB files used during structure analysis can be retrieved using the PDB codes 4O56 and 3P35 on the PDB website: <https://www.rcsb.org>. The final X-ray structure of the PLK1 PBD bound to the phosphorylated BRCA2 peptide is also available on this website, under the code 6GY2.

Received: 8 October 2019; Accepted: 20 March 2020;

Published online: 14 April 2020

References

- Moynahan, M. E., Pierce, A. J. & Jasin, M. BRCA2 is required for homology-directed repair of chromosomal breaks. *Mol. Cell* **7**, 263–272 (2001).
- Jensen, R. B., Carreira, A. & Kowalczykowski, S. C. Purified human BRCA2 stimulates RAD51-mediated recombination. *Nature* **467**, 678–683 (2010).
- Saleh-Gohari, N. & Helleday, T. Conservative homologous recombination preferentially repairs DNA double-strand breaks in the S phase of the cell cycle in human cells. *Nucleic Acids Res.* **32**, 3683–3688 (2004).
- Choi, E. et al. BRCA2 fine-tunes the spindle assembly checkpoint through reinforcement of BubR1 acetylation. *Dev. Cell* **22**, 295–308 (2012).
- Futamura, M. et al. Potential role of BRCA2 in a mitotic checkpoint after phosphorylation by hBUBR1. *Cancer Res.* **60**, 1531–1535 (2000).
- Lampson, M. A. & Kapoor, T. M. The human mitotic checkpoint protein BubR1 regulates chromosome-spindle attachments. *Nat. Cell Biol.* **7**, 93–98 (2005).
- Lara-Gonzalez, P., Westhorpe, F. G. & Taylor, S. S. The spindle assembly checkpoint. *Curr. Biol.* **22**, R966–R980 (2012).
- Elowe, S. et al. Uncoupling of the spindle-checkpoint and chromosome-congression functions of BubR1. *J. Cell Sci.* **123**, 84–94 (2010).
- Zhang, G., Mendez, B. L., Sedgwick, G. G. & Nilsson, J. Two functionally distinct kinetochore pools of BubR1 ensure accurate chromosome segregation. *Nat. Commun.* **7**, 12256 (2016).
- Park, I. et al. HDAC2/3 binding and deacetylation of BubR1 initiates spindle assembly checkpoint silencing. *FEBS J.* **284**, 4035–4050 (2017).
- Mondal, G. et al. BRCA2 localization to the midbody by filamin A regulates cep55 signaling and completion of cytokinesis. *Dev. Cell* **23**, 137–152 (2012).
- Daniels, M. J., Wang, Y., Lee, M. & Venkitaraman, A. R. Abnormal cytokinesis in cells deficient in the breast cancer susceptibility protein BRCA2. *Science* **306**, 876–879 (2004).
- Takaoka, M., Saito, H., Takenaka, K., Miki, Y. & Nakanishi, A. BRCA2 phosphorylated by PLK1 moves to the midbody to regulate cytokinesis mediated by nonmuscle myosin IIC. *Cancer Res.* **74**, 1518–1528 (2014).
- Lin, H.-R., Ting, N. S. Y., Qin, J. & Lee, W.-H. M phase-specific phosphorylation of BRCA2 by Polo-like kinase 1 correlates with the dissociation of the BRCA2-P/CAF complex. *J. Biol. Chem.* **278**, 35979–35987 (2003).
- Lee, M., Daniels, M. J. & Venkitaraman, A. R. Phosphorylation of BRCA2 by the Polo-like kinase Plk1 is regulated by DNA damage and mitotic progression. *Oncogene* **23**, 865–872 (2004).
- Zitouni, S., Nabais, C., Jana, S. C., Guerrero, A. & Bettencourt-Dias, M. Polo-like kinases: structural variations lead to multiple functions. *Nat. Rev. Mol. Cell Biol.* **15**, 433–452 (2014).
- Barr, F. A., Silljé, H. H. W. & Nigg, E. A. Polo-like kinases and the orchestration of cell division. *Nat. Rev. Mol. Cell Biol.* **5**, 429–440 (2004).
- Elowe, S., Hümmel, S., Ultschmid, A., Li, X. & Nigg, E. A. Tension-sensitive Plk1 phosphorylation on BubR1 regulates the stability of kinetochore microtubule interactions. *Genes Dev.* **21**, 2205–2219 (2007).
- Suijkerbuijk, S. J. E., Vleugel, M., Teixeira, A. & Kops, G. J. P. L. Integration of kinase and phosphatase activities by BUBR1 ensures formation of stable kinetochore-microtubule attachments. *Dev. Cell* **23**, 745–755 (2012).
- Hauf, S. et al. The small molecule Hesperadin reveals a role for Aurora B in correcting kinetochore-microtubule attachment and in maintaining the spindle assembly checkpoint. *J. Cell Biol.* **161**, 281–294 (2003).
- Foley, E. A., Maldonado, M. & Kapoor, T. M. Formation of stable attachments between kinetochores and microtubules depends on the B56-PP2A phosphatase. *Nat. Cell Biol.* **13**, 1265–1271 (2011).
- Elia, A. E. H., Cantley, L. C. & Yaffe, M. B. Proteomic screen finds pSer/pThr-binding domain localizing Plk1 to mitotic substrates. *Science* **299**, 1228–1231 (2003).
- Elia, A. E. H. et al. The molecular basis for phosphodependent substrate targeting and regulation of Plks by the Polo-box domain. *Cell* **115**, 83–95 (2003).
- Neef, R. et al. Phosphorylation of mitotic kinesin-like protein 2 by polo-like kinase 1 is required for cytokinesis. *J. Cell Biol.* **162**, 863–875 (2003).
- Kang, Y. H. et al. Self-regulated Plk1 recruitment to kinetochores by the Plk1-PBIP1 interaction is critical for proper chromosome segregation. *Mol. Cell* **24**, 409–422 (2006).
- Szabo, C., Masiello, A., Ryan, J. F. & Brody, L. C. The breast cancer information core: database design, structure, and scope. *Hum. Mutat.* **16**, 123–131 (2000).
- Bérout, C. et al. BRCA share: a collection of clinical BRCA gene variants. *Hum. Mutat.* **37**, 1318–1328 (2016).
- Golsteyn, R. M., Mundt, K. E., Fry, A. M. & Nigg, E. A. Cell cycle regulation of the activity and subcellular localization of Plk1, a human protein kinase implicated in mitotic spindle function. *J. Cell Biol.* **129**, 1617–1628 (1995).
- Yata, K. et al. BRCA2 coordinates the activities of cell-cycle kinases to promote genome stability. *Cell Rep.* **7**, 1547–1559 (2014).
- Santaguida, S. & Amon, A. Short- and long-term effects of chromosome mis-segregation and aneuploidy. *Nat. Rev. Mol. Cell Biol.* **16**, 473–485 (2015).
- Lera, R. F. et al. Decoding Polo-like kinase 1 signaling along the kinetochore-centromere axis. *Nat. Chem. Biol.* **12**, 411–418 (2016).
- Kraakman-van der Zwet, M. et al. Brca2 (XRCC11) deficiency results in radioresistant DNA synthesis and a higher frequency of spontaneous deletions. *Mol. Cell Biol.* **22**, 669–679 (2002).
- Bryant, H. E. et al. Specific killing of BRCA2-deficient tumours with inhibitors of poly(ADP-ribose) polymerase. *Nature* **434**, 913–917 (2005).
- Brunet, E. et al. Chromosomal translocations induced at specified loci in human stem cells. *Proc. Natl Acad. Sci. USA* **106**, 10620–10625 (2009).
- Hockemeyer, D. et al. Efficient targeting of expressed and silent genes in human ESCs and iPSCs using zinc-finger nucleases. *Nat. Biotechnol.* **27**, 851–857 (2009).
- Hertz, E. P. T. et al. A Conserved Motif Provides Binding Specificity to the PP2A-B56 Phosphatase. *Mol. Cell* **63**, 686–695 (2016).
- Wu, C.-G. et al. PP2A-B' holoenzyme substrate recognition, regulation and role in cytokinesis. *Cell Discov.* **3**, 17027–19 (2017).
- Spain, B. H., Larson, C. J., Shihabuddin, L. S., Gage, F. H. & Verma, I. M. Truncated BRCA2 is cytoplasmic: implications for cancer-linked mutations. *Proc. Natl Acad. Sci. USA* **96**, 13920–13925 (1999).
- Gretarsdottir, S. et al. BRCA2 and p53 mutations in primary breast cancer in relation to genetic instability. *Cancer Res.* **58**, 859–862 (1998).
- Hucl, T. et al. A syngeneic variance library for functional annotation of human variation: application to BRCA2. *Cancer Res.* **68**, 5023–5030 (2008).
- Nicolai, von, C., Ehlen, A., Martin, C., Zhang, X. & Carreira, A. A second DNA binding site in human BRCA2 promotes homologous recombination. *Nature Communications* **7**, 12813 (2016).
- Martinez, J. S. et al. BRCA2 regulates DMC1-mediated recombination through the BRC repeats. *Proc Natl Acad Sci USA* **113**, 3515–3520 (2016).
- Schanda, P., Kupče, ě. & Brutscher, B. SOFAST-HMQC experiments for recording two-dimensional heteronuclear correlation spectra of proteins within a few seconds. *J. Biomol. NMR* **33**, 199–211 (2005).
- Vonrhein, C. et al. Data processing and analysis with the autoPROC toolbox. *Acta Crystallogr D Biol Crystallogr* **67**, 293–302 (2011).
- Adams, P. D. et al. PHENIX: a comprehensive Python-based system for macromolecular structure solution. *Acta Crystallogr D Biol Crystallogr* **66**, 213–221 (2010).
- Smart, O. S. et al. Exploiting structure similarity in refinement: automated NCS and target-structure restraints in BUSTER. *Acta Crystallogr D Biol Crystallogr* **68**, 368–380 (2012).
- Afonine, P. V. et al. Towards automated crystallographic structure refinement with phenix.refine. *Acta Crystallogr D Biol Crystallogr* **68**, 352–367 (2012).
- Emsley, P., Lohkamp, B., Scott, W. G. & Cowtan, K. Features and development of Coot. *Acta Crystallogr D Biol Crystallogr* **66**, 486–501 (2010).

Acknowledgements

The authors thank members of the AC lab for fruitful comments on the manuscript and Davide Panigada and Jose M. Jimenez-Gomez for the illustration of chromosomes in Fig. 9. We thank Rene H. Medema for useful discussions on this work including the cell synchronization protocol used in Fig. 7. We also thank Juan S. Martinez for construct BRCA2₁₋₂₅₀, Anne Houdusse for construct PLK1365-603, Carine Giovannangeli for TALEN plasmids, Eric Nigg for pS676-BUBR1 antibody and Geert JPL Kops for BUBR1-RFP construct. We acknowledge the Cell and Tissue Imaging Facility of the Institut Curie (PICT), a member of the France BioImaging National Infrastructure (ANR-10-INBS-04), and the French Infrastructure for Integrated Structural Biology (<https://www.structuralbiology.eu/networks/frisbi>, ANR-10-INBS-05-01). We thank Charlene Lasgi from the Flow Cytometry platform of Institut Curie, Orsay. We thank Guillaume Hoffmann and Jose A. Marquez from the HTXLab (Grenoble, France), funded by the European Community's Seventh Framework Programme H2020 under iNEXT (grant agreement No. 653706). This work was supported by the ATIP-AVENIR CNRS/INSERM Young Investigator grant 201201, FRM "Amorçage Jeunes Equipes" Young Investigator grant AJE20110 and Institut National du Cancer INCa-DGOS_8706 to A.C. and S.Z.J.; A. E. was supported by the Swedish Society for Medical Research.

Author contributions

A.E. purified WT and mutated BRCA2₁₋₂₅₀, established the stable DLD1^{-/-} cell lines, performed kinase assays, pull-down assays, Western blots, time-lapse microscopy experiments, mitotic index measurements by FACS, clonogenic survival and MTT assays as well as the statistical analysis for all the experiments. C.M. performed Western blot of pT207, IF and image acquisition of cold-stable microtubules, metaphase plate alignment, chromosome segregation and karyotype analysis. M.J. performed the NMR experiments

assisted by S. M., F.T., and S.Z.J. M.J. and S.M. purified PLK1_{PBD} and performed the ITC experiments. S.M. solved the X-ray structure assisted by V.R. R.B. and G.S. performed IF, image acquisition and quantification of DNA repair foci. V.B. assisted establishing stable clones and performing clonogenic survival assays. P.D. purified PLK1_{PBD}. A.M. cloned and produced PLK1 and PLK1-KD from insect cells. A.C., A.E., and S.Z.J. designed the experiments. A.C. and S.Z.J. supervised the work. A.C. wrote the paper with important contributions from all authors.

Competing interests

The authors declare no competing interests.

Additional information

Supplementary information is available for this paper at <https://doi.org/10.1038/s41467-020-15689-9>.

Correspondence and requests for materials should be addressed to S.Z.-J. or A.C.

Peer review information *Nature Communications* thanks Georges Mer, Elmar Schiebel and the other, anonymous, reviewer(s) for their contribution to the peer review of this work. Peer reviewer reports are available.

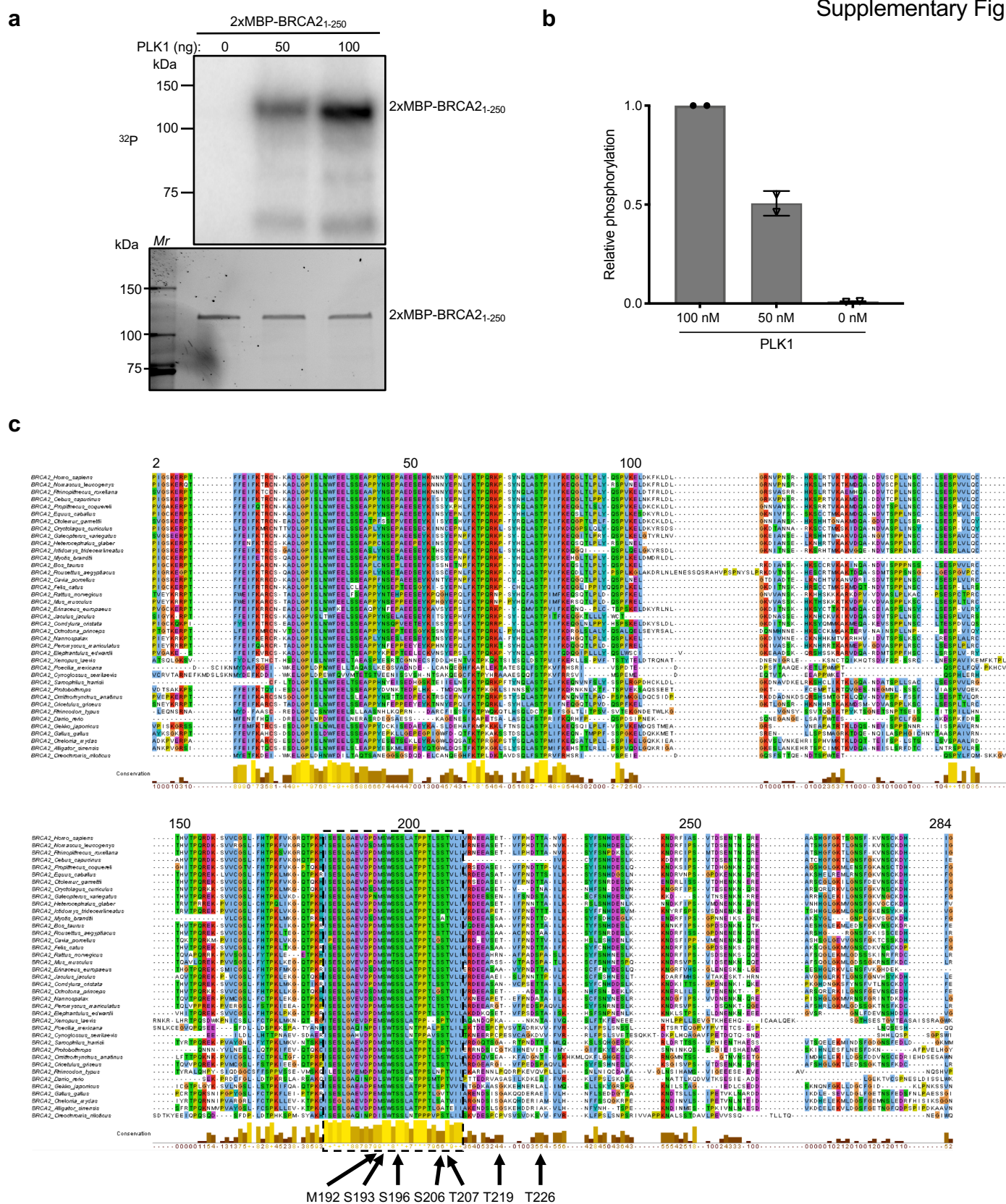
Reprints and permission information is available at <http://www.nature.com/reprints>

Publisher's note Springer Nature remains neutral with regard to jurisdictional claims in published maps and institutional affiliations.



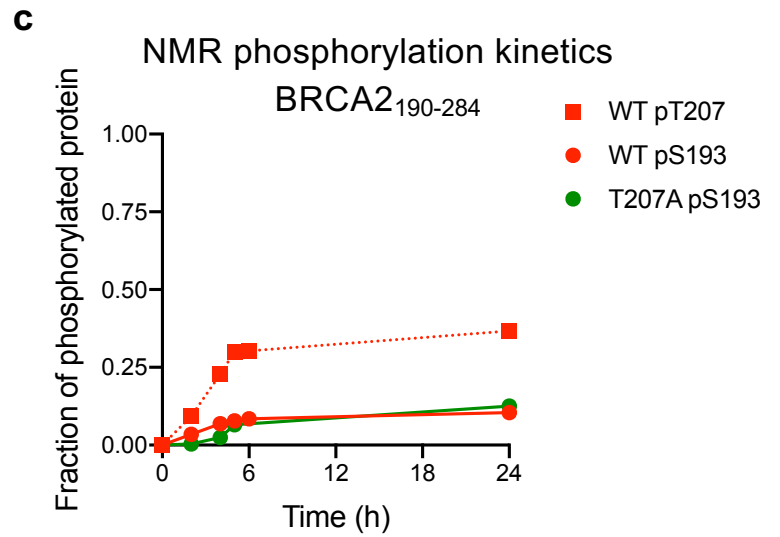
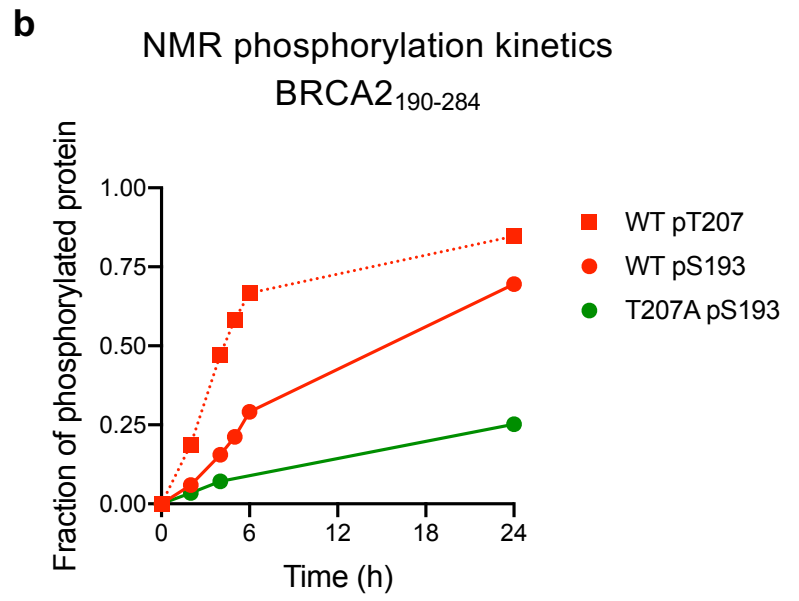
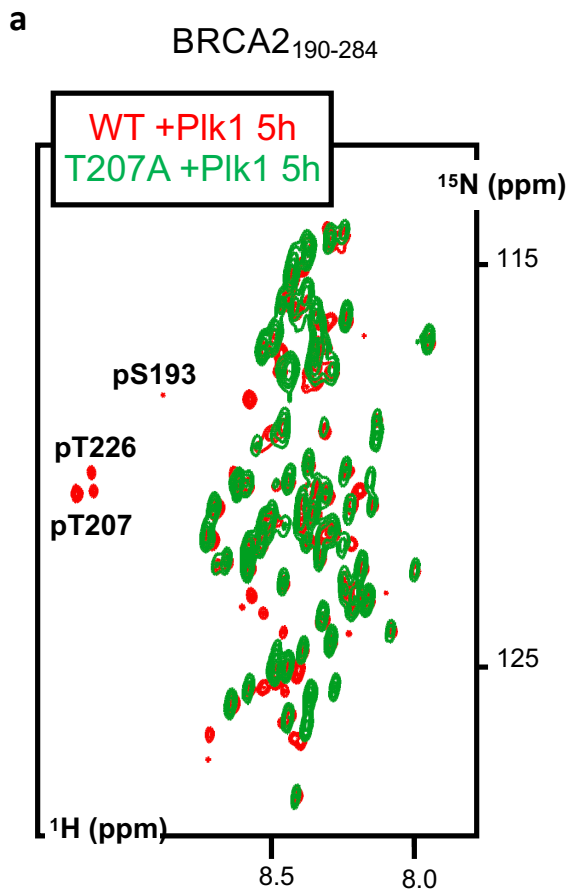
Open Access This article is licensed under a Creative Commons Attribution 4.0 International License, which permits use, sharing, adaptation, distribution and reproduction in any medium or format, as long as you give appropriate credit to the original author(s) and the source, provide a link to the Creative Commons license, and indicate if changes were made. The images or other third party material in this article are included in the article's Creative Commons license, unless indicated otherwise in a credit line to the material. If material is not included in the article's Creative Commons license and your intended use is not permitted by statutory regulation or exceeds the permitted use, you will need to obtain permission directly from the copyright holder. To view a copy of this license, visit <http://creativecommons.org/licenses/by/4.0/>.

© The Author(s) 2020



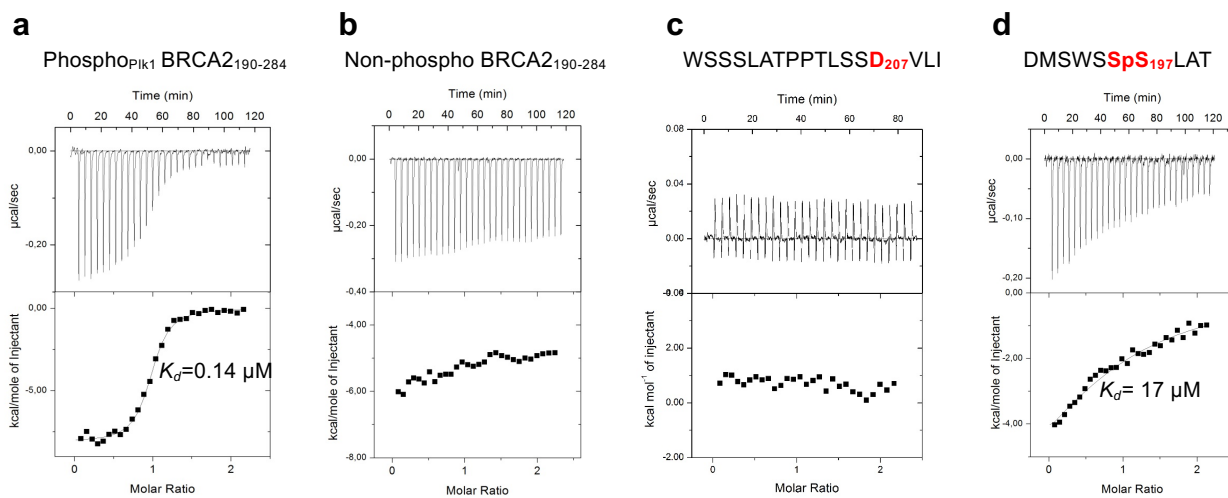
Supplementary Figure 1. Related to Figure 1. PLK1 phosphorylation of the N-terminal region of BRCA2 and conservation of PLK1 phosphosites

(a) PLK1 *in vitro* kinase assay with BRCA2₁₋₂₅₀. Top: The polypeptide 2x-MBP-BRCA2₁₋₂₅₀ WT was incubated with increased concentrations (0, 50 and 100 ng) of recombinant PLK1 in the presence of $\gamma^{32}\text{P}$ -ATP. The samples were resolved on 4-15% SDS-PAGE and the ^{32}P -labeled products were detected by autoradiography. Bottom: 4-15% SDS-PAGE showing the input of 2xMBP-BRCA2₁₋₂₅₀ WT (0.5 μg) used in the reaction. **(b)** Quantification of the relative phosphorylation in (a). Data are represented as mean \pm SD from two independent experiments. **(c)** Alignment of the region 2-284 of human BRCA2 with the N-terminal regions of BRCA2 from 40 different species. Amino acids conserved in more than 30 % of the species are highlighted with coloured background. A dashed line box identifies the highly conserved cluster around S193 (amino acid 180 to amino acid 210). Arrows show the amino acids cited in this manuscript (including the PLK1 phosphosites). Source data is available as a Source Data file.



Supplementary Figure 2. Related to Figure 2. PLK1 phosphorylation kinetics of BRCA2₁₉₀₋₂₈₄ WT vs T207A

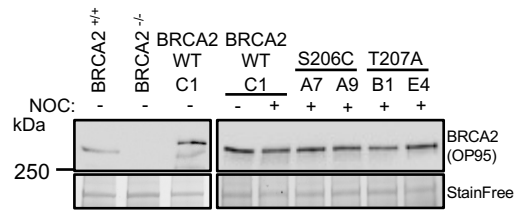
(a) Superimposition of the ¹H-¹⁵N HSQC spectra recorded on the ¹⁵N labelled fragments BRCA2₁₉₀₋₂₈₄ WT (red) and T207A (green) after 5h of incubation with PLK1. The conditions are the same as in Figure 1. **(b,c)** Comparison of the phosphorylation kinetics of BRCA2₁₉₀₋₂₈₄ WT and T207A performed with two different PLK1 samples. The percentage of phosphorylation deduced from the intensities of the peaks corresponding to the non-phosphorylated and phosphorylated residues is plotted as a function of time. WT S193 and T207 time points are represented by red circles and squares, respectively, while T207A S193 timepoints are represented by green circles. Source data is available as a Source Data file.



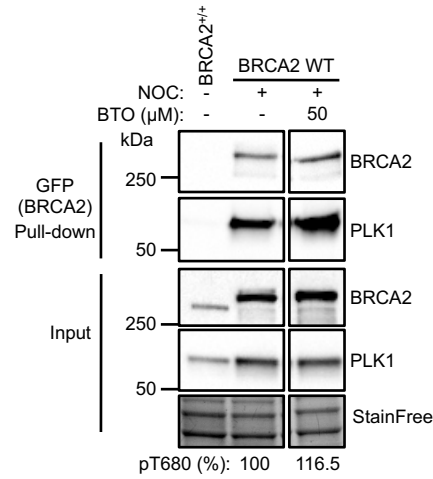
Supplementary Figure 3. Related to Figure 3. Isothermal Titration Calorimetry (ITC) thermogram showing binding of PLK1_{PBD} to the fragment BRCA2₁₉₀₋₂₈₄ or a 10 aa BRCA2 peptide containing pS197

Thermogram showing the binding affinity of PLK1_{PBD} to the **(a)** phosphorylated or **(b)** non-phosphorylated BRCA2₁₉₀₋₂₈₄ fragment, purified from bacteria as explained in the Methods section and also used in the NMR experiments. **(c)** Thermogram showing the binding affinity of PLK1_{PBD} to a 17 aa BRCA2 synthetic peptide comprising T207D (WSSSLATPPTLSSD₂₀₇VLI). **(d)** Thermogram showing the binding affinity of PLK1_{PBD} to a 10 aa BRCA2 synthetic peptide comprising pS197. Source data is available as a Source Data file.

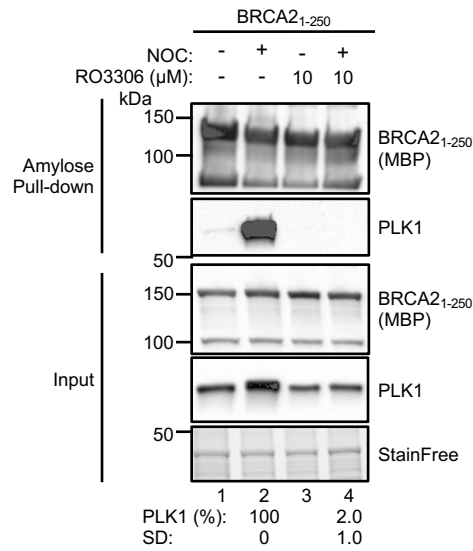
a



b

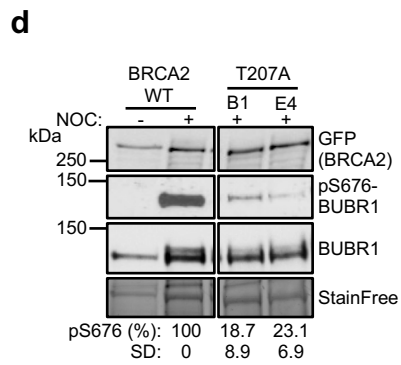
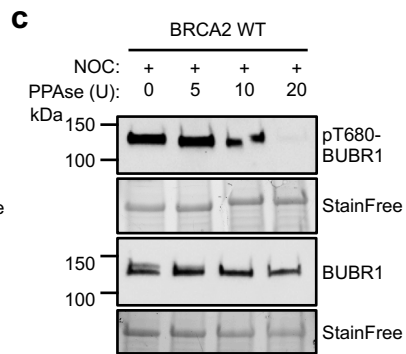
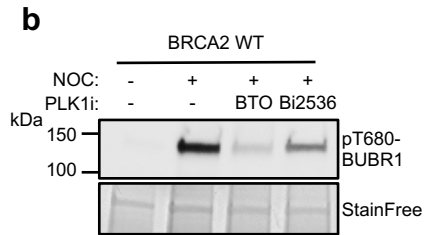
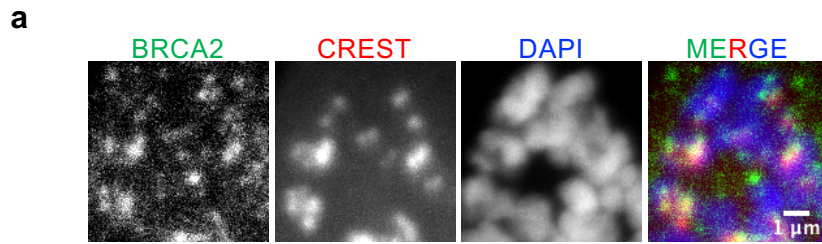


c



Supplementary Figure 4. Related to Figures 3-8. BRCA2 protein levels in DLD1 BRCA2^{-/-} stable clones bearing BRCA2 WT and variants utilized in this study and effect of PLK1 and CDK1 inhibitors on the interaction between BRCA2 and PLK1

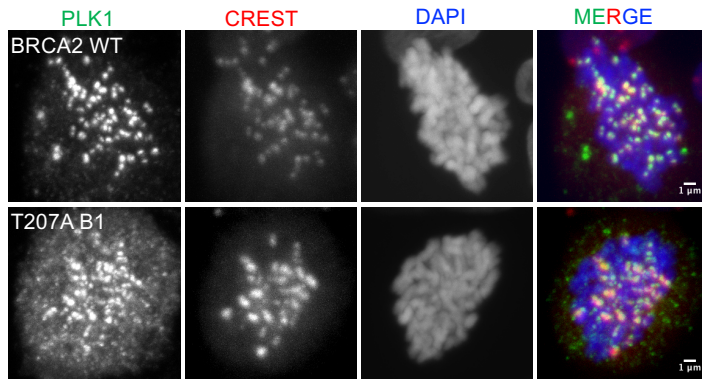
(a) BRCA2 protein levels in total cell extracts from DLD1 cells stably expressing EGFP-MBP-BRCA2 WT (BRCA2 WT C1) or the variants S206C (clones A7 and A9) and T207A (clones B1 and E4) as detected by western blot using anti-BRCA2 (OP95) antibody. **(b)** The effect of PLK1 inhibitors on the interaction between BRCA2 WT and PLK1. BRCA2 WT cells were treated with nocodazole (100 ng/ml, 14h), then treated with the PLK1 inhibitor BTO (50 μ M, 2h) before harvesting. BRCA2 was pull-down with GFP-trap beads, immunocomplexes were resolved on 4-15% SDS-PAGE followed by WB using anti-PLK1 and -MBP antibodies. Unsynchronized BRCA2^{+/+} were used as control of pull-down and StainFree images of the gels before transfer were used as loading control (cropped image is shown). The amount of PLK1 co-IPed with BRCA2 relative to the input levels of PLK1 and the amount of pull-down BRCA2 is presented below the blot, relative to non-treated BRCA2 WT. **(c)** The effect of CDK1 inhibitors on the interaction between 2xMBP-BRCA2₁₋₂₅₀ and PLK1. U2OS cells transiently transfected with the 2xMBP-BRCA2₁₋₂₅₀ WT, were arrested in mitosis with nocodazole (300 ng/ml, 14h) and then treated with CDK1 inhibitor (Ro-3306 50nM, 2h) before amylose pull-down. Complexes were resolved on 4-15% SDS-PAGE followed by WB using anti-PLK1 and anti-MBP antibodies. The amount of PLK1 co-immunoprecipitated with 2xMBP-BRCA2₁₋₂₅₀ relative to the input levels of PLK1 and the amount of pull-down 2xMBP-BRCA2₁₋₂₅₀ is presented below the blot as mean \pm SD from three independent experiments. The data is presented relative to the non-treated BRCA2 WT. Immunoblots in (a) and (c) are representative of three independent experiments. Source data is available as a Source Data file.



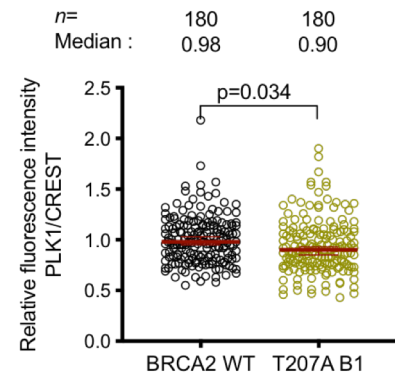
Supplementary Figure 5. Related to Figure 5. BRCA2 at the kinetochores and effect of PLK1 inhibitors and phosphatase treatment on pT680-BUBR1.

(a) Representative images of the localization of BRCA2 in nocodazole-arrested U2OS transient expressing GFP-MBP-BRCA2 WT. BRCA2 is detected by anti-BRCA2 rabbit antibody (CA1033), CREST is used as centromere marker and DNA is counterstained with DAPI. Scale bar represents 1 μ m. The figures are representative of three independent experiments. **(b)** Protein levels of pT680-BUBR1 in BRCA2 WT stable clone after treatment with PLK1 inhibitors. After 14h culture with media containing nocodazole (100 ng/ μ l), PLK1 inhibitors (Bi2536 (50 nM) or BTO (50 μ M)) were added to the media and the cells were cultured for additional 2h before harvesting. The level of pT680-BUBR1 was analyzed in the total protein extract by western blot. **(c)** Phosphatase (Fast AP) treatment of total protein lysate extracted from DLD1 BRCA2 WT cells treated with nocodazole (100 ng/ μ l) for 14h. **(d)** Western blot showing the expression levels of endogenous BUBR1 and pS676-BUBR1 in nocodazole treated stable clones of DLD1 BRCA2 deficient cells (BRCA2^{-/-}) expressing GFPMBP-BRCA2 WT (BRCA2 WT) or T207A variant. The levels of pS676-BUBR1 was analyzed in the total protein extract by western blot. The mean pBUBR1 signal relative to the stain free signal is shown for the nocadazole treated samples below the blots. Results are presented normalized to the protein levels for BRCA2 WT. The data represents the mean \pm SD of two independent experiments. Immunoblots in (b-d) are representative of two (b, d) and three (c) independent experiments. Source data is available as a Source Data file.

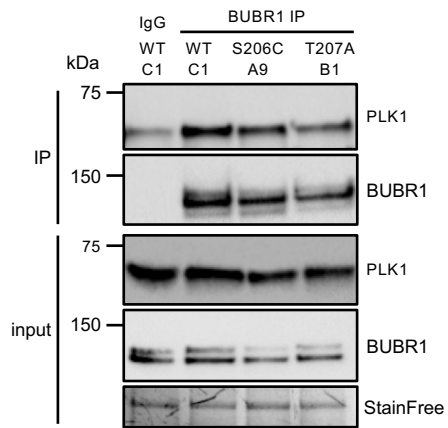
a



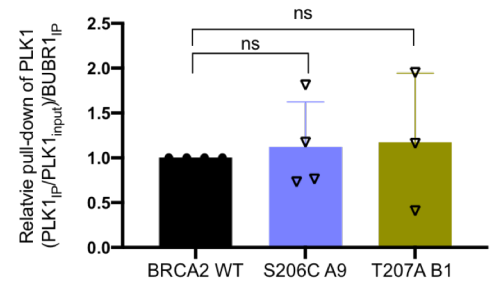
b



c



d



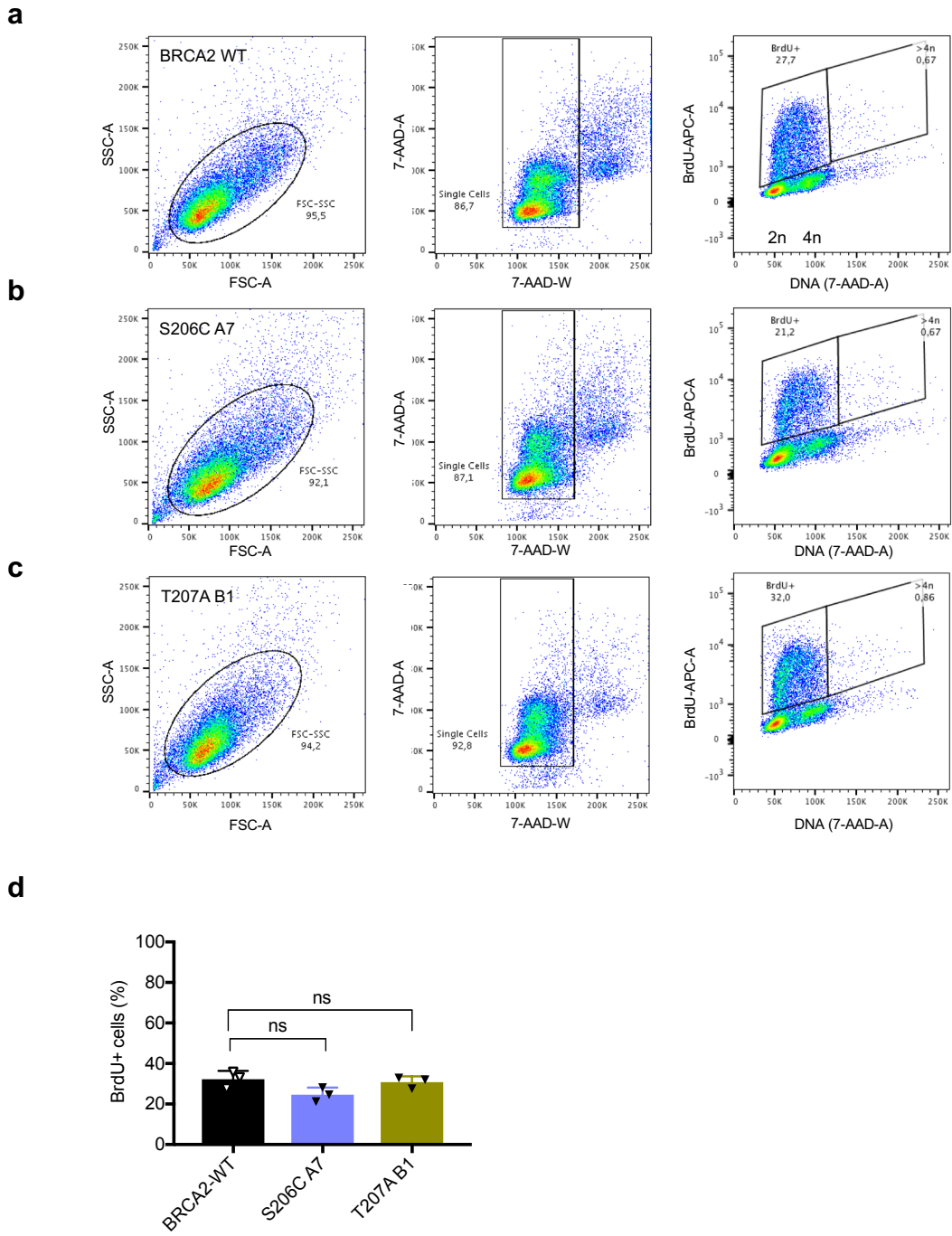
Supplementary Figure 6. Related to Figure 5. Localization of BRCA2 and PLK1 at the kinetochores and PLK1-BUBR1 complex in cells bearing variant T207A compared to WT

(a) Representative images of the localization of PLK1 in nocodazole-arrested DLD1 BRCA2^{-/-} cells stably expressing GFP-MBP-BRCA2 WT or the variant T207A as indicated. CREST is used as centromere marker and DNA is counterstained with DAPI. Scale bar represents 1 μ m.

(b) Quantification of the co-localization of PLK1 and CREST in (a). The data represents the intensity ratio (PLK1:CREST) relative to the mean ratio of PLK1:CREST for the GFP-MBP-BRCA2 WT calculated from a total of 180 pairs of chromosomes analysed from two independent experiments (6 pairs of chromosomes/cell from 15 cells). The red line in the plot indicates the median (95% CI) ratio, each dot represents a pair of chromosomes. For statistical comparison of the differences between the samples we applied a Mann-Whitney two-tailed analysis, the p-values show significant difference.

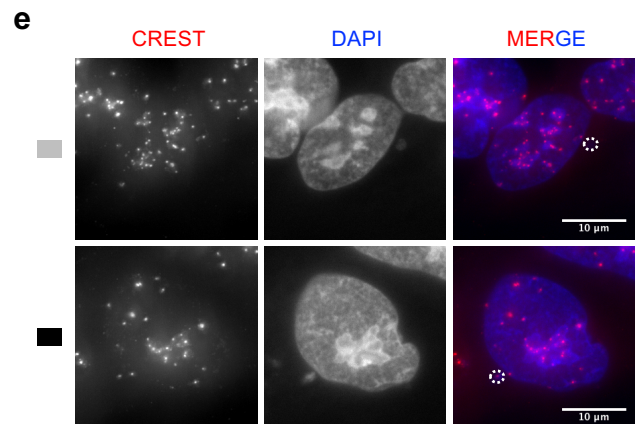
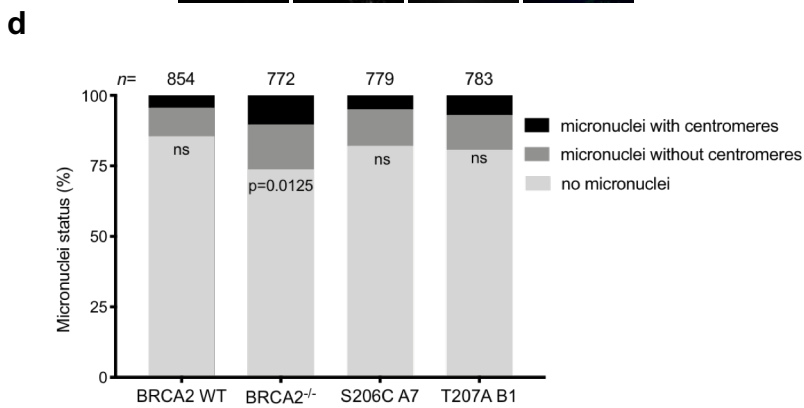
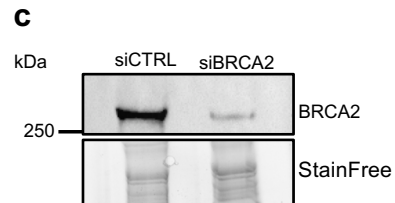
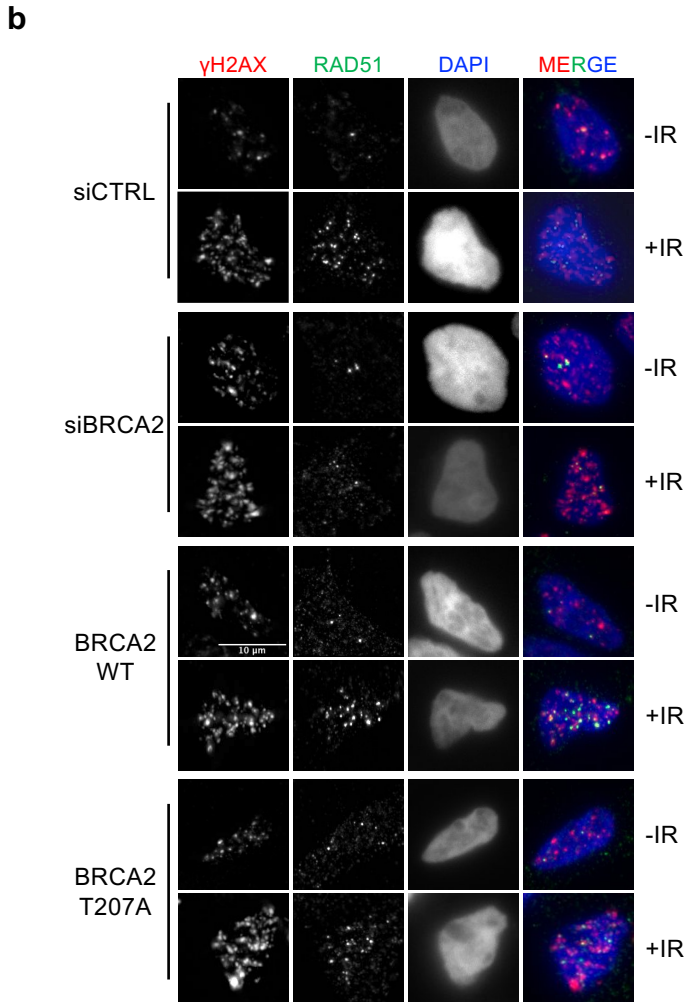
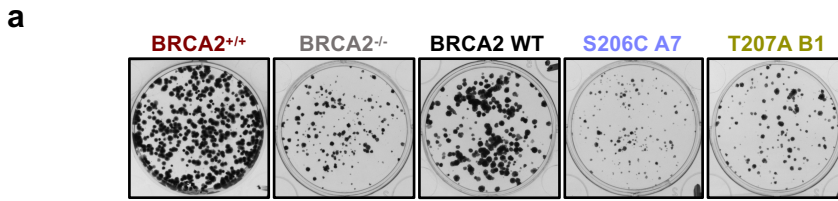
(c) Co-immunoprecipitation of endogenous PLK1 with endogenous BUBR1 from mitotic cell extracts of BRCA2 WT cells or cells expressing the variants S206C or T207A using mouse anti-BUBR1 antibody. Mouse IgG was used as control for the BUBR1 immunoprecipitation. The immuno-complexes were resolved on 4-15% SDS-PAGE followed by western blotting, the interactions were revealed by rabbit anti-BUBR1 and mouse anti-PLK1 antibodies.

(d) Quantification of co-immunoprecipitated PLK1 in (c), relative to the input levels and the amount of immunoprecipitated BUBR1. Results are presented as the fold change compared to the BRCA2 WT clone. The data represents the mean \pm SD of three to four independent experiments (WT (n=4), S206C A9 (n=4) and T207A B1 (n=3)). Statistical significance of the difference was calculated with one-way ANOVA test with Dunnett's multiple comparisons test, the p-values show the significant difference, ns: non-significant. Source data is available as a Source Data file.



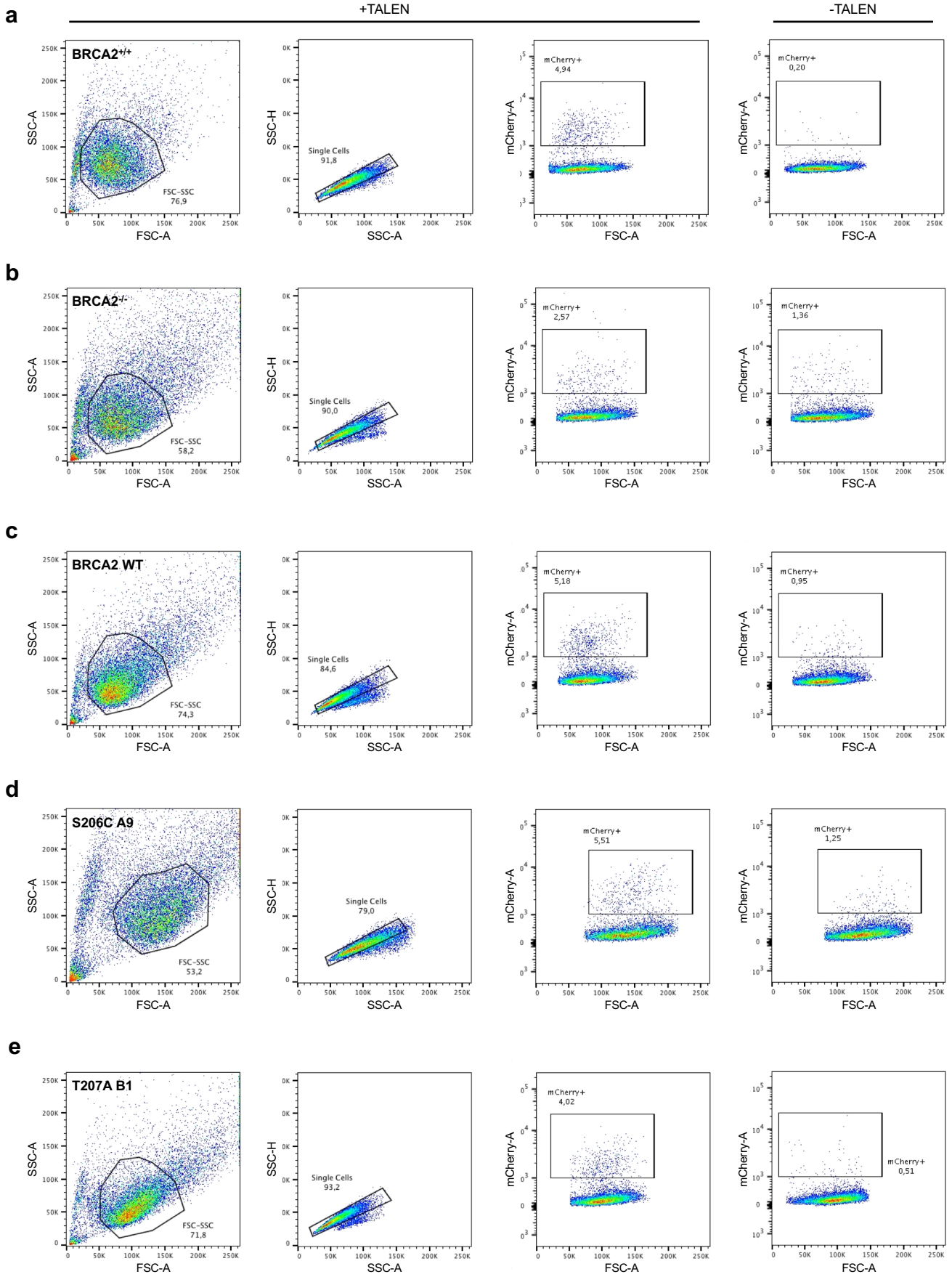
Supplementary Figure 7. Related to Figure 7. BrdU incorporation measured by flow cytometry of DLD1 BRCA2^{-/-} stable cell lines expressing BRCA2 WT or BRCA2 variants S206C and T207A.

(a-c) Representative flow cytometry plots for the analysis of S-phase tetraploid cells (quantified in Figure 7c, d) in the stable DLD1 BRCA2 deficient cells expressing BRCA2 WT (a) or the VUS S206C (b) and T207A (c). Viable cells were gated from the Forward Scatter (FSC-A) versus Side Scatter (SSC-A) plots and displayed in a 7-AAD-W versus 7-AAD-A plot to exclude doublets. The gated singlet population was displayed in a APC-A (BrdU) versus 7-AAD-A (DNA) plot. The S-phase tetraploid population was gated as BrdU⁺ cells with DNA content >4N. 20,000 singlet events were collected for each experiment. **(d)** Frequency of BrdU⁺ cells in the stable clones expressing BRCA2 WT or the VUS as indicated. The data represents the mean \pm SD of three independent experiments. Statistical significance of the difference was calculated with one-way ANOVA test with Tukey's multiple comparisons test (the p value show the difference compared to WT, ns: non-significant). Source data is available as a Source Data file.



Supplementary Figure 8. Related to Figure 8. **Plating efficiency of unchallenged DLD1 BRCA2^{-/-} stable clones expressing EGFP-MBP-BRCA2 WT or the variants, and representative images of DNA damage foci in these cells. Micronuclei in BRCA2^{-/-} stable cell lines and BRCA2^{-/-} expressing BRCA2 WT or BRCA2 variants S206C and T207A.**

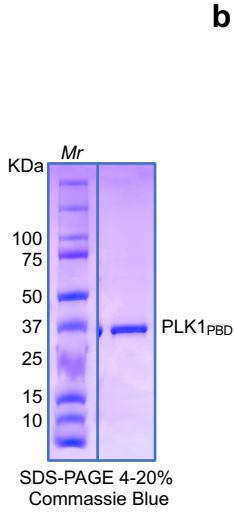
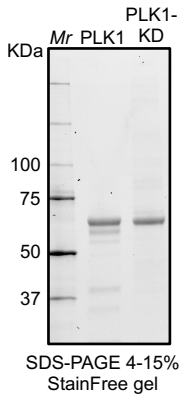
(a) Representative plates showing the number of colonies in unchallenged conditions of the cells assessed for MMC-clonogenic survival assay quantified in Fig. 9a (500 cells seeded per 6-well plate). **(b)** Representative immunofluorescence images of two independent experiments of nuclear γ H2AX and RAD51 foci in DLD1 BRCA2^{+/+} cells depleted of BRCA2 (siBRCA2), BRCA2^{+/+} control cells (siCTRL), DLD1 BRCA2 deficient cells (BRCA2^{-/-}) stably expressing BRCA2 WT or the variant T207A, in non-treated (-IR) or two hours after exposure to 6 Gy of γ -irradiation (+IR), as indicated in the images and as quantified in Fig. 9d, 9e. Scale bar represents 10 μ m. **(c)** Representative Western blot of two independent experiments showing the levels of endogenous BRCA2 in the siRNA transfected cells imaged in (b) and analysed in Fig. 9d, 9e, at the time for radiation. **(d)** Frequency of micronuclei with and without centromeres in DLD1 BRCA2 deficient cells (BRCA2^{-/-}) and BRCA2^{-/-} clones stably expressing BRCA2 WT or the variants S206C and T207A. *n* indicates the total number of cells counted for each clone from two independent experiments. Statistical significance of the difference was calculated with two-way ANOVA test with Tukey's multiple comparisons test, the p-values show the significant difference, ns: non-significant. **(e)** Representative images of micronuclei with and without centromeres observed in cells quantified in (d), scale bar represents 10 μ m. Source data is available as a Source Data file.



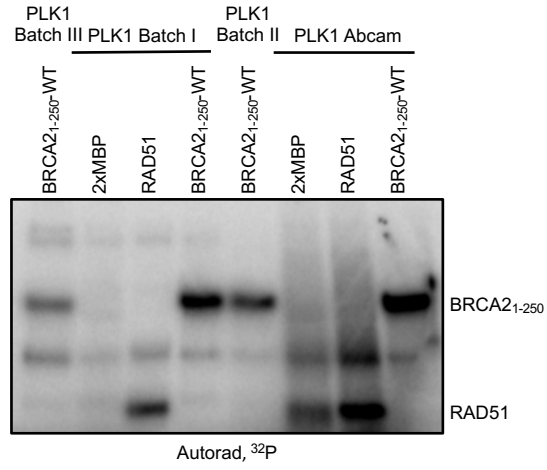
Supplementary Figure 9. Related to Figure 8f. Frequency of mCherry positive cells measured by flow cytometry of DLD1 BRCA2^{-/-} stable cell lines expressing BRCA2 WT or BRCA2 variants S206C and T207A.

(a-e) Representative flow cytometry plots for the analysis of mCherry positive cells in the HR assay (quantified in Fig. 9f) in DLD1 cells with endogenous BRCA2 (BRCA2^{+/+}) (a), DLD1 BRCA2 deficient cells (BRCA2^{-/-}) (b), BRCA2 deficient cells expressing BRCA2 WT (c) or the VUS S206C (d) and T207A (e). Viable cells were gated from the Forward Scatter (FSC-A) versus Side Scatter (SSC-A) plots and displayed in a SSC-H versus SSC-A plot to exclude doublets. The gated singlet population was displayed in a mCherry-A versus FSC-A plot. The mCherry positive population was gated from non-transfected cells. 10 000 singlet events were collected for each experiment. Source data is available as a Source Data file.

a



b



Supplementary Figure 10. SDS-PAGE of the PLK1, PLK1-KD and PLK1-PBD recombinant proteins utilized in this study and comparison of the kinase activity of each batch of PLK1

(a) SDS-PAGE showing purified PLK1, PLK1-K82R mutant (PLK1-KD) and PLK1_{PBD}.

Human PLK1 was expressed and purified from sf9 insect cells using Ni-NTA column followed by a second purification step with a cationic exchange Capto S column. Purified PLK1 and PLK1-K82R protein (3 µg) were loaded on a 4-15% SDS-PAGE Stain-Free gel. For purification of PLK1_{PBD}, 6His-Sumo-PLK1_{PBD} was expressed and purified from bacteria using a His-TRAP column, the His-tag was cleaved with 6xHis-SUMO Protease and the cleaved PLK1_{PBD} was further purified using Ni-NTA agarose resin. The purified protein was loaded on a 4-20% SDS-PAGE (1.4 µg) and detected by Coomassie staining. *Mr*; molecular weight markers. **(b)** *In vitro* kinase assay with the purified PLK1 (0.1 µg) from (a) or PLK1 purchased from Abcam, 0.1 µg PLK1 was used in the kinase reaction with either RAD51 (25 ng) or purified 2xMBP-BRCA2₁₋₂₅₀ WT (0.5 µg) as substrate in the presence of [$\gamma^{32}\text{P}$]-ATP. The samples were resolved by 7.5 % SDS-PAGE and ^{32}P -labeled products were detected by autoradiography. Source data is available as a Source Data file.

Supplementary Table 1: Number of records in ClinVar and BRCAShare data bases of the variants identified in breast cancer patients altering the amino acids investigated in this work. The specific VUS utilized in this study are highlighted in bold.

VUS	ClinVar	BRCAShare
M192T	2	0
S196I	4	0
S196N	4	3
S196T	1	0
S206C	1	1
S206Y	1	0
T207A	3	0
T207I	4	0

Supplementary Table 2: Statistics table for the crystal structure of PBD_pT207, a complex between the Polo-Box Domain of human PLK1 (aa 365 to aa 603) and the 17aa peptide pT207 of BRCA2 (aa 194 to aa 210, threonine 207 being phosphorylated).

	PBD_T207 phosphorylated (PDB 6GY2)
Data collection	
Space group	P ₁
Cell dimensions :	
<i>a</i> , <i>b</i> , <i>c</i> (Å)	50.000 56.040 61.030
α , β , γ (°)	80.79 79.23 65.05
Molecules per a.u	2
Resolution (Å)	59.70 – 3.106 (3.106 – 3.16)
<i>R</i> _{merge}	0.056 (0.346)
<i>R</i> _{meas}	0.076 (0.466)
<i>R</i> _{pim}	0.051 (0.31)
<i>I</i> / σ (<i>I</i>)	10.1 (2.3)
<i>CC</i> _{1/2}	0.997 (0.821)
Completeness (spherical, %)	93.7 (96.9)
Redundancy	1.94 (1.977)
B Wilson (Å ²)	76.9 (78.86)
Multiplicity	1.9 (2.0)

Refinement

Resolution (Å)	22.57 - 3.11 (3.11 – 3.15)
No. reflections	9911
$R_{\text{work}} / R_{\text{free}}$	0.189/0.215
No. Atoms	
Protein	3788
Heterogen atoms	28
Water	22
R.m.s. deviations	
Bond lengths (Å)	0.007
Bond angles (°)	0.97

*Values in parentheses are for highest-resolution shell.

Supplementary Table 3: Primers used to introduce point mutations in EGFMBP-BRCA2, 2xMBP-BRCA2₁₋₂₅₀, GST-BRCA2₁₉₀₋₂₈₄ constructs

Mutation	Oligo name	Sequence (5'-3')
S193A	Fw : oAC543	CCC ACC CTT AGT TCT GCT GTG CTC ATA GTC
	Rv : oAC544	GAC TAT GAG CAC AGC AGA ACT AAG GGT GGG
M192T	Fw : oAC283	GTGGATCCTGATACGTCTTGGTCAAGTTC
	Rv : oAC284	GA ACT TGA CCA AGA CGT ATC AGG ATC CAC
S196N	Fw : oAC026	CCTGATATGTCTTGGTCAAATTCTTTAGCTACA CCACC
	Rv : oAC027	GGTGGTGTAGCTAAAGAATTTGACCAAGACAT ATCAGG
S206C	Fw : oAC028	CCACCCACCCTTAGTTGTACTGTGCTCATAGTC AG
	Rv : oAC029	CTGACTATGAGCACAGTACA ACTAAGGGTGGG TGG
T207A	Fw : oAC545	GGA TCC TGA TAT GGC TTG GTC AAG TTC TTT AGC

	Rv : oAC546	GCT AAA GAA CTT GAC CAA GCC ATA TCA GGA TCC
--	-------------	--

Supplementary Table 4: Sequencing primers

Construct	Oligo name	Binding site	Sequence (5'-3')
GFPMBP- BRCA2, GST- BRCA2 ₁₉₀₋₂₈₄	Rv : oAC131	aa 273 BRCA2	TTAGTTCGACTTATCCAATGTGGTCTTT
2xMBP- BRCA2 ₁₋₂₅₀	Fw : oAC149	aa 1-6 BRCA2	TTATTTGCTAGCCCTATTGGATCCAAAGAG
PLK1	Fw : oAC907	aa 38 PLK1	AAAGAGATCCCGGAGGTCCTAGTG

Supplementary Table 5: Primers used to subclone BRCA2₁₉₀₋₂₈₄ into the pGEX-6P-1 vector

Construct	Oligo name	Sequence (5'-3')
BRCA2 ₁₉₀₋₂₈₄	Fw: oAC130	TTAGGATCCATGTCTTGGTCAAGTTCT
	Rv: oAC131	TTAGTTCGACTTATCCAATGTGGTCTTT

Supplementary Table 6: Primers used to subclone *PLK1* cDNA into pFastBac HT

Primer name	Sequence (5'-3')
GA_pFBtev_R	GCCCTGAAAATACAGGTTTTTCGGTCGTTGGGAT

GA_pFB_UTR _F	TTGTCGAGAAGTACTAGAGGATCATAATCA
GA_hPLK_F	ATCCCAACGACCGAAAACCTGTATTTTCAGGGCATGAGT GCTGCAGTGACTGCA
GA_hPLK_R	TGATTATGATCCTCTAGTACTTCTCGACAATTAGGAGGC CTTGAGACGGTT

Supplementary Table 7: Primers used to introduce K82R point mutation in pFastBAC-PLK1 vector to produce PLK1-KD and to subclone PLK1_{PBD} (aa 326-603) into pT7-His6-SUMO

Product	Oligo name	Sequence (5'-3')
K82R-PLK1	Fw : oAC905	GCG GGCAGGATTGTGCCTAAG
	Rv : oAC906	CTTAGGCACAATCCTGCCCGC
PLK1 _{PBD}	GA_PLKP DBwt_F	ATTGAGGCTCACCGCGAACAGATTGGTGGCTC GATTGCTCCCAGCAGCCT
	GA_PLKPDB wt_R	TTCCTTTCGGGCTTTGTTAGCAGCCGGTCATTA GGAGGCCTTGAGACGGT

Supplementary Table 8: Primers used to introduce S670D, S676D and T680D point mutations in pcDNA3-3xFlagBUBR1-RFP construct

Name	Sequence (5'-3')
oAC884	CAA GAA GCT GGA CCC AAT TAT TGA AGA CGA TCG TGA AGC CGA CCA CTC CTC
oAC885	GAG GAG TGG TCG GCT TCA CGA TCG TCT TCA ATA ATT GGG TCC AGC TTC TTG

Supplementary Table 9: Synthetic peptide sequences for Isothermal Titration Calorimetry (ITC) and X-ray crystallography

Peptide	Sequence
pS197	DMSWSS{pS}LAT
T207	WSSSLATPPTLSSTVLI
pT207	WSSSLATPPTLSS{pT}VLI
T207A	WSSSLATPPTLSSAVLI
T207D	WSSSLATPPTLSSDVLI
CpT207	WSSSLATPPTLSC{pT}VLI

Supplementary Table 10: Primers for amplifying BRCA2 (aa 1-267) from genomic DNA

Primer name	Sequence (5'-3')
Fw : oAC035	GGTCGTCAGACTGTCGATGAAGCC
Rv : oAC056	CAAAGAGAAGCTGCAAGTCATGGATTTGAAAAACATC AGGG

Supplementary Table 11: Oligos used for replacing GFP in AAVS1-2A-GFP to mCherry using Gibson Assembly strategy

Construct	Oligo name	Sequence (5'-3')
AAVS1-2A	Fw: oAC537	TAAAGCGGCCGCGTCGAGTCTAGAGGG
	Rv: oAC538	CATCTCGAGCCTAGGGCCGGG
AAVS1-2A-mCherry	Fw: oAC539	cccggcctaggctcgagatgGTGAGCAAGGGCGA GGAGGATAAC

	Rv: oAC540	ctctagactegacgcgccgctttaCTTGTACAGCTCGT CCATGCCGC
--	------------	---

Supplementary Table 12: TALEN sequences used in DSB-mediated gene targeting assay

Name	Sequence (5'-3')
TALEN AAVS 5'	TCCCCTCCACCCCACAGT
TALEN AAVS 3'	AGGATTGGTGACAGAAAA

In addition to the experiments of the article, I tried to phosphorylate BRCA2₄₈₋₂₁₈ in cell extracts (**Figure 44.A**). Although I have tried a number of conditions (amount of cell extracts, temperature, time of incubation), I observed only one event of phosphorylation after 1.5 h of incubation. Using 2D NMR experiments, I assigned this peak to the phosphorylated version of S70. Because S70 corresponds to a PKA phosphosite, I incubated BRCA2₄₈₋₂₁₈ with purified commercial PKA *in vitro* (NE BioLabs). The first event of phosphorylation was S70 and 2 other phosphoevents appeared after long incubation times in presence of high quantities of kinase conditions (2500 units, i.e. 2500 pmol/min of phosphate transfer on a model peptide). PKA may thus phosphorylate BRCA2_{S70} in cell extracts. Unfortunately, we did not observe any phosphorylation corresponding to the Plk1 activity described above.

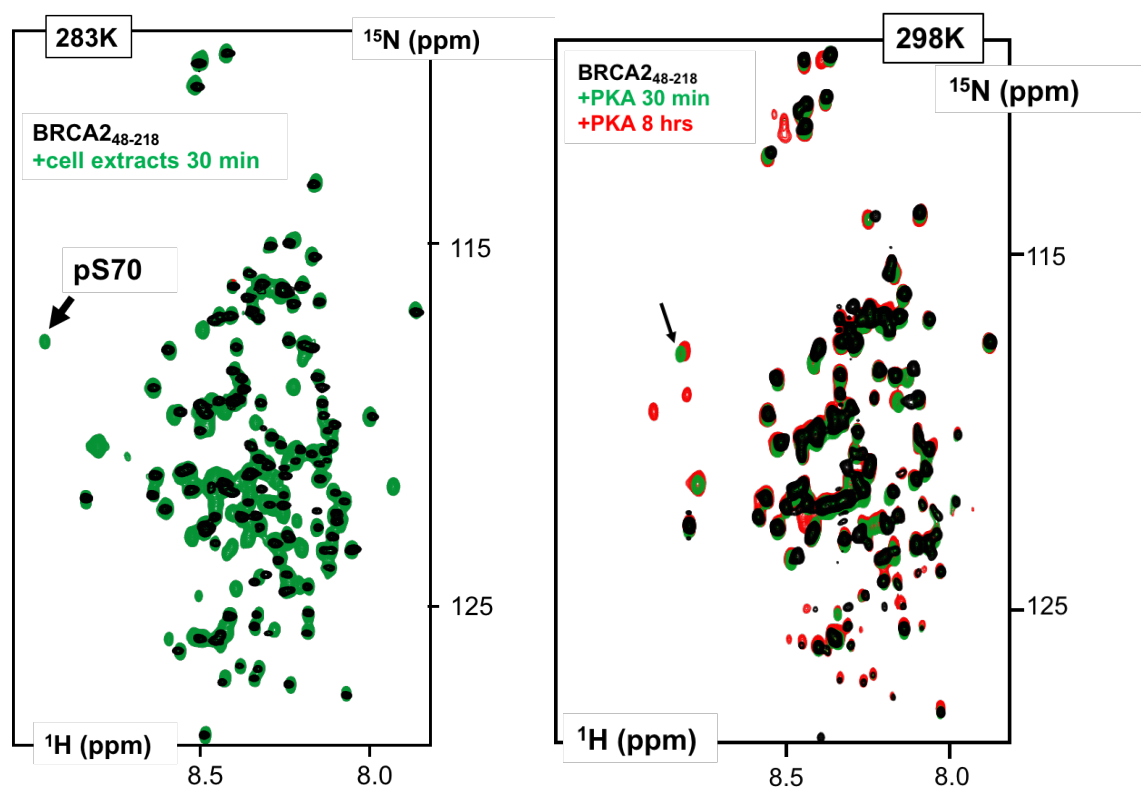


Figure 44. Phosphorylation of BRCA2₄₈₋₂₁₈ in cell extracts reveals the phosphorylation of S70 that may be executed by PKA.

(A) Overlay of ¹H-¹⁵N SOFAST-HMQC spectra of ¹⁵N BRCA2₄₈₋₂₁₈ at 130 μM before (black) and after 1.5 h incubation in mitotic cell extracts (green) in 50 mM HEPES, 150 mM NaCl, 2 mM ATP, 20 mM MgCl₂, 1X PI, 1X Phospho-STOP, 2 mM DTT, 10% D₂O, at pH 7.0, 283 K (600 MHz). **(B)** Superimposition of ¹H-¹⁵N SOFAST-HMQC spectra of ¹⁵N BRCA2₄₈₋₂₁₈ at 50 μM before (black) and after 30 min (green) or 8 hrs (red) of incubation in presence of 2500 units of PKA in NEB Buffer (NE BioLabs), supplemented with 200 μM ATP, 1X PI, 5% D₂O, pH 7.5, 298 K (600 MHz). The peak of pS70 is highlighted by an arrow.

I also performed an NMR analysis of the interaction between phosphorylated BRCA2₁₆₇₋₂₆₀ and Plk1_{PBD} (**Figure 45**). Interestingly, the addition of Plk1_{PBD} decreased the ¹H-¹⁵N peak intensities of almost every BRCA2₁₆₇₋₂₆₀ residue. Residues around T207 show the largest intensity decrease upon addition of Plk1_{PBD}. Here, NMR did not provide a precise delimitation of the binding site within this IDR. We can hypothesize that pBRCA2₁₆₇₋₂₆₀ is anchored to Plk1_{PBD} at the position pT207, and that its positively and negatively charged stretches interact in a very loose fashion with the electrostatic patches present on the surface of Plk1_{PBD}. Such fuzzy interactions are a common theme in the IDP community. We did not go further in the biophysical characterization of this interaction though.

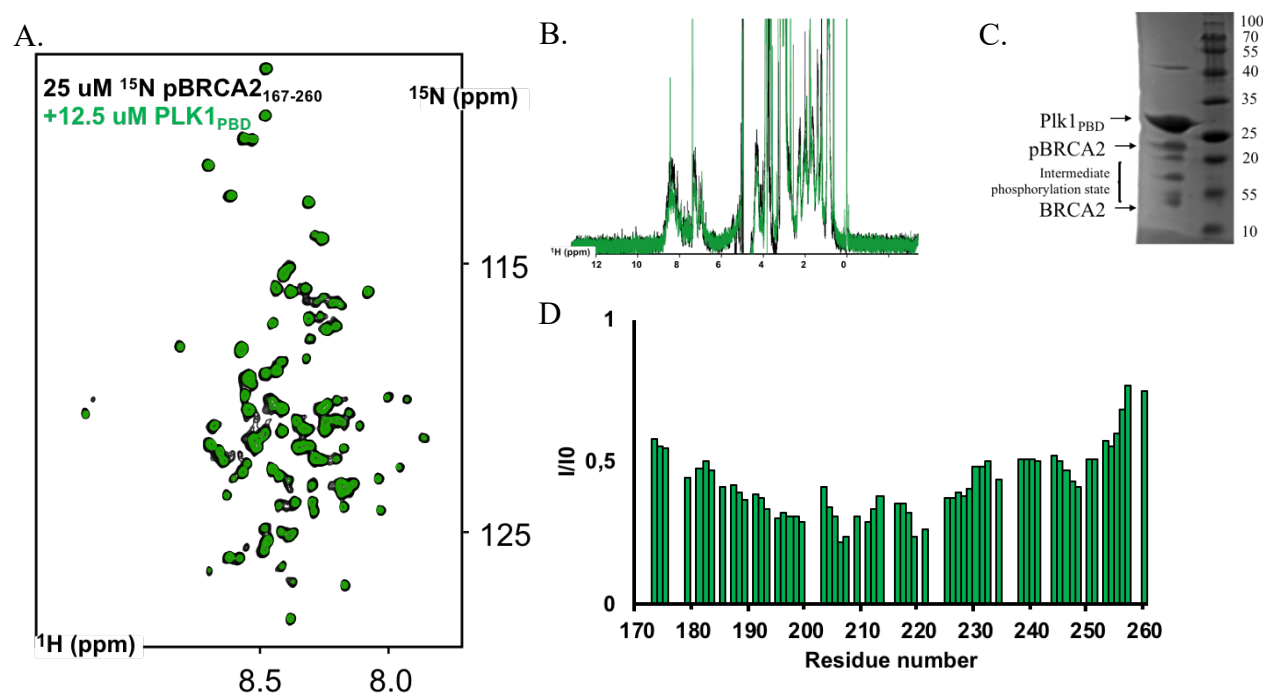


Figure 45. Interaction between pBRCA2₁₆₇₋₂₆₀ and Plk1_{PBD}, as observed by NMR (**A**) Overlay of the ¹H-¹⁵N SOFAST-HMQC spectra and (**B**) ¹H 1D spectra of 25 uM ¹⁵N labeled pBRCA₁₆₇₋₂₆₀ either free (black) or in the presence of 12.5 uM unlabeled Plk1_{PBD} (green), in Dulbecco's PBS (Sigma) pH 7.0, 283K (600 MHz). (**C**) Coomassie-stained 15% SDS-PAGE analysis of the NMR sample containing pBRCA2 and PBD. (**D**) Peak intensity ratio as a function of the residue number and averaged over 3 residues, calculated from the analysis of the NMR experiments displayed in (**A**).

Dr Simona Miron and Dr. Virginie Ropars solved the structure of a complex between a peptide from BRCA2_{pT207} (W194 to I210) and Plk1_{PBD} (PDB code: 6GY2). Combined with ITC experiments, it showed that the motif S206-pT207 is the main determinant of BRCA2_{pT207} recognition by Plk1_{PBD}.

While the BRCA2/Plk1 interaction is new, several other interactions contributing to the formation of the quaternary complex between BRCA2_{pT207}, Plk1, BubR1 and PP2A have already been reported in the literature (**Figure 46**).

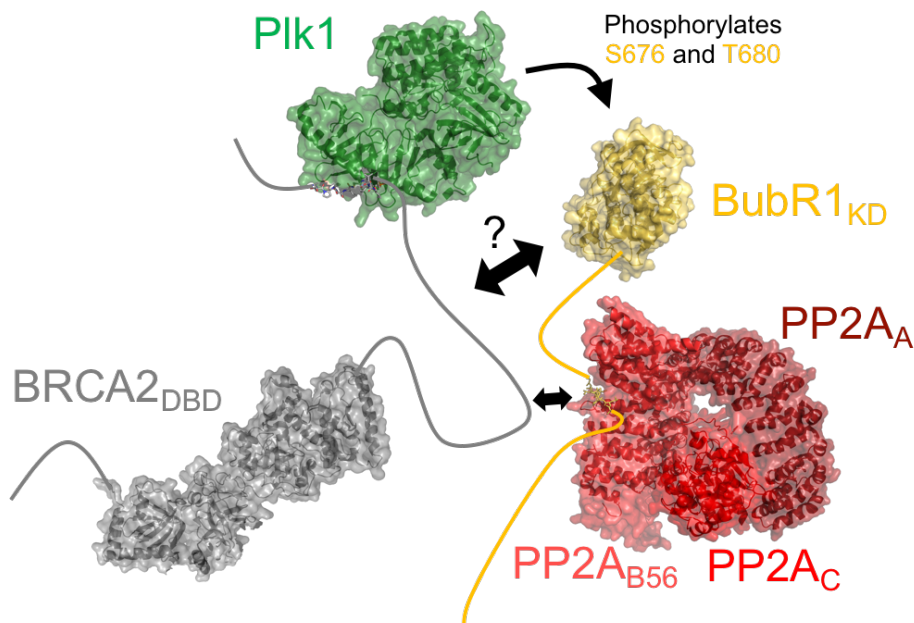


Figure 46. Scheme of the BRCA2/Plk1/BubR1/PP2A quaternary complex, necessary for chromosome segregation.

BRCA2 (in gray) has a C-terminal folded domain (BRCA2_{DBD}; PDB:1IYJ) and a long N-terminal IDR, which interacts with Plk1_{PBD} (PDB:6GY2) upon BRCA2_{T207} phosphorylation by Plk1. No human Plk1 structure has yet been elucidated: my model (in green) is built using the *Danio rerio* Plk1 structure (4J7B). BRCA2 interacts with BubR1 through a controversial interface (Futamura et al., 2000, Choi et al., 2012). The interaction between BRCA2 and Plk1 favors the phosphorylation of the BubR1 catalytic domain (BubR1_{KD}, PDB: 6JKK, in yellow) at its two tension-sensitive sites (S676 and T680). BRCA2 and BubR1 phosphorylated by Plk1 interact with the B56 subunit of the phosphatase PP2A (Hertz et al., 2016, PDB: 5SW9, 5K6S, 5SWF, in red).

2. Interaction between BRCA2₁₀₉₃₋₁₁₅₈ and PP2A_{B56}

To better understand the structure and regulation of this quaternary complex BRCA2_{pT207}:Plk1:BubR1:PP2A, we initiated a study on the BRCA2/PP2A interaction. PP2A is a very common phosphatase accounting for >50% of total Ser/Thr phosphatase activities in many cell types (Virshup & Shenolikar 2009, Sangodkar et al., 2016). It regulates the chromosome segregation and more generally contributes to genome stability (Wurzenberger and Gerlich, 2011, Funabiki and Wynne, 2013). The PP2A phosphatase is an heterotrimer composed of a scaffolding subunit A and a catalytic unit C (Xu et al., 2006, Cho and Xu, 2007,

Xu et al., 2008), plus a variable subunit B. There are four known families of B subunits, B55, B56, PR72, and PR93, which differ in both their primary sequences and tertiary structures. The B subunit determinates the PP2A substrate specificity (Eichhorn et al., 2009). Here, we chose to focus on the B56 subunit, which has already been show to interact with BRCA2(aa1001-1255) by cellular pull-downs (Hertz et al., 2016). B56 presents 2 conserved binding sites: the major one is responsible for target recognition through an interaction with the consensus motif L-X-X-I-X-E, with X for any amino acid (Hertz et al., 2016, Wang et al., 2016), whereas its secondary binding site modulates this interaction through electrostatic interactions (Wang et al., 2020).

We decided to confirm the BRCA2/PP2A interaction and to elucidate if BRCA2 phosphorylation by Plk1 regulates the BRCA2/PP2A interaction. In this project, I was involved in the NMR characterization of this other conserved BRCA2 region (**Figure 10**), in identifying BRCA2 residues phosphorylated by Plk1 and in optimizing the phosphorylation conditions for NMR monitoring.

Rania Ghouil optimized the expression and purification conditions of a BRCA2₁₀₉₃₋₁₁₅₈ fragment, which contains the L-X-X-I-X-E motif at the position aa1114-1119. Then, I recorded 3D heteronuclear NMR experiments on a ¹⁵N-¹³C BRCA2₁₀₉₃₋₁₁₅₈ sample, in order to assign the NMR resonances of this fragment (**Figure 47.A**). Analysis of its NMR chemical shifts experimentally confirmed the disorder propensity of this region, which shows two transient α -helices at positions 1104-1108 and 1123-1128 (**Figure 47.B**). I also conducted T₁, T₂ and ¹H-¹⁵N-NOE NMR analysis under the supervision of Dr. Sophie Zinn-Justin, Dr. Philippe Cuniasse and Dr. François-Xavier Theillet (**Figure 47.C.D.E**). The low values of R₁, R₂ and NOEs confirmed the unfolded character of BRCA2₁₀₉₃₋₁₁₅₈. The T₂ analysis may also reveal us-ms time scale motion around the residues 1009 and 1126 corresponding to the transient α -helices evoked above. Such an advanced interpretation would require to integrate the residue-specific water-amide proton exchange in the T₂ fitting, which would necessitate the measurement of these exchange rates (Kim et al., 2013).

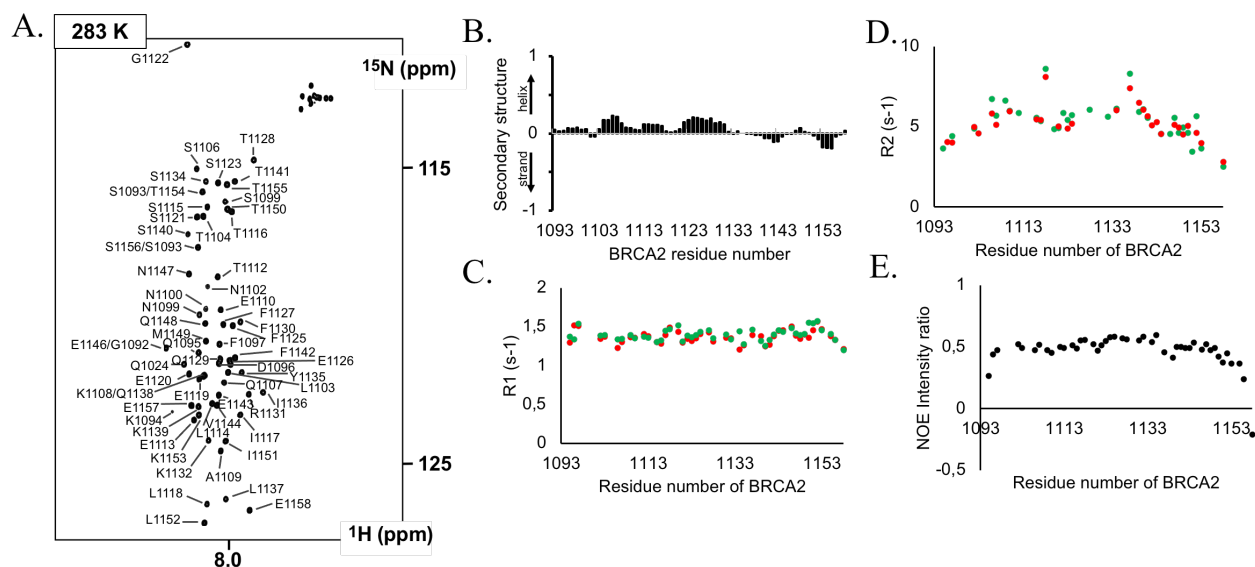


Figure 47. NMR analysis of BRCA2₁₀₉₃₋₁₁₅₈

(A) Assignment of the ^1H - ^{15}N SOFAST-HMQC spectrum of ^{15}N - ^{13}C BRCA2₁₀₉₃₋₁₁₅₈ at 200 μM in 50 mM HEPES, 50 mM NaCl, 1 mM EDTA at pH7.0, 283K (600 MHz). (B) Secondary structure propensity, deduced from the $^1\text{H}_\text{N}$, $^{15}\text{N}_\text{H}$, $\text{C}\alpha$ and $\text{C}\beta$ chemical shifts of BRCA₁₀₉₃₋₁₁₅₈, using: <http://linuxnmr02.chem.rug.nl/ncSPC>. (C) R1, (D) R2 and (E) ^1H - ^{15}N -NOEs measured on ^{15}N - ^{13}C BRCA2₁₀₉₃₋₁₁₅₈ at 500 μM in 50 mM HEPES, 50 mM NaCl, 1 mM EDTA at pH7.0, 283K (950 MHz Gif-sur-Yvette). R1 and R2 were monitored with 2 sets of experiments (green and red).

Then, I tried to characterize the BRCA2/PP2A_{B56} interaction by NMR (**Figure 48**). The sample preparation was performed by Rania Ghoulil. Adding PP2A_{B56} decreased all BRCA2₁₀₉₃₋₁₁₅₈ peak intensities in ^1H - ^{15}N 2D spectra, which is consistent with an interaction between the two proteins. However, this does not help to localize precisely localize the BRCA2 motif binding to PP2A_{B56}, as also observed for the interaction between pBRCA2 and Plk1 (**Chapter 4**).

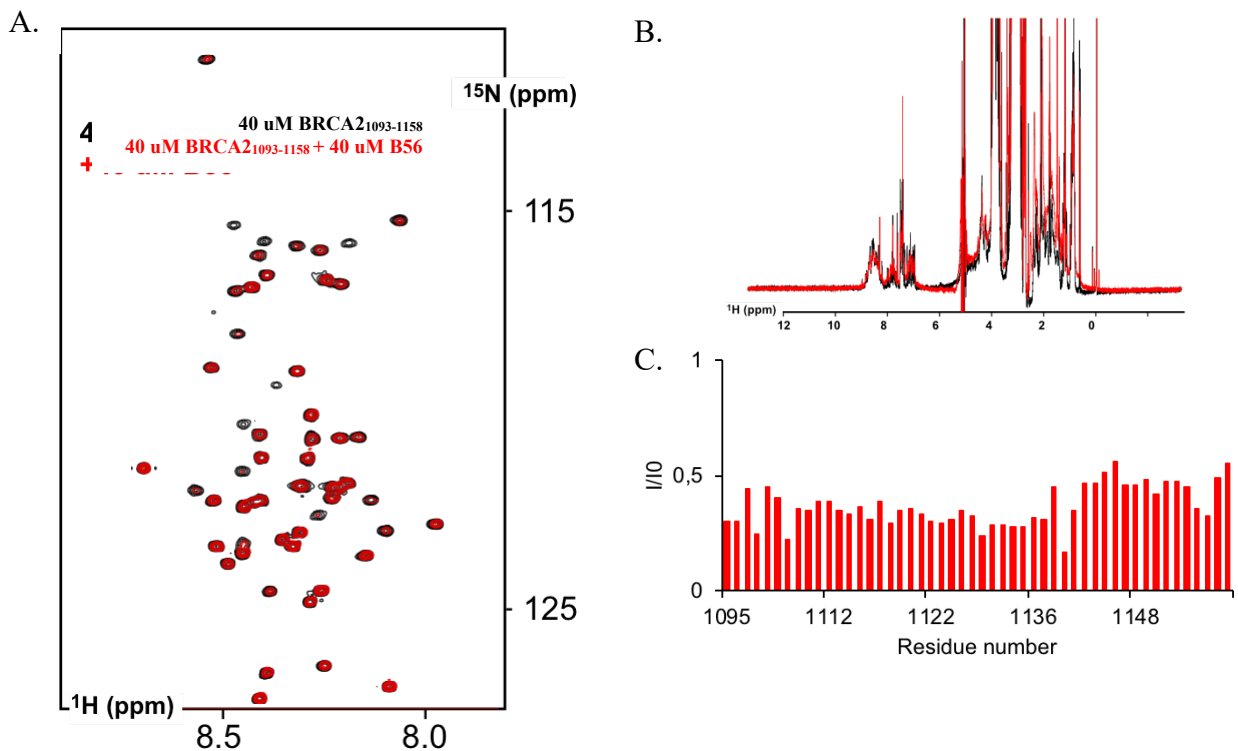


Figure 48. Interaction between BRCA2₁₀₉₃₋₁₁₅₈ and PP2A_{B56}
(A) Overlay of the ¹H-¹⁵N SOFAST-HMQC spectra and **(B)** ¹H 1D spectra of ¹⁵N-labeled BRCA₁₀₉₃₋₁₁₅₈ at 40 μM either free (black) or bound (red) to PP2A_{B56} at 40 μM in PBS 1X pH 7.0, 283K (600 MHz). **(C)** Peak intensity ratio as a function of the residue number, deduced from the analysis of the NMR experiments displayed in **(A)**.

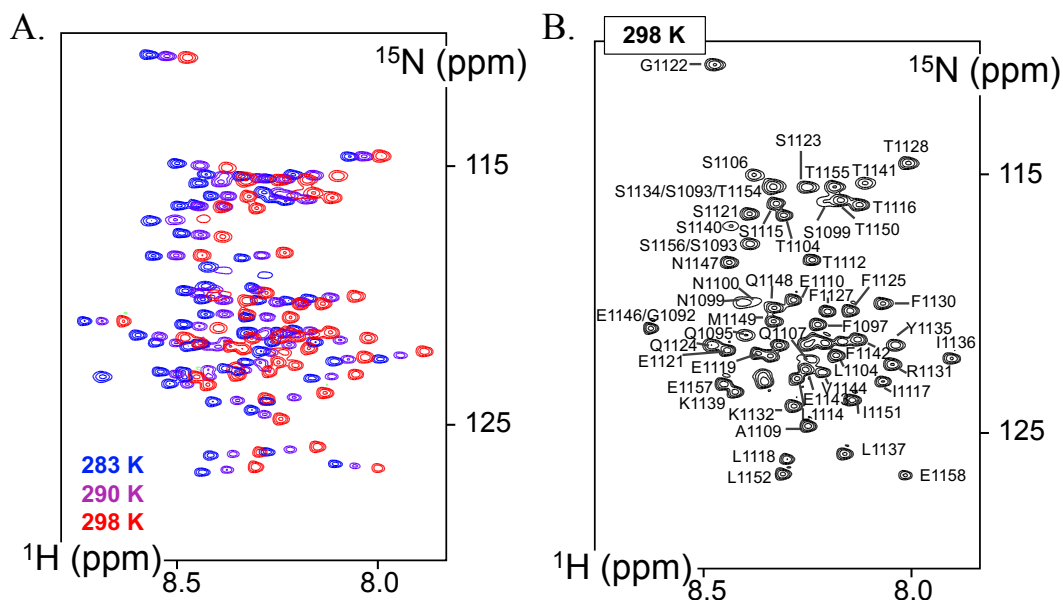


Figure 49. Transfer of the BRCA2₁₀₉₃₋₁₁₅₈ assignment from 283 K to 298 K. **(A)** Overlay of the ¹H-¹⁵N SOFAST-HMQC spectra acquired at 283 K, 290 K and 298 K using ¹⁵N-¹³C BRCA2₁₀₉₃₋₁₁₅₈ at 200 μM in 50 mM HEPES, 50 mM NaCl, 1 mM EDTA at pH7.0 (600MHz). **(B)** The assigned ¹H-¹⁵N SOFAST-HMQC spectrum of BRCA2₁₀₉₃₋₁₁₅₈ at 298 K (600 MHz).

Then, I studied the phosphorylation of BRCA2₁₀₉₃₋₁₁₅₈ by Plk1 and took the opportunity to teach Rania Ghouil the protocols related to this approach. I transferred the assignment from 283 K to 298 K (**Figure 49**), as described in Julien et al. (MiMB) and we tried to phosphorylate BRCA₁₀₉₃₋₁₁₅₈ by Plk1, applying the conditions used for BRCA₁₆₇₋₂₆₀ (**Figure 50**). We did not observe any phosphorylation of BRCA₁₀₉₃₋₁₁₅₈ by Plk1 in the course of our NMR measurements (**Figure 50.A**).

The aliquot of Plk1 that we used to carry out the reaction was produced by the insect cells facility of Institut Curie, the same that we used previously on the N-terminal fragments of BRCA2 presented in the chapter above. It is known that production of Plk1 in insect cells generates an unactivated version of Plk1 (i.e. non-phosphorylated at T210) (Kothe et al., 2007). We must insist on the fact that we used it successfully earlier on BRCA2₁₆₇₋₂₇₀, BRCA2₄₈₋₂₁₈ and BRCA2₁₉₀₋₂₈₄, although unactivated Plk1 is not supposed to phosphorylate efficiently its substrate. Plk1 activation depends on two complementary events i) a major mechanism (activity multiplied by 100) is the phosphorylation of T210 in its activation loop, ii) a secondary mechanism (activity multiplied by 10) consists in the release of the inhibitory interaction between the PBD and KD domains (Xu et al., 2013). This secondary activation can be triggered by an interaction between the PBD and a peptide containing its consensus docking motif S-pS/pT-Pro/X (Johnson et al., 2008, Zhu et al., 2016). Hence, we thought to add a Plk1 “activator” peptide to the reaction mix. We used the BRCA2_{194-210(pT207)} peptide (later named APB207) previously designed for the ITC measurements and X-ray crystallography assays. Rania Ghouil optimized the concentration of APB207 necessary for activating Plk1 (10 μ M of APB207 for 280 nM of Plk1) and we monitored the phosphorylation of BRCA2₁₀₉₃₋₁₁₅₈ in these new conditions (**Figure 50.B**). With this strategy, BRCA2₁₀₉₃₋₁₁₅₈ was efficiently phosphorylated by Plk1.

Incidentally, this result led us to consider that, in the case of BRCA2₁₆₇₋₂₇₀, BRCA2₄₈₋₂₁₈ and BRCA2₁₉₀₋₂₈₄, we may have benefitted of a fortuitous (and providential) activation of Plk1 by the little amounts of pT207 produced in the very early moments of the reaction. Because the first molecules of BRCA2₁₆₇₋₂₇₀, BRCA2₄₈₋₂₁₈ and BRCA2₁₉₀₋₂₈₄ phosphorylated on pT207 behave as Plk1 “activator” peptides, they may have ensured the success of the kinetics presented in the precedent chapters. Addition of APB207 to the BRCA2₁₆₇₋₂₆₀ phosphorylation mix led to decrease the phosphorylation kinetics of all residues, except T207 (**Figure 51**). These results underline the role of BRCA2_{T207} either for Plk1 activation but also the importance of a Plk1 docking site for the phosphorylation. However, in the case of BRCA2₁₀₉₃₋₁₁₅₈, no Plk1 binding site is available, even after BRCA2₁₀₉₃₋₁₁₅₈ phosphorylation (**Figure 50.A**).

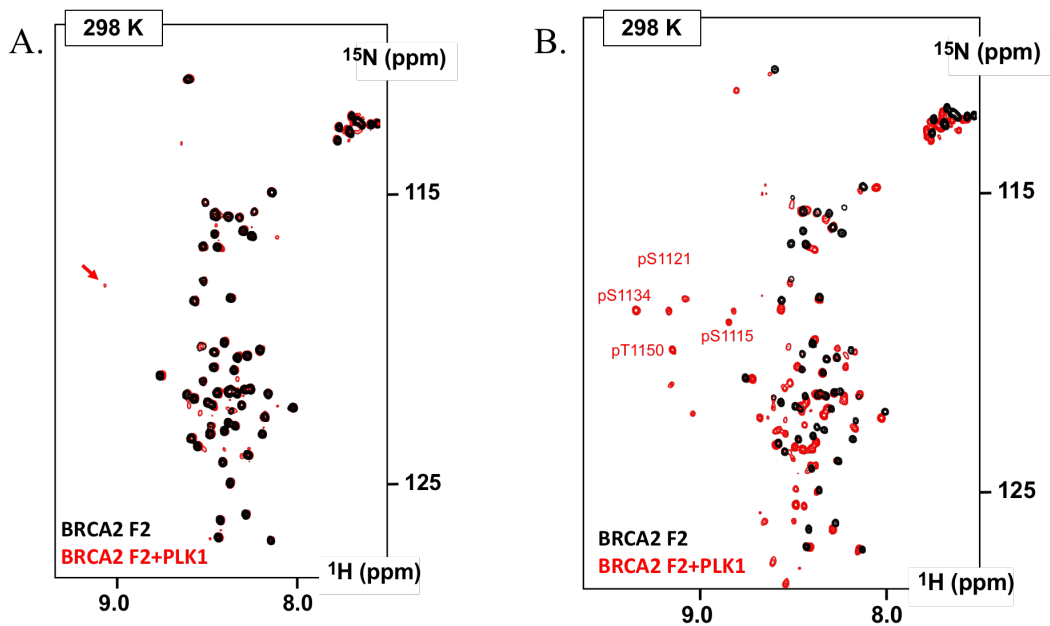


Figure 50. Phosphorylation of BRCA₁₀₉₃₋₁₁₅₈ at 50 μ M by Plk1 at 280 nM in 50 mM HEPES, 75 mM, NaCl 2 mM, ATP 10 mM, MgCl₂, 2 mM DTT, 1X PI at pH7.0, 298K, (600 MHz). **(A)** without activator peptide **(B)** in presence of the activator peptide at 10 μ M.

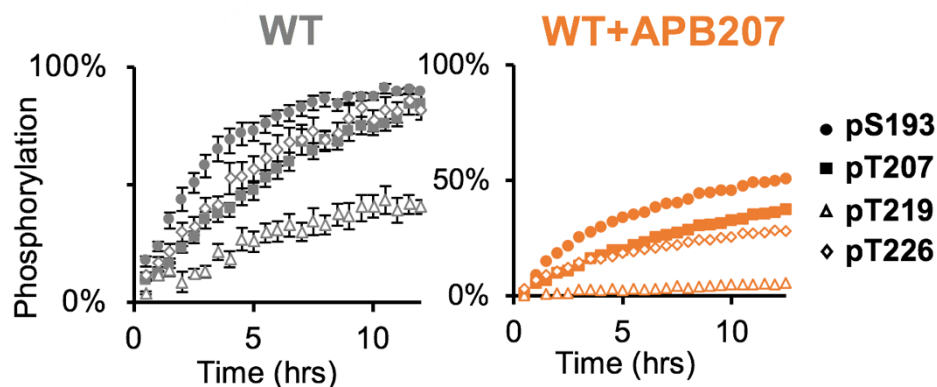


Figure 51. Comparison of S193, T207, T219 and T226 phosphorylation kinetics between BRCA2₁₆₇₋₂₆₀ WT +/- APB207. All these phosphorylation reactions were monitored using ¹H-¹⁵N SOFAST-HMQC spectra for a continuous readout at 298K. BRCA2 fragments at 50 μ M were mixed to Plk1 at 150 nM +/- ABP207 at 10 μ M in 50 mM HEPES at pH 7.0, 75 mM NaCl, 1 mM EDTA, 2 mM DTT, 1X protease inhibitors (Roche), 2 mM ATP, 10 mM MgCl₂, 50 μ M DSS and 5 % D₂O.

To identify the numerous phosphoresidues of BRCA2₁₀₉₃₋₁₁₅₈, I performed 3D NMR experiments. My preliminary analysis led to the conclusion that Plk1 phosphorylates BRCA2₁₀₉₃₋₁₁₅₈ in its PP2A binding site (S1115). This phosphorylation by Plk1 may modulate the BRCA2/PP2A interaction. The next steps will include i) the full identification of Plk1 phosphosites on BRCA2₁₀₉₃₋₁₁₅₈ and ii) the characterization of their impact on the

BRCA2/PP2A interaction. This will serve as a basis for testing the consequences of the identified VUS on BRCA2₁₀₉₃₋₁₁₅₈ phosphorylation by Plk1 and on the BRCA2/PP2A interaction. This work will be carried out in the context of another PhD project.

Chapter 5. Does phosphoBRCA2 recruit other partners?

1. Impact of other VUS on Plk1 phosphorylation of BRCA2

I reported the analysis of the phosphorylation kinetics of BRCA2 WT and of the VUS T207A. In parallel, I also assayed the impact on BRCA2(pT207) phosphorylation of two other VUS: T200K and M192T (**Figure 52**).

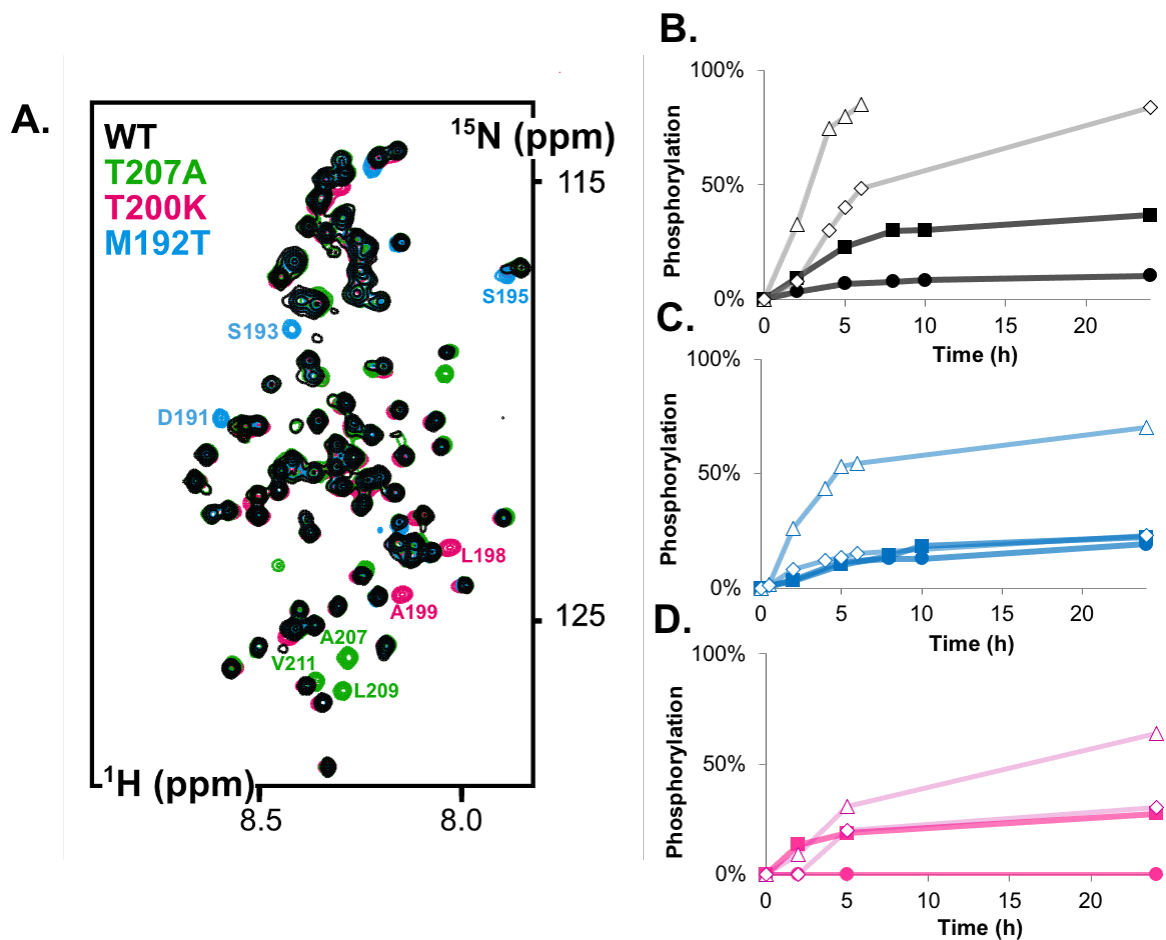
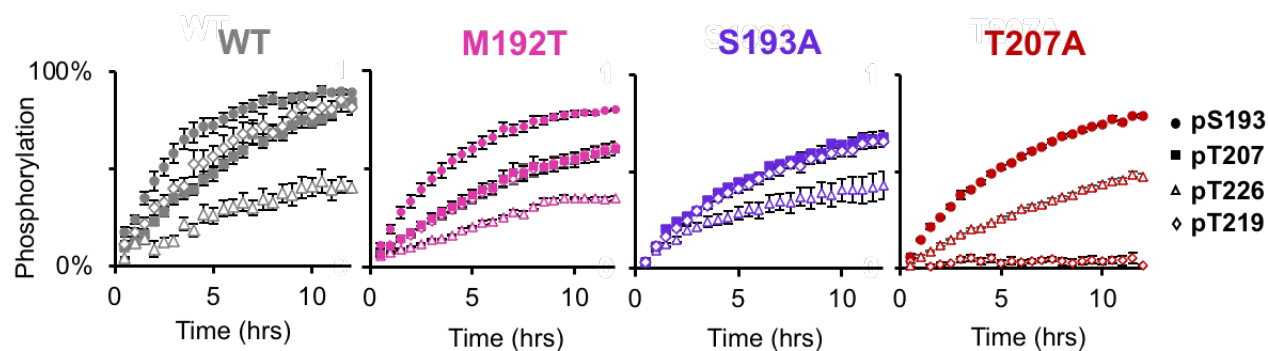


Figure 52. Impact of T200K and M192T VUS on BRCA2₁₉₀₋₂₈₄ phosphorylation by Plk1. **(A)** Overlay of ^1H - ^{15}N SOFAST-HMQC spectra of BRCA2_{WT}, BRCA2_{T207A}, BRCA2_{T200K} and BRCA2_{M192T}. Spectra were recorded using BRCA2 fragments at 200 μM in 50 mM HEPES, 1 mM EDTA, 2 mM DTT at pH7.0, 283K. **(B)**, **(C)** and **(D)** Phosphorylation quantification of S193 (round), T207 (square), T219 (diamond) and T226 (triangle) for BRCA2_{WT} (black), BRCA2_{M192T} (blue) and BRCA2_{T200K} (pink) using the quenched reaction protocol.

Both of these VUS slow down the phosphorylation kinetics in the BRCA2₁₉₀₋₂₈₄ construct (**Figure 52.B.C.**). Interestingly, T200K is not in close proximity from a phosphorylation site but has an impact on all the 4 phosphosites. M192T slows down phosphorylation kinetics of T207, T219 and T226 but not S193. Because M192T is close to the

BRCA2₁₉₀₋₂₈₄ N-terminal extremity, we decided to also test the impact of M192T on the phospho-centered BRCA2₁₆₇₋₂₆₀ fragment (**Figure 53**).



K_{obs} (min^{-1})	WT	M192T	S193A	T207A
pS193	1.97 ± 0.72	0.74 ± 0.21		0.75 ± 0.03
pT207	0.80 ± 0.15	0.34 ± 0.10	0.52 ± 0.13	
pT219	0.25 ± 0.08	0.21 ± 0.04	0.24 ± 0.14	0.01 ± 0.01
pT226	0.99 ± 0.34	0.30 ± 0.08	0.50 ± 0.11	0.31 ± 0.03

Figure 53. Comparison of S193, T207, T219 and T226 phosphorylation kinetics between BRCA2₁₆₇₋₂₆₀ WT, M192T, S193A and T207A. All these phosphorylation reactions were monitored using ^1H - ^{15}N SOFAST-HMQC spectra for a continuous readout at 298K. BRCA2 fragments at 50 μM were mixed to Plk1 at 150 nM in 50 mM HEPES at pH 7.0, 75 mM NaCl, 1 mM EDTA, 2 mM DTT, 1X protease inhibitors (Roche), 2 mM ATP, 10 mM MgCl_2 , 50 μM DSS and 5 % D_2O . All experiments were performed in triplicate, the corresponding error bars are presented. The analysis of the kinetics provided the initial phosphorylation rates of every phosphosite, as described in [Julien et al., 2020](#).

The M192T VUS slows down the phosphorylation rates of all BRCA2₁₆₇₋₂₆₀ phosphosites by a factor of 3. In addition, the phosphorylation rates of S193 and T226 are similar in BRCA2_{M192T} and BRCA2_{T207A}. However, the phosphorylation preference is globally conserved compared to the WT (**Figure 53**). I also tested the mutant S193A, which is not a VUS, but was previously used as a “non-phosphorylatable” control in cell biology experiments ([Lin et al., 2003](#), [Takaoka et al., 2014](#)). Here again, all phosphosites’ kinetics are slowed down (**Figure 53**).

In all these BRCA2 mutants, we have seen that one mutation impacts the overall Plk1 phosphorylation of BRCA2. In the case of M192T, the mutation modifies the motif containing the phosphosite S193. The mutation M192T sufficiently modifies the environment of S193 to impair its preferred recognition by Plk1. The consensus phosphorylation target motif of Plk1 is known to be D/E/S-X-pS/T- Φ , with X for any amino acid in position $i-1$ and Φ for a

hydrophobic amino acid in position $i+1$. We observe here that Met may be preferred than Thr in position $i-1$. Concerning T200K, none of the phosphosites are close to the mutation point. The phosphorylation mechanism of BRCA2 by Plk1 may be more complex than what we thought initially.

All these experiments have been carried out using unphosphorylated Plk1. The observed rates are in the range of those published in the literature: unphosphoPlk1 phosphorylated a substrate called TCTP with a $k_{cat}=1 \text{ min}^{-1}$ ($K_m=170 \text{ uM}$), and a k_{cat} of about 14 min^{-1} in presence of an activating peptide MQSpTPL, while Plk1(pT210) phosphorylated the same substrate with a k_{cat} of 90 min^{-1} ($K_m=80 \text{ uM}$) and of 720 min^{-1} in presence of the activating peptide (Johnson et al., 2008).

2. The VUS M192T impairs cytokinesis

Because the impact of M192T on Plk1 phosphorylation kinetics was similar to that of T207A, the team of Dr. Aura Carreira tested its impact in cells. They observed that BRCA2_{M192T} shows no defect in chromosome segregation. However, in collaboration with Dr. Yoshio Miki, they observed a failure and a mislocalization of BRCA2(M192T) to the midbody as well as cytokinesis delays (data not shown).

Previous studies already showed that S193A impairs BRCA2 localization to the midbody and cytokinesis. However, this is the first report of an impact of M192T. Until now, several partners of BRCA2 such as CEP55 (Morita et al., 2007), Alix (Mondal et al., 2012), NMH-IIC (Takaoka et al., 2014), HMG20b (Marmorstein et al., 2001), Filamin A (Yuan et al., 2001, Mondal et al., 2012) were identified at the midbody and were shown to contribute to BRCA2 midbody functions. However, none of these interactions involves the BRCA2₄₈₋₂₈₄ region. Thus, another partner of BRCA2 may recognize the BRCA2_{pS193} region and drive it to the midbody.

3. Isolating new pBRCA2₁₆₇₋₂₆₀ partners using proteomics

The intriguing consequences of M192T in cells cannot be explained by a molecular mechanism based on the known interactions of BRCA2. They may reveal the existence of BRCA2 partners binding in the vicinity of M192-S193, which may be phospho-dependent. Alternatively, because BRCA2 phosphorylation kinetics by Plk1 are slower in mutants M192T and S193A, these cellular phenotypes may result from impaired phosphodependent interactions at T207, T219 or T226. Following this rationale, we initiated a study for searching new BRCA2₁₆₇₋₂₆₀ partners that would bind specifically to its Plk1-phosphorylated form. For this purpose, I performed pull-down experiments from cell extracts using BRCA2₁₆₇₋₂₆₀ +/- Plk1-phosphorylated as baits, whose results were analyzed by mass-spectrometry proteomics.

To carry out this study, I used a construct based on the BRCA2₁₆₇₋₂₆₀ fragment, which contains the extended conserved region of BRCA2 including the 4 Plk1 phosphosites (**Figure 18**). The new construct was designed to integrate a N-terminal peptide GLNDIFEAQKIEWHE, named Avi-Tag, which can be efficiently biotinylated on its lysine by the enzyme BirA ([Fairhead et al., 2015](#)). Hence, the final construct of interest can be tagged with a biotin, which permits a convenient attachment to streptavidin-coated beads for pull-down assays. I performed the biotinylation reaction of AviTag-BRCA2₁₆₇₋₂₆₀ following the protocol set up for Sox2 by Chafiaa Bouguechtouli and Dr. François-Xavier Theillet in the lab (unpublished). Then, I phosphorylated Biotin-Avi-Tag-BRCA2₁₆₇₋₂₆₀ (phosphorylated or not phosphorylated as a control) was then attached to streptavidin-coated magnetic beads and incubated with cell extracts in order to identify new BRCA2 partners by MS analysis.

For the pull-downs, I adapted the protocol of Asa Ehlen (Aura Carreira team) with advices from Dr. Theillet and from Florent Dingli, member of the Institut Curie proteomics platform, where the MS analysis was performed. BRCA2 was incubated with cells extracts freshly prepared by our collaborators in the team of Dr. Aura Carreira. After washes, the remaining proteins attached to the beads were analyzed by the Institut Curie proteomics platform, under the supervision of Dr. Damarys Loew. Two experimental procedures were utilized with different quantities of BRCA2 fragments on beads (**Figure 55**).

In unsynchronized cell conditions, no partner enrichment was found for BRCA2 +/- phosphorylated by Plk1 (**Figure 55.B**). Upon incubation with G2/M cell extracts, the phosphoBRCA2₁₆₇₋₂₆₀ sample is enriched in several partners compared to that of BRCA2₁₆₇₋₂₆₀

(**Figure 55.A.B**), using 2 or 10 ng of BRCA2 fragments as bait. These results may indicate that this region of BRCA2 interacts with partners in a phospho-dependent manner only during mitosis. Within the identified partners, we found the kinase Plk1, which presents the combined highest enrichment with the strongest p-value. We already knew that Plk1 interacts with BRCA2₁₆₇₋₂₆₀ in a phospho-dependent manner, which reassured us on the validity of our approach. Six others partners were also identified: the kinesin-like protein 2C (Kif2C), the alpha-actinin 1 (ACTN1), the kinesin-like protein 2A (Kif2A), the glyoxalase domain-containing protein 4 (GLOD4), the histone-binding protein RBBP4 and the Chk2 kinase. These partners display a similar enrichment in the second phosphoBRCA2₁₆₇₋₂₆₀ conditions (**Figure 5.B.C**), while Chk2 is found only in the pBRCA2 sample of the first experiment (infinite enrichment). Kif2C and Kif2A are present in both results (2 and 10 ng of BRCA2) and Kif2C presents the second highest p-value after Plk1 and a medium protein abundance in cell (**Figure 55.C**, Wang et al., 2012). Thus, I initiated a study to characterize the BRCA2/Kif2C interaction.

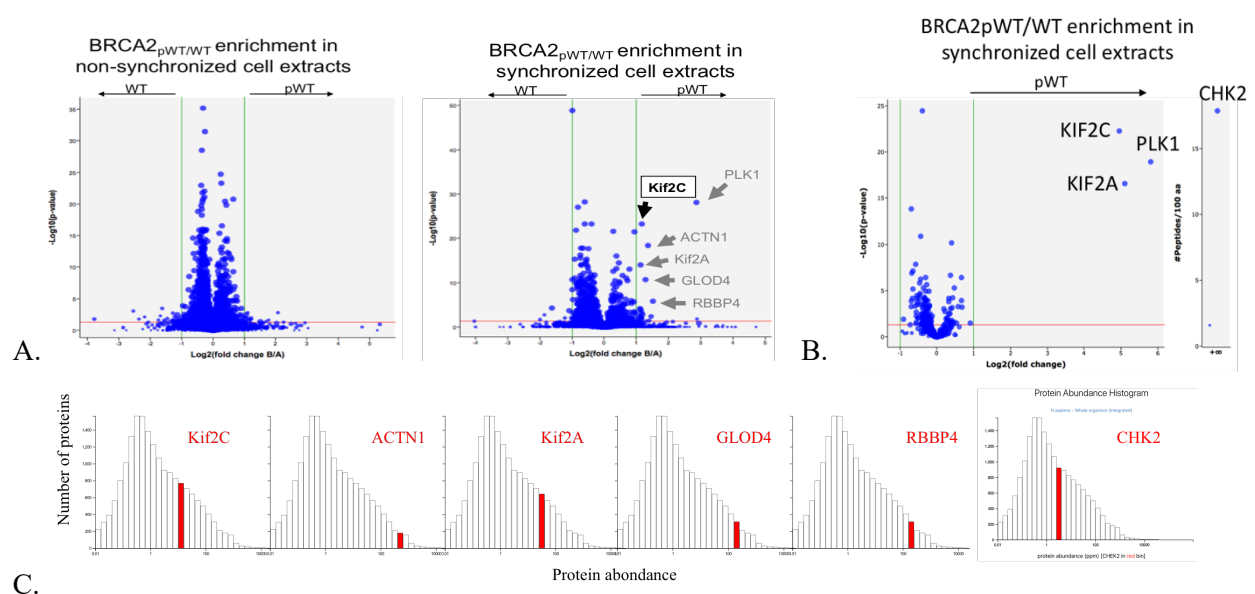


Figure 55. 6 mitotic partners were identified by MS for phosphorylated BRCA2₁₆₇₋₂₆₀. Volcano plots obtained from pull-down and proteomics MS analysis using 2 ng (**A**) or 10 ng (**B**) of phosphoBRCA2₁₆₇₋₂₆₀ versus BRCA2₁₆₇₋₂₆₀ as bait (on 50 μ L (**A**) or 100 μ L (**B**) of resuspended magnetic beads) after incubation with cell extracts from unsynchronized DLD1^{BRCA2-/-} cells (left) or G2/M synchronized cells (right). Five replicates were analyzed for each condition by Institut Curie platform. Partners with an enrichment in one of the two conditions are written. Log2 fold consists in the row enrichment while the p-value is a combination of the number of different peptides identified for a same protein in the sample and the intensity of each peptide. (**C**) Protein abundancy, from Wang 2012 (<https://pax-db.org/>)

4. Study of the BRCA2/Kif2C interaction

Kinesin Kif2C, also known as the Mitotic Centromere Associated Kinesin (MCAK), is a microtubule-associated protein that produces mechanical work upon ATP hydrolysis. It is involved in microtubule disassembly via its depolymerase activity (Hunter et al., 2003) and in chromosome positioning at the kinetochore (Domnitz et al., 2012). Interestingly, dysfunction of Kif2C has been linked to malignance progression of breast cancers (Li et al., 2020). However, no common pathways between Kif2C and BRCA2 were reported yet. Nevertheless, these 2 proteins are simultaneously localized at the kinetochore and at the Flemming body during mitosis, and very interestingly, this localization is also shared by Plk1 (Zhang et al., 2011). The identification of a direct interaction between Kif2C and BRCA2 could thus reveal a new pathway at the kinetochore or midbody during mitosis.

As IDRs commonly interact with globular domains, I first wanted to test the interaction between pBRCA2₁₆₇₋₂₆₀ and the globular region of Kif2C. Only one structure of Kif2C is available, which describes its large globular motor domain Kif2C₂₃₂₋₅₈₆ (Figure 56). Dr. Benoît Gigant kindly gave us a plasmid coding for Kif2C₂₁₆₋₅₉₈, which I used to produce this construct. Then, I tested the interaction between pBRCA2₁₆₇₋₂₆₀ and Kif2C₂₁₆₋₅₉₈.

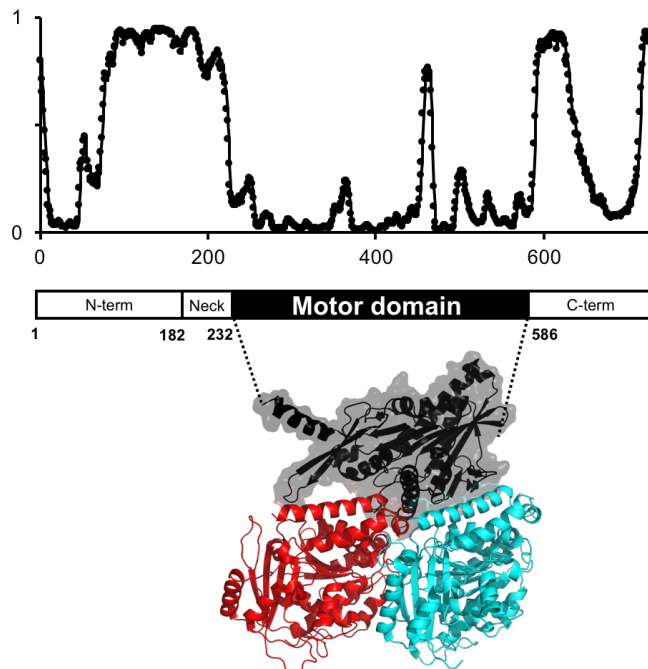


Figure 56. Prediction of Kif2C disorder reveals one large globular domain corresponding to its motor domain (Kif2C₂₃₂₋₅₈₆). Predictions were calculated using the SPOT-dis server (<http://sparks-lab.org/server/SPOT-disorder/index.php>) and the structure of the Kif2C motor domain (grey) is presented in interaction with a dimer of tubulin (monomer: red and blue) (PDB code: 5MIO).

The Kif2C_{neck+motor} domain (Kif2C₂₁₆₋₅₉₈, containing mutations R330A and R379A; [Tan et al., 2008](#)) was produced in bacteria according to the protocol from the team of Dr B. Gigant ([Wang et al., 2012](#)). Its purification was implemented in the lab by Rania Ghouil and I used her protocol to produce large amounts of Kif2C₂₁₆₋₅₉₈ for the interaction tests with pBRCA2₁₆₇₋₂₆₀ (**Figure 57**). First, I tested this interaction using Size Exclusion Chromatography (SEC). The two proteins have similar elution volumes and I did not observe any shift of their elution volumes when I injected their stoichiometric mix in the SEC column. However, this result is ambiguous: we can imagine an interaction mode where pBRCA2₁₆₇₋₂₆₀ would enwrap Kif2C₂₁₆₋₅₉₈, which would generate a similar result. Hence, I decided to test this interaction using ITC.

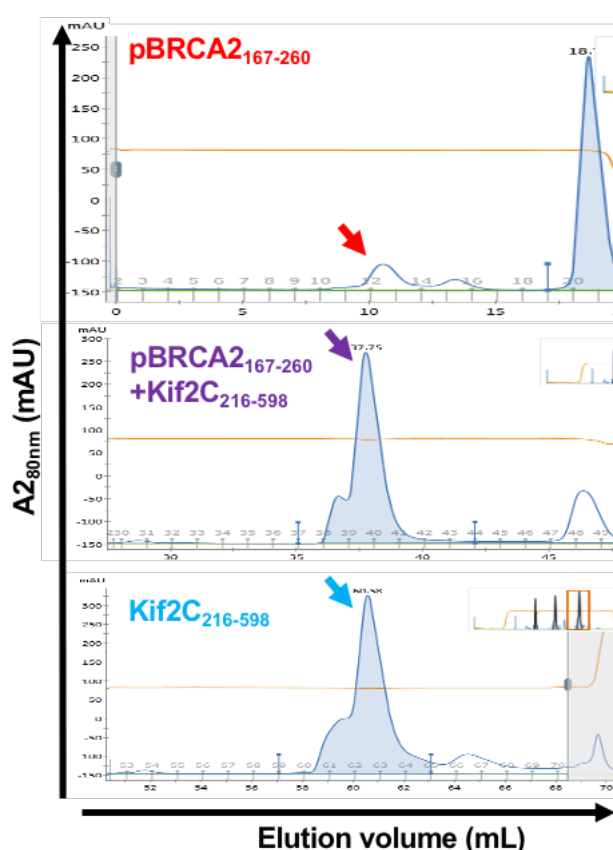


Figure 57. Gel filtration elution profile of pBRCA2₁₆₇₋₂₆₀ and Kif2C₂₁₆₋₅₉₈. BRCA2₁₆₇₋₂₆₀ was previously phosphorylated by Plk1. 500 μ L of pBRCA2₁₆₇₋₂₆₀ (red), Kif2C₂₁₆₋₅₉₈ (blue) and pBRCA2₁₆₇₋₂₆₀+Kif2C₂₁₆₋₅₉₈ both at 50 μ M were injected on a Superdex 75 10/300 column (GE Healthcare). Buffer: 50 mM HEPES, 150 mM NaCl, 5 mM MgCl₂, 2 mM DTT, at pH7.0 and 277 K.

I performed the first ITC trials at 20°C, where we observed a null heat exchange signal. Then I decided to perform further ITC experiments at 10°C. We observed no heat exchange when titrating BRCA2₁₆₇₋₂₆₀ unphosphorylated and Kif2C₂₁₆₋₅₉₈ (**Figure 58.A**). Concerning

pBRCA2₁₆₇₋₂₆₀, we observed an high heat exchange for the first test (**Figure 58.B**). However, further tests showed a weak heat exchange that was poorly reproducible (**Figure 58.C.D.E**). Thinking about possible aggregation events that can occur at such high concentrations, I reversed the injection scheme: when Kif2C was loaded in the syringe and pBRCA2 in the cell, no more convincing results were obtained. My dilution controls showed signals of similar magnitudes than those obtained during the previous titration assays (**Figure 58.F.G**). The first observation (**Figure 58.B**) was thus probably due to a buffer variation in the syringe and cell which led to observe the dilution of buffer constituents.

We can think of different hypotheses: the affinity between pBRCA2₁₆₇₋₂₇₀ may be above 50 μ M, the heat exchange of the possible interaction may be very weak, the observed heat exchange may be the result of a pBRCA2:Kif2C aggregation at high concentration, the buffers in the syringe and the cell may have been slightly different, or Kif2C may interact only with a phospho-form of BRCA2₁₆₇₋₂₆₀ present in low, sub-stoichiometric proportions.

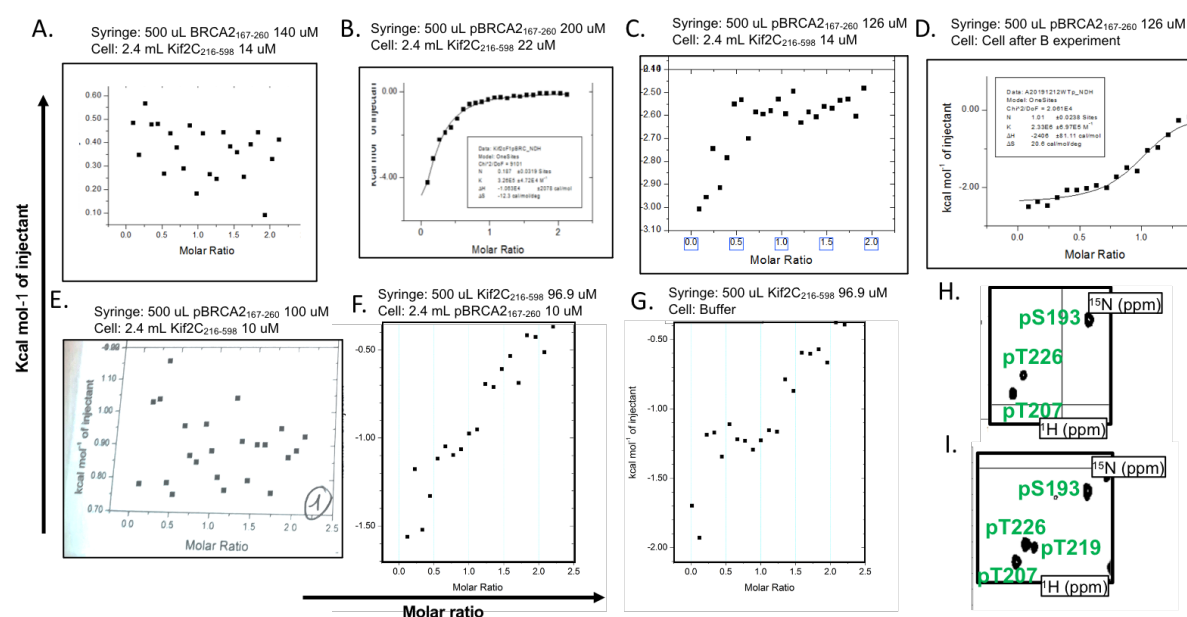


Figure 58. ITC experiments titrating BRCA2₁₆₇₋₂₆₀ and Kif2C₂₁₆₋₅₉₈ (**A**), BRCA2₁₆₇₋₂₆₀ phosphorylated by Plk1 and Kif2C₂₁₆₋₅₉₈ (**B to F**) and Kif2C₂₁₆₋₅₉₈ and buffer. All experiments were performed at 283K using injections of 12 μ L in a 2,4 mL cell in a buffer containing 50 mM HEPES, 150 mM NaCl, 5 mM MgCl₂, 5 mM b-mercaptoethanol, pH 7.0. (**H and I**) Close-up views of ¹H-¹⁵N SOFAST-HMQC NMR spectra of ¹⁵N phosphoBRCA2₁₆₇₋₂₆₀ are displayed and present the phosphoregion (¹⁵N BRCA2₁₆₇₋₂₆₀ at 100 μ M in ITC buffer, 283K, 600MHz). (**H**) corresponds to the BRCA2 sample used for experiments (C and D). and (**I**) corresponds to the BRCA2 sample used for experiments (E and F).

We have seen previously in a number of SDS-PAGE analysis that it was difficult to produce homogeneous, 100% phosphorylated BRCA2₁₆₇₋₂₆₀. The Plk1 kinase that we use is not

extremely active, and it starts to phosphorylate unspecific sites after a prolonged incubation (see **Chapter 2**). Hence, we hypothesized that Kif2C may interact with a phospho-form of BRCA2₁₆₇₋₂₆₀ that represent only a minor fraction of the population. This would greatly hamper the former analysis relying on SEC and ITC observables. In such an eventuality, NMR spectroscopy would be a better approach to reveal the interaction-ready subpopulation of phospho-BRCA2₁₆₇₋₂₆₀, whose resonances would vanish selectively. Hence, I also recorded ¹H-¹⁵N 2D NMR spectra of ¹⁵N-labeled pBRCA2₁₆₇₋₂₆₀ in presence or absence of Kif2C₂₁₆₋₂₉₈ (**Figure 59**). Here again, I did not observe any peak disappearance or chemical shift perturbations that would reveal an interaction, as shown by the homogeneous bar graph representing the peak intensities along the amino acid sequence (**Figure 59**).

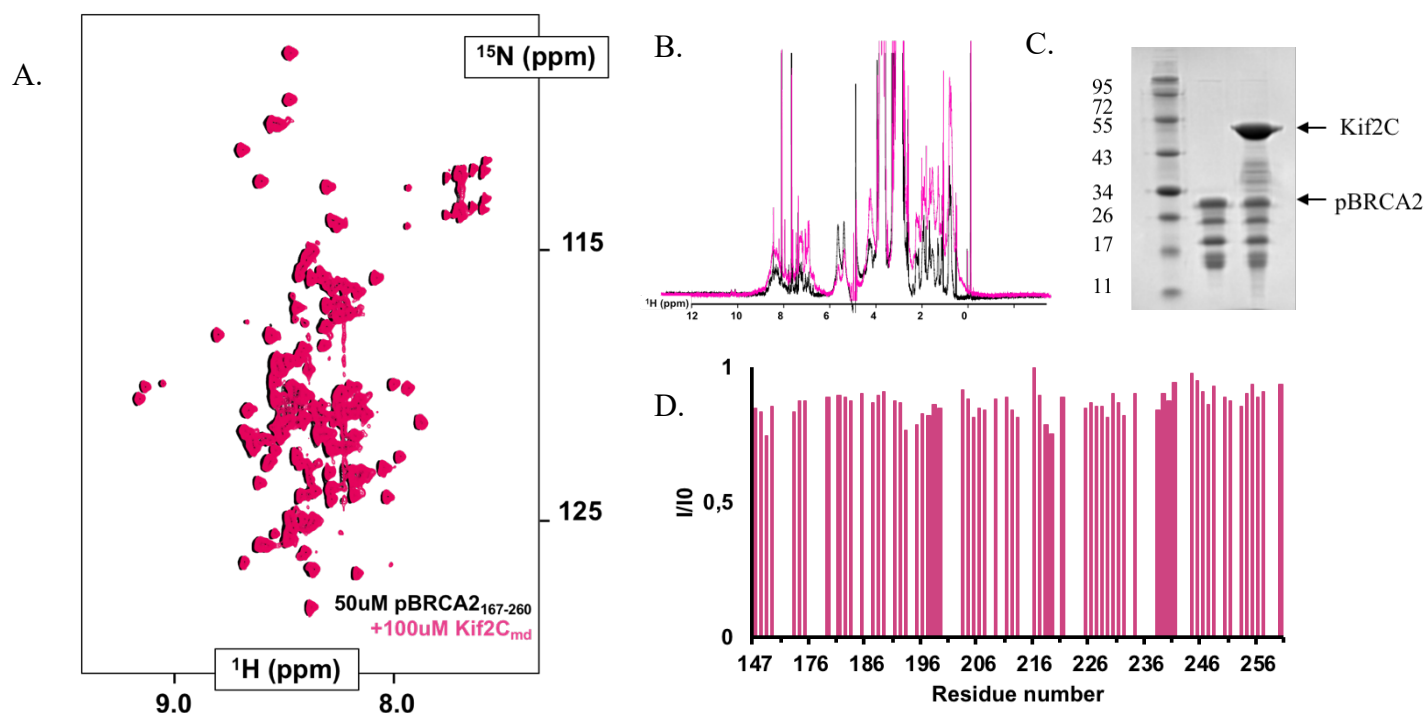


Figure 59. Interaction between pBRCA2₁₆₇₋₂₆₀ and Kif2C₂₁₆₋₅₉₈

(A) Overlay of ¹H-¹⁵N SOFAST-HMQC and (B) ¹H 1D spectra of ¹⁵N-labeled pBRCA₁₆₇₋₂₆₀ at 50 uM free and in presence of 100 uM Kif2C₂₁₆₋₅₉₈ in 50 mM HEPES, 150 mM NaCl, 5 mM MgCl₂, 2 mM DTT at pH 7.1, 283K (600 MHz). (C) Coomassie-stained 15% SDS-PAGE analysis of the NMR sample containing pBRCA2 alone (left) or in presence of Kif2C (right) (D) Peak intensity ratios as measured in the spectra shown in (A).

Interestingly, Kif2C was shown to interact directly with the kinase domain of Plk1 via its neck and motor domain by GST pull-down (Zhang et al., 2011). As shown earlier, Plk1 was clearly identified among the BRCA2 partners in the proteomics study. I hypothesized that the BRCA2/Kif2C interaction may be mediated by Plk1. Thus, I produced the kinase domain of Plk1 (Plk1₁₋₃₂₈) and Kif2C₂₁₆₋₅₉₈ and tested their interaction by size-exclusion chromatography

(**Figure 60**). I did not observe any shift of the elution volume that would reveal an interaction between these two protein domains.

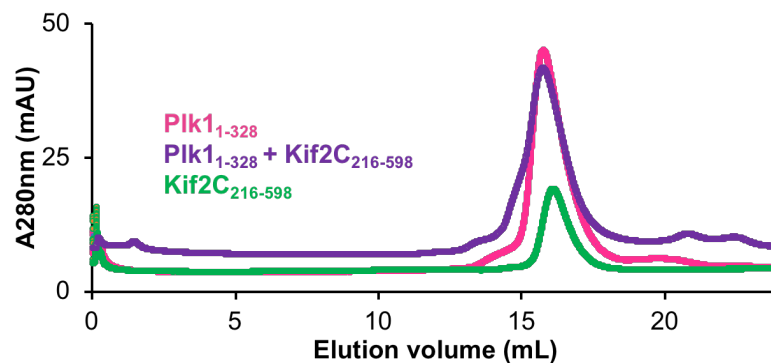


Figure 60. Size exclusion chromatography profiles of Plk1₁₋₃₂₈ (pink), Kif2C₂₁₆₋₅₉₈ (green) and Plk1₁₋₃₂₈+Kif2C₂₁₆₋₅₉₈ (violet), using a Superdex 200 10/300 Increase GL column (GE Healthcare). Buffer: 50 mM HEPES, 150 mM NaCl, 5 mM MgCl₂, 2 mM DTT at pH7.0, 277K.

As the isolated motor domain of Kif2C does apparently not interact with pBRCA2₁₆₇₋₂₆₀, we thought to produce full-length constructs of Kif2C. Two plasmids were generously given by Dr. Claire Friel (WT Kif2C) and by Dr Julie Welburn (mutation S715E, which limits Kif2C dimerization) and used for recombinant productions in insect cells by Rania Ghouil. I purified the obtained proteins according to the protocols published by our colleagues (Helenius et al., 2006, Talapatra et al., 2015). Our first purification tests provided sufficient amounts of proteins for interactions assays only in the case of Kif2C FL WT (**Figure 61**). It was however clear that the homogeneity of the sample was poor, because of low starting quantities from a weak over-expression profile, and because of the poor stability of the constructs resulting in a number of degradation bands as revealed by the SDS-PAGE.

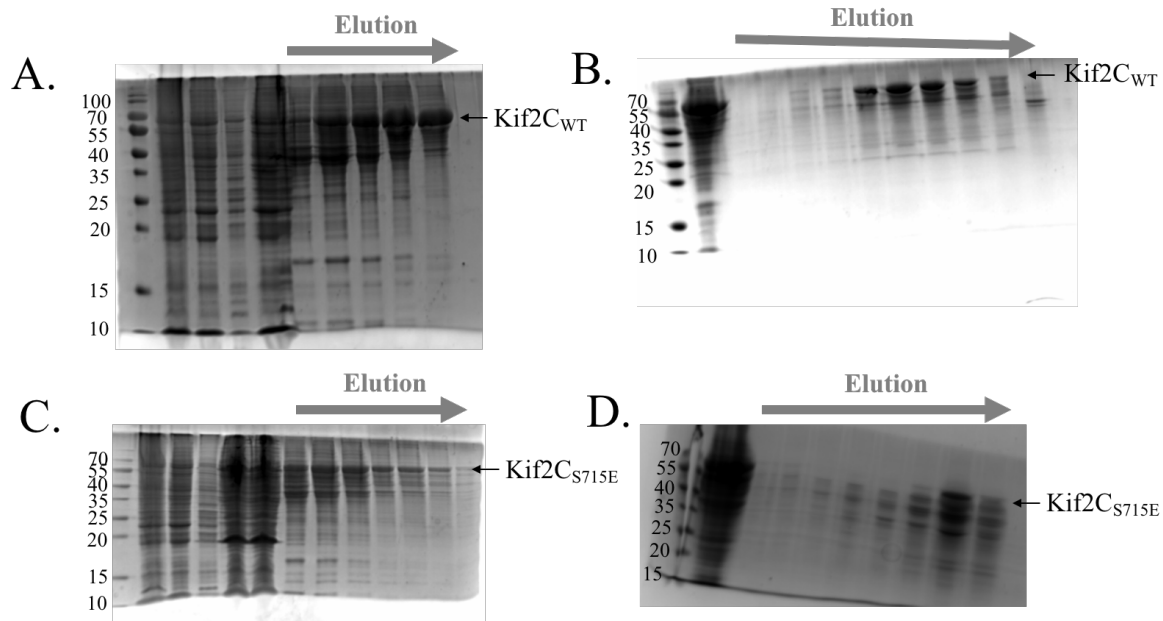


Figure 61. Purification of Kif2C FL WT and S715E

(A and C) Coomassie-stained 15% SDS-PAGE gels of affinity-chromatography elution of Kif2C WT and S715E respectively. **(B and D)** Coomassie-stained 15% SDS-PAGE gels of size-exclusion chromatographies of Kif2C WT and S715E respectively.

I tested the interaction between pBRCA2₁₆₇₋₂₆₀ and FL Kif2C by size-exclusion chromatography (**Figure 62**). However, Kif2C FL was further degraded very quickly during the concentration step, between its purification and the interaction test. In these conditions, I did not observe any interaction with pBRCA2₁₆₇₋₂₆₀. To conclude on this interaction, I will optimize Kif2C FL WT purification and test its interaction with pBRCA2₁₆₇₋₂₆₀ by size-exclusion chromatography and NMR.

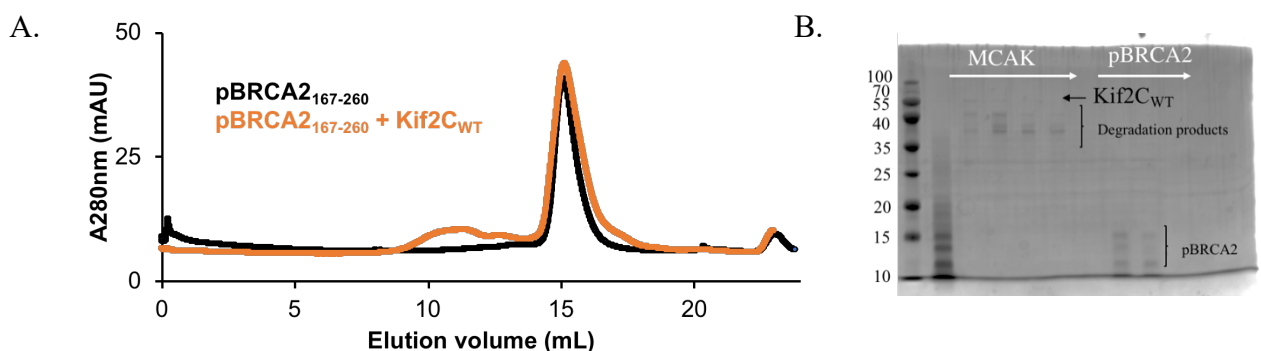


Figure 62. Interaction test between pBRCA2₁₆₇₋₂₆₀ and Kif2C_{FL}. **(A)** BRCA2₁₆₇₋₂₆₀ was previously phosphorylated by Plk1. pBRCA2₁₆₇₋₂₆₀ was injected in presence (orange) or absence (black) of Kif2C WT on a Superdex 200 10/300 GL Increase column (GE Healthcare). Buffer: Dulbecco's PBS (Sigma) adjusted to 200 mM NaCl, 5 mM MgCl₂, 2 mM DTT pH7.2. **(B)** Coomassie-stained 15% SDS-PAGE gel of the elution.

5. Study of the BRCA2/Chk2 interaction

I also tested the interaction between pBRCA2 and the kinase Chk2, which was enriched only in the 10 ng pBRCA2 sample in the proteomics experiments (**Figure 55**).

The kinase Chk2 is a critical mediator of the DNA damage response. Upon damage, Chk2 acts as activator of the checkpoint and can provoke cell cycle arrest if DNA damage is not repaired (Zannini et al., 2014, Li et al., 2002, Mustofa et al., 2020). Interestingly, mutations in Chk2 are associated to an increased risk of sporadic and hereditary breast cancer (Wendt et al., 2019, Badgular et al., 2019). However, no mechanism linking BRCA2 and Chk2 has yet been described in the literature.

Chk2 is constituted of i) a N-terminal region enriched in SQ/TQ motifs that are essential for Chk2 activation by the ATM/ATR/DNA-PK kinases upon DNA damage, ii) a central FHA domain and iii) the kinase domain (**Figure 63**). Interestingly, the FHA domain of Chk2 is known to recognize phosphorylated peptides with a preference for phosphothreonines having an aspartic acid at position -1 and a leucine at position +3, with an optimal affinity of 0.9 μ M (Li et al., 2002). One structure of the human FHA domain of Chk2 in complex with a model phosphopeptide is available (Li et al., 2002, PDB code: 1GXC). Furthermore, the Chk2 FHA domain presents many mutations associated to cancers, including breast cancer (**Figure 63**).

We decided to first test the interaction between Chk2_{FHA} and pBRCA2₁₆₇₋₂₆₀. I produced a construct that we already had in the lab, which contained aa 1 to aa 209 of Chk2 (**Figure 64.A**), that is to say its N-terminal region and the FHA domain. I examined the possible interaction between pBRCA2₁₆₇₋₂₆₀ and Chk2₁₋₂₀₉ by NMR (**Figure 64.B.C.D**).

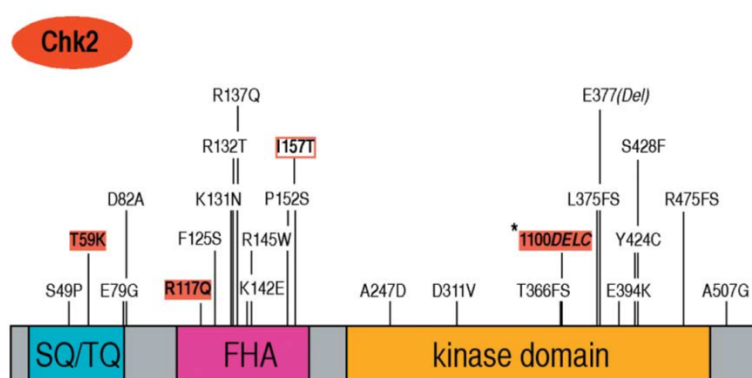


Figure 63. Scheme of the primary structure and domains of Chk2, and the identified mutations in breast, colon, lung, bladder and ovary cancers (from Bartek et al., 2003). Red boxes highlight three mutations associated with familial cancer.

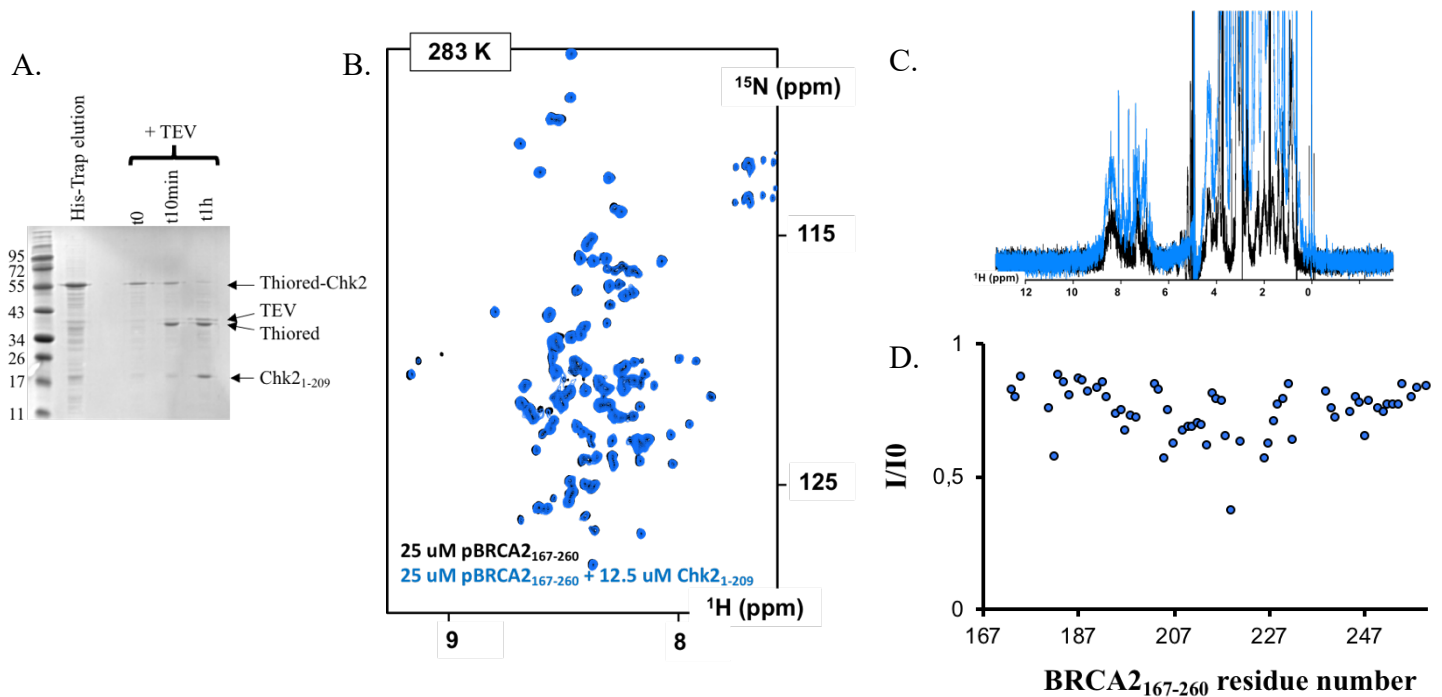


Figure 64. Interaction between pBRCA2₁₆₇₋₂₆₀ and Chk2₁₋₂₀₉
(A) Coomassie-stained 15% SDS-PAGE gel of the thioredoxin-Chk2₁₋₂₀₉ construct after HisTrap elution, and TEV cleavage. A gel-filtration was later performed to polish the purification **(B)** Overlay of ¹H-¹⁵N SOFAST-HMQC and **(C)** ¹H 1D spectra of ¹⁵N-labeled pBRCA₁₆₇₋₂₆₀ at 25 uM free (black) and in presence of Chk2₁₋₂₀₉ at 12.5 uM in Dulbecco's PBS (Sigma), 2 mM DTT at pH 7.0, 283K (600 MHz). **(D)** Peak intensity ratios extracted from the spectra in **(B)**.

After addition, of Chk2₁₋₂₀₉, I observed decreased peak intensities in ¹H-¹⁵N 2D correlation spectra for peaks corresponding to the region spanning residues 214-232. This result should be further confirmed in presence of higher concentrations of the isolated Chk2_{FHA} domain (in progress).

6. Other interactions tested

During my PhD, I also briefly tested interactions between the BRCA2 fragments that I produced and proteins from collaborators. In this context, I tested interaction between BRCA2 and DDX5 (from Dr. Aura Carreira, **Figure 65**) and BRCA2 and PARP1 (from Dr. Aura Carreira) using NMR (**Figure 66**). However, in both cases, I could not observe any significant peaks disappearance or chemical shift perturbations in ¹H-¹⁵N 2D spectra of ¹⁵N-labeled BRCA2₁₉₀₋₂₈₄ or BRCA2₄₈₋₂₁₈ at 50 uM upon addition of DDX5 and PARP1 at high

concentrations up to 100 μM . We thus failed to obtain any evidence of a direct interaction between BRCA2 and DDX5 or PARP1 in these conditions.

Because the amounts of PARP1 provided from our collaborators were not sufficient to carry out supplementary experiments, I also produced unlabeled PARP1₁₋₃₆₆ (**Figure 67.C**) to record NMR spectra in presence of ^{15}N -labeled BRCA2₁₋₂₈₄ produced by Rania Ghoul. However, I could not observe any consistent peak intensity variations (**Figure 67.A**). Only minor chemical shift perturbations were visible and well-dispersed along the sequence, corresponding to pH variations. To cross-validate our results on the opposite side, I also produced ^{15}N PARP1₁₋₃₆₆ samples (**Figure 67.B.D**) in order to test its interaction with non-labeled BRCA2₁₋₅₀₀ produced by Dr. Aura Carreira's team. However, this later PARP1 construct was highly prone to aggregation (loss of ^1H - ^{15}N NMR peak intensities after 1h at 20 $^\circ\text{C}$, **Figure 67.D**). I observed a large and homogeneous peak disappearance upon addition of BRCA2₁₋₅₀₀, except for Asn/Gln side chains and the flexible residues, whose peaks are at the center of the spectrum. It was thus not possible to conclude whether it was due to aggregation or an interaction or both.

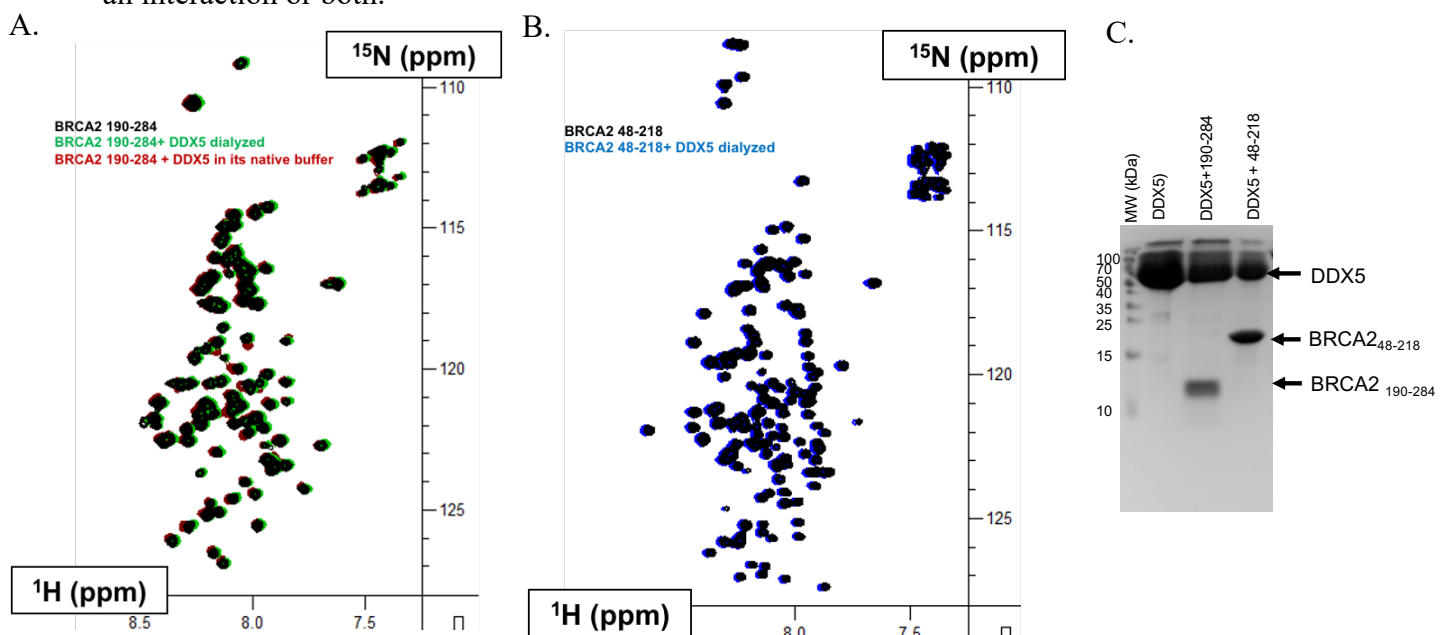


Figure 65. Interaction test between BRCA2 and DDX5.

(A) Overlay of ^1H - ^{15}N SOFAST-HMQC spectra of ^{15}N -labeled BRCA2₁₉₀₋₂₈₄ at 50 μM free (black) or in presence of DDX5 at 100 μM in its “native buffer” (PBS 1.5X, Mg-acetate 1 mM, glycerol 10%, DTT 1 mM, EDTA 1 mM at pH 7.0) (red) or in presence of DDX5 at 100 μM in “dialyzed buffer” (HEPES 50 mM, NaCl 150 mM, EDTA 1 mM, DTT 2 mM at pH7.0) (green). (B) Overlay of ^1H - ^{15}N SOFAST-HMQC spectra of ^{15}N -labeled BRCA2₄₈₋₂₁₈ at 50 μM free (black) or in presence of DDX5 at 100 μM in HEPES 50 mM, NaCl 150 mM, EDTA 1 mM, DTT 2 mM at pH7.0 (blue). All spectra were recorded at 283 K, 700 MHz (CEA Saclay) (C) Coomassie-stained 15% SDS-PAGE gel of ^{15}N BRCA2₁₉₀₋₂₈₄, ^{15}N BRCA2₄₈₋₂₁₈ and DDX5 (from collab.)

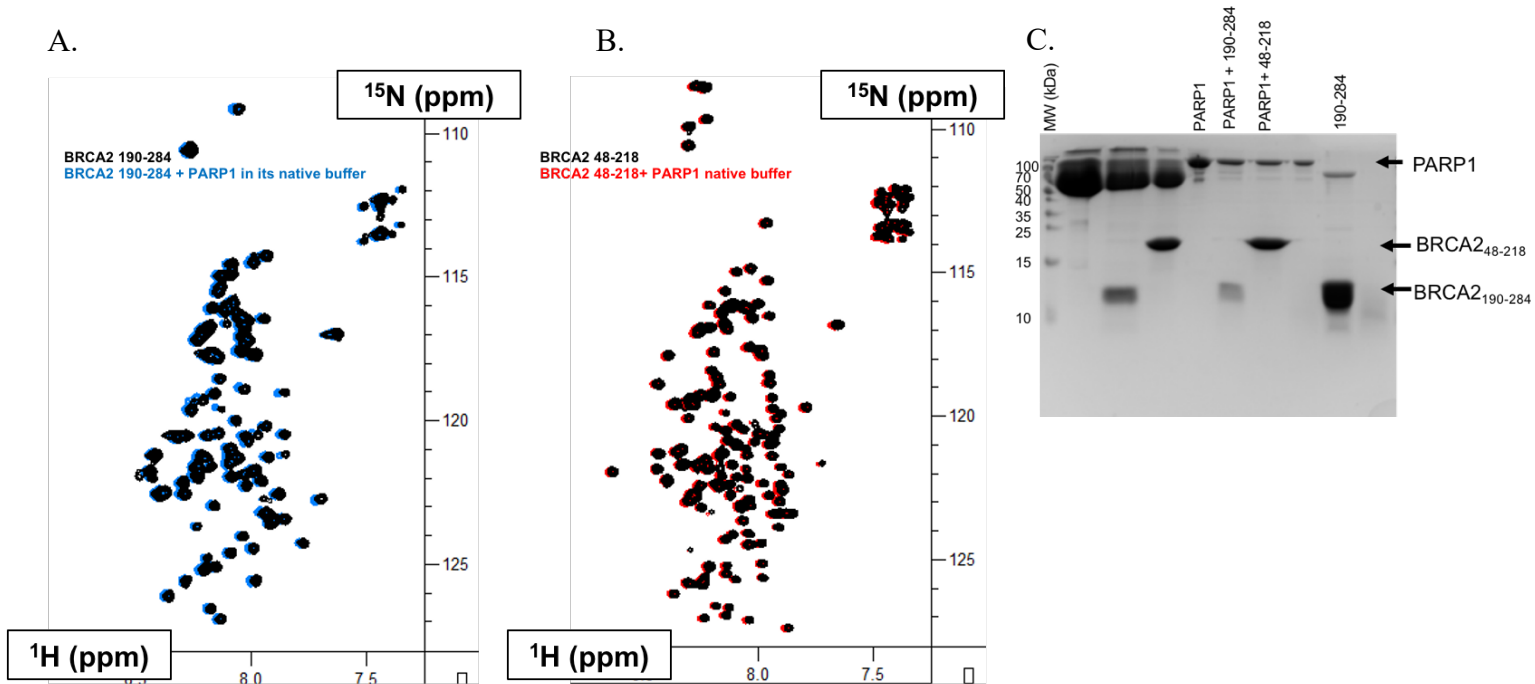


Figure 66. Interaction tests between BRCA2 and PARP1

(A) Overlay of ^1H - ^{15}N SOFAST-HMQC spectra of ^{15}N -labeled BRCA2₁₉₀₋₂₈₄ at 50 μM free (black) or in presence of PARP1 at 100 μM in 25 mM HEPES, 150 mM NaCl, 0.1 mM TCEP, 1 mM EDTA pH 7.0 (blue) (B) Overlay of ^1H - ^{15}N SOFAST-HMQC spectra of ^{15}N -labeled BRCA2₄₈₋₂₁₈ at 50 μM free (black) or in presence of PARP1 at 100 μM in 25 mM HEPES 150 mM NaCl, 0.1 mM TCEP, 1 mM EDTA, pH 7.0 (red). All spectra were recorded at 283 K and 700 MHz (CEA Saclay) (C) Coomassie-stained 15% SDS-PAGE gel of ^{15}N BRCA2₁₉₀₋₂₈₄, ^{15}N BRCA2₄₈₋₂₁₈ and PARP1 (from collab.)

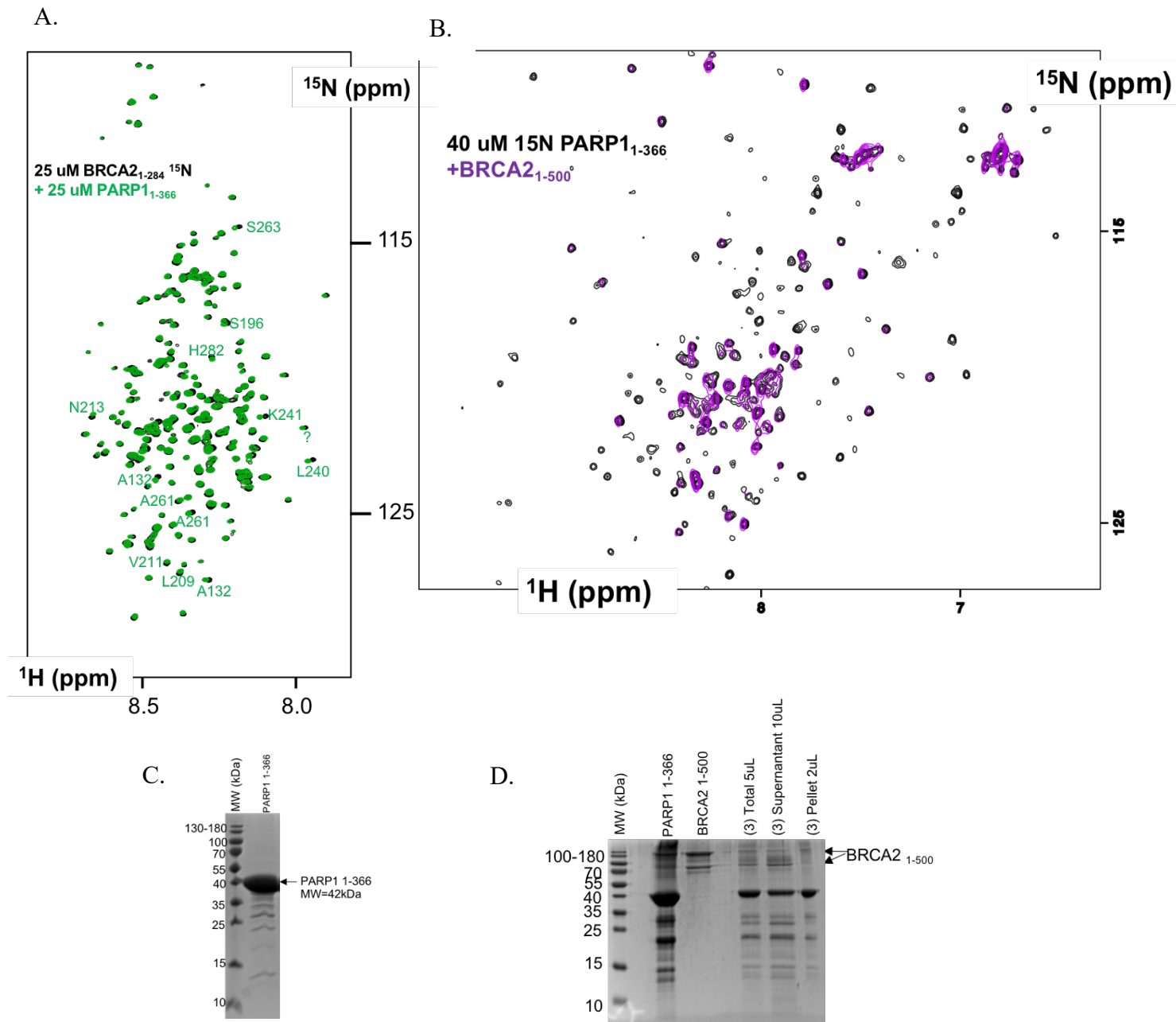


Figure 67. Interaction test between BRCA2 and PARP1₁₋₃₆₆

(A) Overlay of ^1H - ^{15}N SOFAST-HMQC spectra of ^{15}N -labeled BRCA2₁₋₂₈₄ at 25 uM free (black) or in presence of PARP1 at 25 uM in 25 mM HEPES, 150 mM NaCl, 0.1 mM TCEP, 1 mM EDTA at pH 7.0 (blue) **(B)** Overlay of ^1H - ^{15}N SOFAST-HMQC spectra of ^{15}N -labeled PARP1₁₋₃₆₆ at 40 uM free (black) or in presence of BRCA2₁₋₅₀₀ (BRCA2₁₋₅₀₀ provided by Dr. Aura Carreira) in BRCA2₁₋₅₀₀ elution buffer, pH 7.0 (violet). All spectra were recorded at 283 K, 700 MHz (CEA Saclay) **(C)** Coomassie-stained 15% SDS-PAGE gel of ^{15}N PARP1₁₋₃₆₆ (produced in-house) **(D)** Coomassie-stained 15% SDS-PAGE analysis of the ^{15}N PARP1 NMR sample.

Chapter 6. Interplay between BRCA2 phosphorylation by Cdk and Plk1

In **Chapter 3**, I illustrated the discovery of a new Plk1 binding site on BRCA2 (BRCA2_{pT207}). Another Plk1 docking site was previously described in the literature: pT77, which has been reported to be phosphorylated by Cdk1 (Yata et al., 2014, Takaoka et al., 2014).

Here, I was interested in understanding how the two Plk1 docking sites of the N-terminal region BRCA2 (BRCA2_{pT77} and BRCA2_{pT207}) can exert synergistic functions. After demonstrating the affinity of Plk1_{PBD} for a short BRCA2_{pT77} peptide, such a study required to produce phosphorylated constructs BRCA2_{pT77}. Different strategies have been used, which we report in subchapters 2 and 3. Our recent success in producing BRCA2_{pT77-aa48-220} will permit to quantify and understand the influence of the phosphorylation of BRCA2(T77) by Cdk on the later phosphorylation by Plk1.

1. The phosphomimetics approach

The first approach to test the impact of BRCA2_{pT77} on Plk1 phosphorylation was to generate a so-called phosphomimetic of the position T77. This popular method consists in the mutation of a serine or threonine into an aspartate or glutamate. The negative charge and the chain length of these two amino acids mimic, even imperfectly, the presence of a phosphate on a serine or threonine. Thus, the targeted site is so-to-say natively 100% modified. Phosphomimetics are largely used in cell biology for testing the impact of a phosphoresidue on protein functions or interactions.

First, BRCA2_{pT77} interacts with Plk1_{PBD} with a $K_D=240$ nM, which is in the range of PBD affinities for its targets (Elia et al., 2003). In addition, the interaction is phosphodependent because the Plk1_{PBD} does not interact with BRCA2_{T77}. Then, I tested the ability of Plk1_{PBD} to recognize BRCA2_{T77D} and BRCA2_{T77E} by ITC (**Figure 68**). The titrations revealed that BRCA2 fragments carrying T77D or T77E mutations did not interact with Plk1_{PBD}. Hence, Plk1_{PBD} does not recognize phosphomimetics, which is consistent with the prior structural knowledge derived from X-ray crystallography: the phosphate on the threonine side-chain is at the core of the interaction with Plk1_{PBD} and appears to be essential for the binding event. Thus, the phosphomimetic strategy cannot work here.

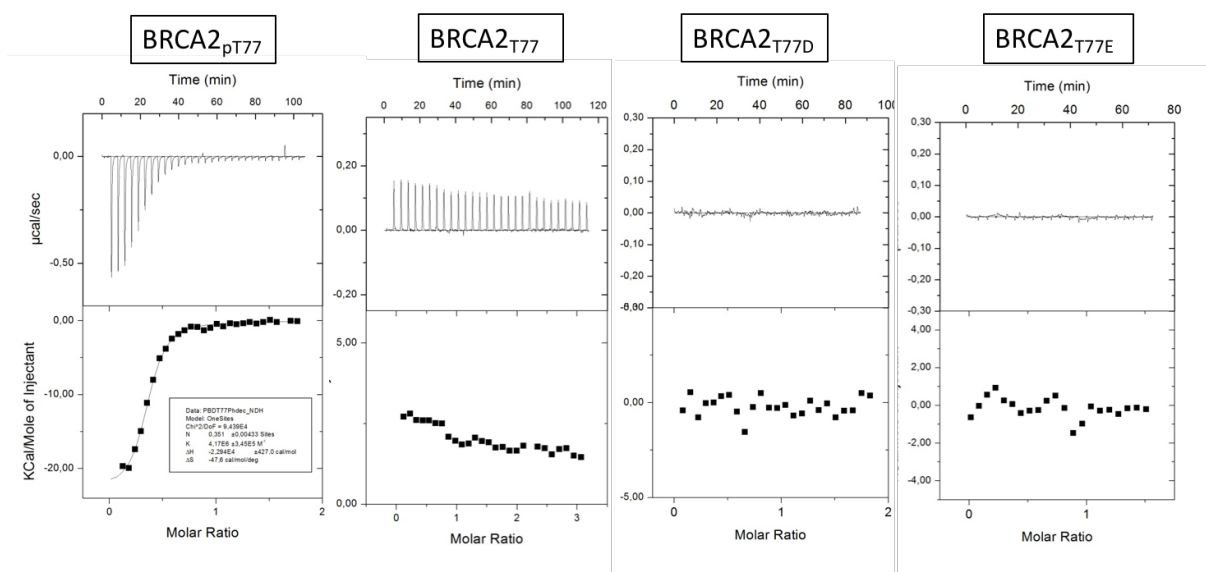


Figure 68. ITC titration of Plk1_{PBD} (100 μ M in the syringe) with BRCA2 peptides (10 μ M in the cell). Experiments were performed at 20°C, with injections of 10 μ L, in a buffer containing 50 mM Tris-HCl, at pH 8.0, 150 mM NaCl, 5 mM b-mercaptoethanol.

2. Pre-phosphorylation of BRCA2 by Cdks

Then, we sought to produce longer BRCA2 constructs pre-phosphorylated by Cdk kinases to analyse their phosphorylation by Plk1. Our strategy was to use a Cdk kinase to phosphorylate BRCA2₄₈₋₂₁₈. The first kinase that we tested was Cdk1/cyclinB1 because it is the most abundant Cdk during mitosis (Ord et al., 2018). After BRCA2₄₈₋₂₁₈ phosphorylation by commercial Cdk1/B1, seven phosphopeaks appeared, including pT77 (Figure 69). This confirmed that Cdk1/B1 directly phosphorylates BRCA2_{T77}. Then I boiled the sample 10 min at 90°C for inactivating Cdk1/B1 and I added Plk1 to the sample with fresh ATP and DTT and monitored Plk1 kinesis (Figure 69). After phosphorylation by Plk1, peaks corresponding to pS193 and pT207 were more intense in the case of pre-Cdk1 phosphorylation. This suggested that pT77 increases BRCA2 phosphorylation by Plk1. Because of the high cost of commercial Cdk1/B1 (the amount of kinase necessary for one experiment costs 360€), we limited our analysis to this early, qualitative observation.

Cdk1/B1 was indeed purchased to Sigma-Aldrich and possesses an activity of 12-16 nmol/min/mg, which is rather low for our approach using NMR spectroscopy. I performed this experiment before the reoptimization of Plk1 phosphorylation that finally allowed a continuous readout. Hence, at that time, I used the quenched reaction strategy for analyzing BRCA2 phosphorylation by Plk1, which was even more demanding in terms of protein

quantities. The recent recombinant production of Cdk1 and Cyclin B1 in-house by FX Theillet at milligram scales (~20 mg per liter of culture) should permit to reproduce these data in more controlled conditions.

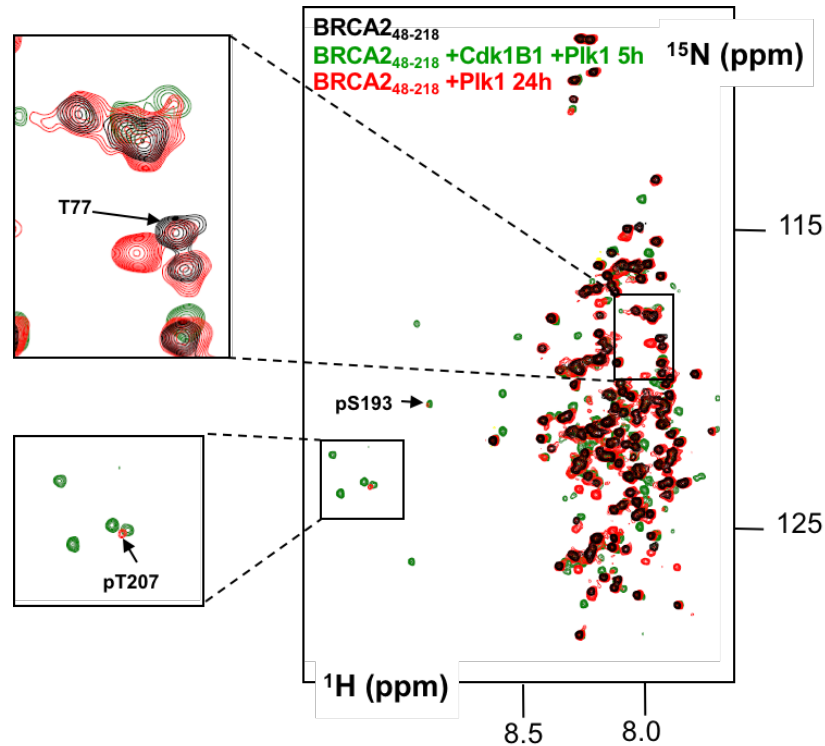


Figure 69. Pre-phosphorylation of BRCA2₄₈₋₂₁₈ by Cdk1/B1 qualitatively increases its phosphorylation by Plk1. Comparison of the ¹H-¹⁵N SOFAST-HMQC spectra of ¹⁵N BRCA2₄₈₋₂₁₈ at 25 μM before phosphorylation (black) and after phosphorylation either by Plk1 (24h, red) or Cdk1/B1 and then Plk1 (5h, green). The spectra were recorded at 283 K and 600 MHz CEA Saclay. Samples were priorily incubated at 25°C, pH 7.0 in the presence of Cdk1/B1 and then at 30°C, pH 7.8 in presence of Plk1, in a buffer containing 50 mM HEPES, 2 mM ATP, 1 mM DTT, 1 mM EDTA, 20 mM MgCl₂. The phosphorylation reactions were stopped by heating the samples during 10 min at 90°C and the pH was readjusted at pH 7.0 before NMR analysis.

In order to carry out a quantitative analysis of the influence of pT77, I tried to phosphorylate T77 with a more affordable kinase: Cdk1/cyclinA2. However, while Cdk1/A2 phosphorylates several BRCA2 sites in common with those modified by Cdk1/B1 (peak superimposition), we observed only a very weak phosphorylation level of T77 in these conditions (**Figure 70**). Perhaps not surprisingly in the absence of a high pT77 stoichiometry, the quantitative analysis of BRCA2₄₈₋₂₁₈ phosphorylation by Plk1 after pre-phosphorylation by Cdk1/A2 revealed no changes in kinetics as compared to those observed on non-modified BRCA2₄₈₋₂₁₈.

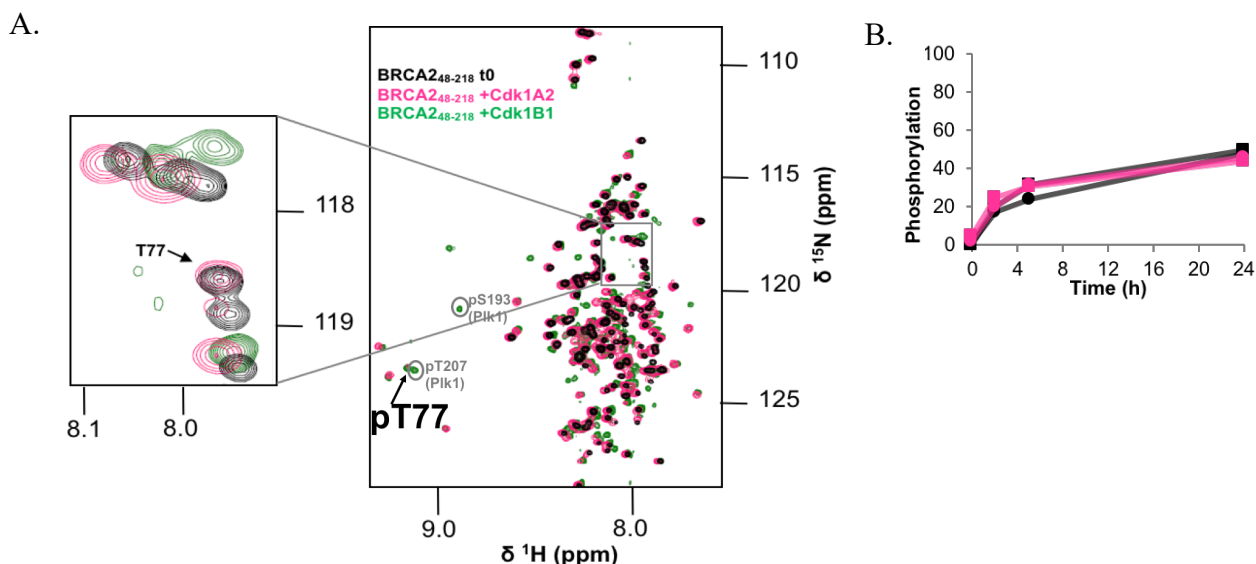


Figure 70. Phosphorylation of BRCA2₄₈₋₂₁₈ by Cdk1/A2 compared to Cdk1/B1. **(A)** Comparison of the ¹H-¹⁵N SOFAST-HMQC spectra of ¹⁵N BRCA2₄₈₋₂₁₈ before phosphorylation (black) and after phosphorylation either by Cdk1/A2 (pink) or Cdk1/B1 + Plk1 (green). The spectra were recorded at 283 K, 600 MHz CEA Saclay. The phosphopeaks due to Plk1 activity are circled in grey. Samples were incubated at 25°C, pH 7.0 in the presence of Cdk1/A2 or Cdk1/B1, in a buffer containing 50 mM HEPES, 2 mM ATP, 1 mM DTT, 1 mM EDTA 20 mM MgCl₂, pH 7.0. The phosphorylation reactions were stopped by heating the samples during 10 min at 90°C and the pH was readjusted at pH 7.0 before NMR analysis. **(B)** Quantification of S193 (circle) and T207 (square) phosphorylation with (pink) or without (black) Cdk1/A2 prephosphorylation.

In order to efficiently phosphorylate efficiently BRCA2_{T77}, I thought to use the p38 α kinase. The MAP kinase p38 α has a minimal S/T-P consensus phosphorylation site, similarly to Cdk1/B1. The fine preferences and the distant secondary docking sites are of course not the same, but we expected to obtain T77 phosphorylation in stoichiometric amounts. This kinase is indeed produced in the lab in high quantities and possesses a good activity. Thus, I tested the phosphorylation of BRCA2₄₈₋₂₁₈ by p38 α .

As illustrated in **Figure 71**, BRCA2₄₈₋₂₁₈ phosphorylation by p38 α led to similar phosphopeaks than Cdk1/B1. In addition, the analysis of the spectra generated by the mutant BRCA2_{T77A} phosphorylated by p38 α permitted to identify the ¹H-¹⁵N crosspeak corresponding to pT77 (**Figure 72**). However, p38 α appeared to be able to phosphorylate a more extended set of peaks on BRCA2 upon prolonged incubation. While T77 phosphorylation required 2 hours to reach ~100% levels, supplementary phosphopeaks already emerged with high intensities. We observed up to 7 phosphopeaks after 4 hours of incubation, although many of them represented minor populations (**Figure 73**).

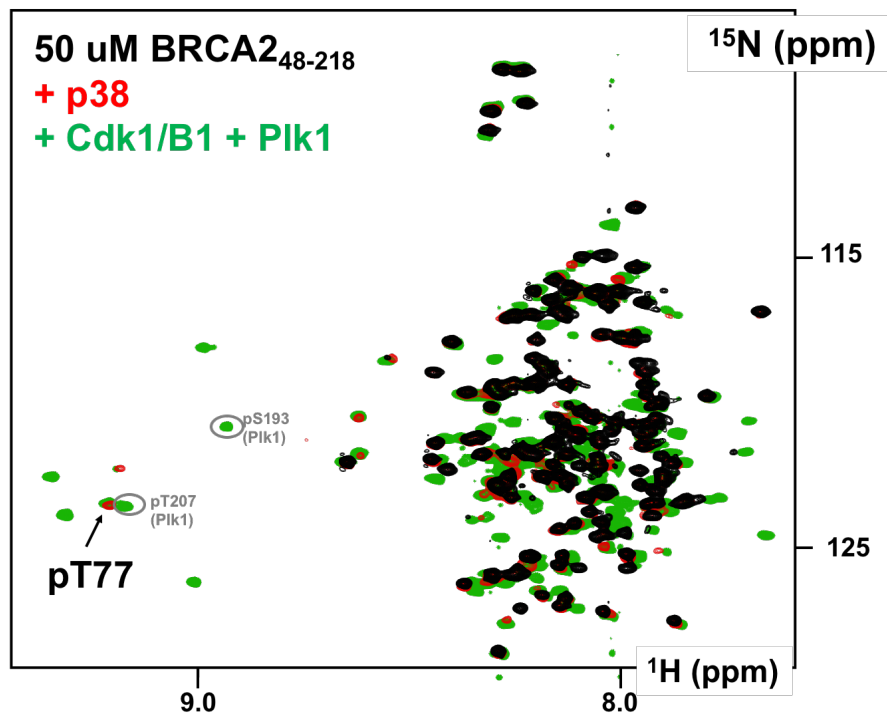


Figure 71. Phosphorylation of BRCA2₄₈₋₂₁₈ by p38 α compared to Cdk1/B1. Superimposition of the ¹⁵N BRCA2₄₈₋₂₁₈ ¹H-¹⁵N SOFAST-HMQC spectra before phosphorylation (black), after p38 α phosphorylation (red) and after Cdk1/B1 phosphorylation and Plk1 phosphorylation (green). The spectra were recorded at 283 K, 600 MHz CEA Saclay. The phosphopeaks due to Plk1 activity are circled in grey. Samples were incubated at 25°C, pH 7.0 in the presence of p38 α or Cdk1/B1, in a buffer containing 50 mM HEPES, 2 mM ATP, 1 mM DTT, 1 mM EDTA 20 mM MgCl₂, pH 7.0. The phosphorylation reactions were stopped by heating the samples during 10 min at 90°C and the pH was readjusted at pH 7.0 before NMR analysis.

Because the observed activity of p38 α on BRCA2 appeared to mimic decently that of Cdk1/B1, I thought it would permit to test quantitatively the impact of BRCA2_{pT77} on Plk1 phosphorylation (**Figure 73**). Similarly to the experiments carried out previously with Cdk1/B1, my strategy was to phosphorylate BRCA2₄₈₋₂₁₈ by p38 α first, boil the sample 10 min at 90°C for inactivating p38 α and then to add Plk1 to the sample with fresh ATP and DTT.

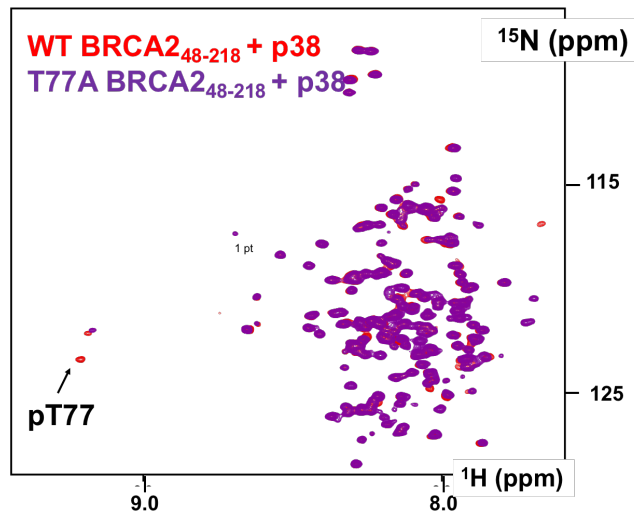


Figure 72. Phosphorylation of WT and T77A BRCA2₄₈₋₂₁₈ by p38 α . Overlay of the ¹⁵N WT (red) and T77A (violet) BRCA2₄₈₋₂₁₈ ¹H-¹⁵N SOFAST-HMQC spectra after phosphorylation by p38 α . The spectra were recorded at 283 K, 600 MHz CEA Saclay. The samples were incubated at 25°C, pH 7.0 in the presence of p38 α , in a buffer containing 50 mM HEPES, 2 mM ATP, 1 mM DTT, 1 mM EDTA 20 mM MgCl₂, at pH 7.0. The phosphorylation reactions were stopped by heating the samples during 10 min at 90°C and the pH was readjusted at pH 7.0 before NMR analysis.

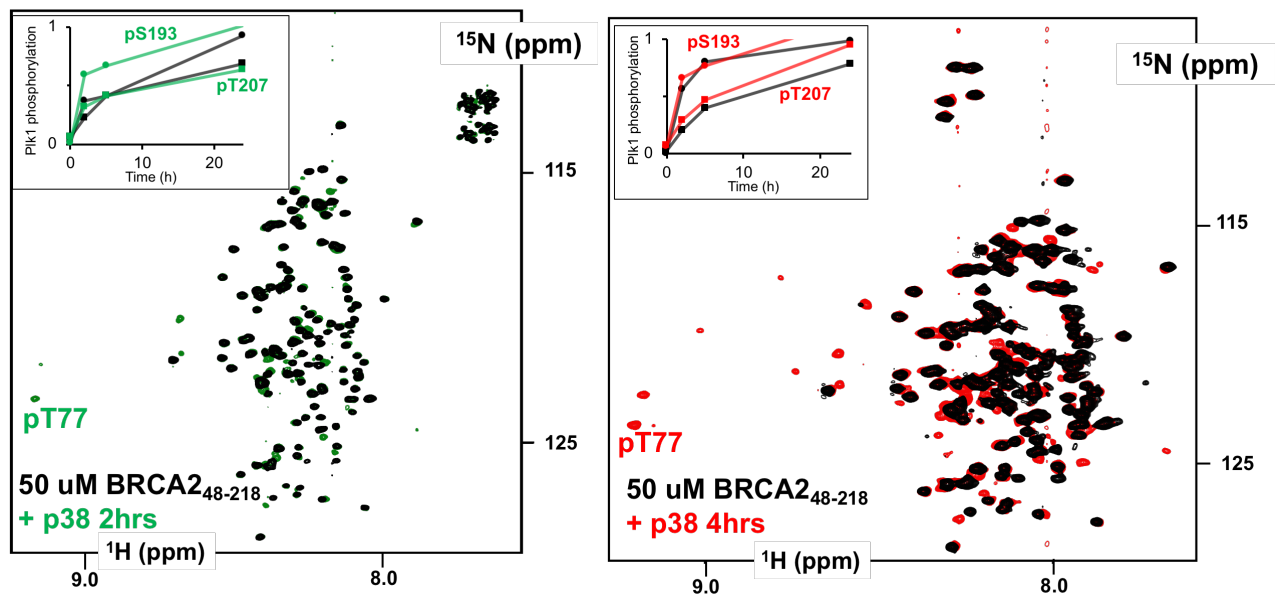


Figure 73. p38 α phosphorylates BRCA2_{T77} and can favor the later phosphorylation of BRCA2_{S193} by Plk1 when the phosphorylation of BRCA2 by p38 α was stopped at an early stage. Overlay of the ¹⁵N BRCA2₄₈₋₂₁₈ ¹H-¹⁵N SOFAST-HMQC spectra before (black) and after 2 hrs (green) or 4 hrs (red) of phosphorylation by p38 α . The spectra were recorded at 283 K, 600 MHz CEA Saclay. The insets show the quantitative phosphorylation kinetics on S193 and T207 by Plk1. The samples were incubated at 25°C, pH 7.0 in the presence of p38 α , in a buffer containing 50 mM HEPES, 2 mM ATP, 1 mM DTT, 1 mM EDTA 20 mM MgCl₂, pH 7.0. The phosphorylation reactions were stopped by heating the samples during 10 min at 90°C and the pH was readjusted at pH 7.0 before NMR analysis. Quantification of Plk1-dependent BRCA2_{pS193} (rounds) and BRCA2_{pT207} (squares) events are displayed in the NMR spectra.

We performed such experiments using BRCA2₄₈₋₂₁₈ incubated with p38 α during either 2 or 4 hours. Interestingly, the phosphorylation reactions executed by Plk1 did not produce the same results on these 2 samples, although they both carry stoichiometric phosphorylation on T77 (**Figure 73**). When pre-phosphorylation by p38 α is stopped after immediately after the full modification of T77, we observed an increased phosphorylation rate on S193 by Plk1, but not on T207. At the opposite, a more extended pre-phosphorylation by p38 α (7 phosphopeaks) does not increase phosphorylation rates by Plk1, neither on S193 nor on T207. Hence, the degree of BRCA2₄₈₋₂₁₈ pre-phosphorylation on secondary sites has clear consequences. This result illustrates the complexity of a multi-phosphosite system. Moreover, we observed that the hyperphosphorylated BRCA2₄₈₋₂₁₈ incubated 4 hours with p38 α was extremely prone to degradation.

In order to characterize the role of BRCA2_{pT77} on Plk1 phosphorylation, we thought that a better defined experimental approach had to be adopted.

3. Native Chemical Ligation (NCL)

Thereby, I used a semi-synthetic strategy: a short BRCA2 peptide precisely phosphorylated at the position T77 is chemically synthesized, and is later covalently linked to a recombinantly produced ¹⁵N labeled peptide, which contains the BRCA2₁₉₃₋₂₂₀ phospho-region or interest (**Figure 74**).

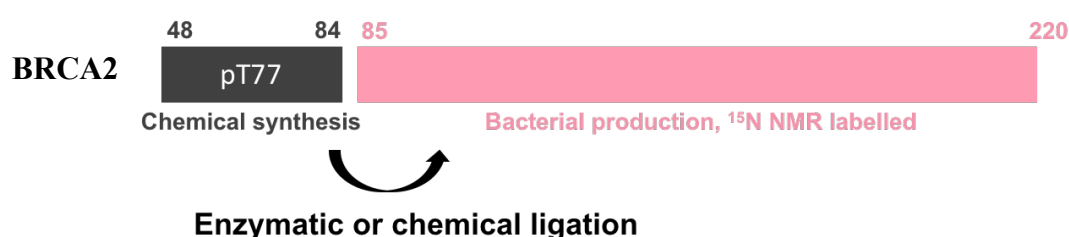


Figure 74. The NCL strategy for studying the effect of pT77 on BRCA2 phosphorylation by Plk1.

A chemically synthesized peptide fragment of BRCA2, containing a phosphothreonine at the position 77, is linked to a ¹⁵N labeled recombinantly produced fragment of BRCA2 containing the 193-220 region of interest. The constructs are discussed in the main text.

Several ligation methods already exist and are extensively reviewed in [Baumann & Hackenberger, 2018](#) and [Berrade & Camarero, 2008](#). These methods can be sorted into two categories: enzymatic and chemical ligation.

Native Chemical Ligation generally designates chemical ligation methods aiming at obtaining native peptide backbones. This is an intense field of research that has greatly progressed in the last years. NCL consists in a transthioesterification via a nucleophilic attack of a thioester (at the C-terminal end of the initial N-terminal fragment) by a cystiolate group (at the N-terminal end of the initial C-terminal fragment). Then, under native conditions, the activated thioester undergoes an intramolecular S->N acyl shift. This reaction generates a peptide bond at the conjugation junction. Finally, post-ligation desulfurization can be used to reduce cysteine and selenocysteine into alanine.

I initiated a collaboration under the supervision of Dr. François-Xavier Theillet with Dr. Vincent Aucagne and Jean-Baptiste Madinier (CBM, Orléans), who are experts in peptide chemical synthesis and NCL. Obtaining a reactive C-terminal peptide thioester function is often considered to be the limiting part of NCL. The group of Dr. Aucagne has designed interesting solutions to this problem (Terrier et al., 2016). Here, the strategy was to produce a synthetic N-terminal peptide containing BRCA2_{pT77} and to link it to a C-terminal ¹⁵N labeled BRCA2 fragment containing the Plk1 phospho-region (**Figure 74**).

The N-terminal peptide has the same N-terminal extremity as BRCA2₄₈₋₂₁₈. The C-terminal extremity of this synthetic peptide is the residue 84, a glycine, which is usually a favorable C-terminal residue for an efficient NCL. The BRCA2₄₈₋₈₄ N-terminal peptide with a phosphothreonine at position 77 was produced using the Fmoc-based solid phase synthesis. A thioester was introduced at the C-terminal extremity for the NCL. This synthesis was performed by Jean-Baptiste Madinier and Dr. Vincent Aucagne according to their published protocol (Terrier et al., 2016). They obtained 14 mg of the BRCA2₄₈₋₈₄ peptide per synthesis, a common yield obtained using this strategy. Then, the peptide was linked to a BRCA2₈₅₋₂₂₀ C-terminal ¹⁵N labeled fragment. I was in charge of the bacterial expression and purification of this fragment. A G85C mutation was introduced in a BRCA2₈₅₋₂₂₀ construct to permit the NCL.

The BRCA2 fragments were purified and analyzed by inverse-phase HPLC, lyophilized by Jean-Baptiste Madinier and redissolved at 0.5-1 mM concentrations. The NCL reactions were carried out according to the published protocol (See Material and Methods) under gaseous argon (**Figure 75.B and C**) at 37°C under agitation over night. The reported pictures were taken when I went to the CBM to attend the experiment and understand how the NCL protocol works. The reaction was monitored using HPLC analysis (**Figure 76**). The reaction was completed after 24 hrs of incubation.

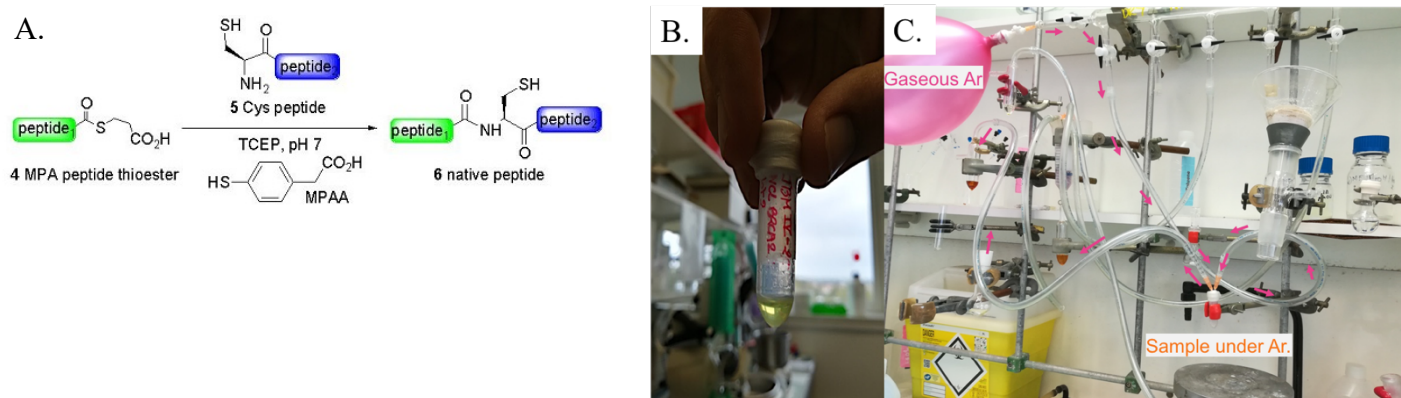


Figure 75. NCL protocol for linking BRCA2₄₈₋₈₄ to BRCA2₈₅₋₂₂₀.

(A) NCL reaction (image from Melnik lab, <http://olegmelnik.cnrs.fr>). BRCA2₄₈₋₈₄ (peptide 1) is synthesized with a C-terminal thioester. NCL is then performed at RT in the presence of BRCA2_{85-220-G85C} (peptide 2), TCEP and MPA, which improves the reactivity of the cryptothioester, at pH 7.0. The reaction generates a covalent peptide bond between peptide 1 and peptide 2. **(B)** The NCL sample after addition of cryptothioester, C-terminal fragment, TCEP, NaOH and MPA. The yellow color indicates that MPA is at a pH higher than 6.5. **(C)** Installation for placing the sample under argon atmosphere. These photos were taken at the CBM when I accompanied Jean-Baptiste Madinier for a day for discovering the NCL protocol.

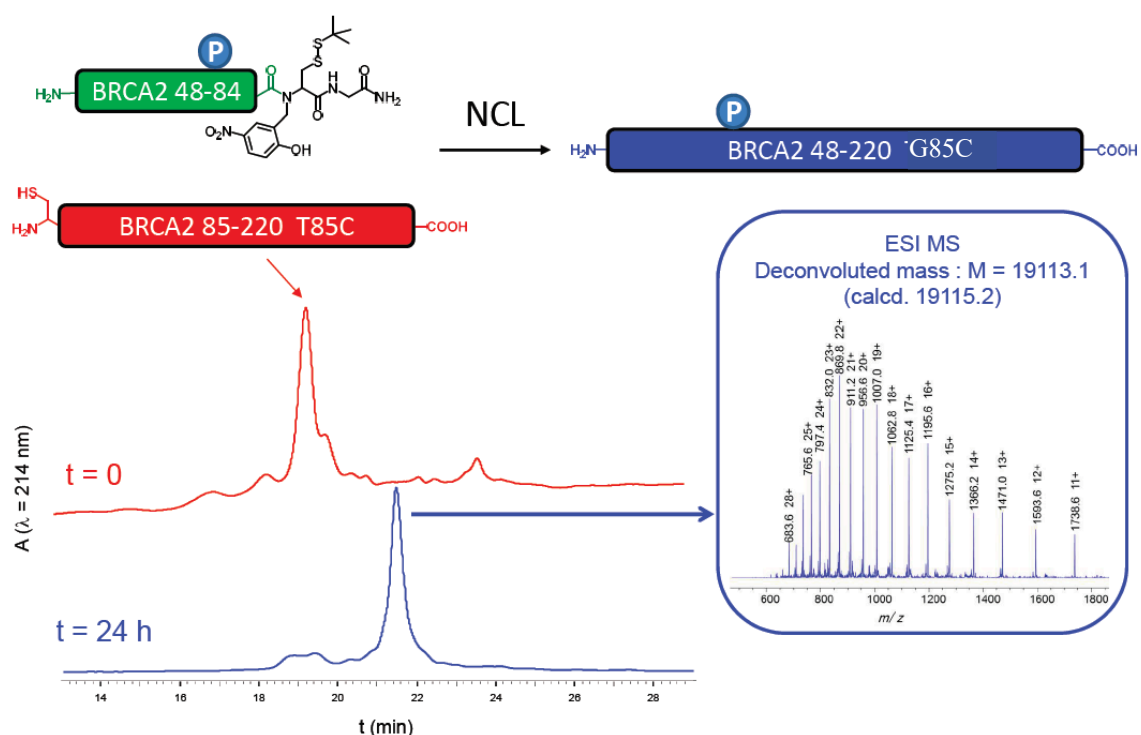


Figure 76. NCL reaction to obtain BRCA2_{48-220-G85C-P77} and its monitorin. The cryptothioester BRCA2₄₈₋₈₄ is linked to ¹⁵N BRCA2_{85-220-G85C} by NCL in order to generate BRCA2_{48-220-G85C}. HPLC elution on a C18 column (gradient H₂O/acetonitrile 20->40%) permits to separate the initial cryptothioester peptide (t=0, red peak) from the final product (t=24h, blue peak). ESI MS analysis of the blue peak reveals a deconvoluted mass corresponding to the BRCA2₄₈₋₂₂₀ ligated fragment (MS platform CBM, Orléans).

The next step of the protocol is the reduction of the Cys85 into alanine. By achieving this final modification, we thought to minimize the impact of the Gly85 mutation and to avoid the usual dimerization troubles that a solvent-exposed cysteine can generate. This step is currently under optimization. Until now the protocol of desulfurization led to a yield of 70% and it generated oxidation of the methionine. In order to obtain higher yields (more than 90%) and better sample quality, the alkylation of this cysteine is now considered.

Hence, I will soon purify the reconstituted BRCA2₄₈₋₂₂₀ by size-exclusion chromatography in the phosphorylation buffer. The sample will be used to study the influence of pT77 phosphorylation on the phosphorylation by Plk1, using the continuous readout that we already achieved with ¹H-¹⁵N SOFAST-HMQC experiments.

Chapter 7. Plk1 production and structural characterization

In parallel to the BRCA2 studies, I was also interested in characterizing the Plk1 kinase. I felt indeed that a number of ambiguous results from BRCA2 phosphorylation experiments may come from a lack of understanding on how Plk1 functions. The intriguing “activation” of Plk1 by peptides binding the PBD had to be elucidated to fully solve the phosphorylation regulation of BRCA2.

Previously, full length Plk1 was produced in insect cells by the Institut Curie protein production platform (Dr. Ahmed El Marjou and Patricia Duchambon, Paris). It permitted to carry out all the experiments reported above. However, the aliquots that we used were clearly containing truncated/proteolyzed versions of Plk1, i.e. separated PBD and kinase domain (KD). Moreover, we could not obtain any information on Plk1 activation state, i.e. its phosphorylation on S137 or T210 (see below), even though it has been reported in the literature that Plk1 is not phosphorylated when produced in insect cells (Kothe et al., 2007). Because Plk1 truncation and phosphorylation have an impact on its activity (Johnson et al., 2008), we thought we would have to produce well-defined versions of Plk1 if we wanted to characterize its activity and its regulation in an accurate fashion. Thus, the first goal was to produce Plk1 in house. The second goal was to obtain activated Plk1, phosphorylation either at S137 or T210.

Then, because we would produce various activated or unactivated versions of Plk1, we thought to carry out structural investigations on them in a synergistic manner. Our goal is to obtain information about the conformations and the interdomain interactions of Plk1 upon activation using NMR. Indeed, a study by Xu et al. on Plk1 from *Danio rerio* (Xu et al., 2013) reported that Plk1_{PBD} binding to Plk1_{KD} regulates Plk1 activity. The authors also showed how the phosphorylation of S123 (human S137) contributes to the dissociation of the KD and the PBD. Finally, they showed that the large linker (about 40 residues) between Plk1_{KD} and Plk1_{PBD} modulates negatively modulates the activity of the kinase (enzymatic tests). Hence, we aimed at collecting information on Plk1 structure and dynamics and the impact of i) the interaction between Plk1_{KD} and Plk1_{PBD}, ii) the long linker between human Plk1_{KD} and Plk1_{PBD}, iii) the peptides binding to Plk1_{PBD} (including BRCA2pT77 or BRCA2pT207), iv) the phosphorylation of Plk1_{KD}.

In order to confirm the phosphorylation state of Plk1 obtained from insect cells production, I asked the MS facility of the CEA Saclay (Steven Dubois) to analyze the Plk1_{Curie}. It was digested by trypsin and analyzed using MALDI-TOF spectroscopy. Unfortunately, the peptides containing S137 and T210 were not detected (**Figure 77**), probably because they were not enough ionizable. According to the literature, FL Plk1 produced in insect cells is not phosphorylated. I hypothesized that Plk1_{Curie} was also not phosphorylated. This would be consistent with the phosphorylation rate values obtained from BRCA2₄₈₋₂₈₄ and BRCA2₁₀₉₃₋₁₁₅₈ kinetic studies (**Chapter 2 and 3**). Thus, we needed to also produce the Plk1 activating kinase: Aurora A which phosphorylates Plk1_{T210} (Macurek et al., 2008, Seki et al., 2008).

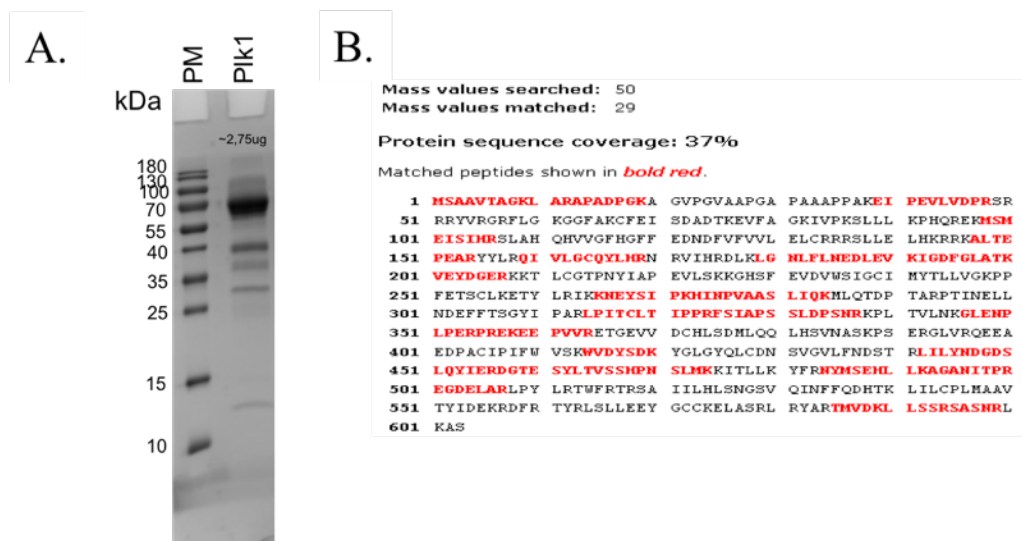


Figure 77. Mass spectrometry identified trypsinization products of Plk1_{Curie} but could not determine the phosphorylation state of Plk1_{S137} and Plk1_{T210}.

(A) SDS-PAGE of the Plk1_{Curie} revealed supplementary bands smaller than the molecular weight of FL-Plk1 (69 kDa). (B) MALDI-TOF analysis of the SDS-PAGE bands digested by trypsin revealed that lower bands correspond to truncated fragments of Plk1. No peptides containing either Plk1_{S137} or Plk1_{T210} could be detected (CEA MS facility, Steven Dubois).

1. Plk1 production in insect cells

I tried to produce Plk1 in insect cells, in order to be able to carry out supplementary purification steps yielding better purity levels. The recombinant expression platform of the Institut Curie was using a vector pFast-Bac HT for producing Plk1 in insect cells using the Bac-to-Bac baculovirus system. Our local platform preferred to use the vector that it classically uses, called pKL, which encodes also for a YFP-reporter of the baculovirus expression (under the promoter of the late infection stage gene polH). Hence, we sought to clone the Plk1 cDNA in pKL. We obtained the Plk1 cDNA cloned in a mammalian expression vector pTK24 (Addgene,

Kiyomitsu et al., 2012) from Dr. Ahmed El Marjou (Institut Curie, Paris). This plasmid encodes for mCherry-Stag-TEV-(cDNA)Plk1_{FL}. With the help of Dr. Virginie Ropars, I first amplified the Plk1 sequence by PCR and cloned it into pKL (**Figure 78.A**). We designed the amplification and the cloning in such a manner that we inserted a sequence encoding for a 6-His tag followed by a TEV cleavage site at the N-terminal extremity of the Plk1 sequence.

After ligation, the plasmid was used to transform DH10-EMBacY bacteria and generate bacmids carrying the Plk1 cDNA. This step relies on colonies screening on LB-agar plates containing IPTG and X-gal (**Figure 78.B**). Bacterial clones containing Plk1 encoding bacmids do not express β -galactosidase do not digest X-gal and remain uncolored/white, while the others generate blue colonies (see Material and Methods for more details) (**Figure 78.B**).

After purification, we used the bacmid to produce virions by infection of Sf9 cells. The baculovirus genome contains two recombinant production systems: one for the gene of interest and the other one for YFP reporting the expression of the bacmid proteins. After infection, the YFP fluorescence level in Sf9 cells is monitored as it reports for the efficiency of infection and protein expression (**Figure 79.A**). All the production was realized with the help of Audrey Coëns.

Then, I tried to purify the recombinant Plk1 expressed in Sf9 insect cells. Unfortunately, the SDS-PAGE analysis of Plk1 expression revealed a weak production equally distributed in the soluble and insoluble fractions (**Figure 79.B**). After Ni-NTA 6His-affinity chromatography of the soluble fraction, no Plk1 was found in the elution. It became clear that the protocol would require further optimization for producing large amounts of Plk1. A codon-optimized gene for insect cell expression has been synthesized by Genscript and inserted in pKL. We should obtain the first results from this approach in January 2021.

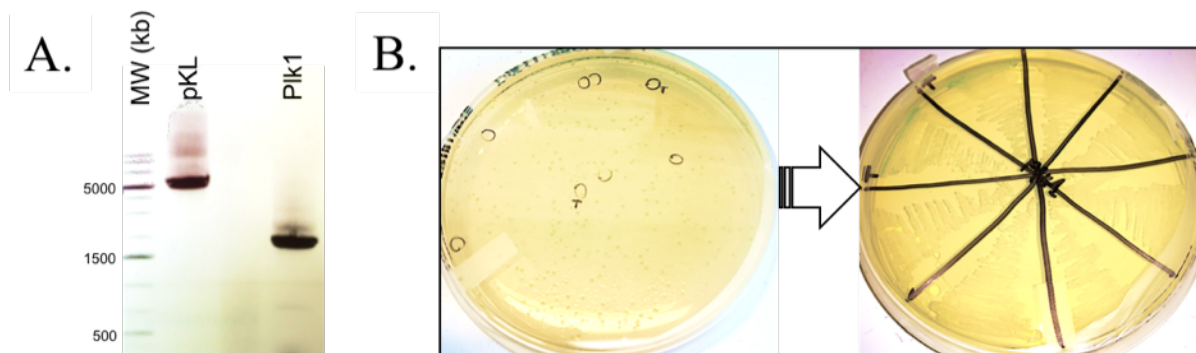


Figure 78. Cloning the Plk1 cDNA sequence into the pKL plasmid for bacmid recombination into DM10EMBacY cells.

(A) Agarose gel of the pKL plasmid and the Plk1 cDNA sequence PCR amplified from pTK24.
(B) Transformation of the ligated pKL-Plk1 plasmid into DH10EMBacY chimio-competent

cells grown on LB+antibiotic (left) and LB+antibiotic+IPTG+X-gal medium (right) after 24 and 48 hrs respectively.

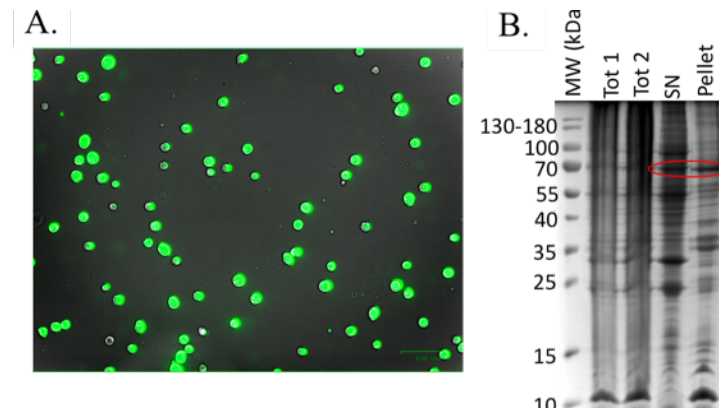


Figure 79. Production of Plk1 in Sf9 cells.

(A) Sf9 cells infected with a bacmid encoding for FL Plk1 and a YFP-reporter sequence, observed with an epifluorescence microscope. **(B)** SDS-PAGE analysis of the cells sonicated before (tot1 and tot2) and after (supernatant SN, pellet) centrifugation of the cell lysate. The bands supposedly corresponding to Plk1 are circled in red.

2. Design of protein constructs for bacterial expression

To carry out a structural characterization of Plk1, we thought to use NMR spectroscopy, which requires $^{13}\text{C}/^{15}\text{N}$ isotope labeling. Isotope labeling in insect cells is only at its beginnings in the lab. Thus, we designed Plk1 constructs for bacterial expression and ordered their codon-optimized synthesis (**Figure 80.A**). Constructs were designed for in house production of the full-length human kinase and of separated domains for the study of Plk1 dynamics.

We designed one PBD construct (Plk1₃₆₆₋₆₀₃) and two kinase domain (KD) constructs: one with the interdomain linker (Plk1₁₋₃₆₆) and one without (Plk1₁₋₃₂₈), which may permit to characterize its potential role on the interdomain interaction.

We also thought to design constructs ready for lanthanide chelating tag attachment. FX Theillet has already used such an approach to derive structural information on GB1 in frog oocytes (Müntener et al., 2016) in collaboration with Pr. Daniel Haüssinger (Univ. Basel, Suisse). This strategy is very convenient, because it can provide tridimensional information from pseudo-contact shifts observed in 2D NMR spectra (Joss et al., 2019). Thus, we designed Plk1 constructs that show only one solvent-accessible cysteine to permit in site-selective attachment of the lanthanid tag. We mutated all exposed cysteines in the KD and in the PBD (**Figure 80.A**). Unfortunately, this require the mutation of Cys212, located in the KD activation loop close to the activating T210. Then, we selected the position L162C for the tag graft. L162

is at the surface of the kinase domain and at an intermediate distance from both the PBD, the linker and the KF activation loop.

For the FL Plk1, we design three constructs: FL_{L162C} (Plk1₁₋₆₀₃), FL_{C212C} (to validate the innocuity of Cys212 mutation on Plk1 activity) and (Plk1₃₇₋₆₀₃), which does not contain the repetitive Pro/Ala rich N-terminal extremity of the kinase.

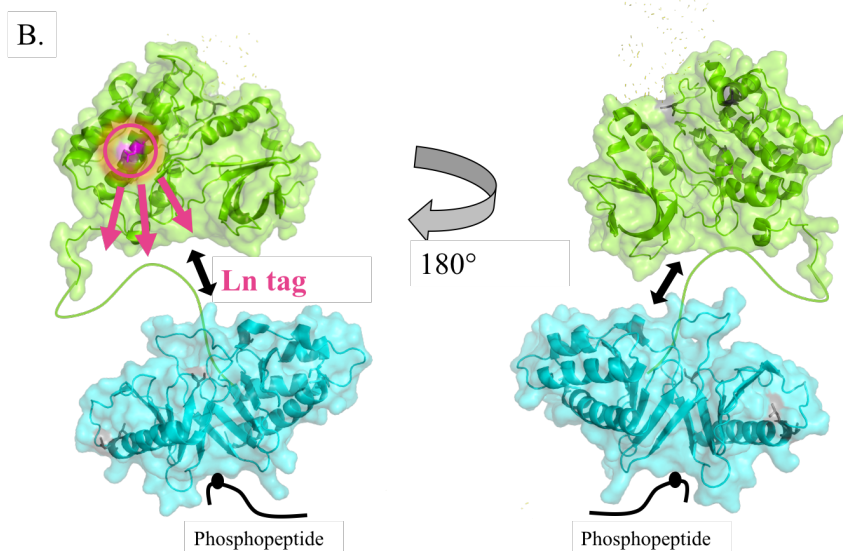
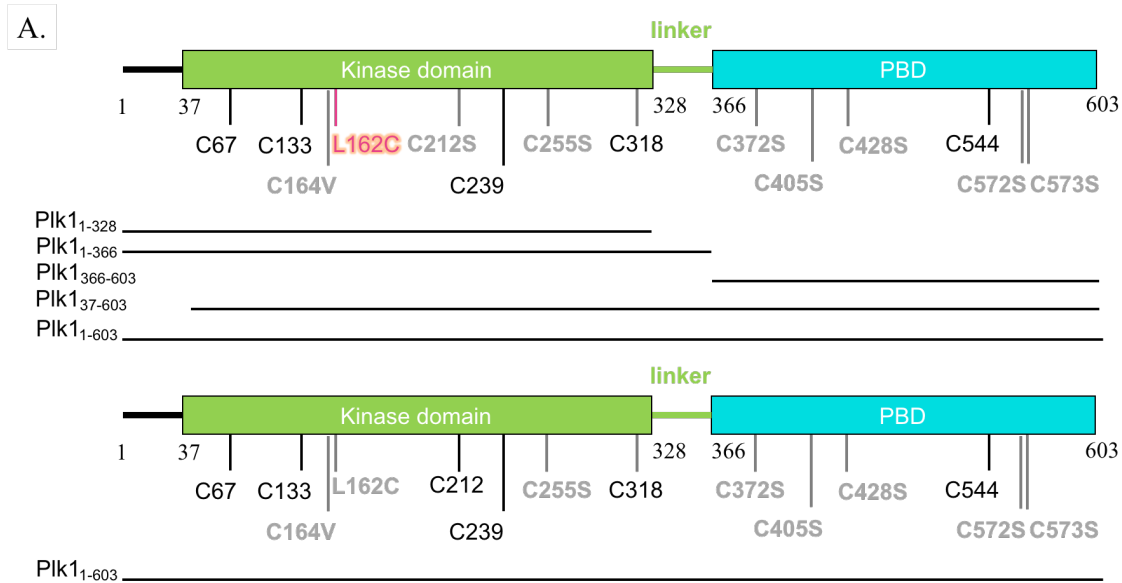


Figure 80. Construct design for the Plk1 study

(A) Plk1 contains 2 domains: the kinase domain (KD) and the Polo-Box Domain (PBD). Solvent-exposed cysteines and the chosen mutations are displayed in grey and non-exposed cysteines in black. Residue L162 was mutated into cysteine in order to create an attachment site for a lanthanide tag. Constructs used for the studies are displayed under the Plk1 schematic sequence. (B) Structure and surface of the human Plk1 KD (green, PDB: 5TA8) and the human Plk1 PBD (blue, PDB: 1UMW) and orientation of the two domains according to the *Danio rerio* Plk1 structure (PDB: 4J7B). Position of the lanthanide tag (pink) and the phosphopeptide substrate of PBD (black) are displayed in the Figure.

Because Aurora A is the kinase that is considered to phosphorylate the activation loop of Plk1 at position T210 (Macurek et al., 2008, Seki et al., 2008), we also designed a plasmid encoding for a AuroraA-TPX2₁₋₄₃ chimera, according to the plasmid construct described in Zorba et al., 2014. TPX2₁₋₄₃ allosterically activates Aurora A by interacting with a hydrophobic pocket in the N-terminal lobe of the Aurora A catalytic domain. This chimera has been shown to activate Aurora A. Activated Plk1 would be useful for phosphorylation kinetics studies, but also for studying the impact of T210 phosphorylation on Plk1 structure and dynamics.

The bacterial production tests of all constructs revealed that expression at 20°C was the most favorable because it provides soluble populations (**Figure 81**). In the optimized protocol, I finally used induction at 15°C, which yielded increased amounts of soluble proteins.

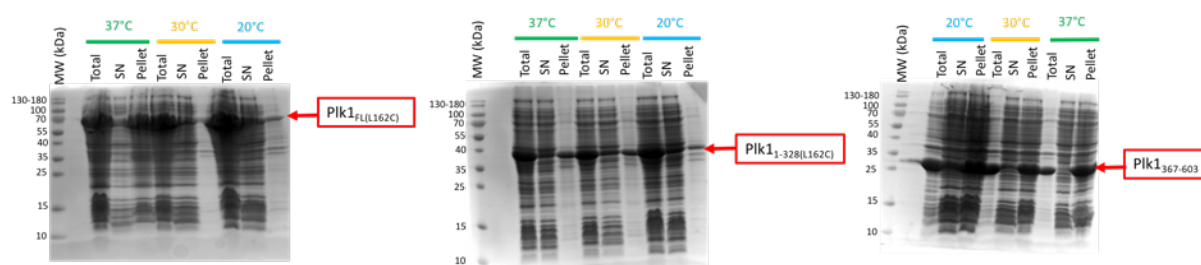


Figure 81. Expression tests of Plk1_{FL}, Plk1₁₋₃₂₈ and Plk1₃₆₇₋₆₀₃ constructs in *E.coli* BL21 (DE3). The conditions tested were: induction at 37°C for 3hrs, 30°C for 4°C and 20°C over night. Total lysed bacteria, soluble and insoluble fractions in 3X Laemmli buffer were loaded on SDS-PAGE 15% gel and revealed by Coomassie-staining.

3. Production of the kinase domain

I started with the production of the kinase domain Plk1₁₋₃₂₈. This domain is prone to degradation (**Figure 82.A**). The lower band observed on the SDS-PAGE gel after gel filtration was confirmed to be a Plk1 degradation product by MS (CEA MS facility, Steven Dubois). This degradation product is very stable over time even at room temperature. Then, I tested the same purification protocol with a systematic addition of 1 mM EDTA. This strategy limited the rate of degradation and was chosen for further Plk1₁₋₃₂₈ production (**Figure 82.B**). For the Plk1₁₋₃₆₆ (kinase+linker) production, a similar degradation pattern was observed (**Figure 83**) and the systematic addition of 1 mM EDTA also limited the degradation of Plk1₋₃₆₆.

These conditions are not perfect because the degradation products cannot be fully removed after gel filtration, however it allowed me to first test the activity of the Plk1 kinase domain. We suspect that the N-terminal Ala-Pro rich disordered region of Plk1 is responsible

for the observed degradation and we designed truncated mutants that will be tested in January 2021.

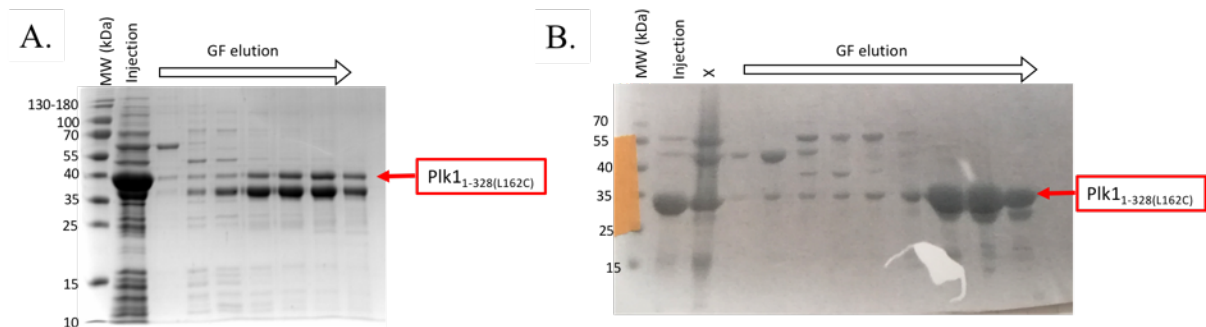


Figure 82. Coomassie-stained 15% SDS-PAGE analysis of the GF purification of Plk1₁₋₃₂₈. **(A)** Purification without EDTA, **(B)** Purification with 1 mM EDTA at each steps. It is worth mentioning here that bacterial DNA/RNA degradation must be carried out more thoroughly than usual to efficiently load this construct on a His-Trap column, before performing the GF.

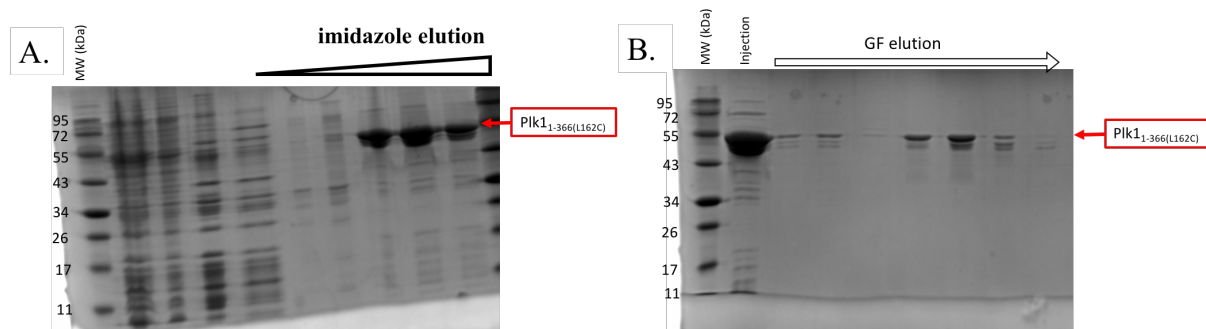


Figure 83. Coomassie-stained 15 % SDS-PAGE analysis of Plk1₁₋₃₆₆ affinity (left) and GF (right) chromatography purifications. Details of the protocol are provided in the Material and Methods section.

After purification optimization, I tested the Plk1₁₋₃₂₈ activity on BRCA2₁₆₇₋₂₆₀. As revealed by SDS-PAGE analysis, Plk1₁₋₃₂₈ phosphorylates its target (**Figure 84.A**). Then, I compared the phosphorylation of BRCA2₁₆₇₋₂₆₀ by Plk1_{FL}, Plk1₁₋₃₂₈ and Plk1₁₋₃₆₆ using NMR monitoring. The NMR spectra revealed that S193, T207, T219 and T226 were phosphorylated in every case, although not with the same rates and preferences (**Figure 84.B**). Hence, the isolated kinase domain is able to correctly recognize its targets. The same profile was observed for Plk1₁₋₃₂₈ and Plk1₁₋₃₆₆, but the corresponding phosphorylation kinetics were about 3 times slower than those obtained with Plk1_{Curie} (**Figure 84.C**). It may be due to the absence of the PBD in Plk1₁₋₃₂₈ and Plk1₁₋₃₆₆ and thus to the absence of binding to pT207. To conclude, the isolated kinase domain can be used to mimic the phosphorylation by Plk1_{FL}. It will be interesting to test whether Plk1₁₋₃₂₈ can phosphorylate BRCA2₁₀₉₃₋₁₁₅₈, with the same rates as those observed with Plk1_{Curie} in the presence of an “activating” peptide.

A.

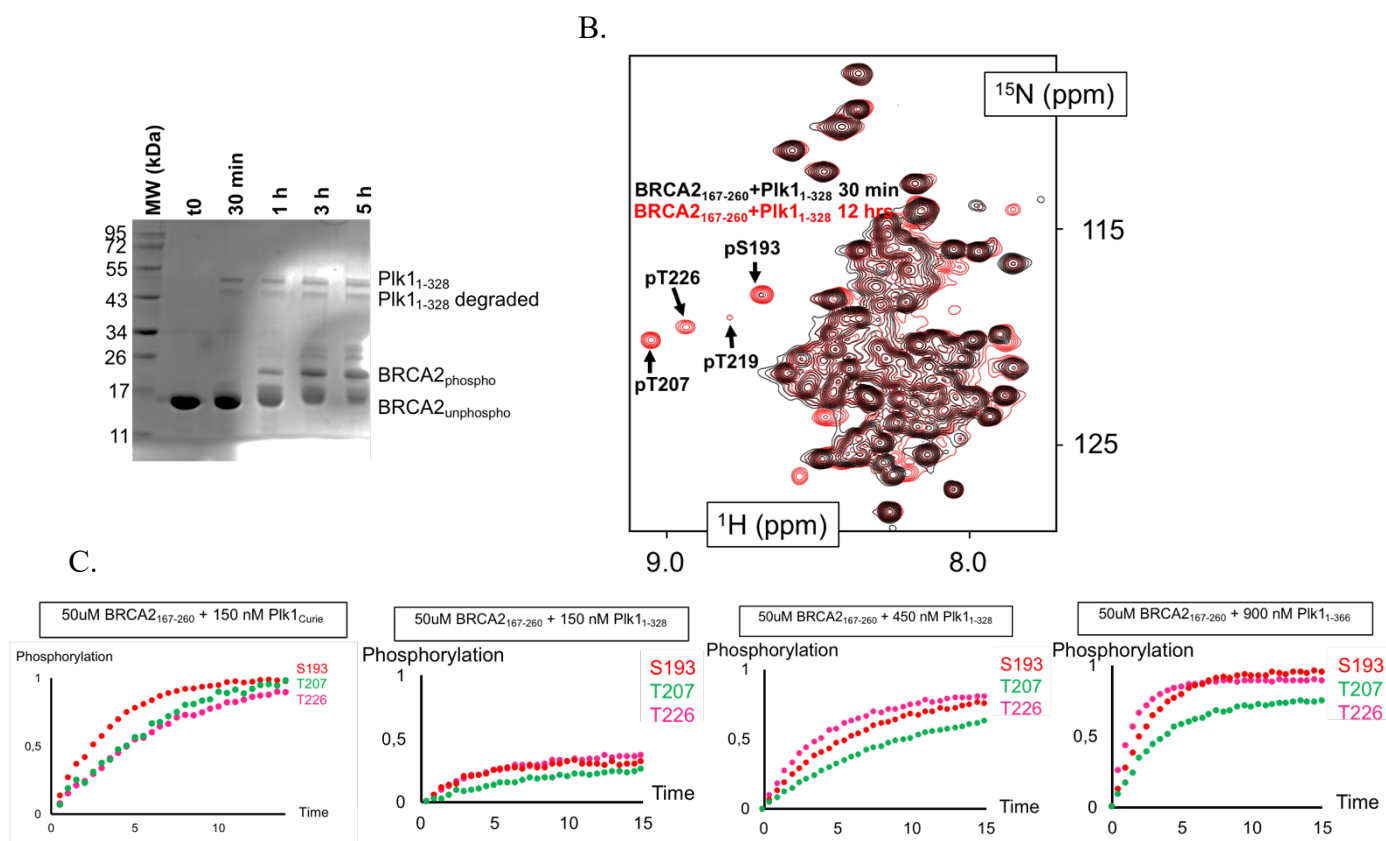


Figure 84. Plk1₁₋₃₂₈ phosphorylates BRCA2₁₆₇₋₂₆₀ at 4 positions: S193, T207, T219 and T226. **(A)** Coomassie-stained 15% SDS-PAGE analysis of BRCA2₁₆₇₋₂₆₀ at 50 uM incubated with Plk1₁₋₃₂₈ at 500 nM for 30 min, 1 h, 3 h or 5 h in HEPES 50 mM, NaCl 75 mM, DTT 2 mM, EDTA 1 mM, ATP 4 mM, MgCl₂ 10 mM, pH 7.0 **(B)** Overlay of ¹H-¹⁵N SOFAST-HMQC spectra of ¹⁵N BRCA2₁₆₇₋₂₆₀ at 50 uM incubated with Plk1₁₋₃₂₈ at 450 nM for 30 min (black) or 12 hrs (red) in HEPES 50 mM, NaCl 75 mM, DTT 2 mM, EDTA 1 mM, ATP 4 mM, MgCl₂ 10 mM, pH 7.0. Spectra were recorded at 298 K, 600 MHz (CEA Saclay). **(C)** Comparison of BRCA2 pS193, pT207 and pT226 phosphokinetics executed by Plk1_{Curie}, Plk1₁₋₃₂₈ or Plk1₁₋₃₆₆. pT219 kinetics were not reported because pT219 phosphopeak showed very weak intensities.

4. Production of Aurora A and phosphorylation of Plk1

To activate the kinase domain of Plk1 by phosphorylation of T210, I produced a AurA-TPX₂₁₋₄₃ chimera in bacteria and purified it using Ni-NTA His-affinity chromatography and a gel filtration chromatography (**Figure 85**). Then, I used it to initiate phosphorylation tests on Plk1₁₋₃₂₈. As the kinase was described to phosphorylate Plk1_{T210} ([Macurek et al., 2008](#), [Seki et al., 2008](#)), we expected at least one phosphorylation event on Plk1₁₋₃₂₈.

To better observe the phosphorylation of Plk1₁₋₃₂₈ by the Aurora kinase A, I used the Phos-tagTM technology ([Kinoshita et al., 2006](#)). It consists in a SDS-PAGE gel polymerized in presence of an acrylamide-attached Phos-tagTM (**Figure 86.A**) chelating Mn²⁺. The Phos-tagTM

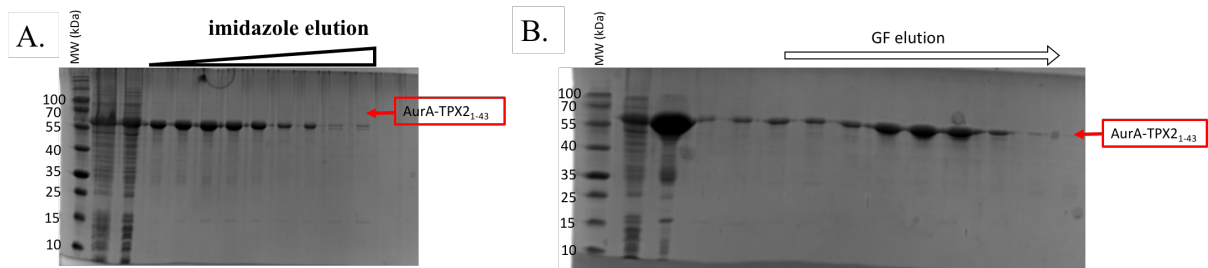


Figure 85. Coomassie-stained 15% SDS-PAGE analysis of AurA-TPX2₁₋₄₃ affinity (left) and GF (right) chromatography purifications. Details of the protocol are in the Material & methods.

has the ability to bind phosphate groups and thus to slow down the migration of phosphorylated protein (**Figure 86.B**). This strategy allows to better distinguish the phosphorylation states of a protein. It is very useful for large, globular proteins, whose migration is poorly affected by one or two phosphorylation events in conventional SDS-PAGE gels.

I mixed Plk1₁₋₃₂₈ to several concentrations of Aurora A (**Figure 86.C.D**). While I used similar buffer conditions than the one previously used for testing Aurora A activity (Zorba et al., 2014, Zorba et al., 2019), I did not observe any phosphorylation of Plk1 upon incubation with AurA-TPX2₁₋₄₃ (and even observed more degradation of Plk1, probably because of remaining contaminants in the AurA-TPX2₁₋₄₃ samples) (**Figure 86.D**). A better defined Plk1₃₇₋₃₂₈ may permit to obtain more satisfying results. We will also test the activity of AurA-TPX2₁₋₄₃ on Plk1 constructs that carry the wild-type Cys212, whose mutation may affect the phosphorylation of T210. We will also test the activity of another kinase, Slk, which has been reported to phosphorylate Plk1 *in vitro* (Johnson et al., 2008).

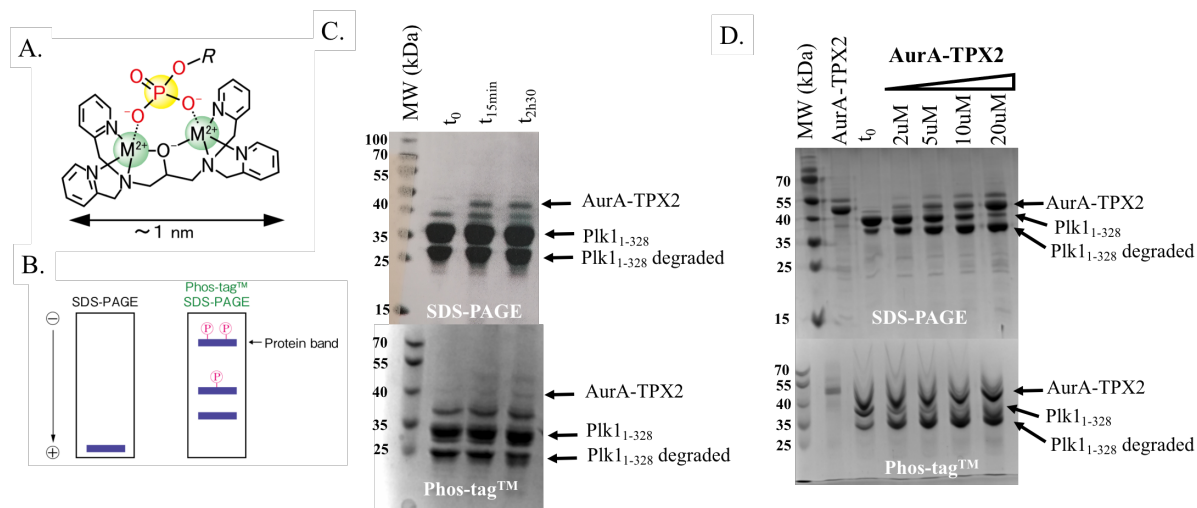


Figure 86. Phosphorylation of Plk1₁₋₃₂₈ by AurA-TPX2₁₋₄₃. **(A)** Chemical structure of the Phos-tagTM (from Wako Chemicals labs) **(B)** Scheme of Phos-tagTM SDS-PAGE principle (from Wako Chemicals labs) **(C)** Conventional SDS-PAGE and Phos-tagTM-SDS-PAGE (15% acrylamide) of Plk1₁₋₃₂₈ at 45 uM incubated with AurA-TPX2₁₋₄₃ at 1 uM, in PBS, supplemented with 2 mM DTT, 2 mM ATP, 5 mM MgCl₂ at pH 7.5 after 0, 15 min or 2.5 h of incubation at 25°C. **(D)** Conventional SDS-PAGE and Phos-tagTM-SDS-PAGE (15% acrylamide) of Plk1₁₋₃₂₈ at 25 uM incubated with AurA-TPX2 at 2 uM, 5 uM, 10 uM or 20 uM in 20 mM TrisHCl, 150 mM NaCl, 5mM DTT, 1 mM PMSF, 20 mM MgCl₂, 2 mM ATP at pH 7.3 during 1 h at 25°C.

5. Production of the PBD

Then, I produced Plk1_{PBD}. After Ni-NTA His-affinity and heparin chromatographies, Plk1₃₆₆₋₆₀₃ (Plk1_{PBD}) was pure enough for structural studies (**Figure 87**). We performed a gel filtration to check the sample quality. The first gel filtration profile showed multiple elution peaks, revealing a high heterogeneity in the sample probably due to oligomerization. This heterogeneity disappeared in the next purification when we removed a concentration step between the His-trap and Heparin purification steps (**Figure 88**).

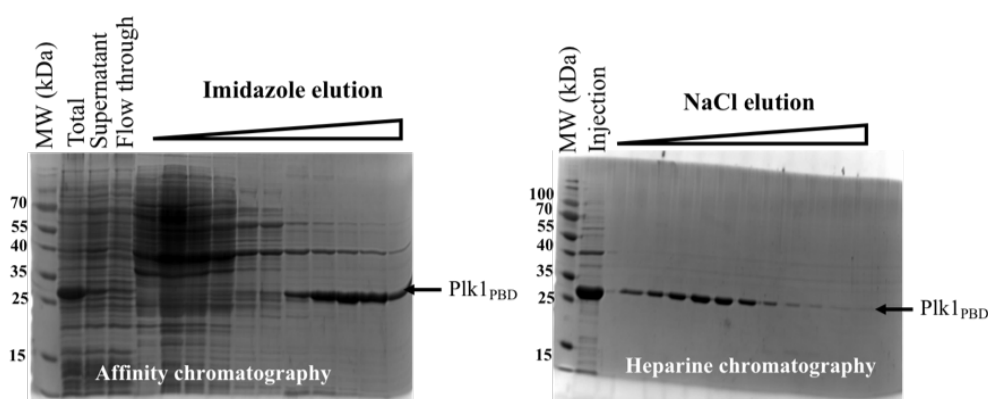


Figure 87. SDS-PAGE analysis of Plk1₃₆₆₋₆₀₃ His-trap (left) and heparine (right) chromatographies. Details of the protocol are provided in the Material and Methods.

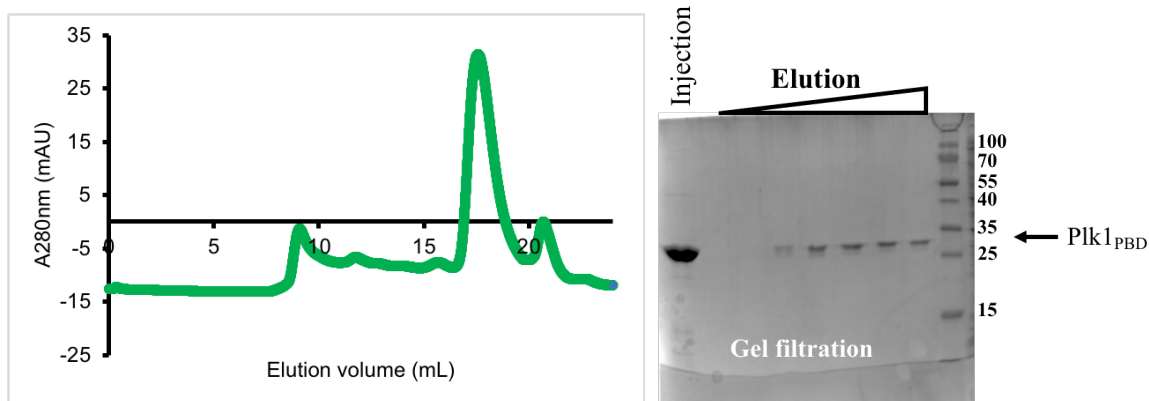


Figure 88. Gel filtration profile of Plk1₃₆₆₋₆₀₃ on a Superdex 200 Increase 10/300 GL (GE Healthcare) and Coomassie-stained 15% SDS-PAGE of the eluted fractions. The monomeric Plk1₃₆₆₋₆₀₃ was eluted at 17 mL.

To test if Plk1₁₋₃₂₈ was able to interact with the PBD, I recorded NMR spectra of Plk1₁₋₃₂₈ in absence or presence of Plk1_{PBD} (**Figure 89**). Upon addition of Plk1_{PBD}, most of the ¹H-¹⁵N NMR signals Plk1₁₋₃₂₈ disappeared, except those from Asn/Gln side chains and from disordered/flexible residues appearing (in the center of the spectra). Importantly, Plk1₁₋₃₂₈ and Plk1_{PBD} were still soluble after NMR acquisition (**Figure 89.B**), as shown by SDS-PAGE analysis. This suggested an interaction between the two domains, even though the sample suffered important degradation, as seen earlier with Plk1₁₋₃₂₈. This result needs to be confirmed by gel filtration and ITC analysis.

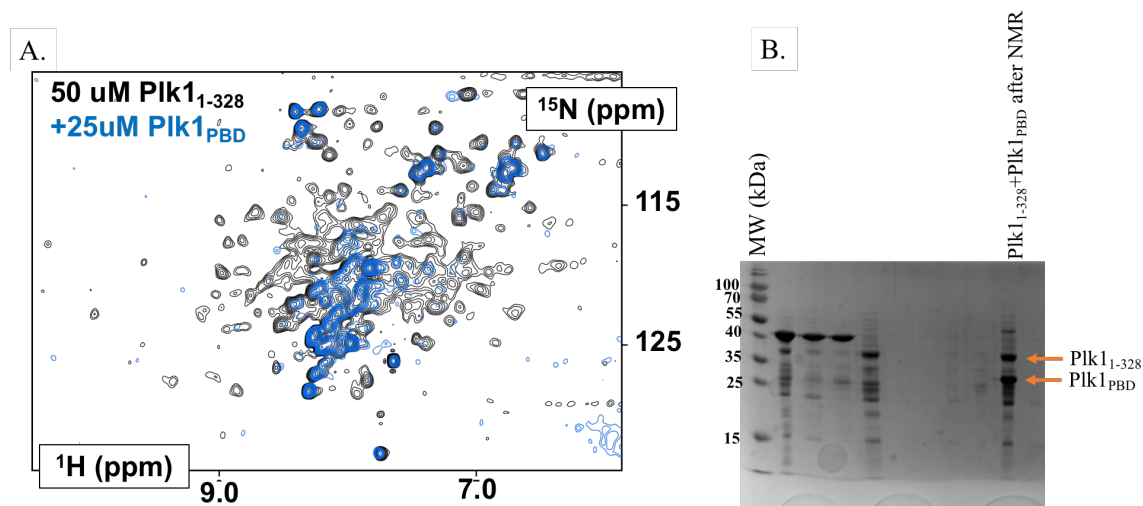


Figure 89. Interaction between Plk1₁₋₃₂₈ and Plk1_{PBD}. **(A)** Overlay of ¹H-¹⁵N HSQC spectra of ¹⁵N Plk1₁₋₃₂₈ at 50 uM and Plk1₃₆₆₋₆₀₃ at 25 uM in PBS, 1 mM DTT at pH 7.0. The spectra were recorded at 293 K and 700 MHz CEA Saclay. **(B)** SDS-PAGE 15% analysis of the soluble fraction of the NMR sample after acquisition.

6. Production of Plk1_{FL}

Finally, I initiated the purification of Plk1 FL produced in bacteria (**Figure 90**). I performed a Ni-NTA His-affinity chromatography. Even though it showed lower yields than those obtained with the isolated domains, this early result is relatively promising. The next steps of the protocol will be carried out in the next months.

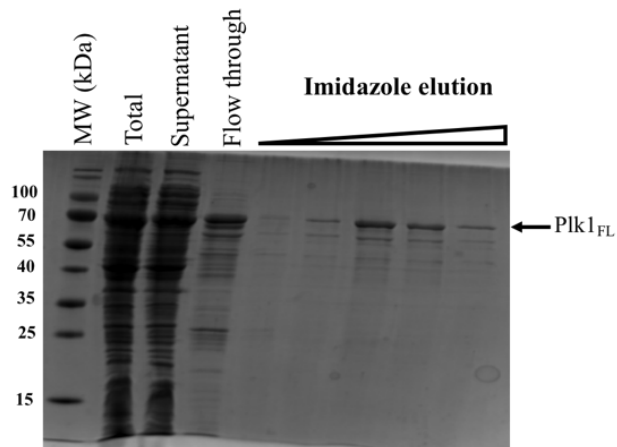


Figure 90. SDS-PAGE 15% analysis of the Plk1_{1-603-L162C} (i.e. Plk1_{FL}) His-trap affinity purification. Details of the protocol are available in the Material and Methods.

Chapter 7. The initial PhD project: characterizing the interaction between DNA and the N-terminal region of BRCA2

Initially, my PhD project was meant to focus on the characterization of a DNA-Binding Domain (DBD) recently identified in the BRCA2 N-terminal region. In 2016, the team of Dr. Aura Carreira discovered that the region 250 to 500 of BRCA2 interacts with several DNA structures (ssDNA, dsDNA, 3' and 5' overhang, **Figure 91**) by EMSA (Electrophoretic Mobility Shift Assay). Quantification of the results revealed an affinity around 0.5-1 μM for all these DNA structures. This result was of high interest because the C-terminal DBD (aa2378-3114) of BRCA2 only interacts with ssDNA. The N-terminal DBD was proposed to cooperate with the C-terminal DBD to promote genome stability.

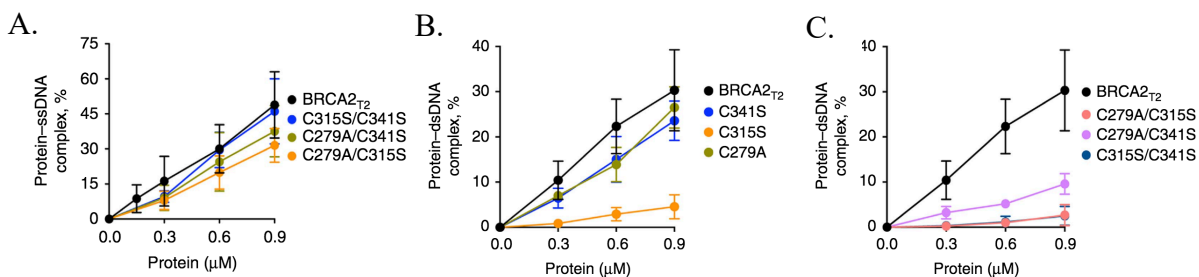


Figure 91. Interaction between BRCA2₂₅₀₋₅₀₀ and ssDNA or dsDNA (from von Nicolai et al., 2016)

(A) Quantification of EMSA assays between BRCA2₂₅₀₋₅₀₀ (WT and mutated) and ssDNA, (B) Quantification of EMSA assays between BRCA2₂₅₀₋₅₀₀ (WT and mutated) and dsDNA, (C) Quantification of EMSA assays between BRCA2₂₅₀₋₅₀₀ (WT and mutated) and dsDNA.

While this N-terminal DBD region is not well conserved and predicted to be disordered (**Figure 92**), the authors identified a potential zinc-finger involving cysteines in this region using the Webserver SMART, although with a low probability score. Therefore, they tested the impact of cysteines on the interaction between BRCA2₂₅₀₋₅₀₀ and different DNA structures. They revealed that, indeed, a loss of dsDNA interaction is observed when C315, C341 or C279 are doubly mutated (**Figure 91.C**). The authors concluded by suggesting that the region may form a zinc-finger domain involving C315, C341 and/or C279. Moreover, the mutations of the cysteines do not strongly impact the interaction with ssDNA. Two different regions may be involved in DNA recognition.

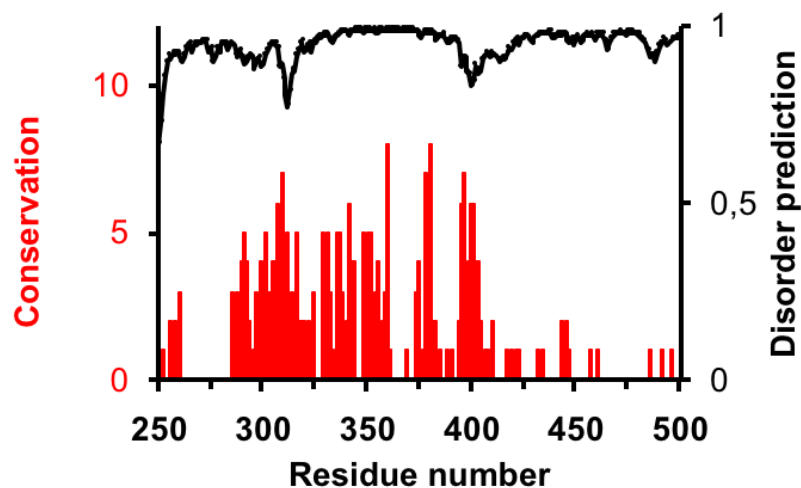


Figure 92. Disordered propensity and conservation analysis of BRCA2₂₅₀₋₅₀₀.

Conservation of the BRCA2 sequence. Human BRCA2 was aligned with 24 sequences from mammals to fishes: *Mus musculus*, *Ratus norvegicus*, *Felis catus*, *Cavia porcellus*, *Bos taurus*, *Myotis brandtii*, *Heterocephalus glaber*, *Oryctolagus cuniculus*, *Otolemur garnettii*, *Equus caballus*, *Propithecus coquereli*, *Cebus capucinus*, *Rhinopithecus roxellana*, *Nomascus leucogenys*, *Erinaceus europaeus*, *Xenopus laevis*, *Sarcophilus harrisii*, *Ornithorhynchus anatinus*, *Danio rerio*, *Gallus gallus*, *Chelonia mydas*, *Alligator sinensis* and *Oreochromis niloticus*. The conservation score was calculated using Jalview 1.0 (Clamp et al., 2004). A score of 11 corresponds to a position identical in 100% of the sequences, while a score of 1 indicates that only one chemical criteria (size, hydrophobicity, global charge) is common to all the variants. The disorder prediction was performed using the server SPOT-disorder (<http://sparks-lab.org/server/SPOT-disorder/index.php>), 1: fully disordered; 0: fully ordered).

I started to investigate the structural aspects of the interaction between BRCA2_{DBD-NTD} and DNA. To characterize the BRCA2₂₅₀₋₅₀₀ region and its interaction with DNA, I produced first the WT fragment of BRCA2₂₅₀₋₅₀₀ and a shorter region predicted to form the zinc-finger domain (BRCA2₂₅₀₋₃₅₀) (Figure 93). However, both fragments were insoluble even in a buffer containing urea at 2 M. I hypothesized that it was due to the large number of cysteines in these fragments, which creates large aggregates upon oxidation. As a second approach, we designed alternative fragments including mutations of the non-conserved cysteines (Figure 93), in order to favor the solubility of this BRCA2 region. The conservation of BRCA2 was quantified from the alignment of BRCA2 sequences from mammals to fishes (Figure 92). Non-conserved cysteines were either mutated into serines when the mouse BRCA2 presented a serine instead of a cysteine, or into alanine in other cases.

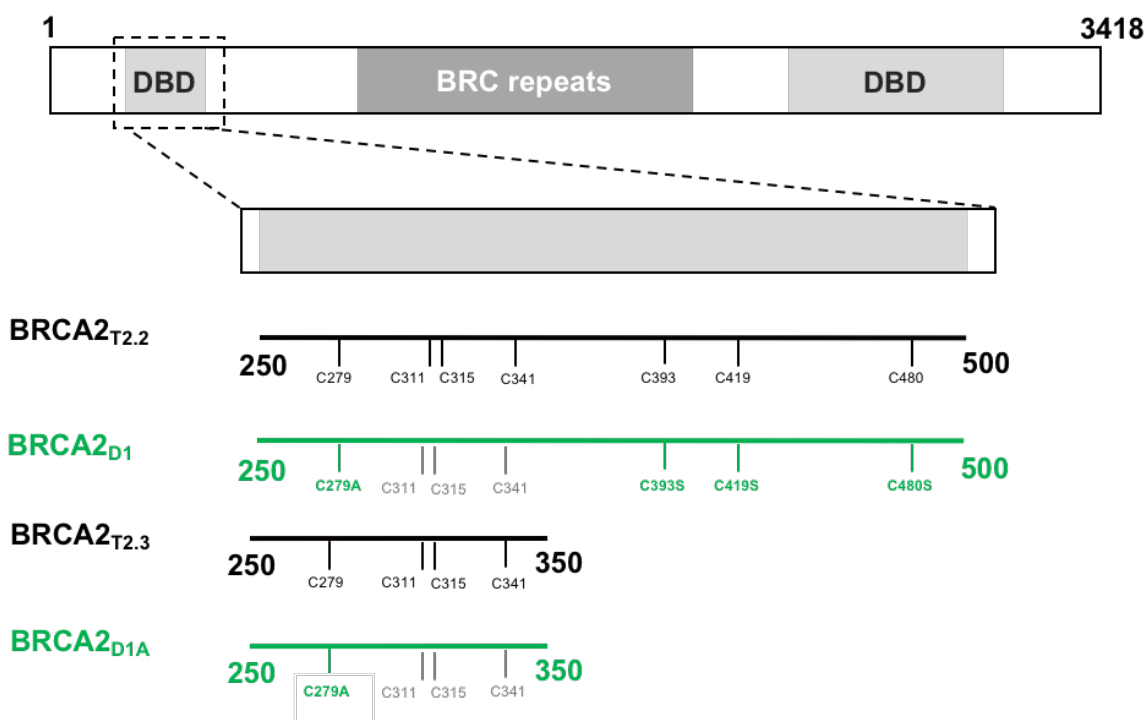


Figure 93. BRCA2 fragments used in the N-terminal DBD study. All cysteines are displayed, mutated cysteines are highlighted in bolded green.

I focused my attention on the larger version of BRCA2₂₅₀₋₅₀₀ mutated at positions C279, C393, C419 and C480 (BRCA2_{D1}). It was impossible to purify it in the standard waterous buffers that we tried: the peptide construct was aggregating. After affinity purification in an 8 M urea buffer, I diluted the sample to obtain a urea concentration of 0.05 M and recorded a ¹H-¹⁵N HMQC spectrum immediately after this dilution (**Figure 94.A**). Surprisingly, the spectrum presented broad peaks and I could not enumerate a reasonable number of peaks in comparison to the number of residues, and I observed a great heterogeneity among peak intensities. This result suggested that the BRCA2_{D1} fragment shows either heterogeneous agregates, or loose interactions with itself, or microsecond-millisecond time scale conformational exchange. In order to test if potential intermolecular interactions or conformational dynamics could be cancelled, I recorded ¹H-¹⁵N HMQC spectra at increasing urea concentrations in the presence of DTT (**Figure 94.B**). Although urea improved the spectral quality, it did not permit to record high quality ¹H-¹⁵N for BRCA2_{D1}. Also, addition of ZnCl₂ did not change the poor quality of the NMR spectra (and ZnCl₂ concentrations higher than 20 μ M led to protein precipitation) (**Figure 95**).

A.

B.

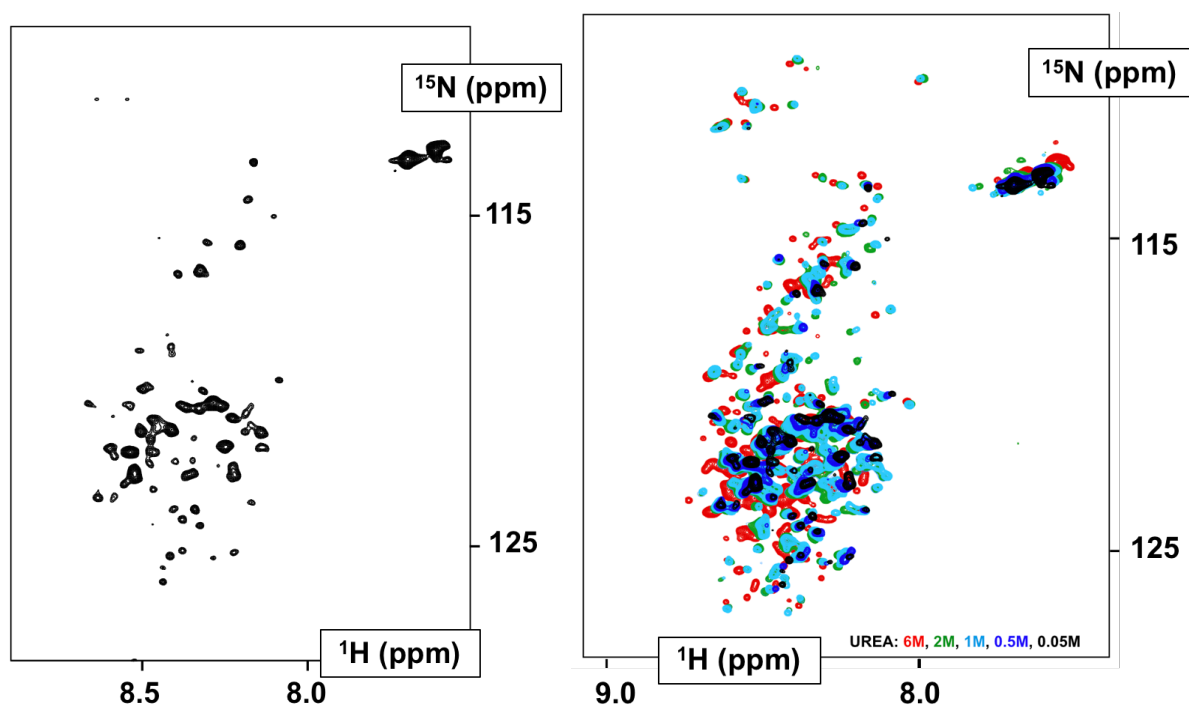


Figure 94. ^1H - ^{15}N SOFAST-HMQC NMR spectra of BRCA2_{D1} (A) BRCA2_{D1} at 100uM in 50 mM HEPES, 150 mM NaCl, 1mM DTT, 0.05 M urea at pH7.0. The spectrum was recorded at 283K, 700 MHz CEA Saclay (ns=16) (B) Urea titration of BRCA2_{D1} at 100 uM in 50 mM HEPES, 150 mM NaCl, 1 mM DTT at pH 7.0 with 6 M (red), 2 M (green), 1 M (light blue), 0.5 M (dark blue) or 0.05 M (black) Urea, 700 MHz CEA Saclay, (ns=16).

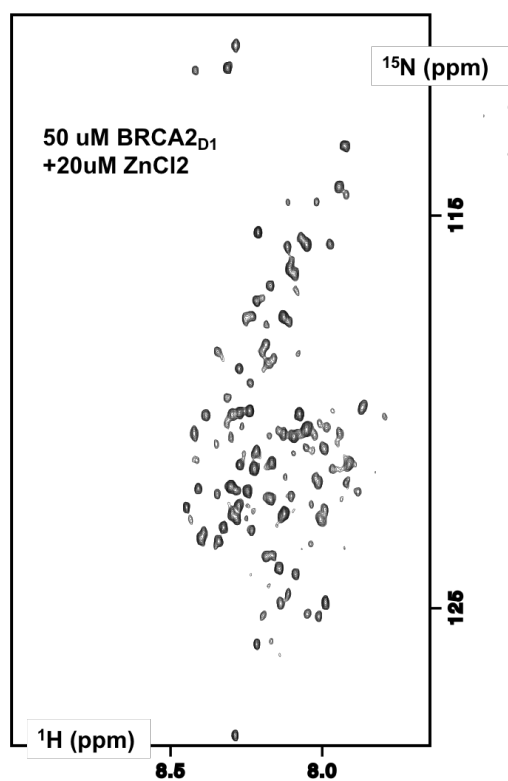


Figure 95. ^1H - ^{15}N SOFAST-HMQC NMR spectrum of ^{15}N BRCA2_{D1} at 50uM in 50 mM Tris at pH 6.1, 2 mM DTT, 20 uM ZnCl₂, recorded at 283K, 600 MHz CEA Saclay (ns=256).

Earlier experiments in the lab suggested that chimeric constructs including GB1 may have improved solubility (cf. pre-laminA-GB1, [thèse F. Celli](#)). S. Zinn-Justin designed a GB1-BRCA2_{D1} fragment, which corresponds to the N-terminal addition of the GB1 protein to the BRCA2_{D1} fragment. However, the ¹H-¹⁵N NMR spectrum of GB1-BRCA2_{D1} after urea dilution also contains a weak number of peaks (**Figure 96**). In addition, ¹H-¹⁵N GB1 NMR peaks are also scarcely observed on the spectrum recorded in the presence of 0.05 M Urea. This could be due to aggregation of the whole constructs, or heterogeneous, transient interactions between GB1 and BRCA2_{D1}.

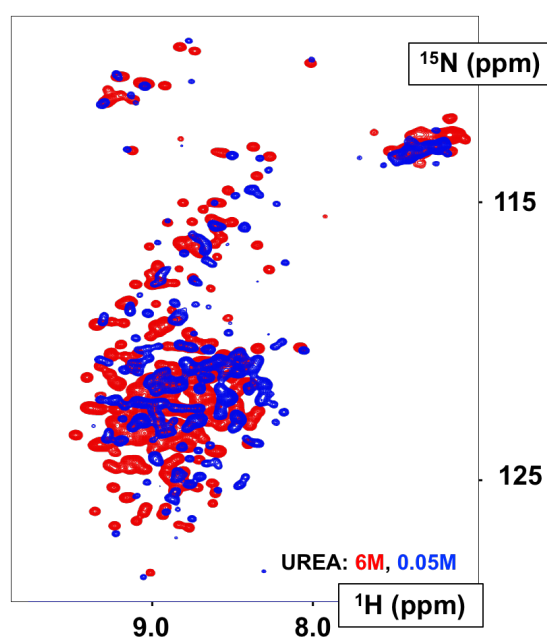


Figure 96. ¹H-¹⁵N SOFAST-HMQC NMR spectrum of GB1-BRCA2_{D1} GB1-BRCA2_{D1} at 100uM in 50 mM HEPES, 150 mM NaCl, 1mM DTT, in presence of 0.05 M urea (blue) or 6 M Urea (red) at pH7.0, recorded at 283K, 700 MHz (CEA Saclay).

Then, I focused my attention on the smaller fragment BRCA2_{D1A} (i.e. BRCA2-aa250-350-C279A), which contains the predicted zinc-finger domain and is in average more conserved than BRCA2_{D1} (**Figure 92**). Although the spectra looked better than those observed with BRCA2_{D1}, we obtained only NMR spectra of poor quality after urea dilution, with a great peak intensity heterogeneity observed in a buffer containing 0.05 M urea (**Figure 97**).

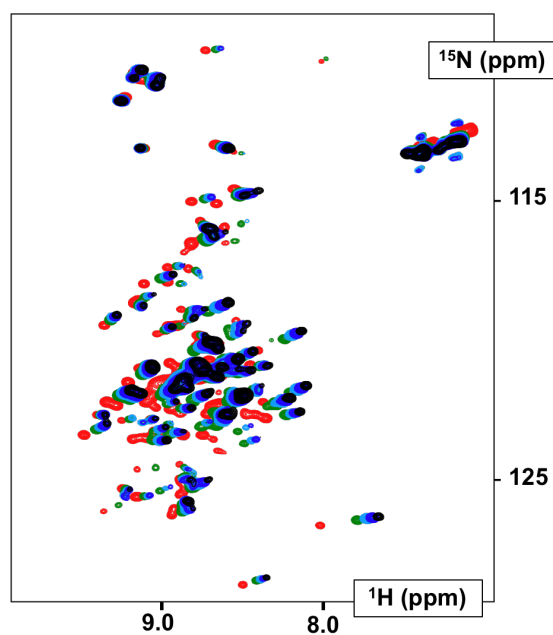


Figure 97. ^1H - ^{15}N SOFAST-HMQC NMR spectra of BRCA2_{D1A}. Urea titration of BRCA2_{D1A} at 100 μM in 50 mM HEPES, 150 mM NaCl, 1 mM DTT at pH 7.0 in presence of 6 M (red), 2 M (green), 1 M (light blue), 0.5 M (dark blue) or 0.05M (black) urea. Spectra were recorded at 283K and 700 MHz (CEA Saclay).

In order to test whether the addition of DNA would improve the BRCA2_{DBD-NTD} behavior, I recorded NMR spectra of BRCA2_{GB1-D1} and BRCA2_{D1A} in the presence of short ssDNA and dsDNA (**Figure 98**). For all constructs, weak intensity peaks disappeared. For BRCA2_{D1}, intense peaks show faint chemical shift perturbations upon addition of dsDNA. However, I did not observe any progressive effect depending on DNA concentration on the BRCA2_{D1} spectrum. The observed effects seem to be the consequence of sample dilution or pH or redox changes upon DNA addition, or eventually of mild aggregation.

In conclusion, the poor quality of the NMR spectra could be interpreted in multiple ways that are difficult to deconvolute. Our efforts to improve the sample quality, to reduce the oxidation or the aggregation appeared to be ineffective. In these conditions, it was difficult to confirm any DNA interaction with these BRCA2 constructs.

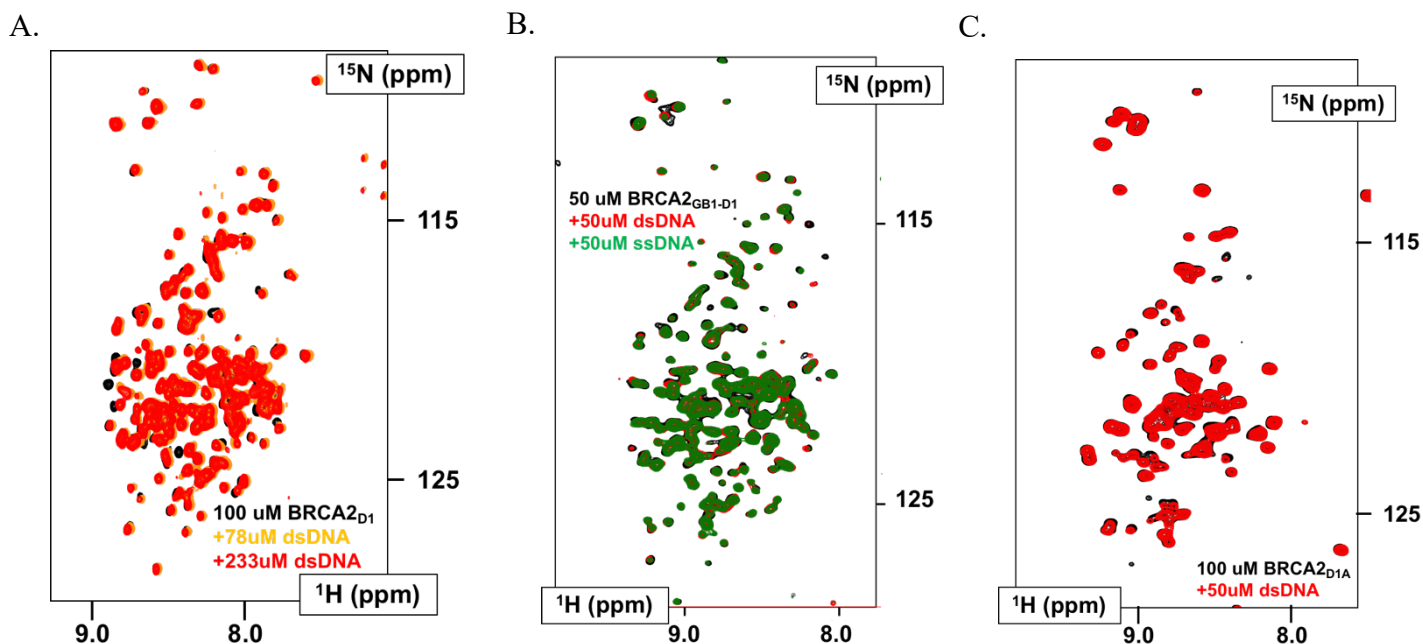


Figure 98. ^1H - ^{15}N SOFAST-HMQC spectra of BRCA2_{D1}, BRCA2_{GB1-D1} and BRCA2_{D1A} in presence of dsDNA or ssDNA.

(A) BRCA2_{D1} at 100uM in 50 mM Tris-HCl at pH6.1, 150 mM NaCl, 1 mM PMSF, 1mM DTT, 2 uM ZnCl₂, 1 M Urea in absence (black) or presence of 78 uM (orange) or 233uM (red) R9R10 dsDNA. (B) BRCA2_{GB1D1} at 50 uM in 50 mM HEPES, 150mM NaCl, 2 mM DTT at pH 7.0 in absence (black) or presence of R9R10 dsDNA at 50 uM (red) or of R9 ssDNA at 50 uM (green). (C) BRCA2_{D1A} at 100uM in HEPES 50 mM, 150 mM NaCl, 0.05M urea at pH 7.0 in the absence (black) or presence of R9R10 dsDNA at 50 uM (red). All spectra were recorded at 283 K and 700 MHz (CEA Saclay)

Because of BRCA2_{DBD-NTD} tendency to aggregate, we thought that this region may interact with DNA through liquid-liquid phase separation and membraneless droplet formation. I tested this hypothesis by observing BRCA2_{DBD-NTD} under a microscope (**Figure 99**). I observed large droplets of BRCA2_{D1} after 36h incubation at 4°C. These early observations did not allow to distinguish aggregation from phase transition advanced droplets. However, it confirmed that BRCA2_{D1} forms large objects in presence or absence of DTT and Urea. Together with the NMR results, this raises concerns about the feasibility of any *in vitro* biochemical study using this region of BRCA2.

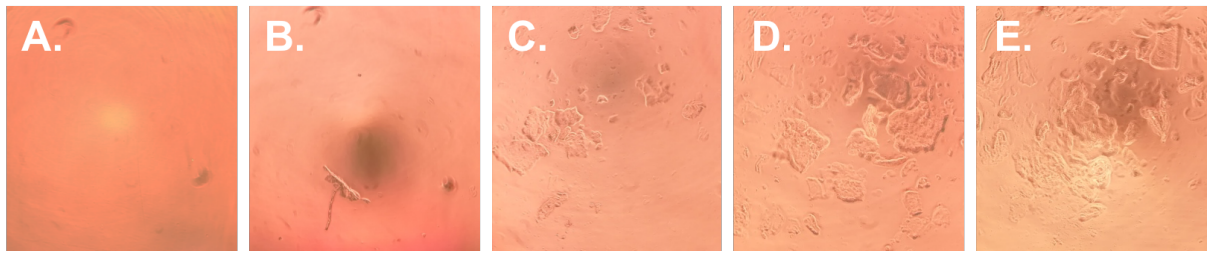


Figure 99. Light microscopy observation of BRCA2_{D1} after 36 hrs at 4°C.

A λ 50 Zeiss microscope was used for these observations, x63. (A) Buffer (B) Aggregates of BAF at 5 uM prepared by Agathe Marcelot (C) BRCA2_{D1} at 10 uM in 20 mM HEPES, 1 mM EDTA, 50 mM NaCl at pH7.0 (D) BRCA2_{D1} at 10 uM in 20 mM HEPES, 1 mM EDTA, 50 mM NaCl, 2mM DTT at pH7.0 (E) BRCA2_{D1} at 10uM in 20 mM HEPES, 1 mM EDTA, 150 mM NaCl, 2M Urea at pH7.0.

To continue the investigation, we benefited from the equipment and the expertise of the microscopy platform of the I2BC, notably the help of Romain Le Bars. Their Differential Interference Contrast (DIC) microscope permitted to test the phase transition hypothesis of BRCA2_{D1}. While the control Sox2₁₁₅₋₃₁₇, prepared by Chafiaa Bouguechtouli, presents small droplets characteristic of phase transition, no similar objects were found for BRCA2_{D1} (**Figure 100**). Even upon varying buffer conditions (1-3X PBS, 100-200mg/mL Ficoll, longer incubation, on ice or at room temperature), we did not observe any signs of phase separation events with BRCA2_{D1}. BRCA2_{D1} primary structure does not correspond to a low-complexity region, and is not enriched in amino-acids (Arg, Tyr, Phe, Gly...) or features (alternated electrostatic patches) that favor transient, multivalent interchain interaction, and thus phase separation (Martin & Mittag, Biochemistry 2018, Wang.. Hyman Cell 2018). Such a description is difficult to render, we attempted to show it below with a color code used by Tanja Mittag (**polar**, **glycine**, **positive**, **negative**, **aromatic**, **hydrophobic**, **cysteines** are highlighted in yellow):

260	270	280	290	300
TDS E NT NQ RE	AASH G FG K T S	G N S F K V N S C K	D H I G K S M P N V	L E D E V Y E T V V
310	320	330	340	350
D T S E E D S F S L	C F S K C R T K N L	Q K V R T S K T R K	K I F H E A N A D E	C E K S K N Q V K E
360	370	380	390	400
K Y S F V S E V E P	N D T D P L D S N V	A N Q K P F E S G S	D K I S K E V V P S	L A C E W S Q L T L
410	420	430	440	450
S G L N G A Q M E K	I P L L H I S S C D	Q N I S E K D L L D	T E N K R K K D F L	T S E N S L P R I S
460	470	480	490	500
S L P K S E K P L N	E E T V V N K R D E	E Q H L E S H T D C	I L A V K Q A I S G	T S P V A S S F Q G

Altogether, it is probable that the previously observed large objects result from cysteines oxidation leading to the the generation of soft protein aggregates.

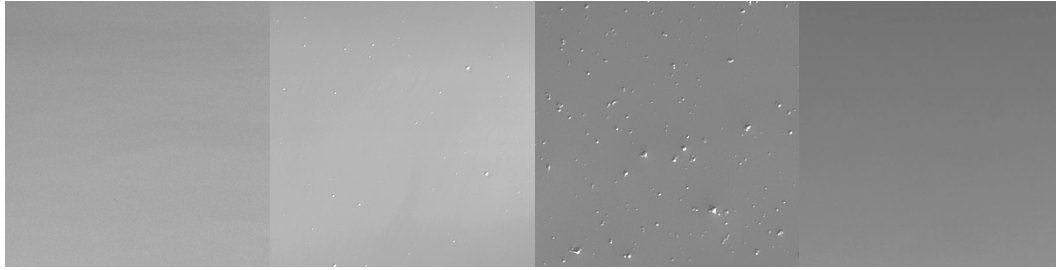


Figure 100. DIC microscopy of Sox2₁₁₅₋₃₁₇ and BRCA2_{D1}
(A) PBS supplemented with 100 mg/mL Ficoll **(B)** Sox2₁₁₅₋₃₁₇ at 4 uM in PBS supplemented with 100 mg/mL Ficoll; **(C)** Sox2₁₁₅₋₃₁₇ at 20 uM in PBS supplemented with 100 mg/mL Ficoll; **(D)** BRCA2_{D1} at 20 uM in PBS supplemented with 200 mg/mL Ficoll.

Because these BRCA2 fragments were extremely difficult to manipulate and to study, we decided to refocus my PhD project on the phosphorylation of BRCA2 by Plk1, which was a project that I started during my Master 2 internship.

Discussion & perspectives

BRCA2 is often mutated in hereditary cancers. In order to improve the diagnosis and treatment of these cancers, it is important to identify the causal mutations. Since the 90's, several databases have listed the observed genetic variations on *BRCA2*. Molecular studies are now necessary to progress in the classification of these variants.

BRCA2 is a large protein that contains a long N-terminal region (about 2,500 residues) predicted to be disordered. The function(s) of this region is (are) not very clear in the literature, although it contains conserved fragments. Among them, I was interested in two N-terminal conserved regions: residue 72 to 84 and 175 to 218. During my PhD, I carried out a molecular characterization of the BRCA2₄₈₋₂₈₄ region, which contains these two conserved patches. I also attempted to look at a poorly conserved N-terminal region, described as binding to ssDNA and dsDNA: residue 250 to 500. However, its weak affinity for short DNA fragments (20 to 48 nt) made it difficult to further characterize its binding mechanisms.

1. BRCA2₄₈₋₂₈₄ phosphorylations

Previous studies identified the fragment BRCA2(1-284) as a region phosphorylated by the kinase Plk1 at the entry into mitosis (Lin et al., 2003). Because the mutation of the S193 residue decreased the phosphorylation signal observed by radiography, the authors of these early studies concluded that S193 is phosphorylated by Plk1. However, they could not precisely identify the phosphoresidues of BRCA2, which thus limited the functional characterization of the N-terminal region.

In the course of my thesis, we proposed to use NMR spectroscopy for monitoring and studying phosphorylation events on BRCA2. I have implemented and updated protocols, based on previously published ones in 2013 (Theillet et al., 2013), for IDR/IDP phosphorylation monitoring using ¹H-¹⁵N SOFAST-HMQC experiments. This pipeline of protocols -from the ¹⁵N labeled peptide production, sample preparation, NMR monitoring to the data analysis- is based on the experimental procedures that we had to optimize to monitor BRCA2 fragments phosphorylation in the lab. We are now able to monitor phosphorylation reactions occurring on the N-terminal domain of BRCA2 in acceptable conditions of pH (7.0), buffer concentrations (PBS or equivalent) and temperature (298 K), in regards to physiological conditions. This set of protocols can be applied to a large number of IDPs.

However, as phosphorylation reactions occur in cells at pH 7.5 and 310 K, and these parameters are likely to affect the site preferences of kinases, as shown for p38 α (Deredge et al., 2019) or CK1 δ (Shinohara et al., 2017), we also developed a new NMR experiment to monitor phosphorylation using the ^{13}C signals. ^1H - ^{15}N NMR spectroscopy of IDPs is difficult at high pH and temperature, because of the fast water-amide proton exchange, whereas ^{13}C - ^{13}CO NMR signals are not pH dependent. I participated to the implementation and tests of this novel approach, which will further expand the range of proteins and conditions accessible to NMR characterization.

In the following subchapters, I summarized, put into context, and draw interpretations and hypotheses on the individual results obtained on BRCA2.

a. BRCA2 phosphorylation by Plk1

Using NMR spectroscopy, I identified and monitored the phosphorylation of four BRCA2 residues by Plk1: S193, T207, T219 and T226. These favored phosphorylation events are followed by late phosphorylation of several additional residues. As the late phosphorylation events were markedly slow and concern residues showing poor conservation, we focused our analysis on the 4 first phosphoresidues. I performed phosphorylation kinetics studies of mutant versions of BRCA2 found in breast cancer patients, focusing on mutations neighboring S193 and T207, like M192T, T200K and T207A. Not only these mutations affected the phosphorylation rates, but our collaborators (team of Dr. Aura Carreira) showed that they were also affecting the recruitment of BRCA2 partners and the localization of BRCA2, leading to mitotic defects in the case of M192T and T207A.

To test the phosphorylation kinetics in a more physiological environment, I tried to phosphorylate BRCA2 by endogenous kinases from a cell extract: first with cell lysate from G2/M synchronized HEK cells, second with HeLa nuclear extracts (data not shown). However, only one phosphoresidue appeared from the total cell lysate experiment: pS70, probably phosphorylated by PKA. It may be useful to optimize such an experimental procedure in order to know whether the order of phosphorylation by Plk1 remains the same in an environment close to cellular conditions. Furthermore, it may permit to identify if the late BRCA2 phosphoresidues observed in *in vitro* experiments correspond to artefacts due to the simplified experimental conditions (notably missing phosphatases) or if they may be biologically relevant.

I also showed that a short BRCA2 synthesized peptide containing pT207A could function as an “activator” of Plk1 for the phosphorylation of a fragment of BRCA2_{aa1093-1158}. This is consistent with published works on Plk1 activation, which show that: i) the interdomain

interactions between Plk1_{KD} and Plk1_{PBD} regulate Plk1_{KD} activity (Xu et al., 2013), and ii) Plk1_{PBD} binding to phosphopeptides containing its consensus recognition motif SpTP activates Plk1_{KD} (Johnson et al., 2008, Zhu et al., 2016). This is also consistent with our prior results showing the diminished phosphorylation rates in BRCA2_{T207A} fragments. However, it is still unclear whether pT207 plays only the role of “activator” by binding to Plk1_{PBD}, or whether this binding also helps to favor further phosphorylation of the neighboring acids, hence playing the role of priming event. We also observed using NMR that the interaction region between pBRCA2₁₆₇₋₂₆₀ and Plk1_{PBD} is larger than the BRCA2 peptide used for X-Ray crystallography study. This suggests that S193 may play a similar role, although it does not correspond to a PBD binding motifs. The exact molecular scenography is not yet fully resolved.

Altogether, we have shown that among the 4 phosphosites, S193 and T207 are important phosphorylation sites of BRCA2.

b. Role of BRCA2_{pT77} for Plk1 phosphorylation

Then, I investigated the role of priming BRCA2 phosphorylation by Cdks on subsequent Plk1 phosphorylation. Indeed, in 2014, Takaoka et al., showed that Cdks phosphorylate BRCA2_{T77} in cells during mitosis (Takaoka et al., 2014). BRCA2_{pT77} has been shown to be a Plk1_{PBD} docking site (Takaoka et al., 2014, Yata et al., 2014), which suggested a role for BRCA2_{T77} in pS193 phosphorylation. Such priming events scenarii appear ever more to be a common theme, according to recent publications in the field (Ord et al., 2020, Singh et al., 2020).

Here, I could obtain early results suggesting that the prior phosphorylation of BRCA2₄₈₋₂₁₈ by Cdk1/B1 could speed up the subsequent phosphorylation of BRCA2_{S193} and BRCA2_{T207} by Plk1. However, I could not pursue this characterization and perform a quantitative analysis because it would have been too costly (the commercial Cdk1/B1 is poorly active, yet very expensive). Then, I tried to phosphorylate BRCA2_{T77} by Cdk1/A2. Interestingly, the exchange of B1 cyclin for A2 cyclin modified the BRCA2 phosphorylation profile and did not yield high levels of pT77 phosphorylation.

Cyclin A2 and B1 have been shown to affect Cdk2 substrate preferences (Brown et al., 2007): i) the RxL consensus binding motif of Cyclin A2 shows poor affinity for Cyclin B1, which does affect the target recruitment to Cdk2; ii) the two cyclins generate different conformations and environments of the activation loop, and thus different binding surfaces for the substrate, i.e. different preferences for the phosphorylation motif. Such a comparative structural knowledge does not yet exist for Cdk1, to the best of our knowledge (Wood &

[Endicott, 2018](#)). However, the structure of Cdk1/CyclinB1 shows a greater flexibility of the activation loop, which correlates with the fact that Cdk1 appears to accommodate better sub-optimal substrate sequences than Cdk2 ([Brown et al., 2015](#)). Waiting for a structure of Cdk1/CyclinA2, we may also hypothesize that supplementary docking sites on CyclinB1 exist. Recently, a LxF motif and a PxxPxP motif have been shown to favor substrate recruitment by yeast homologs of CyclinB1 ([Ord et al., 2018](#), [Ord et al., 2020](#)). We did not find such motifs in the N-terminal region of BRCA2. Anyway, in the context of this study, Cdk1/A2 was not of great help.

I also tried to use the p38 α kinase to pre-phosphorylate BRCA2 because it phosphorylates S/T-P motifs, similarly to Cdk1/B1. The first p38 α phosphorylation events looked similar to those observed with Cdk1/B1. In the chosen conditions, we observed after 2 hours almost stoichiometric phosphorylation of 2 sites on BRCA2, among which T77, and weaker stoichiometry but existing phosphorylation on 5 other sites. A more prolonged incubation led to more populated phosphorylation on these secondary sites. We tested the influence of these phosphosites on subsequent Plk1 phosphorylation. It revealed that:

- BRCA2 incubated with p38 α during 2 hours was phosphorylated by Plk1 faster on S193 but not on T207;
- BRCA2 incubated 4 hours and hyperphosphorylated by p38 α was phosphorylated by Plk1 with the same rates than non-modified BRCA2.

The first observation may confirm the data obtained by [Takaoka et al., \(2014\)](#): BRCA2_{pT77} seems to be linked to BRCA2_{S193} phosphorylation. It is intriguing to observe that a more complete phosphorylation suppresses the BRCA2_{pT77} effect on BRCA2_{pS193} kinetics. It would be interesting to test whether pre-phosphorylation by Cdk1/B1 has the same consequences. The recent production of Cdk1/B1 in the lab may permit such investigations.

Would multiple phosphorylation of BRCA2 by Cdk1 or MAP kinases like p38 α be biologically relevant? Multiple phosphorylation processes have been seen as tunable components for the signaling circuits, permitting either graded responses or signaling thresholds ([Valk et al., 2014](#)). Most examples of multisite phosphorylation correspond to phosphorylations by a single kinase that either activates or inhibits an interaction or an activity. Opposite functions are usually obtained by an equilibrium between kinases and phosphatases. An intriguing mechanism was also shown for the regulation of the transcription factor Elk1 by the MAP kinase ERK2: early phosphorylation sites of Elk1 favor the recruitment of the Mediator complex and the transcription of Elk1 target genes, while later phosphorylation sites

have the opposite effect (Mylona et al., 2016). This example shows that multisite phosphorylation by a single kinase can trigger subsequent, opposite functions. However, it is yet unknown if ERK2 is the only kinase possessing this particularity or if it is a more common mechanism (Whitmarsh et al., 2016). p38 α is also a MAP kinase, but there is no information about any interplay between BRCA2 and p38 α in the literature. In the case of BRCA2:Cdk1/B1, we can not exclude the possibility of a similar mechanism. We observed at least that Cdk1/B1 executes more than a single T77 phosphorylation event on BRCA2. In my opinion, it would be very interesting to investigate whether such a multiple phosphorylation scheme is part of a regulation process in cells.

c. Generating single site phosphorylation on IDRs

As described just above, we observed multiple phosphorylation sites on BRCA2 by Cdk1 and p38 α , which showed varying kinetics, hence varying stoichiometries. This resulted in poorly defined samples and an increased complexity, which hampered the study of the impact of priming phosphorylation events on the subsequent phosphorylation by Plk1. We thought to switch to a chemical synthesis approach and initiated a collaboration with Dr. Vincent Aucagne. Using Native Chemical Ligation, they linked a N-terminal synthesized BRCA2 peptide, precisely phosphorylated at the position T77, to a recombinantly produced, ¹⁵N-labeled C-terminal peptide containing the BRCA2 phosphotargets of Plk1, which I expressed and purified. We are now able to monitor Plk1 phosphorylation kinetics on BRCA2 and quantify the exact impact of pT77.

Another strategy based on the recoding of bacterial amber stop codons would also permit to produce IDRs phosphorylated at chosen sites (**Figure 101**). This approach is apparently better adapted for the incorporation of phosphoserines, although a method has been published to introduce phosphothreonines (Rogerson et al., 2015, Zhang et al., 2017). Currently, Dr. François-Xavier Theillet attempts to implement this method in the lab using the strain described in Phillip Zhu et al. (2019). The authors improved the *E.coli* strain for increasing production yields and enhancing the production of multiphosphorylated proteins. Dr. Richard Cooley gave us the corresponding strain containing the tRNA optimized by the team of Pr. Jason W. Chin (Rogerson et al., 2015, Zhang et al., 2017). This perspective may be a long-term tool in the lab. It will be interesting to compare the efficiency of NCL versus the recombinant production of phosphoproteins.

2. Interactions and functions mediated by phosphoBRCA2

The studies on phosphorylation kinetics of BRCA2 find notably their interest in the regulation of protein:protein interaction by the revealed phosphosites. Since the beginning, we had the feeling that a large part of the functionality of the N-terminal region of BRCA2 would lie in phospho-regulated interactions. This would provide clear explanations for the possible oncogenic role of mutations detected in breast cancer patients.

The interaction between BRCA2_{pT207} and Plk1 emerged soon during my thesis and was shown to have important consequences on mitosis regulation. Some advanced details of this interaction are still missing to really understand the BRCA2_{pT207}:Plk1 interaction and its consequences on Plk1 activity, which we discuss in the next first subchapter. The quaternary complex that BRCA2_{pT207} promotes with BubR1 and PP2A is not fully described yet and we discuss it in the second subchapter.

Then, we had to face a common challenge in the field on IDPs: how to find novel protein partners, which, moreover, are often interacting with the phosphoforms of the IDP of interest. This situation is well exemplified for pS193, the only phosphoresidue among pS193-pT207-pT219-pT226 that was previously characterized in the literature. This phosphorylation has been shown to be essential for the localization of BRCA2 at the midbody (Takaoka et al., 2014): the mutant S193A fails to localize at the midbody but the phosphomimic S193E restores the BRCA2 localization. The team of Dr. Aura Carreira in collaboration with Dr. Yoshio Miki showed that the breast cancer variant M192T also presents cytokinesis defects. We have shown that the cancer patient M192T mutant does not strongly affect the phosphorylation of the BRCA2 phosphosites by Plk1. Thus, although the region around pS193 (including M192) is probably recognized by a partner that drives BRCA2 to the midbody (Mondal et al., 2012), this partner is yet to be identified. Concerning pT219 and pT226, their potential functions remain unclear.

In this purpose, we used a pull-down/MS-proteomics approach, which revealed a few potential protein partners of BRCA2 that we started to test *in vitro*. This is discussed in the three next subchapters.

Altogether, I explored several hypotheses for understanding the role of BRCA2 mitotic phosphorylations. In the meantime, this required to produce the many protein constructs necessary to characterize the corresponding interactions, including phosphorylated BRCA2 constructs. I will not discuss the yet-to-be-proven interactions with DDX5 and PARP1 (see

Results 5.6.). Still, I would like here to stress the fact that finding new protein partners of IDPs is a labor-intensive task with the current approaches, notably because it ends often with disappointing *in vitro* titrations. This illustrates probably that the common pull-down methods used for folded proteins are not adapted to IDPs. These difficulties underline also the unpractical aspects of IDPs for *in vitro* characterization, i.e. their tendency to form soluble aggregates (which is greatly facilitated by solvent accessible cysteines), their capacity to establish weak interactions either specific or unspecific, or to serve as interactions hubs. When I started my PhD, the lab was starting to work in the IDP field and to establish efficient protocols for their study. Since then, our lab tries to tackle the problem of identifying novel IDP partners, but exquisite methods remain to be found.

a. BRCA2/Plk1 interactions

First, I focused my attention on BRCA2_{pT207} as it corresponded to a potential Plk1_{PBD} docking site, according to the known consensus Plk1_{PBD} target motif (Elia et al., 2003, Elia et al., 2003). I confirmed the interaction between BRCA2_{pT207} and Plk1_{PBD} by ITC. ITC data showed an interaction in the range of 200 nM, a classical affinity for Plk1_{PBD} interactions with its known protein partners (Elia et al., 2003, Zhu et al., 2016). Dr. Simona Miron and Dr. Virginie Ropars resolved the X-ray structure of the complex. This structure revealed the importance of pT207 and S206 side chains for the interaction with Plk1_{PBD}. In addition, we have seen that the mutation T207A slows down the phosphorylation profile of all the other residues (S193, T219 and T226). It is clear that BRCA2_{pT207} is important for the Plk1 phosphorylation mechanism of BRCA2, as discussed in the previous section on phosphorylation kinetics.

Further NMR analysis of the interaction suggested that the binding interface of BRCA2_{pT207} on Plk1_{PBD} may be more extended than the core binding motif described by the X-ray structure centered on the pT207 phosphosite. This could be due to the extended cryptic pocket that can arrange a hydrophobic motif at the N-terminus of the core PBD-binding motif (Liu et al., 2011, Sharma et al., 2019). There is a tryptophane at the corresponding position in BRCA2, but it is not observed in our X-ray structure. Tryptophane is a rare residue in IDRs and often reveals the position of an interaction site. The PBD has been also shown to interact with a variety of other non-phosphorylated partners (Archambault et al., 2015). It has a very charged surface that may interact with the N-terminal and C-terminal regions surrounding pT207. My results demonstrated that mutations M192T, S193A and T200K reduce the Plk1 phosphorylation of all the BRCA2 phosphosites, without any clear explanation. If the

BRCA2_{T207} N-terminal region including these residues was to interact with Plk1_{PBD}, it would provide some hints about the impact of these three mutations.

In parallel, we observed that multiple phosphorylation surrounding BRCA2_{pT77} may reduce the impact of its pre-phosphorylation on the subsequent phosphorylation by Plk1. BRCA2_{pT77} is clearly a docking site Plk1_{PBD}, whose recognition may be affected by abundant phosphorylation events in its the vicinity. This could explain the contradicting results obtained with two different levels of priming phosphorylation by p38 α on the subsequent phosphorylation by Plk1.

Altogether, these data underline the role of Plk1 docking sites displayed by BRCA2 on Plk1 activity. Further studies will be necessary to fully decipher the interactions between BRCA2 and Plk1.

b. The role of BRCA2_{pT207} in chromosome segregation: interactions with PP2A and BubR1

The team of Dr. Aura Carreira has shown that BRCA2_{pT207}/Plk1 is part of a quaternary complex also involving BubR1 and PP2A.

The interaction between BRCA2 and BubR1 appears to be a key cellular event. It has been reported to be involved in two essential pathways: the kinetochore-microtubule attachment and the spindle assembly checkpoint (Lampson et al., 2005, Lara-Gonzalez et al., 2012, Elowe et al., 2010, Zhang et al., 2016). On one hand, the regulation of BubR1 by BRCA2, PP2A, Plk1 and Aurora B regulates the kinetochore-microtubule attachment: BubR1 is phosphorylated by Plk1 (Matsumura et al., 2007) at two tension sensitive sites S676 (Elowe et al., 2007) and T680 (Suijkerbuijk et al., 2012) and by Cdk1 at the attachment-sensitive-site S670 (Huang et al., 2008), which controls the chromosome segregation. On the other hand, the BRCA2:BubR1 (Futamura et al., 2000, Choi et al., 2012) and BRCA2:PCAF (Fuks et al., 1998, Lin et al., 2003) interactions promote BubR1 acetylation by PCAF (Choi et al., 2012, Park et al., 2017), activating the SAC. The literature reports two different interaction interfaces between BRCA2 and BubR1: Futamura et al. (Futamura et al., 2000) showed an interaction between BubR1₇₈₆₋₁₀₅₀ with BRCA2₂₈₆₁₋₃₁₇₆, while Choi et al. (Choi et al., 2012) proposed an interaction between BRCA2₃₁₈₉₋₃₄₁₈ and BubR1₁₋₃₂₂. In the lab, Dr. Simona Miron initiated a study to better define which BRCA2 region interacts with BubR1.

In this context, our collaborators showed that the formation of the BRCA2_{pT207}/Plk1/pBUBR1/PP2A complex at the kinetochore leads to an enrichment in phosphorylated BUBR1 (by Plk1) and in phosphatase PP2A. Hence, BRCA2 serves as a

platform to bring together BubR1 and Plk1, which favors BubR1 phosphorylation by Plk1. Furthermore, in cells, the BubR1 phosphorylation is targeted by the kinase Aurora B, which destabilizes erroneous kinetochore-microtubule attachment (Hauf et al., 2003), and by the phosphatase PP2A, which protects the initial kinetochore-microtubule interaction from excessive destabilization by Aurora B (Foley et al., 2011).

While the BRCA2_{pT207}:Plk1 interaction is a new piece of information, several interactions of this quaternary complex were already elucidated. First, it has been reported that BRCA2 directly interacts with PP2A. PP2A-B56 presents 2 consensus binding sites: one mediated by electrostatic interactions (Wang et al., 2020) and the second one that recognizes the core target consensus motif L-X-X-I-X-E, with X for any amino acid (Hertz et al., 2016, Wang et al., 2017). The second one interacts favorably with the fragment 1114-1119 (LSTILE) of BRCA2 (Hertz et al., 2016). During my PhD, I have described the disorder propensity of the BRCA2₁₀₉₃₋₁₁₅₈ region and analyzed the interaction between BRCA2₁₀₉₃₋₁₁₅₈ and PP2A-B56 by NMR. The NMR results showed a global peak intensity decrease for BRCA2₁₀₉₃₋₁₁₅₈ upon addition of PP2A-B56, which is consistent with an interaction. This interaction was further confirmed using ITC by Rania Ghouil. However, we did not yet restrict the exact binding region to the short fragment BRCA2₁₁₁₄₋₁₁₁₉ containing the L-X-X-I-X-E motif. I also identified that Plk1 can phosphorylate BRCA2₁₀₉₃₋₁₁₅₈ at several positions including S1115, comprised in the L-X-X-I-X-E motif. This phosphorylation by Plk1 may favor the formation of the BRCA2/PP2A complex, as reported below for BubR1.

Indeed, BRCA2 and BubR1 bind PP2A through similar sequences: the L-X-X-I-X-E motifs of both BRCA2₁₁₁₄₋₁₁₁₉ and the KARD domain of BubR1. This interaction is promoted by the phosphorylation of the BubR1 KARD domain by Plk1 (Suijkerbuijk et al., 2012, Wu et al., 2017). Thus, there might be a competition between BRCA2 and BubR1 for binding to PP2A. Because Plk1 phosphorylates both BRCA2 and BubR1, a regulation of the PP2A partners may be mediated by Plk1 phosphorylations, which would permit a tight regulation of the Spindle Assembly Checkpoint. All these informations are summarized in **Figure 101**.

Hence, we have shown that N-terminal phosphorylation of BRCA2 by Plk1 promotes BubR1 phosphorylation and a correct kinetochore-microtubule attachment. Phosphorylation of N-terminal BRCA2 by Plk1 was also shown to release PCAF from BRCA2 (Lin et al., 2003), which is suggested to favor the decrease of BubR1 acetylation (Choi et al., 2012) and inhibits the SAC. These two pathways seem to be regulated in time by Plk1-dependent phosphorylations. It may be interesting to explore *in cells* how these two pathways work together to ensure mitotic progression, i.e.: i) the role of BRCA2₁₀₉₃₋₁₁₅₈ phosphorylation in the

regulation of BRCA2:PP2A binding and ii) the competition between BRCA2 and BubR1 for binding to PP2A before and after phosphorylation by Plk1 during mitosis. These questions will be investigated in the context of a new PhD project.

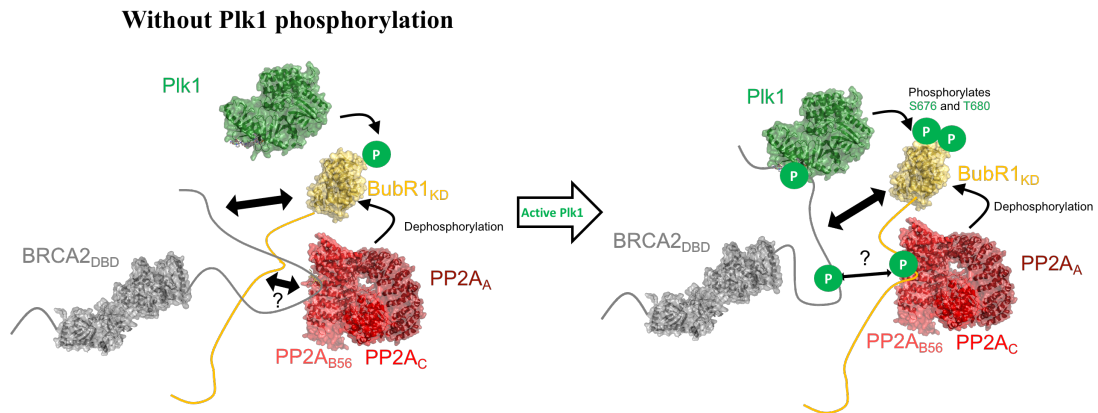


Figure 101. BRCA2/Plk1/BubR1/PP2A quaternary complex upon phosphorylation by Plk1. When Plk1 is not active (left), BRCA2_{T207} does not interact with Plk1_{PBD}. As a result, the phosphorylation of BubR1 by Plk1 is low. BubR1 and BRCA2 interact with the same PP2A docking site. This favors the dephosphorylation of BubR1, which, in turn, disfavors chromosome segregation. Upon Plk1 activation (right), Plk1 phosphorylates BRCA2_{pT207} and interacts directly with BRCA2. This promotes BubR1 phosphorylation by Plk1 on its kinase domain and its LXXIXE motif, which strengthens the BubR1:PP2A interaction. PDB codes used for the Figure: 3D folded domain of BRCA2 (1IYJ), Plk1_{PBD} (6GY2), the kinase domain of BubR1 (6JKK), PP2A (2NPP), PP2A-B56 (5SWF). No human Plk1 structure was yet elucidated, thus the kinase domain (3D5U) was docked onto the PBD domain using the *Danio rerio* Plk1 structure (4J7B).

c. Use of proteomics for searching IDRs partners

In order to identify new phosphoBRCA2 partners, I performed pull-down experiments followed by semi-quantitative mass-spectrometry proteomics analysis, in collaboration with the Institut Curie proteomic platform. François-Xavier Theillet had explored this approach previously and set up the use of AviTag-directed biotinylation by BirA, together with the feasibility of detecting new IDP partners by MS analysis of pull-downs. In attempting to find appropriate experimental conditions, I used two protocols:

- 2 ng of non-phospho- and phospho-BRCA2₁₆₇₋₂₆₀ on 25 uL of dry beads, 2 hrs of incubation with cell extracts and gentle washes;
- 10 ng of non-phospho- or phospho-BRCA2₁₆₇₋₂₆₀ on 50 uL of dry beads, 30 min of incubation with cell extracts and several washes with beads resuspension.

The first condition led to the identification of 6 partners with a low p-value, while the second condition led to identify 4 partners but with a higher p-value. We found that Kif2C, Kif2A and Plk1 were pulled-down in both conditions (2 and 10 ng bait protein), which gave

good hopes that they might be real binding partners. I am currently testing the interactions between phosphoBRCA2 and two of the partners identified, Kif2C and Chk2, in order to validate their direct binding.

Because IDRs interacts with their partners often with affinities in the micromolar range and in transient fashions, it is not straightforward to define optimal conditions for pulling-down new partners. The scarcity of the differentially pulled-down proteins is not very satisfying nor encouraging. Cross-linking methods are likely to lead to a great number of false identifications, because of the great accessibility and unspecific interactions that IDPs experience in the cellular milieu. Identifying IDP partners keeps hampering the field.

d. Kif2C/phosphoBRCA2 interaction

I decided to focus my attention on the interaction between the kinesin Kif2C and BRCA2. Indeed, Kif2C is localized at the kinetochore and the Flemming body, like BRCA2 and Plk1 (Zhang et al., 2011, Takaoka et al., 2014). IDRs establish most often specific interactions with folded domains. Hence, I tested first the interaction between the neck+motor domain of Kif2C and pBRCA2₁₆₇₋₂₆₀. Up to now, I could unfortunately not nail any direct interaction between these two constructs, using ITC, NMR or size-exclusion chromatography assays. In the next months, I will investigate the possible interactions with the full length Kif2C.

It is known from the literature that the kinase domain of Plk1 interacts directly with the motor domain of Kif2C (Zhang et al., 2011). As Plk1 was found in the proteomics result with a high p-value, I proposed the hypothesis that the BRCA2/Kif2C interaction is mediated by Plk1. However, I did not confirm the interaction between Kif2C_{motordomain} and Plk1_{KD} using gel filtration analysis. We should probably test the interaction between Plk1_{KD} and full length Kif2C. We could also hypothesize that the concomitant presence of Plk1, pBRCA2 and Kif2C is necessary to establish a ternary complex (**Figure 102**). These hypotheses will be tested using gel filtration and NMR.

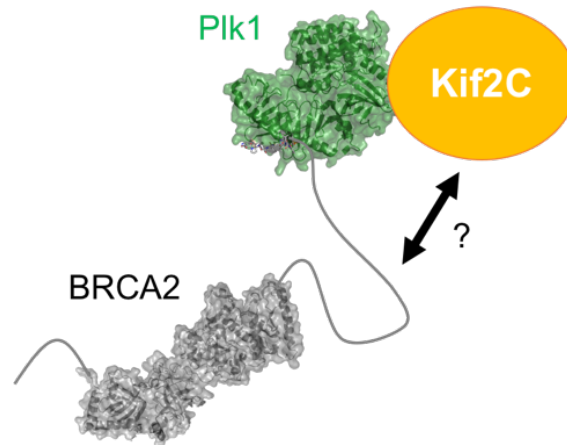


Figure 102. Known interactions between BRCA2, Plk1 and Kif2C. BRCA2_{pT207} interacts with Plk1_{PBD} (6GY2) and Plk1_{KD} with Kif2C_{motor domain} (Zhang et al., 2011)

The question of the functional relevance of such a complex remains. To the best of our knowledge, BRCA2 and Kif2C have not been shown to exert functions in a common pathway. However, they present similar functions, in particular for the kinetochore formation: Kif2C, which is able to depolymerase microtubules, is involved in the centromere-microtubule attachment and in microtubule catastrophes (Tanenbaum et al., 2011), while BRCA2 serves as a platform for sensing the correct alignment of chromosomes along the metaphase plate (Elhen et al., 2020). BRCA2 and Kif2C both interact and are phosphorylated by the kinase Plk1. Plk1 was indeed shown to phosphorylate Kif2C and positively regulate its depolymerase activity during metaphase and anaphase (Zhang et al., 2011, Sanhaji et al., 2011). As Plk1 is known to protect the kinetochore-centromere architecture against tension (Lera et al., 2019), the formation of a BRCA2/Kif2C(+/- Plk1) complex phosphorylated by Plk1 may have a function in the preparation of chromosome segregation.

BRCA2 and Kif2C also both localize at the midbody during cytokinesis (Zhang et al., 2011, Takaoka et al., 2014). During cytokinesis, BRCA2 has been shown to interact with several partners to ensure a correct cytoplasm division at the end of mitosis (Morita et al., 2007, Mondal et al., 2012, Takaoka et al., 2014, Marmorstein et al., 2001, Yuan et al., 2001). While other kinesins are involved in the last step of cell division, a cytokinetic function of Kif2C is absent from the literature (Zhu et al., 2005, Gigant et al., 2017). The BRCA2/Kif2C complex may be involved in the process of cytokinesis but it would be a very new function for Kif2C. Kif2C may also drive the BRCA2 localization to the midbody, for which no protein recognizing the BRCA2_{pS193} region was yet identified.

In addition, Kif2C was recently shown to be involved in the regulation of DSBs DNA repair (Zhu et al., 2020). The microtubule depolymerase activity of Kif2C is linked to the formation of DNA damage foci that are essential for the resolution of DSBs. A function of the BRCA2/Kif2C complex in DSBs repair can not be excluded, but it is doubtful because the two proteins are involved in very different steps of DSBs repair. Furthermore, the mitotic phosphorylation of BRCA2 by Plk1 is needed for the complex formation, which indicates that the complex formation should possess mitotic function.

Finally, Kif2C is highly expressed in testis, where its role in microtubule depolymerization is essential for the first steps of spermatogenesis. During mitotic steps of spermatogenesis, Kif2C acts as in somatic cells by creating microtubule catastrophes for spindle organization (Ma et al., 2017). BRCA2 is also involved in spermatogenesis, however, it functions mainly in the meiosis part of the process.

To conclude, the interaction between BRCA2 and Kif2C would be a new information. However, this hypothesis must be confirmed by *in vitro* experiments. Furthermore, establishing the biological role of this complex would require cell biology experiments, e.g. the comparison of phenotypes of cells expressing either WT BRCA2 or VUS BRCA2 impairing the formation of the complex.

e. Chk2/phosphoBRCA2 interaction

Chk2 was found to interact with phospho-BRCA2 in our pull-down assays analyzed by MS-proteomics. Hence, I tested the interaction between the kinase Chk2 and pBRCA2₁₆₇₋₂₆₀, starting with the FHA domain of Chk2, which is known to interact with phosphopeptides (Li et al., 2002). The comparison between our recent NMR spectra of pBRCA2₁₆₇₋₂₆₀ free and in presence of Chk2-FHA provided an uncertain answer: we observed weaker NMR signals in the region surrounding pBRCA2₁₆₇₋₂₆₀(aa220). We are currently waiting for the FHA alone to confirmed this interaction.

We know that Chk2 phosphorylates BRCA2 at the position 3387 upon DNA damage (Bahassi et al., 2008). This phosphorylation is important for the dissociation of Rad51 from TR2 (Bahassi et al., 2008) and its re-localization to new DNA damage foci. However, no direct interaction between Chk2 and BRCA2 has yet been described. The confirmation of this interaction would be a novel piece of information and may be important for the signalling of DNA repair pathways. Chk2 was also shown to be involved in the mitotic exit upon unattachment of kinetochores (Petsalki & Zachos, 2014). Thus, a BRCA2/Chk2 interaction may also be a part of the chromosome segregation regulation.

f. Is the NTD-DBD of BRCA2 functional?

Initially, I investigated the interaction between another region of BRCA2 (BRCA2₂₅₀₋₅₀₀) and DNA. This project was my initial PhD project and was funded by the ANR FUNBRCA2. Hence, I dedicated quite some time to test this interaction.

In 2016, our collaborators showed by EMSA that BRCA2₂₅₀₋₅₀₀ is able to bind several forms of DNA (dsDNA, ssDNA, 3' overhang and gapped DNA) with better affinity than the well-known C-terminal CTD-DBD (Von Nicolai et al., 2016). They also showed that BRCA2₂₅₀₋₅₀₀ was sufficient to promote Rad51 recombination, suggesting a role of this region in Homologous Recombination. In addition, double mutations including C279, C315 or C341 impacted the formation of BRCA2 complex with dsDNA but not with ssDNA. This led them to suspect the existence of a Zinc-finger folding in the BRCA2₂₆₅₋₃₄₉ region.

In the course of our study, we had great difficulties to obtain soluble WT BRCA2₂₅₀₋₅₀₀ and BRCA2₂₅₀₋₃₅₀. Even upon mutations of non-conserved cysteines, BRCA2₂₅₀₋₅₀₀ and BRCA2₂₅₀₋₃₅₀ remained poorly soluble. In addition, no folding or secondary structure propensities could be perceived for BRCA2₂₅₀₋₅₀₀ in NMR spectra, even upon addition of ZnCl₂. We observed by microscopy that BRCA2₂₅₀₋₅₀₀ forms large, soluble aggregates upon overnight incubation at 277 K, but we did not detect any droplets that would reveal liquid-liquid phase separation. Finally, we could not observe any clear interaction between this BRCA2 region and ssDNA or dsDNA using NMR spectroscopy.

We did not manage to find an appropriate peptide construct to work with, which pushed us to stop the structural characterization of this region.

In the team of Dr A. Carreira, BRCA2₂₅₀₋₅₀₀ was produced in mammalian cells and then purified (Von Nicolai et al., 2016). Thus, two hypotheses may be drawn:

- This region needs to be expressed in mammalian cells to get its DBD characteristics. It may require post-translational modifications or a specific environment to be soluble and bind DNA,
- The aggregation propensity of this region, which is correlated with the number of cysteines in our hands, generates artefacts during the EMSA analysis of its DNA binding. The loss of DNA interaction upon cysteine mutation is consistent with this hypothesis. Soluble aggregates of the studied BRCA2 constructs would slow down DNA migration in the polyacrylamide gels. In our hands, the DTT concentrations (about 1 mM) in EMSA gels were not enough to maintain cysteines of cysteine-rich IDPs in their reduced states in solution, according to NMR characterization. In order to exclude this hypothesis, it may be relevant to use another technique such as ITC or NMR with a sample non-prone to aggregation.

Interestingly, Brh2, the BRCA2 homolog from the fungus *Ustilago maydis*, possesses 2 DBD: one in its N-terminus and one in its C-terminus (Zhou et al., 2009). Sequence alignment between BRCA2 and Brh2 indicated that the C-terminal DBD of Brh2 contains the OB1 and OB2 folds but not OB3 (Zhou et al., 2009) and interacts with DNA. The NTD-DBD of Brh2 collaborate with the single BRC motif of Brh2 to assemble Rad51 on protruding ssDNA (Zhou et al., 2009), independently from the CTD-DBD. Further studies have shown that NTD-DBD is the priming DNA docking site and these two DBDs contribute in different ways to repair processes (Zhou et al., 2014).

The NTD-DBD of Brh2 was shown to interact with several forms of DNA, as the NTD-DBD of BRCA2. However, alignment between BRCA2 and Brh2 sequences did not reveal evident homology between the 2 DBDs (Zhou et al., 2009). Furthermore, if a zinc-finger domain is formed in BRCA2-NTD, it is not conserved among species as the cysteines are not conserved beyond mammals (Zhou et al., 2009). Similarities in structure/mechanism are thus complicated to imagine. The conservation of some basic residues among mammals (human BRCA2₃₁₀₋₃₅₀) suggests that this region may recognize a negatively charge partner, such as DNA. However, mini-BRCA2 constructs that contains only few BRCA repeats and the CTD-DBD are enough to ensure HR in cell (Siaud et al., 2011). Thus, if a N-terminal DBD is present on BRCA2, it is probably not essential for DNA repair involving BRCA2.

3. Plk1, a cancer target with non-elucidated regulation and dynamics

To fully understand the interactions between BRCA2 and Plk1, I needed to obtain high amounts of well-defined and homogeneous samples of Plk1. Hence, I tried to produce it in-house. I thought that it would also permit to obtain structural information on the regulation of Plk1 activity. To achieve these goals, I produced several constructs of Plk1.

We carried out initial trials using human cDNA cloned into the local bacmid systems for production in insect cells. The results were not satisfying. We will try again with codon-optimized genes in 2021. In the meantime, I tried to produce Plk1 constructs in *E. coli*. We found conditions to achieve this recombinant production and the subsequent purification for the separated Plk1_{PBD} and Plk1_{KD}. Hence, we are now capable to produce the kinase domain of Plk1 without the PBD. I have shown that this isolated KD can be used for phosphorylation assays without any severe drawbacks on phosphosite recognition. This will be a useful tool for studying Plk1 targets in the absence of the neighboring Plk1_{PBD} docking site, e.g. in the case of BRCA2₁₀₉₃₋₁₁₅₈.

I also initiated the production of the FL Plk1 kinase. The purification protocol of Plk1_{FL} is still to be optimized. However, the obtained amounts of Plk1_{FL} from bacterial expression are quite low.

In parallel, I attempted to activate Plk1 by the phosphorylation of T210 using the kinase Aurora A. This part of the project is still in progress. Previous tests did not permit to observe a clear phosphorylation of Plk1_{T210} by Aurora A. Because the construct of AurA-TPX2 was previously shown to phosphorylate efficiently its targets (Zorba et al., 2014) and Aurora A-TPX2 and Plk1₁₋₃₂₈ are eluted at a relevant gel filtration elution volume, I do not suspect that the construct design or the protein quality are the limiting factors in this experiment. Thus, four strategies may be considered:

- Optimize buffer conditions for Aurora A phosphorylation. Even if I used conditions close to the previously described ones (Zorba et al., 2014), it may be possible that phosphorylation of Plk1 has to be performed in other conditions (pH, salts);
- Remove the Plk1-C212S mutation that we used in the Plk1₁₋₃₂₈ construct, which may be deleterious for the phosphorylation of Plk1_{T210} by Aurora A;
- Aurora A may not be the kinase that directly phosphorylates Plk1 but only a part of the mechanism. In this case, the use of the Slk kinase may be a solution, as shown 15 years ago in the literature (Johnson et al., 2008);
- Add the mutation T210D in the construct: T210D has been shown to mimic the phosphorylated state of T210 (Macurek et al., 2008).

In the meantime, I started to draw plans for studying structural dynamics between the two Plk1 domains. The study of Plk1 from *Danio rerio* showed that the long linker between Plk1_{KD} and Plk1_{PBD} negatively regulates the activity of Plk1_{KD} (Xu et al., 2013). Our strategy is to use NMR to investigate the dynamics between the two domains in presence or absence of the long linker and in presence or absence of the activating phosphorylation (pT210).

I observed that the linker length does not have any consequence on the phosphorylation activity of the isolated Plk1_{KD}. I also showed that it seems to be possible to reconstitute a Plk1_{KD}/Plk1_{PBD} complex, according to NMR data. This will have to be further confirmed using other techniques (ITC, GF). As the human Plk1 structure is not available yet, we will initiate crystallography assays by reconstituting the Plk1_{KD}/Plk1_{PBD} complex using separated domains or by varying the linker length.

Then, in the short-term, in collaboration with the group of Dr. Daniel Haussinger, we will attach a lanthanide tag to the kinase domain for structural characterization purposes (Joss

et al., 2019). Because the ~70 kDa full-length Plk1 is certainly a challenge for NMR investigations, we have to think of efficient isotope labeling strategies that may provide sufficient NMR signal. Selective ^{13}C -labeling of methionines may be an attractive and affordable solution. Plk1_{KD} contains 4 Met, Plk1_{PBD} 5. We can reasonably expect that a couple of residues in each domain show resolved resonances. The assignment of their ^1H - ^{13}C methyl resonances should be feasible using an Ala-mutation strategy. In Plk1_{PBD}, methionines are well-spread and present mainly at the surface (**Figure 103**). Hence, we propose a strategy consisting in comparing the ^1H - ^{13}C spectrum of Plk1_{PBD} with the ^1H - ^{13}C spectrum Plk1_{FL} and Plk1_{PBD}+Plk1₁₋₃₂₈ labeled with the lanthanide-tag at the L162 position. Pseudo-contact shifts will allow to confirm the orientation between PBD and KD of human Plk1. Then, the same experiments may be carried out with the truncated Plk1_{PBD} and Plk1₁₋₃₆₆ to test the influence of the linker. Finally, the same experiments can be carried out with the T210-phosphorylated kinase domain (Plk1₁₋₃₂₈ and Plk1₁₋₃₆₆) using the T210D mutation. The inverse labeling (lanthanide tag on the Plk1_{PBD} and specific amino acid labeling of Plk1_{KD}) may be considered to complete the information. This study would permit to obtain further information about the cooperation between the 2 domains of human Plk1. Alternative labeling schemes may be more appropriate. The resulting NMR spectral quality can unfortunately not be predicted.

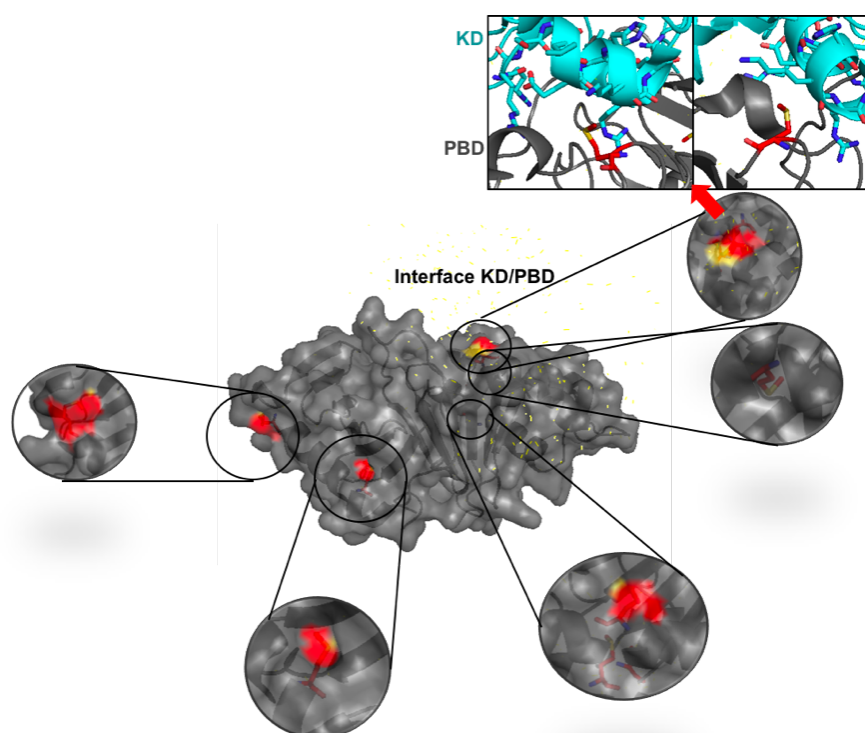


Figure 103. A proposed labeling strategy for studying Plk1_{KD}/Plk1_{PBD} interface. Plk1_{PBD} (grey, PDB code: IUMW) contains 4 exposed methionines (red) and one methionine in the protein core. Interestingly one of them is at the interface with the Plk1_{KD} (PBD: 5TA8 align to the PBD with *Danio rerio* Plk1:4J7B)

In the long-term, such information may be useful for designing Plk1 inhibitors in the context of cancer therapy. Overexpression of Plk1 has been observed in a wide variety of cancers (Strebhardt et al., 2010) including non-small cell lung (Wolf et al., 1997), breast (Wolf et al., 2000), ovarian (Weichert et al., 2004) and head and neck squamous carcinomas (Knecht et al., 2000), as well as melanoma (Strebhardt et al., 2000) and diffuse large B cell lymphoma (Liu et al., 2007). These cancers with an overexpression of Plk1 are often correlated with a poor patient prognosis (Eckerdt et al., 2005). Furthermore, downregulation of Plk1 expression causes reduced proliferation in a variety of cancer cell lines and tumor xenografts but not in normal cells (Lane et al., 1996, Spankuch et al., 2002, Liu et al., 2003, Guan et al., 2005, Elez et al., 2003), suggesting that inhibition of Plk1 as an attractive target for cancer therapy (Liu et al., 2015).

Several Plk1 inhibitors were developed as anti-cancer candidates for tumors overexpressing Plk1. Several were tested in clinical studies, and are listed in the clinicaltrials.gov website, but none of them obtained an authorization for large clinical use (O'Neil et al., 2015). In 2015, a review listed the current Plk1 inhibitors under clinical test (9 in phase I or II, 2 in phase 3, Brandwein et al., 2015). Among them, we can identify some specific inhibitors of Plk1, however, most of the inhibitors also have an inhibitory impact on the other Plks (Strebah et al., 2010, Liu et al., 2015). The most promising molecules are the following (**Figure 107**):

- GSK461363 inhibits Plk1 with a K_i of 2.2 nM, and is more than 1,000-fold selective against Plk2/3 (Gilmartin et al., 2009),
- TAK-960 has an IC_{50} of 0.8 nM against Plk1 but presents also inhibitory activities against Plk2 (IC_{50} : 16.9 nM) and Plk3 (IC_{50} : 50.2 nM) (Hikichi et al., 2012),
- Rigosertib has an IC_{50} of 9 nM for Plk1, it shows 30-fold greater selectivity against Plk2 (Gumireddy et al., 2005),
- BI2536 has an IC_{50} of 0.83 nM for Plk1 and shows a 4- and 11- fold greater selectivity against Plk2 and Plk3 (Steehmaier et al., 2007),
- Volasertib has an IC_{50} of 0.87 nM against Plk1 and a 6- and 65- fold greater selectivity against Plk1 and Plk3 (Rudolph et al., 2009).

The chemical differences between the most promising inhibitors (number of cycles, presence of sulphur, fluor...) show that the optimization of new Plk1 inhibitors offers a large panel of possibilities. Furthermore, not all the molecules have the same inhibition process on

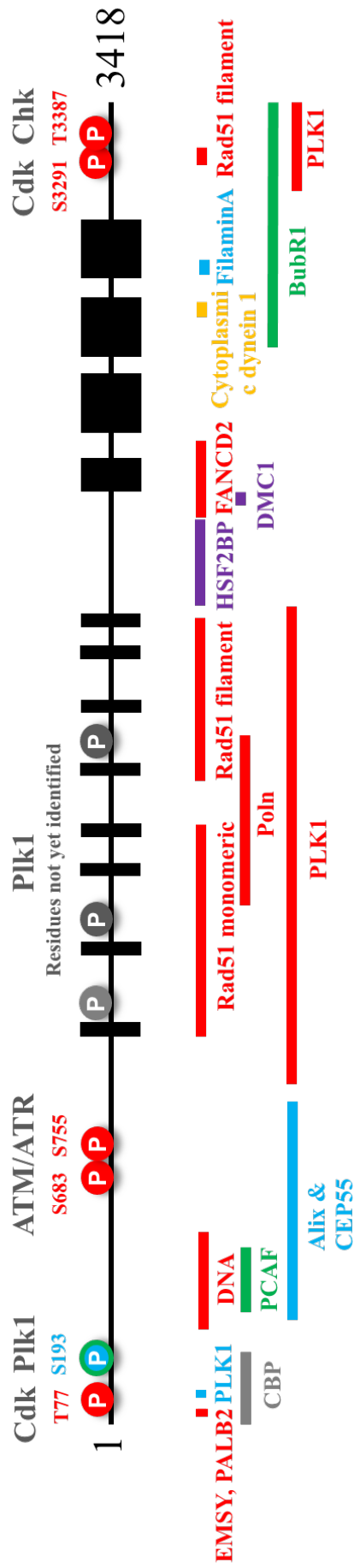
Plk1: some of them target the kinase domain while the others target the PBD. The intrinsic limits of targeting only one of the two Plk1 domains may be an explanation for the non-conclusive clinical tests. Interestingly, in 2018, one compound has been shown to inhibit the interaction between the KD and the PBD of Plk1: AW00551 (Raab et al., 2018). This new class of inhibitors, targeting the interface between the KD and the PBD may be more efficient for the modulation of Plk1 activity and functions.

Hence, it will be interesting to provide further structural details about the Plk1_{KD}/Plk1_{PBD} interaction and to describe their modification upon kinase activation. Hopefully, this will help to design Plk1 inhibitors for treating a large panel of cancers.

4. Conclusion

Throughout my PhD, I characterized the disorder propensity of BRCA2₄₈₋₂₈₄, set up methodologies for the identification and the monitoring of its phosphorylation by Plk1, explored the role of BRCA2 pT77 as a priming event for the phosphorylation by Plk1, and tested several potential interactions for understanding the role of phosphoBRCA2₄₈₋₂₈₄. This led us notably to characterize the interaction between the BRCA2_{pT207} region and Plk1_{PBD}. Hopefully, the identification of Kif2C and Chk2 binding regions in BRCA2 will allow us to extend our knowledge on the regions of high importance for BRCA2 functions.

In conclusion, through the methodology set up and the exploration of several hypothetical BRCA2 interactions, this work probably help to orient future research on BRCA2 in the team. In addition, the identification of functional regions of BRCA2 constitutes a basis for the prediction of causal breast cancer variants in this region. It will also permit to design protein-protein interaction tests for contributing to classify variants of the region.



Annexe 1. Relationships between PTMs or interactions and BRCA2 functions are displayed with the following color code: red for DNA repair, yellow for centrosome localization, green for chromosome segregation, blue for cytokinesis, purple for meiosis, grey for unknown function. BRCA2 directly interacts with a large panel of proteins and contains several phosphorylation sites: T77 (Cdk, Takaoka et al., 2014), S193, (Plk1, Ehlen et al., 2020), S683 and S755 (ATM/ATR, Matsuoka et al., 2007), between the BRC repeats (Plk1, Lee et al., 2004) S3291 (Cdk, Esashi et al., 2005) and T3387 (Chk, Bahassi et al., 2008).

Bibliography

- Alberti, S. et al. A user's guide for phase separation assays with purified proteins. *J Mol Biol* 430, 4806–4820 (2018).
- Alexander, J. et al. Spatial Exclusivity Combined with Positive and Negative Selection of Phosphorylation Motifs Is the Basis for Context-Dependent Mitotic Signaling. *Sci Signal* 4, ra42–ra42 (2011).
- Ambadipudi, S., Biernat, J., Riedel, D., Mandelkow, E. & Zweckstetter, M. Liquid–liquid phase separation of the microtubule-binding repeats of the Alzheimer-related protein Tau. *Nat Commun* 8, 275 (2017).
- ANAES. (1999). Le dépistage du cancer du sein par Mammographie dans la population générale.
- Andresen, C. et al. Transient structure and dynamics in the disordered c-Myc transactivation domain affect Bin1 binding. *Nucleic Acids Res* 40, 6353–6366 (2012).
- Andrew, C. D., et al. Effect of Phosphorylation on α -Helix Stability as a Function of Position†. *Biochemistry-us* 41, 1897–1905 (2002).
- Anjum, F., Razvi, N., Maqbool, A. & Jahan, N. A review of breast cancer risk factors. *Univers J Pharm Res* 2, 40–45 (2017).
- Anothaisintawee, T. et al. Risk Factors of Breast Cancer. *Asia Pac J Public Heal* 25, 368–387 (2013).
- Archambault, V. & Glover, D. M. Polo-like kinases: conservation and divergence in their functions and regulation. *Nat Rev Mol Cell Bio* 10, 265–275 (2009).
- Arrêté du 24 janvier 2008 portant introduction de la mammographie numérique dans le programme de dépistage organisé du cancer du sein, NOR: SJSP0802212A.
- Arrêté du 27 septembre 2001 fixant le modèle de la convention type mentionnée à l'article L. 1411-2 du code de la santé publique, NOR: MESS0123474A
- Arrêté du 29 septembre 2006 relatif aux programmes de dépistage des cancers, NOR: SANP0623877A
- Ayoub, N. et al. The Carboxyl Terminus of Brca2 Links the Disassembly of Rad51 Complexes to Mitotic Entry. *Curr Biol* 19, 1075–1085 (2009).
- Azatian, S. B., Kaur, N. & Latham, M. P. Increasing the buffering capacity of minimal media leads to higher protein yield. *J Biomol Nmr* 73, 11–17 (2019).
- Ba, A. N. N. et al. Proteome-Wide Discovery of Evolutionary Conserved Sequences in Disordered Regions. *Sci Signal* 5, rs1–rs1 (2012).
- Badgujar, N. V., Tarapara, B. V. & Shah, F. D. Computational analysis of high-risk SNPs in human CHK2 gene responsible for hereditary breast cancer: A functional and structural impact. *Plos One* 14, e0220711 (2019).

- Badie, S. et al. BRCA2 acts as a RAD51 loader to facilitate telomere replication and capping. *Nat Struct Mol Biol* 17, 1461–1469 (2010).
- Bah, A. & Forman-Kay, J. D. Modulation of Intrinsically Disordered Protein Function by Post-translational Modifications. *J Biol Chem* 291, 6696–6705 (2016).
- Bah, A. et al. Folding of an intrinsically disordered protein by phosphorylation as a regulatory switch. *Nature* 519, 106–109 (2015).
- Bahassi, E. M. et al. The checkpoint kinases Chk1 and Chk2 regulate the functional associations between hBRCA2 and Rad51 in response to DNA damage. *Oncogene* 27, 3977–3985 (2008).
- Bailey, L. S., Alves, M., Galy, N., Patrick, A. L. & Polfer, N. C. Mechanistic insights into intramolecular phosphate group transfer during collision induced dissociation of phosphopeptides. *J Mass Spectrom* 54, 449–458 (2019).
- Bailey, R. W., et al. Clusterin, a Binding Protein with a Molten Globule-like Region †. *Biochemistry-us* 40, 11828–11840 (2001).
- Banani, S. F., Lee, H. O., Hyman, A. A. & Rosen, M. K. Biomolecular condensates: organizers of cellular biochemistry. *Nat Rev Mol Cell Bio* 18, 285–298 (2017).
- Barr, F. A., Silljé, H. H. W. & Nigg, E. A. Polo-like kinases and the orchestration of cell division. *Nat Rev Mol Cell Bio* 5, 429–441 (2004).
- Barraud, P. et al. Time-resolved NMR monitoring of tRNA maturation. *Nat Commun* 10, 3373 (2019).
- Bartek, J. & Lukas, J. Chk1 and Chk2 kinases in checkpoint control and cancer. *Cancer Cell* 3, 421–429 (2003).
- Baumann, A. L. & Hackenberger, C. P. R. Modern Ligation Methods to Access Natural and Modified Proteins. *Chimia Int J Chem* 72, 802–808 (2018).
- Belloque, J., Fuente, M. A. D. L. & Ramos, M. Qualitative and quantitative analysis of phosphorylated compounds in milk by means of ³¹P-NMR. *J Dairy Res* 67, 529–539 (2000).
- Bergeron-Sandoval, L.-P., Safaee, N. & Michnick, S. W. Mechanisms and Consequences of Macromolecular Phase Separation. *Cell* 165, 1067–1079 (2016).
- Béroud, C. et al. BRCA Share: A Collection of Clinical BRCA Gene Variants. *Hum Mutat* 37, 1318–1328 (2016).
- Berrade, L. & Camarero, J. A. Expressed protein ligation: a resourceful tool to study protein structure and function. *Cell Mol Life Sci* 66, 3909 (2009).
- Bertwistle, D. & Ashworth, A. Functions of the BRCA1 and BRCA2 genes. *Curr Opin Genet Dev* 8, 14–20 (1998).

- Beutel, O., Maraschini, R., Pombo-García, K., Martin-Lemaitre, C. & Honigmann, A. Phase Separation of Zonula Occludens Proteins Drives Formation of Tight Junctions. *Cell* 179, 923-936.e11 (2019).
- Bicker, K. L. & Thompson, P. R. The protein arginine deiminases: Structure, function, inhibition, and disease. *Biopolymers* 99, 155–163 (2013).
- Bienkiewicz, E. A. & Lumb, K. J. Random-coil chemical shifts of phosphorylated amino acids. *J Biomol Nmr* 15, 203–206 (1999).
- Bock, I. et al. Detailed specificity analysis of antibodies binding to modified histone tails with peptide arrays. *Epigenetics* 6, 256–263 (2011).
- Boija, A. et al. Transcription Factors Activate Genes through the Phase-Separation Capacity of Their Activation Domains. *Cell* 175, 1842-1855.e16 (2018).
- Borgia, A. et al. Extreme disorder in an ultrahigh-affinity protein complex. *Nature* 555, 61–66 (2018).
- Brandsma, I. et al. HSF2BP Interacts with a Conserved Domain of BRCA2 and Is Required for Mouse Spermatogenesis. *Cell Reports* 27, 3790-3798.e7 (2019).
- Brandwein. Targeting polo-like kinase 1 in acute myeloid leukemia. *Therapeutic Advances in Hematology* (2015).
- Brown, N.R., et al. Cyclin B and cyclin A confer different substrate recognition properties on CDK2. *Cell Cycle*. 2007 Jun 1;6(11):1350-9.
- Brown, C. J., Johnson, A. K. & Daughdrill, G. W. Comparing Models of Evolution for Ordered and Disordered Proteins. *Mol Biol Evol* 27, 609–621 (2010).
- Brown, N. R. et al. CDK1 structures reveal conserved and unique features of the essential cell cycle CDK. *Nat Commun* 6, 6769 (2015).
- Brzovic, P. S., et al. Structure of a BRCA1–BARD1 heterodimeric RING–RING complex. *Nat Struct Biol* 8, 833–837 (2001).
- Buisson, R. et al. Breast Cancer Proteins PALB2 and BRCA2 Stimulate Polymerase η in Recombination-Associated DNA Synthesis at Blocked Replication Forks. *Cell Reports* 6, 553–564 (2014).
- Burkard, M. E. et al. Chemical genetics reveals the requirement for Polo-like kinase 1 activity in positioning RhoA and triggering cytokinesis in human cells. *Proc National Acad Sci* 104, 4383–4388 (2007).
- Byrum, A. K., Vindigni, A. & Mosammaparast, N. Defining and Modulating ‘BRCAness.’ *Trends Cell Biol* (2019).

- Caputo, S. et al. Description and analysis of genetic variants in French hereditary breast and ovarian cancer families recorded in the UMD-BRCA1/BRCA2 databases. *Nucleic Acids Res* 40, D992–D1002 (2012).
- Carreira, A. & Kowalczykowski, S. C. Two classes of BRC repeats in BRCA2 promote RAD51 nucleoprotein filament function by distinct mechanisms. *Proc National Acad Sci* 108, 10448–10453 (2011).
- Carreira, A. et al. The BRC Repeats of BRCA2 Modulate the DNA-Binding Selectivity of RAD51. *Cell* 136, 1032–1043 (2009).
- Castro, E. & Eeles, R. The role of BRCA1 and BRCA2 in prostate cancer. *Asian J Androl* 14, 409–414 (2012).
- Chajès, V. & Romieu, I. Nutrition and breast cancer. *Maturitas* 77, 7–11 (2014).
- Chase, D. et al. The polo-like kinase PLK-1 is required for nuclear envelope breakdown and the completion of meiosis in *Caenorhabditis elegans*. *Genesis* 26, 26–41 (2000).
- Cheng, J., Sweredoski, M. & Baldi, P. Accurate Prediction of Protein Disordered Regions by Mining Protein Structure Data, *Data Mining and Knowledge Discovery*, 11(3) 213-222 (2005).
- Cho, U. S. & Xu, W. Crystal structure of a protein phosphatase 2A heterotrimeric holoenzyme. *Nature* 445, 53–57 (2007).
- Choi, E. et al. BRCA2 Fine-Tunes the Spindle Assembly Checkpoint through Reinforcement of BubR1 Acetylation. *Dev Cell* 22, 295–308 (2012).
- Choi, E. et al. BubR1 acetylation at prometaphase is required for modulating APC/C activity and timing of mitosis. *Embo J* 28, 2077–2089 (2009).
- Clamp, M., et al. The Jalview Java alignment editor. *Bioinformatics* 20, 426–427 (2004).
- Colicino, E. G. & Hehnl, H. Regulating a key mitotic regulator, polo-like kinase 1 (PLK1). *Cytoskeleton* 75, 481–494 (2018).
- Cordier, F., Chaffotte, A. & Wolff, N. Quantitative and dynamic analysis of PTEN phosphorylation by NMR. *Methods* 77, 82–91 (2015).
- Daniels, M. J., et al. Abnormal Cytokinesis in Cells Deficient in the Breast Cancer Susceptibility Protein BRCA2. *Science* 306, 876–879 (2004).
- Danis, C. et al. Nuclear Magnetic Resonance Spectroscopy for the Identification of Multiple Phosphorylations of Intrinsically Disordered Proteins. *J Vis Exp* (2016) doi:10.3791/55001.
- Davey, N. E. et al. Attributes of short linear motifs. *Mol Biosyst* 8, 268–281 (2011).
- Davey, N. E. et al. Discovery of short linear motif-mediated interactions through phage display of intrinsically disordered regions of the human proteome. *Febs J* 284, 485–498 (2017).

- Densham, R. M. & Morris, J. R. The BRCA1 Ubiquitin ligase function sets a new trend for remodelling in DNA repair. *Nucleus* 8, 116–125 (2017).
- Deredge, D. et al. A temperature-dependent conformational shift in p38 α MAPK substrate-binding region associated with changes in substrate phosphorylation profile. *J Biol Chem* 294, 12624–12637 (2019).
- Deribe, Y. L., Pawson, T. & Dikic, I. Post-translational modifications in signal integration. *Nat Struct Mol Biol* 17, 666–672 (2010).
- Domnitz, S. B., et al. MCAK activity at microtubule tips regulates spindle microtubule length to promote robust kinetochore attachment. *J Cell Biology* 197, 231–237 (2012).
- Dormann, D. et al. Arginine methylation next to the PY-NLS modulates Transportin binding and nuclear import of FUS. *Embo J* 31, 4258–4275 (2012).
- Dosztányi, Z., et al. IUPred: web server for the prediction of intrinsically unstructured regions of proteins based on estimated energy content. *Bioinformatics* 21, 3433–3434 (2005).
- Duncan, P. I., et al. Cloning and Characterization of Plx2 and Plx3, Two Additional Polo-like Kinases from *Xenopus laevis*. *Exp Cell Res* 270, 78–87 (2001).
- Dunker, A. K. & Gough, J. Sequences and topology: intrinsic disorder in the evolving universe of protein structure. *Curr Opin Struc Biol* 21, 379–381 (2011).
- Dunker, A. K. et al. Intrinsically disordered protein. *J Mol Graph Model* 19, 26–59 (2001).
- Dunker, A. K. et al. Protein disorder and the evolution of molecular recognition: theory, predictions and observations. *Pac Symposium Biocomput Pac Symposium Biocomput* 473–84 (1998).
- Dunker, A. K., et al. Function and structure of inherently disordered proteins. *Curr Opin Struc Biol* 18, 756–764 (2008).
- Dunker, A.K., et al. Flexible nets. The roles of intrinsic disorder in protein interaction networks. *FEBS J.* 272(20):5129-48 (2005).
- Dyson, H. J. & Wright, P. E. Coupling of folding and binding for unstructured proteins. *Curr Opin Struc Biol* 12, 54–60 (2002).
- Dyson, H. J. & Wright, P. E. Intrinsically unstructured proteins and their functions. *Nat Rev Mol Cell Bio* 6, 197–208 (2005).
- Eckerdt, F., Yuan, J. & Strebhardt, K. Polo-like kinases and oncogenesis. *Oncogene* 24(2):267-76 (2005).
- Egelhofer, T. A. et al. An assessment of histone-modification antibody quality. *Nat Struct Mol Biol* 18, 91–93 (2011).

- Ehlén, Å. et al. Proper chromosome alignment depends on BRCA2 phosphorylation by PLK1. *Nat Commun* 11, 1819 (2020).
- Eichhorn, P. J. A., Creighton, M. P. & Bernards, R. Protein phosphatase 2A regulatory subunits and cancer. *Biochimica Et Biophysica Acta Bba - Rev Cancer* 1795, 1–15 (2009).
- Elez, R., et al. Tumor regression by combination antisense therapy against Plk1 and Bcl-2. *Oncogene* 22(1):69-80 (2003).
- Elia, A. E. H. et al. The Molecular Basis for Phosphodependent Substrate Targeting and Regulation of Plks by the Polo-Box Domain. *Cell* 115, 83–95 (2003).
- Elia, A. E. H., Cantley, L. C. & Yaffe, M. B. Proteomic Screen Finds pSer/pThr-Binding Domain Localizing Plk1 to Mitotic Substrates. *Science* 299, 1228–1231 (2003).
- Ellis, H. & Mahadevan, V. Anatomy and physiology of the breast. *Surg Oxf* 31, 11–14 (2013).
- Elowe, S. Bub1 and BubR1: at the Interface between Chromosome Attachment and the Spindle Checkpoint. *Mol Cell Biol* 31, 3085–3093 (2011).
- Elowe, S., et al. Tension-sensitive Plk1 phosphorylation on BubR1 regulates the stability of kinetochore–microtubule interactions. *Gene Dev* 21, 2205–2219 (2007).
- Errington, N. & Doig, A. J. A Phosphoserine–Lysine Salt Bridge within an α -Helical Peptide, the Strongest α -Helix Side-Chain Interaction Measured to Date †. *Biochemistry-us* 44, 7553–7558 (2005).
- Esashi, F. et al. CDK-dependent phosphorylation of BRCA2 as a regulatory mechanism for recombinational repair. *Nature* 434, 598–604 (2005).
- Esashi, F., et al. Stabilization of RAD51 nucleoprotein filaments by the C-terminal region of BRCA2. *Nat Struct Mol Biol* 14, 468–474 (2007).
- Fairhead, M. & Howarth, M. Site-Specific Protein Labeling, Methods and Protocols. *Methods Mol Biology* 1266, 171–184 (2014).
- Feldmann, K. & Hull, W. E. ³¹P nuclear magnetic resonance studies of glycogen phosphorylase from rabbit skeletal muscle: ionization states of pyridoxal 5'-phosphate. *Proc National Acad Sci* 74, 856–860 (1977).
- Feng, S. et al. Conservation and divergence of methylation patterning in plants and animals. *Proc National Acad Sci* 107, 8689–8694 (2010).
- Fenyo, D. et al. MALDI Sample Preparation: the Ultra Thin Layer Method. *J Vis Exp* 192 (2007).
- Ferreon, A. C. M., Ferreon, J. C., Wright, P. E. & Deniz, A. A. Modulation of allostery by protein intrinsic disorder. *Nature* 498, 390–394 (2013).
- Fisher, C. K. & Stultz, C. M. Constructing ensembles for intrinsically disordered proteins. *Curr Opin Struc Biol* 21, 426–431 (2011).

Foit, L., George, J. S., Zhang, B. W., Brooks, C. L. & Bardwell, J. C. A. Chaperone activation by unfolding. *Proc National Acad Sci* 110, E1254–E1262 (2013).

Follis, A. V. et al. PUMA binding induces partial unfolding within BCL-xL to disrupt p53 binding and promote apoptosis. *Nat Chem Biol* 9, 163–168 (2013).

Forman-Kay, J. D. & Mittag, T. From Sequence and Forces to Structure, Function, and Evolution of Intrinsically Disordered Proteins. *Structure* 21, 1492–1499 (2013).

Fradet-Turcotte, A., Sitz, J., Grapton, D. & Orthwein, A. BRCA2 functions: from DNA repair to replication fork stabilization. *Endocr-relat Cancer* 23, T1–T17 (2016).

Franzmann, T. M. et al. Phase separation of a yeast prion protein promotes cellular fitness. *Science* 359, eaao5654 (2018).

Fridlich, R., Annamalai, D., Roy, R., Bernheim, G. & Powell, S. N. BRCA1 and BRCA2 protect against oxidative DNA damage converted into double-strand breaks during DNA replication. *Dna Repair* 30, 11–20 (2015).

FRM “Les cancers du sein en chiffre », <https://www.frm.org/>

Fuchs, S. M., et al. Influence of Combinatorial Histone Modifications on Antibody and Effector Protein Recognition. *Curr Biol* 21, 53–58 (2011).

Fujioka, Y. et al. Phase separation organizes the site of autophagosome formation. *Nature* 578, 301–305 (2020).

Fuks, F., Milner, J. & Kouzarides, T. BRCA2 associates with acetyltransferase activity when bound to P/CAF. *Oncogene* 17, 2531–2534 (1998).

Funabiki, H. & Wynne, D. J. Making an effective switch at the kinetochore by phosphorylation and dephosphorylation. *Chromosoma* 122, 135–158 (2013).

Futamura, M. et al. Potential role of BRCA2 in a mitotic checkpoint after phosphorylation by hBUBR1. *Cancer Res* 60, 1531–5 (2000).

Fuxreiter, M., Simon, I. & Bondos, S. Dynamic protein–DNA recognition: beyond what can be seen. *Trends Biochem Sci* 36, 415–423 (2011).

Fuxreiter, M., Tompa, P. & Simon, I. Local structural disorder imparts plasticity on linear motifs. *Bioinformatics* 23, 950–956 (2007).

Gabellieri, C. et al. Therapeutic Target Metabolism Observed Using Hyperpolarized ¹⁵N Choline. *J Am Chem Soc* 130, 4598–4599 (2008).

Galea, C. A., et al. W. Regulation of Cell Division by Intrinsically Unstructured Proteins: Intrinsic Flexibility, Modularity, and Signaling Conduits. *Biochemistry* 47, 7598–7609 (2008).

- Gallivan, J. P. & Dougherty, D. A. Cation- π interactions in structural biology. *Proc National Acad Sci* 96, 9459–9464 (1999).
- Gassner, M. et al. The Phosphoenolpyruvate-Dependent Phosphotransferase System of *Staphylococcus aureus*. *Eur J Biochem* 75, 287–296 (1977).
- Gebel, J. et al. p63 uses a switch-like mechanism to set the threshold for induction of apoptosis. *Nat Chem Biol* 16, 1078–1086 (2020).
- Ghosh, R., Gilda, J. E. & Gomes, A. V. The necessity of and strategies for improving confidence in the accuracy of western blots. *Expert Rev Proteomic* 11, 549–560 (2014).
- Ghousaini, M. & Pharoah, P. D. Polygenic susceptibility to breast cancer: current state-of-the-art. *Future Oncol* 5, 689–701 (2009).
- Gigant, E. et al. Inhibition of ectopic microtubule assembly by the kinesin-13 KLP-7MCAK prevents chromosome segregation and cytokinesis defects in oocytes. *Development* 144, dev.147504 (2017).
- Gilmartin, A. G. et al. Distinct Concentration-Dependent Effects of the Polo-like Kinase 1–Specific Inhibitor GSK461364A, Including Differential Effect on Apoptosis. *Cancer Res* 69, 6969–6977 (2009).
- Gorr, T.A. & Vogel, J. Western blotting revisited: critical perusal of underappreciated technical issues. *Proteomics Clin Appl* 9(3-4):396-405 (2015).
- Group, A. B. C. S. Prevalence and penetrance of BRCA1 and BRCA2 mutations in a population-based series of breast cancer cases. *Brit J Cancer* 83, 1301–1308 (2000).
- Gudmundsdottir, K., et al. DSS1 is required for RAD51 focus formation and genomic stability in mammalian cells. *Embo Rep* 5, 989–993 (2004).
- Guidugli, L. et al. Functional Assays for Analysis of Variants of Uncertain Significance in BRCA2. *Hum Mutat* 35, 151–164 (2014).
- Gumireddy, K. et al. ON01910, a non-ATP-competitive small molecule inhibitor of Plk1, is a potent anticancer agent. *Cancer Cell* 7, 275–286 (2005).
- Guseva, S. et al. Measles virus nucleo- and phosphoproteins form liquid-like phase-separated compartments that promote nucleocapsid assembly. *Sci Adv* 6, eaaz7095 (2020).
- Hall, J. et al. Linkage of early-onset familial breast cancer to chromosome 17q21. *Science* 250, 1684–1689 (1990).
- Hanks, S., et al. Constitutional aneuploidy and cancer predisposition caused by biallelic mutations in BUB1B. *Nat Genet* 36(11):1159-61 (2004).
- Hanson, J., Yang, Y., Paliwal, K. & Zhou, Y. Improving protein disorder prediction by deep bidirectional long short-term memory recurrent neural networks. *Bioinformatics* btw678 (2016) doi:10.1093/bioinformatics/btw678.

Helenius, J., et al. The depolymerizing kinesin MCAK uses lattice diffusion to rapidly target microtubule ends. *Nature* 441, 115–119 (2006).

Helleday, T., Eshtad, S. & Nik-Zainal, S. Mechanisms underlying mutational signatures in human cancers. *Nat Rev Genet* 15, 585–598 (2014).

Hendus-Altenburger, R. et al. Random coil chemical shifts for serine, threonine and tyrosine phosphorylation over a broad pH range. *J Biomol Nmr* 73, 713–725 (2019).

Hernandez, M. A., Avila, J. & Andreu, J. M. Physicochemical characterization of the heat-stable microtubule-associated protein MAP2. *Eur J Biochem* 154, 41–48 (1986).

Hertz, E. P. T. et al. A Conserved Motif Provides Binding Specificity to the PP2A-B56 Phosphatase. *Mol Cell* 63, 686–695 (2016).

Hertz, E. P. T. et al. A Conserved Motif Provides Binding Specificity to the PP2A-B56 Phosphatase. *Mol Cell* 63, 686–95 (2016).

Higurashi, M., Ishida, T. & Kinoshita, K. Identification of transient hub proteins and the possible structural basis for their multiple interactions. *Protein Sci* 17, 72–78 (2008).

Hikichi, Y. et al. TAK-960, a Novel, Orally Available, Selective Inhibitor of Polo-Like Kinase 1, Shows Broad-spectrum Preclinical Antitumor Activity in Multiple Dosing Regimens. *Mol Cancer Ther* 11, 700–709 (2012).

Hirai, H., Yoshioka, K. & Yamada, K. A simple method using ³¹P-NMR spectroscopy for the study of protein phosphorylation. *Brain Res Protoc* 5, 182–189 (2000).

Hoffmann, R. et al. ¹H and ³¹P-NMR spectroscopy of phosphorylated model peptides. *international journal of peptide & protein research* 193–198 (1994).

Hofweber, M. et al. Phase Separation of FUS Is Suppressed by Its Nuclear Import Receptor and Arginine Methylation. *Cell* 173, 706-719.e13 (2018).

Hoult, D. I. et al. Observation of tissue metabolites using ³¹P nuclear magnetic resonance. *Nature* 252, 285–287 (1974).

Houtum, Q. et al. Feasibility of ³¹P spectroscopic imaging at 7 T in lung carcinoma patients. *Nmr Biomed* e4204 (2019).

Houtum, Q. et al. Feasibility of ³¹P spectroscopic imaging at 7 T in lung carcinoma patients. *Nmr Biomed* e4204 (2019).

Huang, B., Liu, Y., Yao, H. & Zhao, Y. NMR-based investigation into protein phosphorylation. *Int J Biol Macromol* 145, 53–63 (2019).

Huang, H. et al. Phosphorylation sites in BubR1 that regulate kinetochore attachment, tension, and mitotic exit. *J Cell Biology* 183, 667–680 (2008).

Huang, H., Lin, S., Garcia, B. A. & Zhao, Y. Quantitative Proteomic Analysis of Histone Modifications. *Chem Rev* 115, 2376–2418 (2015).

Hughes-Davies, L. et al. EMSY Links the BRCA2 Pathway to Sporadic Breast and Ovarian Cancer. *Cell* 115, 523–535 (2003).

Hunter, A. W. et al. The Kinesin-Related Protein MCAK Is a Microtubule Depolymerase that Forms an ATP-Hydrolyzing Complex at Microtubule Ends. *Mol Cell* 11, 445–457 (2003).

Iakoucheva, L. M. et al. The importance of intrinsic disorder for protein phosphorylation. *Nucleic Acids Res* 32, 1037–1049 (2004).

IARC (2018) «Globocan », <http://gco.iarc.fr>.

INCa. (2017). *Cancer en France* ISBN net : 978-2-37219-381-8

Jang, Y.-J., et al. Phosphorylation of Threonine 210 and the Role of Serine 137 in the Regulation of Mammalian Polo-like Kinase. *J Biol Chem* 277, 44115–44120 (2002).

Jensen, O. N. Modification-specific proteomics: characterization of post-translational modifications by mass spectrometry. *Curr Opin Chem Biol* 8, 33–41 (2004).

Jensen, M. R., Ruigrok, R. W. & Blackledge, M. Describing intrinsically disordered proteins at atomic resolution by NMR. *Curr Opin Struct Biol* 23, 426–435 (2013).

Jeyasekharan, A. D. et al. A cancer-associated BRCA2 mutation reveals masked nuclear export signals controlling localization. *Nat Struct Mol Biol* 20, 1191–1198 (2013).

Johnson, T. M., Antrobus, R. & Johnson, L. N. Plk1 Activation by Ste20-like Kinase (Slk) Phosphorylation and Polo-Box Phosphopeptide Binding Assayed with the Substrate Translationally Controlled Tumor Protein (TCTP). *Biochemistry-us* 47, 3688–3696 (2008).

Jones, D. T. & Ward, J. J. Prediction of disordered regions in proteins from position specific score matrices. *Proteins Struct Funct Bioinform* 53, 573–578 (2003).

Jorda, J., et al. Protein tandem repeats - the more perfect, the less structured. *Febs J* 277, 2673–2682 (2010).

Joss, D. & Häussinger, D. Design and applications of lanthanide chelating tags for pseudocontact shift NMR spectroscopy with biomacromolecules. *Prog Nucl Mag Res Sp* 114, 284–312 (2019).

Julien, M., et al. Multiple Site-Specific Phosphorylation of IDPs Monitored by NMR. *Methods Mol Biol*. 2141:793-817 (2020).

Kamińska, M., Ciszewski, T., Łopacka-Szatan, K., Miotła, P. & Starosławska, E. Breast cancer risk factors. *Menopausal Rev* 3, 196–202 (2015).

Kang, Y. H. et al. Self-Regulated Plk1 Recruitment to Kinetochores by the Plk1-PBIP1 Interaction Is Critical for Proper Chromosome Segregation. *Mol Cell* 24, 409–422 (2006).

- Kendrew, J.C., et al. Structure of myoglobin: A three-dimensional Fourier synthesis at 2 Å resolution. *Nature* 185(4711):422–427 (1960).
- Kettenbach, A. N. et al. Rapid Determination of Multiple Linear Kinase Substrate Motifs by Mass Spectrometry. *Chem Biol* 19, 608–618 (2012).
- Kim, S., Wu, K.-P. & Baum, J. Fast hydrogen exchange affects ¹⁵N relaxation measurements in intrinsically disordered proteins. *J Biomol Nmr* 55, 249–256 (2013).
- King, M.-C., Marks, J. H. & Mandell, J. B. Breast and Ovarian Cancer Risks Due to Inherited Mutations in BRCA1 and BRCA2. *Science* 302, 643–646 (2003).
- Kinoshita, E., et al Phosphate-binding Tag, a New Tool to Visualize Phosphorylated Proteins. *Mol Cell Proteomics* 5, 749–757 (2006).
- Kitada, K., et al. A multicopy suppressor gene of the *Saccharomyces cerevisiae* G1 cell cycle mutant gene *dbf4* encodes a protein kinase and is identified as CDC5. *Mol Cell Biol* 13, 4445–4457 (1993).
- Kiyomitsu, T. & Cheeseman, I. M. Chromosome- and spindle-pole-derived signals generate an intrinsic code for spindle position and orientation. *Nat Cell Biol* 14, 311–317 (2012).
- Knecht, R., Oberhauser, C. & Strebhardt, K. PLK (polo-like kinase), a new prognostic marker for oropharyngeal carcinomas. *Int J Cancer*. 89(6):535-6 (2000).
- Kosten, J. et al. Efficient Modification of Alpha-Synuclein Serine 129 by Protein Kinase CK1 Requires Phosphorylation of Tyrosine 125 as a Priming Event. *ACS Chem Neurosci* 5, 1203–1208 (2014).
- Kothe, M. et al. Structure of the Catalytic Domain of Human Polo-like Kinase 1 *Biochemistry* 46, 5960–5971 (2007).
- Kovacs, D. & Tompa, P. Diverse functional manifestations of intrinsic structural disorder in molecular chaperones. *Biochem Soc T* 40, 963–968 (2012).
- Krishnan, N. et al. Targeting the disordered C terminus of PTP1B with an allosteric inhibitor. *Nat Chem Biol* 10, 558–566 (2014).
- Kristensen, C. N., et al. Depletion of DSS1 protein disables homologous recombinational repair in human cells. *Mutat Res Fundam Mol Mech Mutagen* 694, 60–64 (2010).
- Kriwacki, R. W., et al. Structural studies of p21^{Waf1}/Cip1/Sdi1 in the free and Cdk2-bound state: conformational disorder mediates binding diversity. *Proc National Acad Sci* 93, 11504–11509 (1996).
- Kwon, M. et al. Brca2 abrogation engages with the alternative lengthening of telomeres via break-induced replication. *Febs J* 286, 1841–1858 (2019).
- Kwon, M. et al. Paradoxical delay of senescence upon depletion of BRCA2 in telomerase-deficient worms. *Febs Open Bio* 6, 1016–1024 (2016).

- Lacy, E. R. et al. p27 binds cyclin–CDK complexes through a sequential mechanism involving binding-induced protein folding. *Nat Struct Mol Biol* 11, 358–364 (2004).
- Landrieu, I., et al. Exploring the molecular function of PIN1 by nuclear magnetic resonance. *Curr Protein Pept Sci.* (3):179-94 (2006).
- Lara-Gonzalez, P., Westhorpe, F. G. & Taylor, S. S. The Spindle Assembly Checkpoint. *Curr Biol* 22, R966–R980 (2012).
- Le, H. P. et al. DSS1 and ssDNA regulate oligomerization of BRCA2. *Nucleic Acids Res* 48, gkaa555- (2020).
- Lee, C. W., et al. Graded enhancement of p53 binding to CREB-binding protein (CBP) by multisite phosphorylation. *Proc National Acad Sci* 107, 19290–19295 (2010).
- Lee, K. S. et al. Mechanisms of mammalian polo-like kinase 1 (Plk1) localization: Self-versus non-self-priming. *Cell Cycle* 7, 141–145 (2008).
- Lee, K. S., et al. Self-regulated mechanism of Plk1 localization to kinetochores: lessons from the Plk1-PBIP1 interaction. *Cell Div* 3, 4 (2008).
- Lee, M. & Venkitaraman, A. R. A cancer-associated mutation inactivates a region of the high-mobility group protein HMG20b essential for cytokinesis. *Cell Cycle* 13, 2554–2563 (2014).
- Lee, M., Daniels, M. J. & Venkitaraman, A. R. Phosphorylation of BRCA2 by the Polo-like kinase Plk1 is regulated by DNA damage and mitotic progression. *Oncogene* 23, 865–872 (2004).
- Lee, M., et al. A mitotic function for the high-mobility group protein HMG20b regulated by its interaction with the BRC repeats of the BRCA2 tumor suppressor. *Oncogene* 30, 3360–3369 (2011).
- Lee, S. A. & Baker, M. D. Analysis of DNA repair and recombination responses in mouse cells depleted for Brca2 by SiRNA. *Dna Repair* 6, 809–817 (2007).
- Lera, R. F. et al. Plk1 protects kinetochore–centromere architecture against microtubule pulling forces. *Embo Rep* 20, (2019).
- Li, J. et al. Structural and Functional Versatility of the FHA Domain in DNA-Damage Signaling by the Tumor Suppressor Kinase Chk2. *Mol Cell* 9, 1045–1054 (2002).
- Li, P. et al. Phase transitions in the assembly of multivalent signalling proteins. *Nature* 483, 336–340 (2012).
- Li, S. S.-L. et al. Molecular characterization of germline mutations in the BRCA1 and BRCA2 genes from breast cancer families in Taiwan. *Hum Genet* 104, 201–204 (1999).
- Li, T.-F. et al. Overexpression of kinesin superfamily members as prognostic biomarkers of breast cancer. *Cancer Cell Int* 20, 123 (2020).

- Lin, H.-R., et al. M Phase-specific Phosphorylation of BRCA2 by Polo-like Kinase 1 Correlates with the Dissociation of the BRCA2-P/CAF Complex. *J Biol Chem* 278, 35979–35987 (2003).
- Lin, H.R., et al. M phase-specific phosphorylation of BRCA2 by Polo-like kinase 1 correlates with the dissociation of the BRCA2-P/CAF complex. *J Biol Chem* 278(38):35979-87 (2003).
- Liu, J. et al. Ubiquitin-specific protease 21 stabilizes BRCA2 to control DNA repair and tumor growth. *Nat Commun* 8, 137 (2017).
- Liu, F. et al. Serendipitous alkylation of a Plk1 ligand uncovers a new binding channel. *Nat Chem Biol* 7, 595–601 (2011).
- Liu, J., et al. Human BRCA2 protein promotes RAD51 filament formation on RPA-covered single-stranded DNA. *Nat Struct Mol Biol* 17, 1260–1262 (2010).
- Liu, J., et al. Inhibition of breast and brain cancer cell growth by BCCIP α , an evolutionarily conserved nuclear protein that interacts with BRCA2. *Oncogene* 20, 336–345 (2001).
- Liu, L., Zhang, M. & Zou, P. Expression of PLK1 and survivin in diffuse large B-cell lymphoma. *Leuk Lymphoma* 48(11):2179-83 (2007).
- Liu, X. Targeting Polo-Like Kinases: A Promising Therapeutic Approach for Cancer Treatment. *Transl Oncol* 8, 185–195 (2015).
- Livingstone, C.D. & Barton, G. J., Protein Sequence Alignments: A Strategy for the Hierarchical Analysis of Residue Conservation, *Comp. Appl. Bio. Sci.*, 9, 745-756. (1993).
- Lowery, D. M. et al. Proteomic screen defines the Polo-box domain interactome and identifies Rock2 as a Plk1 substrate. *Embo J* 26, 2262–2273 (2007).
- Lu, L.-Y. et al. Polo-Like Kinase 1 Is Essential for Early Embryonic Development and Tumor Suppression ∇ ‡. *Mol Cell Biol* 28, 6870–6876 (2008).
- Ludwig, K. K., Neuner, J., Butler, A., Geurts, J. L. & Kong, A. L. Risk reduction and survival benefit of prophylactic surgery in BRCA mutation carriers, a systematic review. *Am J Surg* 212, 660–669 (2016).
- Luo, Y., Ma, B., Nussinov, R. & Wei, G. Structural Insight into Tau Protein's Paradox of Intrinsically Disordered Behavior, Self-Acetylation Activity, and Aggregation. *J Phys Chem Lett* 5, 3026–3031 (2014).
- Ma, D.-D., Wang, D.-H. & Yang, W.-X. Kinesins in spermatogenesis. *Biol Reprod* 96, 267–276 (2017).
- Macûrek, L. et al. Polo-like kinase-1 is activated by aurora A to promote checkpoint recovery. *Nature* 455, 119–123 (2008).
- Malik, S., Saito, H., Takaoka, M., Miki, Y. & Nakanishi, A. BRCA2 mediates centrosome cohesion via an interaction with cytoplasmic dynein. *Cell Cycle* 15, 1–12 (2016).

- Malinowska, L., Kroschwald, S. & Alberti, S. Protein disorder, prion propensities, and self-organizing macromolecular collectives. *Biochimica Et Biophysica Acta Bba - Proteins Proteom* 1834, 918–931 (2013).
- Manning, G., et al. The Protein Kinase Complement of the Human Genome. *Science* 298, 1912–1934 (2002).
- Mao, A. H., et al. Net charge per residue modulates conformational ensembles of intrinsically disordered proteins. *Proc National Acad Sci* 107, 8183–8188 (2010).
- Marmorstein, L. Y. et al. A Human BRCA2 Complex Containing a Structural DNA Binding Component Influences Cell Cycle Progression. *Cell* 104, 247–257 (2001).
- Marsh, J. A. et al. Structural Diversity in Free and Bound States of Intrinsically Disordered Protein Phosphatase 1 Regulators. *Structure* 18, 1094–1103 (2010).
- Martinez-Useros, J. & Garcia-Foncillas, J. The Role of BRCA2 Mutation Status as Diagnostic, Predictive, and Prognosis Biomarker for Pancreatic Cancer. *Biomed Res Int* 2016, 1–8 (2016).
- Martinez, J. S. et al. BRCA2 regulates DMC1-mediated recombination through the BRC repeats. *Proc National Acad Sci* 113, 3515–3520 (2016).
- Matheis, G. & Whitaker, J. R. 31P NMR chemical shifts of phosphate covalently bound to proteins. *Int J Biochem* 16, 867–873 (1984).
- Matsumoto, T. et al. Polo-like kinases mediate cell survival in mitochondrial dysfunction. *Proc National Acad Sci* 106, 14542–14546 (2009).
- Matsumura, S., Toyoshima, F. & Nishida, E. Polo-like Kinase 1 Facilitates Chromosome Alignment during Prometaphase through BubR1. *J Biol Chem* 282, 15217–15227 (2007).
- Matsuoka, S. et al. ATM and ATR Substrate Analysis Reveals Extensive Protein Networks Responsive to DNA Damage. *Science* 316, 1160–1166 (2007).
- Mazet, F. et al. A high-density immunoblotting methodology for quantification of total protein levels and phosphorylation modifications. *Sci Rep-uk* 5, 16995 (2015).
- Metallo, S. J. Intrinsically disordered proteins are potential drug targets. *Curr Opin Chem Biol* 14, 481–488 (2010).
- Mersch, J. et al. Cancers associated with BRCA1 and BRCA2 mutations other than breast and ovarian. *Cancer* 121, 269–275 (2015).
- Mesman, R. L. S. et al. The functional impact of variants of uncertain significance in BRCA2. *Genetics Medicine Official J Am Coll Medical Genetics* 21, 293–302 (2018).
- Meyer, S. et al. Fanconi anaemia, BRCA2 mutations and childhood cancer: a developmental perspective from clinical and epidemiological observations with implications for genetic counselling. *J Med Genet* 51, 71 (2014).

Midding, E. et al. Men With a “Woman’s Disease”: Stigmatization of Male Breast Cancer Patients—A Mixed Methods Analysis. *Am J Men’s Heal* 12, 2194–2207 (2018).

Midding, E. et al. Social Support of Male Breast Cancer Patients—a Mixed-Methods Analysis. *Am J Men’s Heal* 13, 1557988319870001 (2019).

Milles, S., Salvi, N., Blackledge, M. & Jensen, M. R. Characterization of intrinsically disordered proteins and their dynamic complexes: From in vitro to cell-like environments. *Prog Nucl Mag Res Sp* 109, 79–100 (2018).

Mittag, T. et al. Dynamic equilibrium engagement of a polyvalent ligand with a single-site receptor. *Proc National Acad Sci* 105, 17772–17777 (2008).

Mittag, T. et al. Structure/Function Implications in a Dynamic Complex of the Intrinsically Disordered Sic1 with the Cdc4 Subunit of an SCF Ubiquitin Ligase. *Structure* 18, 494–506 (2010).

Moesa, H. A., et al. Chemical composition is maintained in poorly conserved intrinsically disordered regions and suggests a means for their classification. *Mol Biosyst* 8, 3262–3273 (2012).

Mohan, A. et al. Analysis of Molecular Recognition Features (MoRFs). *J Mol Biol* 362, 1043–1059 (2006).

Monahan, Z. et al. Phosphorylation of the FUS low-complexity domain disrupts phase separation, aggregation, and toxicity. *Embo J* 36, 2951–2967 (2017).

Mondal, G. et al. BRCA2 Localization to the Midbody by Filamin A Regulates CEP55 Signaling and Completion of Cytokinesis. *Dev Cell* 23, 137–152 (2012).

Moon, R. J., Tremblay, E. S. & Morris, K. M. Distribution and Metabolism of ¹⁴C-Tryptophan in Normal and Endotoxin-Poisoned Mice. *Infect Immun* 8, 604–611 (1973).

Moran, A. et al. Risk of cancer other than breast or ovarian in individuals with BRCA1 and BRCA2 mutations. *Fam Cancer* 11, 235–242 (2012).

Morita, E. et al. Human ESCRT and ALIX proteins interact with proteins of the midbody and function in cytokinesis. *Embo J* 26, 4215–4227 (2007).

Müller-Späth, S. et al. From the Cover: Charge interactions can dominate the dimensions of intrinsically disordered proteins. *P Natl Acad Sci Usa* 107, 14609–14 (2010).

Müntener, T., Häussinger, D., Selenko, P. & Theillet, F.-X. In-Cell Protein Structures from 2D NMR Experiments. *J Phys Chem Lett* 7, 2821–2825 (2016).

Musselman, C. A., Lalonde, M.-E., Côté, J. & Kutateladze, T. G. Perceiving the epigenetic landscape through histone readers. *Nat Struct Mol Biol* 19, 1218–1227 (2012).

- Mustofa, Md. K., Tanoue, Y., Tateishi, C., Vaziri, C. & Tateishi, S. Roles of Chk2/CHEK2 in guarding against environmentally induced DNA damage and replication-stress. *Environ Mol Mutagen* 61, 730–735 (2020).
- Mylona, A. et al. Opposing effects of Elk-1 multisite phosphorylation shape its response to ERK activation. *Science* 354, 233–237 (2016).
- Nakajima, H., et al Identification of a Consensus Motif for Plk (Polo-like Kinase) Phosphorylation Reveals Myt1 as a Plk1 Substrate. *J Biol Chem* 278, 25277–25280 (2003).
- Nakanishi, A. et al. Interference with BRCA2, which localizes to the centrosome during S and early M phase, leads to abnormal nuclear division. *Biochem Biophys Res Commun* 355, 34–40 (2007).
- Nash, P. et al. Multisite phosphorylation of a CDK inhibitor sets a threshold for the onset of DNA replication. *Nature* 414, 514–521 (2001).
- Nathanson, K. L., et al. Breast cancer genetics: What we know and what we need. *Nat Med* 7, 552–556 (2001).
- Navon, G., et al. High-resolution ³¹P nuclear magnetic resonance studies of metabolism in aerobic *Escherichia coli* cells. *Proc National Acad Sci* 74, 888–891 (1977).
- Neef, R. et al. Choice of Plk1 docking partners during mitosis and cytokinesis is controlled by the activation state of Cdk1. *Nat Cell Biol* 9, 436–444 (2007).
- Neef, R. et al. Phosphorylation of mitotic kinesin-like protein 2 by polo-like kinase 1 is required for cytokinesis. *J Cell Biology* 162, 863–876 (2003).
- Nicolai, C. von, Ehlén, Å., Martin, C., Zhang, X. & Carreira, A. A second DNA binding site in human BRCA2 promotes homologous recombination. *Nat Commun* 7, 12813 (2016).
- Nielsen, J. T. & Mulder, F. A. A. Quality and bias of protein disorder predictors. *Sci Rep-uk* 9, 5137 (2019).
- Nogueira, M. O. et al. Monitoring HPV-16 E7 phosphorylation events. *Virology* 503, 70–75 (2017).
- Nott, T. J. et al. Phase Transition of a Disordered Nuage Protein Generates Environmentally Responsive Membraneless Organelles. *Mol Cell* 57, 936–947 (2015).
- Nuland, N. A. J. van et al. The High-resolution Structure of the Histidine-containing Phosphocarrier Protein HPr from *Escherichia coli* Determined by Restrained Molecular Dynamics from Nuclear Magnetic Resonance Nuclear Overhauser Effect Data. *J Mol Biol* 237, 544–559 (1994).
- Nuland, N. A. J. van et al. The NMR determination of the IIAMtl binding site on HPr of the *Escherichia coli* phosphoenol pyruvate-dependent phosphotransferase system. *FEBS Lett* 315, 11–15 (1993).

- O’Neil, B. H. et al. A phase II/III randomized study to compare the efficacy and safety of rigosertib plus gemcitabine versus gemcitabine alone in patients with previously untreated metastatic pancreatic cancer. *Ann Oncol* 26, 1923–1929 (2015).
- Oates, M. E. et al. D2P2: database of disordered protein predictions. *Nucleic Acids Res* 41, D508–D516 (2013).
- Ohkura, H., Hagan, I.M. & Glover, D.M. The conserved *Schizosaccharomyces pombe* kinase *plp1*, required to form a bipolar spindle, the actin ring, and septum, can drive septum formation in G1 and G2 cells. *Genes Dev* 9(9):1059-73 (1995).
- Ohta, T., Sato, K. & Wu, W. The BRCA1 ubiquitin ligase and homologous recombination repair. *FEBS Lett* 585, 2836–2844 (2011).
- Oldfield, C. J. et al. Flexible nets: disorder and induced fit in the associations of p53 and 14-3-3 with their partners. *BMC Genomics* 9, S1 (2008).
- Oliver, A. W., et al. Structural basis for recruitment of BRCA2 by PALB2. *EMBO Rep* 10, 990–996 (2009).
- Örd, M., et al. Cyclin-Specific Docking Mechanisms Reveal the Complexity of M-CDK Function in the Cell Cycle. *Mol Cell*. 2019 Jul 11;75(1):76-89.e3
- Örd, M., et al. Proline-Rich Motifs Control G2-CDK Target Phosphorylation and Priming an Anchoring Protein for Polo Kinase Localization. *Cell Rep*. 2020;31(11):107757.
- Ottman, R., et al. Familial breast cancer in a population-based series. *Am J Epidemiol* 123, 15–21 (1986).
- Ouyang, B., Wang, Y. & Wei, D. *Caenorhabditis elegans* contains structural homologs of human *prk* and *plk*. *DNA Seq* 10(2):109-13 (1999).
- Page, F. L. et al. BRCA1 and BRCA2 are necessary for the transcription-coupled repair of the oxidative 8-oxoguanine lesion in human cells. *Cancer Res* 60, 5548–52 (2000).
- Pak, C. W. et al. Sequence Determinants of Intracellular Phase Separation by Complex Coacervation of a Disordered Protein. *Mol Cell* 63, 72–85 (2016).
- Park, I. et al. HDAC2/3 binding and deacetylation of BubR1 initiates spindle assembly checkpoint silencing. *FEBS J* 284, 4035–4050 (2017).
- Park, J.-Y., Zhang, F. & Andreassen, P. R. PALB2: The hub of a network of tumor suppressors involved in DNA damage responses. *Biochimica Et Biophysica Acta Bba - Rev Cancer* 1846, 263–275 (2014).
- Patel, A. et al. A Liquid-to-Solid Phase Transition of the ALS Protein FUS Accelerated by Disease Mutation. *Cell* 162, 1066–1077 (2015).
- Patel, K. J. et al. Involvement of *Brca2* in DNA Repair. *Mol Cell* 1, 347–357 (1998).

Patil, A. A., Chiang, C.-K., Wen, C.-H. & Peng, W.-P. Forced dried droplet method for MALDI sample preparation. *Anal Chim Acta* 1031, 128–133 (2018).

Pellegrini, L. et al. Insights into DNA recombination from the structure of a RAD51–BRCA2 complex. *Nature* 420, 287–293 (2002).

Peng, Z. et al. Exceptionally abundant exceptions: comprehensive characterization of intrinsic disorder in all domains of life. *Cell Mol Life Sci* 72, 137–151 (2015).

Perutz, M.F., et al. Structure of haemoglobin: a three-dimensional Fourier synthesis at 5.5-Å resolution, obtained by X-ray analysis. *Nature* 185(4711):416–422 (1960).

Petitalot, A. et al. Combining Homologous Recombination and Phosphopeptide-binding Data to Predict the Impact of BRCA1 BRCT Variants on Cancer Risk. *Mol Cancer Res* 17, molcanres.0357.2017 (2018).

Petsalaki, E. & Zachos, G. Chk2 prevents mitotic exit when the majority of kinetochores are unattached Chk2 delays anaphase onset. *J Cell Biology* 205, 339–356 (2014).

Pillai-Kastoori, L. et al. Antibody validation for Western blot: By the user, for the user. *J Biol Chem* 295, 926–939 (2020).

Pillai-Kastoori, L., Schutz-Geschwender, A. R. & Harford, J. A. A systematic approach to quantitative Western blot analysis. *Anal Biochem* 593, 113608 (2020).

Plon, S. E. et al. Sequence variant classification and reporting: recommendations for improving the interpretation of cancer susceptibility genetic test results. *Hum Mutat* 29, 1282–1291 (2008).

Prabakaran, S. et al. Comparative analysis of Erk phosphorylation suggests a mixed strategy for measuring phospho-form distributions. *Mol Syst Biol* 7, 482 (2011).

Prates, E. T. et al. The impact of O -glycan chemistry on the stability of intrinsically disordered proteins. *Chem Sci* 9, 3710–3715 (2018).

Prus, G., Hoegl, A., Weinert, B. T. & Choudhary, C. Analysis and Interpretation of Protein Post-Translational Modification Site Stoichiometry. *Trends Biochem Sci* 44, 943–960 (2019).

Qi, H. et al. Nuclear Magnetic Resonance Spectroscopy Characterization of Interaction of Tau with DNA and Its Regulation by Phosphorylation. *Biochemistry-us* 54, 1525–1533 (2015).

Qian, Y.-W., Erikson, E. & Maller, J. L. Mitotic Effects of a Constitutively Active Mutant of the *Xenopus* Polo-Like Kinase Plx1. *Mol Cell Biol* 19, 8625–8632 (1999).

Raab, M. et al. Modulation of the Allosteric Communication between the Polo-Box Domain and the Catalytic Domain in Plk1 by Small Compounds. *Acs Chem Biol* 13, 1921–1931 (2018).

Ravi, A., et al. Breast Cancer in Men. *Am J Men's Heal* 6, 51–58 (2012).

- Reinhardt, H. C. & Yaffe, M. B. Phospho-Ser/Thr-binding domains: navigating the cell cycle and DNA damage response. *Nat Rev Mol Cell Bio* 14, 563–580 (2013).
- Rezaei-Ghaleh, N., Blackledge, M. & Zweckstetter, M. Intrinsically Disordered Proteins: From Sequence and Conformational Properties toward Drug Discovery. *Chembiochem* 13, 930–950 (2012).
- Riback, J. A. et al. Stress-Triggered Phase Separation Is an Adaptive, Evolutionarily Tuned Response. *Cell* 168, 1028–1040.e19 (2017).
- Richet, N. et al. Structural insight into how the human helicase subunit MCM2 may act as a histone chaperone together with ASF1 at the replication fork. *Nucleic Acids Res* 43, 1905–1917 (2015).
- Roey, K. V., Gibson, T. J. & Davey, N. E. Motif switches: decision-making in cell regulation. *Curr Opin Struc Biol* 22, 378–385 (2012).
- Rogerson, D. T. et al. Efficient genetic encoding of phosphoserine and its nonhydrolyzable analog. *Nat Chem Biol* 11, 496–503 (2015).
- Romero, P. et al. Sequence complexity of disordered protein. *Proteins Struct Funct Genetics* 42, 38–48 (2000).
- Romero, P., Obradovic, Z. & Dunker, A.K. Natively disordered proteins: functions and predictions. *Appl Bioinformatics* 3(2-3):105-13 (2004).
- Rudolf, A. F., Skovgaard, T., Knapp, S., Jensen, L. J. & Berthelsen, J. A Comparison of Protein Kinases Inhibitor Screening Methods Using Both Enzymatic Activity and Binding Affinity Determination. *Plos One* 9, e98800 (2014).
- Ryser, S. et al. Distinct Roles of BARD1 Isoforms in Mitosis: Full-Length BARD1 Mediates Aurora B Degradation, Cancer-Associated BARD1 β Scaffolds Aurora B and BRCA2. *Cancer Res* 69, 1125–1134 (2009).
- Sangodkar, J. et al. All roads lead to PP2A: exploiting the therapeutic potential of this phosphatase. *Febs J* 283, 1004–1024 (2016).
- Sanhaji, M., et al. Mitotic centromere-associated kinesin (MCAK): a potential cancer drug target. *Oncotarget* 2, 935–947 (2011).
- Santaguida, S. & Amon, A. Short- and long-term effects of chromosome mis-segregation and aneuploidy. *Nat Rev Mol Cell Bio* 16, 473–485 (2015).
- Santé publique (2019) « Taux de participation au programme de dépistage organisé du cancer du sein 2017-2018 », <https://www.santepubliquefrance.fr/maladies-et-traumatismes/cancers/cancer-du-sein/articles/taux-de-participation-au-programme-de-dépistage-organise-du-cancer-du-sein-2017-2018> (19/06/2019)
- Santner, A. A. et al. Sweeping Away Protein Aggregation with Entropic Bristles: Intrinsically Disordered Protein Fusions Enhance Soluble Expression. *Biochemistry-us* 51, 7250–7262 (2012).

Sato, K. et al. HSF2BP negatively regulates homologous recombination in DNA interstrand crosslink repair. *Nucleic Acids Res* 48, 2442–2456 (2020).

Savage, K. I. & Harkin, D. P. BRCA1, a ‘complex’ protein involved in the maintenance of genomic stability. *Febs J* 282, 630–646 (2015).

Schanda, P., Kupče, Ě. & Brutscher, B. SOFAST-HMQC Experiments for Recording Two-dimensional Deteronuclear Correlation Spectra of Proteins within a Few Seconds. *J Biomol Nmr* 33, 199–211 (2005).

Scheeff, E. D., et al. Structure of the Pseudokinase VRK3 Reveals a Degraded Catalytic Site, a Highly Conserved Kinase Fold, and a Putative Regulatory Binding Site. *Structure* 17, 128–138 (2009).

Schlacher, K. et al. Double-Strand Break Repair-Independent Role for BRCA2 in Blocking Stalled Replication Fork Degradation by MRE11. *Cell* 145, 529–542 (2011).

Schlessinger, A. et al. Protein disorder—a breakthrough invention of evolution? *Curr Opin Struc Biol* 21, 412–418 (2011).

Schmucker, S. & Sumara, I. Molecular dynamics of PLK1 during mitosis. *Mol Cell Oncol* 1, e954507 (2014).

Schneider, R., Blackledge, M. & Jensen, M. R. Elucidating binding mechanisms and dynamics of intrinsically disordered protein complexes using NMR spectroscopy. *Curr Opin Struc Biol* 54, 10–18 (2019).

Schweiger, R. & Linial, M. Cooperativity within proximal phosphorylation sites is revealed from large-scale proteomics data. *Biol Direct* 5, 6 (2010).

Segall, Y., et al. Direct observation and elucidation of the structures of aged and nonaged phosphorylated cholinesterases by ³¹P NMR spectroscopy. *Biochemistry* 32(49):13441-50 (1993).

Seki, A., et al. Bora and the Kinase Aurora A Cooperatively Activate the Kinase Plk1 and Control Mitotic Entry. *Science* 320, 1655–1658 (2008).

Selenko, P. et al. In situ observation of protein phosphorylation by high-resolution NMR spectroscopy. *Nat Struct Mol Biol* 15, 321–329 (2008).

Shahid, T. et al. Structure and mechanism of action of the BRCA2 breast cancer tumor suppressor. *Nat Struct Mol Biol* 21, 962–968 (2014).

Shahid, T. et al. Structure and mechanism of action of the BRCA2 breast cancer tumor suppressor. *Nat Struct Mol Biol* 21, 962–968 (2014).

Shammas, S. L., Rogers, J. M., Hill, S. A. & Clarke, J. Slow, Reversible, Coupled Folding and Binding of the Spectrin Tetramerization Domain. *Biophys J* 103, 2203–2214 (2012).

- Sharan, S. K. et al. BRCA2 deficiency in mice leads to meiotic impairment and infertility. *Development* 131, 131–142 (2004).
- Sharan, S. K. et al. Embryonic lethality and radiation hypersensitivity mediated by Rad51 in mice lacking Brca2. *Nature* 386, 804–810 (1997).
- Sharma, B., Kaur, R. P., Raut, S. & Munshi, A. BRCA1 mutation spectrum, functions and therapeutic strategies: The story so far. *Curr Prob Cancer* 42, 189–207 (2018).
- Sharma, P. et al. A cryptic hydrophobic pocket in the polo-box domain of the polo-like kinase PLK1 regulates substrate recognition and mitotic chromosome segregation. *Sci Rep-uk* 9, 15930 (2019).
- Shinohara, Y. et al. Temperature-Sensitive Substrate and Product Binding Underlie Temperature-Compensated Phosphorylation in the Clock. *Mol Cell* 67, 783-798.e20 (2017).
- Siaud, N. et al. Plasticity of BRCA2 Function in Homologous Recombination: Genetic Interactions of the PALB2 and DNA Binding Domains. *Plos Genet* 7, e1002409 (2011).
- Siddique, Rao & Reddy. CBP-mediated post-translational N-glycosylation of BRCA2. *Int J Oncol* (2009).
- Siddiqui, M. Q. et al. Studies of protein–protein interactions in Fanconi anemia pathway to unravel the DNA interstrand crosslink repair mechanism. *Int J Biol Macromol* 104, 1338–1344 (2017).
- Simidzu, M., et al. In Vivo Phosphorylation of Histones H1 and H5 in Calf Thymus and Chicken Erythrocyte as Studied by ³¹P Nuclear Magnetic Resonance Spectroscopy. *J Biochem* 351–358 (1987).
- Singh, P. et al. BUB1 and CENP-U, Primed by CDK1, Are the Main PLK1 Kinetochores Receptors in Mitosis. *Mol Cell* (2020)
- Skop, M., Lorentz, J., Jassi, M., Vesprini, D. & Einstein, G. “Guys Don’t Have Breasts”: The Lived Experience of Men Who Have BRCA Gene Mutations and Are at Risk for Male Breast Cancer. *Am J Men’s Heal* 12, 961–972 (2017).
- Smith, M. J. et al. Real-time NMR monitoring of biological activities in complex physiological environments. *Curr Opin Struc Biol* 32, 39–47 (2015).
- Smith, M. J., Neel, B. G. & Ikura, M. NMR-based functional profiling of RASopathies and oncogenic RAS mutations. *Proc National Acad Sci* 110, 4574–4579 (2013).
- Sopik, V., Phelan, C., Cybulski, C. & Narod, S. A. BRCA1 and BRCA2 mutations and the risk for colorectal cancer. *Clin Genet* 87, 411–418 (2015).
- Spänkuch-Schmitt, B., et al. Downregulation of human polo-like kinase activity by antisense oligonucleotides induces growth inhibition in cancer cells. *Oncogene* 21(20):3162-71 (2002).
- Steggmaier, M. et al. BI 2536, a Potent and Selective Inhibitor of Polo-like Kinase 1, Inhibits Tumor Growth In Vivo. *Curr Biol* 17, 316–322 (2007).

- Stein, A., Mosca, R. & Aloy, P. Three-dimensional modeling of protein interactions and complexes is going 'omics. *Curr Opin Struc Biol* 21, 200–208 (2011).
- Stevens, L. M. et al. Modulators of 14-3-3 Protein–Protein Interactions. *J Med Chem* 61, 3755–3778 (2017).
- Strebhardt, K. Multifaceted polo-like kinases: drug targets and antitargets for cancer therapy. *Nat Rev Drug Discov* 9, 643–660 (2010).
- Studer, R. A. et al. Evolution of protein phosphorylation across 18 fungal species. *Science* 354, 229–232 (2016).
- Suijkerbuijk, S. J. E., et al. Integration of Kinase and Phosphatase Activities by BUBR1 Ensures Formation of Stable Kinetochore-Microtubule Attachments. *Dev Cell* 23, 745–755 (2012).
- Sunkel, C. E. & Glover, D. M. polo, a mitotic mutant of *Drosophila* displaying abnormal spindle poles. *J Cell Sci* 89 (Pt 1), 25–38 (1988).
- Sy, S. M. H., Huen, M. S. Y. & Chen, J. PALB2 is an integral component of the BRCA complex required for homologous recombination repair. *Proc National Acad Sci* 106, 7155–7160 (2009).
- Szabo, C., et al. The Breast Cancer Information Core: Database design, structure, and scope. *Hum Mutat* 16, 123–131 (2000).
- Takahashi, K. et al. Tyrosine-Specific Dephosphorylation-Phosphorylation with Alkaline Phosphatases and Epidermal Growth Factor Receptor Kinase as Evidenced by 31P NMR Spectroscopy1. *J Biochem* 101, 1107–1114 (1987).
- Takaoka, M. & Miki, Y. BRCA1 gene: function and deficiency. *Int J Clin Oncol* 23, 36–44 (2018).
- Takaoka, M., Saito, H., Takenaka, K., Miki, Y. & Nakanishi, A. BRCA2 Phosphorylated by PLK1 Moves to the Midbody to Regulate Cytokinesis Mediated by Nonmuscle Myosin IIC. *Cancer Res* 74, 1518–1528 (2014).
- Talapatra, S. K., Harker, B. & Welburn, J. P. The C-terminal region of the motor protein MCAK controls its structure and activity through a conformational switch. *Elife* 4, e06421 (2015).
- Tan, D., Rice, W. J. & Sosa, H. Structure of the Kinesin13-Microtubule Ring Complex. *Structure* 16, 1732–1739 (2008).
- Tanenbaum, M. E., Medema, R. & Akhmanova, A. Regulation of localization and activity of the microtubule depolymerase MCAK. *Bioarchitecture* 1, 80–87 (2011).
- Tang, X. et al. Composite low affinity interactions dictate recognition of the cyclin-dependent kinase inhibitor Sic1 by the SCFCdc4 ubiquitin ligase. *Proc National Acad Sci* 109, 3287–3292 (2012).

Taniguchi, E., et al. Nuclear Translocation of Plk1 Mediated by Its Bipartite Nuclear Localization Signal. *J Biol Chem* 277, 48884–48888 (2002).

Tavtigian, S. V. et al. The complete BRCA2 gene and mutations in chromosome 13q-linked kindreds. *Nat Genet* 12, 333–337 (1996).

Terrier, V. P., Adihou, H., Arnould, M., Delmas, A. F. & Aucagne, V. A straightforward method for automated Fmoc-based synthesis of bio-inspired peptide crypto-thioesters. *Chem Sci* 7, 339–345 (2015).

Theillet, F.-X. et al. Cell signaling, post-translational protein modifications and NMR spectroscopy. *J Biomol Nmr* 54, 217–236 (2012).

Theillet, F.-X. et al. Site-Specific Mapping and Time-Resolved Monitoring of Lysine Methylation by High-Resolution NMR Spectroscopy. *J Am Chem Soc* 134, 7616–7619 (2012).

Theillet, F.-X. et al. Site-specific NMR mapping and time-resolved monitoring of serine and threonine phosphorylation in reconstituted kinase reactions and mammalian cell extracts. *Nat Protoc* 8, 1416–1432 (2013).

Theillet, F.-X. et al. The alphabet of intrinsic disorder. *Intrinsically Disord Proteins* 1, e24360 (2013).

Theillet, F.-X., et al. Paramagnetic relaxation enhancement to improve sensitivity of fast NMR methods: application to intrinsically disordered proteins. *J Biomol Nmr* 51, 487–495 (2011).

Thongwichian, R. et al. A Multiplexed NMR-Reporter Approach to Measure Cellular Kinase and Phosphatase Activities in Real-Time. *J Am Chem Soc* 137, 6468–6471 (2015).

Thorlacius, S. et al. Linkage to BRCA2 region in hereditary male breast cancer. *Lancet* 346, 544–545 (1995).

Thorslund, T., Esashi, F. & West, S. C. Interactions between human BRCA2 protein and the meiosis-specific recombinase DMC1. *Embo J* 26, 2915–2922 (2007).

Thorslund, T. et al. The breast cancer tumor suppressor BRCA2 promotes the specific targeting of RAD51 to single-stranded DNA. *Nat Struct Mol Biol* 17, 1263–1265 (2010).

Tokuriki, N., et al. Do viral proteins possess unique biophysical features? *Trends Biochem Sci* 34, 53–59 (2009).

Tompa, P. & Fuxreiter, M. Fuzzy complexes: polymorphism and structural disorder in protein–protein interactions. *Trends Biochem Sci* 33, 2–8 (2008).

Tompa, P., Davey, N. E., Gibson, T. J. & Babu, M. M. A Million Peptide Motifs for the Molecular Biologist. *Mol Cell* 55, 161–169 (2014).

Tompa, P., Schad, E., Tantos, A. & Kalmar, L. Intrinsically disordered proteins: emerging interaction specialists. *Curr Opin Struc Biol* 35, 49–59 (2015).

1. Thorslund, T. et al. The breast cancer tumor suppressor BRCA2 promotes the specific targeting of RAD51 to single-stranded DNA. *Nat Struct Mol Biol* 17, 1263–1265 (2010).
- Trego, K. S. et al. Non-catalytic Roles for XPG with BRCA1 and BRCA2 in Homologous Recombination and Genome Stability. *Mol Cell* 61, 535–546 (2016).
- Uversky, V. N. & Dunker, A. K. Understanding protein non-folding. *Biochimica Et Biophysica Acta Bba - Proteins Proteom* 1804, 1231–1264 (2010).
- Uversky, V. N. The alphabet of intrinsic disorder. *Intrinsically Disord Proteins* 1, e24684 (2013).
- Uversky, V. N. & Dunker, A. K. Understanding protein non-folding. *Biochimica Et Biophysica Acta Bba - Proteins Proteom* 1804, 1231–1264 (2010).
- Uversky, V. N., Gillespie, J. R. & Fink, A. L. Why are natively unfolded proteins unstructured under physiologic conditions? *Proteins Struct Funct Genetics* 41, 415–427 (2000).
- Vacic, V. & Iakoucheva, L. M. Disease mutations in disordered regions—exception to the rule? *Mol Biosyst* 8, 27–32 (2011).
- Valk, E. & Loog, M. Multiple Pho85-Dependent Mechanisms Control G1 Cyclin Abundance in Response to Nutrient Stress. *Mol Cell Biol* 33, 1270–1272 (2013).
- Van de Weerd, B.C.M. & Medema, R.H. Polo Like Kinases A Team in Control of the Division. *Cell cycle* 5, 853–864 (2005).
- Van Roey, K., et al. ELM resource: a compendium of conditional regulatory interaction interfaces. *Sci Signal*. 6(269) (2013).
- Varma, A. K., et al. Structural Basis for Cell Cycle Checkpoint Control by the BRCA1–CtIP Complex †, ‡. *Biochemistry-us* 44, 10941–10946 (2005).
- Virshup, D. M. & Shenolikar, S. From Promiscuity to Precision: Protein Phosphatases Get a Makeover. *Mol Cell* 33, 537–545 (2009).
- Vogel, H.J. & Bridger, W.A., Phosphorus-31 nuclear magnetic resonance pH titration studies of the phosphoproteins tropomyosin and glycogen phosphorylase a. *Can J Biochem Cell Biol*. 61(6):363-9 (1983).
- Vuzman, D. & Levy, Y. Intrinsically disordered regions as affinity tuners in protein–DNA interactions. *Mol Biosyst* 8, 47–57 (2011).
- Wang, J. et al. Crystal structure of a PP2A B56-BubR1 complex and its implications for PP2A substrate recruitment and localization. *Protein Cell* 7, 516–526 (2016).
- Wang, M. et al. PaxDb, a Database of Protein Abundance Averages Across All Three Domains of Life. *Mol Cell Proteomics* 11, 492–500 (2012).
- Wang, S.-C., et al. Changes in BRCA2 Expression during Progression of the Cell Cycle. *Biochem Bioph Res Co* 234, 247–251 (1997).

- Wang, X. et al. A dynamic charge-charge interaction modulates PP2A:B56 substrate recruitment. *Elife* 9, e55966 (2020).
- Wang, X., Andreassen, P. R. & D'Andrea, A. D. Functional Interaction of Monoubiquitinated FANCD2 and BRCA2/FANCD1 in Chromatin. *Mol Cell Biol* 24, 5850–5862 (2004).
- Wang, X., Bajaj, R., Bollen, M., Peti, W. & Page, R. Expanding the PP2A Interactome by Defining a B56-Specific SLiM. *Structure* 24, 2174–2181 (2016).
- Ward, J. J., et al. Prediction and Functional Analysis of Native Disorder in Proteins from the Three Kingdoms of Life. *J Mol Biol* 337, 635–645 (2004).
- Wauer, T. et al. Ubiquitin Ser65 phosphorylation affects ubiquitin structure, chain assembly and hydrolysis. *Embo J* 34, 307–325 (2015).
- Weinreb, P. H., et al, A Protein Implicated in Alzheimer's Disease and Learning, Is Natively Unfolded †. *Biochemistry-us* 35, 13709–13715 (1996).
- Wendt, C. & Margolin, S. Identifying breast cancer susceptibility genes – a review of the genetic background in familial breast cancer. *Acta Oncol* 1–12 (2019)
- Whitmarsh, A. J. & Davis, R. J. Multisite phosphorylation by MAPK. *Science* 354, 179–180 (2016).
- Williams, R. S., Green, R. & Glover, J. N. M. Crystal structure of the BRCT repeat region from the breast cancer-associated protein BRCA1. *Nat Struct Biol* 8, 838–842 (2001).
- Wong, L. E., Kim, T. H., Muhandiram, D. R., Forman-Kay, J. D. & Kay, L. E. NMR Experiments for Studies of Dilute and Condensed Protein Phases: Application to the Phase-Separating Protein CAPRIN1. *J Am Chem Soc* 142, 2471–2489 (2020).
- Wong, O. K. & Fang, G. Cdk1 phosphorylation of BubR1 controls spindle checkpoint arrest and Plk1-mediated formation of the 3F3/2 epitope. *J Cell Biology* 179, 611–617 (2007).
- Wood, D. J. & Endicott, J. A. Structural insights into the functional diversity of the CDK–cyclin family. *Open Biol* 8, 180112 (2018).
- Wooster, R. et al. Localization of a breast cancer susceptibility gene, BRCA2, to chromosome 13q12-13. *Science* 265, 2088–2090 (1994).
- Wright, P. E. & Dyson, H. J. Linking folding and binding. *Curr Opin Struc Biol* 19, 31–38 (2009).
- Wu, C.-G. et al. PP2A-B' holoenzyme substrate recognition, regulation and role in cytokinesis. *Cell Discov* 3, 17027 (2017).
- Wurzenberger, C. & Gerlich, D. W. Phosphatases: providing safe passage through mitotic exit. *Nat Rev Mol Cell Bio* 12, 469–482 (2011).

- Xu, J., Shen, C., Wang, T. & Quan, J. Structural basis for the inhibition of Polo-like kinase 1. *Nat Struct Mol Biol* 20, 1047–1053 (2013).
- Xu, Y. et al. Structure of the Protein Phosphatase 2A Holoenzyme. *Cell* 127, 1239–1251 (2006).
- Xu, Y., et al. Structure of a Protein Phosphatase 2A Holoenzyme: Insights into B55-Mediated Tau Dephosphorylation. *Mol Cell* 31, 873–885 (2008).
- Xue, B., Dunker, A.K. & Uversky, V.N. Orderly order in protein intrinsic disorder distribution: disorder in 3500 proteomes from viruses and the three domains of life. *J Biomol Struct Dyn* 30(2):137-49 (2012).
- Xue, B., Mizianty, M. J., Kurgan, L. & Uversky, V. N. Protein intrinsic disorder as a flexible armor and a weapon of HIV-1. *Cell Mol Life Sci* 69, 1211–1259 (2012).
- Yamaguchi, T. et al. Phosphorylation by Cdk1 induces Plk1-mediated vimentin phosphorylation during mitosis. *J Cell Biology* 171, 431–436 (2005).
- Yamashiro, S. et al. Myosin Phosphatase-Targeting Subunit 1 Regulates Mitosis by Antagonizing Polo-like Kinase 1. *Dev Cell* 14, 787–797 (2008).
- Yang, H. et al. BRCA2 Function in DNA Binding and Recombination from a BRCA2-DSS1-ssDNA Structure. *Science* 297, 1837–1848 (2002).
- Yano, K. et al. Nuclear Localization Signals of the BRCA2 Protein. *Biochem Bioph Res Co* 270, 171–175 (2000).
- Yata, K. et al. BRCA2 Coordinates the Activities of Cell-Cycle Kinases to Promote Genome Stability. *Cell Reports* 7, 1547–1559 (2014).
- Yata, K. et al. Plk1 and CK2 Act in Concert to Regulate Rad51 during DNA Double Strand Break Repair. *Mol Cell* 45, 371–383 (2012).
- Yekezare, M. & Pines, J. Escaping the firing squad: acetylation of BubR1 protects it from degradation in checkpoint cells. *Embo J* 28, 1991–1993 (2009).
- Yi, Y. W., Kang, H. J. & Bae, I. BRCA1 and Oxidative Stress. *Cancers* 6, 771–795 (2014).
- Young, M. A., et al. Dynamic Coupling between the SH2 and SH3 Domains of c-Src and Hck Underlies Their Inactivation by C-Terminal Tyrosine Phosphorylation. *Cell* 105, 115–126 (2001).
- Yuan, Y. & Shen, Z. Interaction with BRCA2 Suggests a Role for Filamin-1 (hsFLNa) in DNA Damage Response. *J Biol Chem* 276, 48318–48324 (2001).
- Zandt, S. E. V., Edwards, L. & Jordan, E. T. Lower epidural anesthesia use associated with labor support by student nurse doulas: Implications for intrapartal nursing practice. *Complement Ther Clin* 11, 153–160 (2005).

- Zannini, L., Delia, D. & Buscemi, G. CHK2 kinase in the DNA damage response and beyond. *J Mol Cell Biol* 6, 442–457 (2014).
- Zarin, T. et al. Proteome-wide signatures of function in highly diverged intrinsically disordered regions. *Elife* 8, e46883 (2019).
- Zemach, A., et al. Genome-Wide Evolutionary Analysis of Eukaryotic DNA Methylation. *Science* 328, 916–919 (2010).
- Zhang, G., Mendez, B. L., Sedgwick, G. G. & Nilsson, J. Two functionally distinct kinetochore pools of BubR1 ensure accurate chromosome segregation. *Nat Commun* 7, 12256 (2016).
- Zhang, J., Fujiwara, Y., Yamamoto, S. & Shibuya, H. A meiosis-specific BRCA2 binding protein recruits recombinases to DNA double-strand breaks to ensure homologous recombination. *Nat Commun* 10, 722 (2019).
- Zhang, L. et al. PLK1 Phosphorylates Mitotic Centromere-associated Kinesin and Promotes Its Depolymerase Activity. *J Biol Chem* 286, 3033–3046 (2011).
- Zhang, M. S. et al. Biosynthesis and genetic encoding of phosphothreonine through parallel selection and deep sequencing. *Nat Methods* 14, 729–736 (2017).
- Zhou, H. et al. Mechanism of DNA-Induced Phase Separation for Transcriptional Repressor VRN1. *Angewandte Chemie Int Ed* 58, 4858–4862 (2019).
- Zhou, Q. & Holloman, W. K. Dual DNA-binding domains shape the interaction of Brh2 with DNA. *Dna Repair* 22, 104–111 (2014).
- Zhou, Q., Kojic, M. & Holloman, W. K. DNA-binding Domain within the Brh2 N Terminus Is the Primary Interaction Site for Association with DNA. *J Biol Chem* 284, 8265–8273 (2009).
- Zhu, C. et al. Functional Analysis of Human Microtubule-based Motor Proteins, the Kinesins and Dyneins, in Mitosis/Cytokinesis Using RNA Interference. *Mol Biol Cell* 16, 3187–3199 (2005).
- Zhu, K., Shan, Z., Zhang, L. & Wen, W. Phospho-Pon Binding-Mediated Fine-Tuning of Plk1 Activity. *Structure* 24, 1110–1119 (2016).
- Zhu, P., Gafken, P. R., Mehl, R. A. & Cooley, R. B. A Highly Versatile Expression System for the Production of Multiply Phosphorylated Proteins. *Acs Chem Biol* 14, 1564–1572 (2019).
- Zhu, S. et al. Kinesin Kif2C in regulation of DNA double strand break dynamics and repair. *Elife* 9, e53402 (2020).
- Zorba, A. et al. Allosteric modulation of a human protein kinase with monobodies. *Proc National Acad Sci* 116, 13937–13942 (2019).
- Zorba, A. et al. Molecular mechanism of Aurora A kinase autophosphorylation and its allosteric activation by TPX2. *Elife* 3, e02667 (2014).

Titre : Phosphorylation mitotique de la région N-terminal de la protéine BRCA2 par la kinase Plk1 : identification, caractérisation et rôle dans les interactions protéine-protéine

Mots clés : phosphorylation, BRCA2, Plk1, RMN, interaction protéine-protéine

Résumé : BRCA2 est une oncoprotéine fréquemment mutée dans les cancers du sein héréditaires. Pour améliorer le diagnostic de ces cancers, plusieurs études moléculaires ont localisées des régions clés de BRCA2 et ont caractérisées l'impact de mutations sur les fonctions portées par ces régions.

Ici, je m'intéresse à la région aa 48 à aa 284 (BRCA2₄₈₋₂₈₄) de la protéine. Cette région conservée est désordonnée (Julien et al. 2020 Biomol. NMR Assign), c.à.d. qu'elle ne contient pas de structure secondaire stable. Cette région est également phosphorylée par la kinase Plk1 à l'entrée en mitose. Cependant, des études précédentes utilisant la spectrométrie de masse n'ont pas permis d'identifier précisément les sites phosphorylés, limitant ainsi leur caractérisation fonctionnelle. Pour contourner ce problème, nous avons utilisé la RMN en temps réel pour identifier et caractériser les phosphorylations de BRCA2₄₈₋₂₈₄, à l'échelle du résidu. Nous avons développé deux protocoles permettant d'étudier la phosphorylation de régions désordonnées pour une grande gamme de pH et températures (Julien et al. 2020 Methods Mol. Biol; Alik et al. 2020 Angew. Chem.). Ainsi, nous avons identifié que Plk1 phosphoryle BRCA2₄₈₋₂₈₄ sur deux sites conservés : pS193 et pT207. Ceci nous a servi de base pour la caractérisation de ces sites.

D'abord, nous avons identifié grâce à des méthodes biophysiques que BRCA2_{pT207} est un site d'interaction pour le domaine régulateur de Plk1. En collaboration avec l'équipe de Dr. Aura Carreira, nous avons montré que cette interaction est à la base d'un complexe quaternaire (BRCA2, Plk1, BubR1 et PP2A) qui régule l'alignement des chromosomes en métaphase (Ehlen et al. 2020. Nat Commun.). Nous avons aussi démontré que des mutations de BRCA2 issues de patientes ont un impact sur la phosphorylation de BRCA2 et la formation du complexe. Puis, nous avons réalisé des expériences de protéomique pour identifier de nouveaux partenaires mitotiques reconnaissant pBRCA2₄₈₋₂₈₄. Nous avons identifié Plk1 et d'autres protéines impliquées dans la mitose. J'ai débuté l'analyse structurale de deux nouveaux partenaires prometteurs : Kif2C et Chk2.

Nous avons aussi étudié le rôle de la préphosphorylation de BRCA2_{T77} par Cdk sur la phosphorylation par Plk1. Nous avons trouvé que BRCA2_{pT77} favorisait la phosphorylation de BRCA2_{S193} par Plk1.

Enfin, nous avons initié une étude structurale sur la kinase Plk1, surexprimée dans de nombreux cancers dont le cancer du sein. Ici, j'ai produit plusieurs constructions de la kinase qui serviront à sa caractérisation structurale.

Title : Plk1 mitotic phosphorylation in the N-terminal region of the BRCA2 protein: identification, characterization and role in protein interactions

Keywords : Phosphorylation, BRCA2, Plk1, NMR, protein-protein interaction

Abstract : BRCA2 is an oncoprotein frequently mutated in hereditary breast cancers. To improve the diagnosis of these cancers, several molecular studies have identified BRCA2 key positions and characterized mutations in these regions causing a BRCA2 loss of function. However, these studies mainly focused on the C-terminal globular domain of BRCA2.

Here, we characterized the N-terminal region of BRCA2 from aa 48 to aa 284 (BRCA2₄₈₋₂₈₄). This well-conserved region is disordered, i.e. it lacks stable secondary structure (Julien et al. 2020 Biomol. NMR Assign). It is also highly phosphorylated by the kinase Plk1 at the entry into mitosis. However, previous studies using mass spectrometry didn't allow to precisely identify all the phosphorylation sites, limiting their characterization. To circumvent this problem, we used real-time NMR to monitor phosphorylations of the N-terminal region of BRCA2, at the residue level. We developed 2 protocols for disordered regions allowing phosphorylation in a large range of temperatures and pHs (Julien et al. 2020 Methods Mol. Biol; Alik et al. 2020 Angew. Chem.). Then, we identified that Plk1 phosphorylates BRCA2 at 2 conserved positions: pS193 and pT207. We further searched for the function of these phosphoresidues.

First, we identified by biophysical methods that BRCA2_{pT207} creates a docking site for the regulatory domain of Plk1. In collaboration with the group of Dr. Aura Carreira, we showed that this interaction contributes to the assembly of a quaternary complex involving BRCA2, Plk1, BubR1 and PP2A that regulates chromosome alignment in mitosis (Ehlen et al. 2020. Nat Commun.). We also demonstrated that breast cancer variants impact the phosphorylation of BRCA2 and the formation of the complex in vitro and in cell. Then, we performed proteomics experiments to identify new mitotic partners specific to phospho-BRCA2, and found Plk1 as well as other proteins involved in mitosis. I started the characterization of two new BRCA2 partners: Ki2C and Chk2.

We also explored the role of Cdk1 phosphorylation of BRCA2_{T77} on further Plk1 phosphorylation. We found that early BRCA2_{T77} phosphorylation increases the phosphorylation rate of BRCA2_{S193} by Plk1.

Finally, we initiated a project about the Plk1 kinase, an interesting cancer-target as it is often overexpressed in several cancers, including breast cancers. Here, I produced several constructs of the kinase for further structural characterization.